Aptamers and Peptides:
Finding and Guiding CAR T Cells for Better Cancer Care

Ian Israel Cardle

A dissertation

submitted in partial fulfillment of the

requirements for the degree of

Doctor of Philosophy

University of Washington

2022

Reading Committee:

Suzie H. Pun, Chair

Michael C. Jensen, Chair

Hao Yuan Kueh

Jonathan T. C. Liu

Program Authorized to Offer Degree:

Bioengineering

University of Washington

Abstract

Aptamers and Peptides:
Finding and Guiding CAR T Cells for Better Cancer Care

Ian Israel Cardle

Chairs of the Supervisory Committee:

Suzie H. Pun

Michael C. Jensen

Department of Bioengineering

Chimeric antigen receptor (CAR) T-cell therapy has prompted a new age of cancer treatments, in which a patient's T cells are genetically programmed with a cancer-targeting receptor *ex vivo* and reinfused for immune-mediated clearance of the tumor. However, despite some success in treating $CD19^+$ B-cell malignancies in pediatric and adult patients, commercial CAR T-cell therapies currently suffer from an expensive manufacturing process that limits access to care and an inflexible design that cannot prevent treatment-associated side-effects and cancer relapse from antigen escape. Accordingly, new strategies for making more cost-effective, safe, and versatile CAR T-cell therapies are urgently needed to broaden and increase their therapeutic impact on the cancer community. Synthetic DNA aptamer and peptide targeting ligands are uniquely positioned to address these issues, owing to their specificity, low cost, small size, and ease of modification

for a variety of applications (**Chapter 1**). To this end, we developed aptamer selection reagents that inexpensively isolate label-free $CD8^+$ T cells (**Chapter 2**) and efficiently deplete $TfR1^+$ cancer cells (**Chapter 3**) for CAR T-cell manufacturing. We also generated aptamer and peptide targeting reagents that selectively bind integrins expressed on liquid and sold tumors (**Chapter 4** and **Chapter 5**, respectively) and integrated them into heterobifunctional intermediates that direct the anti-cancer activity of a novel universal CAR T-cell platform via covalent SpyCatcher003-SpyTag003 chemistry (**Chapter 6**). At the end of each chapter, we discuss limitations and future directions of this work.

Table of Contents

List of Figures

List of Tables

Acknowledgements

My journey through graduate school would not have been possible without an amazing support network of advisors, mentors, colleagues, friends, and family. A Ph.D. is a roller coaster of successes and failures, sleepless nights, good and bad coffee, and occasional motivational struggle, so having a group of people to pull me up when I was down or push me to a greater standard when I was high has been invaluable for getting through this process. You all have continuously reaffirmed my passion for science and research, and I am incredibly thankful.

To my advisors, **Suzie Pun** and **Michael Jensen**. Suzie, your astounding work ethic inspires me to this very day, and I just hope that I can emulate half of it in my future career endeavors. You have built a remarkable research lab that fosters critical thinking and creative liberty, and I feel very fortunate that I was able to be a part of it. I have grown considerably as a scientist and independent thinker under your wing, and I can't wait to spread my own and fly to greater heights. Dr. J, your passion for immunotherapy never ceases to impress me, and I've learned greatly from your outside-the-box thinking and attention to detail. Despite overseeing so many projects, you effortlessly ask all the right questions and come up with the most amazing ideas, and I hope some of your ideation rubs off on me. To both of you, thank you for allowing me to engage in interdisciplinary research that challenged and nurtured me.

To my pseudo third advisor, mentor, and fellow caffeine addict, **Drew Sellers**. I will miss our daily walks to get coffee, our productive science conversations, and our occasional not so productive venting over things happening in the lab. You work harder and more efficiently than anyone I know, and I have had the fortune to learn from your incredible wealth of knowledge and lab skills. We kickstarted a project together back in Fall 2018, and while it has entailed more work and time

than what we would have ever expected, it has been gratifying to see how far we have come. I'm excited for what the future has in store.

To my reading and supervisory committee, **Suzie Pun**, **Michael Jensen**, **Hao Yuan Kueh**, and **Jonathan T. C. Liu**. Thank you for taking time out of your busy schedules to provide guidance throughout my Ph.D. adventure. It is easy to get tunnel vision when delving deep into a research project, so your rigorous questions and high-level input were greatly appreciated.

To my Pun Lab and aptamer mentor, **Nataly Kacherovsky**. Your dry humor and choleric personality always bring a smile to my face, and you have a magical touch when it comes to aptamer discovery and receptor identification. I greatly admire (and occasionally disprove) your unwavering approach to research and will miss our friendly banter. Thank you for introducing me to the world of aptamers, and I look forward to more mushroom hunting, cross-country skiing, and oysters together in the future!

To my former Jensen Lab mentor, **James Matthaei**. Your positive and funny attitude always made even the longest days in lab enjoyable, and you supported my professional development in more than one way. Thank you for showing me how to do everything from cloning to manufacturing CAR T cells and for taking me on morning swims. I will always fondly look back at our late nights working together in the lab and gorging ourselves with Red Bull.

To past senior Pun Lab members, including **Chayanon Ngambenjawong**, **Bob Lamm**, **Gary Liu**, **Brynn Olden**, **David Peeler**, **Daniel Lee**, and **Albert Yen**. You were all pillars that held up the lab when I joined, and embodied the hard work, perseverance, and cordiality that inspired future generations of Punions. Thank you for making the lab such a fun and supportive place to work.

To past and current senior Jensen Lab members, including **Adam Johnson**, **Michael Baldwin**, **Jason Yokoyama**, **Joshua Gustafson**, **Kamila Gwiazda**, **Ashley Wilson**, **Jacob Appelbaum**, **James Rosser**, **Jia Wei**, **Emi Tokuda**, **Tracy Ooi**, **Karen Spratt**, **Joseph Cheng**, **Giacomo Tampella**, and **Leanne Rubin**. Thank you for your advice, support, expertise, and humor over the years. You all made me feel welcome in the Jensen Lab and gave me the tools I needed to succeed.

To my Pun Lab cohort, **Emmeline Cheng**, **Alex Prossnitz**, and **Meilyn Sylvestre**. Graduate school is not easy, so being able to commiserate with you all when an experiment failed and to celebrate with you all when there was a success in the lab meant the world to me. You all are such wonderful and smart people, and I greatly value the friendships we formed over the years. As the last one to graduate from our cohort, I am sad that our era in the lab is ending, but I take comfort in the long-lasting impact that we have left on the lab.

To Jensen Lab graduate students, **Chris Saxby**, **Clinton Heinze**, **Ian Blumenthal**, and **Benjamin Curtis**. I recently found myself in awe of each of your research presentations at the weekly Immunotherapy Program Science Meetings. You all have pioneered such an impressive body of work that I have no doubt will change how we treat cancer with CAR T-cell therapy. I will miss our adrenaline-pumping Spikeball games together, and I look forward to seeing your future accomplishments.

To past and current junior Pun Lab members, **Audrey Olshefsky**, **Clinton Heinze**, **Trey Pichon**, **Lucy Yang**, **Melissa Ling**, **Ben Nguyen**, and **Kefan Song**. I have had the joy of working alongside you all for the past few years. You all are so fun, cheerful, and exceptionally talented, and I know I'm leaving the Pun Lab in good hands. Don't stop excelling at what you do and foster the next generation of Punions that will lead the lab to greater heights.

To my past and current undergraduate mentees, **Jai Raman** and **Dylan Scherer**. Both of you helped me become a better mentor and teacher, and it was gratifying to watch each of you grow as young scientists. Thank you for your patience, willingness to take risks, passion, and contributions to these projects. I can't wait to see what you do in your future careers.

To my Seattle friends, **Alfredo Quijano-Rubio**, **Camilla Bortolami**, **Daniel De Córdoba Gil**, **Mitchell Kirby**, **Jamie Hernandez**, **Sara Keller**, and **Ian Hull**. Sharing our love for food, beer, the outdoors, and telling stories made the graduate school experience all the much better. Thank you for getting me out of the lab to enjoy life and all the great things the PNW has to offer. I will cherish our time spent together and laugh over the silly things we've done.

To my East Coast family, **Scott Shirken**, **Susan Shirken**, **Adam Gelles**, and **Angela Gelles**. Thank you for showing interest in what I do and for your love and support. I may not have found "the cure," but I will make it my life's mission to continue pursuing research and scientific breakthroughs that will have an impact on people's lives.

To my West Coast family, **Sharon Whaley**, **Max Whaley**, **Conner Whaley**, **Austin Whaley**, **Brett Whaley**, **Spencer Whaley**, **Barbara Israel**, **Christine Joshel**, **David Joshel**, **Julia Worthen**, **Adam Ramirez**, and the **Worthen/Gilbride family**. Thank you for believing in me and showering me with love and encouragement. You all mean so much to me, and I'm so glad that many of you were able to visit Seattle and understand my affection for this place.

To my parents, **Beryl Israel** and **Robert Cardle**, and their respective partners, **Ken Worthen** and **Catherine Church**. You all have been my biggest cheerleaders through this process. Thank you for supporting my passion and education and for not once doubting that I could succeed. Our talks

over the phone always lifted my spirits, and I promise to call more in the future. I owe this Ph.D. to all of you.

Lastly, to my partner, **Emmeline Cheng**. Finding you was undoubtedly the best part of graduate school. You are one of the most sweet, kind, and hardworking people that I know, and you always find a way to make me smile. You have always had my back and knowing that continually motivates me to be better. I could not imagine getting through this process without you. While this chapter of our lives is ending, a new one is beginning, and I can't wait to explore that with you.

Dedication

To my grandparents, Robert Israel, James Cardle, and Peggy Cardle; to my great-uncles, Maurice Shirken and David Gelles; and to my great-aunts, Arlene Shirken and Judith Gelles:

gone but never forgotten.

Chapter 1: Synthetic Targeting Ligands for Tackling Barriers in CAR T-Cell Therapy

ABSTRACT

Chimeric antigen receptor (CAR) T-cell therapy has transformed the cancer treatment landscape, utilizing *ex vivo* modified autologous T cells to treat relapsed or refractory B-cell leukemias and lymphomas. However, the therapy's broader impact has been limited, in part, by its expensive production process, severe side effects, and its narrow single-target design. Therefore, as CAR T-cell therapies are further advanced to treat other cancers, continual innovation in cell manufacturing and CAR architecture will be critical to their successful clinical implementation. Synthetic DNA aptamers and peptides, either as reversible cell isolation reagents or cancer-targeting intermediates, can solve CAR T-cell manufacturing and therapy needs. This work integrates DNA aptamers and peptides into the production and application of CAR T cells, paving the way for more economical, safe, and effective cancer care with adoptive T-cell immunotherapy.

[1]Parts of this chapter are adapted from: Cardle, I.I., Cheng, E.L. *et al*. Biomaterials in Chimeric Antigen Receptor T-Cell Process Development. *Acc. Chem. Res.* **53**, 1724-1738 (2020). Copyright 2020 American Chemical Society. http://pubs.acs.org/articlesonrequest/AOR-IZPQ38T5WAJTYSETXIXA

1.1 BACKGROUND

1.1.1 CAR T-cell therapy

Adoptive cell therapy (ACT), also known as cellular immunotherapy, has greatly diversified the toolkit for treating certain cancers, offering a smart, patient-tailored therapeutic option in contrast to traditional "one-size-fits-all" chemotherapy. In ACT, immune cells are isolated from the patient, activated *ex vivo*, genetically engineered to express a cancer-targeting receptor, expanded to therapeutically relevant numbers, and administered back into the patient for immune-mediated clearance of the cancer. Chimeric antigen receptor (CAR) T-cell therapy is the most successful example of ACT to date, in which autologous T cells are programed with a CAR that redirects their immune responses in a non-major histocompatibility complex (MHC)-restricted manner.[1,2] The CAR usually consists of: (1) an extracellular antibody-derived antigen binding domain that provides cancer specificity and (2) a linked intracellular signaling domain, comprised of stimulatory CD3ζ and costimulatory CD28 and/or 4-1BB subdomains, that induces cytotoxic and helper T-cell function upon cancer cell recognition. As of October 2022, there are six FDA-approved CAR T-cell therapies (Novartis's Kymriah, Gilead's Yescarta and Tecartus, Bristol Myers Squibb's Breyanzi and Abecma, and Johnson & Johnson's Carvykti) for treating $CD19^+$ or $BCMA^+$ relapsed or refractory B-cell leukemia/lymphoma and multiple myeloma with >50% objective response rates,[3–5] and many others are in the clinical trial pipeline.[6] Furthermore, two of these therapies (Yescarta and Breyanzi) recently received FDA clearance for use as second-line treatments, broadening patient eligibility for these life-saving interventions.[7,8]

1.2 MOTIVATION

1.2.1 Expensive and inefficient cell manufacturing process

Despite the promise of CAR T-cell therapy, the manufacturing of cellular therapeutics is complex and costly compared to small molecule- and protein-based counterparts (**Figure 1.1**). This is underscored by the fact that while the critical quality attributes that ensure therapeutic safety and efficacy of a CAR T-cell product are well known —that is, viable and not terminally differentiated $CD3^+CAR^+$ cells (identify), balanced CD4/CD8 ratio (purity), and *in vitro* cytotoxicity and cytokine release against cells expressing the target antigen (potency)—current manufacturing challenges prevent reliable production of CAR T cells with these attributes at an acceptable cost.[9] As an example, the approximate price per dose for Kymriah and Yescarta are $475,000 and $373,000, respectively,[10] with estimated manufacturing materials costs being $20,000-40,000 per production.[11–13] The respective median manufacturing turnaround times are also 22 and 17 days, with some products requiring 4 weeks to obtain sufficient cell numbers.[14–16] Importantly, manufacturing of cell products that inconsistently meet their critical quality attributes prohibits predictable linking of other product properties to patient outcomes. Streamlining the manufacturing of engineered T-cell products will thus be imperative to their successful and widespread clinical translation.

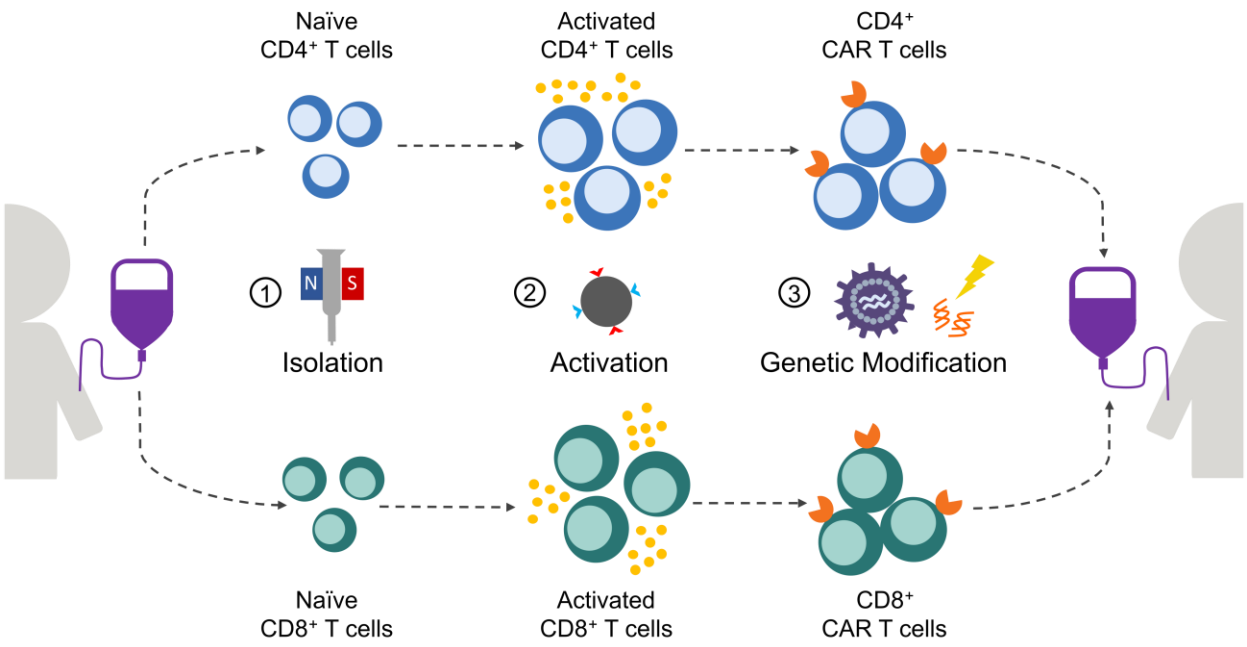

Figure 1.1 | CAR T-cell manufacturing steps. Schematic includes separate $CD4^+$ and $CD8^+$ CAR T-cell production for therapies that use balanced CD4/CD8 compositions. Reproduced from Cardle et al.[17]

1.2.2 Treatment-associated toxicities and antigen escape

In addition to manufacturing issues, the therapeutic application of CAR T cells is fraught with challenges. CAR T cells are living, responsive drugs that are capable of persisting in patients for more than 10 years,[18,19] meaning they do not follow the predictable pharmacokinetics and pharmacodynamics of conventional drugs. Especially with the rigid design of current commercial CAR T-cell products, physicians have little control of the cells following their infusion. As a result, systemic, high-level immune activation, known as cytokine release syndrome (CRS), often occurs in patients, which can be potentially fatal.[20–22] Less understood neurological toxicities also occur,[22,23] and in some cases, CAR T cells can destroy non-malignant tissue due to target antigen expression not being restricted to tumor cells, resulting in dangerous on-target, off-tumor toxicity.[24,25] Antigen escape, either due to pre-existing tumor heterogeneity or cancer cell

plasticity, is another obstacle for commercial therapies that target just CD19. Approximately 14% of patients that respond to CAR T-cell therapy across different institutions relapse with $CD19^-$ disease,[26] often due to mutation of the CD19 protein that leads to truncation and loss of surface antigen.[27] Single antigen targeting is even more problematic for solid tumors, which are much more antigenically complex than B-cell malignancies,[28,29] resulting in adaptive resistance to therapy due to loss or decreased expression of the target antigen.[30,31] For these reasons, greater control of CAR T-cell activity and targeting after infusion is needed for safer and more comprehensive treatment.

1.3 OPPORTUNITIES

1.3.1 Cost-effective and traceless T-cell isolations reagents

CAR T-cell therapies are beginning to use defined product compositions for treatment, such as balanced ratios of $CD4^+$ and $CD8^+$ T cells, since this contributes to low patient-to-patient variability in CAR T-cell dose, *in vitro* cytokine production, and health.[32] Not only does this strategy allow clinicians to better associate certain product qualities with patient outcomes, but it also has led to remarkably high rates of cancer remission in the clinic.[33] However, this approach also compounds the cost of T-cell isolation, requiring sequential isolation of $CD4^+$ and $CD8^+$ T cells so that they can be separately manufactured into CAR T cells for later infusion into the patient at a 1:1 ratio (**Figure 1.1**). Even for CAR T-cell therapies that are not administered at defined T-cell compositions, circulating malignant cells must be adequately removed prior to cell manufacturing to prevent rare transduction of these cells that can mediate cancer resistance to treatment and disease relapse.[34] Antibody-coated magnetic beads are commonly used for clinical-scale cell sorting, and the estimated cost of these materials for just a single separation is ~$5000

(source: Miltenyi), amounting to 10-15% of the overall materials expenses required for CAR T-cell production.[13] Additionally, antibody-coated magnetic beads are retained on the cell surface, raising safety concerns and preventing downstream cell isolation. Given the high cost of using biologically produced antibodies for cell separation and their inflexible binding, the development of inexpensive and traceless cell capture ligands could greatly benefit CAR T-cell manufacturing.

1.3.2 Small, synthetic cancer targeting adaptors for use with universal CARs

Combinatorial antigen targeting presents a new path for making safer, broader-targeting CAR T-cell therapies. A relatively simple multi-targeting approach that has been championed by the research community is to use universal CAR receptors that rely on bifunctional adaptor ligands for cancer targeting (**Figure 1.2**).[35] In this system, a single CAR recognizes a shared tag on a panel of distinct targeting intermediates, which in turn direct CAR T-cell responses against multiple tumor-associated antigens (TAAs). Not only does this mitigate antigen escape,[36] but it also allows quantitative and temporal control of CAR T-cell responses based on the amount and frequency at which the intermediate ligands are dosed.[37] As the intermediates control antigen presentation to the CAR T cells, CRS symptoms and on-target, off-tumor toxicity can be easily managed and rapidly reversed depending on the pharmacokinetics of the intermediate ligand.[38] Unfortunately, the majority of universal CAR systems to-date use large antibody intermediates,[39–41] which have long circulation half-lives that prevent swift manipulation of their concentrations *in vivo*. Furthermore, the use of tagged antibody intermediates significantly increases the costs of already expensive CAR T-cell therapy. Using small, synthetic targeting intermediates, however, would allow for highly cost-effective treatment with universal CAR T cells that is both safe and powerful.

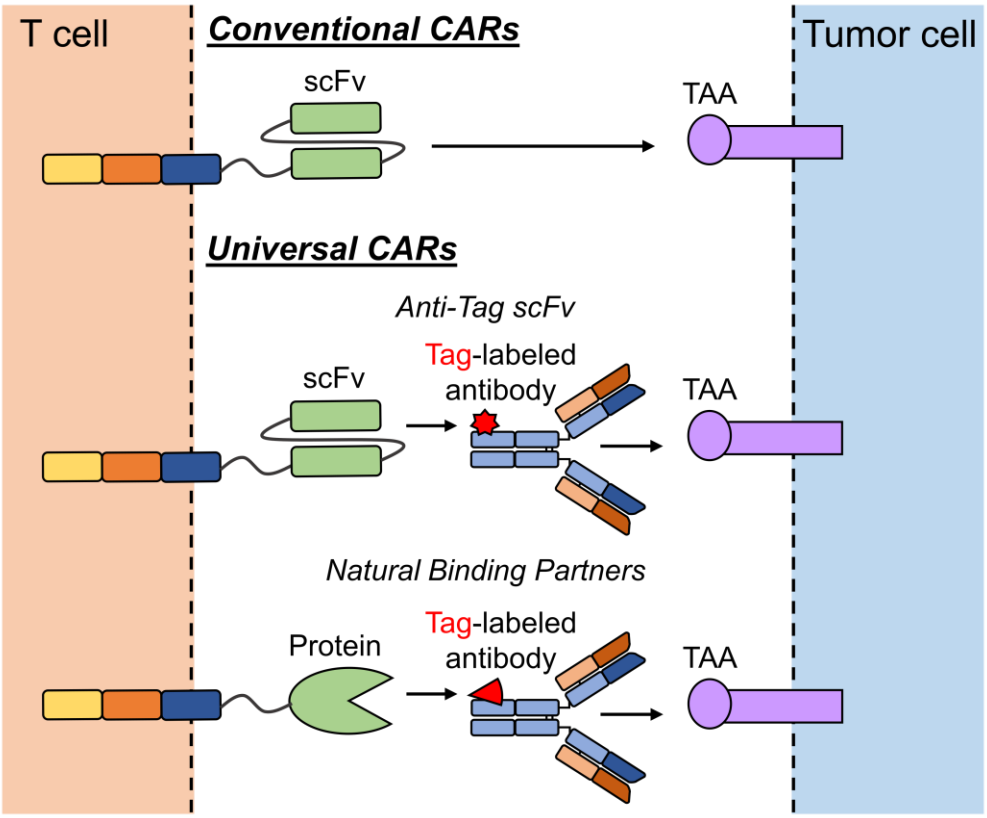

Figure 1.2 | Universal CARs that use bifunctional adaptor intermediates for cancer targeting. Unlike conventional CARs that directly bind the tumor-associated antigen (TAA), the universal CAR recognizes a tag moiety on the targeting intermediate, which in turn redirects the CAR T-cell responses against a tumor-associated antigen (TAA). This can be achieved through an anti-tag scFv that binds to a specific tag, such as fluorescein or a peptide, or using natural binding partners, such as avidin and biotin or leucine zippers.

1.3.3 Universal CAR platform with covalent tag recognition

Another pitfall of current universal CAR systems if that they must bridge together two noncovalent interactions to elicit T-cell responses, unlike conventional CARs that require only a single noncovalent interaction. The use of two noncovalent interactions that each have the propensity to dissociate may reduce the strength and duration of the immune synapse, especially at low intermediate concentrations where the avidity between CAR T cells and tumor cells is small. This poor synapse formation can in turn impair CAR T-cell effector function, leading to suboptimal treatment efficacy. Accordingly, development of a universal CAR approach that utilizes covalent

recognition of tag-labeled targeting intermediates would allow for more stable bridging of CAR T cells with cancer cells, better resembling immune synapses seen with conventional CARs.

1.4 INNOVATION

1.4.1 DNA aptamers for reversible T-cell capture and efficient cancer cell depletion at low cost

Nucleic acid aptamers—single-stranded oligonucleotides with sequence-driven folding structures capable of binding proteins of interest—can address several drawbacks of using antibodies for clinical cell separation (**Figure 1.3**). Aptamers are chemically produced, enabling more affordable production, lower batch-to-batch variability, improved control over conjugation to substrates, and higher shelf-life compared to antibody counterparts.[42] Aptamers also bind antigen targets with specificities and affinities comparable to antibodies. Importantly, they can further be modified to include unique toeholds and stems for complementary oligonucleotide displacement,[43,44] in which an aptamer-specific sequence anneals to the aptamer, thereby disrupting its structure and reversing binding. Along these lines, part of this work seeks to develop DNA aptamers for both reversible isolation of T cells (Chapter 2) and efficient depletion of cancers cells (Chapter 3) for cost-effective and safe CAR T-cell manufacturing. The findings from these goals are published in *Nature Biomedical Engineering* and the *Journal of the American Chemical Society*, respectively.

1.4.2 Small aptamer and peptide intermediates for covalently guiding universal CAR T cells

Given their chemical synthesis, peptides share many of the same cost advantages as aptamers over antibodies (**Figure 1.3**). From a targeting perspective, aptamers and peptides are also small, giving them higher tumor penetration and shorter circulation half-lives than antibodies.[45,46] This is an attractive quality for directing universal CAR T cells against cancers, as *in vivo* concentrations of aptamers and peptides can be readily manipulated by their fast clearance rates for safer treatment.

Additionally, cancer-target aptamers and peptides can be easily modified with synthetic peptide tags that spontaneously undergo isopeptide bond formation with genetically encodable proteins,[47,48] permitting covalent tag recognition with universal CARs. Hence, this work also seeks to develop synthetic, cancer-targeting aptamer (Chapter 4) and peptide (Chapter 5) intermediates that interface covalently with a novel universal CAR platform for directing T cell function (Chapters 6). The findings from Chapter 5 are published in the *Journal of Biological Chemistry*. whereas the research in Chapters 4 and 6 is ongoing and has yet to be published at the time of this writing.

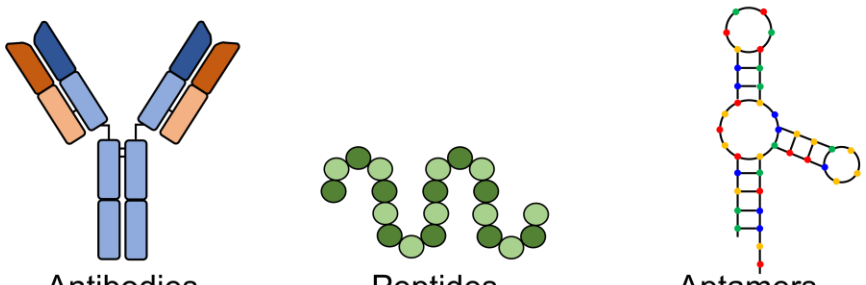

	Antibodies	Peptides	Aptamers
Synthesis	Biological	Chemical	Chemical
Modification	Random	Controlled	Controlled
Batch-to-Batch Variability	High	Low	Low
Affinity	pM-nM	nM-μM	pM-nM
Size	50-150 kDa	1-5 kDa	10-30 kDa
Shelf Life	Limited	Long (dry)	Long (dry/frozen)

Figure 1.3 | Advantages of peptide and aptamer ligands over antibodies.

1.5 REFERENCES

(1) Kuwana, Y.; Asakura, Y.; Utsunomiya, N.; Nakanishi, M.; Arata, Y.; Itoh, S.; Nagase, F.; Kurosawa, Y. Expression of Chimeric Receptor Composed of Immunoglobulin-Derived V

Resions and T-Cell Receptor-Derived C Regions. *Biochemical and Biophysical Research Communications* **1987**, *149* (3), 960–968.

(2) Gross, G.; Waks, T.; Eshhar, Z. Expression of Immunoglobulin-T-Cell Receptor Chimeric Molecules as Functional Receptors with Antibody-Type Specificity. *Proceedings of the National Academy of Sciences of the United States of America* **1989**, *86* (24), 10024–10028.

(3) Sengsayadeth, S.; Savani, B. N.; Oluwole, O.; Dholaria, B. Overview of Approved CAR-T Therapies, Ongoing Clinical Trials, and Its Impact on Clinical Practice. *eJHaem* **2022**, *3* (S1), 6–10.

(4) Sheikh, S.; Migliorini, D.; Lang, N. CAR T-Based Therapies in Lymphoma: A Review of Current Practice and Perspectives. *Biomedicines* **2022**, *10* (8), 1960.

(5) Berdeja, J. G.; Madduri, D.; Usmani, S. Z.; Jakubowiak, A.; Agha, M.; Cohen, A. D.; Stewart, A. K.; Hari, P.; Htut, M.; Lesokhin, A.; Deol, A.; Munshi, N. C.; O'Donnell, E.; Avigan, D.; Singh, I.; Zudaire, E.; Yeh, T.-M.; Allred, A. J.; Olyslager, Y.; Banerjee, A.; Jackson, C. C.; Goldberg, J. D.; Schecter, J. M.; Deraedt, W.; Zhuang, S. H.; Infante, J.; Geng, D.; Wu, X.; Carrasco-Alfonso, M. J.; Akram, M.; Hossain, F.; Rizvi, S.; Fan, F.; Lin, Y.; Martin, T.; Jagannath, S. Ciltacabtagene Autoleucel, a B-Cell Maturation Antigen-Directed Chimeric Antigen Receptor T-Cell Therapy in Patients with Relapsed or Refractory Multiple Myeloma (CARTITUDE-1): A Phase 1b/2 Open-Label Study. *The Lancet* **2021**, *398* (10297), 314–324.

(6) Upadhaya, S.; Yu, J. X.; Shah, M.; Correa, D.; Partridge, T.; Campbell, J. The Clinical Pipeline for Cancer Cell Therapies. *Nature Reviews Drug Discovery* **2021**, *20* (7), 503–504.

(7) Locke, F. L.; Miklos, D. B.; Jacobson, C. A.; Perales, M.-A.; Kersten, M.-J.; Oluwole, O. O.; Ghobadi, A.; Rapoport, A. P.; McGuirk, J.; Pagel, J. M.; Muñoz, J.; Farooq, U.; van Meerten, T.; Reagan, P. M.; Sureda, A.; Flinn, I. W.; Vandenberghe, P.; Song, K. W.; Dickinson, M.; Minnema, M. C.; Riedell, P. A.; Leslie, L. A.; Chaganti, S.; Yang, Y.; Filosto, S.; Shah, J.; Schupp, M.; To, C.; Cheng, P.; Gordon, L. I.; Westin, J. R. Axicabtagene Ciloleucel as Second-Line Therapy for Large B-Cell Lymphoma. *New England Journal of Medicine* **2021**, *386* (7), 640–654.

(8) Kamdar, M.; Solomon, S. R.; Arnason, J.; Johnston, P. B.; Glass, B.; Bachanova, V.; Ibrahimi, S.; Mielke, S.; Mutsaers, P.; Hernandez-Ilizaliturri, F.; Izutsu, K.; Morschhauser, F.; Lunning, M.; Maloney, D. G.; Crotta, A.; Montheard, S.; Previtali, A.; Stepan, L.; Ogasawara, K.; Mack, T.; Abramson, J. S. Lisocabtagene Maraleucel versus Standard of Care with Salvage Chemotherapy Followed by Autologous Stem Cell Transplantation as Second-Line Treatment in Patients with Relapsed or Refractory Large B-Cell Lymphoma (TRANSFORM): Results from an Interim Analysis of an Open-Label, Randomised, Phase 3 Trial. *The Lancet* **2022**, *399* (10343), 2294–2308.

(9) Lipsitz, Y. Y.; Timmins, N. E.; Zandstra, P. W. Quality Cell Therapy Manufacturing by Design. *Nature Biotechnology* **2016**, *34* (4), 393–400.

(10) Yip, A.; Webster, R. M. The Market for Chimeric Antigen Receptor T Cell Therapies. *Nature Reviews Drug Discovery* **2018**, *17* (3), 161–162.

(11) Zhu, F.; Shah, N.; Xu, H.; Schneider, D.; Orentas, R.; Dropulic, B.; Hari, P.; Keever-Taylor, C. A. Closed-System Manufacturing of CD19 and Dual-Targeted CD20/19 Chimeric Antigen Receptor T Cells Using the CliniMACS Prodigy Device at an Academic Medical Center. *Cytotherapy* **2018**, *20* (3), 394–406.

(12) Spink, K.; Steinsapir, A. The Long Road to Affordability: A Cost of Goods Analysis for an Autologous CAR-T Process. *Cell and Gene Therapy Insights* **2018**, *4* (11), 1105–1116.

(13) Ran, T.; Eichmüller, S. B.; Schmidt, P.; Schlander, M. Cost of Decentralized CAR T-Cell Production in an Academic Nonprofit Setting. *International Journal of Cancer* **2020**, *147* (12), 3438–3445.
(14) Tyagarajan, S.; Spencer, T.; Smith, J. Optimizing CAR-T Cell Manufacturing Processes during Pivotal Clinical Trials. *Molecular Therapy - Methods & Clinical Development* **2020**, *16*, 136–144.
(15) Neelapu, S. S.; Locke, F. L.; Bartlett, N. L.; Lekakis, L. J.; Miklos, D. B.; Jacobson, C. A.; Braunschweig, I.; Oluwole, O. O.; Siddiqi, T.; Lin, Y.; Timmerman, J. M.; Stiff, P. J.; Friedberg, J. W.; Flinn, I. W.; Goy, A.; Hill, B. T.; Smith, M. R.; Deol, A.; Farooq, U.; McSweeney, P.; Munoz, J.; Avivi, I.; Castro, J. E.; Westin, J. R.; Chavez, J. C.; Ghobadi, A.; Komanduri, K. V; Levy, R.; Jacobsen, E. D.; Witzig, T. E.; Reagan, P.; Bot, A.; Rossi, J.; Navale, L.; Jiang, Y.; Aycock, J.; Elias, M.; Chang, D.; Wiezorek, J.; Go, W. Y. Axicabtagene Ciloleucel CAR T-Cell Therapy in Refractory Large B-Cell Lymphoma. *New England Journal of Medicine* **2017**, *377* (26), 2531–2544.
(16) Perica, K.; Curran, K. J.; Brentjens, R. J.; Giralt, S. A. Building a CAR Garage: Preparing for the Delivery of Commercial CAR T Cell Products at Memorial Sloan Kettering Cancer Center. *Biology of Blood and Marrow Transplantation* **2018**, *24* (6), 1135–1141.
(17) Cardle, I. I.; Cheng, E. L.; Jensen, M. C.; Pun, S. H. Biomaterials in Chimeric Antigen Receptor T-Cell Process Development. *Accounts of Chemical Research* **2020**, *53* (9), 1724–1738.
(18) Scholler, J.; Brady, T. L.; Binder-Scholl, G.; Hwang, W.-T.; Plesa, G.; Hege, K. M.; Vogel, A. N.; Kalos, M.; Riley, J. L.; Deeks, S. G.; Mitsuyasu, R. T.; Bernstein, W. B.; Aronson, N. E.; Levine, B. L.; Bushman, F. D.; June, C. H. Decade-Long Safety and Function of Retroviral-Modified Chimeric Antigen Receptor T Cells. *Science Translational Medicine* **2012**, *4* (132), 132ra53.
(19) Melenhorst, J. J.; Chen, G. M.; Wang, M.; Porter, D. L.; Chen, C.; Collins, M. A.; Gao, P.; Bandyopadhyay, S.; Sun, H.; Zhao, Z.; Lundh, S.; Pruteanu-Malinici, I.; Nobles, C. L.; Maji, S.; Frey, N. v; Gill, S. I.; Tian, L.; Kulikovskaya, I.; Gupta, M.; Ambrose, D. E.; Davis, M. M.; Fraietta, J. A.; Brogdon, J. L.; Young, R. M.; Chew, A.; Levine, B. L.; Siegel, D. L.; Alanio, C.; Wherry, E. J.; Bushman, F. D.; Lacey, S. F.; Tan, K.; June, C. H. Decade-Long Leukaemia Remissions with Persistence of CD4+ CAR T Cells. *Nature* **2022**, *602* (7897), 503–509.
(20) Bonifant, C. L.; Jackson, H. J.; Brentjens, R. J.; Curran, K. J. Toxicity and Management in CAR T-Cell Therapy. *Molecular Therapy - Oncolytics* **2016**, *3*, 16011.
(21) Li, D.; Que, Y.; Ding, S.; Hu, G.; Wang, W.; Mao, X.; Wang, Y.; Li, C.; Huang, L.; Zhou, J.; Zhang, W.; Xiao, M. Anti-BCMA CAR-T Cells Therapy for a Patient with Extremely High Membrane BCMA Expression: A Case Report. *Journal for ImmunoTherapy of Cancer* **2022**, *10* (9), e005403.
(22) Sheth, V. S.; Gauthier, J. Taming the Beast: CRS and ICANS after CAR T-Cell Therapy for ALL. *Bone Marrow Transplantation* **2021**, *56* (3), 552–566.
(23) Neill, L.; Rees, J.; Roddie, C. Neurotoxicity—CAR T-Cell Therapy: What the Neurologist Needs to Know. *Practical Neurology* **2020**, *20* (4), 285–293.
(24) Morgan, R. A.; Yang, J. C.; Kitano, M.; Dudley, M. E.; Laurencot, C. M.; Rosenberg, S. A. Case Report of a Serious Adverse Event Following the Administration of T Cells Transduced With a Chimeric Antigen Receptor Recognizing ERBB2. *Molecular Therapy* **2010**, *18* (4), 843–851.

(25) Parkhurst, M. R.; Yang, J. C.; Langan, R. C.; Dudley, M. E.; Nathan, D.-A. N.; Feldman, S. A.; Davis, J. L.; Morgan, R. A.; Merino, M. J.; Sherry, R. M.; Hughes, M. S.; Kammula, U. S.; Phan, G. Q.; Lim, R. M.; Wank, S. A.; Restifo, N. P.; Robbins, P. F.; Laurencot, C. M.; Rosenberg, S. A. T Cells Targeting Carcinoembryonic Antigen Can Mediate Regression of Metastatic Colorectal Cancer but Induce Severe Transient Colitis. *Molecular Therapy* **2011**, *19* (3), 620–626.

(26) Wang, Z.; Wu, Z.; Liu, Y.; Han, W. New Development in CAR-T Cell Therapy. *Journal of Hematology & Oncology* **2017**, *10*, 53.

(27) Orlando, E. J.; Han, X.; Tribouley, C.; Wood, P. A.; Leary, R. J.; Riester, M.; Levine, J. E.; Qayed, M.; Grupp, S. A.; Boyer, M.; De Moerloose, B.; Nemecek, E. R.; Bittencourt, H.; Hiramatsu, H.; Buechner, J.; Davies, S. M.; Verneris, M. R.; Nguyen, K.; Brogdon, J. L.; Bitter, H.; Morrissey, M.; Pierog, P.; Pantano, S.; Engelman, J. A.; Winckler, W. Genetic Mechanisms of Target Antigen Loss in CAR19 Therapy of Acute Lymphoblastic Leukemia. *Nature Medicine* **2018**, *24* (10), 1504–1506.

(28) Hegde, M.; Corder, A.; Chow, K. K.; Mukherjee, M.; Ashoori, A.; Kew, Y.; Zhang, Y. J.; Baskin, D. S.; Merchant, F. A.; Brawley, V. S.; Byrd, T. T.; Krebs, S.; Wu, M. F.; Liu, H.; Heslop, H. E.; Gottachalk, S.; Yvon, E.; Ahmed, N. Combinational Targeting Offsets Antigen Escape and Enhances Effector Functions of Adoptively Transferred T Cells in Glioblastoma. *Molecular Therapy* **2013**, *21* (11), 2087–2101.

(29) Bielamowicz, K.; Fousek, K.; Byrd, T. T.; Samaha, H.; Mukherjee, M.; Aware, N.; Wu, M. F.; Orange, J. S.; Sumazin, P.; Man, T. K.; Joseph, S. K.; Hegde, M.; Ahmed, N. Trivalent CAR T Cells Overcome Interpatient Antigenic Variability in Glioblastoma. *Neuro-Oncology* **2018**, *20* (4), 506–518.

(30) Brown, C. E.; Ph, D.; Alizadeh, D.; Ph, D.; Starr, R.; Ostberg, J. R.; Ph, D.; Blanchard, M. S.; Ph, D.; Kilpatrick, J.; Simpson, J.; Kurien, A.; Priceman, S. J.; Ph, D.; Wang, X.; Ph, D.; Harshbarger, T. L.; Apuzzo, M. D.; Ressler, J. A.; Jensen, M. C.; Barish, M. E.; Ph, D.; Chen, M.; Ph, D.; Portnow, J.; Forman, S. J.; Badie, B. Regression of Glioblastoma after Chimeric Antigen Receptor T-Cell Therapy. *The New England Journal of Medicine* **2016**, 2561–2569.

(31) O'Rourke, D. M.; Nasrallah, M. P.; Desai, A.; Melenhorst, J. J.; Mansfield, K.; Morrissette, J. J. D.; Martinez-Lage, M.; Brem, S.; Maloney, E.; Shen, A.; Isaacs, R.; Mohan, S.; Plesa, G.; Lacey, S. F.; Navenot, J. M.; Zheng, Z.; Levine, B. L.; Okada, H.; June, C. H.; Brogdon, J. L.; Maus, M. V. A Single Dose of Peripherally Infused EGFRvIII-Directed CAR T Cells Mediates Antigen Loss and Induces Adaptive Resistance in Patients with Recurrent Glioblastoma. *Science Translational Medicine* **2017**, *9* (399), eaaa0984.

(32) Ramsborg, C. G.; Guptill, P.; Weber, C.; Christin, B.; Larson, R. P.; Lewis, K.; Mallaney, M.; Bowen, M.; Higham, E.; Albertson, T. JCAR017 Is a Defined Composition CAR T Cell Product with Product and Process Controls That Deliver Precise Doses of CD4 and CD8 CAR T Cell to Patients with NHL. *Blood* **2017**, *130* (Supplement 1), 4471.

(33) Turtle, C. J.; Hanafi, L.-A.; Berger, C.; Gooley, T. A.; Cherian, S.; Hudecek, M.; Sommermeyer, D.; Melville, K.; Pender, B.; Budiarto, T. M.; Robinson, E.; Steevens, N. N.; Chaney, C.; Soma, L.; Chen, X.; Yeung, C.; Wood, B.; Li, D.; Cao, J.; Heimfeld, S.; Jensen, M. C.; Riddell, S. R.; Maloney, D. G. CD19 CAR–T Cells of Defined CD4+:CD8+ Composition in Adult B Cell ALL Patients. *The Journal of Clinical Investigation* **2016**, *126* (6), 2123–2138.

(34) Ruella, M.; Xu, J.; Barrett, D. M.; Fraietta, J. A.; Reich, T. J.; Ambrose, D. E.; Klichinsky, M.; Shestova, O.; Patel, P. R.; Kulikovskaya, I.; Nazimuddin, F.; Bhoj, V. G.; Orlando, E. J.; Fry, T. J.; Bitter, H.; Maude, S. L.; Levine, B. L.; Nobles, C. L.; Bushman, F. D.; Young, R. M.; Scholler, J.; Gill, S. I.; June, C. H.; Grupp, S. A.; Lacey, S. F.; Melenhorst, J. J. Induction of Resistance to Chimeric Antigen Receptor T Cell Therapy by Transduction of a Single Leukemic B Cell. *Nature Medicine* **2018**, *24* (10), 1499–1503.

(35) Minutolo, N. G.; Hollander, E. E.; Powell Jr, D. J. The Emergence of Universal Immune Receptor T Cell Therapy for Cancer. *Frontiers in Oncology* **2019**, *9*, 176.

(36) Lee, Y. G.; Marks, I.; Srinivasarao, M.; Kanduluru, A. K.; Mahalingam, S. M.; Liu, X.; Chu, H.; Low, P. S. Use of a Single CAR T Cell and Several Bispecific Adapters Facilitates Eradication of Multiple Antigenically Different Solid Tumors. *Cancer Research* **2019**, *79* (2), 387–396.

(37) Cho, J. H.; Collins, J. J.; Wong, W. W. Universal Chimeric Antigen Receptors for Multiplexed and Logical Control of T Cell Responses. *Cell* **2018**, *173* (6), 1426–1438.

(38) Lee, Y. G.; Chu, H.; Lu, Y.; Leamon, C. P.; Srinivasarao, M.; Putt, K. S.; Low, P. S. Regulation of CAR T Cell-Mediated Cytokine Release Syndrome-like Toxicity Using Low Molecular Weight Adapters. *Nature Communications* **2019**, *10* (1), 2681.

(39) Tamada, K.; Geng, D.; Sakoda, Y.; Bansal, N.; Srivastava, R.; Li, Z.; Davila, E. Redirecting Gene-Modified T Cells toward Various Cancer Types Using Tagged Antibodies. *Clinical Cancer Research* **2012**, *18* (23), 6436–6445.

(40) Ma, J. S. Y.; Kim, J. Y.; Kazane, S. A.; Choi, S.-H.; Yun, H. Y.; Kim, M. S.; Rodgers, D. T.; Pugh, H. M.; Singer, O.; Sun, S. B.; Fonslow, B. R.; Kochenderfer, J. N.; Wright, T. M.; Schultz, P. G.; Young, T. S.; Kim, C. H.; Cao, Y. Versatile Strategy for Controlling the Specificity and Activity of Engineered T Cells. *Proceedings of the National Academy of Sciences* **2016**, *113* (4), E450–E458.

(41) Cao, Y.; Rodgers, D. T.; Du, J.; Ahmad, I.; Hampton, E. N.; Ma, J. S. Y.; Mazagova, M.; Choi, S.-H.; Yun, H. Y.; Xiao, H.; Yang, P.; Luo, X.; Lim, R. K. V; Pugh, H. M.; Wang, F.; Kazane, S. A.; Wright, T. M.; Kim, C. H.; Schultz, P. G.; Young, T. S. Design of Switchable Chimeric Antigen Receptor T Cells Targeting Breast Cancer. *Angewandte Chemie (International ed. in English)* **2016**, *55* (26), 7520–7524.

(42) Keefe, A. D.; Pai, S.; Ellington, A. Aptamers as Therapeutics. *Nature Reviews Drug Discovery* **2010**, *9* (7), 537–550.

(43) Zhang, D. Y.; Winfree, E. Control of DNA Strand Displacement Kinetics Using Toehold Exchange. *Journal of the American Chemical Society* **2009**, *131* (47), 17303–17314.

(44) Zhang, D. Y.; Seelig, G. Dynamic DNA Nanotechnology Using Strand-Displacement Reactions. *Nature Chemistry* **2011**, *3* (2), 103–113.

(45) Xiang, D.; Zheng, C.; Zhou, S. F.; Qiao, S.; Tran, P. H. L.; Pu, C.; Li, Y.; Kong, L.; Kouzani, A. Z.; Lin, J.; Liu, K.; Li, L.; Shigdar, S.; Duan, W. Superior Performance of Aptamer in Tumor Penetration over Antibody: Implication of Aptamer-Based Theranostics in Solid Tumors. *Theranostics* **2015**, *5* (10), 1083–1097.

(46) Liu, H.; Zhao, Z.; Zhang, L.; Li, Y.; Jain, A.; Barve, A.; Jin, W.; Liu, Y.; Fetse, J.; Cheng, K. Discovery of Low-Molecular Weight Anti-PD-L1 Peptides for Cancer Immunotherapy. *Journal for ImmunoTherapy of Cancer* **2019**, *7* (1), 270.

(47) Zakeri, B.; Fierer, J. O.; Celik, E.; Chittock, E. C.; Schwarz-Linek, U.; Moy, V. T.; Howarth, M. Peptide Tag Forming a Rapid Covalent Bond to a Protein, through Engineering a

Bacterial Adhesin. *Proceedings of the National Academy of Sciences* **2012**, *109* (12), E690–E697.

(48) Keeble, A. H.; Turkki, P.; Stokes, S.; Khairil Anuar, I. N. A.; Rahikainen, R.; Hytönen, V. P.; Howarth, M. Approaching Infinite Affinity through Engineering of Peptide–Protein Interaction. *Proceedings of the National Academy of Sciences* **2019**, *116* (52), 26523–26533.

Chapter 2: Traceless aptamer-mediated isolation of $CD8^+$ T cells for chimeric antigen receptor T-cell therapy

Nataly Kacherovsky, Ian I. Cardle,* Emmeline L. Cheng, Jonathan L. Yu, Michael L. Baldwin, Stephen J. Salipante, Michael C. Jensen, Suzie H. Pun*

ABSTRACT

Chimeric antigen receptor T-cell therapies using defined product compositions require high-purity T-cell isolation systems that, unlike immunomagnetic positive enrichment, are inexpensive and leave no trace on the final cell product. Here, we show that DNA aptamers (generated with a modified cell−SELEX procedure to display low-nanomolar affinity for the T-cell marker CD8) enable the traceless isolation of pure $CD8^+$ T cells at low cost and high yield. Captured $CD8^+$ T cells are released label-free by complementary oligonucleotides that undergo toehold-mediated strand displacement with the aptamer. We also show that chimeric antigen receptor T cells manufactured from these cells are comparable to antibody-isolated chimeric antigen receptor T cells in proliferation, phenotype, effector function and antitumor activity in a mouse model of B-cell lymphoma. By employing multiple aptamers and the corresponding complementary oligonucleotides, aptamer-mediated cell selection could enable the fully synthetic, sequential and traceless isolation of desired lymphocyte subsets from a single system.[2]

[2]Chapter reproduced from: Kacherovsky, N., Cardle, I.I. *et al*. Traceless aptamer-mediated isolation of CD8+ T cells for chimeric antigen receptor T-cell therapy. *Nat. Biomed. Eng.* **3**, 783-795 (2019).

2.1 INTRODUCTION

The clinical impact of T-cell therapies is being rapidly realized with two recent FDA approvals for chimeric antigen receptor (CAR) T-cell therapies treating acute lymphoblastic leukaemia and diffuse large B-cell lymphoma (Novartis's Kymriah and Gilead−Kite's Yescarta, respectively), as well as many promising results in clinical trials.[1–4] CAR T cells have also been generated as potential anti-HIV therapies.[5,6] The production and administration of autologous CAR T-cell therapy involves harvesting and genetically manipulating T cells before reintroducing the engineered cells back into the patients. The first step in this process, cell harvesting, requires high-purity isolation of the desired cell populations. For example, CAR T cells with defined 1:1 $CD4^+$ to $CD8^+$ cell populations have been reported to be more potent than $CD4^+$ or $CD8^+$ cells alone, or unselected populations in animal models of leukaemia, and are also very effective in human clinical trials for acute lymphoblastic leukaemia.[7,8]

T cells for CAR T-cell manufacturing are typically isolated from peripheral blood mononuclear cells (PBMCs) collected by leukapheresis. One method reported for use in clinical-scale T-cell isolation is the sequential isolation of $CD8^+$ and $CD4^+$ T cells from the apheresis product by immunomagnetic positive enrichment (CliniMACS, for example).[9] This approach can achieve high purity and yield but may suffer from: high costs associated with biologically produced antibodies; potential safety concerns stemming from a final cell population that may still be associated with antibody-coated magnetic beads; and low throughput due to the need for multiple selection apparatuses in sequence.[10] Furthermore, the magnetic beads retained on the cells may prevent the downstream selection of cell subsets that could be beneficial for therapy. Although clinical selection strategies that immunodeplete undesired cell populations allow for the isolation of untouched cells and downstream positive selection of specific cell subsets, they also: introduce

more costs by relying on a large panel of antibodies for depletion; reduce the yield by half as the apheresis product has to be split to obtain separate subsets of both $CD4^+$ and $CD8^+$ T cells; and may result in target cells with a low purity.[11,12]

Streptamer-based cell-selection technology that avoids some of these undesirable outcomes through fragment antigen-binding constructs (Fabs) fused with peptide tags that bind reversibly to magnetic beads coated with engineered streptavidin has been reported.[13–15] Fabs can be released from the beads as a result of competition with high-affinity D-biotin and therefore must be engineered with relatively low receptor-binding affinity so that they dissociate rapidly from the cell once released in the monovalent form.[14–17] While the extent of Fab internalization into the cells after release from the solid support is unclear, Fabs engineered with relatively low receptor binding are not substantially retained on the cell surface.[16] However, this method is still costly due to its reliance on biologically produced engineered streptavidin and modified Fabs. Additionally, all the aforementioned approaches have low throughput and high supply requirements for $CD4^+$ and $CD8^+$ T-cell isolation and rely on multiple selection apparatus either in sequence or in parallel. Thus, despite technological advances in cell selection, an overall approach that has low cost, traceless selection and high throughput while maintaining a reasonable yield and purity has remained elusive (**Table S2.1**).

Nucleic acid aptamers (single-stranded oligonucleotides capable of binding target molecules) are an attractive alternative to antibodies and Fabs for cell selection. First developed in the 1990s,[18–20] aptamers can possess binding affinities comparable to (or even higher than) antibodies. Importantly, aptamers are produced synthetically as well-defined, low-variability products with a long storage stability, making them inexpensive and easy to manufacture.[21–23] Aptamers are commonly discovered through a library selection method known as systematic evolution of ligands

by exponential enrichment (SELEX) and can be further optimized for chemical stability. With their favourable attributes, as summarized in **Table S2.1**, the application field for aptamers has escalated in the last quarter of a century to encompass areas including sensing, purification, diagnostics, drug delivery and therapeutics.[24]

Here, we report a reversible aptamer-selection technology for the isolation of label-free $CD8^+$ T cells. Three main facets of the work are presented. First, we identified several high-affinity DNA aptamers specific for CD8 using a modified cell−SELEX procedure and validated the binding characteristics of selected aptamers. We compared magnetic-activated cell sorting (MACS) with one of the aptamers to the antibody-based CD8 Microbead system that is used clinically and found that the aptamer isolated $CD8^+$ T cells from PBMCs with efficiencies comparable to the standard method. Second, we developed a method to reverse aptamer binding using a complementary oligonucleotide reversal agent to disrupt aptamer folding. We show that $CD8^+$ cells can be released from aptamer-immobilized supports with high yield and purity using this approach. Finally, we generated and fully characterized CAR T cells from both our reversible aptamer selection approach and standard, antibody-based selection. CAR T cells isolated using traceless aptamer selection were phenotypically similar to those isolated using antibodies and exhibited nearly identical effector functions, both in vitro and in vivo. This aptamer-based selection approach therefore enables highly efficient, label-free and inexpensive selection of T cells for potential clinical-scale cell therapy applications. With the future discovery of other T-cell-specific aptamers, such as a CD4 aptamer, this technique could be readily expanded for high-throughput, serial selection of multiple T-cell populations from a single apparatus using a panel of aptamers and corresponding reversal agents.

2.2 RESULTS

2.2.1 Identification of T-cell-binding aptamers by cell−SELEX incorporating competitive and counter selection

The generation of highly specific aptamers is critical for cell isolation applications. As our initial efforts to identify T-cell-specific aptamers using either traditional protein−SELEX with recombinant proteins or cell−SELEX[25,26] with engineered cell lines were unsuccessful and yielded aptamers with poor specificity, we hypothesized that both the native display of receptors on cell surfaces afforded by cell−SELEX and the increased stringency of selection provided by competitive selection[27] would be required to discover a T-cell-specific aptamer. We therefore modified the published cell−SELEX protocol[28] to include both competitive selection (selection in the presence of relevant undesired cells) and counter selection (the depletion of aptamers binding undesired targets) (**Figure 2.1**). After an initial round of positive selection against T cells using a single-stranded DNA library with a 52 base pair (bp) random region (10^{16} variants), the selected aptamer pool underwent multiple rounds of competitive/counter selection. Each round included the competitive selection of T-cell-binding aptamers, which was achieved by incubating aptamer pools with PBMCs and then isolating untouched T cells and extracting the bound aptamers. Collected aptamers were then subjected to counter selection by incubation with J.RT3-T3.5, a $CD3^-$ $CD4^{lo}CD8^-$ human T-cell leukaemia line, to remove aptamers binding non-selective surface proteins expressed on T cells. Selection stringency in each of five selection rounds was increased as summarized in **Table S2.2** and selection progress was monitored by flow cytometry (**Figure S2.1**). Binding to a subset of T cells was observed by round 3 and increased in rounds 4 and 5. Selection was halted after five rounds due to the non-specific binding to counter-selection cells observed in round 5.

Aptamer pools from each round of selection were identified by next generation sequencing (NGS) using the primers detailed in **Table S2.3** and analyzed using FASTAptamer.[29] Phylogenetic trees of the top 100 aptamers were generated using FigTree[30] and consensus motifs identified using MEME analysis[31] (**Figure S2.2**). Aptamer sequences collapsed in round 4 to two major branches with two overlapping motifs (Motifs 1 and 2). In round 5, a new motif, Motif 3, emerged, as well as Motif 4, which overlaps with Motif 1. **Table S2.4** shows the top 20 aptamers identified from round 5 in order of prevalence, the predicted motif, and the enrichment of each aptamer in successive rounds.

Five aptamers (named according to their rank in **Table S2.4** and listed in **Table S2.5**) were selected for binding studies with primary T cells and counter selection with J.RT3-T3.5 cells on the basis of on their abundance, motif, enrichment between rounds, family representation on the phylogenetic tree and the low energy state of their secondary structure (**Figure S2.3**). Fluorescein-labeled aptamers A1, A3 and A8 displayed specific binding to a subset of mixed T cells whereas A2 and A7 exhibited whole-population binding to both T cells and J.RT3-T3.5 cells, compared to a randomly chosen aptamer from the naive library (RN) (**Figure S2.4**). Interestingly, A2 and A7, but not A1, A3 or A8, belong to the unique Motif 3 that emerged in round 5 and showed significant enrichment (>100-fold) between rounds 4 and 5 when non-specific binding to J.RT3-T3.5 cells in the bulk aptamer pool was observed.

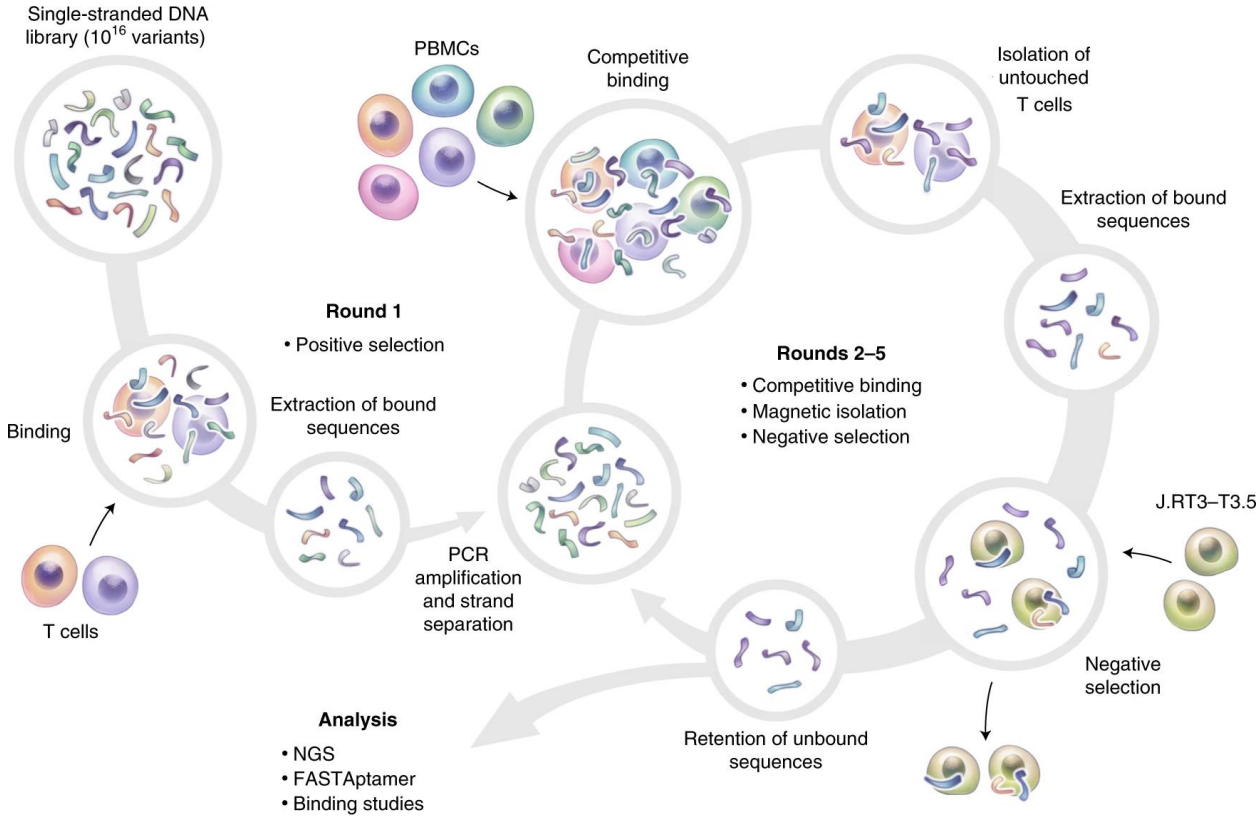

Figure 2.1 | Schematic representation of competitive cell−SELEX with magnetic depletion from PBMCs. A DNA aptamer library underwent one round of positive selection against mixed T cells, followed by four rounds of consecutive competitive selection and negative selection against PBMCs and $CD4^{lo}CD8^{-}$ J.RT3-T3.5 cells, respectively, under increasingly stringent conditions. After competitive selection, untouched T cells and bound aptamers were isolated from PBMCs by depleting the non-target cells using a Pan T Cell Isolation Kit.

2.2.2 Characterization of T-cell-binding aptamers

We hypothesized that aptamers A1, A3 and A8 probably bind to the same receptor due to their overlapping motifs. Furthermore, we suspected that the aptamers bind to CD8 as this protein is not expressed on the counter-selection cell line and CD8:CD4 T-cell ratios are low in healthy donor pan-T-cell isolates, consistent with the 20–30% binding observed in the mixed T-cell population (**Figure S2.4**). We therefore analyzed aptamer binding to mixed human T cells with CD4 and CD8 antibody labelling and demonstrated that all three aptamers bind to $CD8^{+}$ but not $CD4^{+}$ T cells, suggesting that aptamers bind to human CD8 (**Figure 2.2a**). A similar binding study against

murine splenocytes did not, however, show any binding to the T-lymphocyte subset, suggesting that the aptamers, like antihuman CD8 antibodies, do not bind murine CD8 (**Figure S2.5a**). Aptamers A1, A3 and A8, however, do bind to $CD8^+$ T cells in rhesus macaque PBMCs, which is consistent with the rhesus cross-reactivity observed in many antihuman CD8 antibody clones (**Figure S2.5b**). We confirmed that these aptamers bind the human CD8 alpha chain isoform (CD8a) expressed on cells using three techniques: competitive binding with a CD8-specific antibody; short interfering RNA (siRNA) knockdown of CD8a in T cells; and enforced CD8a expression in $CD8^-$ cells. Increasing concentrations of an unlabeled CD8-specific antibody (clone RPA-T8), but not a CD3-specific antibody, robustly outcompeted all three aptamers for binding to CD8+ T cells during a co-incubation (**Figure S2.6**). CD8a knockdown (75%) by siRNA (**Table S2.6**) in primary $CD8^+$ T cells was confirmed by antibody staining and correlated with a 73–77% reduction in the binding of all three aptamers (**Figure 2.2b**). Transient expression of CD8a from a green fluorescent protein (GFP) reporter plasmid in $CD8^-$ Jurkat immortalized human lymphocyte cells introduced aptamer binding specifically to GFP^+ cells (**Figure 2.2c**).

To validate aptamer binding to the CD8a protein itself, we measured association and dissociation kinetics by biolayer interferometry (BLI), in which a serial dilution of recombinant extracellular CD8a protein (Ser22-Asp182) was screened against aptamers immobilized on streptavidin-coated BLI sensors. Whereas the RN aptamer negative control exhibited no detectable association with the CD8a protein (data not shown), the A1, A3 and A8 aptamers bound the protein with binding affinities (K_D values) of 20.1 ± 0.2, 14.7 ± 0.1 and 5.59 ± 0.11 nM, respectively (**Figure 2.2d** and **Table S2.7**). Interestingly, the A3 aptamer had both the highest association (K_{on}) and dissociation (K_{dis}) rate constants of the three aptamers, whereas A8 had the lowest K_{dis}. We also evaluated the apparent K_D values of aptamer binding to $CD8^+$ T cells by flow cytometry, and the A1, A3 and A8

aptamers have apparent K_D values of 18.3 ± 4.6, 1.9 ± 0.8 and 2.4 ± 0.9 nM, respectively (**Figure 2.2e**). The observed differences in K_D values determined by the two methods were expected. Mass transport limitations not present with BLI but present when staining cells in static wells favor re-binding and thereby limit dissociation, improving the apparent K_D of the faster-dissociating A3 relative to the other aptamers. Furthermore, at saturating concentrations of aptamer, where binding advantages stemming from high K_{on} values are diminished given enough time (that is, binding at or near steady-state), the A8 aptamer displays increased binding over A3, consistent with the large difference in K_{dis} between the two aptamers. Regardless, all three aptamers have a high binding affinity to CD8a protein and CD8+ T cells, with K_D values comparable to monoclonal antibodies.

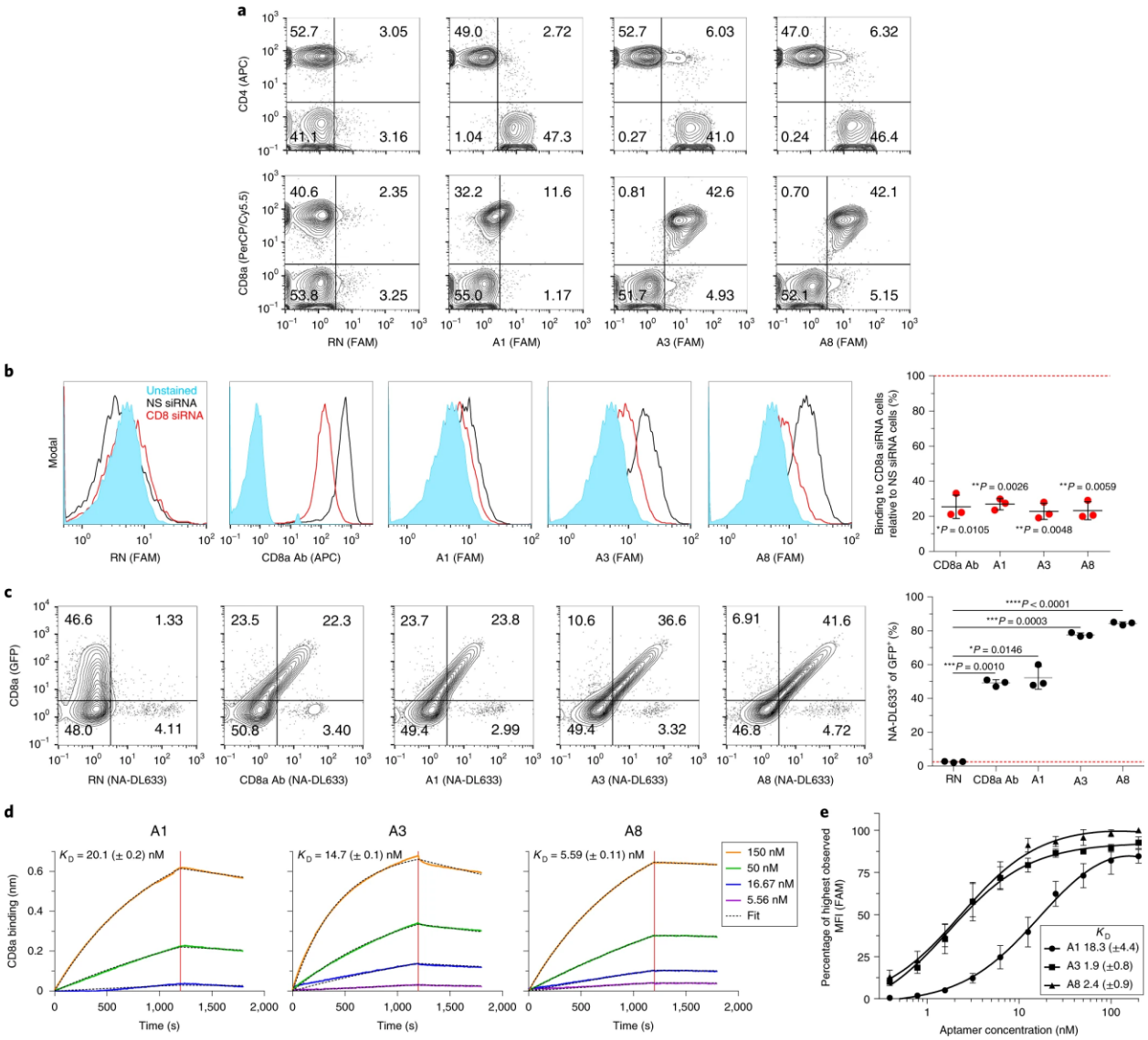

Figure 2.2 | A1, A3, and A8 bind to CD8a glycoprotein. (a) Flow cytometry plots of 50 nM random (RN), A1, A3 and A8 aptamer binding to $CD4^+$ and $CD8^+$ T cells in a mixed T-cell population. The plots represent one independent experiment. (b) Flow cytometry analysis of CD8a antibody (CD8a Ab) and 10 nM RN, A1, A3 and A8 aptamer binding to $CD8^+$ T cells 24 h after nucleofection with non-specific siRNA or CD8 siRNA duplexes. Left, five graphs showing three independent experiments with technical triplicates. Right, a chart showing the binding to CD8 siRNA-treated cells relative to non-specific siRNA-treated controls. Red, dashed horizontal line represents binding to non-specific siRNA-treated controls to which the CD8 siRNA data points were normalized (that is, 100% binding). Horizontal lines and error bars represent the mean ± s.d.; $n = 3$ independent experiments. $*P < 0.05$ and $**P < 0.01$ (one-way analysis of variance (ANOVA) with Bonferroni correction). (c) Flow cytometry analysis of CD8a Ab and 10 nM RN, A1, A3 and A8 aptamer binding to $CD8^-$ Jurkat cells 24 h after nucleofection with a CD8a-hnRNP-M-EGFP plasmid. Left, flow cytometry plots representing three biological replicates with technical triplicates. Right, a chart indicating the percentage of GFP^+ Jurkat cells that were also positive for antibody or aptamer binding. Red, dashed horizontal line represents the mean of RN binding. Horizontal lines and error bars represent the mean ± s.d.; $n = 3$ biologically

independent samples. *$P < 0.05$, ***$P < 0.001$ and ****$P < 0.0001$ (paired one-way ANOVA with Dunnett's test). (d) BLI-measured association and dissociation kinetics of serially diluted CD8a protein binding to immobilized A1, A3 and A8 aptamers. The association phase is illustrated from 0−1,200 s, whereas dissociation is shown from 1,200–1,800 s (separated by the vertical red line). K_D values were calculated by performing a global fit of the kinetic data at the different concentrations of CD8a protein to a 1:1 binding model. K_D values are the mean ± s.d.; $n = 3$ individual concentrations for A1 and 4 individual concentrations for A3 and A8. (e) The flow cytometry binding curves of A1, A3 and A8 aptamers to $CD8^+$ T cells, normalized to 200 nM of A8 binding. The curves represent a nonlinear regression assuming one-site total binding of three independent experiments with technical triplicates. K_D values were calculated by averaging the individual regression values of the independent experiments. Data points and error bars, and K_D values, are the mean ± s.d.; $n = 3$ independent experiments. APC, allophycocyanin; PerCP/Cy5.5, peridinin-chlorophyll-protein complex: cyanine-5.5 conjugate; FAM, carboxyfluorescein; NS, non-specific; NA-DL633, neutravidin DyLight 633.

2.2.3 Reversing aptamer binding with a complementary oligonucleotide

To achieve traceless cell isolation using an aptamer-based affinity agent, a method to reverse aptamer binding to the cell is needed in the cell recovery step. Aptamer binding can be disrupted by nuclease-mediated degradation of the aptamer,[32,33] applied force,[34] competitive binding,[35] or denaturing the secondary structure, either through heat[36] or complementary oligonucleotide binding.[37–40] Of these methods, complementary oligonucleotide displacement is a preferred approach due to its advantages of being gentle (compared to heat or force), with a high yield (compared to competitive binding) and relatively low cost (compared to nuclease degradation). We therefore designed a CD8-binding aptamer that could be released from cells by binding with a complementary displacement strand (reversal agent).

Two major considerations in the design of the selection aptamer and reversal agent are: high-affinity binding to target cells by the selection aptamer; and rapid disruption of the aptamer secondary structure, which is critical for receptor binding by the reversal agent. We therefore chose the A3 aptamer for cell selection, not only due to its low apparent K_D for $CD8^+$ T cells, but also

because of its high K_{on} and K_{dis} for CD8a protein. As multivalent display of the aptamer on a selection medium would potentially mitigate passive cell dissociation, because there are aptamers in cis to retain cell binding even if a few aptamers dissociate, we rationalized that faster association kinetics would probably be more important for cell isolation. Furthermore, a high K_{dis} implies less stable binding, suggesting that strategies to reverse aptamer binding by complementary oligonucleotide displacement may be more successful. We also tested a reported CD8 aptamer from the literature[41,42]; however, low binding was observed under the binding conditions in the published research and our study (**Figure S2.7**). A toehold region was then extended on the 3′ end of the original A3 sequence (A3t) to facilitate the initiation of cell release by the complementary reversal agent (**Figure 2.3a** and **Table S2.5**). Toeholds are single-strand sequences that allow for complementary sequence binding and the supplanting of prepaired bases through a method known as strand displacement.[43–47] In this case, the reversal agent would undergo strand displacement via the toehold to abrogate intrastrand base pairing in the aptamer necessary for its secondary structure. It has been previously described that the rate constant of strand displacement depends critically on the toehold length, varying over up to six orders of magnitude, with maximum rates reached with toeholds over six bases in length;[47] an octanucleotide toehold was therefore used in our CD8-aptamer selection agent. The reversal agent was designed to be 36 bases in length based on the predicted change in secondary structure on binding (**Figure 2.3b** and **Table S2.5**).

We demonstrated effective and rapid aptamer release from cells by the reversal agent using a fluorescently labeled aptamer with flow cytometry analysis. To determine the appropriate conditions for release, various concentrations of reversal agent (ranging from 25- to 100-fold excess), temperatures (4 °C, room temperature and 37 °C) and times of incubation (5, 10 and 20 min) were evaluated (**Figure S2.8**). While >70% A3t aptamer release was observed in all conditions, 90% release could be achieved with just a 10 min incubation at room temperature with 100-fold excess reversal agent. We therefore chose these parameters for our label-free isolation strategy.

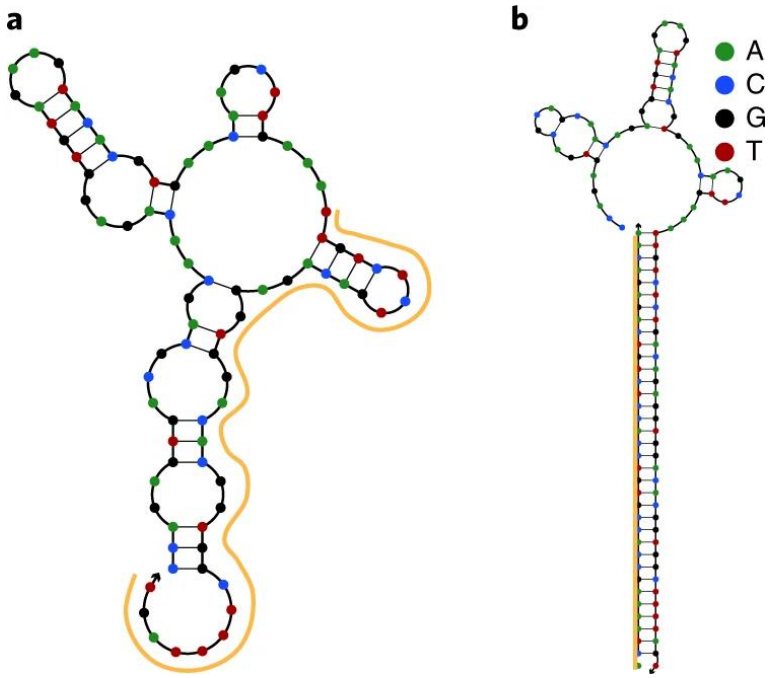

Figure 2.3 | Complementary reversal agent designed to occlude binding of A3 aptamer with modified toehold. (a) The minimum free energy secondary structure of a modified A3 aptamer with a 3′ 8 bp toehold (A3t), predicted using NUPACK (temperature = 4 °C; Na^+ = 137 mM; Mg^{2+} = 5.5 mM). The orange line represents the 36 bp region that a complementary reversal agent was designed to anneal. (b) The predicted minimum free energy secondary structure of the A3t aptamer after strand displacement with the reversal agent (temperature = 20 °C; Na^+ = 137 mM; Mg^{2+} = 5.5 mM).

2.2.4 An aptamer-based strategy for traceless T-cell isolation

Before applying the A3t aptamer to a cell selection process, it was imperative to ensure that the aptamer selectively binds T cells when other types of PBMCs are present. At the concentration used for cell isolation (5 nM), minimal binding to $CD3^{-}CD56^{-}CD14^{+}$ monocytes and $CD3^{-}CD56^{-}CD19^{+}$ B cells was observed and binding to these cell populations was not above the RN aptamer control (**Figure S2.9**). Binding to B cells was especially low (close to 0%)—a desirable trait given that the transduction of a single, highly competent leukaemic B cell with a CAR was recently shown to induce resistance to therapy.[48] In addition to $CD3^{+}CD56^{-}$ T cells, the A3t aptamer displayed substantial binding to $CD3^{+}CD56^{+}$ natural killer T (NKT) cells and $CD3^{-}CD56^{+}$ natural killer (NK) cells (as expected), which are known to have subsets that express CD8. As NKT cells have been found to improve CAR T-cell therapy,[49] binding to these cells was seen as beneficial. Importantly, the median fluorescent intensity (MFI) of aptamer binding on A3t-positive monocytes, B cells and NK cells is much lower compared to that of A3t-positive T and NKT cells, suggesting that binding events would minimally capture the contaminant cells at this aptamer concentration.

We predicted that the selection aptamer A3t and its cognate reversal agent could be used to achieve traceless T-cell isolation in a completely synthetic system in which immobilized aptamers are used to isolate T cells that are then released by the addition of the reversal agent, which disrupts the secondary structure of the aptamer that is critical for binding (**Figure 2.4a**). We tested this strategy using the A3t aptamer immobilized on immunomagnetic Anti-Biotin Microbeads (Miltenyi Biotec). We compared the aptamer strategy to antibody-based CD8 Microbeads (Miltenyi Biotec) in terms of their abilities to isolate $CD8^{+}$ T cells with high purity and yield from three healthy donor PBMC populations, as CD8 Microbeads are the only selection technology approved for

clinical-scale CAR T-cell manufacture at present. PBMCs were incubated with functionalized beads and applied onto a column under a magnetic field, after which the flow-through fraction was collected. Antibody-isolated cells were then removed from the column using a column flush whereas aptamer-isolated cells were exposed to a 100-fold excess of reversal agent for 10 min on the column. The column was then unplugged and washed, which constituted the reversal agent elution (RAE) fraction. Any remaining cells on the column were removed using a column flush. The fractions of both isolation methods were analyzed via flow cytometry (**Figure S2.10**)

We observed near-complete depletion of $CD8^+$ cells from the flow-through fraction using aptamer-loaded microbeads, comparable to that obtained using antibody-based CD8 Microbeads. This corresponded to the enrichment of $CD8^+$ cells in the RAE and column flush fractions (**Figure 2.4b**). Further analysis of the $CD8^+$ cells in the RAE fraction showed that these cells were predominantly $CD3^+CD16^-$ T cells (>97%), with only a small fraction of the population being $CD8^{lo}CD16^+$ monocytes and NK cells (**Figure 2.4c**). Importantly, this purity analysis is conservative, as it does not account for $CD3^+CD16^+$ NKT cells. On average, the combined RAE and column flush of the aptamer-based isolation yielded 97.5% of the $CD8^+$ T cells from the starting PBMC population (comparable to that obtained from antibody-based isolation) and the traceless isolation alone (RAE fraction) yielded 72.3% (**Figure 2.4d**). Even if contaminating $CD8^-$ cells are included, the average purity of $CD8^+$ T cells in the RAE fraction was 95.6%, illustrating that the A3t aptamer displays minimal non-specific binding to $CD8^-$ cells in PBMCs (**Figure 2.4e**). The CD8 staining of aptamer-isolated $CD8^+$ T cells in the RAE fraction with the RPA-T8 antibody clone was comparable to that of $CD8^+$ T cells in the starting PBMC population, whereas that of antibody-isolated $CD8^+$ T cells was lower (**Figure 2.4f**). Given that the antibody-based method depletes nearly the whole $CD8^+$ T-cell population (**Figure 2.4b, d**), the lower CD8

staining is probably a result of the cell-bound CD8 Microbeads hindering the binding of the staining antibody clone used (**Figure 2.4f**). This further emphasizes certain advantages of the traceless nature of reversal agent strand displacement, which can enable accurate, downstream phenotyping of capture antigens without needing to optimize the staining antibody clone. Interestingly, aptamer-isolated $CD8^+$ T cells in the column flush fraction that were not stripped off in the RAE were just as pure as those in the RAE fraction (**Figure 2.4e**). However, they also had higher CD8 expression than those in the RAE fraction (**Figure 2.4f**), albeit not significantly so, indicating that cells with higher CD8 expression and thus aptamer-bead labelling may be more difficult to remove from the column by RAE. Although simply flushing the column would provide a similarly pure product with higher yield than using a reversal agent, RAE allows the isolation of cells free of magnetic beads in a manner that is specific to each selection aptamer used. In addition to providing traceless cell recovery, this approach affords the potential for both further downstream selection of different cell subsets and the serial selection of different cell types from a single selection process.

To confirm that aptamer-isolated cells are similar to antibody-isolated cells, we compared the $CD8^+$ T cells in the RAE fraction of the aptamer-based isolation to those of the antibody-based isolation using flow cytometry phenotyping and NanoString nCounter transcript profiling. Whereas $CD8^+$ T cells in the aptamer-isolated RAE fraction were phenotypically identical to those in PBMCs, antibody-isolated $CD8^+$ T cells comprised a slightly larger percentage of cells in a transitional stage of dual CD45RA/RO expression that coincided with a small reduction in effector memory cells (**Figure S2.11a**). Transcriptionally, however, aptamer- and antibody-isolated cells were identical (**Figure S2.11b**). No gene transcripts were differentially expressed in significantly

higher or lower amounts, suggesting that there are no immediate side effects to briefly exposing the cells to high reversal agent concentrations.

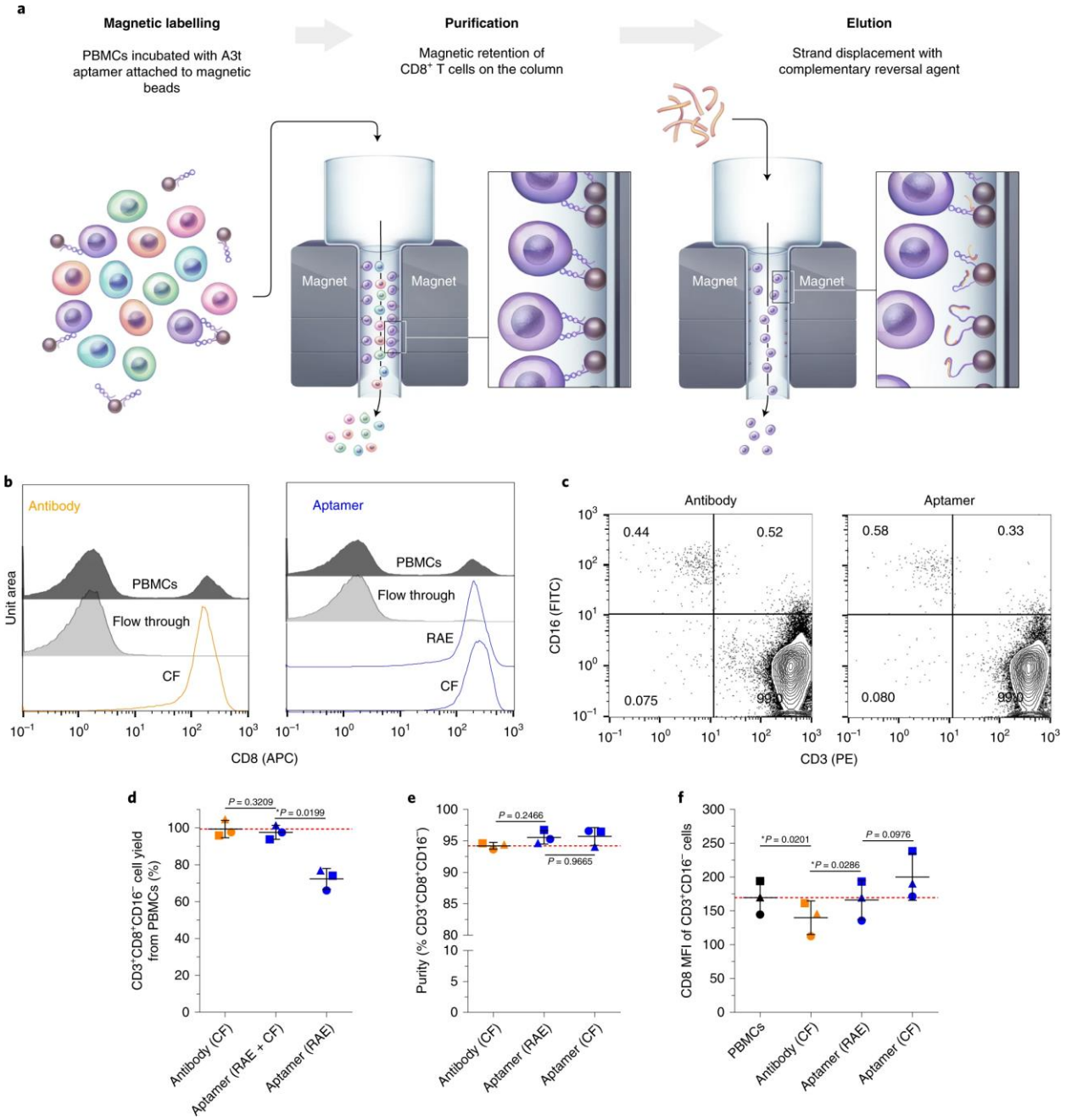

Figure 2.4 | Isolation of label-free CD8$^+$ T cells from PBMCs using a reversible, aptamer-based selection strategy. (a) A schematic representation of the traceless selection of CD8$^+$ T cells using the A3t aptamer. Biotinylated aptamer (5 nM) preloaded onto Miltenyi Anti-Biotin Microbeads was incubated with PBMCs to magnetically label CD8$^+$ T cells. The cell suspension was applied onto an LS column under a magnetic field, in which unlabeled cells were removed in the flow-through fraction. Microbead-labeled CD8$^+$ T cells that remained on the column were incubated with a 100-fold excess of the complementary reversal agent and released CD8$^+$ T cells

were washed off the column in the RAE fraction. Any remaining cells on the column were removed using a plunger column flush in the absence of the magnetic field. (b) Flow cytometry graphs of CD8 expression in the different fractions of standard, antibody-based Miltenyi CD8 Microbead isolation (left) and traceless aptamer-based isolation (right). The graphs represent three independent experiments with technical triplicates. (c) Flow cytometry plots of CD3 and CD16 expression in $CD8^+$ antibody-isolated column flush (left) and aptamer-isolated RAE cell fractions (right) to distinguish between $CD3^+CD16^-$ T cells and $CD3^-CD16^+$ monocytes and NK cells. The plots represent three independent experiments with technical triplicates. (d-f), Flow cytometry analysis of yield (d), purity (e) and CD8 MFI (f) of $CD3^+CD8^+CD16^-$ T cells in different fractions of antibody- and aptamer-based isolations. The circles, squares and triangles represent different donors from separate isolation experiments, and all data were collected in technical triplicates. The red, dashed horizontal line represents the corresponding mean value of the antibody group (d-e) or PBMC group (f). Horizontal lines and error bars represent the mean ± s.d.; $n = 3$; $P > 0.05$ and $^*P < 0.05$ (paired one-way ANOVA with Tukey's test). APC, allophycocyanin; FITC, fluorescein isothiocyanate; PE, phycoerythrin.

2.2.5 Generation of CAR T cells from aptamer-based traceless cell isolates

Few differences were observed between aptamer- and antibody-isolated cells immediately after isolation and we sought to confirm whether this would stay true for a final CAR T-cell product generated using these different isolation methods. We thus generated $CD8^+$ CAR T cells from both the antibody-isolated cells and the traceless aptamer-isolated cells (RAE fraction) shown in **Figure 2.4d-f** and fully compared their outgrowth, phenotype, gene expression and effector function. Antibody-isolated $CD4^+$ T cells were not included in these studies so as not to convolute any differences between the $CD8^+$ T cells isolated from the different methods. We transduced cells with the PLAT-02 lentiviral vector, which encodes a second generation CD19scFv-41BB-CD3ζ CAR (and the truncated version of the epidermal growth factor receptor, EGFRt, as a surrogate transduction marker) that is used in ongoing clinical trials (**Figure 2.5a**).[9] CD19 CAR T cells were manufactured using a sequential two week stimulation bead outgrowth from days S1D0 to S1D14 and a two week rapid expansion protocol (REP) with irradiated $CD19^+$ feeder cells from days S1R1D0 to S1R1D14, as summarized in **Figure S2.12**, where S1 denotes the bead stimulation, R1

indicates the REP and D# signifies the number of days since stimulation or REP onset. After transduction, high expression of the surrogate transduction marker EGFRt (>60%) was observed on S1D9 without additional selection and was further increased using immunomagnetic enrichment and over the REP period to at least 94% on S1R1D13 before functional assays were run (**Figure 2.5b**). Importantly, although transduction copy number was probably variable, given the variation in surrogate transduction marker expression, there was no difference in the mean EGFRt MFI between antibody- and aptamer-isolated cells (**Figure 2.5b**).

Over the two week stimulation period, we observed no differences in the outgrowth between untransduced antibody- and aptamer-isolated mock T cells (**Figure 2.5c**). This was consistent with the similar Ki-67 expression between both mocks and CD19 CAR T cells from the different isolation methods at the end of the two week stimulation outgrowth (**Figure 2.5d**) and unsurprisingly the cells grew identically during the REP (**Figure S2.13**). On S1D14, while staining for PD1, TIM3 and LAG3 coexpression (markers of both activation and exhaustion) we observed small differences in the accumulation of these markers between cells from the different isolation methods at the end of the two week stimulation outgrowth (**Figure 2.5e** and **Figure S2.14**). Whereas aptamer-isolated CD19 CAR T cells had a loss of $TIM3^{+}PD1^{-}TIM3^{-}$ cells and a gain of $PD1^{+}TIM3^{+}$ cells compared to antibody-isolated cells, opposite trends were seen in the mock cells between the two isolation methods, suggesting that these differences are probably artifacts of transduction and the stimulation process and not the isolation strategy. Consistent with the exhaustion/activation data, aptamer-isolated CD19 CAR T cells from the same day exhibited more differentiation than the antibody-isolated cells, as indicated by the greater proportion of $CD45RA^{-}CD62L^{+}$, but the mock cells of the two isolation methods were equivalently differentiated (**Figure 2.5f** (left) and **Figure S2.15**). However, after a two week REP process, the

aptamer-isolated CD19 CAR T cells were less terminally differentiated than the antibody-isolated cells while the mocks remained the same, again suggesting that the isolation strategy is not the principal cause of these small differences (**Figure 2.5f** (right) and **Figure S2.15**). NanoString nCounter transcript profiling of immune-associated genes further confirmed that there were minimal differences between the two isolation methods with zero genes being differentially expressed in significantly higher or lower amounts between aptamer- and antibody-isolated mock and CD19 CAR T cells at the end of the REP before functional testing (**Figure S2.16**). These results reaffirm that the aptamer selection strategy did not have any durable, long-term side effects on CAR T-cell fitness.

We evaluated the antitumor effector function of these cells against both myelogenous leukaemia K562 cells lines that were transduced to stably express OKT3 Fab and CD19 for CD3 and CAR engagement, respectively, as well as B lymphoma Raji cells that constitutively express moderate levels of CD19 (**Figure S2.17**). On tumor challenge in vitro, aptamer-isolated CD19 CAR T cells lysed all three cell types to similar extents to antibody-isolated cells and secreted identical amounts of the effector cytokines tumor necrosis factor (TNF)-α and interferon (IFN)-γ (**Figure 2.5g, h**). Thus, CAR T cells derived from an aptamer-based traceless isolation strategy perform in vitro to the standard of cells derived from the widely used antibody-based isolation.

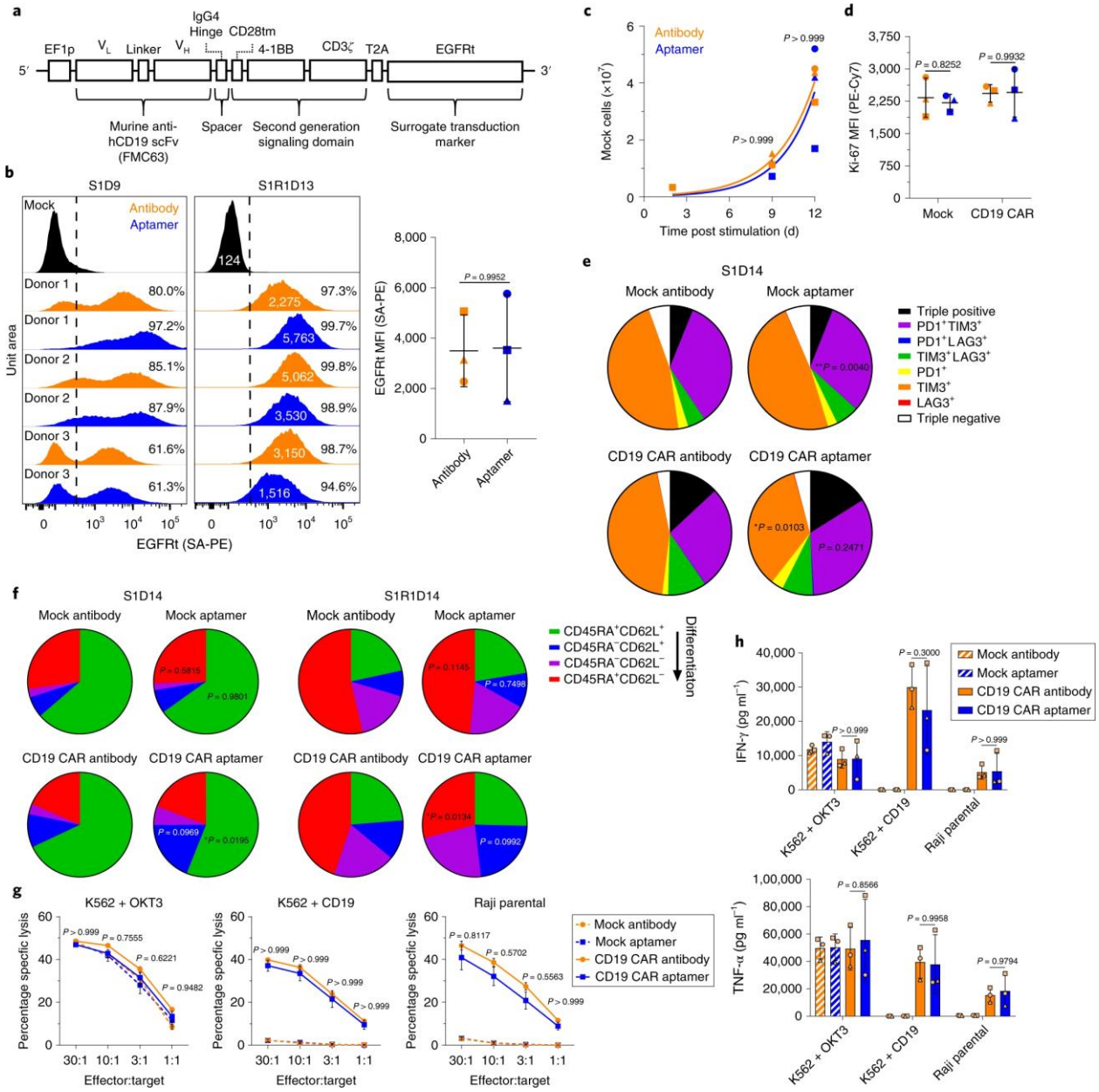

Figure 2.5 | Characterization of CD19 CAR T cells generated from antibody- and aptamer-isolated cells. (a) The second generation CD19 CAR T-cell construct with EGFRt reporter that was used to retrovirally transduce isolated T cells. (b) Left, flow cytometry analysis of EGFRt expression in antibody- and aptamer-isolated T cells 9 d after initial bead stimulation (S1D9) and 13 d after the REP (S1R1D13) with irradiated CD19$^+$ TM-LCL cells. The timeline for cell expansion is shown in **Figure S2.12**. The flow graphs represent one independent experiment. Right, a chart indicating EGFRt reporter MFI at S1R1D13, using the symbols from **Figure 2.4d-f**. Horizontal lines and error bars represent the mean ± s.d.; $n = 3$; $P > 0.05$ (two-sided paired *t*-test). (c) The growth of non-transduced mock T cells after bead stimulation. The symbols are as in **Figure 2.4d-f**; $n = 3$; $P > 0.05$ (paired two-way ANOVA with Bonferroni correction). The curves represent a least-squares fit to the exponential growth equation. (d) Flow cytometry analysis of Ki-67 expression in mock and CD19 CAR T cells on S1D14 immediately before the REP. The symbols are as in **Figure 2.4d-f**. Horizontal lines and error bars represent the

mean ± s.d.; $n = 3$; $P > 0.05$ (paired two-way ANOVA with Sidak correction). (e) Flow cytometry analysis of PD1/TIM3/LAG3 expression in mock and CD19 CAR T cells on S1D14 immediately before the REP. Individual donor values can be found in **Figure S2.14**. The pie charts show the mean phenotype of the cells; $n = 3$ biologically independent samples; $P > 0.05$, $*P < 0.05$ and $**P < 0.01$ (paired two-way ANOVA with Bonferroni correction). (f) Flow cytometry analysis of CD62L/CD45RA expression in mock and CD19 CAR T cells on S1D14 immediately before the REP and on S1R1D14 immediately before the functional assays. Individual donor values can be found in **Figure S2.15**. The pie charts show the mean phenotype of the cells; $n = 3$ biologically independent samples; $P > 0.05$ and $*P < 0.05$ (paired two-way ANOVA with Bonferroni correction). (g,h) In vitro antitumor cytotoxicity and cytokine release of mock and CD19 CAR T cells. For (h), the symbols are as in **Figure 2.4d-f**. Data points and error bars (g) and graph bars and error bars (h) represent the mean ± s.d.; $n = 3$ biologically independent samples; $P > 0.05$ (paired two-way ANOVA with Bonferroni correction (g); paired two-way ANOVA with Sidak correction (h)). SA–PE, streptavidin–phycoerythrin; PE-Cy7, phycoerythrin:cyanine-7 tandem conjugate.

2.2.6 Aptamer-isolated CAR T-cell performance in systemic Raji tumor mouse model

In vitro cytotoxicity results with CAR T cells do not always corroborate with in vivo results.[50] Thus, despite observing little difference in the effector function of antibody- and aptamer-isolated $CD8^+$ CAR T cells in vitro, it was important to further show that this would translate in vivo. To this end, we used a less stringent version of the previously described CAR T-cell stress test,[50,51] in which Raji-bearing NOD/SCID/IL-2R-γ null (NSG) mice were treated with a non-curative dose of $CD8^+$ CD19 CAR T cells from the different isolation methods at the end of the REP (S1R1D14). Mice were injected with 5×10^5 GFP-ffluc $CD19^+$ Raji cells and treated 7 d later with 10^7 antibody- or aptamer-isolated S1R1D14 $CD8^+$ CAR T cells, as previously described.[52] $CD8^+$ mock T cells from both isolation methods were included as placebo controls.

Administration of 2×10^7 $CD8^+$ CAR T cells was previously shown to be only 50% curative long term with this model due to the absence of the $CD4^+$ CAR T-cell subset critical for therapy persistence.[52] The $CD8^+$ CAR T cells in this study were also expanded by both a two week bead stimulation and two week REP, and thus displayed markedly more exhaustion and differentiation

than the one or two week expanded CAR T cells described in other publications.[50,51] Consequently, using only 10^7 $CD8^+$ CD19 CAR T cells in the same model was found to be non-curative with a maximal survival of approximately ten weeks (A. Johnson, unpublished observations). We therefore postulated that this T-cell stress study design would be able to rigorously identify any differences in antitumor effector function between antibody- and aptamer-isolated CAR T cells. Even so, in vivo, we continued to observe identical antitumor activity between both antibody- and aptamer-isolated $CD8^+$ CAR T cells. Tumor regression and relapse kinetics, as measured using the photon flux of the tumor, overlapped between mice that received CAR T cells derived from the different isolation methods across multiple donors. (**Figure 2.6a**). Although the therapy was non-curative for both CAR T-cell treatment groups, indicative of a successful stress test model, mice receiving aptamer-isolated CAR T cells exhibited similar prolonged survival compared to mice receiving antibody-isolated CAR T cells as determined by both biological significance (median survival time) and log-rank statistical significance (**Figure 2.6b**). These results further illustrate that traceless aptamer-based cell isolation with strand displacement is a viable replacement for antibody-based isolation in the initial production step of CAR T-cell therapy, having negligible downstream impact on the quality of the final cell product.

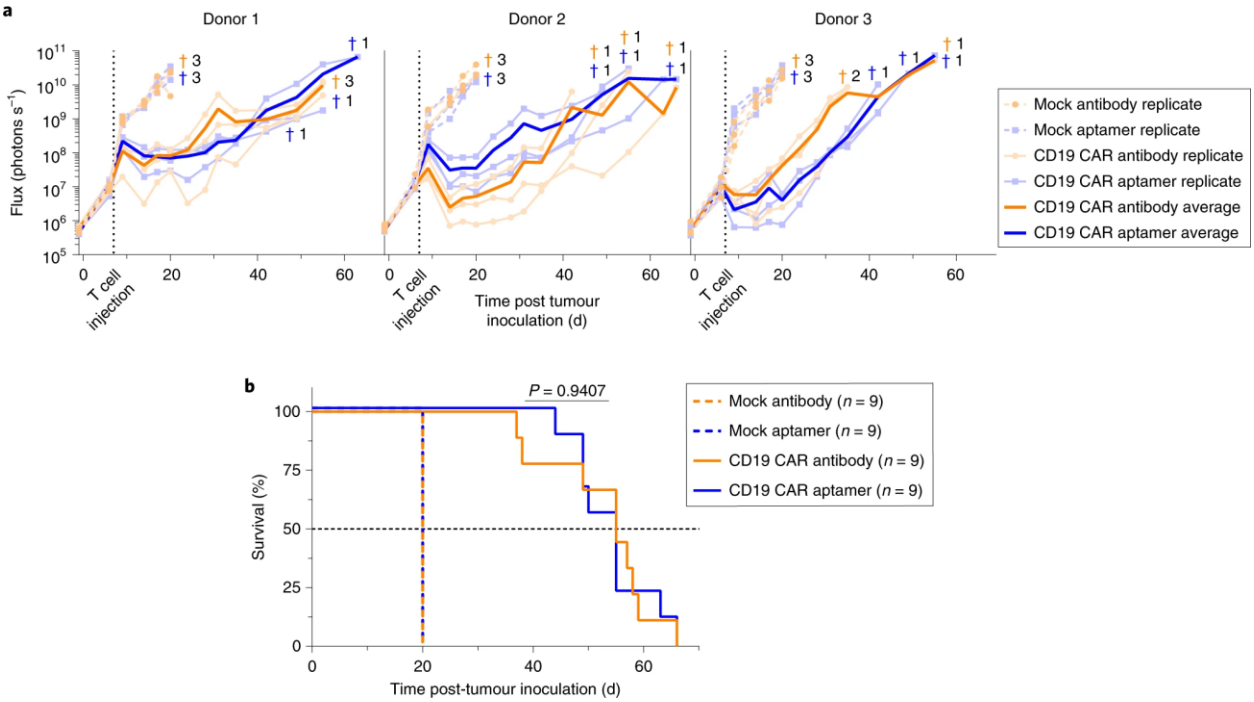

Figure 2.6 | Tumor stress test with antibody- and aptamer-isolated CD8$^+$ CD19 CAR T cells. NSG mice were inoculated intravenously with 5×10^5 CD19$^+$ Raji cells and treated 7 d later with 10^7 CD8$^+$ mock or CD19 CAR T cells from antibody- or aptamer-isolated donor cells. (a) The flux of the systemic tumors. †Individual mice were killed at these points. The pale curves are the tumor flux values for the individual mice (three mice per donor per group). (b) Kaplan−Meier survival curves. The black, dashed horizontal line represents 50% survival, otherwise known as the median survival time. Median survival times of the CD19 CAR T-cell treatment groups were as follows: antibody: 55 d; aptamer: 55 d. $n = 9$ (3 mice per donor); $P > 0.05$ (two-sided log-rank test).

2.3 DISCUSSION AND FUTURE WORK

A challenge with CAR T-cell therapy is the time and cost associated with manufacturing a clinical product. As recent literature has shown that the selection of different T-cell subsets for therapy may provide improved and consistent clinical outcomes compared to undefined products starting from heterogenous PBMCs, it is increasingly imperative that efficient and cost-effective selection approaches are developed to meet the demands of these new therapeutic composition.[7,8] At present, CD8$^+$ and CD4$^+$ T cells are selected by either: splitting the starting leukapheresis product and immunomagnetically depleting undesired cells for further downstream positive selections; or

sequential isolation from the leukapheresis product using immunomagnetic positive selections. Both approaches are far from perfect: the former wastes a portion of the cells in the starting population by splitting the cells, but saves time with parallel isolations; the latter is time consuming as it uses the whole population in each step. Furthermore, labels remaining on the cells prevent further selection and present regulatory barriers for clinical translation into patients. Two recent reports have used DNA-labeled antibodies followed by strand displacement to isolate multiple cell populations; however, antibodies and DNA tags remain attached to selected cells.[53,54] The advent of Streptamer technology and similar avidity-reliant Fab multimerization strategies have partially mitigated these issues by enabling label-free isolation; however, these approaches still rely on expensive, biologically produced selection agents and require two or more apparatus in sequence to isolate pure, separate cell subsets.[16,17] These technologies are also perishable and frequently have a sole supplier of consumables, which adds supply-chain risk to a cell therapy manufacturing process that is often time-sensitive for patients with refractory disease.[10]

DNA aptamers and complementary strand displacement with a reversal agent present a unique opportunity to improve the selection of T cells for use in adoptive cell therapy. Aptamers are synthetic and thereby inexpensive to produce at large scales. Furthermore, their manufacture can be outsourced to one of many available companies and they have a long-shelf life, so they bear minimal supply-chain risk. High-affinity DNA aptamers can be developed against multiple targets and their sequences can be further modified after SELEX to include unique toeholds and stems for aptamer-specific strand displacement. Thus, panels of aptamers against diverse T-cell antigens can be developed with corresponding unique reversal agents for sequential label-free isolation of different cell subsets off the same column. As an example, microbeads loaded with CD4 and CD8 aptamers that have unique toeholds and sequences could be added at the same time to one whole

leukapheresis product, and $CD4^+$ and $CD8^+$ T cells could be serially eluted off one column by sequential incubations with the corresponding reversal agents. A similar outcome can be achieved using a CD3 aptamer in combination with either a CD4 or CD8 aptamer. Alternatively, one could deplete $CD8^+$ T cells and other unwanted cell subsets using a CD8-specific aptamer and other aptamers that bind monocytes, B cells and NK cells, respectively. Untouched $CD4^+$ T cells could then be enriched in the flow-through fraction and $CD8^+$ T cells could be selectively eluted from the column using a reversal agent specific to the CD8 aptamer. The key to executing these strategies is the identification of highly cell-specific aptamers.

In this study, we report the discovery of high-affinity CD8a-specific aptamers and the successful application of one aptamer with a reversal agent in a traceless $CD8^+$ T-cell isolation system. Using the aptamer alone, we report an equivalent $CD8^+$ T-cell selection yield compared to a widely used antibody-based approach. With a reversal agent for label-free elution, we observed a >70% selection yield and >95% purity of $CD8^+$ T cells. Given that a 350–450 ml apheresis product from a person with acute lymphoblastic leukaemia will have $3–9 \times 10^9$ T cells, and only $200–600 \times 10^6$ $CD8^+$ T cells are needed to manufacture a 1:1 $CD4^+$:$CD8^+$ CAR T-cell therapy, the trade of lower yield for high purity, lower cost and label-free selection with this approach has little consequence but many benefits. Importantly, on the basis of anecdotal observations of the maximal capacity of this system at a small scale, we estimate that only US$5−10 of aptamer would be needed for reliable clinical-scale isolation. CD19-directed CAR T cells manufactured from label-free, aptamer-isolated cells also exhibited identical performance to CAR T cells generated from antibody-selected cells in assays designed to measure antitumor effector function, showing that aptamer-based traceless cell isolation is a practical selection strategy for CAR T-cell therapy.

Although the competitive SELEX approach was designed to identify multiple T-cell-specific aptamers, only CD8-specific aptamers were discovered with this strategy. We speculate that this occurred due to the strong partitioning of the library towards the high-affinity CD8 aptamers. SELEX strategies using untouched $CD4^+$ primary T cells or the $CD8^-$ Jurkat T-cell line may thus be required to identify aptamers that bind to alternative T-cell antigens like CD3 or CD4. Furthermore, due to the limited binding chemistry available to unmodified DNA aptamers, certain proteins may not be amenable to high-affinity aptamer discovery using unmodified DNA libraries. For these targets, increased chemical diversity including one or two modified base pairs in the library design may be needed for the successful partitioning of high-affinity binders.[55]

In the future, aptamers could be readily functionalized for attachment to solid supports for affinity chromatography separation, thus resulting in a purely synthetic isolation system without the need for recombinant proteins, magnetic supports, and pre-incubation with selection agents. Cell-release efficiency could be potentially improved, for example by refining the strand displacement kinetics between aptamer and reversal agent through further sequence optimization (higher toehold GC content, aptamer truncation) and chemical modification of the aptamer and reversal agent (locked nucleic acids).[47,56] Further discovery of aptamers against the T-cell markers CD3 and CD4 will also be required to realize a serial selection strategy that can isolate multiple cell subsets tracelessly from a single column. With these advances, aptamer and reversal agent-based isolation approaches could be inexpensively applied in process-engineering strategies to prepare engineered $CD4^+$ and $CD8^+$ T cells through continuous flow methods, thus increasing the accessibility of T-cell immunotherapy.

2.4 MATERIALS AND METHODS

2.4.1 Oligonucleotides

All oligonucleotides studied were synthesized by Integrated DNA Technologies. The ssDNA library used in the T-cell−SELEX process was purified using high-performance liquid chromatography and consisted of a 52 bp random sequence flanked by two 18 bp constant regions. The primers used for library amplification between SELEX rounds, with IDT modification codes, are as follows: forward 5′-/56-FAM/ATCCAGAGTGACGCAGCA-3′ and reverse 5′-/5BiosG/ACTAAGCCACCGTGTCCA-3′. The individually synthesized ssDNA aptamers are listed in **Table S2.5**.

2.4.2 Antibodies and flow cytometry

The following dyes, antibodies and secondaries were used to stain cells: Zombie Violet (1:500 in 100 μl 10^{-6} cells, BioLegend), Zombie Yellow (1:500 in 100 μl 10^{-6} cells, BioLegend), APC antihuman CD4 (1:100, 300514, BioLegend), PerCP/Cy5.5 antihuman CD8a (1:100, 301031, BioLegend), APC antihuman CD8a (rhesus cross-reactivity, 1:100, 301014, BioLegend), CD8−biotin (1:100, 130-098-556, Miltenyi), antimouse CD16/CD32 Fc block (1:100, 14-0161-86, eBioscience), FITC antimouse CD3e (1:50, 100305, BioLegend), BV421 antimouse CD8a (1:50, 100737, BioLegend), FITC mouse antihuman CD3e (rhesus cross-reactivity, 1:20, 55611, BD Biosciences), purified antihuman CD3 (Clone UCHT1, 300402, BioLegend), purified antihuman CD8a (Clone RPA-T8, 301002, BioLegend), Super Bright 600 antihuman CD19 (1:20, 63-0198-42, eBioscience), Super Bright 702 antihuman CD56 (1:100, 67-0566-42, eBioscience), PE antihuman CD3 (1:100, 300308, BioLegend), APC/Cy7 antihuman CD14 (1:40, 325619, BioLegend), FITC antihuman CD16 (1:50, 302006, BioLegend), Alexa Fluor 700 antihuman CD3

(1:50, 300424, BioLegend), Brilliant Violet 785 antihuman CD4 (1:50, 317442, BioLegend), PE/Cy7 antihuman CD8a (1:200, 300914, BioLegend), BUV737 mouse antihuman CD45RA (1:25, 564442, BD Biosciences), BUV395 mouse antihuman CD45RO (1:25, 564291, BD Biosciences), PE antihuman CD62L (1:400, 304806, BioLegend), Brilliant Violet 421 antihuman CCR7 (1:25, 353208, BioLegend), Erbitux−biotin (1:500, Jensen Lab), PE-Cy7 mouse anti-Ki-67 (1:20, 561283, BD Biosciences), BUV737 mouse antihuman PD1 (1:20, 565299, BD Biosciences), Brilliant Violet 785 antihuman TIM3 (1:20, 345032, BioLegend), PE mouse antihuman LAG3 (1:20, 565616, BD Biosciences), Brilliant Violet 785 antihuman CD45RA (1:160, 304140, BioLegend), NeutrAvidin Protein DyLight 633 (1:500, 22844, Invitrogen), Alexa Fluor 647 streptavidin (1:500, 405237, BioLegend) and PE streptavidin (1:500, 405204, BioLegend). OneComp eBeads (Invitrogen) were used to prepare single-colour controls for compensation, if needed. Stained samples were analyzed with a MACSQuant Analyzer 10 (Miltenyi), Attune NxT (Invitrogen) or BD LSRFortessa (BD Biosciences) flow cytometer.

2.4.3 Cell line culture and PBMC isolation

The J.RT3-T3.5 and Jurkat (clone E6-1) cell lines used for counter selection and nucleofection, respectively, were purchased from ATCC. The Epstein−Barr virus-transformed lymphoblastoid cell line (TM-LCL) used in the REP of T cells was made from mononuclear cells as previously described.[57] The $CD19^+$ and $OKT3^+$ K562 cells used for functional assays were generated by lentivirally transducing parental K562 parental cells (ATCC) with CD19- or OKT3-expressing constructs. Raji parental cells were also purchased from ATCC. All the above cell lines were cultured in RPMI 1640 medium (Gibco) with 10% heat-inactivated FBS (Life Tech and VWR). Human PBMCs were isolated from Leukocyte Reduction System cones (Bloodworks Northwest) using Ficoll-Paque density gradient centrifugation (GE). The mixed or $CD8^+$ T cells used in non-

isolation experiments were a gift from Juno Therapeutics. Rhesus PBMCs were a gift from A. Taraseviciute (Seattle Children's Research Institute).

2.4.4 Competitive cell-SELEX with T-cell depletion

The SELEX protocol was adapted from a reported method.[28] A schematic of the SELEX procedure is shown in **Figure 2.1** and the conditions used in the individual rounds are summarized in **Table S2.2**. In brief, positive selection was conducted for round 1, in which 4×10^7 thawed mixed T cells, depleted of dead cells (Miltenyi), were incubated with 40 nmol of ssDNA library (~10^{16} individual sequences) for 1 h at 4 °C in binding buffer. Bound aptamers were extracted and amplified by PCR using Phusion High Fidelity DNA Polymerize (NEB) with forward and reverse primers. Strand separation was performed with High Capacity Neutravidin Agarose Resin (Thermo Scientific), as described previously,[28] and the FAM-labeled ssDNA aptamer pool was used in the next round. For rounds 2−5, the ssDNA aptamer pools were incubated with thawed PBMCs depleted of dead cells, a process termed competitive selection. After three washes, T cells and bound ssDNA sequences were then enriched using a Pan T Cell Isolation Kit (Miltenyi). The ssDNA pool was then extracted and incubated with 10^7 $CD3^-CD8^-$ J.RT3-T3.5 cells at 4 °C as a form of negative selection in each round, and unbound ssDNA sequences were PCR amplified and used to generate ssDNA aptamer pools for use in the sequential round. The wash and binding buffer formulations, as well as folding conditions, are as described previously.[28]

2.4.5 Aptamer binding assays

Cells (2×10^5) were incubated with 100 µl of folded FAM-labeled ssDNA pools or FAM/biotin-labeled individual aptamers for 20–30 min at 4 °C in binding buffer at the indicated concentrations. For antibody competition and multicolor flow cytometry staining with antibodies, antibodies were

added to the primary incubation with aptamer. Cells were washed twice (or three times for large flow panels) in 200 µl of wash buffer supplemented with 1% BSA to remove excess aptamer. If the aptamers or antibodies used were biotinylated, the cells underwent a second incubation with 100 µl of fluorescently labeled streptavidin or neutravidin secondary for 15–20 min at 4 ^{o}C in wash buffer with 1% BSA and were washed twice. Stained cells were fixed in 200 µl of wash buffer with 1% BSA and 0.1% PFA before analysis via flow cytometry.

2.4.6 NGS and data analysis

The starting RN and ssDNA pools from each SELEX round were PCR amplified with the barcoded primers listed in **Table S2.3** for sequencing using the MiSeq Reagent Kit v2 (300 cycles) and MiSeq System (Illumina) according to the manufacturer's instructions. Exported FASTA files were analyzed with FASTAptamer v1.0.3.[29] Specifically, FASTAptamer-Count was first used to determine rank and reads per million for each sequence, whereafter FASTAptamer-Compare was used to conduct pairwise comparison of reads per million for sequences between adjacent rounds and thus calculated fold enrichment (**Table S2.4**). Neighbor joining trees were constructed for the top 100 sequences from rounds 2–4 and were further analyzed by both FigTree v1.4.3 (tree.bio.ed.ac.uk/software/figtree/) for phylogenetic tree generation and MEME Suite v4.12.0 for motif prediction.[31] The NUPACK web application was used to generate predicted secondary structures of aptamer sequences.[58]

2.4.7 Murine splenocyte isolation and staining

For mouse spleen harvesting, animal work was conducted under protocol no. 4053-01 approved by the Institutional Animal Care and Use Committee at the University of Washington. 20-week-old Tg(Aldh1l1-EGFP,-DTA)D8Rth/J male mice (Jackson Laboratory) were euthanized with

avertin and perfused with 20 ml PBS to limit coagulation.[59] Spleens were harvested, minced with scissors and dissociated by sieving over a 40-μm cell strainer (Falcon). Red blood cells were removed by incubation with ACK Lysing Buffer (Gibco) and cells were stained with both anti-mCD3 and anti-mCD8 antibodies and aptamers.

2.4.8 siRNA knockdown

Some 10^7 thawed $CD8^+$ T cells were activated with Dynabeads Human T-activator CD3/CD28 (Life Tech) at 1.5×10^6 cells ml^{-1} for 3 d in complete RPMI supplemented with 100 U ml^{-1} rhIL-2 (Miltenyi, NIBSC calibrated value). On day 3, 3×10^6 activated T cells were nucleofected with 50 pmol of both CD8a-targeting duplex siRNA 1 and 2, listed in **Table S2.6**, or 100 pmol of scrambled duplex siRNA (IDT) using the Human T Cell Nucleofector Kit (Lonza) with Program T-023 according to the manufacturer's instructions. Aptamer and anti-CD8 antibody staining, as discussed in the previous section, were performed 24 h later and analyzed via flow cytometry.

2.4.9 Plasmid transfection

CD8a-hnRNP-M-EGFP was a gift from L. Lu (Addgene plasmid no. 86054).[60] 2×10^6 $CD8^-$ Jurkat cells were nucleofected (Lonza) with 2 μg of the plasmid using the Nucleofector Kit V (Lonza) with Program X-001 according to the manufacturer's instructions. The cells were analyzed 24 h later for both GFP expression and anti-CD8 antibody and aptamer binding via flow cytometry.

2.4.10 BLI

BLI studies were conducted on a FortéBio Octet Red96 instrument at 25 ºC with sample agitation at 1,000 r.p.m. The sample buffer used for all steps comprised binding buffer with 0.01% Tween

20. Streptavidin-coated biosensors were loaded with 50 nM biotinylated aptamer until all sensors (except for the reference) reached a capture threshold of 0.5 nm. After a 100 s rinse and baseline steps in buffer alone, sensors were exposed to a 1:3 dilution series of recombinant human CD8a protein (Sino Biological) ranging from 150 to 5.56 nM. Association with protein was monitored for 1,200 s and dissociation was carried out for 600 s in buffer alone. Data analysis was carried out using Octet Data Analysis 9.0 (FortéBio). Kinetic constants were calculated by conducting a global fit of the several processed association and dissociation curves from the protein dilution series to a 1:1 binding model. The quality of the fit was evaluated using R^2 and χ^2 values.

2.4.11 Comparison to previously reported aptamer

CD8Ap17s, as described by Wang et al.,[42] was synthesized with the sequence 5′-CTACAGCTTGCTATGCTCCCCTTGGGGTA/iSp18//3Bio/-3′. Binding to $CD8^+$ T cells was compared to our aptamer A3t (**Table S2.5**), and CD8Ap17s binding buffer (A-BB) and folding conditions were used in addition to our binding buffer (T-BB) and folding conditions. For the CD8Ap17s conditions, 1 μM of each aptamer was folded by denaturation at 95 ºC for 5 min and cooled to 37 ºC in its wash buffer (40 mM HEPES, 150 mM NaCl, 5 mM KCl, 1 mM $MgCl_2$, 1 mM $CaCl_2$, pH 7.5). Binding was similarly carried out and analyzed as detailed above but in CD8Ap17s binding buffer, which comprised the wash buffer supplemented with 5% FBS.

2.4.12 Reversal agent optimization

A 36 bp reversal agent was designed complementary to the 3′ end of aptamer A3t (**Table S2.5**). Binding to $CD8^+$ T cells with 5 nM aptamer A3t was first carried out with secondary fluorescent streptavidin labelling, as discussed above. Labeled cells were then incubated with varying fold excesses (over the amount of aptamer used) of 200 μl of reversal agent in wash buffer with 1%

BSA for different times and temperatures. Cells were washed twice with the wash buffer with 1% BSA to remove eluted aptamers, fixed and analyzed via flow cytometry.

2.4.13 Traceless selection of $CD8^+$ T cells from PBMCs

For each PBMC donor, 200 µl of Anti-Biotin Microbeads (Miltenyi) were diluted to 1,000 µl in binding buffer with 5 nM aptamer A3t and incubated for 15 min at 4 °C under gentle rotation. The aptamer-labeled bead suspensions were then added to 2×10^8 Ficoll-isolated PBMCs and allowed to incubate for another 15 min at 4 °C under gentle rotation. Cells were subsequently washed with 10 ml of autoMACS Rinsing Solution (Miltenyi) supplemented with 0.5% BSA, resuspended in the same buffer and applied over two LS columns in parallel on a QuadroMACS separator (Miltenyi) according to the manufacturer's instructions. A flow-through fraction, which includes the flow through from the initial application of cells and the three subsequent 3 ml column washes, was collected. Afterwards, 1 ml of 500 nM reversal agent (100-fold excess) in autoMACS solution with 0.5% BSA and 5 mM $MgCl_2$ was applied to the column on the magnet containing cells labeled with aptamer-functionalized microbeads. Approximately 600–700 µl of the reversal agent solution passed through the column before it was plugged with a M/F Luer Lock Plug (Smiths Medical) for a 10 min incubation at room temperature. On removal of the plug, the column was washed three times with 3 ml of autoMACS solution with 0.5% BSA and 5 mM EDTA, which constituted the RAE fraction. The RAE cells were immediately spun down and resuspended in fresh buffer to remove any reversal agent. Remaining cells on the column were removed with a column flush according to the manufacturer's instructions. In parallel, $CD8^+$ cells from the same donor were isolated from 200×10^6 PBMCs in the column flush fraction with antibody-based CD8 Microbeads (Miltenyi), according to the manufacturer's instructions.

All fractions were counted and analyzed via flow cytometry with two antibody panels: a yield panel staining for CD3, CD8 and CD16 expression; and a phenotype panel staining for CD3, CD4, CD8, CD45RA, CD45RO, CCR7 and CD62L expression. Furthermore, 10^6 cell pellets from both the antibody-isolated column flush fraction and aptamer-isolated RAE fraction were flash frozen on dry ice and ethanol for NanoString nCounter analysis. The remaining cells were banked for downstream CAR T-cell production.

2.4.14 CD19 CAR T-cell manufacturing

$CD8^+$ T cells from both isolation methods from each donor were thawed and 3.3×10^6 cells for both mock and CD19 CAR T-cell groups were stimulated 1:1 with Dynabeads Human T-Activator CD3/CD28 (Invitrogen) in 4 ml complete RPMI with 50 U ml^{-1} rhIL-2 (Miltenyi) and 0.5 ng ml^{-1} rhIL-15 (Miltenyi) in a 12-well plate. After 2 d (S1D2), cells designated for CAR T-cell production were transduced with clinical-grade PLAT-02 CD19 CAR lentiviral vector (a gift from the City of Hope) at a multiplicity of infection of 0.3 with 40 μg ml^{-1} protamine sulphate via spinoculation for 30 min at 800*g* at 32 ºC. Thereafter, media exchanges were conducted every 2–3 d to replenish cytokines and cells were moved to larger culture vessels when cell concentrations reached $1.5–2 \times 10^6$ cells ml^{-1}. The activator beads were removed 9 d poststimulation, termed S1D9, and cells were stained for EGFRt surrogate marker expression to assess transduction efficiency. CAR^+ cells were magnetically enriched 12 d poststimulation (S1D12) using biotinylated Erbitux antibody and Anti-Biotin Microbeads according to the manufacturer's instructions. On day 14 poststimulation (S1D14), cells were analyzed via flow cytometry by staining for: activation/proliferation with Ki-67; exhaustion/activation with PD1, TIM3 and LAG3; and differentiation with CD62L and CD45RA.

The two-week-stimulated T cells were further expanded using a two week REP, as previously described.[61] Briefly, 1.5×10^6 CD19 CAR T cells were co-incubated with 10.5×10^6 irradiated $CD19^+$ TM-LCL feeder cells in 25 ml of complete RPMI supplemented with the aforementioned cytokine concentrations in T-25 flasks (Corning). Similarly, 1.5×10^6 mock T cells were co-incubated with 10×10^6 irradiated $CD19^+$ TM-LCL feeder cells and 50×10^6 irradiated donor-mismatched PBMC feeder cells in 25 ml complete RPMI supplemented with the same cytokines and 30 ng ml^{-1} OKT3 in T-25 flasks (Corning). PBMCs and TM-LCL cells were irradiated at 3,500 and 8,000 rad, respectively, using a caesium source irradiator. Cells were maintained as for the two week activator bead expansion, except that OKT3 was replaced only on day 2. On day 13 after the REP (S1R1D13), the CD19 CAR T cells were stained for EGFRt surrogate transduction marker expression to assess the enrichment and purity of the CAR^+ cells after magnetic selection and the REP. On day 14 after the REP (S1R1D14), the cells were characterized again for differentiation and a 10^6 cell pellet of each cell lot was flash frozen for downstream NanoString nCounter analysis. The remaining cells were used for in vitro functional assays or banked for in vivo studies.

2.4.15 NanoString nCounter gene profiling

Thawed cell pellets were resuspended in RLT lysis buffer with β-mercaptoethanol at 3,500 cells μl^{-1} and overnight hybridization reactions with the nCounter Immunology Panel (Human V2) Reporter CodeSet and Capture ProbeSet were run according to the manufacturer's instructions. Samples were run on the nCounter SPRINT Profiler (NanoString) and mRNA counts were normalized in groups by day and cell type (D0, S1R1D14 mocks, S1R1D14 CD19 CAR) using nSolver 4.0 (NanoString) and Advanced Analysis 2.0 (NanoString), which selects the housekeeping genes that minimize the pairwise variation statistic. Each group has six samples:

three biological replicates for antibody-based isolation and three biological replicates for aptamer-based isolation. Using Excel (Microsoft), mRNA probes that gave normalized counts of less than 25 for more than 50% of the samples in a group (four or more samples) were removed from the analysis as they were mostly below the background. The unadjusted *P* values of the $\log_2$ fold changes in the probe counts of aptamer-isolated cells over antibody-isolated cells were determined using a paired two-tailed *t*-test in Excel and the threshold for significance was calculated using the Benjamini−Yekutieli multiple-testing correction in R software v3.3.2 (http://www.R-project.org/).

2.4.16 Antitumor cytotoxicity assay

K562 + OKT3, K562 + CD19 and Raji parental target cells were each seeded at 5×10^6 cells in 4 ml of complete RPMI in a well of a 12-well plate and 75 µl of Cr-51 (PerkinElmer) was added to each well with cells. Cells were harvested a day later and seeded at 5×10^3 cells per well in a 96-well plate at 100 µl. S1R1D14 $CD8^+$ mock and CD19 CAR effector T cells in 100 µl were added to the target cells at different effector-to-target ratios ranging from 1:1 to 30:1. Media without cells or with 2% SDS were also added to wells with target cells as minimum and maximum lysis controls, respectively. Target and effector cell mixtures were lightly pelleted at 700 r.p.m. for 2 min before incubating for 4 h at 37 °C in an incubator. 50 µl of supernatant was then harvested into LUMA plates (PerkinElmer) and allowed to dry overnight. The plates were analyzed by a TopCount NXT Microplate Scintillation and Luminescence Counter (PerkinElmer).

2.4.17 Antitumor cytokine release assay

K562 + OKT3, K562 + CD19 and Raji parental target cells were plated at 5×10^4 cells per well in a 96-well plate at 100 µl. S1R1D14 $CD8^+$ mock and CD19 CAR effector T cells were added to target cells at 10^5 cells per well in 100 µl and allowed to co-incubate for 24 h. Cells were then

pelleted at 1,200 r.p.m. for 3 min and 120 µl of supernatant was collected and frozen at −80 °C until ready to analyze. Thawed supernatants were diluted 1:5 or 1:20 in RPMI without FBS, and IL-2, IFN-γ and TNF-α in the supernatants and a standard (Bio-Rad) were captured and fluorescently detected on magnetic beads using a 3-plex Bio-Plex custom kit with flat magnetic plates (Bio-Rad) according to the manufacturer's instructions. The beads with captured cytokines were analyzed using a Bio-Plex 200 system (Bio-Rad).

2.4.18 T-cell stress test mouse model

All animal work described in this Article complied with local animal ethical and welfare standards. The T-cell stress test mouse model was conducted under protocol no. 13853 approved by the IACUC at the Seattle Children's Research Institute. 9- to 11-week-old NSG female mice (Jackson Laboratory) were inoculated with 5×10^5 GFP-ffluc Raji cells in 200 µl of PBS by tail vein injection, followed by 10^7 S1R1D14 antibody- or aptamer-isolated $CD8^+$ mock or CD19 CAR T cells 7 d later. The same three donors from the in vitro studies were tested and for each of the four T-cell populations evaluated, three mice were used per donor (for a total of nine mice in each treatment group across all donors). For bioluminescence imaging, mice were injected subcutaneously with 150 µl of D-luciferin (PerkinElmer) in PBS (4.29 mg per mouse) and unsaturated images were acquired with the Xenogen IVIS Imaging System (PerkinElmer) after 7 and 10 min using medium or small binning and an acquisition time of 30 s to 1 min. Photon flux was analyzed using Living Image software v4.5 (PerkinElmer). On day 6 following tumor inoculation, mice were arranged into groups of three mice each for each donor and treatment group, such that the average photon flux of the pre-established systemic tumors was approximately equal across all groups. Accordingly, no randomization or blinding methods were used. Mice that

developed hind-limb paralysis were killed with carbon dioxide. The log-rank test was performed using Prism 7.0 (GraphPad).

2.4.19 Statistical analysis

Data are expressed as mean ± s.d., unless otherwise stated, and the number of biological and technical replicates is indicated in the figure caption. If only two populations were being compared, a two-tailed *t*-test was used for hypothesis testing; ANOVA was used for hypothesis testing when more than two populations were being compared. Paired hypothesis testing was often implemented to account for large donor-to-donor variability. When conducting multiple comparisons, Tukey's test or Dunnett's test was used to adjust the *P* values when every mean was compared to every other mean or a control mean, respectively, whereas the Sidak correction was used to adjust *P* values when select sets of means were compared, assuming independence. If comparisons could not be assumed to be independent from each other, Bonferroni correction was used instead of the Sidak correction to adjust *P* values. The Benjamini−Yekutieli correction was used for the analysis of NanoString data, as this method handles the dependence between the expression of different genes well. Differences were considered significant if $P < 0.05$ after any adjustment. Unless otherwise stated, graphing and statistical tests were performed using GraphPad Prism v7.00 for Windows, GraphPad Software, La Jolla California USA, www.graphpad.com.

2.5 AUTHOR CONTRIBUTIONS

S.H.P. and M.C.J. conceived the idea and provided experimental advice and funding support. N.K., I.I.C. and S.H.P. designed the project. N.K. and I.I.C. conceived, performed and interpreted the experiments. N.K. designed and performed the SELEX procedure. I.I.C. and E.L.C. evaluated the binding of aptamer libraries and select aptamers and I.I.C., E.L.C., S.J.S. and N.K. analyzed the

NGS data. I.I.C. performed murine splenocyte and rhesus binding experiments. N.K., J.L.Y., I.I.C. and E.L.C. conducted receptor-binding studies using siRNA knockdown and gene transfection. I.I.C. and N.K. conducted antibody competition and Octet studies. J.L.Y. and E.L.C. performed binding curve studies and E.L.C. and I.I.C. evaluated aptamer binding to human PBMCs. N.K., I.I.C. and J.L.Y. optimized reversal agent and traceless cell isolation conditions. I.I.C. performed CAR T-cell production and characterization studies. M.L.B. conducted in vivo tumor studies and bioluminescence imaging. I.I.C. prepared the figures and performed statistical analyses. I.I.C., N.K., E.L.C. and S.H.P. wrote the manuscript.

2.6 ACKNOWLEDGEMENTS

This work was supported by a sponsored research agreement from Juno Therapeutics. We are grateful to C. Ramsborg (Juno Therapeutics), A. Bianchi (Juno Therapeutics), J. Shi (Juno Therapeutics), C. Chan (Juno Therapeutics), B. Olden (University of Washington) and J. Gustafson (Seattle Children's Research Institute) for their critical discussion and helpful advice and to A. Mills (Juno Therapeutics) for manuscript feedback. We are also grateful to all Pun and Jensen Lab members, especially J. Yokoyama (Seattle Children's Research Institute) and A. Johnson (Seattle Children's Research Institute), for experimental support and helpful advice. We also thank the Baker Lab, especially B. Langan, for assistance with Octet BLI studies. We thank C. Saxby (University of Washington) and R. Mukherjee (Seattle Children's Research Institute) for their valuable input relating to NGS and NanoString nCounter analysis, respectively. We thank M. Meechan (Seattle Children's Research Institute) for assisting with mouse bioluminescence imaging and cage monitoring. We also thank members of the Statistical Consulting Program in the Departments of Biostatistics and Statistics, especially T. H. Wai (University of Washington), for their valuable input regarding the statistical analysis. We thank H. Y. Lin for preparing the SELEX

and cell isolation figures. I. Cardle was supported partly by the National Cancer Institute of the National Institutes of Health under award no. 5T32CA080416-19 for research reported in this publication.

2.7 REFERENCES

(1) Brentjens, R. J.; Davila, M. L.; Riviere, I.; Park, J.; Wang, X.; Cowell, L. G.; Bartido, S.; Stefanski, J.; Taylor, C.; Olszewska, M.; Borquez-Ojeda, O.; Qu, J.; Wasielewska, T.; He, Q.; Bernal, Y.; Rijo, I. V.; Hedvat, C.; Kobos, R.; Curran, K.; Steinherz, P.; Jurcic, J.; Rosenblat, T.; Maslak, P.; Frattini, M.; Sadelain, M. CD19-Targeted T Cells Rapidly Induce Molecular Remissions in Adults with Chemotherapy-Refractory Acute Lymphoblastic Leukemia. *Science Translational Medicine* **2013**, *5* (177), 177ra38.

(2) Davila, M. L.; Riviere, I.; Wang, X.; Bartido, S.; Park, J.; Curran, K.; Chung, S. S.; Stefanski, J.; Borquez-Ojeda, O.; Olszewska, M.; Qu, J.; Wasielewska, T.; He, Q.; Fink, M.; Shinglot, H.; Youssif, M.; Satter, M.; Wang, Y.; Hosey, J.; Quintanilla, H.; Halton, E.; Bernal, Y.; Bouhassira, D. C. G.; Arcila, M. E.; Gonen, M.; Roboz, G. J.; Maslak, P.; Douer, D.; Frattini, M. G.; Giralt, S.; Sadelain, M.; Brentjens, R. Efficacy and Toxicity Management of 19-28z CAR T Cell Therapy in B Cell Acute Lymphoblastic Leukemia. *Science Translational Medicine* **2014**, *6* (224), 224ra25.

(3) Lee, D. W.; Kochenderfer, J. N.; Stetler-Stevenson, M.; Cui, Y. K.; Delbrook, C.; Feldman, S. A.; Fry, T. J.; Orentas, R.; Sabatino, M.; Shah, N. N.; Steinberg, S. M.; Stroncek, D.; Tschernia, N.; Yuan, C.; Zhang, H.; Zhang, L.; Rosenberg, S. A.; Wayne, A. S.; Mackall, C. L. T Cells Expressing CD19 Chimeric Antigen Receptors for Acute Lymphoblastic Leukaemia in Children and Young Adults: A Phase 1 Dose-Escalation Trial. *The Lancet* **2015**, *385* (9967), 517–528.

(4) Mirzaei, H. R.; Rodriguez, A.; Shepphird, J.; Brown, C. E.; Badie, B. Chimeric Antigen Receptors T Cell Therapy in Solid Tumor: Challenges and Clinical Applications . *Frontiers in Immunology* . 2017, p 1850.

(5) Hale, M.; Mesojednik, T.; Romano Ibarra, G. S.; Sahni, J.; Bernard, A.; Sommer, K.; Scharenberg, A. M.; Rawlings, D. J.; Wagner, T. A. Engineering HIV-Resistant, Anti-HIV Chimeric Antigen Receptor T Cells. *Molecular Therapy* **2017**, *25* (3), 570–579.

(6) Scholler, J.; Brady, T. L.; Binder-Scholl, G.; Hwang, W.-T.; Plesa, G.; Hege, K. M.; Vogel, A. N.; Kalos, M.; Riley, J. L.; Deeks, S. G.; Mitsuyasu, R. T.; Bernstein, W. B.; Aronson, N. E.; Levine, B. L.; Bushman, F. D.; June, C. H. Decade-Long Safety and Function of Retroviral-Modified Chimeric Antigen Receptor T Cells. *Science Translational Medicine* **2012**, *4* (132), 132ra53.

(7) Sommermeyer, D.; Hudecek, M.; Kosasih, P. L.; Gogishvili, T.; Maloney, D. G.; Turtle, C. J.; Riddell, S. R. Chimeric Antigen Receptor-Modified T Cells Derived from Defined CD8+ and CD4+ Subsets Confer Superior Antitumor Reactivity in Vivo. *Leukemia* **2016**, *30* (2), 492–500.

(8) Turtle, C. J.; Hanafi, L.; Berger, C.; Gooley, T. A.; Cherian, S.; Hudecek, M.; Sommermeyer, D.; Melville, K.; Pender, B.; Budiarto, T. M.; Robinson, E.; Steevens, N. N.; Chaney, C.; Soma, L.; Chen, X.; Yeung, C.; Wood, B.; Li, D.; Cao, J.; Heimfeld, S.; Jensen, M. C.; Riddell, S. R.; Maloney, D. G. CD19 CAR–T Cells of Defined CD4+:CD8+

Composition in Adult B Cell ALL Patients. *Journal of Clinical Investigation* **2016**, *126* (6), 2123–2138.

(9) Gardner, R. A.; Finney, O.; Annesley, C.; Brakke, H.; Summers, C.; Leger, K.; Bleakley, M.; Brown, C.; Mgebroff, S.; Kelly-Spratt, K. S.; Hoglund, V.; Lindgren, C.; Oron, A. P.; Li, D.; Riddell, S. R.; Park, J. R.; Jensen, M. C. Intent-to-Treat Leukemia Remission by CD19 CAR T Cells of Defined Formulation and Dose in Children and Young Adults. *Blood* **2017**, *129* (25), 3322–3331.

(10) Aijaz, A.; Li, M.; Smith, D.; Khong, D.; LeBlon, C.; Fenton, O. S.; Olabisi, R. M.; Libutti, S.; Tischfield, J.; Maus, M. V; Deans, R.; Barcia, R. N.; Anderson, D. G.; Ritz, J.; Preti, R.; Parekkadan, B. Biomanufacturing for Clinically Advanced Cell Therapies. *Nature Biomedical Engineering* **2018**, *2* (6), 362–376.

(11) Terakura, S.; Yamamoto, T. N.; Gardner, R. A.; Turtle, C. J.; Jensen, M. C.; Riddell, S. R. Generation of CD19-Chimeric Antigen Receptor Modified CD8+ T Cells Derived from Virus-Specific Central Memory T Cells. *Blood* **2012**, *119* (1), 72–82.

(12) Wang, X.; Naranjo, A.; Brown, C. E.; Bautista, C.; Wong, C. W.; Chang, W.-C.; Aguilar, B.; Ostberg, J. R.; Riddell, S. R.; Forman, S. J.; Jensen, M. C. Phenotypic and Functional Attributes of Lentivirus-Modified CD19-Specific Human CD8+ Central Memory T Cells Manufactured at Clinical Scale. *Journal of Immunotherapy* **2012**, *35* (9), 689–701.

(13) Voss, S.; Skerra, A. Mutagenesis of a Flexible Loop in Streptavidin Leads to Higher Affinity for the Strep-Tag II Peptide and Improved Performance in Recombinant Protein Purification. *Protein Engineering, Design and Selection* **1997**, *10* (8), 975–982.

(14) Knabel, M.; Franz, T. J.; Schiemann, M.; Wulf, A.; Villmow, B.; Schmidt, B.; Bernhard, H.; Wagner, H.; Busch, D. H. Reversible MHC Multimer Staining for Functional Isolation of T-Cell Populations and Effective Adoptive Transfer. *Nature Medicine* **2002**, *8* (6), 631–637.

(15) Schmitt, A.; Tonn, T.; Busch, D. H.; Grigoleit, G. U.; Einsele, H.; Odendahl, M.; Germeroth, L.; Ringhoffer, M.; Ringhoffer, S.; Wiesneth, M. Adoptive Transfer and Selective Reconstitution of Streptamer-selected Cytomegalovirus-specific CD8+ T Cells Leads to Virus Clearance in Patients after Allogeneic Peripheral Blood Stem Cell Transplantation. *Transfusion* **2011**, *51* (3), 591–599.

(16) Stemberger, C.; Dreher, S.; Tschulik, C.; Piossek, C.; Bet, J.; Yamamoto, T. N.; Schiemann, M.; Neuenhahn, M.; Martin, K.; Schlapschy, M.; Skerra, A.; Schmidt, T.; Edinger, M.; Riddell, S. R.; Germeroth, L.; Busch, D. H. Novel Serial Positive Enrichment Technology Enables Clinical Multiparameter Cell Sorting. *PLoS ONE* **2012**, *7* (4), e35798.

(17) Sabatino, M.; Hu, J.; Sommariva, M.; Gautam, S.; Fellowes, V.; Hocker, J. D.; Dougherty, S.; Qin, H.; Klebanoff, C. A.; Fry, T. J.; Gress, R. E.; Kochenderfer, J. N.; Stroncek, D. F.; Ji, Y.; Gattinoni, L. Generation of Clinical-Grade CD19-Specific CAR-Modified CD8+ Memory Stem Cells for the Treatment of Human B-Cell Malignancies. *Blood* **2016**, *128* (4), 519–528.

(18) Ellington, A. D.; Szostak, J. W. In Vitro Selection of RNA Molecules That Bind Specific Ligands. *Nature* **1990**, *346*, 818–822.

(19) Tuerk, C.; Gold, L. Systematic Evolution of Ligands by Exponential Enrichment: RNA Ligands to Bacteriophage T4 DNA Polymerase. *Science* **1990**, *249* (4968), 505–510.

(20) Robertson, D. L.; Joyce, G. F. Selection in Vitro of an RNA Enzyme That Specifically Cleaves Single-Stranded DNA. *Nature* **1990**, *344*, 467–468.

(21) Bunka, D. H. J.; Stockley, P. G. Aptamers Come of Age – at Last. *Nature Reviews*

Microbiology **2006**, *4* (8), 588–596.
(22) Hernandez, L. I.; Machado, I.; Hernandez, T. S. and F. J. Aptamers Overview: Selection, Features and Applications. *Current Topics in Medicinal Chemistry*. 2015, pp 1066–1081.
(23) Zhou, J.; Rossi, J. Aptamers as Targeted Therapeutics: Current Potential and Challenges. *Nature Reviews Drug Discovery* **2017**, *16* (6), 440.
(24) Dunn, M. R.; Jimenez, R. M.; Chaput, J. C. Analysis of Aptamer Discovery and Technology. *Nature Reviews Chemistry* **2017**, *1* (10), 0076.
(25) Daniels, D. a; Chen, H.; Hicke, B. J.; Swiderek, K. M.; Gold, L. A Tenascin-C Aptamer Identified by Tumor Cell SELEX: Systematic Evolution of Ligands by Exponential Enrichment. *Proceedings of the National Academy of Sciences of the United States of America* **2003**, *100* (26), 15416–15421.
(26) Shangguan, D.; Li, Y.; Tang, Z.; Cao, Z. C.; Chen, H. W.; Mallikaratchy, P.; Sefah, K.; Yang, C. J.; Tan, W. Aptamers Evolved from Live Cells as Effective Molecular Probes for Cancer Study. *Proceedings of the National Academy of Sciences* **2006**, *103* (32), 11838–11843.
(27) Ogasawara, D.; Hasegawa, H.; Kaneko, K.; Sode, K.; Ikebukuro, K. Screening of DNA Aptamer Against Mouse Prion Protein by Competitive Selection. *Prion* **2007**, *1* (4), 248–254.
(28) Sefah, K.; Shangguan, D.; Xiong, X.; O'Donoghue, M. B.; Tan, W. Development of DNA Aptamers Using Cell-Selex. *Nature Protocols* **2010**, *5* (6), 1169–1185.
(29) Alam, K. K.; Chang, J. L.; Burke, D. H. FASTAptamer: A Bioinformatic Toolkit for High-Throughput Sequence Analysis of Combinatorial Selections. *Molecular Therapy - Nucleic Acids* **2015**, *4* (3), e230.
(30) Caroli, J.; Taccioli, C.; De La Fuente, A.; Serafini, P.; Bicciato, S. APTANI: A Computational Tool to Select Aptamers through Sequence-Structure Motif Analysis of HT-SELEX Data. *Bioinformatics* **2016**, *32* (2), 161–164.
(31) Bailey, T. L.; Boden, M.; Buske, F. A.; Frith, M.; Grant, C. E.; Clementi, L.; Ren, J.; Li, W. W.; Noble, W. S. MEME Suite: Tools for Motif Discovery and Searching. *Nucleic Acids Research* **2009**, *37*, W202–W208.
(32) Chen, L.; Liu, X.; Su, B.; Li, J.; Jiang, L.; Han, D.; Wang, S. Aptamer-Mediated Efficient Capture and Release of T Lymphocytes on Nanostructured Surfaces. *Advanced Materials* **2011**, *23* (38), 4376–4380.
(33) Li, S.; Chen, N.; Zhang, Z.; Wang, Y. Endonuclease-Responsive Aptamer-Functionalized Hydrogel Coating for Sequential Catch and Release of Cancer Cells. *Biomaterials* **2013**, *34* (2), 460–469.
(34) Xu, Y.; Phillips, J. A.; Yan, J.; Li, Q.; Fan, Z. H.; Tan, W. Aptamer-Based Microfluidic Device for Enrichment, Sorting, and Detection of Multiple Cancer Cells. *Analytical Chemistry* **2009**, *81* (17), 7436–7442.
(35) Yoon, J. W.; Jang, I. H.; Heo, S. C.; Kwon, Y. W.; Choi, E. J.; Bae, K.-H.; Suh, D.-S.; Kim, S.-C.; Han, S.; Haam, S.; Jung, J.; Kim, K.; Ryu, S. H.; Kim, J. H. Isolation of Foreign Material-Free Endothelial Progenitor Cells Using CD31 Aptamer and Therapeutic Application for Ischemic Injury. *PloS one* **2015**, *10* (7), e0131785.
(36) Zhu, J.; Nguyen, T.; Pei, R.; Stojanovic, M.; Lin, Q. Specific Capture and Temperature-Mediated Release of Cells in an Aptamer-Based Microfluidic Device. *Lab on a Chip* **2012**, *12* (18), 3504–3513.
(37) Labib, M.; Green, B.; Mohamadi, R. M.; Mepham, A.; Ahmed, S. U.; Mahmoudian, L.;

Chang, I. H.; Sargent, E. H.; Kelley, S. O. Aptamer and Antisense-Mediated Two-Dimensional Isolation of Specific Cancer Cell Subpopulations. *Journal of the American Chemical Society* **2016**, *138* (8), 2476–2479.

(38) Sun, N.; Liu, M.; Wang, J.; Wang, Z.; Li, X.; Jiang, B.; Pei, R. Chitosan Nanofibers for Specific Capture and Nondestructive Release of CTCs Assisted by PCBMA Brushes. *Small* **2016**, *12* (36), 5090–5097.

(39) Wan, Y.; Liu, Y.; Allen, P. B.; Asghar, W.; Mahmood, M. A. I.; Tan, J.; Duhon, H.; Kim, Y.; Ellington, A. D.; Iqbal, S. M. Capture, Isolation and Release of Cancer Cells with Aptamer-Functionalized Glass Bead Array. *Lab on a Chip* **2012**, *12* (22), 4693–4701.

(40) Zhang, Z.; Chen, N.; Li, S.; Battig, M. R.; Wang, Y. Programmable Hydrogels for Controlled Cell Catch and Release Using Hybridized Aptamers and Complementary Sequences. *Journal of the American Chemical Society* **2012**, *134* (38), 15716–15719.

(41) Nozari, A.; Berezovski, M. V. Aptamers for CD Antigens: From Cell Profiling to Activity Modulation. *Molecular Therapy - Nucleic Acids* **2017**, *6* (March), 29–44.

(42) Wang, C. W.; Chung, W. H.; Cheng, Y. F.; Ying, N. W.; Peck, K.; Chen, Y. T.; Hung, S. I. A New Nucleic Acid-Based Agent Inhibits Cytotoxic T Lymphocyte-Mediated Immune Disorders. *Journal of Allergy and Clinical Immunology* **2013**, *132* (3), 713–722.

(43) Seelig, G.; Soloveichik, D.; Zhang, D. Y.; Winfree, E. Enzyme-Free Nucleic Acid Logic Circuits. *Science* **2006**, *314* (5805), 1585–1588.

(44) Yurke, B.; Mills, A. P. Using DNA to Power Nanostructures. *Genetic Programming and Evolvable Machines* **2003**, *4* (2), 111–122.

(45) Yurke, B.; Turberfield, A. J.; Mills, A. P.; Simmel, F. C.; Neumann, J. L. A DNA-Fuelled Molecular Machine Made of DNA. *Nature* **2000**, *406* (6796), 605–608.

(46) Zhang, D. Y.; Seelig, G. Dynamic DNA Nanotechnology Using Strand-Displacement Reactions. *Nature Chemistry* **2011**, *3* (2), 103–113.

(47) Zhang, D. Y.; Winfree, E. Control of DNA Strand Displacement Kinetics Using Toehold Exchange. *Journal of the American Chemical Society* **2009**, *131* (47), 17303–17314.

(48) Ruella, M.; Xu, J.; Barrett, D. M.; Fraietta, J. A.; Reich, T. J.; Ambrose, D. E.; Klichinsky, M.; Shestova, O.; Patel, P. R.; Kulikovskaya, I.; Nazimuddin, F.; Bhoj, V. G.; Orlando, E. J.; Fry, T. J.; Bitter, H.; Maude, S. L.; Levine, B. L.; Nobles, C. L.; Bushman, F. D.; Young, R. M.; Scholler, J.; Gill, S. I.; June, C. H.; Grupp, S. A.; Lacey, S. F.; Melenhorst, J. J. Induction of Resistance to Chimeric Antigen Receptor T Cell Therapy by Transduction of a Single Leukemic B Cell. *Nature Medicine* **2018**, *24* (10), 1499–1503.

(49) Heczey, A.; Liu, D.; Tian, G.; Courtney, A. N.; Wei, J.; Marinova, E.; Gao, X.; Guo, L.; Yvon, E.; Hicks, J.; Liu, H.; Dotti, G.; Metelitsa, L. S. Invariant NKT Cells with Chimeric Antigen Receptor Provide a Novel Platform for Safe and Effective Cancer Immunotherapy. *Blood* **2014**, *124* (18), 2824–2833.

(50) Eyquem, J.; Mansilla-Soto, J.; Giavridis, T.; Van Der Stegen, S. J. C.; Hamieh, M.; Cunanan, K. M.; Odak, A.; Gönen, M.; Sadelain, M. Targeting a CAR to the TRAC Locus with CRISPR/Cas9 Enhances Tumour Rejection. *Nature* **2017**, *543* (7643), 113–117.

(51) Zhao, Z.; Condomines, M.; van der Stegen, S. J. C.; Perna, F.; Kloss, C. C.; Gunset, G.; Plotkin, J.; Sadelain, M. Structural Design of Engineered Costimulation Determines Tumor Rejection Kinetics and Persistence of CAR T Cells. *Cancer Cell* **2015**, *28* (4), 415–428.

(52) Brentjens, R. J.; Latouche, J.-B.; Santos, E.; Marti, F.; Gong, M. C.; Lyddane, C.; King, P. D.; Larson, S.; Weiss, M.; Rivière, I.; Sadelain, M. Eradication of Systemic B-Cell Tumors by Genetically Targeted Human T Lymphocytes Co-Stimulated by CD80 and Interleukin-

15. *Nature Medicine* **2003**, *9* (3), 279–286.
(53) Dahotre, S. N.; Chang, Y. M.; Wieland, A.; Stammen, S. R.; Kwong, G. A. Individually Addressable and Dynamic DNA Gates for Multiplexed Cell Sorting. *Proceedings of the National Academy of Sciences of the United States of America* **2018**, *115* (17), 4357–4362.
(54) Probst, C. E.; Zrazhevskiy, P.; Gao, X. Rapid Multitarget Immunomagnetic Separation through Programmable DNA Linker Displacement. *Journal of the American Chemical Society* **2011**, *133* (43), 17126–17129.
(55) Gawande, B. N.; Rohloff, J. C.; Carter, J. D.; von Carlowitz, I.; Zhang, C.; Schneider, D. J.; Janjic, N. Selection of DNA Aptamers with Two Modified Bases. *Proceedings of the National Academy of Sciences* **2017**, *114* (11), 2898–2903.
(56) Ni, S.; Yao, H.; Wang, L.; Lu, J.; Jiang, F.; Lu, A.; Zhang, G. Chemical Modifications of Nucleic Acid Aptamers for Therapeutic Purposes. *International Journal of Molecular Sciences* **2017**, *18* (8), 1683.
(57) Pelloquin, F.; Lamelin, J. P.; Lenoir, G. M. Human Blymphocytes Immortalization by Epstein-Barr Virus in the Presence of Cyclosporin A. *In Vitro Cellular & Developmental Biology* **1986**, *22* (12), 689–694.
(58) Zadeh, J. N.; Steenberg, C. D.; Bois, J. S.; Wolfe, B. R.; Pierce, M. B.; Khan, A. R.; Dirks, R. M.; Pierce, N. A. NUPACK: Analysis and Design of Nucleic Acid Systems. *Journal of Computational Chemistry* **2011**, *32* (1), 170–173.
(59) Tsai, H.-H.; Li, H.; Fuentealba, L. C.; Molofsky, A. V; Taveira-Marques, R.; Zhuang, H.; Tenney, A.; Murnen, A. T.; Fancy, S. P. J.; Merkle, F.; Kessaris, N.; Alvarez-Buylla, A.; Richardson, W. D.; Rowitch, D. H. Regional Astrocyte Allocation Regulates CNS Synaptogenesis and Repair. *Science* **2012**, *337* (6092), 358–362.
(60) Madugula, V.; Lu, L. A Ternary Complex Comprising Transportin1, Rab8 and the Ciliary Targeting Signal Directs Proteins to Ciliary Membranes. *Journal of Cell Science* **2016**, *129* (20), 3922–3934.
(61) Wang, J.; Jensen, M.; Lin, Y.; Sui, X.; Chen, E.; Lindgren, C. G.; Till, B.; Raubitschek, A.; Forman, S. J.; Qian, X.; James, S.; Greenberg, P.; Riddell, S.; Press, O. W. Optimizing Adoptive Polyclonal T Cell Immunotherapy of Lymphomas, Using a Chimeric T Cell Receptor Possessing CD28 and CD137 Costimulatory Domains. *Human Gene Therapy* **2007**, *18* (8), 712–725.

2.8 SUPPORTING INFORMATION

Table S2.1 | Comparison of different antibody-based cell selection approaches with aptamer-based cell selection. Advantages are marked in green.

	CliniMACS Positive Selection	CliniMACS Depletion	Streptamer-Based Selection	Aptamer-Based Selection
Affinity of Selection Agent	pM-nM	pM-nM	pM-nM (avidity-based)	pM-nM
Method of Production	Biological	Biological	Biological	Chemical
Cost of Production	High, lower if recombinant	High, lower if recombinant	High, lower if recombinant	Low cost if DNA
Batch-to-Batch Variability	High, lower if recombinant	High, lower if recombinant	High, lower if recombinant	Low
Ease of Chemical Modification	Low	Low	Low	High
Traceless Selection	No	Yes	Yes	Yes
Isolation of Multiple, Pure Cell Populations from a Single Selection	No	No	No	Potentially Yes

Table S2.2 | Experimental conditions used in rounds of T cell SELEX.

SELEX Round	Positive Selection	Magnetic Separation	Negative Selection	Aptamer Pool (µM)	BSA (%)	Time (min)
1	4×10^7 T Cells	None	None	14	0.1	60
2	10^7 PBMCs	Depletion	10^7 JRT.3-T3.5 Cells	0.5	0.5	60
3	5×10^6 PBMCs	Depletion	10^7 JRT.3-T3.5 Cells	0.5	0.5	60
4	5×10^6 PBMCs	Depletion	10^7 JRT.3-T3.5 Cells	0.5	1	30
5	2×10^6 PMBCs	Depletion	10^7 JRT.3-T3.5 Cells	0.25	1	30

Table S2.3 | Primers used for next generation sequencing (NGS) of naive library (NL) and T cell SELEX rounds 1-5.

Primer Name	SELEX Round	Sequence	Barcode (in red)
Aptamer_F	NL, 1-5	AATGATACGGCGACCACCGAGATCTACACCGAGGAG ATACCACTAAGCCACCGTGTCCA	
Aptamer_R_77	NL	CAAGCAGAAGACGGCATACGAGATGCAATTCGACAG ACCGTCGATCCAGAGTGACGCAGCA	CGAATTGC
Aptamer_R_78	1	CAAGCAGAAGACGGCATACGAGATCAAGAGGTACAG ACCGTCGATCCAGAGTGACGCAGCA	ACCTCTTG
Aptamer_R_79	2	CAAGCAGAAGACGGCATACGAGATTCGATTAAACAG ACCGTCGATCCAGAGTGACGCAGCA	TTAATCGA
Aptamer_R_80	3	CAAGCAGAAGACGGCATACGAGATGAATGGACACAG ACCGTCGATCCAGAGTGACGCAGCA	GTCCATTC
Aptamer_R_81	4	CAAGCAGAAGACGGCATACGAGATAGAATCAGACAG ACCGTCGATCCAGAGTGACGCAGCA	CTGATTCT
Aptamer_R_82	5	CAAGCAGAAGACGGCATACGAGATAACTGCCAACAG ACCGTCGATCCAGAGTGACGCAGCA	TGGCAGTT

Table S2.4 | Enrichment of top 20 Round 5 (R5) aptamer sequences between rounds of T cell SELEX. Fold enrichment is calculated by dividing the reads per million (RPM) of the sequence from a round by the value of the former round.

				Fold Enrichment			
R5 Rank	**% Representation**	**Motif**	**Sequence**	**R5/R4**	**R4/R3**	**R3/R2**	**R2/R1**
1	63.37	1 (4,2)	CGCAGCACCCGTGGTAGTGTATCAGG GAGACACTACGTGATGCAGCTTGAAA	1.0	317.6	73.4	0.8
2	3.05	3	CGCAGCAAGGTGGCTGTGGGCGGATG GTGGGCTCGCGTGGGCGGCCACCTGA	178.1	152.8		
3	1.10	4,2	ACAGAGGTGTAGAAGTACACGTGAAC AAGCTTGAAATTGTCTCTGACAGAGG	4.6	708.5		
4	0.57	1	CGCAGCACCCGTGGTAGTGTATCATGG AGACACTACGTGATGCAGCTTGAAA	1.3	763.1		
5	0.49	1	CGCAGCACCCGTGGTAGTGTATCAGG GATACACTACGTGATGCAGCTTGAAA	1.7	873.0		
6	0.37	1	CGCAGCACCCGTGGTAGTGTATCAGA GAGACACTACGTGATGCAGCTTGAAA	1.6	409.1		
7	0.36	3	TTAGGAGGTGGGCTCGCGTGCACCAA TCCATGGTCGGCGGGAATTTTAAGGG	116.2			
8	0.34	4,2	GCTCGATCGTATAGCCGTGACGCAGCT TGAAATGGGATCGCGTCCACAGTTT	6.6			
9	0.27	1	CGCAGCGCCCGTGGTAGTGTATCAGG GAGACACTACGTGATGCAGCTTGAAA	0.9	450.6		
10	0.25	3	CGGCCGAACCTCCACCCTTCCGCAGCG TAGGCAGACTCGGATCATGATAATC	1.7	0.7	0.7	0.7
11	0.18	1	CGCAGCAGCCGTGGTAGTGTATCAGG GAGACACTACGTGATGCAGCTTGAAA	1.3	254.5		
12	0.17	1	CGCAGCAACCGTGGTAGTGTATCAGG GAGACACTACGTGATGCAGCTTGAAA	1.6	136.5		
13	0.17	1	CGCAGCACCCGTGGTAGTGTATCGGG GAGACACTACGTGATGCAGCTTGAAA	1.5	331.3		
14	0.12	3	CGCAGCAACGTTATCCCCTTTACGGGG TCCTAGAGCCCCGTGAGTGCTCACG	81.6			
15	0.11	1	CGCAGCTCCCGTGGTAGTGTATCAGGG AGACACTACGTGATGCAGCTTGAAA	1.0	342.9		
16	0.10	1	CGCATCACCCGTGGTAGTGTATCAGGG AGACACTACGTGATGCAGCTTGAAA	0.8	535.4		
17	0.09	1	CGCAGCACCCGTGGTAGTGTATCAGTG AGACACTACGTGATGCAGCTTGAAA	0.8	317.0		
18	0.07	1	CGCAGCCCCCGTGGTAGTGTATCAGG GAGACACTACGTGATGCAGCTTGAAA	1.1	309.6		
19	0.05	1	ACGCAGCACCCGTGGTAGTGTATCAG GAGACACTACGTGATGCAGCTTGAAA	1.0	151.5		
20	0.05	1	CGCAGCACCCGTGGTAGTGTATCAGG GAGACACTACGTGATGCAGCTTAAAA	3.0			

Table S2.5 | Sequences of aptamers and reversal agent used in experiments. Text within slashes "/" represent IDT modification codes, and underlined base pairs represent constant regions. Red and green text represent base pairs that were deleted and inserted, respectively, to make the A3t aptamer with an extended 8-bp toehold.

Name	Sequence
A1	5'-/56-FAM/ATCCAGAGTGACGCAGCACGCAGCACCCGTGGTAGTGTATCAGGGAGACACTACGTGATG CAGCTTGAAATGGACACGGTGGCTTAGT-3'
A2	5'-/56-FAM/ATCCAGAGTGACGCAGCACGCAGCAAGGTGGCTGTGGGCGGATGGTGGGCTCGCGTGGG CGGCCACCTGATGGACACGGTGGCTTAGT-3'
A3	5'-/56-FAM/ATCCAGAGTGACGCAGCAACAGAGGTGTAGAAGTACACGTGAACAAGCTTGAAATTGTCTC TGACAGAGGTGGACACGGTGGCTTAGT-3'
A7	5'-/56-FAM/ATCCAGAGTGACGCAGCATTAGGAGGTGGGCTCGCGTGCACCAATCCATGGTCGGCGGGA ATTTTAAGGGTGGACACGGTGGCTTAGT-3'
A8	5'-/56-FAM/ATCCAGAGTGACGCAGCAGCTCGATCGTATAGCCGTGACGCAGCTTGAAATGGGATCGCG TCCACAGTTTTGGACACGGTGGCTTAGT-3'
A3t	5'-/5BiosG//iSp18/CCAGAGTGACGCAGCAACAGAGGTGTAGAAGTACACGTGAACAAGCTTGAAATTGTC TCTGACAGAGGTGGACACGGTGGCTTTTAGT-3'
RA	ACTAAAAGCCACCGTGTCCACCTCTGTCAGAGACAA

Table S2.6 | siRNA duplexes used for CD8 knockdown.

Name	Sequence
hs.Ri.CD8A.13.1-SEQ1	rCrGrArGrGrArGrGrUrArArUrGrArArUrUrArArArGrArAGA
hs.Ri.CD8A.13.1-SEQ2	rUrCrUrUrCrUrUrUrArArUrUrCrArUrUrArCrCrUrCrCrUrCrGrArG
hs.Ri.CD8A.13.2-SEQ1	rCrUrUrGrCrUrUrArArGrGrUrArUrGrGrUrArCrArArGrCAA
hs.Ri.CD8A.13.2-SEQ2	rUrUrGrCrUrUrGrUrArCrCrArUrArCrCrUrUrArArGrCrArArGrGrA

Table S2.7 | Bio-layer interferometry (BLI) measured affinity and kinetics of A1, A3, and A8 aptamer binding to recombinant CD8a protein. Data are mean ± s.d., n = 3 individual concentrations for A1 and 4 individual concentrations for A3 and A8. Values were calculated by performing a global fit of the binding curve data in **Figure 2.2d** to a 1:1 binding model. The ratio between the dissociation rate constant (K_{dis}) and the association rate constant (K_{on}) give the equilibrium dissociation constant (K_D). The goodness of fit was evaluated by a reduced chi-square (χ^2) and a R^2 value approaching 1.

Aptamer	K_D (nM)	K_{on} ($nM^{-1}s^{-1}$) × 10^{-6}	K_{dis} (s^{-1}) × 10^{-4}	Full χ^2	Full R^2
A1	20.1 (±0.2)	6.079 (±0.026)	1.222 (±0.013)	0.1234	0.9995
A3	14.7 (±0.1)	13.850 (±0.035)	2.036 (±0.014)	0.2700	0.9992
A8	5.59 (±0.11)	6.364 (±0.014)	0.356 (±0.004)	0.0595	0.9998

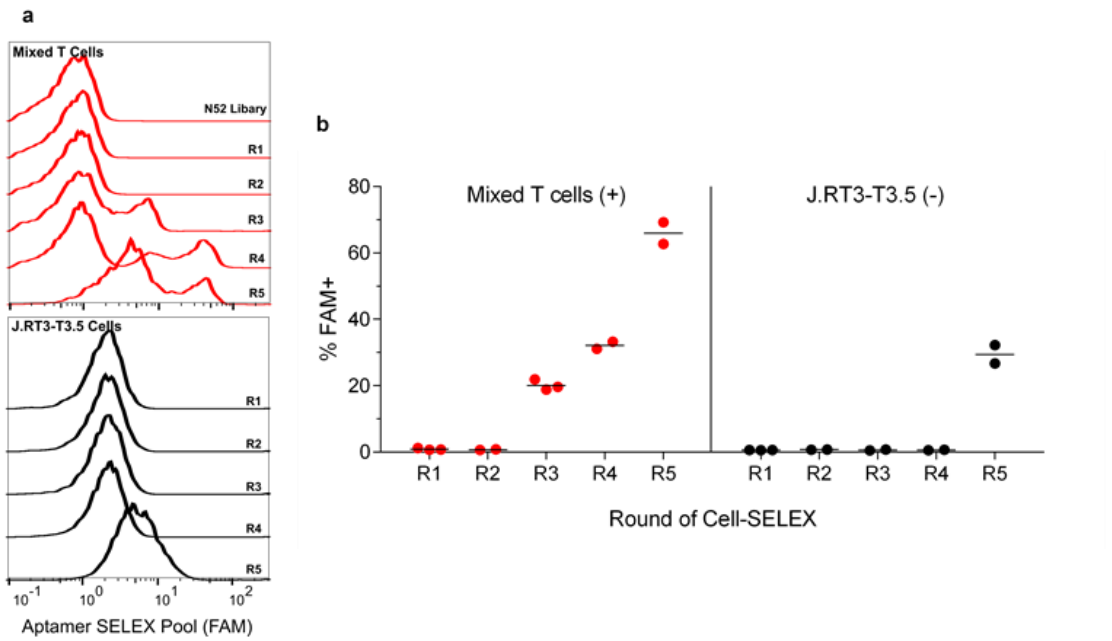

Figure S2.1 | Binding of aptamer pools from different rounds of T cell SELEX to T cells and J.RT3-T3.5 cells. (a) Flow cytometry histograms of 250 nM aptamer pool binding to positive selection mixed T cells and negative selection J.RT3-T3.5 cells after consecutive rounds of SELEX. (b) Corresponding percentages of cells that stained positive with the aptamer pools from the different rounds. Individual data points represent technical replicates with the horizontal bar representing the mean.

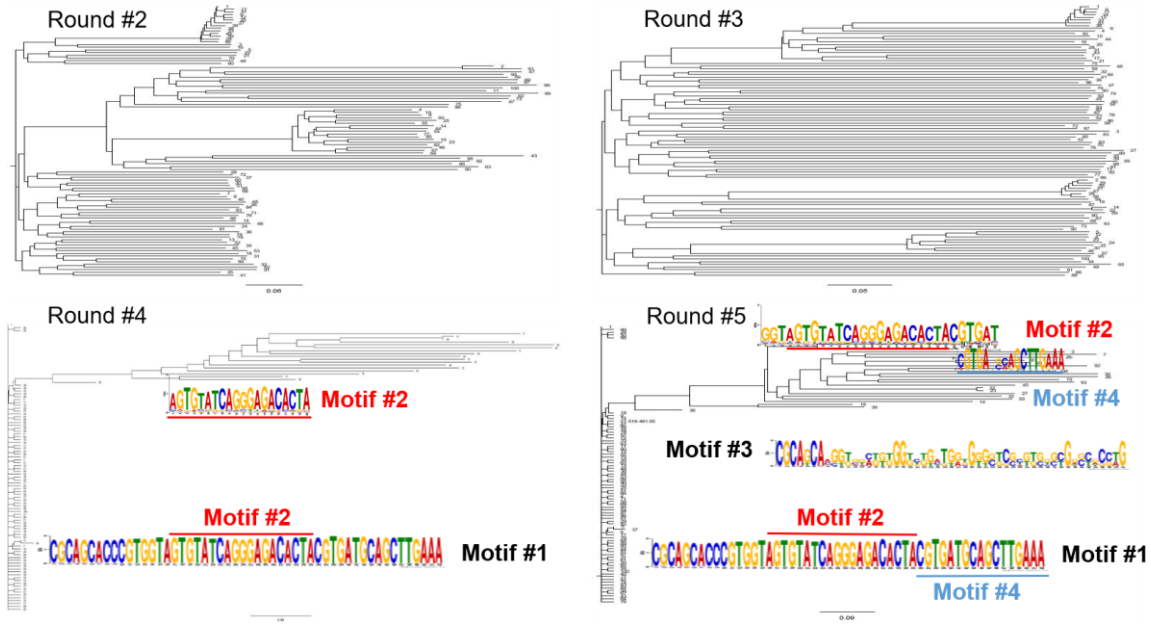

Figure S2.2 | Phylogenetic trees of top 100 aptamers from consecutive rounds of T cell SELEX and emerging consensus motifs. Phylogenetic trees were generated with FigTree software (http://tree.bio.ed.ac.uk/software/figtree/), and binding motifs predicted using MEME analysis (MEME-suite.org).

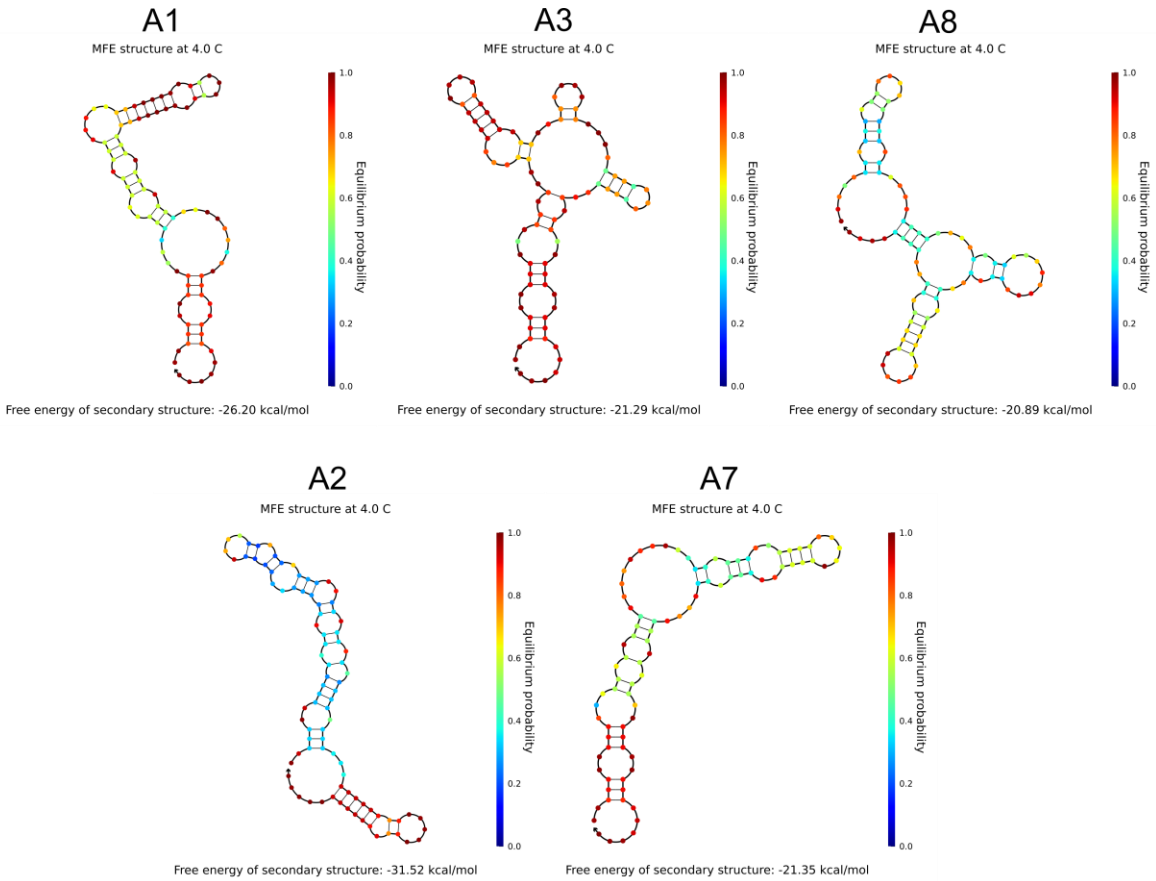

Figure S2.3 | Predicted minimum free energy (MFE) secondary structures of A1, A2, A3, A7, and A8 aptamers. Aptamers are named according to their Round 5 rank. Structures were calculated using NUPACK software (*temp* = 4C; Na^{+} = 137mM; Mg^{++} = 5.5mM).

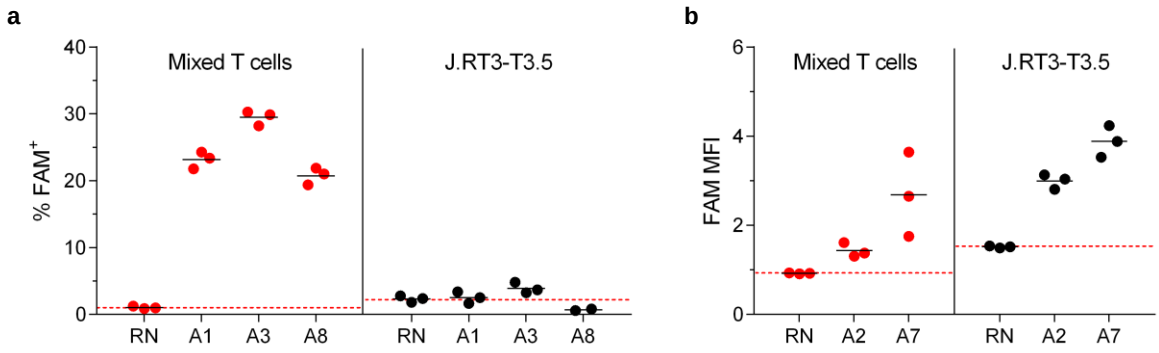

Figure S2.4 | Binding of selected individual aptamers to T cells and J.RT3-T3.5 cells. (a) Flow cytometry analysis of the percentage of mixed T cells and J.RT3-T3.5 cells that stained positive with 50 nM of a random (RN) aptamer and A1, A3, and A8 aptamers. Individual data points represent technical replicates with the horizontal bar representing the mean. (b) Flow cytometry analysis of the median fluorescence intensity (MFI) of 50 nM RN, A2, and A7 aptamer binding to mixed T cells and J.RT3-T3.5 cells. Individual data points represent technical replicates (n = 3) with the horizontal bar representing the mean.

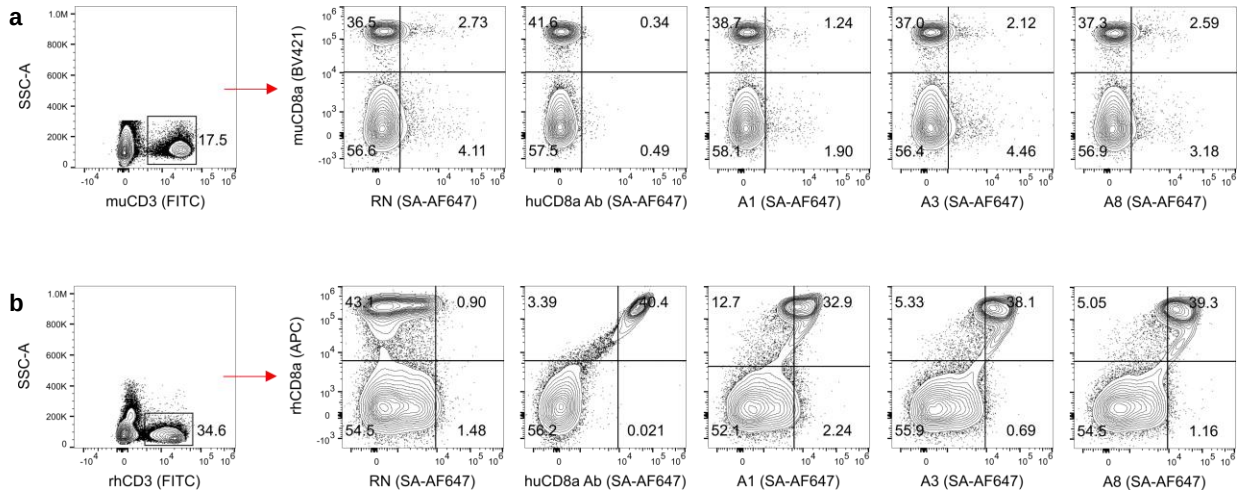

Figure S2.5 | A1, A3, and A8 aptamer binding to murine spleen T cells and rhesus macaque PBMCs. (a) Flow cytometry plots show CD8a Ab and 50 nM RN, A1, A3, and A8 binding to $CD3^+CD8^+$ murine (mu) spleen T cells. Plots are representative of 3 biological replicates. (b) Similar plots that show binding to $CD3^+CD8^+$ rhesus (rh) PBMCs. Plots are representative of 1 biological replicate.

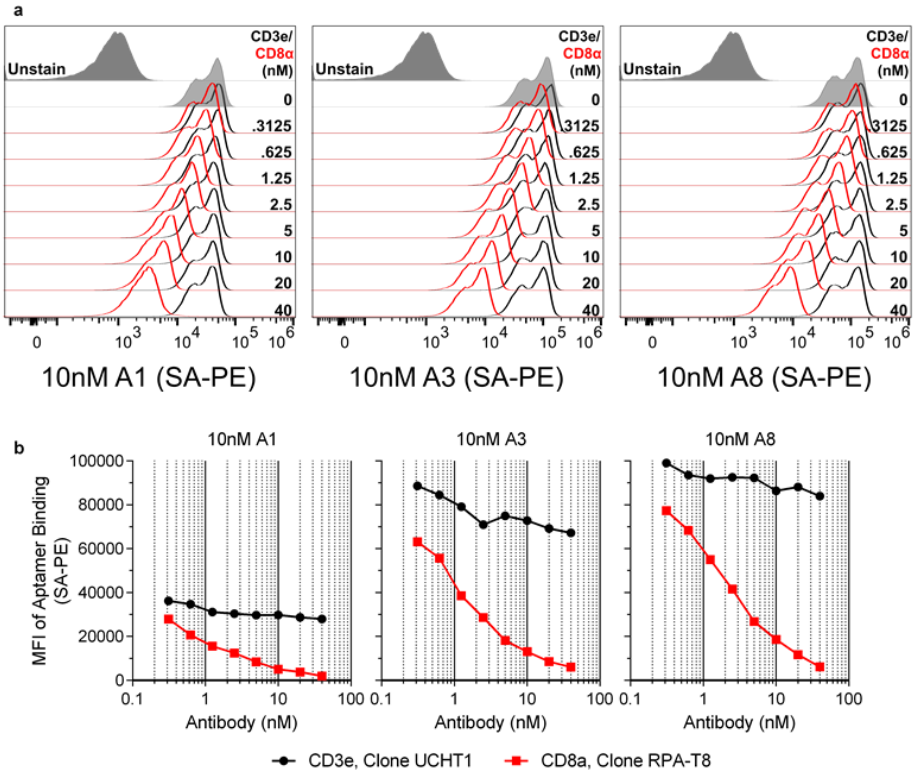

Figure S2.6 | Competitive binding of different CD8a antibody concentrations with fixed concentration of A1, A3, and A8 aptamers. (a) Flow cytometry histograms of 10 nM A1, A3, & A8 binding to $CD8^+$ T cells in the presence of 0 to 40 nM of control CD3e antibody or competitive CD8a antibody. Histograms are representative of 1 biological replicate. (b) Corresponding MFIs of aptamer binding. Data are $n = 1$ biological replicate.

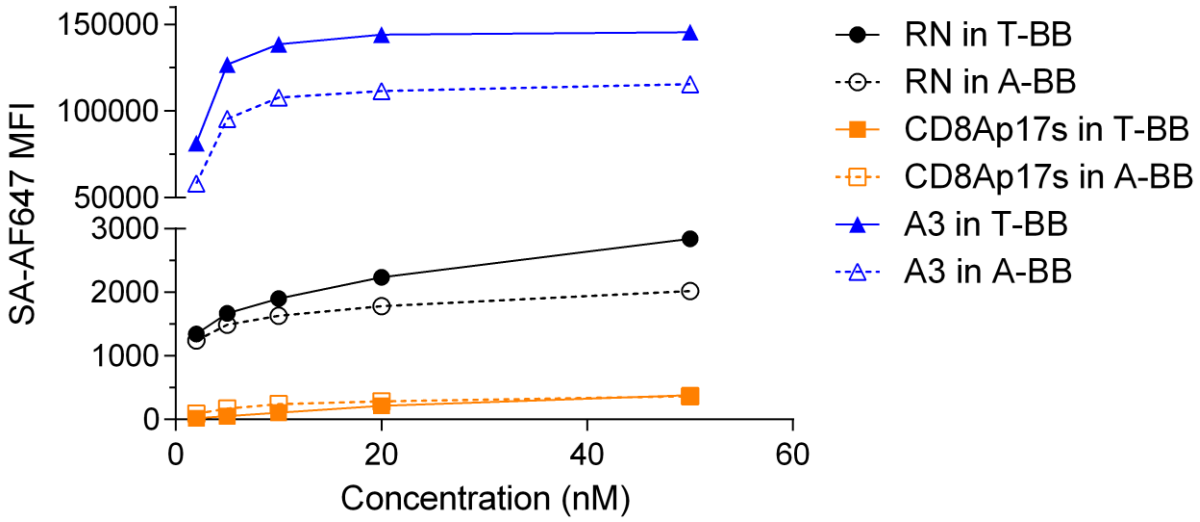

Figure S2.7 | Binding of A3 aptamer and a previously reported CD8 DNA aptamer from the literature to CD8$^+$ T cells. Chart shows MFI of RN, published CD8Ap17s, and A3 binding to CD8$^+$ T cells at a range of concentrations under our binding conditions (T-BB) and the published aptamer's binding conditions (A-BB). Binding conditions account for the buffer used and the annealing conditions. Data are mean, *n* = 3 technical replicates.

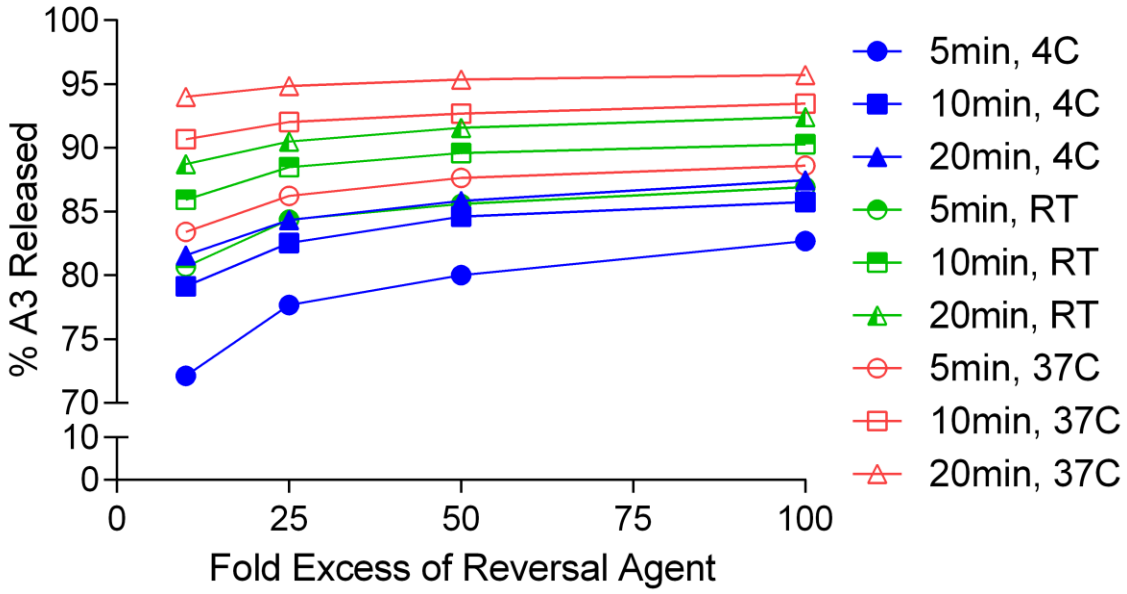

Figure S2.8 | Optimization of A3t aptamer release using complementary reversal agent. Flow cytometry analysis of the percentage of A3t aptamer released (5 nM) from CD8$^+$ T cells at different fold excess concentrations of and incubation times and temperatures with reversal agent (RA). Release was calculated using the MFI at the given condition and dividing it by the MFI of staining without reversal agent at a given temperature. Data are mean, *n* = 3 technical replicates.

a

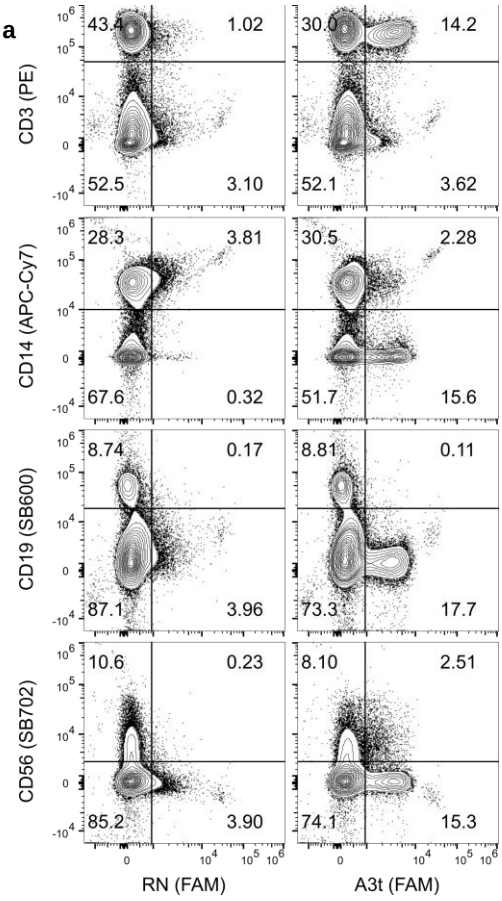

b

Cell Type	% of PBMCs	% RN+ of Cell Type (FAM)	MFI of RN+ Cells (FAM)	% A3t+ of Cell Type (FAM)	MFI of A3t+ Cells (FAM)
$CD3^+CD56^-$ T Cells	44.7 (±1.3)	2.2 (±0.7)	565 (±139)	34.6 (±3.6)	2166 (±138)
$CD3^+CD56^+$ NKT Cells	3.0 (±1.3)	2.0 (±0.6)	493 (±111)	69.2 (±25.5)	2595 (±775)
$CD3^-CD56^+$ NK Cells	11.1 (±3.8)	1.5 (±0.3)	375 (±80)	18.4 (±12.3)	422 (±116)
$CD3^-CD56^-CD14^+$ Monocytes	21.5 (±8.2)	7.5 (±0.9)	752 (±283)	3.6 (±0.3)	407 (±105)
$CD3^-CD56^-CD19^+$ B Cells	11.6 (±9.3)	0.0 (±0.0)	213 (±54)	0.0 (±0.0)	132 (±42)
Sum	91.9 (±1.3)				

Figure S2.9 | RN and A3t aptamer binding to different cell types within PBMCs. (a) Flow cytometry plots show CD3, CD14, CD19, and CD56 antibody and 5 nM RN and A3t aptamer binding to PBMCs. Plots are representative of 3 biological replicates. (b) Corresponding statistics of RN and A3t aptamer binding to different cell types that make up approximately 92% of the PBMC population. The percentage of each cell type that stained positive with aptamer is a statistic of the parent population and not total PBMCs. MFI values were normalized by subtracting out the fluorescence value that was used to delineate aptamer negative and positive cells. Data are mean ± s.d., n = 3 biological replicates.

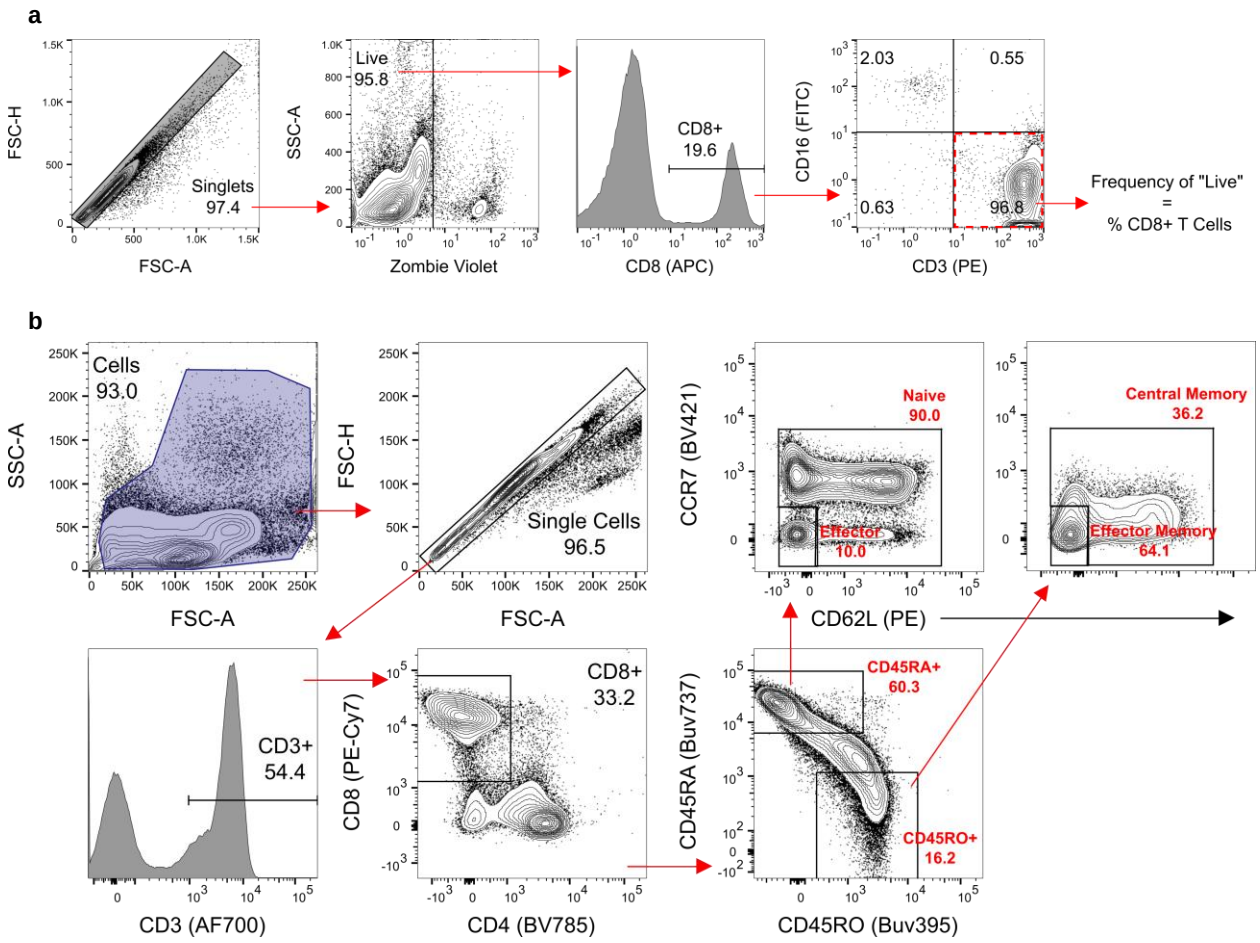

Figure S2.10 | Flow cytometry gating strategies for yield, purity, and phenotype analyses. (a) Gating schemes for determining the percentage of $CD8^+$ T cells in a sample and thus the purity and yield of an isolation fraction. The percentage of $CD8^+$ T cells was determined by using the percentage of $CD8^+CD3^+CD16^-$ cells of live cells, as $CD8^{lo}CD3^-CD16^+$ cells represent monocytes and NK cells. Pre-selected PBMCs are shown in this example. (b) Gating schemes for determining the phenotype of $CD8^+$ T cells in either PBMCs or isolated cell fractions. CD45RA and CD45RO expression was used to differentiate naive/effector (N/E) cells from central/effector memory (CM/EM) cells, respectively, and CD62L and CCR7 expression (single or double) were used together to identify N/CM cells from non-expressing E/EM cells. Cells that were CD45RA/RO double positive and not gated on were identified as transitioning cells. Pre-selected PBMCs are shown in this example.

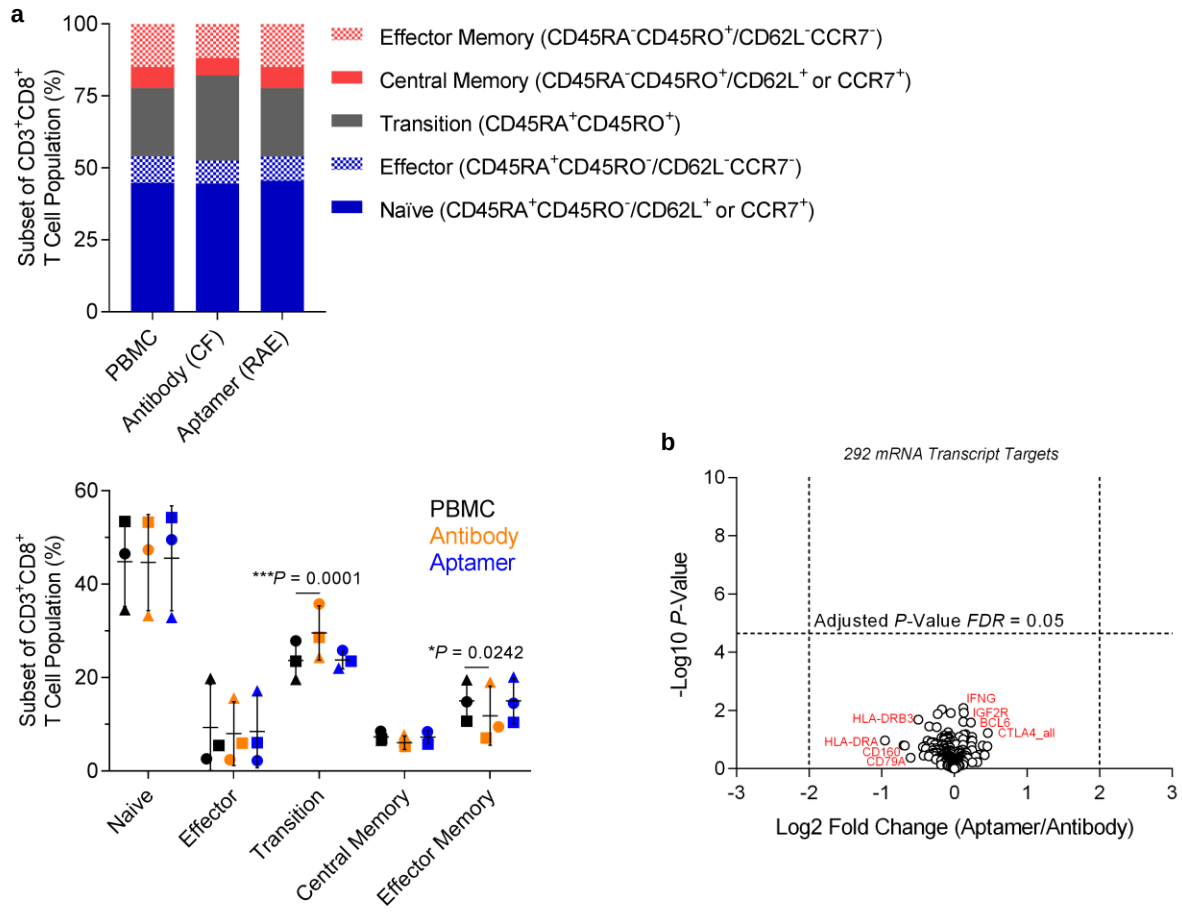

Figure S2.11 | Flow cytometry phenotype and NanoString gene expression profiling of antibody- and aptamer-isolated CD8$^+$ T cells. (a) Flow cytometry analysis of the different phenotypes of CD8$^+$ T cells in PBMCs, antibody-isolated cell fraction, and traceless aptamer-isolated cell fraction. Bar chart (top) shows mean percentages of the phenotypes (normalized to add up to 100) of 3 independent experiments. Grouped chart (bottom, left) indicates corresponding individual values of the different phenotypes, with symbols representing different donors from separate isolation experiments. Data are mean ± s.d., $n = 3$, $^*P < 0.05$ and $^{***}P < 0.001$ (paired two-way ANOVA with Dunnett's test). All other pair-wise comparisons to PBMCs have $P > 0.4$. (b) NanoString differential expression analysis of 292 genes identified as being expressed above background in the nCounter Human Immunology v2 Panel. Fold change values indicate the expression of traceless aptamer-isolated cells relative to antibody-isolated cells and are representative of 3 biological replicates. Data are mean ± s.d., $n = 3$ (two-sided paired t-test with Benjamini-Yekutieli correction).

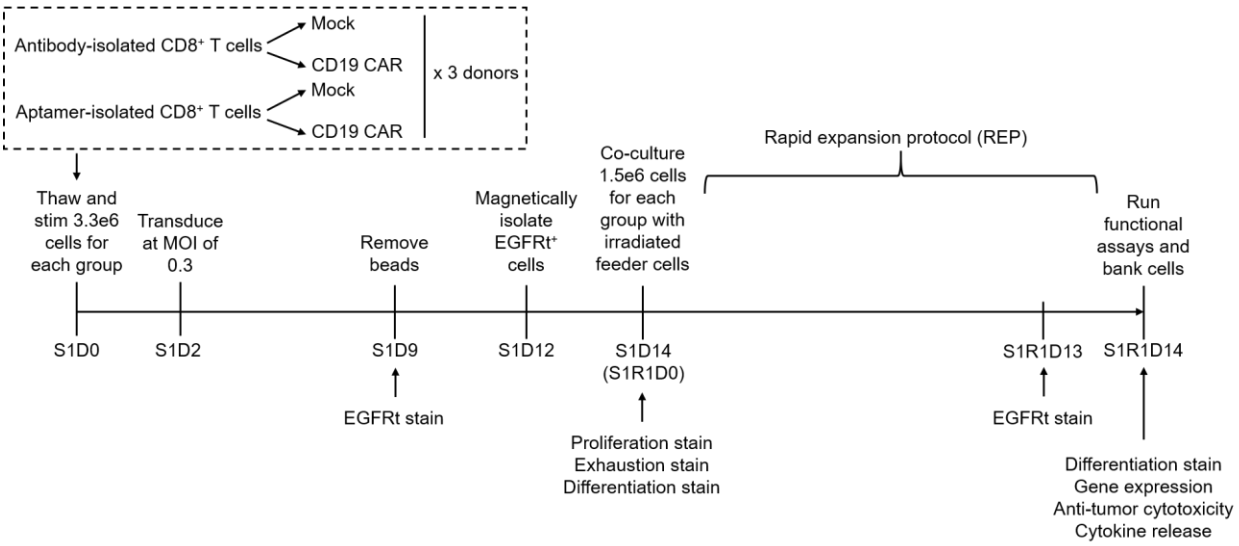

Figure S2.12 | Timeline of CAR T cell production, outgrowth, and characterization. Banked antibody-isolated and traceless aptamer-isolated $CD8^+$ T cells from 3 healthy donors were thawed, split into two groups of 3.3×10^6 cells, and stimulated with activator beads. Stimulation-mediated outgrowth was carried out for two weeks: one of the groups was transduced retrovirally with CD19 CAR on day 2 (S1D2), cells were removed from beads and stained for EGFRt transduction reporter on day 9 (S1D9), $EGFRt^+$ cells were magnetically enriched on day 12 (S1D12), and lastly cells were characterized for differentiation, activation/proliferation, and exhaustion on day 14 (S1D14). On S1D14, 1.5×10^6 cells from each sample were then placed into a two-week rapid expansion protocol (REP), in which they were co-cultured with irradiated feeder cells. On day 13 or REP (S1R1D13), enrichment of CAR^+ T cells was assessed via EGFRt stain. Lastly, on day 14 of REP (S1R1D14), cells were functionally characterized using anti-tumor cytotoxicity and cytokine release assays and phenotypically characterized for differentiation and gene expression.

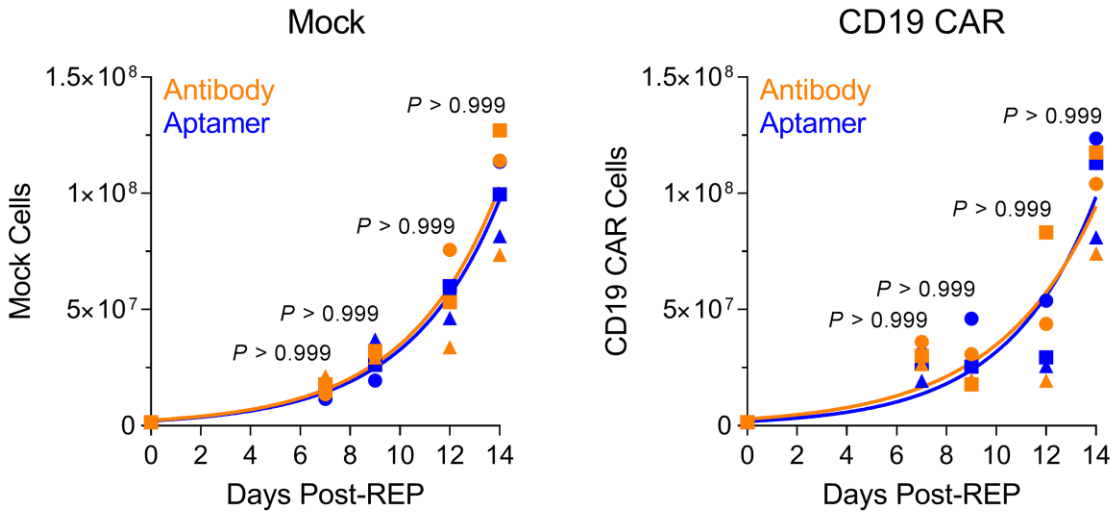

Figure S2.13 | Growth of non-transduced mock and transduced CD19 CAR T cells post-REP. Symbols as in **Figure S2.11a**, $n = 3$, $P > 0.05$ (paired two-way ANOVA with Bonferroni correction). Curves represent a least-squares fit to the exponential growth equation.

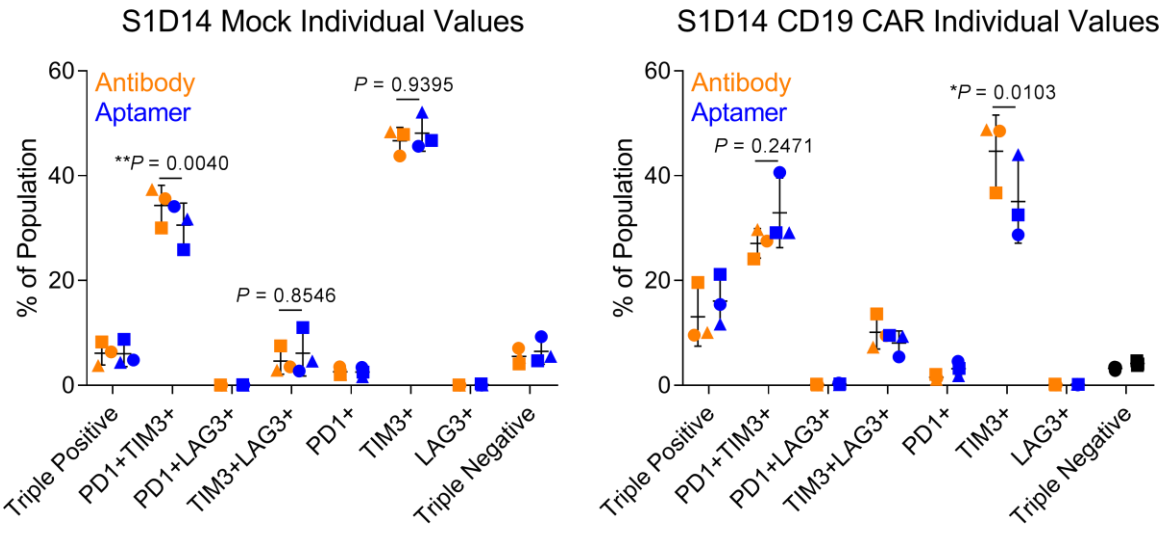

Figure S2.14 | Individual values of PD1/TIM3/LAG3 expression in S1D14 antibody- and aptamer-isolated mock and CD19 CAR T cells. Data is representative of the pie charts in **Figure 2.5e**. Symbols as in **Figure S2.11a**. Data are mean ± s.d., $n = 3$, $P > 0.05$, $*P < 0.05$ and $**P < 0.01$ (paired two-way ANOVA with Bonferroni correction). All other pair-wise comparisons between antibody- and aptamer-isolated cells have $P > 0.999$.

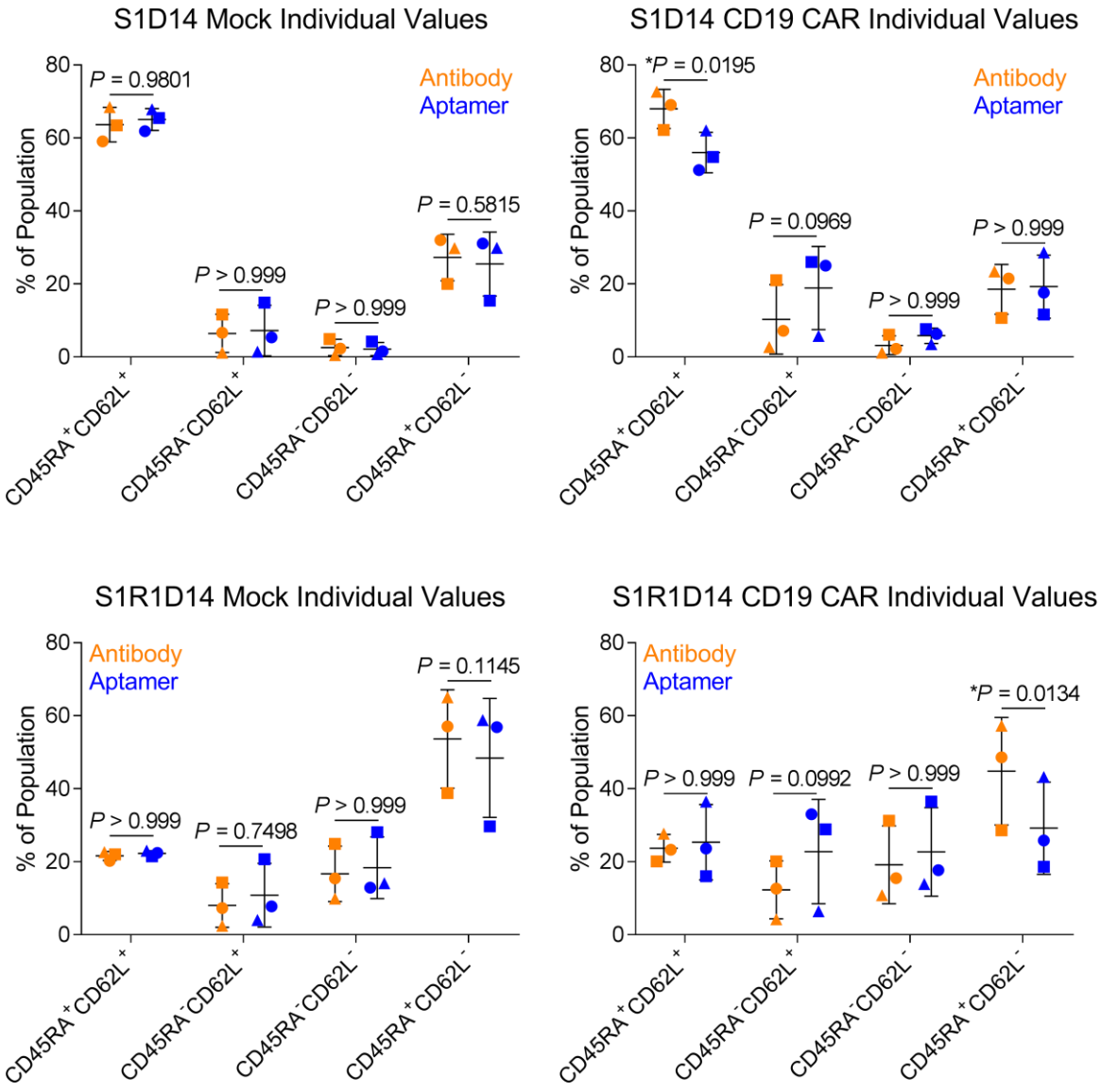

Figure S2.15 | Individual values of CD62L/CD45RA expression in S1D14 and S1R1D14 antibody- and aptamer-isolated mock and CD19 CAR T cells. Data is representative of the pie charts in **Figure 2.5f**. Symbols as in **Figure S2.11a**. Data are mean ± s.d., $n = 3$, and $P > 0.05$ and $*P < 0.05$ (paired two-way ANOVA with Bonferroni correction).

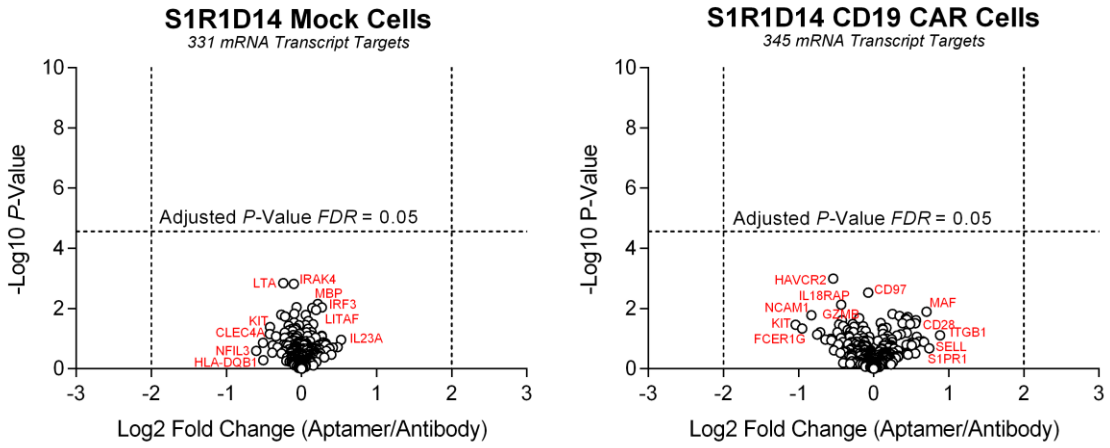

Figure S2.16 | NanoString gene expression profiling of S1R1D14 antibody- and aptamer-isolated mock and CD19 CAR T cells. Differential expression analysis was conducted for 331 and 335 genes identified as being expressed above background in the nCounter Human Immunology v2 Panel for mock and CD19 CAR T cells, respectively. Fold change values indicate the expression of traceless aptamer-isolated cells relative to antibody-isolated cells and are representative of 3 biological replicates. Data are mean ± s.d., n = 3 (two-sided paired t-test with Benjamini-Yekutieli correction).

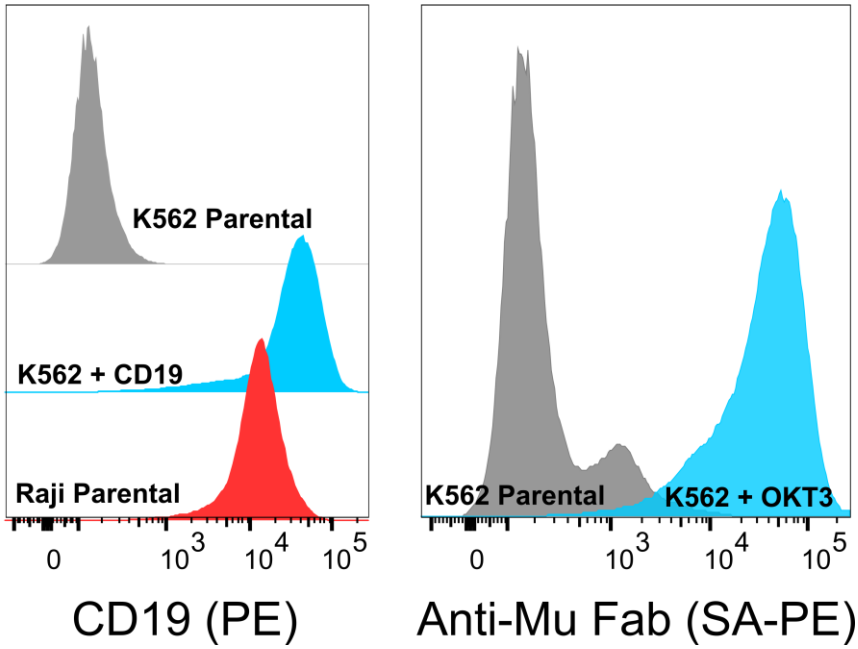

Figure S2.17 | Expression of tumor antigens on target cell lines used for T cell functional studies. Histograms (left) indicate extracellular CD19 expression in K562 parental (negative control), K562 + CD19, and Raji parental cells that is targeted by the CAR. Histograms (right) indicate extracellular OKT3 Fab expression in K562 parental and K562 + OKT3 (positive control) cells that is targeted by the TCR/CD3. Histograms are representative of 1 independent experiment.

Chapter 3: Discovery of a transferrin receptor 1-binding aptamer and its application in cancer cell depletion for adoptive T-cell therapy manufacturing

Emmeline L. Cheng, Ian I. Cardle,* Nataly Kacherovsky,* Harsh Bansia,* Tong Wang,* Yunshi Zhou, Jai Raman, Albert Yen, Dominique Gutierrez, Stephen J. Salipante, Amédée des Georges, Michael C. Jensen, Suzie H. Pun*

ABSTRACT

The clinical manufacturing of chimeric antigen receptor (CAR) T cells includes cell selection, activation, gene transduction, and expansion. While the method of T-cell selection varies across companies, current methods do not actively eliminate the cancer cells in the patient's apheresis product from the healthy immune cells. Alarmingly, it has been found that transduction of a single leukemic B cell with the CAR gene can confer resistance to CAR T-cell therapy and lead to treatment failure. In this study, we report the identification of a novel high-affinity DNA aptamer, termed tJBA8.1, that binds transferrin receptor 1 (TfR1), a receptor broadly upregulated by cancer cells. Using competition assays, high resolution cryo-EM, and *de novo* model building of the aptamer into the resulting electron density, we reveal that tJBA8.1 shares a binding site on TfR1 with holo-transferrin, the natural ligand of TfR1. We use tJBA8.1 to effectively deplete B lymphoma cells spiked into PBMCs with minimal impact on the healthy immune cell composition. Lastly, we present opportunities for affinity improvement of tJBA8.1. As TfR1 expression is broadly upregulated on many cancers, including difficult to treat T-cell leukemias and lymphomas, our work provides a facile, universal, and inexpensive approach for comprehensively removing cancerous cells from patient apheresis product for safe manufacturing of adoptive T-cell therapies.[3]

[3]Chapter reproduced from: Cheng, E.L., Cardle, I.I., Kacherovsky, N., Bansia, H., Wang, T. *et al*. Discovery of a Transferrin Receptor 1-Binding Aptamer and Its Application in Cancer Cell Depletion for Adoptive T-Cell Therapy Manufacturing. *J. Am. Chem. Soc.* **3**, 13851-13864 (2022). Copyright 2022 American Chemical Society. http://pubs.acs.org/articlesonrequest/AOR-WSFIRECG3TNBGG2G64UG

3.1 INTRODUCTION

Chimeric antigen receptor (CAR) T-cell therapy has gained significant traction in the oncology field, with six FDA-approved therapies to-date: four for treating relapsed or refractory (r/r) $CD19^+$ B-cell malignancies (Novartis's Kymriah, Gilead-Kite's Yescarta and Tecartus, and Bristol Myers Squibb-Juno Therapeutic's Breyanzi) and another two for treating r/r $BCMA^+$ multiple myeloma (Bristol Myers Squibb-2seventy bio's Abecma and Janssen Pharmaceuticals-Legend Biotech's Carvykti).[1–8] In these treatments, a patient's T cells journey through an elaborate manufacturing process that consists of 1) enrichment from a leukapheresis product, 2) activation *ex vivo*, 3) lentiviral or retroviral expression of a CAR that directs T-cell function against a tumor-associated antigen, 4) expansion to therapeutically relevant numbers, and 5) re-infusion into the patient's body for cancer elimination.[9] Given the intricate nature of this operation, there is a continual need for further innovation at each production step to reduce the costs and increase the efficacy and safety of these adoptive T-cell therapies.[10]

T-cell enrichment or selection is a pivotal step in CAR T-cell manufacturing, as the cell composition and purity used in subsequent activation and transduction steps can influence the outcome of the therapy. For Kymriah, Yescarta, and Abecma, T cells are indirectly enriched by collecting peripheral blood mononuclear cells (PBMCs) from leukapheresis product using counterflow centrifugal elutriation, which removes most monocytes, granulocytes, platelets, and residual red blood cells based on differences in cell size and density relative to lymphocytes.[11–13] However, this selection approach is unable to discriminate healthy T cells from circulating cancerous lymphocytes, thereby retaining tumor cells in downstream manufacturing steps that can drive uncontrollable activation and exhaustion of the CAR T-cell product.[14] Additionally transduction of a single leukemic B cell with the CAR gene during CAR T-cell manufacturing

caused in *cis* epitope masking that led to a patient's relapse and eventual death.[15] These issues highlight the need for complete removal of cancerous lymphocytes during the selection step prior to further CAR T-cell manufacturing.

To address this problem, especially for patients with high circulating blast and leukemia cell counts, Tecartus, Breyanzi, and Carvykti rely on direct isolation of T cells. Whereas Tecartus and Carvykti isolate bulk $CD3^+$ T cells,[5,16] Breyanzi separately isolates helper $CD4^+$ T cells and cytotoxic $CD8^+$ T cells for CAR T-cell production and later infuses the patient with a defined 1:1 composition of the subsets.[6] Breyanzi is associated with lower rates of cytokine release syndrome and neurotoxicity than Kymriah and Yescarta while remaining equally effective.[2,3,6] However, the direct isolation of T cells is expensive, typically relying on costly antibody- or multimerized Fab-coated magnetic beads that target either the CD3, CD4, and/or CD8 T-cell markers for positive enrichment or unwanted immune cell markers for negative enrichment.[17] Furthermore, these approaches do not actively remove the cancer cells from a patient's leukapheresis product. In contrast to B-cell malignancies, malignant T cells can be difficult to separate from healthy T cells used for manufacturing CAR T-cell therapies.[18,19] Accordingly, as autologous CAR T-cell therapies are broadened to treat diverse hematological malignancies, an inexpensive and universal method for removing cancerous cells from healthy PBMCs will be imperative for their safe manufacturing.

DNA aptamers, single-stranded oligonucleotides that fold into sequence-specific secondary structures, are molecular recognition agents that can address the current deficiencies of cancer cell removal in adoptive T-cell manufacturing. Aptamers can bind their targets with affinities comparable to antibodies, but unlike antibodies they are synthesized chemically with high reproducibility and relatively low cost.[20] Aptamers can also be controllably modified at any

position for facile immobilization onto solid supports (e.g., hydrogels) for affinity-based separations.[21] Finally, aptamer binding to their targets can be reversed by disrupting aptamer structure, for example, by use of a complementary sequence.[21,22] Demonstrating these points, our group previously identified CD8-binding DNA aptamers and used them to tracelessly isolate $CD8^+$ T cells via magnetic-activated cell sorting (MACS) with comparable purity, yield, and downstream CAR functionality as those isolated from commercial antibody-based methods.[23]

Aptamers can be identified through a library selection approach.[24–26] The panning process in which aptamers go through rounds of positive and negative selection against whole cells, termed cell-SELEX (systematic evolution of ligands by exponential enrichment), has become an attractive method for discovering aptamers that can differentiate malignant cells from healthy normal cells.[27] Cell-SELEX thus holds great promise for discovering DNA aptamers that can selectively bind and deplete circulating leukemia and lymphoma cells from PBMCs at low cost prior to CAR T-cell manufacturing.

Here, we report the discovery, characterization, and application of a high-affinity transferrin receptor 1 (TfR1, also known as CD71)-binding aptamer for cancer cell depletion in CAR T-cell manufacturing. The aptamer, named tJBA8.1 after its truncation, was discovered by cell-SELEX using Jurkat T-leukemia cells for positive selection. Pull-down assays identified TfR1, an iron-uptake receptor not expressed on resting immune cells but upregulated on actively dividing and cancerous cells, as the binding target of tJBA8.1. We characterized the tJBA8.1-TfR1 interaction by flow cytometry, biolayer interferometry, and competition studies with holo-transferrin. In addition, we present the first cryogenic electron microscopy (cryo-EM) map of TfR1 in complex with an aptamer, which we used to guide *de novo* model building of tJBA8.1 and its interactions with TfR1. As proof of concept, we further employed tJBA8.1 in MACS to remove spiked Raji B-

lymphoma cells from PBMCs with high yield and minimal impact on the healthy immune cell composition. Lastly, we describe a point mutation to the aptamer sequence for affinity improvement. Given the broad expression of TfR1 on many cancers, including difficult-to-distinguish T-cell leukemias and lymphomas, we anticipate that this method could be universally used for the depletion of circulating cancer cells from patient PBMCs prior to downstream CAR T-cell manufacturing, leading to a safer, more potent, and cost-mindful therapy.

3.2 RESULTS

3.2.1 Discovery of the Jurkat-Binding Aptamer 8.1 (JBA8.1) by cell-SELEX and stem truncation to tJBA8.1

In an initial effort to identify aptamers that bind the human CD3 and CD28 T-cell receptors, we performed cell-SELEX using $CD3^+CD28^+$ Jurkat T-leukemia cells for positive selection and $CD3^-CD28^-$ J.RT3-T3.5 cells, a chemically-generated mutant of the Jurkat cell line, for negative/counter selection (**Figure 3.1A**).[28] We started with an initial positive selection against Jurkat cells with a naive library of 10^{16} theoretical unique ssDNA sequences and then completed seven additional rounds of sequential positive selection with Jurkat cells and negative selection with J.RT3-T3.5 cells with increased stringency (**Table S3.1**). Prior to cell binding, aptamer sequences were folded by heating in DPBS supplemented with ~0.9 mM Ca^{2+} and ~5.5 mM Mg^{2+} ions for 5 min at 95 °C followed by snap cooling on ice, and further details on folding and binding conditions are provided in the Methods section. Flow cytometry binding of aptamer pools from the individual SELEX rounds revealed substantial binding to both Jurkat and J.RT3-T3.5 cells starting in round 5 that plateaued by round 8 (**Figure S3.1**). We observed preferential binding of aptamer pools to Jurkat

cells in later selection rounds, but differences in cell size and absolute number of receptors per cell may have biased binding to larger Jurkat cells.

We conducted next generation sequencing (NGS) of the ssDNA pools from all 8 rounds using the primers detailed in **Table S3.2** and analyzed the results using FASTAptamer toolkit to calculate fold-enrichment of unique aptamer sequences over rounds of cell-SELEX.[29] As unique sequence reads were low for rounds 1-4, we only used FigTree software and MEME analysis on the top 50 aptamers sequences over later rounds 5-8 to generate phylogenetic trees and identify consensus motifs, respectively (**Figure S3.2**).[30,31] In round 5, top aptamer sequences were primarily characterized by one of three short motifs (Motifs 1, 2, and 3) with low individual sequence representation (<0.4%). Sequence representation progressively increased in rounds 6 and 7, with top sequences representing as much as 6.3% and 10.6% of the pool, respectively. By round 8, Motif 3 expanded to encompass the whole 45-nucleotide (nt) random region and a new 40-nt motif, Motif 5, emerged, with top aptamers belonging to each motif displaying robust tree clustering and thus high sequence similarity. Notably, the most prevalent aptamer in round 8, which belonged to Motif 3, represented 21.1% of the entire sequence pool. **Table S3.3** lists the predicted motifs, sequences, and the round-by-round enrichment of the top 50 aptamers identified from round 8.

We selected nine Jurkat-binding aptamers from round 8 (**Table S3.4**), named JBA8.X (where "X" is the aptamer's rank in **Table S3.3**), for cell binding studies based on their representation, motif, and enrichment across rounds. None of the selected fluorescein-labeled aptamers displayed specific binding for Jurkat cells over J.RT3-T3.5 cells, indicating that the SELEX process did not enrich CD3- or CD28-binding aptamers (**Figure 3.1B**). Fluorescein-labeled JBA8.1 from Motif 3, JBA8.3, JBA8.7, and JBA8.11 from Motif 2, and JBA8.4 without a motif all displayed robust binding to both Jurkat and J.RT3-T3.5 cells compared to a random aptamer from the naïve library

(RANL), with JBA8.1 distinguishing itself with greater than 2-fold higher binding than the other aptamers. JBA8.8 did not significantly bind to either cell line despite belonging to the 40-nt Motif 5, whereas JBA8.17 without a motif displayed preferential binding for J.RT3-T3.5 cells. Given these data, we speculate our negative selection steps were ineffective, possibly due to the order of selection steps (positive/negative versus negative/positive) or the insufficient number of J.RT3-T3.5 cells used. In the future, negative selection can be attempted in the first round of SELEX for added stringency, and the input of positive and negative selection cells in each round can be adjusted in real time using a formula that incorporates the binding data from the previous round.[32] We chose the JBA8.1 aptamer for further testing due to it having the most pronounced binding to Jurkat T-leukemia cells.

To reduce aptamer production cost in downstream assays, we first sought to truncate the JBA8.1 aptamer. Using the NUPACK application to predict the minimum free energy (MFE) structure of JBA8.1,[33] we find that the simulated structure of JBA8.1 conforms well to the intended library design, with the majority of the 45-nt Motif 3 forming a multi-hairpin structure that sits on top of a stem comprised of the partially complementary 18-nt flanking primer sequences (**Figure 3.1C**). As we hypothesized that the stem does not directly contribute to aptamer binding, we truncated the stem of JBA8.1 sequence, removing 12 nt from the 5' constant region and all 18 nt from the 3' constant region, yielding the 51-nt tJBA8.1 aptamer sequence (**Figure 3.1C** and **Table S3.4**). In binding studies with Jurkat cells, we found that JBA8.1 has an apparent binding affinity (K_D) of 5.5 ± 1.2 nM versus that of 10.9 ± 2.4 nM for tJBA8.1, demonstrating a minimal impact from the truncation on aptamer binding. (**Figure 3.1D**). We thus proceeded with the more cost-effective tJBA8.1 for receptor identification, further characterization, and application studies.

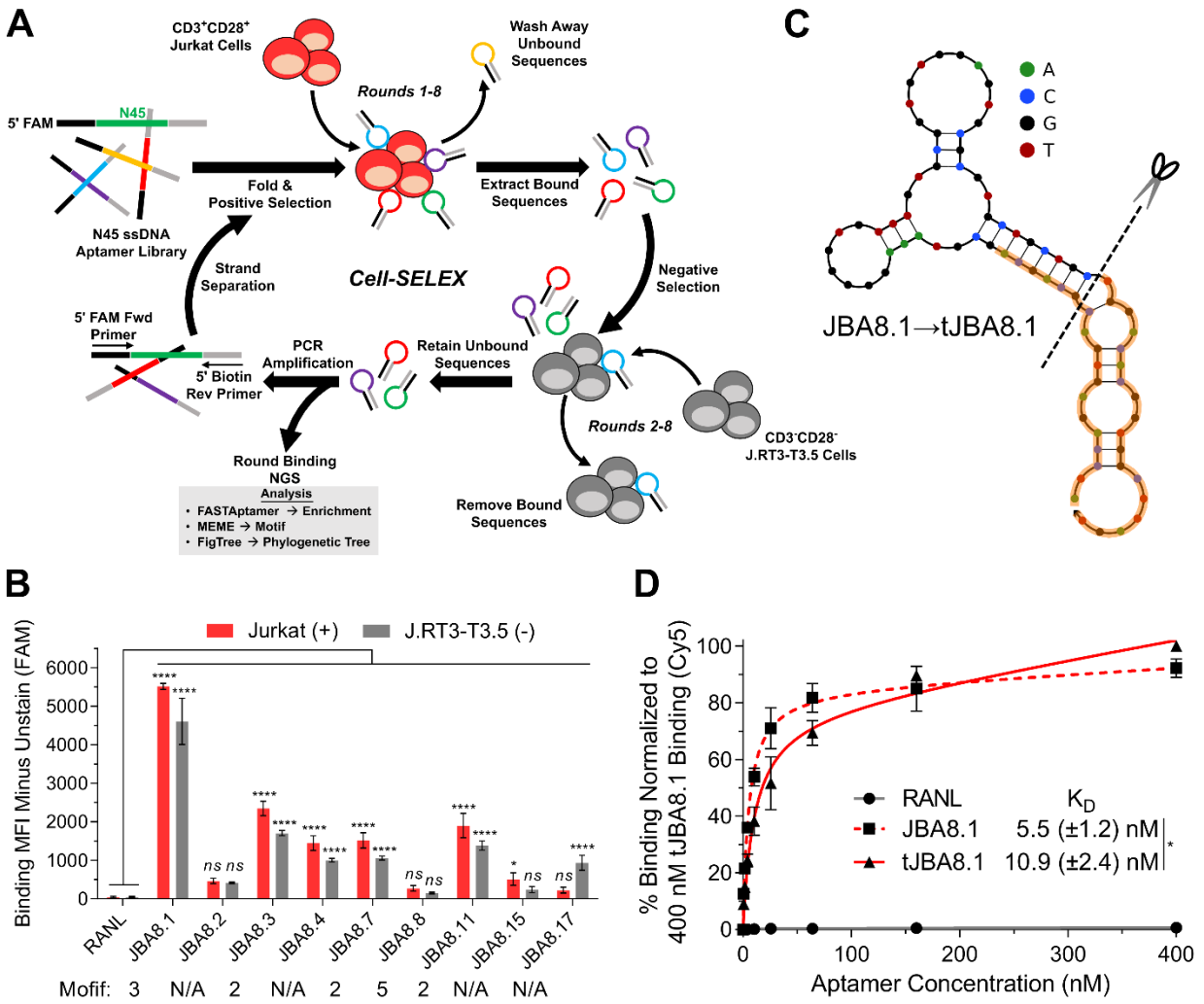

Figure 3.1 | Cell-SELEX and post-SELEX truncation lead to the development of the tJBA8.1 aptamer. (A) Schematic of cell-SELEX using $CD3^+CD28^+$ Jurkat cells for positive selection and $CD3^-CD28^-$ J.RT3-T3.5 cells for negative selection. (B) Binding median fluorescence intensity (MFI) of 100 nM RANL and individual aptamers identified from round 8 of cell-SELEX to Jurkat cells and J.RT3-T3.5 cells by flow cytometry. Aptamers belonging to predicted motifs are indicated. Graph bars and error bars represent mean ± standard deviation; n = 3 independent experiments. *ns* > 0.05, **P* < 0.05, *****P* < 0.0001 (ordinary two-way ANOVA with Šídák correction). (C) MFE secondary structures of JBA8.1 and its truncation (tJBA8.1), predicted using NUPACK (temperature = 4 °C; Na^+ = 137 mM; Mg^{2+} = 5.5 mM). The dashed line indicates the site of truncation, whereas the orange highlighting denotes the 18-nt flanking constant regions. (D) Flow cytometry binding curves of RANL, JBA8.1, and tJBA8.1 to Jurkat cells, normalized to 400 nM tJBA8.1 binding. The curves represent a nonlinear regression assuming one-site total binding. K_D values were calculated by averaging the individual regression values of the independent experiments. Data points and error bars, and K_D values, represent mean ± standard deviation; n = 3 independent experiments with technical duplicates. **P* < 0.05 (two-sided unpaired *t*-test). FAM, 6-carboxyfluorescein; Cy5, cyanine 5.

3.2.2 Identification and validation of transferrin receptor 1 (TfR1) as a target of tJBA8.1

To investigate the type of molecule targeted by tJBA8.1, we labeled Jurkat cells with Cy5-labeled tJBA8.1 at 4 °C followed by enzymatic treatment with trypsin, a serine endopeptidase that cleaves extracellular proteins. tJBA8.1 binding was almost completely abolished after trypsin treatment (**Figure S3.3A**), suggesting that the aptamer targets trypsin-sensitive cell membrane proteins. We also visualized Cy5-labeled tJBA8.1 binding to Jurkat cell membranes at 4 °C by confocal microscopy (**Figure S3.3B**).

We next adapted a reported aptamer-based pull-down assay designed for identification of target membrane receptors.[34] Briefly, we bound biotinylated tJBA8.1 to precleared proteins in solubilized Jurkat cell membrane extracts, isolated the aptamer-bound membrane proteins using streptavidin-coated magnetic beads, and analyzed the recovered protein by SDS-PAGE. Compared to a control sample that was purified with biotin-saturated streptavidin beads without tJBA8.1, we observed two distinct protein bands that were highly enriched by tJBA8.1 at approximately 200 kDa (band a) and 100 kDa (band b) (**Figure 3.2A**). The protein bands were extracted, digested, analyzed by mass spectrometry, and matched to the human transferrin receptor protein 1 (TfR1; also known as CD71) (**Figure 3.2B**). Peptides extracted from the higher molecular weight band (a) covered 62% of the TfR1 amino acid sequence, whereas the lower molecular weight band (b) covered 58%. The presence of two bands is consistent with the structure of TfR1, which is a homodimer composed of two disulfide-linked monomers.[35]

TfR1 is a type II transmembrane glycoprotein that regulates the uptake of transferrin-bound iron needed for cellular metabolism and proliferation.[36] TfR1 is thus ubiquitously expressed at low levels on many cell types, with elevated expression on rapidly dividing cells such as activated

lymphocytes and cancer cells.[37–39] To validate that tJBA8.1 binds TfR1, we used short interfering RNA (siRNA) duplexes (**Table S3.5**) to knockdown the expression of TfR1 encoded by the *TFRC* gene in Jurkat cells and evaluated aptamer binding. Compared to cells that were nucleofected with non-specific (NS) siRNA, cells nucleofected with TFRC siRNA had 51% reduced TfR1 expression as evaluated by anti-CD71 antibody (CD71 Ab) staining, which matched closely with the observed 49% reduction in tJBA8.1 binding (**Figure 3.2C**). We also evaluated TfR1 expression on the Jurkat cells and J.RT3-T3.5 cells used in cell-SELEX. In agreement with the binding profiles of the cell-SELEX aptamer pools and JBA8.1 (**Figure S3.1** and **Figure 3.1B**), both cell lines robustly express TfR1 (**Figure S3.4A**), with Jurkat cells having higher expression than J.RT3-T3.5 cells (**Figure S3.4B**). Lastly, as TfR1 is expressed negligibly on resting T cells but is upregulated upon antigen and cytokine stimulation,[38] we evaluated tJBA8.1 binding to unactivated and day 3 CD3/CD28 Dynabead-activated $CD4^+$ and $CD8^+$ T cells. For both subsets, tJBA8.1 binding was low to unactivated T cells but greatly increased after Dynabead activation (**Figure S3.5A**). Furthermore, we found that JBA8.1 binding correlated strongly with TfR1 expression on $CD4^+$ and $CD8^+$ T cells over 7 days of Dynabead activation (**Figure S3.5B**). Collectively, these results confirm that TfR1 is a binding target of JBA8.1/tJBA8.1.

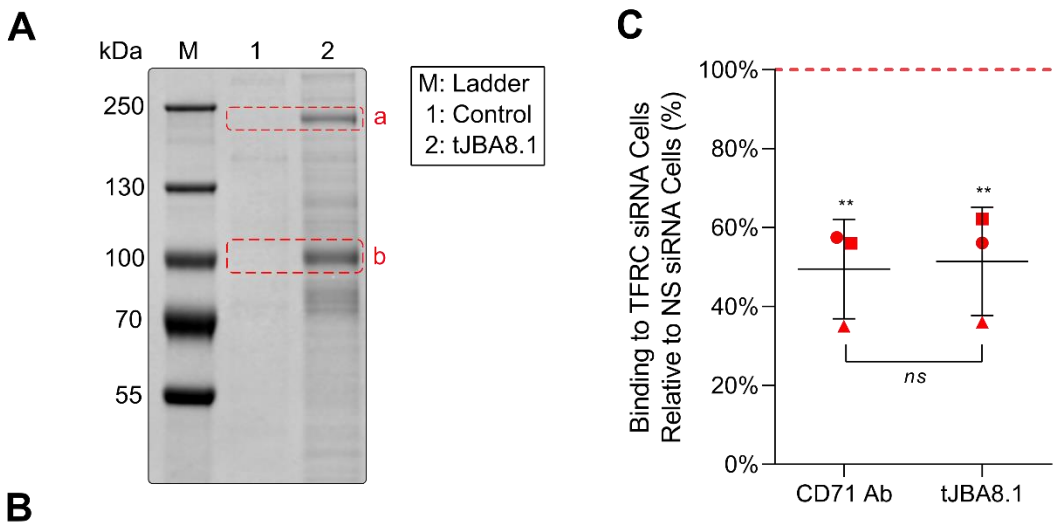

B

Band	Description	Lane 1: Peptide Coverage (Control)	Lane 2: Peptide Coverage (tJBA8.1)	Lane 1: # of Peptides (Control)	Lane 2: # of Peptides (tJBA8.1)
a	Transferrin receptor protein 1	9%	62%	4	52
b	Transferrin receptor protein 1	13%	58%	5	50

Figure 3.2 | TfR1 is identified as the target of tJBA8.1. (A) Colloidal blue-stained 8% SDS-PAGE gel of Jurkat cell membrane proteins pulled down by tJBA8.1. The control lane represents proteins captured by biotin-saturated magnetic beads only. Bands a and b (dashed red boxes) from both lanes were excised for mass spectrometry analysis. (B) Summary of the protein with the highest peptide coverage and number of peptides identified in each excised band by mass spectrometry. (C) Flow cytometry analysis of FITC-labeled CD71 Ab and 25 nM Cy5-labeled tJBA8.1 binding to Jurkat cells 24 h after nucleofection with TFRC siRNA duplexes. Red, dashed horizontal line represents binding to non-specific (NS) siRNA-treated controls to which the TFRC siRNA data points were normalized. Horizontal lines and error bars represent mean ± standard deviation; $n = 3$ independent experiments. $^{**}P < 0.01$ (significance between ligand staining on TFRC siRNA- and NS siRNA-treated cells; one-way ANOVA with Bonferroni correction). *ns* > 0.05 (significance between the relative CD71 Ab and tJBA8.1 staining in pairwise experiments; two-sided paired *t*-test). Cy5, cyanine 5; FITC, fluorescein isothiocyanate.

3.2.3 Characterization of tJBA8.1 binding to TfR1 and competition with other TfR1 ligands

We next used bio-layer interferometry (BLI) to characterize tJBA8.1 binding kinetics to recombinant TfR1. We immobilized biotinylated TfR1 onto streptavidin biosensors to avoid avidity effects from homodimeric TfR1 binding to immobilized aptamers. Demonstrating fast and high-affinity binding kinetics, tJBA8.1 bound the TfR1 protein with a K_D value of 25.11 ± 0.19 nM (**Figure 3.3A** and **Table S3.6**). We further tested by BLI whether aptamers JBA8.3, JBA8.4,

JBA8.7, JBA8.11, and JBA8.15, bind to TfR1. Despite these aptamers displaying statistically significant binding to Jurkat cells in **Figure 3.1B**, none of them appreciably bound TfR1 besides JBA8.1 (**Figure S3.6**). Lastly, we evaluated binding of His-tagged mouse recombinant TfR1 to immobilized tJBA8.1 by BLI, but results were negative despite positive control antibody binding, demonstrating that tJBA8.1 does not interact with mouse TfR1 (**Figure S3.7A,B**).

Iron is delivered intracellularly to cells via a transferrin cycle. Specifically, iron-bound transferrin (holo-Tf) binds to TfR1 for uptake, after which iron is released from transferrin under acidic endosomal pH and the resulting iron-free transferrin (apo-Tf) is recycled to the cell surface for receptor dissociation at neutral pH.[40] To test if tJBA8.1 competes with holo-Tf for binding to TfR1, we co-incubated Jurkat cells with a fixed concentration of labeled tJBA8.1 and varying concentrations of holo-Tf as a competitor. tJBA8.1 binding was reduced by half upon competition with just 1-fold excess of holo-Tf, confirming that tJBA8.1 and holo-Tf share proximal binding sites on TfR1 (**Figure 3.3B**). However, relative tJBA8.1 binding plateaued at 50% and did not further decrease even when holo-Tf was added at 32-fold excess, suggesting that tJBA8.1 has a transferrin- or TfR1-independent binding component to Jurkat cells. We also co-stained Jurkat cells with tJBA8.1 and the CD71 Ab (clone CY1G4) used previously, which is known to bind a TfR1 epitope distinct from that of holo-Tf.[41] We observed a striking positive correlation between CD71 Ab and tJBA8.1 staining, demonstrating that tJBA8.1 can bind TfR1 on cells simultaneously with the CD71 Ab (**Figure 3.3C**). Furthermore, the binding behavior of tJBA8.1 to Jurkat cells in the presence of various concentrations of the CD71 Ab (clone CY1G4) was statistically indistinguishable from binding in the presence of an anti-CD3 antibody (CD3 Ab) control (**Figure 3.3D**). Thus, tJBA8.1 and the CD71 Ab (clone CY1G4) do not share an overlapping binding epitope on TfR1.

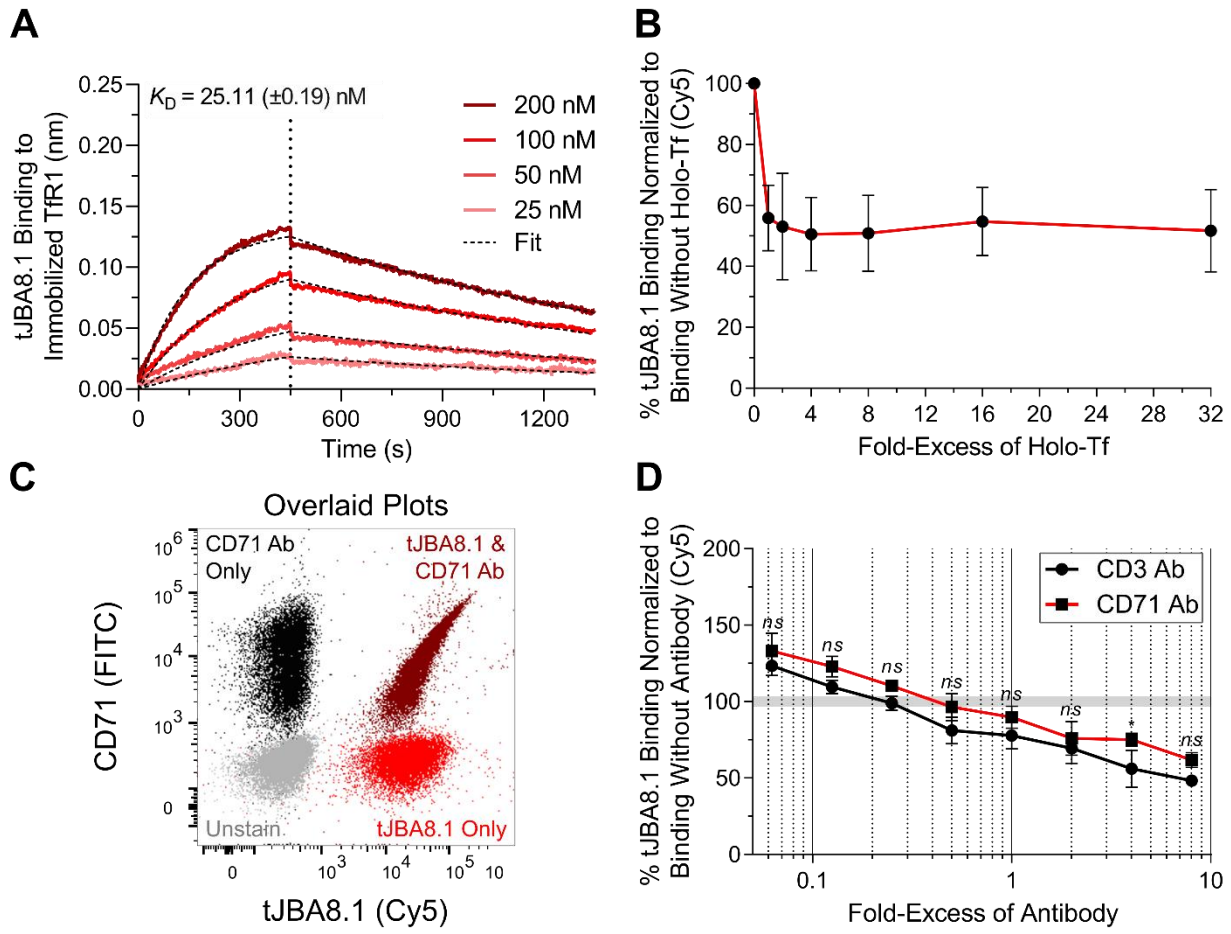

Figure 3.3 | tJBA8.1 competes with holo-Tf but not antibody clone CY1G4 for binding to TfR1. (A) Association and dissociation kinetics of serially diluted FAM-labeled tJBA8.1 binding to biotinylated TfR1 immobilized on streptavidin biosensors by BLI. The association phase is illustrated from 0-450 s, whereas dissociation is shown from 450-1350 s (separated by the vertical dotted line). K_D values were calculated by performing a global fit of the multi-concentration kinetic data to a 1:1 binding model. K_D values represent mean ± standard deviation; n = 4 individual concentrations of aptamers. (B) Competitive binding of 25 nM Cy5-labeled tJBA8.1 with varying fold-excess of holo-Tf to Jurkat cells by flow cytometry. Binding was normalized to aptamer-stained controls without holo-Tf. Data points and error bars represent mean ± standard deviation; n = 3 independent experiments. *ns* > 0.05, **P* < 0.05 (ordinary two-way ANOVA with Šídák correction). (C) Overlaid flow cytometry plots of unstained (grey), FITC-labeled CD71 Ab single-stained (black), 25 nM Cy5-labeled tJBA8.1 single-stained (red), and antibody and aptamer co-stained (dark red) Jurkat cells. Plots are representative of n = 2 independent experiments. (D) Competitive binding of 25 nM Cy5-labeled tJBA8.1 with varying fold-excess of CD3 or CD71 Ab to Jurkat cells by flow cytometry. Binding was normalized to aptamer-stained controls without antibody. Data points and error bars represent mean ± standard deviation; n = 3 independent experiments. *ns* > 0.05, **P* < 0.05 (ordinary two-way ANOVA with Šídák correction). FITC, fluorescein isothiocyanate; Cy5, cyanine 5; FAM, 6-carboxyfluorescein.

3.2.4 Cryo-EM of tJBA8.1-TfR1 complex

To better elucidate the binding interaction between tJBA8.1 and TfR1, we first performed cryo-EM on homodimeric His-tagged TfR1 bound to tJBA8.1. We obtained a cryo-EM map at an overall 2.54 Å resolution and refined an existing crystal structure of homodimeric TfR1 (PDB 1CX8) against the map (parameters for collection and processing listed in **Table S3.7**),[42] which revealed two tJBA8.1 aptamers (yellow) binding to a single TfR1 homodimer (grey), with each TfR1 monomer (light blue and light purple) bound independently by an aptamer (**Figure 3.4**). Each tJBA8.1 aptamer adopts a distal double-stranded helical structure and a more complicated structure proximal to the binding site. Analyzing this binding epitope, we find that tJBA8.1 contacts α helices 1, 2, and 3 (dark blue and dark purple) of each TfR1 monomer helical domain (**Figure 3.4**).

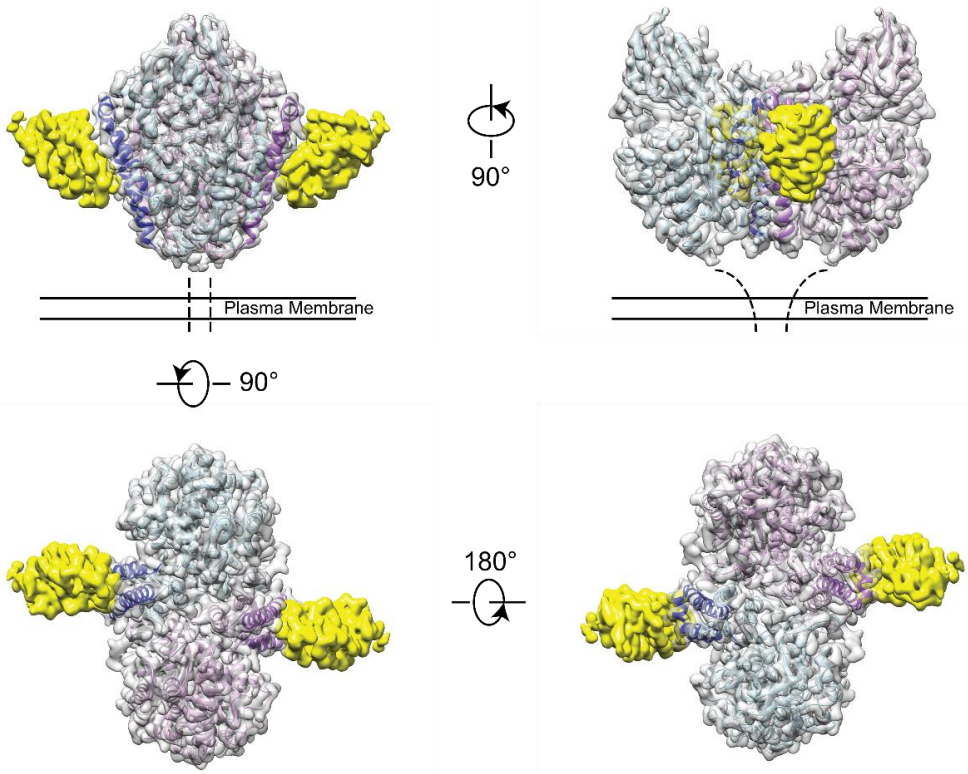

Figure 3.4 | tJBA8.1 binds the helical domain of TfR1. Cryo-EM density map and refined structure of tJBA8.1-bound TfR1. Four views are shown with color coding (yellow: tJBA8.1 density; gray: TfR1 homodimer density; light blue and light purple: individual TfR1 monomer structures; dark blue and dark purple: α helices 1, 2, and 3 of each TfR1 monomer helical domain).

3.2.5 *De novo* modeling of TfR1-bound tJBA8.1 and interactions at the tJBA8.1-TfR1 interface

We next modeled the three-dimensional (3D) structure of tJBA8.1 within its electron density from the cryo-EM data in **Figure 3.4**. Our attempts to convert the predicted 2D structure of tJBA8.1 into a 3D structure followed by rigid-body fitting into the aptamer density failed, perhaps because aptamers can conformationally change upon target binding due to their structural plasticity and/or current DNA folding software do not account for non-Watson-Crick base pairing interactions.[43–46] Since the electron density at the tJBA8.1 core nearest to the TfR1 binding site could be resolved to the level of DNA bases, we conducted unambiguous *de novo* model building of the aptamer structure. While it was difficult to distinguish the different purines and pyrimidines at certain places in the electron density, we were able to sufficiently differentiate purines from pyrimidines. To our benefit, tJBA8.1 has a unique instance of three consecutive pyrimidines (T21, T22, and T23), providing us a definitive starting point for aptamer model building within the electron density map. The resulting *de novo* built model of TfR1-bound tJBA8.1 is shown in **Figure 3.5A**, and parameters concerning structure refinement and validation are listed in **Table S3.7**. We were only able to model tJBA8.1 from A11 to G40; there was no interpretable density to model nucleotides 1-GCAGCAGCGT-10 and 41-CGTGCTGCTGC-51 at the aptamer's 5' end and 3' end, respectively. As these two sequences of nucleotides should mostly base pair to form the distal tJBA8.1 stem, we hypothesize that this non-binding stem region was too flexible to be resolved by cryo-EM.

Analyzing the tJBA8.1-TfR1 binding interface within the cryo-EM density map using the *de novo* built aptamer model and refined structure of TfR1, we found that tJBA8.1 has a single continuous nucleotide sequence comprised of 17-GGTGTTTGTG-26 that contacts Leu619 and Arg623 of helix α1 (aa 613-626), Gln627 that connects helix α1 with helix α2, Arg629 of helix α2 (aa 629-

634), and Gln640, Ser644, Arg646, Phe650, and Arg651 of helix α3 (aa 640-662) in the TfR1 helical domain (**Figure 3.5B**). We inputted the modeled tJBA8.1-TfR1 complex into PDBePISA and PLIP programs to identify the types of interactions that occur at the tJBA8.1-TfR1 binding interface between individual protein residues and nucleotides.[47,48] Notably, we detected an extensive hydrogen bonding network formed by Arg623, Gln627, Arg629, Gln640, Ser644, Arg646, and Arg 651 of TfR1 with the bases, sugars, and/or phosphates of G18, T19, G20, T21, T23, T25, and G26 in tJBA8.1 (**Figure 3.5C** and **Table S3.8**). In addition to these, we also detected stabilizing hydrophobic interactions between Leu619 and the base of T21 and Phe650 and the base and sugar of T23, a pi-stacking interaction between the same Phe650 and T23 pair, a cation-pi interaction between Arg646 and the base of G20, and lastly salt bridges between Arg623, Arg646, and Arg651 and the phosphates of T19, T25, an T24, respectively. Using NUCPLOT to organize many of the detected tJBA8.1-TfR1 interactions into a simple schematic diagram,[49] we intriguingly found that TfR1 does not directly interact with the bases of T19, T22, G24, and G26 but instead with their associated sugar and phosphate groups (**Figure 3.5D**). This may suggest that these nucleotide positions can tolerate base substitutions without affecting tJBA8.1 binding to TfR1, assuming the substitutions do not change aptamer structure or cause steric hindrance with other TfR1 residues. NUCPLOT also identified that Tyr643 and Gly647, while not strongly interacting with tJBA8.1, may form weak non-bonded contacts with T23 and T25 due to their <3.9 Å proximity that results in possible van der Waals forces.

Besides the direct DNA-protein interactions detected at the tJBA8.1-TfR1 binding interface, we identified two other sets of interactions that may contribute to tJBA8.1 structure and/or binding. One interaction is an intramolecular G-quartet (also known as G-tetrad) comprised of G16, G28, G33, and G38 that may stabilize the 3D folding of TfR1-bound tJBA8.1 (**Figure S3.8A**). When

modeled into their electron densities, these guanine nucleotides have a planar arrangement with Hoogsteen hydrogen bonding between their bases consistent with that of a G-quartet. The second set of interactions involves two metal ions found in the cryo-EM density. One metal ion coordinates the bases of G17 and G18, the phosphates of G26 and G28, and the guanidino group of Arg629 and the other metal ion coordinates the phosphates of G34, A35, and G36 and the base of T37 (**Figure S3.8B,C**). Of importance, G28 is shared by both sets of interactions, bridging the two into an expansive interaction network that may play a large role in complexed tJBA8.1 structural stability and its binding to TfR1.

The C-lobe of holo-Tf is known to bind α helices 1, 2, and 3 of the TfR1 helical domain, specifically to Leu619 and Arg623 of helix α1, Arg629 of helix α2, and Gln640, Tyr643, Arg646, Phe650, and Arg651 of helix α3.[50] All these amino acid residues are similarly bound by tJBA8.1 on TfR1, definitively demonstrating that tJBA8.1 and holo-Tf share highly overlapping binding epitopes on TfR1. Besides holo-Tf, TfR1 has other natural ligands that may share TfR1-binding epitopes with tJBA8.1. HFE is a major histocompatibility complex (MHC) class I-like membrane protein that is known to compete with holo-Tf at its TfR1-binding site to regulate iron uptake,[50–53] and mutation of HFE can cause iron overload that resembles hereditary hemochromatosis via hepatic hepcidin deficiency.[54,55] HFE has previously been shown to have a large binding interface with TfR1, interacting with the same α helices in the TfR1 helical domain that both tJBA8.1 and holo-Tf bind.[51] Notably, Leu619 of TfR1 contributes to a strong hydrophobic core with Val78 and Trp81 of HFE, Arg623 has contact with Leu22 of HFE, Arg629 has several polar interactions with residues in both helices α1 and α2 of HFE, and Gln640 forms hydrogen bonds with Glu146 and His150 of HFE. As these key TfR1 residues are also targeted by tJBA8.1, it is probable that

tJBA8.1 competes with membrane-bound HFE for binding to TfR1, like holo-Tf does. The binding interface that tJBA8.1, holo-Tf, and HFE share on TfR1 is depicted in **Figure S3.9A-C**.

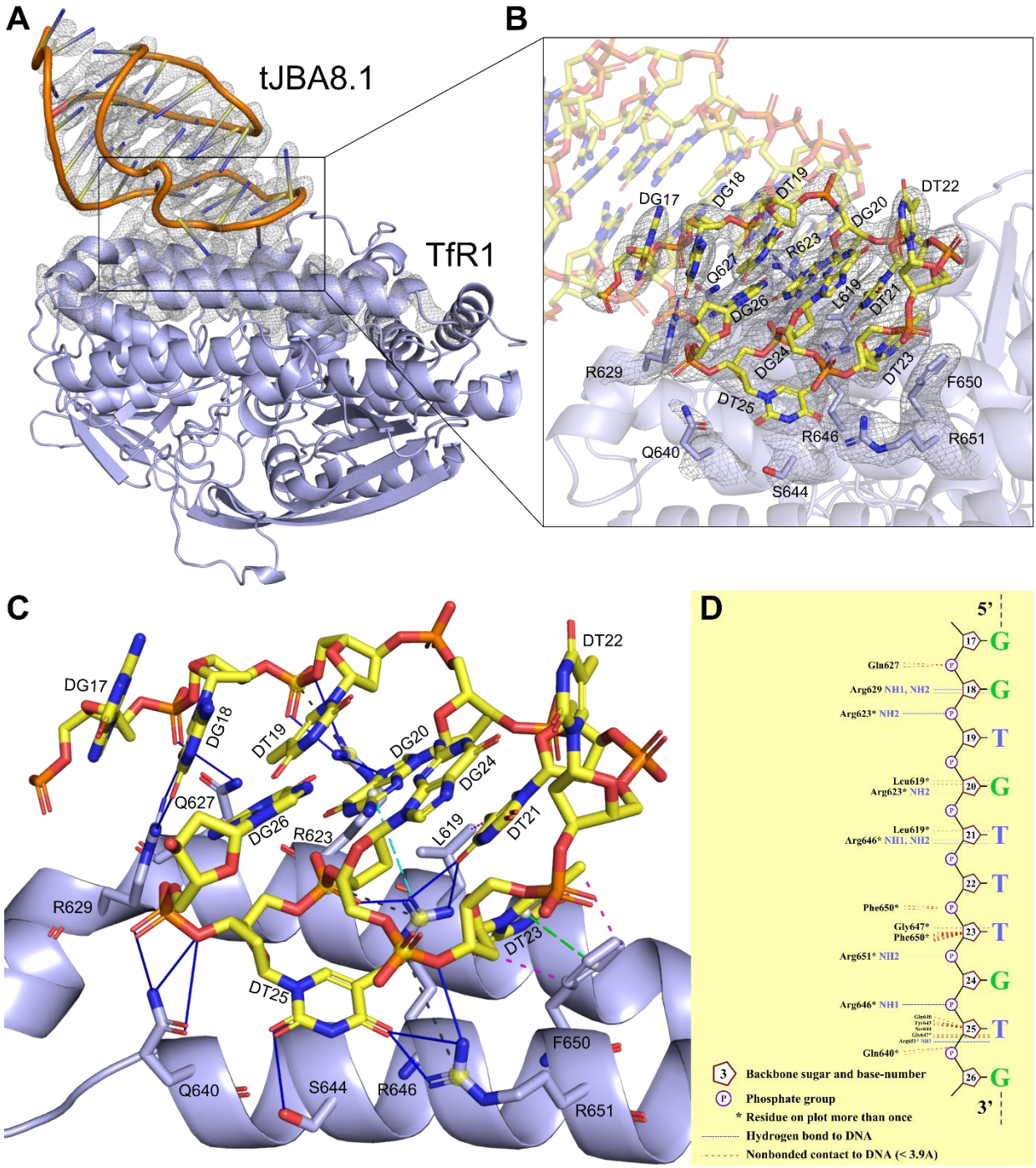

Figure 3.5 | *De novo* model of tJBA8.1 built into the cryo-EM map enables detailed characterization of the interactions at the tJBA8.1-TfR1 interface. (A) Cartoon representation of tJBA8.1-TfR1 complex (yellow: tJBA8.1; lavender blue: TfR1) modeled in the cryo-EM density maps (overlayed grey mesh). For clarity, only one monomer of the tJBA8.1-TfR1 complex is shown, and the overlaid cryo-EM density maps are restricted to tJBA8.1 and the binding

interface on TfR1. (B) Zoomed-in view of the modeled tJBA8.1-TfR1 interface within the cryo-EM density maps showing the overall fit of the model. tJBA8.1 nucleotides and TfR1 protein residues in close contact at the binding interface are labeled and shown as sticks with atom color coding (yellow: nucleotide carbon; lavender blue: protein carbon; blue: nitrogen; red: oxygen; orange: phosphate). (C) Molecular interactions at the modeled tJBA8.1-TfR1 interface, calculated using PDBePISA and PLIP. Different lines and color coding are used to denote the different interactions (blue solid: hydrogen bonds; black dashed: salt bridges; magenta dashed: hydrophobic interactions; green dashed with ring centroids: pi-stacking; cyan dashed with centroids: cation-pi). The list of detected interactions at the tJBA8.1-TfR1 interface can be found in **Table S3.8**. (D) Schematic diagram of hydrogen bonds and nonbonded contacts at the modeled tJBA8.1-TfR1 interface, generated using NUCPLOT.

3.2.6 tJBA8.1-mediated depletion of B-lymphoma cells from PBMCs

Because TfR1 is overexpressed in many cancer types including leukemias (both lymphocytic and myeloid),[56,57] lymphomas,[58,59] and myelomas,[39] and the level of TfR1 expression marks the proliferative potential of these malignant cells,[60] we recognized that tJBA8.1 might be utilized as a malignant cell depletion agent in CAR T-cell manufacturing. We therefore developed a MACS-based approach combining biotinylated tJBA8.1 and Anti-Biotin Microbeads (Miltenyi Biotec) for selective depletion of cancerous cells from PBMCs (**Figure 3.6A**, top). We used immortalized Raji B-lymphoma cells, which robustly express TfR1 in contrast to healthy PBMCs (**Figure S3.10A,B**), to mimic cancers currently treated by FDA-approved CD19-directed CAR T-cell therapies. Raji cells were pre-labeled with a CM-Dil membrane dye (**Figure S3.11A**) and spiked into healthy PBMCs at low (~0.1%), medium (~1%), and high (~10%) percentages to reproduce circulating malignant cell heterogeneity found in patient leukapheresis populations.[61] We incubated the mixed cells sequentially with biotinylated tJBA8.1 and anti-biotin beads before separating them on a magnetic column. The pre-sort, depleted, and flow through fractions were analyzed by flow cytometry to detect CM-Dil$^+$ Raji cells (**Figure 3.6B** and **Figure S3.11B,C**). We observed that tJBA8.1-mediated depletion effectively removed CM-Dil$^+$ Raji cells from all spiked

PBMC populations, with flow-through populations that were statistically indistinguishable from un-spiked PBMC controls (**Figure 3.6C**). Analyzing the depleted fractions, we detected enrichment of CM-Dil^{+} Raji cells, as expected, although their purity scaled with the amount of spike cells and never peaked past 60%. As this indicates some CM-Dil^{-} PBMCs were depleted as well, we further examined the percentages of immune cells in the CM-Dil^{-} pre-sort and flow through fractions to determine if the PBMC composition was being impacted by the depletion process. There were no significant changes in the percentages of CD19^{+} B cells, CD14^{+} monocytes, CD56^{+} NK cells, and CD3^{+} T cells between the pre-sort and flow through fractions (**Figure 3.6D, Figure S3.12A,B**), suggesting that loss of CM-Dil^{-} PBMCs in the depleted fraction was low and likely non-specific. Taken together, these data demonstrate proof-of-concept removal of TfR1^{+} malignant cells from PBMCs using tJBA8.1, yielding healthy and uncompromised cell product that can be used in downstream CAR T-cell manufacturing with improved safety.

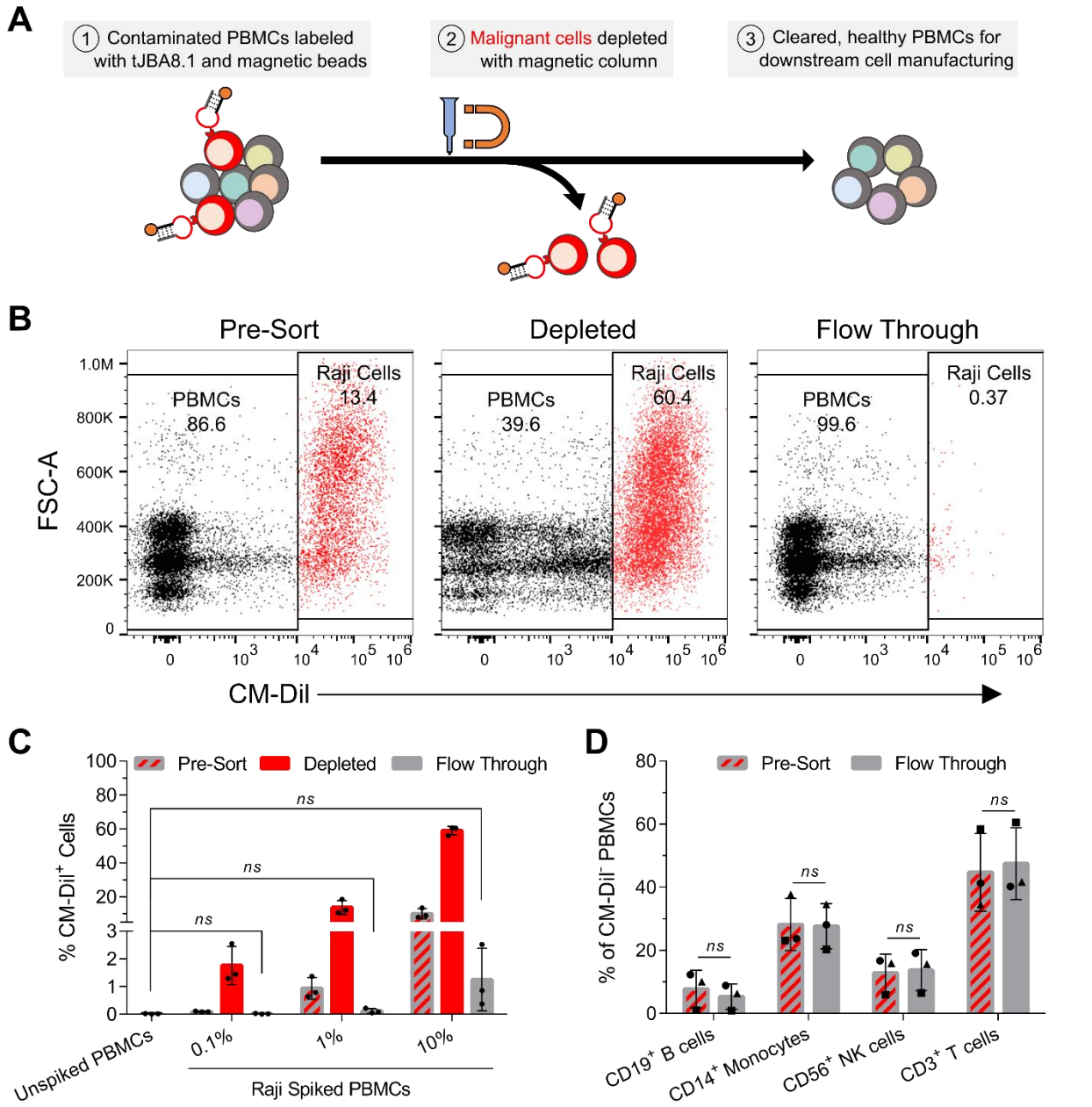

Figure 3.6 | tJBA8.1 thoroughly depletes Raji B-lymphoma cells from PBMCs without altering healthy immune cell composition. (A) Schematic of malignant cell depletion from PBMCs using tJBA8.1-mediated MACS. (B) Flow cytometry plots of CM-Dil$^+$ Raji cell depletion from high (10%) Raji spiked PBMCs. The different cell fractions from the depletion process are shown. Plots for low (0.1%) and medium (1%) Raji spiked PBMCs can be found in **Figure S3.11B,C**. Plots are representative of $n = 3$ independent experiments with different PBMC donors. (C) Flow cytometry analysis of the percentage of CM-Dil$^+$ Raji cells in each cell fraction of the depletion process using low (0.1%), medium (1%), and high (10%) Raji spiked PBMCs. Unspiked PBMCs were included as a benchmark of complete depletion. Graph bars and error bars represent mean ± standard deviation; $n = 3$ independent experiments with different PBMC donors. *ns* > 0.05 (ordinary one-way ANOVA with Dunnett's correction). (D) Flow cytometry analysis of the healthy immune cell composition within CM-Dil$^-$ PBMCs before (pre-sort) and after (flow

through) Raji depletion from high (10%) Raji spiked PBMCs. Analysis for low (0.1%) and medium (1%) Raji spiked PBMCs can be found in **Figure S3.12A,B**. The circles, squares and triangles represent different PBMC donors from separate depletion studies. Graph bars and error bars represent mean ± standard deviation; $n = 3$ independent experiments with different PBMC donors. *ns* > 0.05 (paired two-way ANOVA with Šídák correction). CM-Dil, chloromethylbenzamido-1,1'-dioctadecyl-3,3,3',3'-tetramethylindocarbocyanine perchlorate.

3.2.7 tJBA8.1 affinity optimization

We lastly revisited the NGS results to identify alternative Motif 3 aptamers that could have improved affinity for TfR1. Besides JBA8.1, there were three other aptamers belonging to Motif 3 in the top 50 sequences of the round 8 cell-SELEX pool, namely JBA8.10, JBA8.26, and JBA8.45 (**Table S3.3**). Notably, all three aptamers were single-point variants of JBA8.1 that displayed approximately 20-fold enrichment in round 8, which was significantly greater than the 6.9-fold round 8 enrichment for JBA8.1. We selected JBA8.26 for further characterization because it had the highest fold enrichment of the three aptamers. Analyzing the predicted MFE secondary structure of JBA8.26 by NUPACK, we noticed that JBA8.26 has an extended stem region compared to JBA8.1, owing to a T55C mutation (T43C mutation in tJBA8.1) that induces complementary base pairing (**Figure S3.13A**). We theorized that these predicted changes would increase the structural stability of JBA8.26 relative to JBA8.1, which may elevate its binding affinity for TfR1. Confirming this, JBA8.26 bound $TfR1^{hi}$ H9 T-lymphoma cells with an apparent K_D of 3.3 ± 0.6 nM, a near 8-fold improvement compared to tJBA8.1's apparent K_D of 25.6 ± 13.0 nM for these cells (**Figure S3.13B**). Using BLI, JBA8.26 was found to bind immobilized TfR1 with a K_D of 6.87 ± 0.04 nM (**Figure S3.13C**), displaying both a 2-fold faster association rate and a nearly 2-fold slower dissociation rate than those of tJBA8.1 (**Table S3.6**). Given these upgraded TfR1-binding kinetics, we predict that JBA8.26 and its future truncations will increase the partitioning efficiency of our cancer cell depletion strategy.

3.3 DISCUSSION AND FUTURE WORK

As expensive living drugs, CAR T cells require stringent manufacturing to maximize their safety and efficacy. In rare cases with T-cell isolation approaches currently employed in commercial therapies, malignant cells advance through the isolation process and contaminate enriched T cells, which can inadvertently exhaust produced CAR T cells or even create a cancer resistant to therapy.[14,15] Accordingly, an inexpensive approach that actively removes cancerous cells from patient PBMCs while leaving healthy T cells untouched would be of high value to CAR T-cell manufacturing and safety.

Here, we report the discovery of a nanomolar-affinity DNA aptamer, named tJBA8.1, that binds the iron importer TfR1 overexpressed by cancer cells but not expressed by healthy PBMCs. In proof-of-concept MACS-based depletion studies, tJBA8.1 was capable of efficiently removing Raji B-lymphoma cells spiked into PBMCs at various concentrations, yielding uncontaminated, label-free PBMCs. Importantly, the composition of healthy immune cells was unaltered by the depletion steps, showing the precise partitioning afforded by tJBA8.1. This work provides a straightforward, cost-effective approach for selectively removing malignant cells before CAR T-cell production, enabling safer and more reproducible manufacturing of this precious therapy.

Comprehensive validation and detailed characterization of aptamer binding to their cognate receptors is a necessary step to their widespread recognition and use, especially within the context of other ligands. tJBA8.1 binding to $TfR1^+$ cells was competed off by iron-bearing transferrin, and structure solution of the tJBA8.1-TfR1 complex using cryo-EM and subsequent analysis of the tJBA8.1-TfR1 interface verified that tJBA8.1 has a binding epitope in the TfR1 helical domain that overlaps with that of the transferrin C-lobe.[50] Additionally, the tJBA8.1 binding site on TfR1

appears to coincide with that of HFE, another natural TfR1 ligand that is co-expressed on the cell surface.

We also demonstrated that tJBA8.1 does not bind mouse TfR1 despite the protein sharing ~75% identity in its extracellular domain with human TfR1. Mouse TfR1 has mutations at two of the ten residues bound by tJBA8.1, specifically Arg623 and Arg629 that are instead lysine residues (**Figure S3.14**). Our cryo-EM density-guided modeling of the tJBA8.1-TfR1 interface demonstrated that Arg623 and Arg629 form extensive hydrogen bonds and salt bridges with the guanine bases and thymine phosphate groups of tJBA8.1. Compared to arginine residues that have guanidine side chains, lysine residues have a lower propensity for hydrogen bonding with DNA bases, especially with guanines,[62] and they also electrostatically bind to phosphate with lower affinity due to not having multivalent hydrogen bonding,[63] providing a plausible mechanism for the lack of tJBA8.1 binding to mouse TfR1. Also of potential interest to tJBA8.1 binding is TfR2, a hepatic-localized homolog of TfR1 that shares ~47% identity in its extracellular domain with TfR1.[64] TfR2 has even less conservation of the TfR1 interface with tJBA8.1, with mutations at Arg623 that is instead a glycine, Gln627 that is instead a glutamic acid, Arg629 that is instead a serine, and Phe650 that is instead an isoleucine (**Figure S3.15**). Given these large changes, we predict that tJBA8.1 would not bind or have severely reduced affinity for TfR2.

tJBA8.1 is not the first TfR1-binding DNA aptamer to be reported—XQ-2d is a 56-nt, human TfR1-binding aptamer previously discovered by the Tan group.[65,66] Similar to tJBA8.1, XQ-2d competes with transferrin for TfR1 binding; however, molecular dynamics simulation of the XQ-2d binding site on TfR1 predicts that XQ-2d binds slightly upstream of tJBA8.1 at TfR1 residues Ser638, Gln640, Lys673, Tyr683, Pro688, Tyr689, Ser691, Lys693, Ala736, Trp740, Asn747, Val753, Trp754, and Asn758.[66] As Gln640 is the only shared TfR1 residue predicted to be bound

by both aptamers, comparison of tJBA8.1 and XQ-2d binding properties and competition assays will be critical to ascertain if tJBA8.1 and XQ-2d share an overlapping binding epitope on TfR1. In addition to XQ-2d, the Levy and Shangguan groups have respectively reported a 42-nt 2'-fluoro RNA aptamer called c2.min and a 35-nt DNA aptamer called HG1-9 that both also compete with transferrin for binding to human TfR1.[67–69] Given that tJBA8.1 and these other human TfR1-binding aptamers have unique sequences, understanding the molecular basis by which TfR1 is commonly targeted by these different aptamers may identify protein traits that are amenable to aptamer binding and even help screen protein targets for SELEX.

Besides TfR1, we speculate that tJBA8.1 has other target receptors on Jurkat cells. Aptamer binding to these cells was only partially abrogated by large molar excesses of holo-transferrin despite cryo-EM mapping showing they have highly overlapping binding epitopes on TfR1. As tJBA8.1 binding is only reduced by ~50% under these conditions, it is likely that tJBA8.1 has a TfR1-independent binding component to Jurkat cells. Compellingly, none of the other Jurkat-binding aptamers identified from the cell-SELEX have appreciable binding to TfR1, suggesting they bind other cellular proteins that may be the same targets of tJBA8.1 TfR1-independent binding. A sequence comparison of these aptamers reveals multiple motifs of two or more consecutive guanine bases. This G-rich patterning may suggest that JBA8.1 and some of the other aptamers identified from the SELEX have a propensity for forming intramolecular or intermolecular G-quadruplexes,[70] which may allow the aptamers to bind a number of different target proteins.[71] Supporting this, our modeling of TfR1-bound tJBA8.1 found a stabilizing G-quartet motif within its structure and metal ions coordinating bases, which together are the building blocks of G-quadruplexes.

While we showed efficient tJBA8.1-mediated depletion of malignant cells, our studies were conducted using an idealized model of immortalized cell lines and healthy donor PBMCs. TfR1 expression on patient-derived malignant cells may not be as robust as on *ex vivo* cultured cancer cells, and expression will vary with cancer type, disease stage, and patient history. Validating that tJBA8.1 binds to malignant cells within an array of patient samples will thus be imperative to this system's translation, and the aptamer affinity improvements detailed at the end of this study (JBA8.26) will be important for increasing the depletion system's sensitivity to lower levels of TfR1 expression. Also unexplored in this study is the effect of malignant cell depletion on CAR T-cell differentiation, exhaustion, and expansion during manufacturing. Early expression of differentiation and exhaustion markers on CAR T cells prior to patient infusion is associated with remission induction failure,[72] and poor CAR T-cell expansion can prevent reaching target doses needed for therapy.[73] Removing malignant cell contamination prior to CAR T-cell manufacturing is expected to prevent uncontrolled differentiation and exhaustion of CAR T cells *ex vivo* and thus improve their expansion.

While we used B-lymphoma cells in our depletion studies to mimic cancers currently treated by commercial CAR T-cell therapies, we anticipate the depletion strategy described here will have a greater impact on the treatment of T-cell malignancies. Presently, autologous CAR T-cell manufacturing for treating T-cell leukemias and lymphomas is impractical since malignant T cells are often found in the peripheral blood of patients with these diseases and immunoaffinity purification approaches that target common T-cell antigens are unable to distinguish normal T cells from these malignant T cells.[18,19] To circumvent these challenges, CAR NK cells or allogeneic CAR T cells can be used for treatment,[74,75] but the former is difficult to manufacture at a clinical scale whereas the latter requires gene editing to prevent fatal graft-versus-host-disease

and likely has limited persistence due to host-versus-graft effects. For these reasons, CAR T-cell manufacturing for T-cell malignancies would serve to benefit the most from the depletion strategy developed here, as it would allow selective harvesting of healthy autologous T cells that are otherwise unattainable. Furthermore, as T-lineage leukemias and lymphomas have been shown to have greater TfR1 expression and positivity than B-lineage counterparts,[57,59] these cancers should be especially amenable to tJBA8.1 recognition and capture.

In the future, the aptamer-based malignant cell depletion strategy described here could be adapted to affinity chromatography approaches, eliminating cell processing steps associated with MACS. Chemical conjugation of aptamers to chromatography solid supports will also realize a fully synthetic, low-cost cell depletion system, unlike the anti-biotin coupling used here that relies on expensive antibodies. As contaminating myeloid cells also inhibit the production of CAR T cells,[76] tJBA8.1 could be applied in combination with our reported monocyte-binding aptamer to deplete malignant cells and monocytes from patient PBMC concentrates in a single processing step.[77] Besides cell isolation, we foresee other applications of tJBA8.1 within CAR T-cell manufacturing. Our group previously used cationic comb polymers and polymer-lytic peptide conjugates (VIPER) for non-viral gene delivery to T cells, and low uptake was one of the limiting barriers to activated T-cell transfection.[78,79] Of relevance, we show in this work that activated T cells have upregulated TfR1 expression and high tJBA8.1 binding, and TfR1 is well known to be rapidly internalized upon ligand binding via clathrin-mediated endocytosis.[40] Comb polymer and VIPER formulations could thus be decorated with tJBA8.1 to enhance their binding to activated T cells via TfR1, improving their uptake for T-cell transfection. Outside of CAR T-cell therapy, TfR1 targeting with tJBA8.1 could have implications in the detection of circulating tumor cells and the delivery of

drugs across the blood-brain barrier,[80,81] paving the way for tJBA8.1-based diagnostics and therapeutics.

3.4 MATERIALS AND METHODS

3.4.1 Cell line and primary cell culture

The Jurkat, J.RT3-T3.5, H9, and Raji cell lines used in this work were purchased from ATCC and cultured in RPMI 1640 medium (Corning, Gibco) with 10% FBS (Life Tech). Primary healthy donor PBMCs were isolated from Leukocyte Reduction System (LRS) chambers (Bloodworks Northwest) by Ficoll-Paque density gradient centrifugation (GE). Positively enriched primary $CD4^+$ and $CD8^+$ T cells were gifted by Juno Therapeutics. For T-cell activation studies, T cells were thawed and stimulated 1:1 with Dynabeads Human T-Activator CD3/CD28 (Gibco) in RPMI 1640 10% FBS supplemented with 20 ng/mL recombinant human IL-2 (Miltenyi) for $CD8^+$ T cells, 5 ng/mL recombinant human IL-7 (Miltenyi) for $CD4^+$ T cells, and 0.5 ng/mL recombinant human IL-15 (Miltenyi) for both $CD4^+$ and $CD8^+$ T cells. Fresh media exchanges were conducted every 2-3 days to replenish cytokines, and T cells were passaged to larger plates or flasks upon reaching high densities ($2\text{-}3\times10^6$ cells/mL) with visible yellow coloration of the culture media.

3.4.2 Oligonucleotides, PCR reagents, and recombinant proteins

Aptamer sequences used in this work are listed in **Table S3.4**. All oligonucleotides, including the randomized naïve library, primers, and individual aptamers, were synthesized by Integrated DNA Technologies with either HPLC purification (naïve library and individual aptamers) or standard desalting (primers). The FAM-labeled forward primer and biotin-labeled reverse primer used to amplify aptamer pools between rounds of cell-SELEX are as previously described.[23] dNTPs and Phusion High-Fidelity Polymerase used in PCR reactions were purchased from QIAGEN and

NEB, respectively. For BLI studies, the following recombinant proteins were used: biotinylated human TfR1 (TfR-H82E5, ACROBiosystems) and His-tagged mouse TfR1 (50741-M07H, Sino Biological). Recombinant human holo-Tf used in competition studies was purchased from Sigma-Aldrich. For cryo-EM, recombinant His-tagged human TfR1 was purchased from ACROBiosystems (CD1-H5243).

3.4.3 Flow cytometry reagents and staining

For flow cytometry cell staining and competition studies, we used the following dyes and antibodies: Zombie Violet (1:500, 10^7 cells/mL, BioLegend), CM-Dil (1:200, 10^6 cells/mL, Invitrogen), FITC anti-human CD71 (1:100, BioLegend, CY1G4), FITC anti-human CD14 (1:100, BioLegend, M5E2), FITC anti-human CD3 antibody (1:100, BioLegend, UCHT1), APC-Cy7 anti-human CD14 (1:200, Invitrogen, 61D3), Super Bright 702 anti-human CD19 (1:100, Invitrogen, SJ25C), Super Bright 600 anti-human CD56 (1:100, Invitrogen, TULY56), and Alexa Fluor 647 streptavidin (1:500, BioLegend). Antibody dilutions were adjusted when used as isotype/negative controls to match the concentration of experimental antibody used, or when doing serial dilutions for competition studies.

The base wash buffer used for aptamer folding, cell staining, and washing was comprised of DPBS with calcium and magnesium (Corning; ~0.9 mM $CaCl_2$ and ~0.5 mM $MgCl_2$) further supplemented with 5 mM $MgCl_2$ (Fisher) and 25 mM D-glucose (Sigma-Aldrich). For antibody staining without aptamers, wash buffer supplemented with 1% BSA (Miltenyi) was used. For aptamer binding/staining with or without antibodies, wash buffer supplemented with 1% BSA and 0.1 mg/mL yeast tRNA (Invitrogen) was used. Wash buffer supplemented with 1% BSA was used for all wash steps. Aptamers were folded at 1 µM in wash buffer by heating the solution at 95 °C

for 5 min followed by snap cooling on ice for at least 10 min before binding. For flow cytometry staining, cells were first removed from culture or thawed and washed with DPBS (Gibco) to remove residual media and serum. Cells were then incubated with live/dead Zombie Violet dye diluted in DPBS for 15 min at room temperature. After live/dead staining, cells were washed with wash buffer 1% BSA to neutralize remaining Zombie Violet and aliquoted into a polypropylene U-bottom 96-well plate (Corning) at 1-2×10^5 cells/well for immortalized cell lines and primary T cells and 2-5×10^5 cells/well for PBMCs. Cells were then blocked with 10 µL FcR Blocking Reagent (Miltenyi) for 5-10 min at 4 °C (only if they were to be stained with antibodies) and subsequently stained with 100 µL antibodies and/or aptamers for 20-30 min at 4 °C in the appropriate binding buffer at the indicated concentrations. For competition assays, unlabeled anti-CD3 antibody (BioLegend, UCHT1), unlabeled anti-CD71 antibody (BioLegend, CY1G4), or recombinant human holo-Tf were added to the primary incubation with aptamer at different concentrations. After staining, cells were washed twice with 200 µL wash buffer 1% BSA to remove excess antibodies and/or aptamers. If the aptamers used were biotinylated, cells underwent a further incubation with 100 µL of fluorescently labeled streptavidin for 20 min at 4 °C in wash buffer 1% BSA and subsequently washed twice as before. Fully stained cells were lightly fixed in 200 µL wash buffer 1% BSA further supplemented with 0.1-0.2% PFA (Alfa Aesar) and immediately analyzed on an Attune NxT Cytometer (Invitrogen). If required, unstained and single-stained cell controls were used for compensation.

3.4.4 Cell-SELEX

The experimental design of cell-SELEX used in this study is summarized in **Figure 3.1A** and **Table S3.1** and was modified from a published protocol.[27] Briefly, we started cell-SELEX with an input of 10 nmol randomized naïve library (theoretically ~10^{16} unique sequences), with each

sequence consisting of a 45-nt random region flanked by two 18-nt constant regions. A total volume of 700 µL naïve library was used (~14 µM) for incubation in the first round of SELEX, whereas 0.2 nmol aptamer pools in 400 µL (~0.2 µM, ~10^{14} sequences) were used in subsequent rounds. In positive selection steps across SELEX rounds, decreasing amounts of Jurkat cells were resuspended with the aptamer pools in wash buffer supplemented with 0.1 mg/mL yeast tRNA, 0.1% BSA, and increasing concentrations of FBS and incubate for decreasing times at 4 °C. Aptamer-bound Jurkat cells were then washed an increasing number of times with wash buffer before aptamers were eluted from the cells by heating at 95 °C for 10 min in 500 µL water (only first round since there was no negative selection) or wash buffer with 0.1 mg/mL yeast tRNA and 0.1% BSA. Cell debris from the elution step was pelleted and heat-eluted aptamers were refolded simultaneously by centrifugation at 13,100 xg for 5 min at 4 °C, and the supernatant with refolded aptamers was collected for immediate PCR amplification (only first round) or negative selection. In negative selection steps across SELEX rounds, the eluted and refolded aptamer pools were incubated with 10^6 J.RT3-T3.5 cells at 4 °C for the corresponding time that was used in positive selection. Aptamer-bound J.RT3-T3.5 cells were removed by centrifugation, and the supernatant with unbound aptamer pool was collected for PCR amplification. After each SELEX round, we optimized the PCR cycle number required to amplify the aptamers pools. For preparation of ssDNA aptamer pools from the PCR product, the amplified double-stranded DNA (dsDNA) pool was captured via the biotinylated reverse strand using High Capacity Streptavidin Agarose (Thermo Fisher) and the FAM-labeled forward strand ssDNA was then selectively eluted using 200 mM sodium hydroxide. The eluted forward ssDNA was desalted into water using a NAP-5 desalting column (GE Healthcare), dried using a SpeedVac concentrator (Thermo Fisher), and resuspended and folded at 1 µM in wash buffer for the next round of SELEX.

3.4.5 Next generation sequencing (NGS) and sequence analysis

The aptamer pools from each SELEX round were amplified using the barcoded primers listed in **Table S3.2** and sequenced on the MiSeq System (Illumina) using a MiSeq Reagent Kit v2 (300 cycles). FASTAptamer v1.0.3 toolkit was used to analyze the FASTA files from sequencing.[29] Specifically, *FASTAptamer-Count* was first used to measure the reads for each unique sequence and rank sequences by abundance (reads per million or RPM), and *FASTAptamer-Enrich* was then used to analyze the fold-enrichment of each unique sequence across adjacent rounds (e.g., RPM in Round Y divided by RMP in Round X). MEME Suite v5.3.3 Motif Discovery tool was used to find recurring motifs within the top 50 aptamer sequences in rounds 5-8 with the following settings: zero or one site per sequence for motif distribution, 0-order model of sequences for the background model, minimum motif width of 6 bases, maximum motif width of 45 bases, minimum sites per motif of 2, maximum sites per motif of 50, and search given strand only.[31] Phylogenetic trees of the top 50 aptamer sequences in rounds 5-8 were generated using the FigTree v1.4.3 graphical viewer to map sequence similarities and differences.[30] The NUPACK web application was used to predict the minimum free energy structure of aptamer sequences at 4 °C with 137 mM Na^{+} and 5.5 mM Mg^{++} concentrations.[33]

3.4.6 Subcellular localization of aptamer binding by trypsin flow and confocal imaging

Both flow cytometry and confocal imaging were used to determine the subcellular localization of tJBA8.1 binding to Jurkat cells at 4 °C. In the flow cytometry assay, Jurkat cells were first stained with Cy5-labeled tJBA8.1 as described above. After washing away unbound aptamer, 50 µL 0.25% trypsin or wash buffer 1% BSA was added to the cells for a 5-min incubation at 37 °C. Immediately after incubation, 200 µL RPMI 1640 10% FBS was added to the cells to neutralize

trypsin activity, and the cells were washed twice with 200 µL wash buffer 1% BSA before fixation in wash buffer 1% BSA further supplemented with 0.2% PFA. The change in Cy5-labeled tJBA8.1 binding on the Jurkat cell surface due to trypsin treatment was evaluated by flow cytometry.

For confocal imaging of tJBA8.1 subcellular compartment binding at 4 °C, 15-mm round glass cover slips (Bellco Glass) were first sanitized in 95% ethanol for 5 min and subsequently dried over a 24-well plate for 15 min. Cover slips were next coated with 150 µL 10 µg/mL poly-D-lysine (Sigma) for 2 hr at 37 °C in a 24-well plate. Meanwhile, 5×10^6 Jurkat cells were washed twice with wash buffer 1% BSA and stained with 300 µL 200 nM Cy5-labeled RANL or tJBA8.1 aptamer in binding buffer for 30 min at 4 °C. After aptamer binding, excess aptamer was removed by washing cells twice with 200 µL wash buffer 1% BSA, and cells were resuspended in 200 µL wash buffer 1% BSA for cover slip plating. For this, poly-D-lysine-coated cover slips were washed once with 1 mL water in a 24-well plate to remove excess poly-D-lysine before adding cells. Jurkat cells were adhered to the coated cover slips by centrifugation at 650 xg for 10 min at 4 °C. After cell attachment, the excess buffer was aspirated, and adhered cells were fixed with 200 µL 4% PFA for 10 min at room temperature. Fixative was washed off the cell-coated cover slips three times with 1 mL DPBS for 1 min each, and fixed cells were then permeabilized with 200 µL 0.1% Triton X-100 (Sigma) for 10 min at room temperature. After washing as before, FITC Phalloidin (1:100, Invitrogen) and DAPI (300 nM, Thermo Fisher) in 200 µL DPBS were applied onto the fixed and permeabilized cells for 30 min at room temperature. Stained cells were then washed as before except in longer 5-min increments, and the stained cell-coated glass cover slips were mounted onto larger microscope slides (Fisher) with 10 µL polyvinyl acetate. Fluorescent images were taken at 60X magnification on a Leica SP8X confocal microscope in the Keck Microscopy

Center at the University of Washington, and image processing and overlaying was performed using Fiji/ImageJ.[82]

3.4.7 Target receptor pull-down and identification

The membrane protein extraction and subsequent aptamer pull-down process was modified from a previously published method.[34] For each group (control and tJBA8.1), approximately 85×10^6 Jurkat cells were washed three times in DPBS to remove media-derived proteins and then lysed for 30 min at 4 °C with end-over-end mixing in ~3.3 mL hypotonic buffer comprised of 10 mM Tris-HCl pH 7.5 supplemented with EDTA-free cOmplete Protease Inhibitor Cocktail (Roche) and 1 mM PMSF (Thermo Fisher). The resulting cell membrane debris were pelleted at 16,000 xg for 15 min at 4 °C and washed three times with 3.3 mL of the same hypotonic buffer to remove released intracellular proteins. The membrane pellets were then each resuspended in 1 mL wash buffer containing 1% Triton X-100, protease inhibitors, and 1 mM PMSF to extract and solubilize membrane proteins. The extraction was conducted for 30 min at 4 °C with end-over-end mixing followed by a brief 5-min sonication in an ice water bath. Afterwards, the samples were centrifuged as before and the supernatant containing the extracted proteins was collected and stored at -80 °C or immediately used.

For pre-clearing, the extracts (1 mL) were thawed and spiked with 100nM of RANL and 0.1 mg/mL yeast tRNA. After incubating for 30 min at 4 °C with end-over-end mixing, 200 µL (2 mg) MyOne Streptavidin C1 Dynabeads (Thermo Fisher) were added to the extracts and incubated for another 15 min at 4 °C to magnetically remove RANL-bound proteins. For the tJBA8.1 group, the pre-cleared extract was then spiked with 0.1 mg/mL salmon sperm DNA (Invitrogen) as an additional anionic blocker and 100 nM biotinylated tJBA8.1. After incubating for 30 min at 4 °C

with end-over-end mixing, 150 µL (1.5 mg) Streptavidin Dynabeads were added to the binding reaction and incubated for another 15 min at 4 °C to capture tJBA8.1-bound proteins. For the control group, 150 µL (1.5 mg) Streptavidin Dynabeads were instead saturated with 50 nmol biotin and added to the pre-cleared extract for a 30-min incubation at 4 °C. Afterwards, the beads for both groups were washed 5 times for 5 min each with 1 mL cold wash buffer containing 0.01% Triton X-100 to remove unbound proteins. To minimize stripping off streptavidin from the beads, the captured proteins were mildly eluted by heating the beads for 15 min a 47 °C in 50 µL Laemmli Sample Buffer (Bio-Rad) containing 2.5% 2-mercaptoethanol (Bio-Rad), 4.6M urea (Fisher), and 0.01% Triton X-100. Eluted proteins were stored at -80 °C unless used immediately.

Eluted proteins (25 µL) were loaded onto a Novex WedgeWell 8% Tris-Glycine gel (Invitrogen) and separated by SDS-PAGE. The gel was stained with a Colloidal Blue Staining Kit (Invitrogen) according to the manufacturer's instructions and imaged on a Gel Doc EZ system (Bio-Rad). Enriched protein bands were excised and submitted to the Proteomics and Metabolomics shared resource at the Fred Hutchinson Cancer Research Center for processing by tandem mass spectrometry on an OrbiTrap Elite (Thermo Fisher). The data were searched using Proteome Discoverer 2.2 against a Uniprot Human database that included common contaminants. Results were filtered for high confidence 1% false discovery rate at the peptide level.

3.4.8 siRNA knockdown

Some 10^6 Jurkat cells in logarithmic growth phase were nucleofected with 30 pmol NS or TFRC siRNA listed in **Table S3.5** using the Human T cell Nucleofector Kit (Lonza) with Program X-001 following the manufacturer's instructions. The cells were analyzed 22 h later for tJBA8.1 binding and antibody-measured TfR1 expression by flow cytometry.

3.4.9 BLI

BLI studies were performed on an Octet RED96 instrument (Sartorius) using either streptavidin or Ni-NTA biosensors (Sartorius). The sample buffer used for equilibration, loading, rinse, baseline, association, and dissociation steps was comprised of wash buffer supplemented with 1% BSA, 0.1 mg/mL yeast tRNA, 0.1 mg/mL salmon sperm DNA, and 0.01% Tween-20 (Sigma). All steps were performed at 25 °C with sample agitation at 1000 r.p.m. Biosensors were allowed to equilibrate in buffer for at least 10 min before loading. Loading thresholds were optimized for each capture ligand and analyte used. For streptavidin biosensors, 25 nM recombinant biotinylated human TfR1 was loaded until a 3.5 nm threshold and 50 nM biotinylated aptamers were loaded until a 0.5 nm threshold before performing rinse and baseline steps in buffer alone for 100 s each. For Ni-NTA biosensors, 150 nM recombinant His-tagged mouse TfR1 was loaded until a 0.7 nm threshold before performing cross-linking with 0.1 M EDC + 0.025 M NHS in water for 60 s to stabilize the captured protein. The cross-linking reaction was quenched with 1M ethanolamine pH 8.5 for 60 s before performing rinse and baseline steps as before. Afterwards, loaded sensors were associated with appropriate analytes at concentrations and times indicated in the figures and captions. Lastly, sensors were transferred to wells containing buffer alone for dissociation. Data analysis was performed with the Octet Data Analysis 9.0 software (Sartorius). Association and dissociation curves were normalized to sensors that received capture ligand alone, and kinetic constants were calculated for datasets with several analyte concentrations by conducting a global fit of the association and dissociation curves to a 1:1 ligand binding model. The quality of each fit was evaluated using R^2 and χ^2 values, which are listed in **Table S3.6** for the applicable datasets along with the calculated kinetic constants.

3.4.10 Cryo-EM sample preparation, data collection, and processing

Lyophilized His-tagged human TfR1 was first reconstituted in deionized water to 600 µg/mL per the manufacture's instruction (ACROBiosystems). The resuspended protein was then buffer exchanged and concentrated to 3 mg/mL in TBS pH 8.0 using a 30 kDa MWCO polyethersulfone ultrafiltration centrifugal device (Pierce). Before conducting cryo-EM, a small aliquot of the concentrated TfR1 protein was diluted 1:200 in wash buffer and screened by negative stain transmission electron microscopy (TEM). Briefly, 5 µL of diluted sample was applied onto glow-discharged continuous carbon grids (Electron Microscopy Sciences, CF400-CU). After a 1-min incubation, excess protein solution was wicked away using filter paper, and the grids were subsequently wash twice with 5 µL distilled water and once with 5 µL 2% phosphotungerstic acid (PTA) pH 7.4. The sample was then stained for 30 s using another application of the same PTA solution, and excess staining solution was wicked away using filter paper such that a thin layer of staining solution was left on the grid. The stained sample was air dried before analysis on a Tecnai G2 Spirit TEM (Thermo Fisher).

For cryo-EM of tJBA8.1 binding to TfR1, the concentrated TfR1 protein was incubated with tJBA8.1 at a 1:2 molar ratio of TfR1 monomer to tJBA8.1 in DPBS with calcium and magnesium further supplemented with 5 mM $MgCl_2$ for 1 h at 4 °C. The binding reaction was then diluted to 0.03 mg/mL of TfR1 protein, and 3 µL of the diluted reaction was applied to plasma-cleaned lacey carbon grids with a continuous layer of ultrathin carbon (Electron Microscopy Sciences, LC325-CU-CC). Afterwards, the grids were plunge frozen in liquid ethane pre-cooled by liquid nitrogen using a Vitrobot Mark IV (Thermo Fisher) with the following settings: 4 °C, 100% humidity, 60 s wait time, 3.5 s blot time, and 4 blot force. The grids were analyzed using a Titan Halo (Thermo Fisher) equipped with a Gatan K3 camera. The nominal magnification was 37,000x and the

calibrated pixel size was 0.8465 Å. A total dose of 79.2 $e^-/Å^2$ was fractioned into 80 frames using SerialEM,[83] and 1,397 movies were collected.

Cryo-EM data was processed with cryoSPARC.[84] Specifically, beam-induced motion correction was performed with *Patch motion correction*, and the resulting averaged micrographs were further corrected by CTF estimation using *Patch CTF estimation*. Particle picking was then performed using *Blob picker* followed by particle extraction from micrographs, which resulted in a total of 1,070,200 particles with a box size of 256 pixels. Three rounds of *2D classification* and *Select 2D classes* were then conducted for initial particle cleanup, yielding 247,146 particles. The selected particles were ported to *Ab-initio Reconstruction* to generate three initial 3D maps, each of which was refined according to its own particle set using *Homogenous Refinement* with C1 symmetry. A total of 216,817 particles generated the initial map with the highest resolution, and that map was selected for further refinement using *Non-uniform Refinement* with C1 symmetry followed with C2 symmetry.[85] The final refinement was performed using *Non-uniform Refinement* (C2 symmetry) with defocus and CTF refinement. The estimated resolution is 2.54 Å based on gold standard Fourier shell correlation of 0.143. We obtained raw (unsharpened) and sharpened density maps from the final non-uniform refinement, and the sharpened map was further filtered with a gaussian filter. Both raw and sharpened (filtered) maps were deposited in the Electron Microscopy Data Bank (EMDB) and used in the following model building and refinement. Parameters concerning cryo-EM data collection and processing are listed in **Table S3.7**.

3.4.11 *De novo* modeling of TfR1-bound tJBA8.1 into the cryo-EM density map and refinement of the tJBA8.1-TfR1 complex

Initial coordinates for TfR1 were taken from PDB code 1CX8, rigid-body fitted into the cryo-EM density map using CHIMERA,[86] and subjected to *Auto Fit Rotamers* and *Chain Refine* in COOT.[87] The model of tJBA8.1 was built manually using COOT. Briefly, the phosphate backbone of tJBA8.1 was first traced into the cryo-EM density map followed by modeling the bases. Base assignment was guided by the resolution of the electron densities, the unique patterning of pyrimidines and purines within the tJBA8.1 sequence, and the consideration of base-pairing geometries. Rigid-body fitted TfR1 and *ab initio* modeled tJBA8.1 were then subjected to iterative rounds of real space refinement and manual model building in PHENIX and COOT.[87–89] The final model was validated using MolProbity,[90,91] and analysis of structures and generation of molecular graphics were performed with CHIMERA and PyMOL.[86,92] Detailed statistics regarding structure refinement and validation are given in **Table S3.7**. Interactions at the modeled tJBA8.1-TfR1 interface were determined using PDBePISA, PLIP, and NUCPLOT,[47–49] and the calculated interactions from the former two programs are listed in **Table S3.8**.

3.4.12 Raji cell depletion from PBMCs

Raji cells (5×10^6) were first pre-stained with Vybrant™ CM-Dil dye (1:200 or 5 μM, Invitrogen) in serum-free RPMI 1640 medium at 10^6 cells/mL for 30 min at room temperature. After washing the stained cells twice with wash buffer, approximately 3×10^4, 3×10^5, and 3×10^6 CM-Dil stained Raji cells were spiked into three aliquots of 30×10^6 freeze-thawed PBMCs to achieve 0.1%, 1%, and 10% spiked cell percentages. The mixed PBMC-Raji cells were then each stained with 500 μL 80 nM biotinylated tJBA8.1 in wash buffer supplemented with 0.5% BSA and 0.1 mg/mL yeast

tRNA for 30 min at 4 °C. Meanwhile, three aliquots of 150 µL Anti-Biotin MicroBeads (Miltenyi) were blocked in 500 µL of the same buffer for 30 min at 4 °C to prevent non-specific interactions. After staining, each group of aptamer-labeled mixed cells was washed once with wash buffer 0.5% BSA 0.1 mg/mL yeast tRNA and resuspended in 650 µL of the blocked microbead-containing solution for a 15-min incubation at 4 °C. After attaching the microbeads to the aptamer-labeled cells, each group of fully labeled mixed cells was washed once as before and resuspended in 1 mL wash buffer 0.5% BSA 0.1 mg/mL yeast tRNA.

Prior to Raji cell depletion, three LS Columns (Miltenyi) were anchored onto a QuadroMACS Separator (Miltenyi) and each washed once with 3 mL cold wash buffer 0.5% BSA 0.1 mg/ml yeast tRNA. Each column was then equipped with a 30 µm Pre-Separation Filter (Miltenyi) before applying the fully labeled mixed cells. The Raji cell-depleted PBMCs in the flow through were collected, and each filter-equipped column was washed three times with 3 mL cold wash buffer 0.5% BSA into the same flow through collection tube. The captured Raji cells were collected by removing the columns from the magnet and flushing each with 5 mL autoMACS Rinsing Solution (Miltenyi; 2 mM EDTA) further supplemented with 3 mM EDTA (Invitrogen) and 0.5% BSA using a plunger. The cell composition in each fraction and corresponding depletion efficiencies were determined by antibody staining and flow cytometry.

3.4.13 Protein sequence alignment of TfR1 with mouse ortholog and hepatic homolog

Protein sequence alignment of human TfR1 (UniProt entry P02786) with mouse TfR1 (UniProt entry Q62351) and human TfR2 (UniProt entry Q9UP52) was performed with Clustal Omega v1.2.4.[93,94] The percent identity between the extracellular domain of human TfR1 (residues 89-

760) with each of the extracellular domains of mouse TfR1 (residues 89-763) and human TfR2 (residues 105-801) was calculated in the same program.

3.4.14 Statistical analysis

Data are expressed as mean ± standard deviation, unless otherwise stated, and the number of biological and technical replicates is specified in the figure captions. A two-tailed *t*-test was used for hypothesis testing when comparing only two populations. ANOVA was used for hypothesis testing when comparing more than two populations to each other. Paired hypothesis testing was sometimes performed to account for large donor-to-donor or experimental (e.g., nucleofection) variability. To correct for multiple comparisons, Dunnett's test was used to adjust the *P* values when every mean was compared to a control mean, whereas Šídák correction was used to adjust *P* values when select sets of means were compared, assuming independence. If comparisons could not be assumed to be independent from each other, Bonferroni correction was used instead of the Šídák correction to adjust *P* values. Tested differences were considered significant if $P < 0.05$. Unless otherwise stated in the methods, graphing and statistical tests were performed using GraphPad Prism v6.01 (GraphPad Software Inc.) for Windows.

3.5 AUTHOR CONTRIBUTIONS

S.H.P. and M.C.J. conceived the idea. S.H.P., M.C.J., and A.dG. provided experimental advice and funding support. E.L.C., I.I.C., N.K., and S.H.P. designed the project. E.L.C., I.I.C., N.K., H.B., and T.W. conceived, performed, and interpreted the experiments. N.K. designed and performed the SELEX procedure. I.I.C., J.R., and N.K. evaluated the binding of aptamer libraries and select aptamers. I.I.C., S.J.S., and N.K. analyzed the NGS data. I.I.C. and E.LC. performed binding curve studies. A.Y. and I.I.C performed subcellular localization studies. E.C. designed and

performed the pull-down study for receptor identification. N.K. and Y.Z. conducted siRNA knockdown. E.L.C., A.Y., and I.I.C. evaluated TfR1 expression on immortalized cell lines and PBMCs. N.K. and E.L.C. performed aptamer binding studies with activated T cells. I.I.C. performed BLI studies. J.R. assessed aptamer co-staining and competition with other ligands. T.W. and D.G. performed cryo-EM, and H.B. performed *de novo* modeling of the tJBA8.1-TfR1 complex. E.L.C. conducted Raji depletion from PBMCs. I.I.C. performed protein sequence alignments. E.L.C., I.I.C., H.B., and T.W. prepared the figures. E.L.C. and I.I.C. performed statistical analyses. E.L.C. and I.I.C. wrote the manuscript with input from N.K., H.B., T.W., A.dG., and S.H.P.

3.6 ACKNOWLEDGEMENTS

This work was supported by a sponsored research agreement from Juno Therapeutics, a Bristol-Myers Squibb company, and by the NIH (U54CA199090 and R01AG063845). Ian Cardle was supported by a National Science Foundation Graduate Research Fellowship under grant no. DGE-1762114 and by the National Cancer Institute of the National Institutes of Health under award no. 5T32CA080416-19. Amédée des Georges was supported by NIH grant no. R35GM133598 during his contributions to this research. We thank Dr. Chris Ramsborg, Dr. Allison Bianchi, Dr. Julie Shi, and Calvin Chan from Juno Therapeutics for their valuable discussion and suggestions. We acknowledge support from both the NIH under grant no. S10 OD016240 and the UW Student Technology Fee to the W. M. Keck Microscopy Center that funds the Leica SP8X confocal microscope used in our studies, and we thank Keck Center manager Dr. Nathaniel Peters for his assistance. We are also grateful to Dr. Philip Gafken and Lisa Jones from the Fred Hutchinson Cancer Research Center for preparing and processing our mass spectrometry samples. We lastly

thank the Imaging Facility of the CUNY Advanced Science Research Center for cryo-EM instrument use as well as scientific and technical assistance.

3.7 REFERENCES

(1) Maude, S. L.; Laetsch, T. W.; Buechner, J.; Rives, S.; Boyer, M.; Bittencourt, H.; Bader, P.; Verneris, M. R.; Stefanski, H. E.; Myers, G. D.; Qayed, M.; De Moerloose, B.; Hiramatsu, H.; Schlis, K.; Davis, K. L.; Martin, P. L.; Nemecek, E. R.; Yanik, G. A.; Peters, C.; Baruchel, A.; Boissel, N.; Mechinaud, F.; Balduzzi, A.; Krueger, J.; June, C. H.; Levine, B. L.; Wood, P.; Taran, T.; Leung, M.; Mueller, K. T.; Zhang, Y.; Sen, K.; Lebwohl, D.; Pulsipher, M. A.; Grupp, S. A. Tisagenlecleucel in Children and Young Adults with B-Cell Lymphoblastic Leukemia. *New England Journal of Medicine* **2018**, *378* (5), 439–448.

(2) Schuster, S. J.; Bishop, M. R.; Tam, C. S.; Waller, E. K.; Borchmann, P.; McGuirk, J. P.; Jäger, U.; Jaglowski, S.; Andreadis, C.; Westin, J. R.; Fleury, I.; Bachanova, V.; Foley, S. R.; Ho, P. J.; Mielke, S.; Magenau, J. M.; Holte, H.; Pantano, S.; Pacaud, L. B.; Awasthi, R.; Chu, J.; Anak, Ö.; Salles, G.; Maziarz, R. T. Tisagenlecleucel in Adult Relapsed or Refractory Diffuse Large B-Cell Lymphoma. *New England Journal of Medicine* **2018**, *380* (1), 45–56.

(3) Neelapu, S. S.; Locke, F. L.; Bartlett, N. L.; Lekakis, L. J.; Miklos, D. B.; Jacobson, C. A.; Braunschweig, I.; Oluwole, O. O.; Siddiqi, T.; Lin, Y.; Timmerman, J. M.; Stiff, P. J.; Friedberg, J. W.; Flinn, I. W.; Goy, A.; Hill, B. T.; Smith, M. R.; Deol, A.; Farooq, U.; McSweeney, P.; Munoz, J.; Avivi, I.; Castro, J. E.; Westin, J. R.; Chavez, J. C.; Ghobadi, A.; Komanduri, K. V; Levy, R.; Jacobsen, E. D.; Witzig, T. E.; Reagan, P.; Bot, A.; Rossi, J.; Navale, L.; Jiang, Y.; Aycock, J.; Elias, M.; Chang, D.; Wiezorek, J.; Go, W. Y. Axicabtagene Ciloleucel CAR T-Cell Therapy in Refractory Large B-Cell Lymphoma. *New England Journal of Medicine* **2017**, *377* (26), 2531–2544.

(4) Locke, F. L.; Ghobadi, A.; Jacobson, C. A.; Miklos, D. B.; Lekakis, L. J.; Oluwole, O. O.; Lin, Y.; Braunschweig, I.; Hill, B. T.; Timmerman, J. M.; Deol, A.; Reagan, P. M.; Stiff, P.; Flinn, I. W.; Farooq, U.; Goy, A.; McSweeney, P. A.; Munoz, J.; Siddiqi, T.; Chavez, J. C.; Herrera, A. F.; Bartlett, N. L.; Wiezorek, J. S.; Navale, L.; Xue, A.; Jiang, Y.; Bot, A.; Rossi, J. M.; Kim, J. J.; Go, W. Y.; Neelapu, S. S. Long-Term Safety and Activity of Axicabtagene Ciloleucel in Refractory Large B-Cell Lymphoma (ZUMA-1): A Single-Arm, Multicentre, Phase 1-2 Trial. *The Lancet Oncology* **2019**, *20* (1), 31–42.

(5) Wang, M.; Munoz, J.; Goy, A.; Locke, F. L.; Jacobson, C. A.; Hill, B. T.; Timmerman, J. M.; Holmes, H.; Jaglowski, S.; Flinn, I. W.; McSweeney, P. A.; Miklos, D. B.; Pagel, J. M.; Kersten, M.-J.; Milpied, N.; Fung, H.; Topp, M. S.; Houot, R.; Beitinjaneh, A.; Peng, W.; Zheng, L.; Rossi, J. M.; Jain, R. K.; Rao, A. V; Reagan, P. M. KTE-X19 CAR T-Cell Therapy in Relapsed or Refractory Mantle-Cell Lymphoma. *New England Journal of Medicine* **2020**, *382* (14), 1331–1342.

(6) Abramson, J. S.; Palomba, M. L.; Gordon, L. I.; Lunning, M. A.; Wang, M.; Arnason, J.; Mehta, A.; Purev, E.; Maloney, D. G.; Andreadis, C.; Sehgal, A.; Solomon, S. R.; Ghosh, N.; Albertson, T. M.; Garcia, J.; Kostic, A.; Mallaney, M.; Ogasawara, K.; Newhall, K.; Kim, Y.; Li, D.; Siddiqi, T. Lisocabtagene Maraleucel for Patients with Relapsed or Refractory Large B-Cell Lymphomas (TRANSCEND NHL 001): A Multicentre Seamless Design Study. *The Lancet* **2020**, *396* (10254), 839–852.

(7) Munshi, N. C.; Anderson, L. D.; Shah, N.; Madduri, D.; Berdeja, J.; Lonial, S.; Raje, N.; Lin, Y.; Siegel, D.; Oriol, A.; Moreau, P.; Yakoub-Agha, I.; Delforge, M.; Cavo, M.; Einsele, H.; Goldschmidt, H.; Weisel, K.; Rambaldi, A.; Reece, D.; Petrocca, F.; Massaro, M.; Connarn, J. N.; Kaiser, S.; Patel, P.; Huang, L.; Campbell, T. B.; Hege, K.; San-Miguel, J. Idecabtagene Vicleucel in Relapsed and Refractory Multiple Myeloma. *New England Journal of Medicine* **2021**, *384* (8), 705–716.

(8) Berdeja, J. G.; Madduri, D.; Usmani, S. Z.; Jakubowiak, A.; Agha, M.; Cohen, A. D.; Stewart, A. K.; Hari, P.; Htut, M.; Lesokhin, A.; Deol, A.; Munshi, N. C.; O'Donnell, E.; Avigan, D.; Singh, I.; Zudaire, E.; Yeh, T.-M.; Allred, A. J.; Olyslager, Y.; Banerjee, A.; Jackson, C. C.; Goldberg, J. D.; Schecter, J. M.; Deraedt, W.; Zhuang, S. H.; Infante, J.; Geng, D.; Wu, X.; Carrasco-Alfonso, M. J.; Akram, M.; Hossain, F.; Rizvi, S.; Fan, F.; Lin, Y.; Martin, T.; Jagannath, S. Ciltacabtagene Autoleucel, a B-Cell Maturation Antigen-Directed Chimeric Antigen Receptor T-Cell Therapy in Patients with Relapsed or Refractory Multiple Myeloma (CARTITUDE-1): A Phase 1b/2 Open-Label Study. *The Lancet* **2021**, *398* (10297), 314–324.

(9) Vormittag, P.; Gunn, R.; Ghorashian, S.; Veraitch, F. S. A Guide to Manufacturing CAR T Cell Therapies. *Current Opinion in Biotechnology* **2018**, *53*, 164–181.

(10) Cardle, I. I.; Cheng, E. L.; Jensen, M. C.; Pun, S. H. Biomaterials in Chimeric Antigen Receptor T-Cell Process Development. *Accounts of Chemical Research* **2020**, *53* (9), 1724–1738.

(11) Powell, D. J.; Brennan, A. L.; Zheng, Z.; Huynh, H.; Cotte, J.; Levine, B. L. Efficient Clinical-Scale Enrichment of Lymphocytes for Use in Adoptive Immunotherapy Using a Modified Counterflow Centrifugal Elutriation Program. *Cytotherapy* **2009**, *11* (7), 923–935.

(12) Maude, S. L.; Frey, N.; Shaw, P. A.; Aplenc, R.; Barrett, D. M.; Bunin, N. J.; Chew, A.; Gonzalez, V. E.; Zheng, Z.; Lacey, S. F.; Mahnke, Y. D.; Melenhorst, J. J.; Rheingold, S. R.; Shen, A.; Teachey, D. T.; Levine, B. L.; June, C. H.; Porter, D. L.; Grupp, S. A. Chimeric Antigen Receptor T Cells for Sustained Remissions in Leukemia. *New England Journal of Medicine* **2014**, *371* (16), 1507–1517.

(13) Iyer, R. K.; Bowles, P. A.; Kim, H.; Dulgar-Tulloch, A. Industrializing Autologous Adoptive Immunotherapies: Manufacturing Advances and Challenges. *Frontiers in Medicine* **2018**, *5*, 150.

(14) Hoffmann, J.-M.; Schubert, M.-L.; Wang, L.; Hückelhoven, A.; Sellner, L.; Stock, S.; Schmitt, A.; Kleist, C.; Gern, U.; Loskog, A.; Wuchter, P.; Hofmann, S.; Ho, A. D.; Müller-Tidow, C.; Dreger, P.; Schmitt, M. Differences in Expansion Potential of Naive Chimeric Antigen Receptor T Cells from Healthy Donors and Untreated Chronic Lymphocytic Leukemia Patients. *Frontiers in Immunology* **2018**, *8*, 1956.

(15) Ruella, M.; Xu, J.; Barrett, D. M.; Fraietta, J. A.; Reich, T. J.; Ambrose, D. E.; Klichinsky, M.; Shestova, O.; Patel, P. R.; Kulikovskaya, I.; Nazimuddin, F.; Bhoj, V. G.; Orlando, E. J.; Fry, T. J.; Bitter, H.; Maude, S. L.; Levine, B. L.; Nobles, C. L.; Bushman, F. D.; Young, R. M.; Scholler, J.; Gill, S. I.; June, C. H.; Grupp, S. A.; Lacey, S. F.; Melenhorst, J. J. Induction of Resistance to Chimeric Antigen Receptor T Cell Therapy by Transduction of a Single Leukemic B Cell. *Nature Medicine* **2018**, *24* (10), 1499–1503.

(16) Jie, X.; Li-Juan, C.; Shuang-Shuang, Y.; Yan, S.; Wen, W.; Yuan-Fang, L.; Ji, X.; Yan, Z.; Wu, Z.; Xiang-Qin, W.; Jing, W.; Yan, W.; Jin, W.; Hua, Y.; Wen-Bin, X.; Hua, J.; Juan, D.; Xiao-Yi, D.; Biao, L.; Jun-Min, L.; Wei-Jun, F.; Jiang, Z.; Li, Z.; Zhu, C.; (Frank), F.

X.-H.; Jian, H.; Jian-Yong, L.; Jian-Qing, M.; Sai-Juan, C. Exploratory Trial of a Biepitopic CAR T-Targeting B Cell Maturation Antigen in Relapsed/Refractory Multiple Myeloma. *Proceedings of the National Academy of Sciences* **2019**, *116* (19), 9543–9551.

(17) Miltenyi, S.; Müller, W.; Weichel, W.; Radbruch, A. High Gradient Magnetic Cell Separation with MACS. *Cytometry* **1990**, *11* (2), 231–238.

(18) Alcantara, M.; Tesio, M.; June, C. H.; Houot, R. CAR T-Cells for T-Cell Malignancies: Challenges in Distinguishing between Therapeutic, Normal, and Neoplastic T-Cells. *Leukemia* **2018**, *32* (11), 2307–2315.

(19) Fleischer, L. C.; Spencer, H. T.; Raikar, S. S. Targeting T Cell Malignancies Using CAR-Based Immunotherapy: Challenges and Potential Solutions. *Journal of Hematology & Oncology* **2019**, *12* (1), 141.

(20) Zhou, J.; Rossi, J. Aptamers as Targeted Therapeutics: Current Potential and Challenges. *Nature Reviews Drug Discovery* **2017**, *16* (6), 440.

(21) Zhang, Z.; Chen, N.; Li, S.; Battig, M. R.; Wang, Y. Programmable Hydrogels for Controlled Cell Catch and Release Using Hybridized Aptamers and Complementary Sequences. *Journal of the American Chemical Society* **2012**, *134* (38), 15716–15719.

(22) Rusconi, C. P.; Scardino, E.; Layzer, J.; Pitoc, G. A.; Ortel, T. L.; Monroe, D.; Sullenger, B. A. RNA Aptamers as Reversible Antagonists of Coagulation Factor IXa. *Nature* **2002**, *419*, 90–94.

(23) Kacherovsky, N.; Cardle, I. I.; Cheng, E. L.; Yu, J. L.; Baldwin, M. L.; Salipante, S. J.; Jensen, M. C.; Pun, S. H. Traceless Aptamer-Mediated Isolation of CD8+ T Cells for Chimeric Antigen Receptor T-Cell Therapy. *Nature Biomedical Engineering* **2019**, *3* (10), 783–795.

(24) Robertson, D. L.; Joyce, G. F. Selection in Vitro of an RNA Enzyme That Specifically Cleaves Single-Stranded DNA. *Nature* **1990**, *344*, 467–468.

(25) Tuerk, C.; Gold, L. Systematic Evolution of Ligands by Exponential Enrichment: RNA Ligands to Bacteriophage T4 DNA Polymerase. *Science* **1990**, *249* (4968), 505–510.

(26) Ellington, A. D.; Szostak, J. W. In Vitro Selection of RNA Molecules That Bind Specific Ligands. *Nature* **1990**, *346*, 818–822.

(27) Sefah, K.; Shangguan, D.; Xiong, X.; O'Donoghue, M. B.; Tan, W. Development of DNA Aptamers Using Cell-Selex. *Nature Protocols* **2010**, *5*, 1169–1185.

(28) Weiss, A.; Stobo, J. D. Requirement for the Coexpression of T3 and the T Cell Antigen Receptor on a Malignant Human T Cell Line. *Journal of Experimental Medicine* **1984**, *160* (5), 1284–1299.

(29) Alam, K. K.; Chang, J. L.; Burke, D. H. FASTAptamer: A Bioinformatic Toolkit for High-Throughput Sequence Analysis of Combinatorial Selections. *Molecular Therapy - Nucleic Acids* **2015**, *4* (3), e230.

(30) Rambaut, A. *FigTree-version 1.4. 3, a graphical viewer of phylogenetic trees*. http://tree.bio.ed.ac.uk/software/figtree (accessed 2021-03-03).

(31) Bailey, T. L.; Boden, M.; Buske, F. A.; Frith, M.; Grant, C. E.; Clementi, L.; Ren, J.; Li, W. W.; Noble, W. S. MEME Suite: Tools for Motif Discovery and Searching. *Nucleic Acids Research* **2009**, *37*, W202–W208.

(32) Gold, L.; Ayers, D.; Bertino, J.; Bock, C.; Bock, A.; Brody, E. N.; Carter, J.; Dalby, A. B.; Eaton, B. E.; Fitzwater, T.; Flather, D.; Forbes, A.; Foreman, T.; Fowler, C.; Gawande, B.; Goss, M.; Gunn, M.; Gupta, S.; Halladay, D.; Heil, J.; Heilig, J.; Hicke, B.; Husar, G.; Janjic, N.; Jarvis, T.; Jennings, S.; Katilius, E.; Keeney, T. R.; Kim, N.; Koch, T. H.; Kraemer, S.;

Kroiss, L.; Le, N.; Levine, D.; Lindsey, W.; Lollo, B.; Mayfield, W.; Mehan, M.; Mehler, R.; Nelson, S. K.; Nelson, M.; Nieuwlandt, D.; Nikrad, M.; Ochsner, U.; Ostroff, R. M.; Otis, M.; Parker, T.; Pietrasiewicz, S.; Resnicow, D. I.; Rohloff, J.; Sanders, G.; Sattin, S.; Schneider, D.; Singer, B.; Stanton, M.; Sterkel, A.; Stewart, A.; Stratford, S.; Vaught, J. D.; Vrkljan, M.; Walker, J. J.; Watrobka, M.; Waugh, S.; Weiss, A.; Wilcox, S. K.; Wolfson, A.; Wolk, S. K.; Zhang, C.; Zichi, D. Aptamer-Based Multiplexed Proteomic Technology for Biomarker Discovery. *PLOS ONE* **2010**, *5* (12), e15004.

(33) Zadeh, J. N.; Steenberg, C. D.; Bois, J. S.; Wolfe, B. R.; Pierce, M. B.; Khan, A. R.; Dirks, R. M.; Pierce, N. A. NUPACK: Analysis and Design of Nucleic Acid Systems. *Journal of Computational Chemistry* **2011**, *32* (1), 170–173.

(34) Shangguan, D.; Cao, Z.; Meng, L.; Mallikaratchy, P.; Sefah, K.; Wang, H.; Li, Y.; Tan, W. Cell-Specific Aptamer Probes for Membrane Protein Elucidation in Cancer Cells. *Journal of Proteome Research* **2008**, *7* (5), 2133–2139.

(35) Montemiglio, L. C.; Testi, C.; Ceci, P.; Falvo, E.; Pitea, M.; Savino, C.; Arcovito, A.; Peruzzi, G.; Baiocco, P.; Mancia, F.; Boffi, A.; des Georges, A.; Vallone, B. Cryo-EM Structure of the Human Ferritin–Transferrin Receptor 1 Complex. *Nature Communications* **2019**, *10*, 1121.

(36) Tortorella, S.; Karagiannis, T. C. Transferrin Receptor-Mediated Endocytosis: A Useful Target for Cancer Therapy. *Journal of Membrane Biology* **2014**, *247*, 291–307.

(37) Gatter, K. C.; Brown, G.; Trowbridge, I. S.; Woolston, R. E.; Mason, D. Y. Transferrin Receptors in Human Tissues: Their Distribution and Possible Clinical Relevance. *Journal of Clinical Pathology* **1983**, *36* (5), 539–545.

(38) Caruso, A.; Licenziati, S.; Corulli, M.; Canaris, A. D.; De Francesco, M. A.; Fiorentini, S.; Peroni, L.; Fallacara, F.; Dima, F.; Balsari, A.; Turano, A. Flow Cytometric Analysis of Activation Markers on Stimulated T Cells and Their Correlation with Cell Proliferation. *Cytometry* **1997**, *27*, 71–76.

(39) Yeh, C.-J. G.; Taylor, C. G.; Faulka, W. P. Transferrin Binding by Peripheral Blood Mononuclear Cells in Human Lymphomas, Myelomas and Leukemias. *Vox Sanguinis* **1984**, *46* (4), 217–223.

(40) Mayle, K. M.; Le, A. M.; Kamei, D. T. The Intracellular Trafficking Pathway of Transferrin. *Biochimica et Biophysica Acta (BBA) - General Subjects* **2012**, *1820* (3), 264–281.

(41) Boumsell, L.; Bensussan, A.; Kadouche, J. Anti-CD71 Monoclonal Antibodies and Uses Thereof for Treating Malignant Tumor Cells. US 8,409,573 B2, April 2, 2013.

(42) Lawrence, C. M.; Ray, S.; Babyonyshev, M.; Galluser, R.; Borhani, D. W.; Harrison, S. C. Crystal Structure of the Ectodomain of Human Transferrin Receptor. *Science* **1999**, *286* (5440), 779–782.

(43) Lee, J.-H.; Jucker, F.; Pardi, A. Imino Proton Exchange Rates Imply an Induced-Fit Binding Mechanism for the VEGF165-Targeting Aptamer, Macugen. *FEBS Letters* **2008**, *582* (13), 1835–1839.

(44) Davlieva, M.; Donarski, J.; Wang, J.; Shamoo, Y.; Nikonowicz, E. P. Structure Analysis of Free and Bound States of an RNA Aptamer against Ribosomal Protein S8 from Bacillus Anthracis. *Nucleic Acids Research* **2014**, *42* (16), 10795–10808.

(45) Gelinas, A. D.; Davies, D. R.; Janjic, N. Embracing Proteins: Structural Themes in Aptamer–Protein Complexes. *Current Opinion in Structural Biology* **2016**, *36*, 122–132.

(46) Chu, B.; Zhang, D.; Paukstelis, P. J. A DNA G-Quadruplex/i-Motif Hybrid. *Nucleic Acids Research* **2019**, *47* (22), 11921–11930.

(47) Krissinel, E.; Henrick, K. Inference of Macromolecular Assemblies from Crystalline State. *Journal of Molecular Biology* **2007**, *372* (3), 774–797.
(48) Adasme, M. F.; Linnemann, K. L.; Bolz, S. N.; Kaiser, F.; Salentin, S.; Haupt, V. J.; Schroeder, M. PLIP 2021: Expanding the Scope of the Protein–Ligand Interaction Profiler to DNA and RNA. *Nucleic Acids Research* **2021**, *49* (W1), W530–W534.
(49) Luscombe, N. M.; Laskowski, R. A.; Thornton, J. M. NUCPLOT: A Program to Generate Schematic Diagrams of Protein-Nucleic Acid Interactions. *Nucleic Acids Research* **1997**, *25* (24), 4940–4945.
(50) Cheng, Y.; Zak, O.; Aisen, P.; Harrison, S. C.; Walz, T. Structure of the Human Transferrin Receptor-Transferrin Complex. *Cell* **2004**, *116* (4), 565–576.
(51) Bennett, M. J.; Lebrón, J. A.; Bjorkman, P. J. Crystal Structure of the Hereditary Haemochromatosis Protein HFE Complexed with Transferrin Receptor. *Nature* **2000**, *403*, 46–53.
(52) Feder, J. N.; Penny, D. M.; Irrinki, A.; Lee, V. K.; Lebrón, J. A.; Watson, N.; Tsuchihashi, Z.; Sigal, E.; Bjorkman, P. J.; Schatzman, R. C. The Hemochromatosis Gene Product Complexes with the Transferrin Receptor and Lowers Its Affinity for Ligand Binding. *Proceedings of the National Academy of Sciences* **1998**, *95* (4), 1472–1477.
(53) Waheed, A.; Grubb, J. H.; Zhou, X. Y.; Tomatsu, S.; Fleming, R. E.; Costaldi, M. E.; Britton, R. S.; Bacon, B. R.; Sly, W. S. Regulation of Transferrin-Mediated Iron Uptake by HFE, the Protein Defective in Hereditary Hemochromatosis. *Proceedings of the National Academy of Sciences* **2002**, *99* (5), 3117–3122.
(54) Feder, J. N.; Gnirke, A.; Thomas, W.; Tsuchihashi, Z.; Ruddy, D. A.; Basava, A.; Dormishian, F.; Domingo, R.; Ellis, M. C.; Fullan, A.; Hinton, L. M.; Jones, N. L.; Kimmel, B. E.; Kronmal, G. S.; Lauer, P.; Lee, V. K.; Loeb, D. B.; Mapa, F. A.; McClelland, E.; Meyer, N. C.; Mintier, G. A.; Moeller, N.; Moore, T.; Morikang, E.; Prass, C. E.; Quintana, L.; Starnes, S. M.; Schatzman, R. C.; Brunke, K. J.; Drayna, D. T.; Risch, N. J.; Bacon, B. R.; Wolff, R. K. A Novel MHC Class I–like Gene Is Mutated in Patients with Hereditary Haemochromatosis. *Nature Genetics* **1996**, *13* (4), 399–408.
(55) Schmidt, P. J.; Toran, P. T.; Giannetti, A. M.; Bjorkman, P. J.; Andrews, N. C. The Transferrin Receptor Modulates Hfe-Dependent Regulation of Hepcidin Expression. *Cell Metabolism* **2008**, *7* (3), 205–214.
(56) Scott, C. S.; Ramsden, W.; Limbert, H. J.; Master, P. S.; Roberts, B. E. Membrane Transferrin Receptor (TfR) and Nuclear Proliferation-Associated Ki-67 Expression in Hemopoietic Malignancies. *Leukemia* **1988**, *2* (7), 438–442.
(57) Płoszyńska, A.; Ruckemann-Dziurdzińska, K.; Jóźwik, A.; Mikosik, A.; Lisowska, K.; Balcerska, A.; Witkowski, J. M. Cytometric Evaluation of Transferrin Receptor 1 (CD71) in Childhood Acute Lymphoblastic Leukemia. *Folia Histochemica et Cytobiologica* **2012**, *50* (2), 304–311.
(58) Habeshaw, J. A.; Lister, T. A.; Stansfeld, A. G.; Greaves, M. F. Correlation of Transferrin Receptor Expression with Histological Class and Outcome in Non-Hodgkin Lymphoma. *The Lancet* **1983**, *321* (8323), 498–501.
(59) das Gupta, A.; Shah, V. I. Correlation of Transferrin Receptor Expression with Histologic Grade and Immunophenotype in Chronic Lymphocytic Leukemia and Non-Hodgkin's Lymphoma. *Hematologic Pathology* **1990**, *4* (1), 37–41.

(60) Kozlowski, R.; Reilly, I. A. G.; Sowter, D.; Robins, R. A.; Russell, N. H. Transferrin Receptor Expression on AML Blasts Is Related to Their Proliferative Potential. *British Journal of Haematology* **1988**, *69* (2), 275–280.
(61) Allen, E. S.; Stroncek, D. F.; Ren, J.; Eder, A. F.; West, K. A.; Fry, T. J.; Lee, D. W.; Mackall, C. L.; Conry-Cantilena, C. Autologous Lymphapheresis for the Production of Chimeric Antigen Receptor T Cells. *Transfusion* **2017**, *57* (5), 1133–1141.
(62) Luscombe, N. M.; Laskowski, R. A.; Thornton, J. M. Amino Acid–Base Interactions: A Three-Dimensional Analysis of Protein–DNA Interactions at an Atomic Level. *Nucleic Acids Research* **2001**, *29* (13), 2860–2874.
(63) Schug, K. A.; Lindner, W. Noncovalent Binding between Guanidinium and Anionic Groups: Focus on Biological- and Synthetic-Based Arginine/Guanidinium Interactions with Phosph[on]Ate and Sulf[on]Ate Residues. *Chemical Reviews* **2005**, *105* (1), 67–114.
(64) Worthen, C.; Enns, C. The Role of Hepatic Transferrin Receptor 2 in the Regulation of Iron Homeostasis in the Body. *Frontiers in Pharmacology* **2014**, *5*, 34.
(65) Wu, X.; Zhao, Z.; Bai, H.; Fu, T.; Yang, C.; Hu, X.; Liu, Q.; Champanhac, C.; Teng, I.-T.; Ye, M.; Tan, W. DNA Aptamer Selected against Pancreatic Ductal Adenocarcinoma for In Vivo Imaging and Clinical Tissue Recognition. *Theranostics* **2015**, *5* (9), 985–994.
(66) Wu, X.; Liu, H.; Han, D.; Peng, B.; Zhang, H.; Zhang, L.; Li, J.; Liu, J.; Cui, C.; Fang, S.; Li, M.; Ye, M.; Tan, W. Elucidation and Structural Modeling of CD71 as a Molecular Target for Cell-Specific Aptamer Binding. *Journal of the American Chemical Society* **2019**, *141* (27), 10760–10769.
(67) Wilner, S. E.; Wengerter, B.; Maier, K.; de Lourdes Borba Magalhães, M.; del Amo, D. S.; Pai, S.; Opazo, F.; Rizzoli, S. O.; Yan, A.; Levy, M. An RNA Alternative to Human Transferrin: A New Tool for Targeting Human Cells. *Molecular Therapy - Nucleic Acids* **2012**, *1*, e21.
(68) Zhang, N.; Bing, T.; Shen, L.; Feng, L.; Liu, X.; Shangguan, D. A DNA Aptameric Ligand of Human Transferrin Receptor Generated by Cell-SELEX. *International Journal of Molecular Sciences* **2021**, *22* (16), 8923.
(69) Zhang, N.; Wang, J.; Bing, T.; Liu, X.; Shangguan, D. Transferrin Receptor-Mediated Internalization and Intracellular Fate of Conjugates of a DNA Aptamer. *Molecular Therapy - Nucleic Acids* **2022**, *27*, 1249–1259.
(70) Kikin, O.; D'Antonio, L.; Bagga, P. S. QGRS Mapper: A Web-Based Server for Predicting G-Quadruplexes in Nucleotide Sequences. *Nucleic Acids Research* **2006**, *34* (suppl_2), W676–W682.
(71) Roxo, C.; Kotkowiak, W.; Pasternak, A. G-Quadruplex-Forming Aptamers—Characteristics, Applications, and Perspectives. *Molecules* **2019**, *24* (20), 3781.
(72) Finney, O. C.; Brakke, H.; Rawlings-Rhea, S.; Hicks, R.; Doolittle, D.; Lopez, M.; Futrell, B.; Orentas, R. J.; Li, D.; Gardner, R.; Jensen, M. C. CD19 CAR T Cell Product and Disease Attributes Predict Leukemia Remission Durability. *The Journal of Clinical Investigation* **2019**, *129* (5), 2123–2132.
(73) Bersenev, A. CAR-T Cell Manufacturing: Time to Put It in Gear. *Transfusion* **2017**, *57* (5), 1104–1106.
(74) Cooper, M. L.; Choi, J.; Staser, K.; Ritchey, J. K.; Devenport, J. M.; Eckardt, K.; Rettig, M. P.; Wang, B.; Eissenberg, L. G.; Ghobadi, A.; Gehrs, L. N.; Prior, J. L.; Achilefu, S.; Miller, C. A.; Fronick, C. C.; O'Neal, J.; Gao, F.; Weinstock, D. M.; Gutierrez, A.; Fulton, R. S.;

DiPersio, J. F. An "off-the-Shelf" Fratricide-Resistant CAR-T for the Treatment of T Cell Hematologic Malignancies. *Leukemia* **2018**, *32* (9), 1970–1983.

(75) Xu, Y.; Liu, Q.; Zhong, M.; Wang, Z.; Chen, Z.; Zhang, Y.; Xing, H.; Tian, Z.; Tang, K.; Liao, X.; Rao, Q.; Wang, M.; Wang, J. 2B4 Costimulatory Domain Enhancing Cytotoxic Ability of Anti-CD5 Chimeric Antigen Receptor Engineered Natural Killer Cells against T Cell Malignancies. *Journal of Hematology & Oncology* **2019**, *12* (1), 49.

(76) Stroncek, D. F.; Ren, J.; Lee, D. W.; Tran, M.; Frodigh, S. E.; Sabatino, M.; Khuu, H.; Merchant, M. S.; Mackall, C. L. Myeloid Cells in Peripheral Blood Mononuclear Cell Concentrates Inhibit the Expansion of Chimeric Antigen Receptor T Cells. *Cytotherapy* **2016**, *18* (7), 893–901.

(77) Sylvestre, M.; Saxby, C. P.; Kacherovsky, N.; Gustafson, H.; Salipante, S. J.; Pun, S. H. Identification of a DNA Aptamer That Binds to Human Monocytes and Macrophages. *Bioconjugate Chemistry* **2020**, *31* (8), 1899–1907.

(78) Olden, B. R.; Cheng, Y.; Yu, J. L.; Pun, S. H. Cationic Polymers for Non-Viral Gene Delivery to Human T Cells. *Journal of Controlled Release* **2018**, *282*, 140–147.

(79) Olden, B. R.; Cheng, E.; Cheng, Y.; Pun, S. H. Identifying Key Barriers in Cationic Polymer Gene Delivery to Human T Cells. *Biomaterials Science* **2019**, *7* (3), 789–797.

(80) Biglione, C.; Bergueiro, J.; Asadian-Birjand, M.; Weise, C.; Khobragade, V.; Chate, G.; Dongare, M.; Khandare, J.; Strumia, M. C.; Calderón, M. Optimizing Circulating Tumor Cells' Capture Efficiency of Magnetic Nanogels by Transferrin Decoration. *Polymers* **2018**, *10* (2), 174.

(81) Li, X.; Yang, Y.; Zhao, H.; Zhu, T.; Yang, Z.; Xu, H.; Fu, Y.; Lin, F.; Pan, X.; Li, L.; Cui, C.; Hong, M.; Yang, L.; Wang, K. K.; Tan, W. Enhanced in Vivo Blood–Brain Barrier Penetration by Circular Tau–Transferrin Receptor Bifunctional Aptamer for Tauopathy Therapy. *Journal of the American Chemical Society* **2020**, *142* (8), 3862–3872.

(82) Schindelin, J.; Arganda-Carreras, I.; Frise, E.; Kaynig, V.; Longair, M.; Pietzsch, T.; Preibisch, S.; Rueden, C.; Saalfeld, S.; Schmid, B.; Tinevez, J.-Y.; White, D. J.; Hartenstein, V.; Eliceiri, K.; Tomancak, P.; Cardona, A. Fiji: An Open-Source Platform for Biological-Image Analysis. *Nature Methods* **2012**, *9* (7), 676–682.

(83) Mastronarde, D. N. Automated Electron Microscope Tomography Using Robust Prediction of Specimen Movements. *Journal of Structural Biology* **2005**, *152* (1), 36–51.

(84) Punjani, A.; Rubinstein, J. L.; Fleet, D. J.; Brubaker, M. A. CryoSPARC: Algorithms for Rapid Unsupervised Cryo-EM Structure Determination. *Nature Methods* **2017**, *14* (3), 290–296.

(85) Punjani, A.; Zhang, H.; Fleet, D. J. Non-Uniform Refinement: Adaptive Regularization Improves Single-Particle Cryo-EM Reconstruction. *Nature Methods* **2020**, *17* (12), 1214–1221.

(86) Pettersen, E. F.; Goddard, T. D.; Huang, C. C.; Couch, G. S.; Greenblatt, D. M.; Meng, E. C.; Ferrin, T. E. UCSF Chimera—A Visualization System for Exploratory Research and Analysis. *Journal of Computational Chemistry* **2004**, *25* (13), 1605–1612.

(87) Casañal, A.; Lohkamp, B.; Emsley, P. Current Developments in Coot for Macromolecular Model Building of Electron Cryo-Microscopy and Crystallographic Data. *Protein Science* **2020**, *29* (4), 1055–1064.

(88) Adams, P. D.; Afonine, P. v; Bunkóczi, G.; Chen, V. B.; Davis, I. W.; Echols, N.; Headd, J. J.; Hung, L.-W.; Kapral, G. J.; Grosse-Kunstleve, R. W.; McCoy, A. J.; Moriarty, N. W.; Oeffner, R.; Read, R. J.; Richardson, D. C.; Richardson, J. S.; Terwilliger, T. C.; Zwart, P.

H. PHENIX: A Comprehensive Python-Based System for Macromolecular Structure Solution. *Acta Crystallographica* **2010**, *D66*, 213–221.

(89) Afonine, P. v; Poon, B. K.; Read, R. J.; Sobolev, O. v; Terwilliger, T. C.; Urzhumtsev, A.; Adams, P. D. Real-Space Refinement in PHENIX for Cryo-EM and Crystallography. *Acta Crystallographica. Section D, Structural Biology* **2018**, *74*, 531–544.

(90) Chen, V. B.; Arendall W. Bryan, I. I. I.; Headd, J. J.; Keedy, D. A.; Immormino, R. M.; Kapral, G. J.; Murray, L. W.; Richardson, J. S.; Richardson E-mail: dcr@kinemage.biochem.duke.edu, D. C. MolProbity: All-Atom Structure Validation for Macromolecular Crystallography. *Acta Crystallographica. Section D, Biological Crystallography* **2010**, *66*, 12–21.

(91) Williams, C. J.; Headd, J. J.; Moriarty, N. W.; Prisant, M. G.; Videau, L. L.; Deis, L. N.; Verma, V.; Keedy, D. A.; Hintze, B. J.; Chen, V. B.; Jain, S.; Lewis, S. M.; Arendall III, W. B.; Snoeyink, J.; Adams, P. D.; Lovell, S. C.; Richardson, J. S.; Richardson, D. C. MolProbity: More and Better Reference Data for Improved All-Atom Structure Validation. *Protein Science* **2018**, *27* (1), 293–315.

(92) DeLano, W. L. Pymol: An Open-Source Molecular Graphics Tool. *CCP4 Newsletter on Protein Crystallography* **2002**, *40*, 82–92.

(93) Goujon, M.; McWilliam, H.; Li, W.; Valentin, F.; Squizzato, S.; Paern, J.; Lopez, R. A New Bioinformatics Analysis Tools Framework at EMBL–EBI. *Nucleic Acids Research* **2010**, *38* (suppl_2), W695–W699.

(94) Sievers, F.; Wilm, A.; Dineen, D.; Gibson, T. J.; Karplus, K.; Li, W.; Lopez, R.; McWilliam, H.; Remmert, M.; Söding, J.; Thompson, J. D.; Higgins, D. G. Fast, Scalable Generation of High-Quality Protein Multiple Sequence Alignments Using Clustal Omega. *Molecular Systems Biology* **2011**, *7* (1), 539.

3.8 SUPPORTING INFORMATION

Table S3.1 | Experimental conditions used in rounds of cell-SELEX.

SELEX Round	Positive Selection (Jurkat)	Negative Selection (J.RT3-T3.5)	Aptamer Pool (μM)	FBS (%)	Time (min)	# of Washes
1	10^7 Cells	-	14	-	60	3
2	5×10^6 Cells	10^7 Cells	0.5	-	60	3
3	4×10^6 Cells	10^7 Cells	0.5	-	60	3
4	2×10^6 Cells	10^7 Cells	0.5	5	45	4
5	1×10^6 Cells	10^7 Cells	0.5	5	45	4
6	1×10^6 Cells	10^7 Cells	0.5	10	45	5
7	1×10^6 Cells	10^7 Cells	0.5	10	30	5
8	1×10^6 Cells	10^7 Cells	0.5	20	30	6

Table S3.2 | Primers used for next generation sequencing (NGS) of naive library (NL) and cell-SELEX rounds 1-8. The NL and Rounds 7-8 were sequenced initially, followed by Rounds 1-6 in a separate run. Accordingly, there is some overlap in the barcoded reverse primers used between the separate runs.

Primer Name	SELEX Round	Sequence	Barcode (in red)
Aptamer_F	NL, 1-8	AATGATACGGCGACCACCGAGATCTACACCGAGGAGATACC ACTAAGCCACCGTGTCCA	
Aptamer_R_77	NL	CAAGCAGAAGACGGCATACGAGATGCAATTCGACAGACCG TCGATCCAGAGTGACGCAGCA	CGAATTGC
Aptamer_R_79	1	CAAGCAGAAGACGGCATACGAGATTCGATTAAACAGACCG TCGATCCAGAGTGACGCAGCA	TTAATCGA
Aptamer_R_80	2	CAAGCAGAAGACGGCATACGAGATGAATGGACACAGACCG TCGATCCAGAGTGACGCAGCA	GTCCATTC
Aptamer_R_81	3	CAAGCAGAAGACGGCATACGAGATAGAATCAGACAGACCG TCGATCCAGAGTGACGCAGCA	CTGATTCT
Aptamer_R_82	4	CAAGCAGAAGACGGCATACGAGATAACTGCCAACAGACCG TCGATCCAGAGTGACGCAGCA	TGGCAGTT
Aptamer_R_83	5	CAAGCAGAAGACGGCATACGAGATAAGTAACGACAGACCG TCGATCCAGAGTGACGCAGCA	CGTTACTT
Aptamer_R_84	6	CAAGCAGAAGACGGCATACGAGATACTCAATGACAGACCG TCGATCCAGAGTGACGCAGCA	CATTGAGT
Aptamer_R_78	7	CAAGCAGAAGACGGCATACGAGATCAAGAGGTACAGACCG TCGATCCAGAGTGACGCAGCA	ACCTCTTG
Aptamer_R_79	8	CAAGCAGAAGACGGCATACGAGATTCGATTAAACAGACCG TCGATCCAGAGTGACGCAGCA	TTAATCGA

Table S3.3 | Enrichment of top 50 Round 8 (R8) aptamer sequences between rounds of cell-SELEX. Fold enrichment is calculated by dividing the reads per million (RPM) of the sequence from a round by the value of the former round.

				Fold Enrichment		
R8 Rank	**% Rep.**	**Motif**	**Random Region Sequence**	**R8/R7**	**R7/R6**	**R6/R5**
1	21.08	3	GCGTAAAGGGGGTGTTTGTGCGGTGTGGAGTGCGCGTGCTGCTGC	6.9	7.8	19.5
2	11.15		ATCCGGGAGAGTCGTTGTGTTGAGGTCCGCCCCTGCTCGCCCGCG	11.1	20.3	
3	6.41	2	GGGGCCGCGGATGCAAACGCCCGATAGGGGGACGGCACTGGAGCT	0.6	4.1	89.4
4	5.59		ACCCAAACCACCAGCCGGGGATGCAAACACCGCACAGGGAACGGC	1.3	6.7	104.6
5	5.07		AAGCGGTTTTCGGGTTCGGGTCTGGGGGTTGGGTTGTCGGCACTA	0.8	15.9	
6	4.61		ACAGACAGCTGCGCCGCCGGGAGGGCACCCGGACGGGCTGGGCGG	1.7	0.4	55.1
7	4.01	2	ACCACAGATGCAAATGCGCGAGAGCGGGACGGTTTGCTAGGCTCA	0.7	5.3	80.8
8	3.88	5	GTGGGCCAAATGGATTGGATTAGGGTTGGGCCGCCCGGGAGGGGT	0.6	28.2	51.4
9	3.29	1	AGGCGCTAGACGCAATCCCGCAAGCGGAGCCGGATTCCCTAGTGG	0.7	2.0	13.9
10	3.17	3	GCATAAAGGGGGTGTTTGTGCGGTGTGGAGTGCGCGTGCTGCTGC	20.1	17.4	
11	2.88	2	GCCGGTCGCAGATGCAAATGCCCGACAGGGGGACGCGGGCTGCCA	0.6	4.4	65.7
12	2.70	2	CAGATGCAAATGCCTGACCAGGGAACTGCGACTGGATGGCTCTTG	1.0	5.3	60.4
13	2.26	1	ATCACAGGGCTACAAGGTGCTAAACGTAAACTAGCAAGAGAACTA	0.8	1.8	20.1
14	1.82	2	GATGCAAATGCTCGAGAGAGGACCGGCGGCACTGGTGAACGTAGG	1.0	5.6	70.8
15	1.55		CTCTCGGGGGGTAGGTGGGAAGGGGGCCGCCCCCTGGGTTAGGCT	2.4	9.8	
16	1.18	2	AGCGGGGATGCAAACACCCGAAAGGGGAACGGGAGCTGCGTCAAG	1.7	1.1	73.4
17	0.93		AGGTGGCTGTGGGCGGATGGTGGGCTCGCGTGGGCGGCCACCTGA	0.9	0.9	12.4
18	0.90		ACGTTATCCCCTTTACGGGGTCCTAGAGCCCCGTGAGTGCTCACG	1.0	1.7	19.4
19	0.83		TCGGTGTTTATGGTGTCTGTCGGTGCGTACTCGGGGCTTCACTAG	0.8	9.9	15.3
20	0.69	2	TTGGAGGTGGCGGATGCAAACGCTAGACAGAGGCACCAGCTCCAA	0.8	3.9	
21	0.64		GACTGCTGTGCCACCGGGAGTGCCTTCAGCGCCGTACGGTCTGCT	1.2	0.2	31.9
22	0.63	1	ACGCAGCAAGGTGCTAAACGCAATCCCGGATTCTCGTGCGTCAAG	1.3	1.2	18.3
23	0.49	2	GATGCAAATGCCCGAATGGGGGACGGCGGACACGGGGTGTGCCGA	0.6	4.4	
24	0.43		TACGGCTTATGCTCAGAGGGGCTGTGGGCCGAGGGGAGCGTCGCG	0.9	1.2	9.5
25	0.35		TGTAAGCCGAATGTTGGTGCTTGGGTAGGCGCCATTGTGAGCTCG	0.8	3.2	12.8
26	0.33	3	GCGTAAAGGGGGTGTTTGTGCGGTGTGGAGTGCGCGCGCTGCTGC	22.3		
27	0.25		CTGTGGGGTCACATTGGGGGACGGGACCGTGCGTGAGATCTAAGA	2.6	12.6	
28	0.21		GGGTTCCGGATGTGGTGGGGCTTAGGGGGGTTTCACTGCTAGCGT	0.5	5.2	
29	0.19		AAGGTTGCCATACCACCGGGAGCGTTCGAGTACGGCCTGTCGCGC	0.6	0.5	23.3
30	0.18	1	AGGGGTACAAGGTGTTAAACGTAAATTCTGCGCGGAGGGGAACTT	0.8	1.5	11.0
31	0.16		GACGCAGCAGTGCCATCGGGGGGGATTTCCTTGTACGACGTCACC	0.6	0.8	16.0

32	0.15		GTGCCATCGGGAGGCGCGAGTCCGTACGACGTCATTTGGCAAAAC	0.8	0.8	19.3
33	0.14		AAAAGAAGCGACCGAGACCACGGATGCAAACGCCCAGGCGGGGAA	0.7	2.8	
34	0.13	1	CTGTGGCGTAATTCTGGTCGGCGGTCACGTGCGTGAGAGCTGGGG	3.7	10.7	
35	0.11	1	AGGTGTTAAACGCTAACGCCAGTTATCTTAAAGAAAGTAAACGAC	0.5	1.3	7.5
36	0.11		TCAAGGGGTTACACGAAAAGATAGGCTTTCACGCTAGTGGGCTTG	0.6	1.3	7.5
37	0.10		GTGGTATGGTCTAAGAGCCGTCTGGCGAGTCGGTGGGAGTAGCGA	0.7	1.5	6.4
38	0.09	2	CAGATGCAAATGCCTGACCAGGGAACTGCGACTGGATGGCTCTTT	1.5	6.8	
39	0.09		CGAAAATTTCAAGCTTTATGCTCTAGCGCAGCGCCTCGTACCCCT	1.8	1.5	
40	0.08		GGTGAAGGGCAGTGGTTTGCTGTGGTGGGCGCCCGTGAGCGTTGC	2.2	6.1	
41	0.08		GGGAGTTCGGGCATGATTTGCCCTGGGGGGCACGGGAAGGTACCG	1.0	7.7	2.7
42	0.08	1	CGCACCAAGGCGTTAGACGGAATGGATTTGGAACTTCATGCGAAG	0.4	1.3	6.4
43	0.08		GTTGGGCTAAGCGGAGGATGGTAATGGTGCTTGGGCAGGCGCTCA	0.8	2.5	11.3
44	0.07	2	CAGATGCAAATGCCTGACCAGGGAACTGCGACTTGATGGCTCTTG	1.5	5.8	
45	0.07	3	GCGCAAAGGGGGTGTTTGTGCGGTGTGGAGTGCGCGTGCTGCTGC	20.6		
46	0.07		GTGCCATCGGGAAGGTGTTGACCTGTACGACGTCATAGGATGGAC	1.2	1.0	
47	0.07		GGGGTGTAGGGTGGGGTAGTGGGAACATTGCGTAAAGTGTAGCTC	0.9	6.2	
48	0.06		ACTGTTTGTACGGAGTTAGGGTGTGCCTTTATTGCGCGGGGGGGA	5.6		
49	0.06		TCATTGGAGTGGGTAGGGGTGTTTGTGCGGGATGCGGTGGCTAGG	3.4	5.4	
50	0.06	5	GTTGGCCAAATGGATTGGATTAGGGTTGGGCCGCCCGGGAGGGGT	1.0		

Table S3.4 | Sequences of aptamers used in experiments. Aptamers were modified on their 5'-end with either 6-FAM, Cy5, or biotin-hexa-ethyleneglycol depending on the assay. The exact modifications are specified in the figures and captions. For 5' modification of tJBA8.1 with 6-FAM, a thymidine nucleotide was added at the 5' end to prevent fluorescence quenching by guanosine. Underlined nucleotides represent constant regions. Red text represents nucleotides that were deleted to make the truncated tJBA8.1 aptamer, and blue text represents nucleotides that were substituted to create JBA8.26.

Name	Sequence
RANL	5'-ATCCAGAGTGACGCAGCAAATTCCAAACTCGAGTAAGCGTAGAGCCTCTCATCGCCTCAATA ATGGACACGGTGGCTTAGT-3'
JBA8.1	5'-ATCCAGAGTGACGCAGCAGCGTAAAGGGGGTGTTTGTGCGGTGTGGAGTGCGCGTGCTGCTG CTGGACACGGTGGCTTAGT-3'
JBA8.2	5'-ATCCAGAGTGACGCAGCAATCCGGGAGAGTCGTTGTGTTGAGGTCCGCCCCTGCTCGCCCGCG TGGACACGGTGGCTTAGT-3'
JBA8.3	5'-ATCCAGAGTGACGCAGCAGGGGCCGCGGATGCAAACGCCCGATAGGGGGACGGCACTGGAGC TTGGACACGGTGGCTTAGT-3'
JBA8.4	5'-ATCCAGAGTGACGCAGCAACCCAAACCACCAGCCGGGGATGCAAACACCGCACAGGGAACGG CTGGACACGGTGGCTTAGT-3'
JBA8.7	5'-ATCCAGAGTGACGCAGCAACCACAGATGCAAATGCGCGAGAGCGGGACGGTTTGCTAGGCTCA TGGACACGGTGGCTTAGT-3'
JBA8.8	5'-ATCCAGAGTGACGCAGCAGTGGGCCAAATGGATTGGATTAGGGTTGGGCCGCCCGGGAGGGG TTGGACACGGTGGCTTAGT-3'
JBA8.11	5'-ATCCAGAGTGACGCAGCAGCCGGTCGCAGATGCAAATGCCCGACAGGGGGACGCGGGCTGCC ATGGACACGGTGGCTTAGT-3'
JBA8.15	5'-ATCCAGAGTGACGCAGCACTCTCGGGGGGTAGGTGGGAAGGGGGCCGCCCCCTGGGTTAGGC TTGGACACGGTGGCTTAGT-3'
JBA8.17	5'-ATCCAGAGTGACGCAGCAAGGTGGCTGTGGGCGGATGGTGGGCTCGCGTGGGCGGCCACCTG ATGGACACGGTGGCTTAGT-3'
tJBA8.1	5'-GCAGCAGCGTAAAGGGGGTGTTTGTGCGGTGTGGAGTGCGCGTGCTGCTGC-3'
JBA8.26	5'-ATCCAGAGTGACGCAGCAGCGTAAAGGGGGTGTTTGTGCGGTGTGGAGTGCGCGCGCTGCTG CTGGACACGGTGGCTTAGT-3'

Table S3.5 | siRNA duplexes used for transferrin receptor 1 (TfR1) knockdown.

Name	Sequence
hs.Ri.TFRC.13.1-SEQ1	5'-rCrArGrUrUrCrArGrArArUrGrArUrGrGrArUrCrArArGrCTA-3'
hs.Ri.TFRC.13.1-SEQ2	5'-rUrArGrCrUrUrGrArUrCrCrArUrCrArUrUrCrUrGrArArCrUrGrCrC-3'

Table S3.6 | Bio-layer interferometry (BLI) measured affinity kinetics of tJBA8.1 and JBA8.26 aptamer binding to immobilized TfR1 protein. Data are mean ± standard deviation; *n* = 4-5 individual aptamer concentrations. Values were calculated by performing a global fit of the multi-concentration kinetic data in **Figure 3.3A** and **Figure S3.13C** to a 1:1 binding model. The ratio between the dissociation rate constant (K_{dis}) and the association rate constant (K_{on}) gives the equilibrium dissociation constant (K_D). The goodness of fit was evaluated by a reduced chi-square (χ^2) and a R^2 value approaching 1.

Aptamer	K_D (nM)	K_{on} ($nM^{-1}s^{-1}$) × 10^{-5}	K_{dis} (s^{-1}) × 10^{-4}	Full χ^2	Full R^2
tJBA8.1	25.11 (±0.19)	3.05 (±0.02)	7.66 (±0.03)	0.0402	0.9928
JBA8.26	6.87 (±0.04)	6.24 (±0.03)	4.29 (±0.02)	0.0439	0.9968

Table S3.7 | Parameters and statistics for cryo-EM data collection, processing, structure refinement, and validation.

Codes			
EMDB	EMD-14874		
PDB	7ZQS		
Data Collection and Processing			
Magnification	37000x		
Voltage (kV)	300		
Electron Exposure (e-/Å^2)	79.2		
Defocus Range (μm)	0.9-1.6		
Pixel Size (Å)	0.8465		
Symmetry Imposed	C2		
Initial Micrographs (#)	1397		
Final Micrographs (#)	1397		
Initial Particle Images (#)	1070200		
Final Particle Images (#)	216817		
Map Resolution (Å)	2.54		
FSC Threshold	0.143		
Map Sharpening B Factor (Å^2)	-88.3		
Model Composition		**Average B Factors (Å^2)**	
Nonhydrogen Atoms	11354	Protein	64.61
Protein Residues	1278	Nucleotide	95.09
Nucleotides	60	Ligand	80.25
Ligands: MG, NAG	4, 10		
R.M.S. Deviations			
Bond lengths (Å)	0.004		
Bond angles (°)	0.541		
Validation		**Ramachandran plot (%)**	
Molprobity Score	1.38	Favored	97.65
Clashscore	5.66	Allowed	2.35
Poor rotamers (%)	0.00	Disallowed	0.00

Table S3.8 | Molecular interactions detected at the tJBA8.1-TfR1 interface. PDBePISA (https://www.ebi.ac.uk/pdbe/pisa/) and PLIP (https://plip-tool.biotec.tu-dresden.de/plip-web/plip/index) programs were used for calculating the interactions at the binding interface of the tJBA8.1-TfR1 complex structure solved by cryo-EM. As two tJBA8.1 aptamers bind to one TfR1 dimer, interactions for each tJBA8.1-TfR1 monomer are recorded. Listed atomic coordinates follow standard IUPAC nomenclature for atoms in protein residues, DNA bases (i.e., N1, C2, N2, O2, N3, C4, N4, O4 C5, C6, N6, O6, C7, N7, C8, and N9), DNA sugars (i.e., C1', C2', C3', O3', C4', C5', O5'), and DNA phosphates (OP1 and OP2).

tJBA8.1-TfR1 Monomer 1

Hydrophobic Interactions						
Residue # TfR1	**Residue Type TfR1**	**Atom Type TfR1**	**Nucleotide # tJBA8.1**	**Nucleotide Type tJBA8.1**	**Atom Type tJBA8.1**	**Distance (Å)**
619	LEU	CD2	21	DT	C7	3.6
650	PHE	CE1	23	DT	C7	3.5
650	PHE	CD2	23	DT	C2'	3.4
Pi-Stacking Interactions						
Residue # TfR1	**Residue Type TfR1**	**Nucleotide # tJBA8.1**	**Nucleotide Type tJBA8.1**	**Center Distance (Å)**	**Angle (°)**	**Offset (Å)**
650	PHE	23	DT	3.5	5.0	0.9
Cation-Pi Interactions						
Residue # TfR1	**Residue Type TfR1**	**Nucleotide # tJBA8.1**	**Nucleotide Type tJBA8.1**	**ProtCharged**	**Distance (Å)**	**Offset (Å)**
646	ARG	20	DG	True	5.5	1.8
Salt Bridges						
Residue # TfR1	**Residue Type TfR1**	**Protein Group**	**Nucleotide # tJBA8.1**	**Nucleotide Type tJBA8.1**	**DNA Group**	**Distance (Å)**
623	ARG	Guanidino	19	DT	Phosphate	4.1
646	ARG	Guanidino	25	DT	Phosphate	4.7
651	ARG	Guanidino	24	DG	Phosphate	5.2
Hydrogen Bonds						
Residue # TfR1	**Residue Type TfR1**	**Atom Type TfR1**	**Nucleotide # tJBA8.1**	**Nucleotide Type tJBA8.1**	**Atom Type tJBA8.1**	**Distance (Å)**
623	ARG	NH1	19	DT	OP2	3.3
623	ARG	NH2	19	DT	OP1	2.7
623	ARG	NH2	20	DG	N7	3.3
627	GLN	NE2	18	DG	OP1	3.7
629	ARG	NH1	18	DG	N7	2.6
629	ARG	NH2	18	DG	O6	2.8

640	GLN	OE1	25	DT	O3’	3.8
640	GLN	NE2	25	DT	O3’	3.5
640	GLN	NE2	26	DG	OP1	3.5
644	SER	OG	25	DT	O2	3.8
646	ARG	NH1	21	DT	O4	2.8
646	ARG	NH1	25	DT	OP1	2.3
646	ARG	NH2	21	DT	O4	3.1
651	ARG	NH1	25	DT	O4	2.7
651	ARG	NH2	25	DT	O4	3.7
651	ARG	NH2	23	DT	O3’	3.3

tJBA8.1-TfR1 Monomer 2

Hydrophobic Interactions						
Residue # TfR1	**Residue Type TfR1**	**Atom Type TfR1**	**Nucleotide # tJBA8.1**	**Nucleotide Type tJBA8.1**	**Atom Type tJBA8.1**	**Distance (Å)**
619	LEU	CD2	21	DT	C7	3.6
650	PHE	CE1	23	DT	C7	3.5
650	PHE	CD2	23	DT	C2’	3.5
Pi-Stacking Interactions						
Residue # TfR1	**Residue Type TfR1**	**Nucleotide # tJBA8.1**	**Nucleotide Type tJBA8.1**	**Center Distance (Å)**	**Angle (°)**	**Offset (Å)**
650	PHE	23	DT	3.6	4.9	1.0
Cation-Pi Interactions						
Residue # TfR1	**Residue Type TfR1**	**Nucleotide # tJBA8.1**	**Nucleotide Type tJBA8.1**	**ProtCharged**	**Distance (Å)**	**Offset (Å)**
646	ARG	20	DG	True	5.6	1.8
Salt Bridges						
Residue # TfR1	**Residue Type TfR1**	**Protein Group**	**Nucleotide # tJBA8.1**	**Nucleotide Type tJBA8.1**	**DNA Group**	**Distance (Å)**
623	ARG	Guanidino	19	DT	Phosphate	4.2
646	ARG	Guanidino	25	DT	Phosphate	4.7
651	ARG	Guanidino	24	DG	Phosphate	5.2
Hydrogen Bonds						
Residue # TfR1	**Residue Type TfR1**	**Atom Type TfR1**	**Nucleotide # tJBA8.1**	**Nucleotide Type tJBA8.1**	**Atom Type tJBA8.1**	**Distance (Å)**
623	ARG	NH1	19	DT	OP2	3.4
623	ARG	NH1	20	DG	N7	3.2
623	ARG	NH2	19	DT	OP1	2.8

627	GLN	NE2	18	DG	OP1	3.8
629	ARG	NH1	18	DG	N7	2.6
629	ARG	NH2	18	DG	O6	2.8
640	GLN	OE1	25	DT	O3’	3.8
640	GLN	NE2	25	DT	O3’	3.3
640	GLN	NE2	26	DG	OP1	3.6
644	SER	OG	25	DT	O2	3.8
646	ARG	NH1	21	DT	O4	2.7
646	ARG	NH1	25	DT	OP1	2.4
646	ARG	NH2	21	DT	O4	3.0
651	ARG	NH1	25	DT	O4	2.8
651	ARG	NH2	25	DT	O4	3.8
651	ARG	NH2	23	DT	O3’	3.3

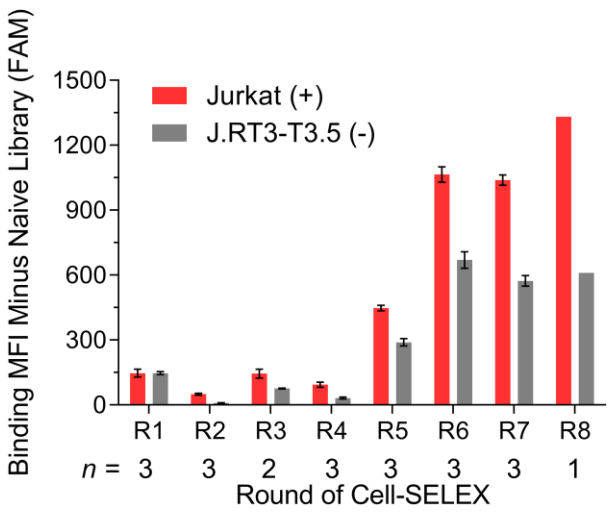

Figure S3.1 | Cell-SELEX enriches aptamer pools that bind both positive selection Jurkat and negative selection J.RT3-T3.5 cells. Binding median fluorescence intensity (MFI) of 250 nM aptamer pools from consecutive rounds of cell-SELEX to Jurkat cells and J.RT3-T3.5 cells by flow cytometry. Graph bars and error bars represent mean ± standard deviation; *n* = 1-3 technical replicates. Replicates vary due to some rounds having limited aptamer pool.

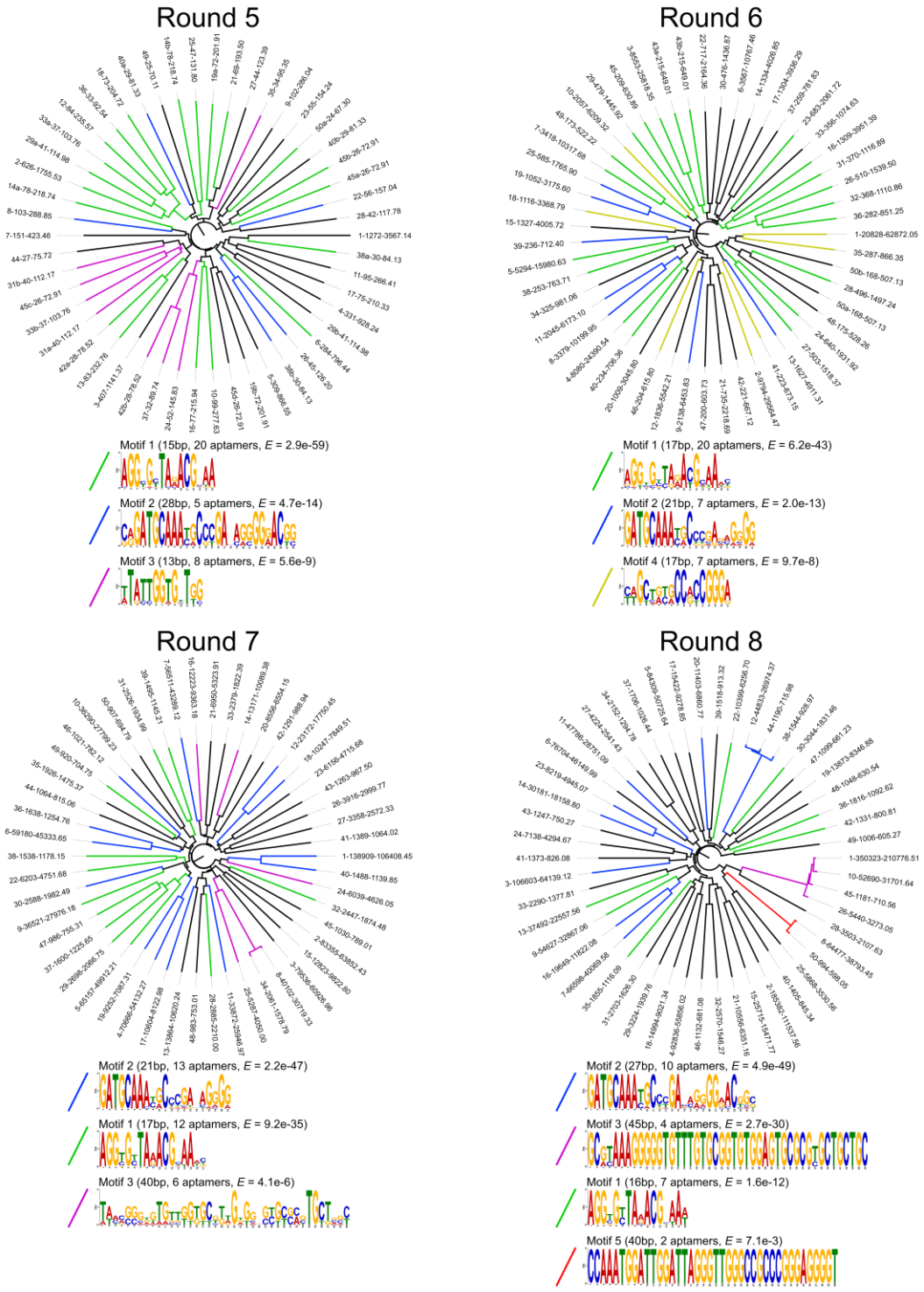

Figure S3.2 | Phylogenetic trees of the top 50 aptamers from rounds 5-8 of Jurkat cell-SELEX and emerging consensus motifs. Phylogenetic trees were generated with FigTree software (http://tree.bio.ed.ac.uk/software/figtree/), and statistically significant binding motifs were predicted using MEME analysis (MEME-suite.org). Phylogenetic trees are colored to denote aptamers belonging to identified motifs. Branch labels denote the aptamer rank followed by raw reads and reads per million.

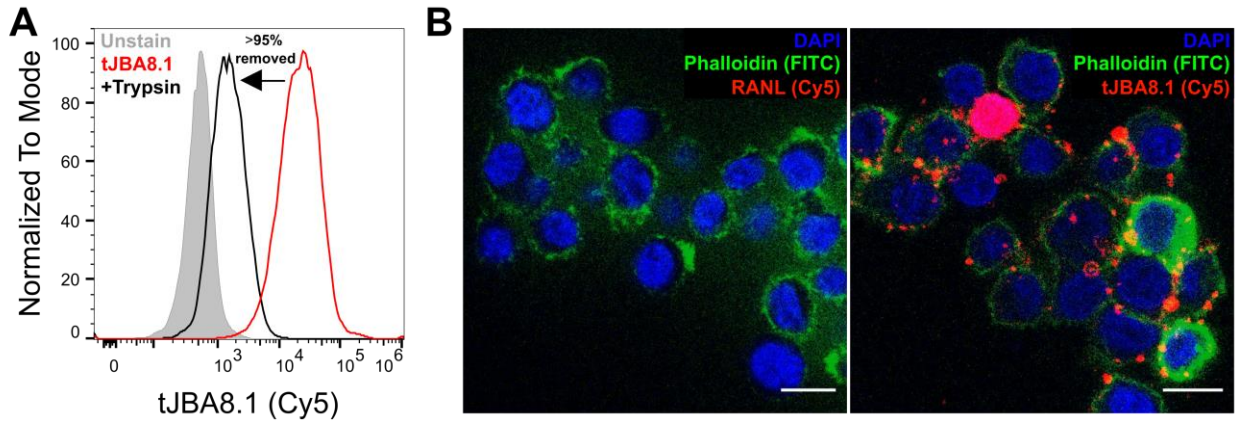

Figure S3.3 | tJBA8.1 targets membrane-bound proteins on Jurkat cells. (A) Flow cytometry histograms of 100 nM Cy5-labeled tJBA8.1 binding to Jurkat cells with and without trypsin treatment. Histograms are representative of *n* = 1 independent experiment with technical triplicates. (B) Subcellular localization of 200 nM Cy5-labeled RANL (left) and tJBA8.1 (right) binding to Jurkat cells at 4 °C by confocal microscopy imaging. Phalloidin recognizes F-actin, which primarily localizes to the cell membrane in Jurkat cells. Scale bars = 10 μm. Cy5, cyanine 5; DAPI, 4′,6-diamidino-2-phenylindole; FITC, fluorescein isothiocyanate.

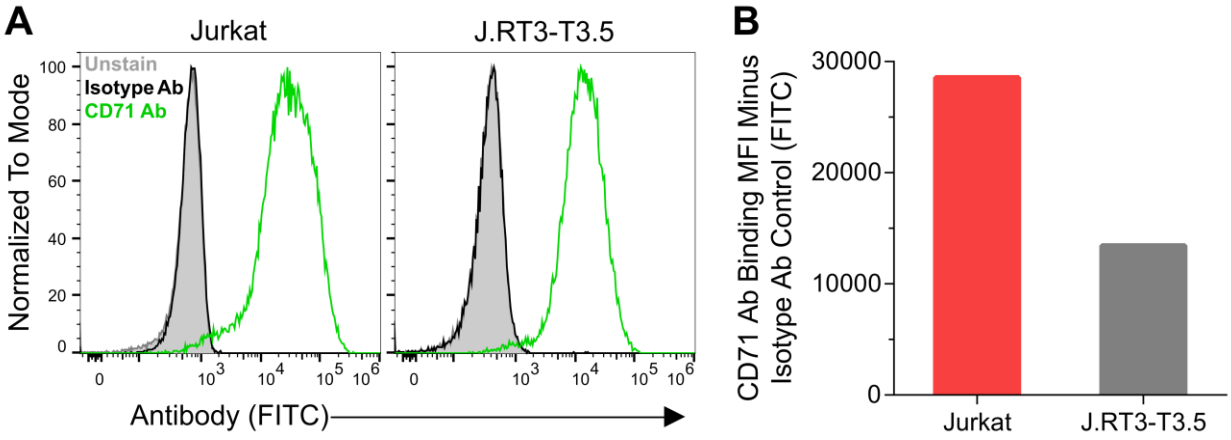

Figure S3.4 | Jurkat and J.RT3-T3.5 cells robustly and differentially express TfR1. (A) Flow cytometry histograms of FITC-labeled anti-CD71 antibody (CD71 Ab) binding to Jurkat and J.RT3-T3.5 cells. A FITC-labeled anti-CD14 antibody was used as an isotype control (Isotype Ab). Histograms are representative of *n* = 1 independent experiment. (B) Corresponding median fluorescence intensity (MFI) of CD71 Ab binding to Jurkat and J.RT3-T3.5 cells minus Isotype Ab binding. Data are representative of *n* = 1 independent experiment. FITC, fluorescein isothiocyanate.

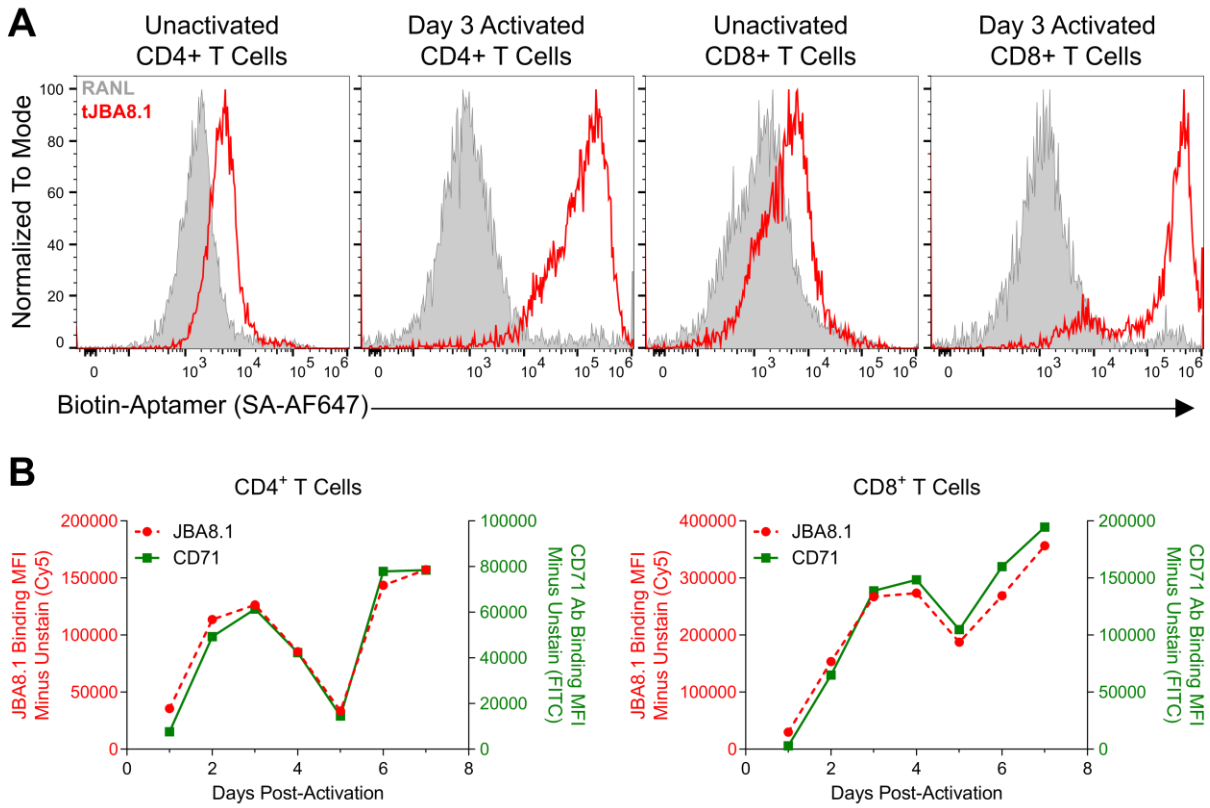

Figure S3.5 | JBA8.1 and tJBA8.1 binding correlates with TfR1 upregulation on activated CD4$^+$ and CD8$^+$ T cells. (A) Flow cytometry histograms of 100 nM biotinylated RANL and tJBA8.1 binding to unactivated and day 3 CD3/CD28 Dynabead-activated CD4$^+$ and CD8$^+$ T cells. Histograms are representative of n = 2 independent experiment. (B) MFI of 25 nM Cy5-labeled JBA8.1 (red, left y-axis) and FITC-labeled CD71 Ab (green, right y-axis) binding to CD4$^+$ and CD8$^+$ T cells over 7 days of CD3/CD28 Dynabead activation by flow cytometry. Data are representative of n = 1 independent experiment carried out on each day of activation. SA-AF647, streptavidin Alexa Fluor 647; Cy5, cyanine 5; FITC, fluorescein isothiocyanate.

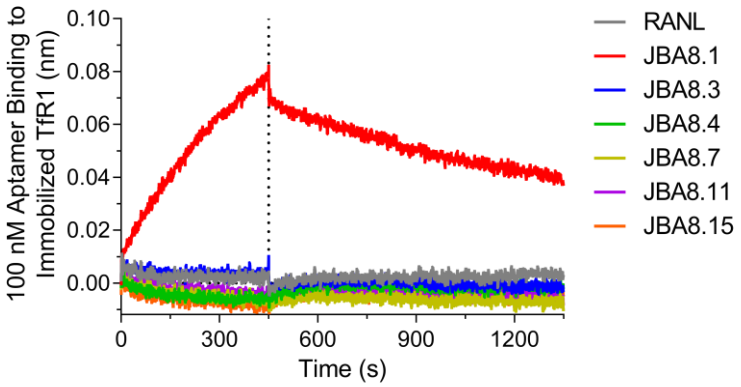

Figure S3.6 | Other Jurkat-binding aptamers identified from cell-SELEX do not bind TfR1. Association and dissociation kinetics of 100 nM FAM-labeled RANL, JBA8.1, JBA8.3, JBA8.4, JBA8.7, JBA8.11, and JBA8.15 to biotinylated TfR1 immobilized on streptavidin biosensors by BLI. The association phase is illustrated from 0-450 s, whereas dissociation is shown from 450-1350 s (separated by the vertical dotted line. Data are representative of n = 1 independent experiment with one individual concentration of each aptamer.

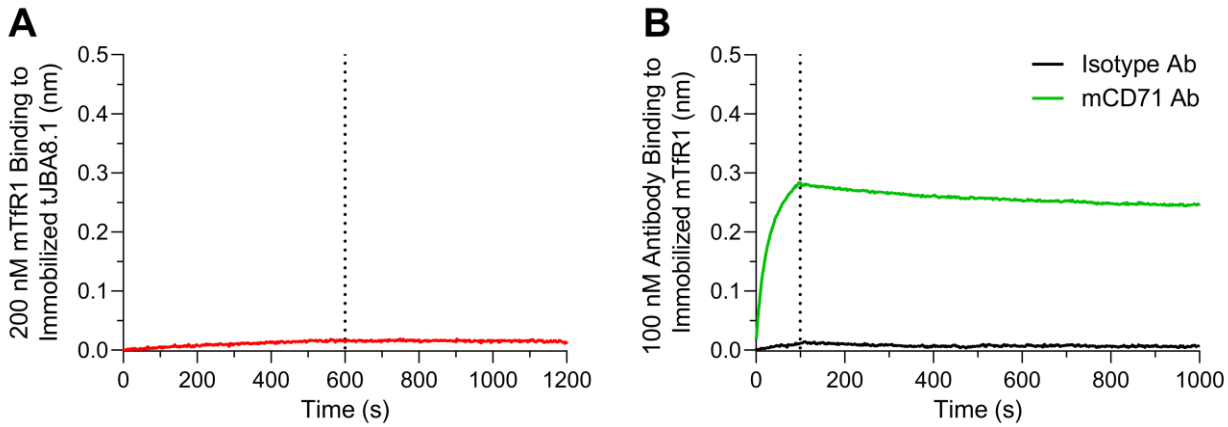

Figure S3.7 | tJBA8.1 does not bind mouse TfR1. (A) Association and dissociation kinetics of 200 nM His-tagged mouse TfR1 (mTfR1) protein binding to biotinylated tJBA8.1 immobilized on streptavidin biosensors by BLI. The association phase is illustrated from 0-600 s, whereas dissociation is shown from 600-1200 s (separated by the vertical dotted line). Data are representative of n = 1 independent experiment with one individual concentration of mTFR1. (B) Positive control binding of 100 nM FITC-labeled anti-mCD71 antibody (mCD71 Ab) to his-tagged mTfR1 immobilized on nickel-charged tris-nitriloacetic acid biosensors by BLI. A FITC-labeled anti-mCD3e antibody was used as an isotype control (Isotype Ab). The association phase is illustrated from 0-100 s, whereas dissociation is shown from 100-1000 s (separated by the vertical dotted line). Data are representative of n = 1 independent experiment with one individual concentration of antibody.

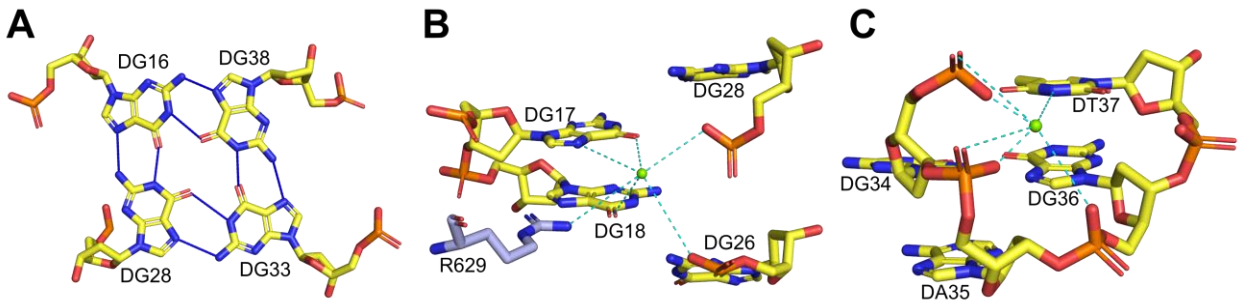

Figure S3.8 | *De novo* modeled tJBA8.1 structure has stabilizing G-quartet motif and nucleotides coordinated by two metal ions. (A) Four adjacent guanine bases in the modeled tJBA8.1 structure that form hydrogen bonds (blue lines) with each other and create a stabilizing G-quartet motif. Guanine nucleotides are labeled and shown as sticks with atom color coding (yellow: carbon; blue: nitrogen; red: oxygen; orange: phosphate). (B and C) Proximal nucleotides and protein residues in the modeled tJBA8.1-TfR1 interface coordinated (blue dashes) by metal ions (green spheres). Nucleotides and protein residues are labeled and shown as sticks with atom color coding (yellow: nucleotide carbon; lavender blue: protein carbon; blue: nitrogen; red: oxygen; orange: phosphate).

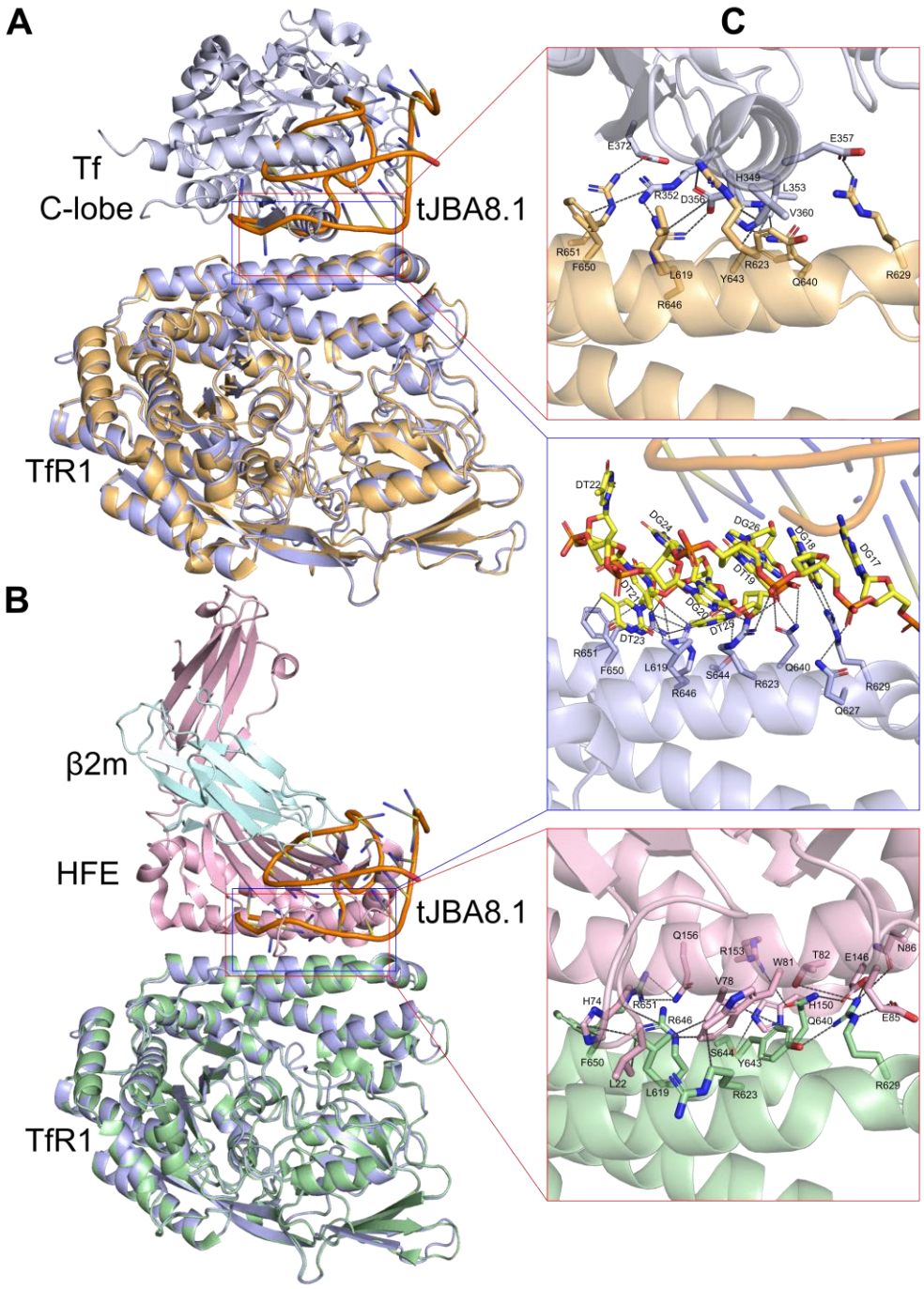

Figure S3.9 | tJBA8.1, holo-Tf, and HFE share a highly overlapping binding epitope on TfR1. Cartoon structural superposition of tJBA8.1-TfR1 complex (yellow: tJBA8.1; lavender blue: TfR1) with (A) Tf C-lobe-TfR1 complex (PDB code 1SUV; silver: Tf C-lobe; gold: TfR1) and (B) β2m-HFE-TfR1 complex (PDB code 1DE4; light blue: β2m; pink: HFE; green: TfR1). For clarity, only one monomer of TfR1 in complex with each ligand is shown. (C) Common TfR1 residues engaged by Tf (top), tJBA8.1 (middle), and HFE (bottom). Interacting residues at the interface are labeled and shown as sticks with carbon color coding that matches that of their respective complexes. Other atoms are commonly colored (blue: nitrogen; red: oxygen; orange: phosphate) and interactions are shown as black dashes.

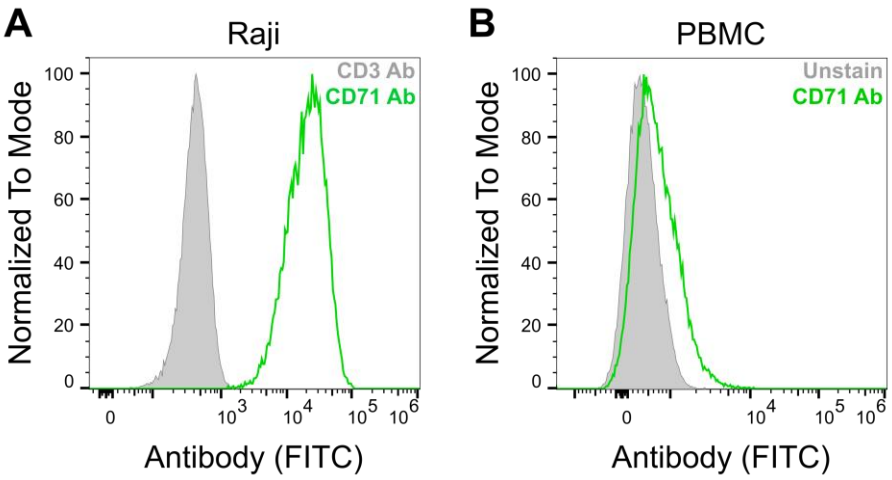

Figure S3.10 | TfR1 expression distinguishes Raji B-lymphoma cells from healthy PBMCs. (A and B) Flow cytometry histograms of FITC-labeled CD71 Ab binding to Raji cells (A) and healthy donor PBMCs (B). For Raji cells, a FITC-labeled anti-CD3 antibody (CD3 Ab) was used as a negative/isotype control. Histograms are representative of n = 1 independent experiment. FITC, fluorescein isothiocyanate.

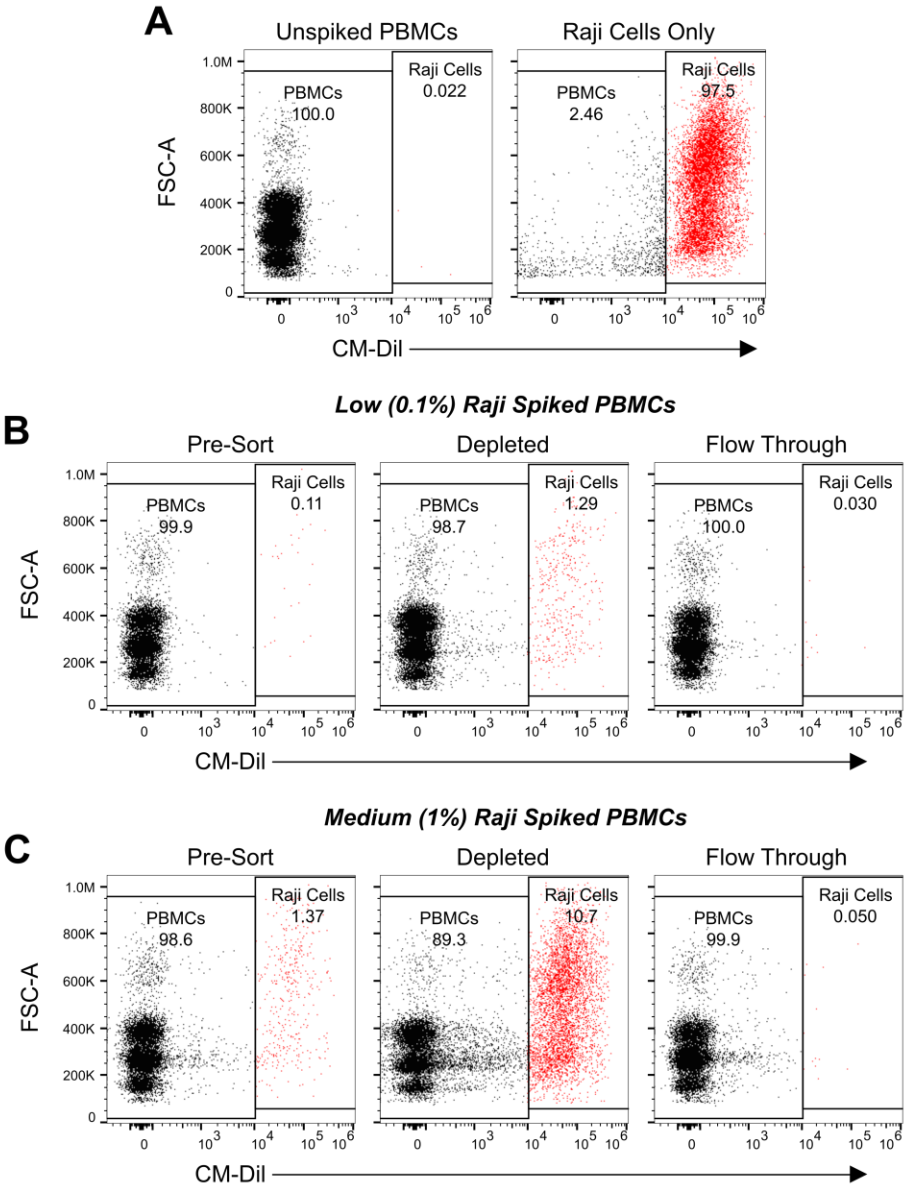

Figure S3.11 | tJBA8.1 efficiently depletes Raji cells from PBMCs even at low spiked percentages. (A) Flow cytometry plots demonstrating gating strategy for tracking CM-Dil-labeled Raji cells in depletion studies. CM-Dil$^-$ unspiked PBMCs and CM-Dil$^+$ Raji cells are shown. Plots are representative of n = 3 independent experiments with different PBMC donors. (B and C) Flow cytometry plots of CM-Dil$^+$ Raji cell depletion from low (0.1%) (B) and medium (1%) (C) Raji spiked PBMCs. The different cell fractions from the depletion process are shown. Plots are representative of n = 3 independent experiments with different PBMC donors. CM-Dil, chloromethylbenzamido-1,1'-dioctadecyl-3,3,3',3'-tetramethylindocarbocyanine perchlorate.

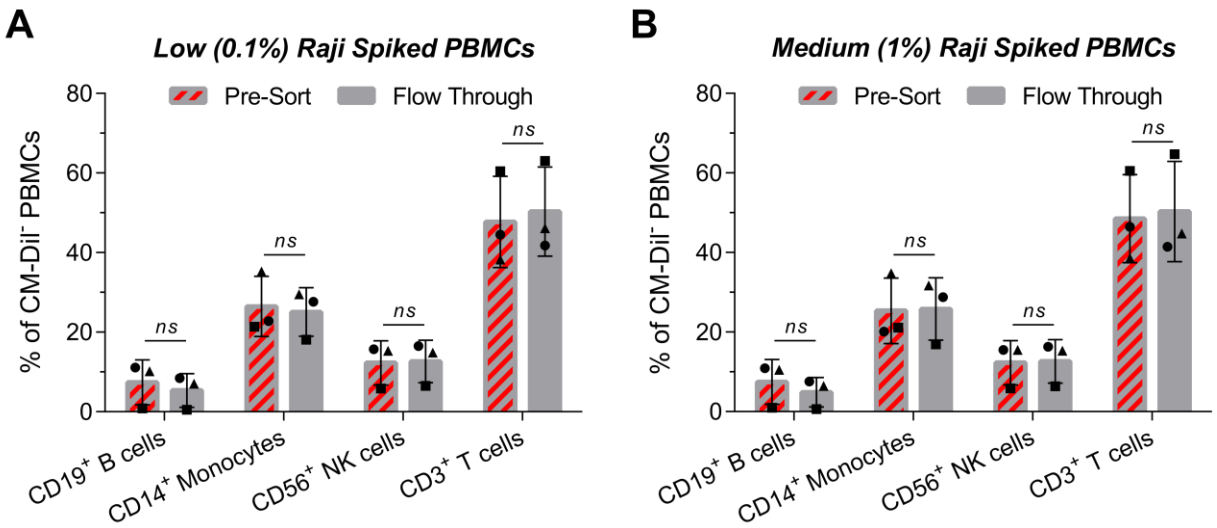

Figure S3.12 | tJBA8.1-mediated depletion of Raji cells from low and medium spiked PBMCs does not affect the healthy immune cell composition. (A and B) Flow cytometry analysis of the healthy immune cell composition within CM-Dil$^-$ PBMCs before (pre-sort) and after (flow through) Raji depletion from low (0.1%) (A) and medium (1%) (B) Raji spiked PBMCs. The circles, squares and triangles represent different PBMC donors from separate depletion studies. Graph bars and error bars represent mean ± standard deviation; *n* = 3 independent experiments with different PBMC donors. *ns* > 0.05 (paired two-way ANOVA with Šídák correction). CM-Dil, chloromethylbenzamido-1,1'-dioctadecyl-3,3,3',3'-tetramethylindocarbocyanine perchlorate.

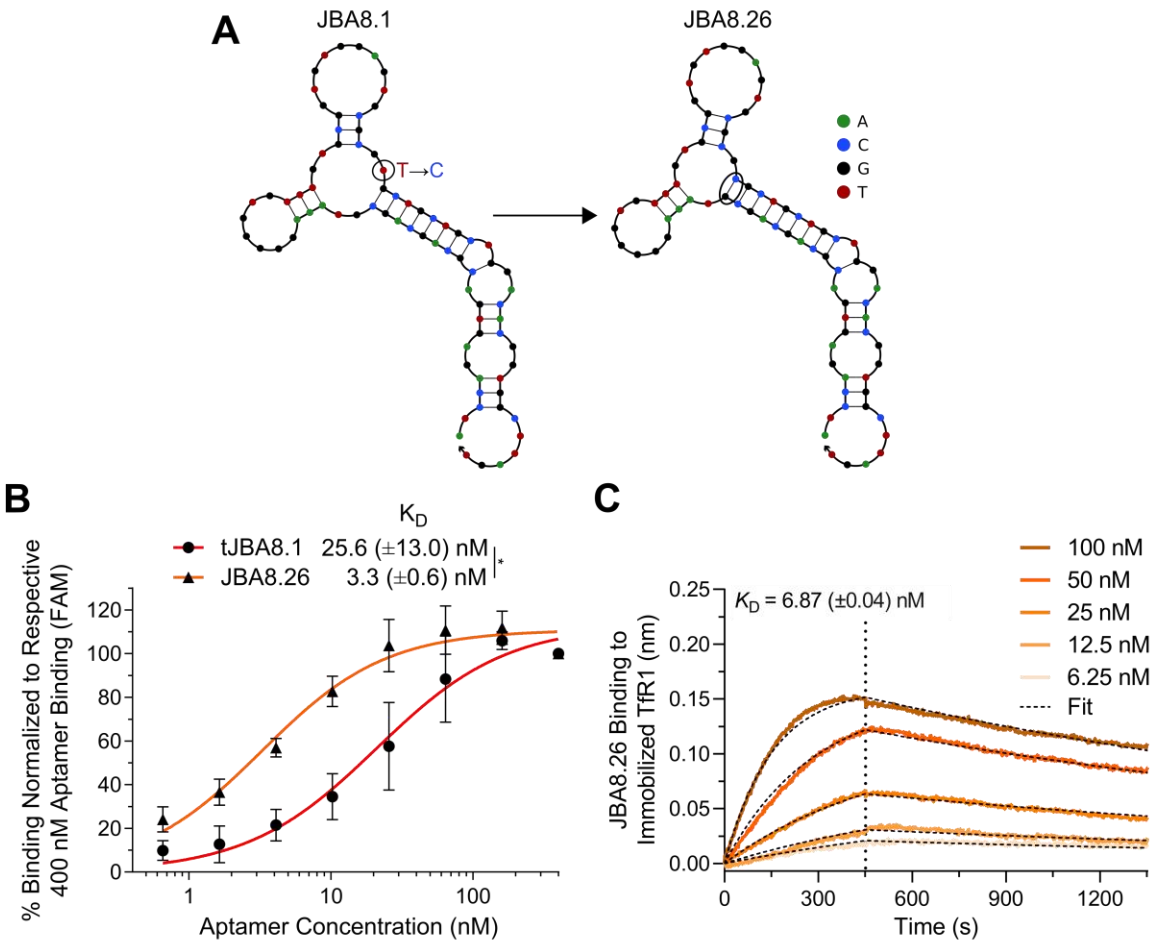

Figure S3.13 | JBA8.26 is a higher affinity point variant of JBA8.1. (A) MFE structure of JBA8.1 and JBA8.26, predicted using NUPACK (temperature = 4 °C; Na^+ = 137 mM; Mg^{2+} = 5.5 mM). Circles indicate T→C point mutation from original JBA8.1 sequence and subsequent predicted base pairing. (B) Flow cytometry binding curves of FAM-labeled tJBA8.1 and JBA8.26 to H9 cells, normalized to 400 nM aptamer binding. The curves represent a nonlinear regression assuming one-site specific binding with Hill slope. K_D values were calculated by averaging the individual regression values of the independent experiments. Data points and error bars, and K_D values, represent mean ± standard deviation; n = 3 independent experiments. *P < 0.05 (two-sided unpaired t-test). (C) Association and dissociation kinetics of serially diluted FAM-labeled JBA8.26 binding to biotinylated TfR1 immobilized on streptavidin biosensors by BLI. The association phase is illustrated from 0-450 s, whereas dissociation is shown from 450-1350 s (separated by the vertical dotted line). K_D values were calculated by performing a global fit of the multi-concentration kinetic data to a 1:1 binding model. K_D values represent mean ± standard deviation; n = 5 individual concentrations of aptamers. FAM, 6-carboxyfluorescein.

```
SP|P02786|TFR1_HUMAN MMDQARSAFSNLFGGEPLSYTRFSLARQVDGDNSHVEMKLAVDEEENADNNTKANVTKPK 60
SP|Q62351|TFR1_MOUSE MMDQARSAFSNLFGGEPLSYTRFSLARQVDGDNSHVEMKLAADEEENADNNMKASVRKPK 60
                     ****************************************.********* **.* ***

SP|P02786|TFR1_HUMAN RCSGSICYGTIAVIVFFLIGFMIGYLGYCKGVEPKTECERLAGTESPVREE--PGEDFPA 118
SP|Q62351|TFR1_MOUSE RFNGRLCFAAIALVIFFLIGFMSGYLGYCKRVEQKEECVKLAETEETDKSETMETEDVPT 120
                     * .* :*:.:**:::******* ******* ** * ** :** **.  :.*    **.*:

SP|P02786|TFR1_HUMAN ARRLYWDDLKRKLSEKLDSTDFTGTIKLLNENSYVPREAGSQKDENLALYVENQFREFKL 178
SP|Q62351|TFR1_MOUSE SSRLYWADLKTLLSEKLNSIEFADTIKQLSQNTYTPREAGSQKDESLAYYIENQFHEFKF 180
                     : **** ***  *****:* :*:.*** *.:*:*.**********.** *:****:***:

SP|P02786|TFR1_HUMAN SKVWRDQHFVKIQVKDSAQNSVIIVDKNGRLVYLVENPGGYVAYSKAATVTGKLVHANFG 238
SP|Q62351|TFR1_MOUSE SKVWRDEHYVKIQVKSSIGQNMVTIVQSNGNLDPVESPEGYVAFSKPTEVSGKLVHANFG 240
                     ******:*:******.*  :.:: : :..  :  **.* ****:** : *:**********

SP|P02786|TFR1_HUMAN TKKDFEDLYTPVNGSIVIVRAGKITFAEKVANAESLNAIGVLIYMDQTKFPIVNAELSFF 298
SP|Q62351|TFR1_MOUSE TKKDFEELSYSVNGSLVIVRAGEITFAEKVANAQSFNAIGVLIYMDKNKFPVVEADLALF 300
                     ******:*   ****:******:**********:*:**********:.***:*:*:*::*

SP|P02786|TFR1_HUMAN GHAHLGTGDPYTPGFPSFNHTQFPPSRSSGLPNIPVQTISRAAAEKLFGNMEGDCPSDWK 358
SP|Q62351|TFR1_MOUSE GHAHLGTGDPYTPGFPSFNHTQFPPSQSSGLPNIPVQTISRAAAEKLFGKMEGSCPARWN 360
                     *************************:**********************:***.**: *:

SP|P02786|TFR1_HUMAN TDSTCRMVTSESKNVKLTVSNVLKEIKILNIFGVIKGFVEPDHYVVVGAQRDAWGPGA-A 417
SP|Q62351|TFR1_MOUSE IDSSCKLELSQNQNVKLIVKNVLKERRILNIFGVIKGYEEPDRYVVVGAQRDALGAGVAA 420
                      **:*::  *:.:**** *.***** :**********: ***:********** * *. *

SP|P02786|TFR1_HUMAN KSGVGTALLLKLAQMFSDMVLKDGFQPSRSIIFASWSAGDFGSVGATEWLEGYLSSLHLK 477
SP|Q62351|TFR1_MOUSE KSSVGTGLLLKLAQVFSDMISKDGFRPSRSIIFASWTAGDFGAVGATEWLEGYLSSLHLK 480
                     **.***.*******:****: ****:**********:*****:****************

SP|P02786|TFR1_HUMAN AFTYINLDKAVLGTSNFKVSASPLLYTLIEKTMQNVKHPVTGQFLYQDSNWASKVEKLTL 537
SP|Q62351|TFR1_MOUSE AFTYINLDKVVLGTSNFKVSASPLLYTLMGKIMQDVKHPVDGKSLYRDSNWISKVEKLSF 540
                     *********.*****************: * **:***** *: **:**** ******::

SP|P02786|TFR1_HUMAN DNAAFPFLAYSGIPAVSFCFCEDTDYPYLGTTMDTYKELIERIPELNKVARAAAEVAGQF 597
SP|Q62351|TFR1_MOUSE DNAAYPFLAYSGIPAVSFCFCEDADYPYLGTRLDTYEALTQKVPQLNQMVRTAAEVAGQL 600
                     ****:******************:******* :***: * :::*:**::.*:********:

SP|P02786|TFR1_HUMAN VIKLTHDVELNLDYERYNSQLLSFVRDLNQYRADIKEMGLSLQWLYSARGDFFRATSRLT 657
SP|Q62351|TFR1_MOUSE IIKLTHDVELNLDYEMYNSKLLSFMKDLNQFKTDIRDMGLSLQWLYSARGDYFRATSRLT 660
                     :************** ***:****::****:::**::*********.******:********

SP|P02786|TFR1_HUMAN TDFGNAEKTDRFVMKKLNDRVMRVEYHFLSPYVSPKESPFRHVFWGSGSHTLPALLENLK 717
SP|Q62351|TFR1_MOUSE TDFHNAEKTNRFVMREINDRIMKVEYHFLSPYVSPRESPFRHIFWGSGSHTLSALVENLK 720
                     *** *****:****:::***:*:************:******:********* **:****

SP|P02786|TFR1_HUMAN LRKQNNGAFNETLFRNQLALATWTIQGAANALSGDVWDIDNEF 760
SP|Q62351|TFR1_MOUSE LRQKNITAFNETLFRNQLALATWTIQGVANALSGDIWNIDNEF 763
                     **::*  ********************.*******:*:*****
```

Figure S3.14 | Mouse TfR1 has lysine mutations at two human TfR1 arginine residues bound by tJBA8.1. Protein sequence alignment of human TfR1 and mouse TfR1 using the Clustal Omega program. Underlined groups of amino acids in the human sequence indicate the α helices 1, 2, and 3 of the TfR1 helical domain. Green font and highlighting represent the TfR1 residues bound by tJBA8.1 that overlap between the human and mouse sequences, whereas red font and highlighting represent the TfR1 residues bound by tJBA8.1 that do not overlap between the mouse and human sequences (i.e., the human TfR1 residues bound by tJBA8.1 mutated in mouse TfR1).

```
SP|P02786|TFR1_HUMAN MMDQARSAFSNLFGGEPLSYTRFSLARQVDGDN-SHVEMKLAVDEEENAD---------- 49
SP|Q9UP52|TFR2_HUMAN -MERLWGLFQRAQQLSPRSS--QTVYQRVEGPRKGHLEEEE-EDGEEGAETLAHFCPMEL 56
                      *::  . *..    .* *    :: ::*:* . .*:* :   * **.*:

SP|P02786|TFR1_HUMAN -------NNTKANVTKPKRCS--GSICYGTIAVIVFFLIGFMIGYLGYCKGVEPKTECER 100
SP|Q9UP52|TFR2_HUMAN RGPEPLGSRPRQPNLIPWAAAGRRAAPYLVLTALLIFTGAFLLGYVAFRGSCQACGDS-- 114
                            .. :     *  .:   :  * .::.:::*  .*::**:.:  . :   :.

SP|P02786|TFR1_HUMAN LAGTESPVREEPGEDFPAARRLYWDDLKRKLSEKLDSTDFTGTIKLLNENSYVPREAGSQ 160
SP|Q9UP52|TFR2_HUMAN VLVVSEDVNYEPDLDFH-QGRLYWSDLQAMFLQFLGEGRLEDTIRQ---TSLRERVAGSA 170
                      :  ... *. **. **    ****.**:  : : *..  : .**:    .*   * ***

SP|P02786|TFR1_HUMAN KDENLALYVENQFREFKLSKVWRDQHFVKIQVKDSAQNSV-IIVDKNGRL--VYLVENPG 217
SP|Q9UP52|TFR2_HUMAN GMAALTQDIRAALSRQKLDHVWTDTHYVGLQFPDPAHPNTLHWVDEAGKVGEQLPLEDPD 230
                          *:  :.  : . **.:** * *:* :*. * *: ..   **: *::     :*:*.

SP|P02786|TFR1_HUMAN GYVAYSKAATVTGKLVHANFGTKKDFEDLYTP---VNGSIVIVRAGKITFAEKVANAESL 274
SP|Q9UP52|TFR2_HUMAN VYCPYSAIGNVTGELVYAHYGRPEDLQDLRARGVDPVGRLLLVRVGVISFAQKVTNAQDF 290
                       *  **  ..***:**:*::*  :*::** :      * :::**.* *:**:**:**:.:

SP|P02786|TFR1_HUMAN NAIGVLIYMDQTKF------PIVNAELSFFGHAHLGTGDPYTPGFPSFNHTQFPPSRSSG 328
SP|Q9UP52|TFR2_HUMAN GAQGVLIYPEPADFSQDPPKPSLSSQQAVYGHVHLGTGDPYTPGFPSFNQTQFPPVASSG 350
                      .* ***** : :.*      * :.:: :.:**.****************:*****  ***

SP|P02786|TFR1_HUMAN LPNIPVQTISRAAAEKLFGNMEGDC-PSDWKTDSTCR-MVTSESKNVKLTVSNVLKEIKI 386
SP|Q9UP52|TFR2_HUMAN LPSIPAQPISADIASRLLRKLKGPVAPQEWQGSLLGSPYHLGPGPRLRLVVNNHRTSTPI 410
                      **.**.* **   *.:*: :::*   *.:*: .        . . .::*.*.*  ..  *

SP|P02786|TFR1_HUMAN LNIFGVIKGFVEPDHYVVVGAQRDAWGPGAAKSGVGTALLLKLAQMFSDMVLKDGFQPSR 446
SP|Q9UP52|TFR2_HUMAN NNIFGCIEGRSEPDHYVVIGAQRDAWGPGAAKSAVGTAILLELVRTFSSMV-SNGFRPRR 469
                       **** *:*  *******:***************.****:**:*.: **.** .:**:* *

SP|P02786|TFR1_HUMAN SIIFASWSAGDFGSVGATEWLEGYLSSLHLKAFTYINLDKAVLGTSNFKVSASPLLYTLI 506
SP|Q9UP52|TFR2_HUMAN SLLFISWDGGDFGSVGSTEWLEGYLSVLHLKAVVYVSLDNAVLGDDKFHAKTSPLLTSLI 529
                      *::* **..*******:********* *****..*:.**:**** .:*:..:**** :**

SP|P02786|TFR1_HUMAN EKTMQNVKHPVT------GQFLYQDSNWASK-VEKLTLDNAAFPFLAYSGIPAVSFCFCE 559
SP|Q9UP52|TFR2_HUMAN ESVLKQVDSPNHSGQTLYEQVVFTNPSWDAEVIRPLPMDSSAYSFTAFVGVPAVEFSFME 589
                      *..:::*. *         *.:: : .* :: :. * :*.:*: * *: *:***.*.* *

SP|P02786|TFR1_HUMAN D-TDYPYLGTTMDTYKELIERIP-ELNKVARAAAEVAGQFVIKLTHDVELNLDYERYNSQ 617
SP|Q9UP52|TFR2_HUMAN DDQAYPFLHTKEDTYENLHKVLQGRLPAVAQAVAQLAGQLLIRLSHDRLLPLDFGRYGDV 649
                      *   **:* *. ***::* : :  .*  **:*.*::***::*:*:**  * **: **..

SP|P02786|TFR1_HUMAN LLSFVRDLNQYRADIKEMGLSLQWLYSARGDFFRATSRLTTDFGNAEKTDRFVMKKLNDR 677
SP|Q9UP52|TFR2_HUMAN VLRHIGNLNEFSGDLKARGLTLQWVYSARGDYIRAAEKLRQEIYSSEERDERLTRMYNVR 709
                      :* .: :**:: .*:*  **:***:******:**:.:*  :: .:*: *. : :  * *

SP|P02786|TFR1_HUMAN VMRVEYHFLSPYVSPKESPFRHVFWGSGSHTLPALLENLKLRKQNN---------GAFNE 728
SP|Q9UP52|TFR2_HUMAN IMRVEFYFLSQYVSPADSPFRHIFMGRGDHTLGALLDHLRLLRSNSSGTPGATSSTGFQE 769
                      :****::*** **** :*****:* * *.*** ***::*:* :.*.          .*:*
SP|P02786|TFR1_HUMAN TLFRNQLALATWTIQGAANALSGDVWDIDNEF 760
SP|Q9UP52|TFR2_HUMAN SRFRRQLALLTWTLQGAANALSGDVWNIDNNF 801
                      : **.**** ***:************:***:*
```

Figure S3.15 | TfR2 has mutations at four TfR1 residues bound by tJBA8.1. Protein sequence alignment of TfR1 and TfR2 using the Clustal Omega program. Underlined groups of amino acids in the TfR1 sequence indicate the α helices 1, 2, and 3 of the helical domain. Green font and highlighting represent the TfR1 residues bound by tJBA8.1 that overlap with TfR2, whereas red font and highlighting represent the TfR1 residues bound by tJBA8.1 that do not overlap with TfR2 (i.e., the human TfR1 residues bound by tJBA8.1 mutated in TfR2).

Chapter 4: Development of a multivalent DNA aptamer-polymer conjugate for selective targeting of integrin $\alpha4\beta1^+$ T-Lineage leukemias and lymphomas

Ian I. Cardle, Jai Raman, Dinh Chuong Nguyen, Drew L. Sellers, Nataly Kacherovsky, Stephen J. Salipante, Michael C. Jensen, & Suzie H. Pun

ABSTRACT

Selective therapeutic targeting of T-cell malignancies is notoriously difficult due to the shared lineage between healthy and malignant T cells. Current front-line chemotherapy for these cancers is largely non-specific, resulting in frequent cases of relapsed or refractory disease that have especially grim outcomes. The development of novel targeting approaches for effectively treating T-cell leukemia and lymphoma thus remains a critical goal for the oncology field. In this work, we report the discovery of a novel DNA aptamer, named HR7A1, that displays single-digit to sub-nanomolar affinity for the heterodimeric integrin α4β1 (also known as VLA-4), a marker associated with chemoresistance and relapse in leukemia patients. After rational truncation of HR7A1 to a minimal binding motif, we demonstrate elevated binding of the aptamer to T-lineage leukemia and lymphoma cell lines over healthy immune cells. We last characterize barriers to *in vivo* translation of the aptamer, including temperature-sensitive binding and short circulation half-life, and synthesize an aptamer-polymer conjugate to address these challenges. Future work will seek to validate *in vivo* targeting of α4β1-expressing tumors with the aptamer-polymer conjugate, thereby establishing an aptamer-based biomaterial that can be readily adapted for targeted treatment of T-cell malignancies.

4.1 INTRODUCTION

Lymphomas and lymphocytic leukemias are estimated to account for 6.0% and 4.5% of new cancer cases and deaths, respectively, in the United States in 2022, and children and young adults are disproportionately afflicted with these cancers.[1,2] While the overall survival rate of children and young adults diagnosed with these conditions has improved dramatically in recent decades,[3] approximately 10-20% of them will suffer from progressive disease or relapse.[4–8] Of these patients with relapsed or refractory (r/r) disease, only ~15-50% will survive,[4,5,7,9–12] with especially poor outcomes associated with lymphomas and leukemias derived from T cells.[5,8,9,13] Accordingly, new therapeutic strategies that can achieve durable responses in these subsets of patients are urgently required.

Designing targeted therapies for T-cell leukemia and lymphoma has been a challenging task. Due to the shared lineage between healthy and malignant T cells, biomarkers that can be uniquely or preferentially targeted for an anti-cancer therapy are limited.[14,15] Therapeutic targeting of pan T-cell markers such as CD2, CD3, CD5, and CD7 carries the risk of T-cell aplasia, which would result in severe immunodeficiency that exposes patients to fatal opportunistic infections.[16] More restricted T-cell antigens, including terminal deoxynucleotidyl transferase (TdT), T cell receptor beta constant 1 (TRBC1), CD1a, and CD30, are either expressed intracellularly or only on a subset of T-cell malignancies, hampering their broader targeting appeal.[15,17,18] For these reasons, the identification of antigens selectively and uniformly expressed on T-cell malignancies and the development of associated targeting ligands remain important goals for treating these cancers.

Monoclonal antibodies have been widely used at targeting ligands for theranostic applications, owing to their high specificities and nanomolar binding affinities. However, antibodies are

expensive for oncology use due to their biological production (>$100,000 annually),[19] and their large size (~150 kDa) prohibits deep tissue penetration needed for comprehensive tumor targeting.[20] Additionally, antibodies are recycled via neonatal Fc receptor binding, leading to long circulation half-lives in patients (several days to weeks) that can prevent rapid management of treatment-associated side effects.[21,22] For treating T-cell malignancies, more short-lived targeting approaches may be preferred to prevent prolonged T-cell aplasia and preferentially target antigens that are upregulated on malignant cells but not strictly tumor-specific.[23]

Considered nucleic acid analogues of monoclonal antibodies, aptamers fulfill many of the unique needs for safe and effective targeting of T-cell malignancies. Aptamers are single-stranded oligonucleotides that fold into sequence-specific structures capable of recognizing almost any kind of target with high affinity and specificity. The small size of aptamers (6-30 kDa) allows them to possess higher tumor penetration and shorter circulation half-lives than antibodies, simplifying the management of their concentrations *in vivo*.[24,25] Aptamers are also synthetic, making them inexpensive to manufacture and permissible to many chemical modifications for diverse functions.[26] Given these favorable properties, aptamers have garnered considerable interest as targeting ligands for cancer theranostic applications.[27,28]

Aptamers are selected through a process known as Systematic Evolution of Ligands by EXponential enrichment (SELEX), in which a library of aptamer sequences is screened for binding to desired targets in iterative rounds of positive and negative selection. Targets used for SELEX can include small molecules, proteins, viruses, bacteria, cells, tissues, and even live animals.[29–35] Importantly, SELEX can be performed without knowledge of the target antigen. For example, cancer cell-specific aptamers can first be developed and then used to identify the target protein, leading to the discovery of novel biomarkers for targeted therapy.[36] Using SELEX, our lab has

discovered a portfolio of aptamers for targeting $CD8^+$ T cells, monocytes, $TfR1^+$ tumor cells, and SARS-CoV-2 in just a short-span of five years.[37–40]

Here, via a "failed" cell-SELEX, we report the accidental discovery of a DNA aptamer named HR7A1 that binds to immortalized leukemia and lymphoma cells. Using membrane protein pull-down, we identified the integrin α4β1 (also known as VLA-4), a marker associated with pediatric r/r lymphoma and lymphocytic leukemia, as a potential target of HR7A1. Aptamer and antibody co-staining, siRNA knockdown, and bio-layer interferometry studies confirmed aptamer targeting of the α4β1 heterodimer and not just one of individual subunits. We rationally and progressively truncated the 88-nucleotide (nt) HR7A1 sequence, generating aptamers as small as 37 nt that retain nanomolar affinity to the α4β1 protein and $\alpha4^+\beta1^+$ cell lines. Of relevance, these truncated HR7A1 aptamers robustly and selectively bind T-lineage malignant cell lines over healthy peripheral immune cells, suggesting that they could be used for therapeutic targeting of T-cell leukemias and lymphomas. We lastly explore modification of one of the truncated aptamers, including nucleotide substitutions and multivalent grafting to a soluble polymer backbone, to overcome barriers of *in vivo* translation, laying the foundation for future targeting studies in tumor-bearing mice.

4.2 RESULTS

4.2.1 Accidental discovery of HR7A1, a leukemia and lymphoma binding aptamer, by cell-SELEX

In an initial effort to identify DNA aptamers that bind B7H3 (CD276), a marker upregulated on solid tumors, we performed cell-SELEX on H9 T-lymphoma cells that were lentivirally transduced to express the predominant isoform of B7H3, 4IgB7H3 (>97% expression, **Figure S4.1A**). H9 cells were chosen due to being a readily available suspension cell line in the lab, eliminating the need for enzymatic dissociation during culturing that can undesirably cleave target extracellular

proteins. An initial round of positive selection was conducted against these H9 4IgB7H3 cells using a single-stranded DNA (ssDNA) library with a theoretical 10^{15}-10^{16} unique sequences. Afterwards, the selected aptamer pool underwent multiple rounds of positive and negative selection against H9 4IgB7H3 cells and H9 parental cells, respectively. Selection pressure was increased by decreasing DNA concentration and the number of positive selection cells, switching BSA for FBS, adding additional anion competitors such as salmon sperm DNA and poly(I:C), decreasing positive selection incubation time, increasing washes, and implementing multiple sequential negative selections in a single round, as summarized in **Table S4.1**. The enrichment of cell-binding aptamers was monitored by flow cytometry starting after round 4, and non-selective binding to both H9 + 4IgB7H3 cells and H9 parental cells was observed after round 6 (**Figure S4.1B**). To enrich B7H3 binders from the non-selective pool, we attempted ligand-guided selection (LIGS) in round 7, which uses antibody competition after the positive selection step to outcompete and elute antigen-specific aptamers.[41] However, even greater non-selective binding was found in round 7 (**Figure S4.1B**), indicating failure of the SELEX process to identify B7H3-specific aptamers. We speculate that our aptamers failed to re-fold properly after extracting them at the end of positive selection, making the subsequent negative selection steps obsolete. Indeed, our lab has had a greater hit-rate with SELEX when reversing the order of positive and negative selection.[42]

Nonetheless, we proceeded with next generation sequencing (NGS) of the round 7 pool using the primers detailed in **Table S4.2** to identify H9-binding aptamers of potential interest. FASTAptamer was used to analyze the sequencing data,[43] and phylogenetic trees and consensus motifs of the top 50 aptamers were generated using FigTree and MEME software, respectively (**Figure 4.1A**).[44,45] **Table S4.3** shows the top 50 aptamers identified from round 7 in order of prevalence with predicted motifs. Top aptamer sequences collapsed into five motifs, with Motifs

1, 2, and 4 spanning at least 40 nt of the 52-nt random region and containing the rank 1, 2, and 3 aptamers, respectively. In contrast, motifs 3 and 5 were smaller (~20 nt), contained lower ranking aptamers, and their respective aptamer sequences clustered less closely on the phylogenetic trees with each other. Surprisingly, Motifs 2 and 4 corresponded to aptamers that our lab previously identified by SELEX with different selection cells (Motifs 2 and 4) and starting libraries (Motif 4). Motif 2 represents an aptamer that binds an unknown antigen on cultured $CD4^+$ T cells (unpublished) and Motif 4 represents our published tJBA8.1 aptamer that binds the transferrin receptor.[39] Motif 1 was a unique motif that we had not previously observed; importantly, it was the most statistically significant motif of the five, encompassing the whole 52-nt random region and containing 10 of the top 50 aptamers with 96-98% sequence identity. The rank 1 aptamer from this motif, which we named H9 SELEX Round 7 Aptamer 1 (HR7A1), represented 41.6% of the whole round 7 sequence pool, demonstrating excellent enrichment. The minimum free energy (MFE) structure of HR7A1, predicted by NUPACK,[46] also conformed well to the library design, with the binding motif residing on top of a stem formed by two flanking 18-nt constant regions (**Figure 4.1B**). Due to these promising properties, we selected the HR7A1 sequence (**Table S4.4**) for further characterization.

We evaluated the binding of fluorescein-labeled HR7A1 to four cell lines: H9 parental cells, H9 4IgB7H3 cells, T-leukemia Jurkat cells, and B-lymphoma Raji cells. HR7A1 exhibited broad binding to all these cell lines, with the highest and lowest binding observed on Jurkat and Raji cells, respectively (**Figure 4.1C**). Binding to H9 parental cells was moderate and equivalent to that of the H9 4IgB7H3 cells, indicating that HR7A1 does not bind B7H3. Impressively, HR7A1 binding to all these cells was already saturated at the lowest concentration we tested (12.5 nM), suggesting that HR7A1 has at least single digit nanomolar affinity.

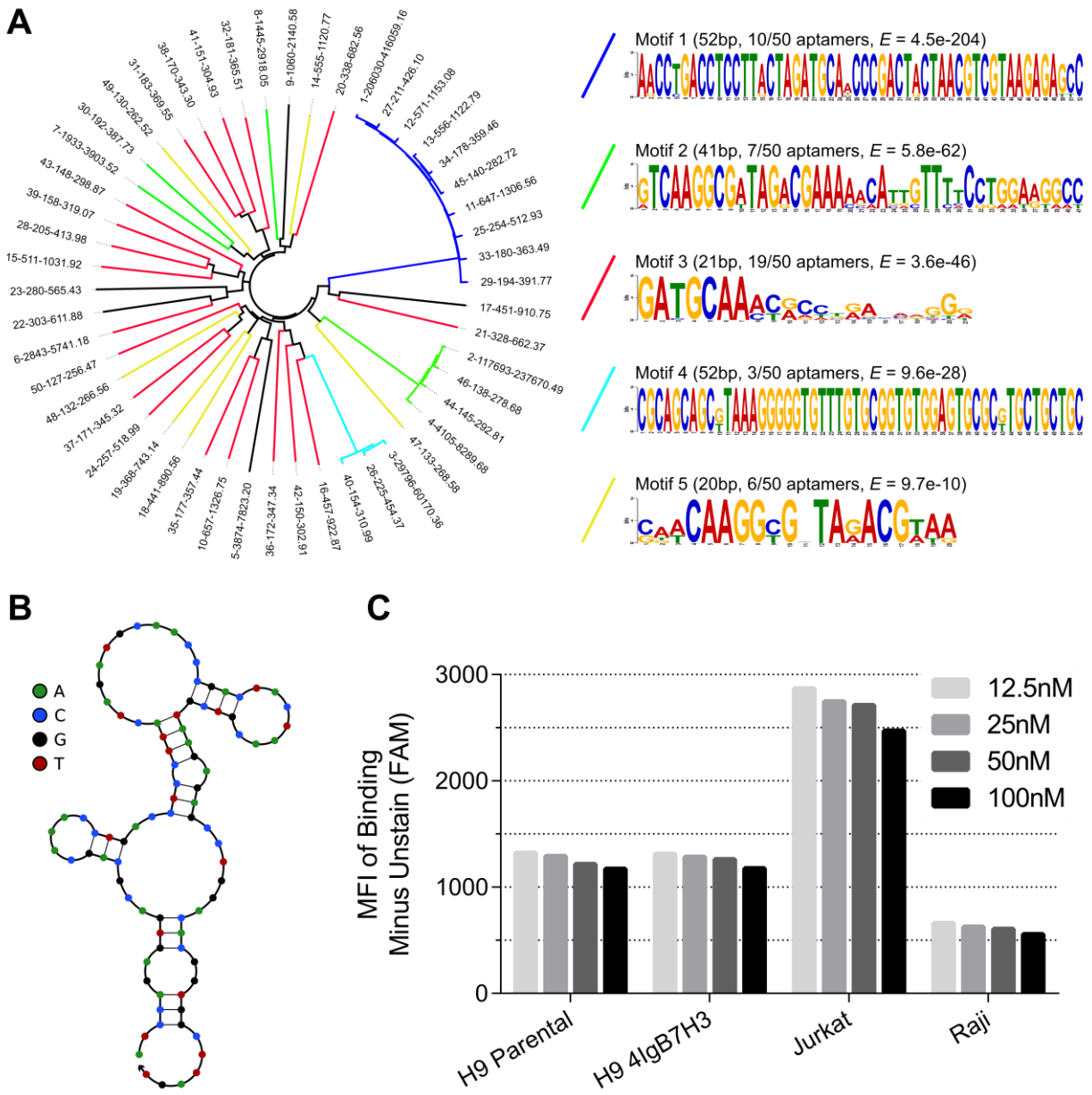

Figure 4.1 | Failed cell-SELEX accidentally identifies HR7A1, a highly enriched aptamer that broadly binds lymphoma and lymphocytic leukemia cells. (A) Phylogenetic tree of the top 50 aptamers from round 7 of cell-SELEX with H9 cells and corresponding consensus motifs. Aptamers with different consensus motifs are highlighted by color in the phylogenetic tree. The *E*-values of the consensus motifs represents their statistical significance. (B) The minimum free energy structure of the HR7A1 aptamer, predicted using NUPACK (temperature = 4 °C; Na^+ = 137 mM; Mg^{2+} = 5.5 mM). (C) Flow cytometry binding of FAM-labeled HR7A1 to H9 parental, H9 4IgB7H3, Jurkat, and Raji cells at different concentrations, as determined by median fluorescence intensity (MFI). The bars graphs are representative of n = 1 independent experiment. FAM, 6-carboxyfluorescein.

4.2.2 HR7A1 aptamer receptor identification

To identify the target receptor of HR7A1, we used a pull-down procedure described by Shangguan et al. (**Figure 4.2A**).[36] Briefly, membrane proteins were extracted from Jurkat and H9 cells and incubated with and without biotinylated HR7A1 aptamer, the latter group serving as the negative control. Biotinylated tJBA8.1, which binds to the transferrin receptor, was also included as a positive control. Aptamer-bound proteins were then isolated using streptavidin-coated magnetic beads, and SDS-PAGE was used to separate and visualize enriched protein bands under mild reducing conditions (**Figure 4.2B**). HR7A1 enriched three protein bands relative to the no aptamer and tJBA8.1 controls: an intense band between 130-250 kDa (Band 1), a moderate band between 100-130 kDa (Band 2), and a faint band between 70-100 kDa (Band 3). Encouragingly, these enriched protein bands were found in the membrane protein pull-downs from both Jurkat and H9 cells, although they were noticeably darker for the Jurkat extracts. This tracks with the HR7A1 aptamer's higher binding to Jurkat cells, which points to higher target receptor expression on Jurkat versus H9 cells.

The enriched protein bands from the Jurkat extracts along with corresponding regions of the negative control were excised, digested, and submitted for LC-MS/MS analysis. Ignoring contaminating skin/hair proteins and intracellular proteins, the top protein hit for each excised Jurkat band is shown in **Figure 4.3C**. The integrin α4 (CD49d) was the first ranked candidate from Bands 1 and 3 whereas the integrin β1 (CD29) was the first ranked candidate from Band 2, with minimal representation of these proteins in the corresponding control bands. The presence of multiple integrin α4 bands is consistent with reports that the protein can be expressed fully intact (~150 kDa) or as two cleaved, non-covalently associated fragments (70-80 kDa).[47] Together, the integrins α4 and β1 partner to form the α4β1 (CD49d/CD29) heterodimer, also known as very late

antigen-4 (VLA-4), which is expressed on a variety of immune cells and interacts with VCAM-1 and fibronectin for cell adhesion and migration during hematopoiesis and inflammation.[48] Of relevance to cancer targeting, the integrin α4β1 is overexpressed on many leukemias and lymphomas, and its expression is associated with chemotherapy refractory disease due to the integrin's interaction with stromal cells that promotes cancer cell survival and drug resistance via PI3/AKT/Bcl2 signaling.[49–51] Similarly, the expression of integrin α4β1 is also an adverse risk factor in childhood acute lymphoblastic leukemia (ALL) at first relapse.[52] The tumor-associated expression of this integrin has thus prompted research efforts to target α4β1 for anti-cancer therapy.[53,54] On account of this and the fact that the expression profile of α4β1 closely resembles the binding profile of the HR7A1 aptamer, we focused on this integrin for further binding validation.

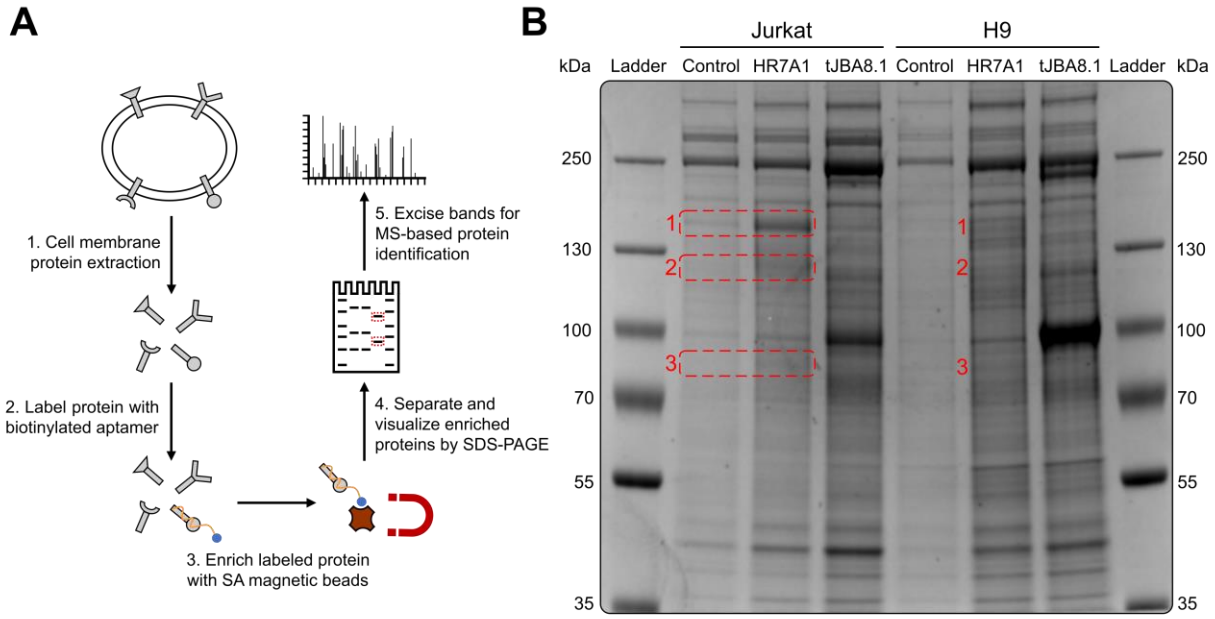

C

			Peptide Coverage		# of Peptides		SEQUEST HT Score	
Band	**Molecular Weight**	**Description**	**Control**	**HR7A1**	**Control**	**HR7A1**	**Control**	**HR7A1**
1	>130 kDa & <250 kDa	Integrin alpha 4	0%	34%	0	41	0	224
2	>100 kDa & <130 kDa	Integrin beta 1	1%	35%	1	40	1.65	311
3	>70 kDa & <100 kDa	Integrin alpha 4	0%	18%	0	17	0	72

**Integrin alpha 4: 114.8 kDa (migrates as 150 kDa and 70-80 kDa) | Integrin beta 1: 88.4 kDa (migrates as 110-130 kDa)*

Figure 4.2 | Integrin α4β1 is identified as a potential target of HR7A1. (A) Schematic representation of aptamer pull-down procedure for identifying candidate target proteins. (B) Colloidal blue-stained 8% SDS-PAGE gel of enriched proteins from aptamer pull-down assay with Jurkat and H9 membrane protein extracts. Protein bands that were enriched by HR7A1 relative to the no aptamer and tJBA8.1 controls are marked by numbers, and the dotted boxes represent the bands that were excised for mass spectrometry analysis. (C) Summary of the top extracellular protein hit for each excised band identified by mass spectrometry. A higher SEQUEST HT score represents a better identification.

4.2.3 Validation of HR7A1 binding to α4β1

To confirm the mass spectrometry results, we examined co-staining of the HR7A1 aptamer with anti-CD49d (anti-α4) and anti-CD29 (anti-β1) antibodies on various target cell lines (**Figure 4.3A**), including H9 and Jurkat cells, as well as erythroleukemia K562 cells, which have previously been shown to express α5β1 (CD49e/CD29) but not α4β1.[55,56] On H9 and Jurkat cells, HR7A1

aptamer binding correlated strongly with anti-CD49d and anti-CD29 antibody staining, whereas binding of a tJBA8.1 aptamer control did not correlate with antibody staining. The HR7A1 aptamer did not bind to $CD49d^{-}CD29^{+}$ K562 cells, suggesting that HR7A1 is specific for either the integrin α4 alone or the α4β1 dimer. We could not further distinguish which of these possibilities was true with this assay since correlation between anti-CD49d and anti-CD29 antibody staining was also observed (**Figure S4.2**). Consequentially, the correlation between HR7A1 aptamer binding and anti-CD29 antibody staining could be either a direct effect of binding to the α4β1 dimer or an indirect effect of binding to the integrin α4, necessitating further testing.

Accordingly, we nucleofected Jurkat cells with non-specific (NS) and CD29-specific short interfering RNA (siRNA) duplexes (**Table S4.5**) and evaluated changes in protein expression and aptamer binding to distinguish if HR7A1 binds the integrin α4 alone or the α4β1 dimer. Interestingly, nucleofection with CD29 siRNA caused not only a 41% reduction in CD29 expression but also a 29% reduction in CD49d expression, suggesting that CD29 is required for proper expression of CD49d (**Figure 4.3B**). HR7A1 aptamer binding to CD29 siRNA-nucleofected cells was also reduced and strikingly matched the loss of CD29 expression but not the decrease in CD49d expression. Given that we show above that HR7A1 does not bind to $CD49d^{-}CD29^{+}$ K562 cells, these results indicate that the aptamer specifically binds the α4β1 heterodimer and not just one of the individual subunits.

To further validate the integrin specificity of HR7A1, we performed bio-layer interferometry (BLI) binding of immobilized HR7A1 to recombinant α4β1 and α4β7, the latter of which is an integrin involved in homing of lymphocytes to the gut.[57,58] Compared to our published CD8-binding A3 aptamer (CD8.A3) that served as a negative control,[37] HR7A1 displayed fast and robust binding to α4β1 that dissociated slowly upon removing excess protein (**Figure 4.3C**). In contrast, while

HR7A1 did bind α4β7 over the control CD8.A3 aptamer, the resulting binding signal was at least 10-fold lower than it was for α4β1, and α4β7 dissociated quickly from HR7A1 after removal of excess protein. This weak binding to α4β7 presents further evidence that α4 alone is not able to mediate tight HR7A1 binding. Taken together, these assays definitively demonstrate that HR7A1 simultaneously interacts with both the integrin α4 and the integrin β1 to facilitate high-affinity, selective targeting of the α4β1 heterodimer.

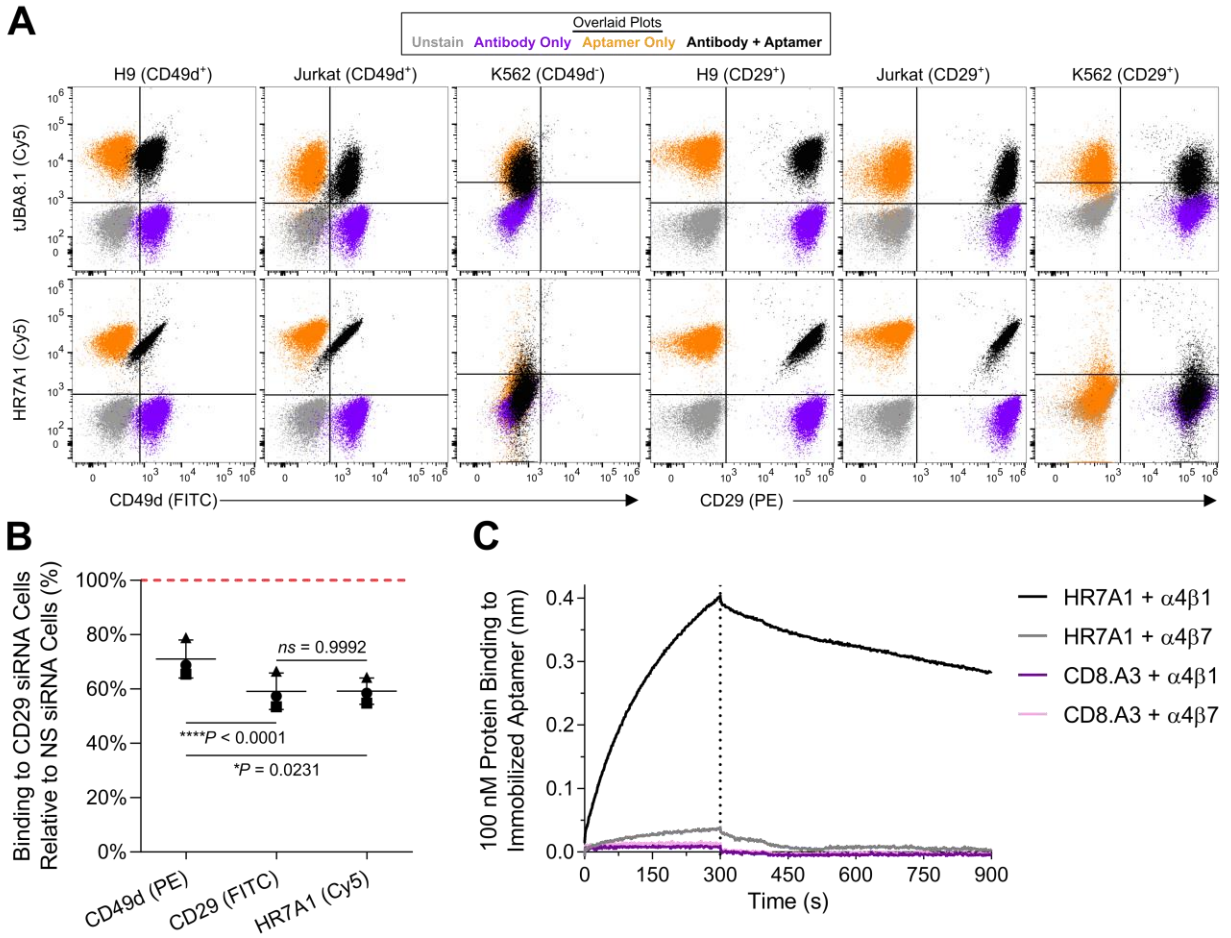

Figure 4.3 | HR7A1 interacts with both CD49d (α4) and CD29 (β1) for selective recognition of α4β1. (A) Overlaid flow cytometry plots of 10 nM Cy5-labeled tJBA8.1 and HR7A1 aptamer co-staining with FITC-labeled anti-CD49d and PE-labeled anti-CD29 antibodies on H9, Jurkat, and K562 cells. Plots are representative of n = 1 independent experiment. (B) Flow cytometry analysis of FITC-labeled anti-CD49d antibody, PE-labeled anti-CD29 antibody, and 20 nM Cy5-labeled HR7A1 binding to Jurkat cells, 42 h after nucleofection with a CD29 siRNA duplex. Red dashed horizonal line represents binding to non-specific (NS) siRNA-treated controls to which the CD29 siRNA data points were normalized. Horizonal lines and error bars

represent mean ± SD; n = 3 independent experiment. *ns* > 0.05, *P < 0.05, ****P < 0.0001 (paired one-way ANOVA with Tukey's test). (C) Association and dissociation kinetics of 100 nM α4β1 and α4β7 binding to biotinylated HR7A1 and CD8.A3 aptamers immobilized on streptavidin biosensors by BLI. The association phase is illustrated from 0-300 s, and the dissociation phase is illustrated from 300-900 s (separated by the vertical dotted line). Data are representative of n = 1 independent experiment with one individual concentration of proteins. Cy5, cyanine 5; FITC, fluorescein isothiocyanate; PE, phycoerythrin.

4.2.4 HR7A1 aptamer truncation and binding affinity comparison to other α4β1-binding aptamers

The full-length HR7A1 aptamer contains 88 nt, including two 18-nt flanking constant regions that were used for PCR amplification during SELEX. While constant regions can be important for stabilizing aptamer structure, often they can be omitted or partially truncated without impacting aptamer binding.[59] By shortening the DNA sequence, aptamer production costs can be reduced even further while increasing synthesis yields, which is especially important for producing large quantities of aptamers needed for *in vivo* applications. Given that the two constant regions of HR7A1 are predicted to form a stem and minimally interact with the aptamer consensus motif (**Figure 4.1B**), we hypothesized that they could be removed without impacting aptamer binding. Accordingly, two truncated versions of the HR7A1 aptamer were synthesized by gradually removing nucleotides from the 5' and 3' termini (**Figure 4.4A**). The first truncation (minus 33 nt from the original sequence) removed the majority of the 5' and 3' constant regions except for 5 nt at the end of the 5' constant region that was predicted to form a small hairpin structure with the consensus motif. The second truncation (minus 46 nt from the original sequence) was added onto the first truncation to further remove that small hairpin structure. These truncations yielded the sequences HR7A1.Tr1 and HR7A1.Tr2, respectively (**Table S4.4**).

We first compared the binding kinetics of the full-length HR7A1 aptamer and these truncated variants to recombinant α4β1 by BLI. HR7A1.Tr1 and HR7A1.Tr2 bound to the α4β1 protein with

K_D values of 7.74 ± 0.03 and 9.89 ± 0.05 nM, respectively, demonstrating negligible loss in binding ability compared to the K_D of 6.28 ± 0.04 nM for the full-length HR7A1 aptamer (**Figure 4.4B** and **Table S4.6**). Interestingly, both the association rate and dissociation rate of aptamer binding to α4β1 decreased with cumulative truncation, indicating that the truncated variants have slower but also more stable binding to α4β1. We further attempted to truncate off the predicted lower stem of HR7A1.Tr2, resulting in the 27-nt HR7A1.Tr3 sequence (**Figure S4.3A** and **Table S4.4**), but this aptamer failed to bind to Jurkat and H9 cells (**Figure S4.3B**). However, partial truncation of the HR7A1.Tr2 stem that further included stabilizing guanine-cytosine (GC) base pair substitutions/additions did yield a smaller (minus 5 nt) aptamer, named HR7A1.Tr4 (**Figure S4.4A** and **Table S4.4**), that retained binding affinity to Jurkat cells (**Figure S4.4B**). While we did not use HR7A1.Tr4 in subsequent studies since it was developed at the time of writing, we recognize that this sequence represents the minimal binding motif required for high affinity α4β1 recognition.

HR7A1 is likely not the first α4β1-specific aptamer to have been discovered. Sgc4 and its truncated 60-nt Sgc4e and 56-nt Sgc4f sequences are aptamers discovered by the Tan group that reportedly bind the α4 integrin.[33,55,60] Of relevance to our intended application of targeting T-cell malignancies, Sgc4 was found to robustly bind T cell acute lymphoblastic leukemia (T-ALL) cell lines and patient samples over healthy immune cells in normal bone marrow.[61] Given this encouraging data, we sought to compare the cell binding capabilities of our HR7A1, HR7A1.Tr1, and HR7A1.Tr2 aptamers against Sgc4f by flow cytometry (**Figure 4.4C**). Like the HR7A1 aptamer, HR7A1.Tr1, HR7A1.Tr2, and Sgc4f did not bind $\alpha4^{-}\beta1^{+}$ K562 cells, again showing that β1 alone is not able to facilitate binding of these aptamers. Analyzing binding to H9 cells and Jurkat cells that express α4β1 at different levels, all four aptamers boasted apparent K_D values of 0.9-2.1 nM and 1.5-4.7 nM for the respective cells. HR7A1.Tr1 and HR7A1.Tr2 bound H9 and

Jurkat cells with two- to three-fold lower K_D values than those of HR7A1 and Sgc4f, suggesting that the truncations we made to HR7A1 may have provided small enhancements in equilibrium (i.e., steady-state) binding affinity at 4 °C that were not reflected in the 25 °C kinetic BLI studies. Additionally, HR7A1.Tr2 exhibited lower maximum binding MFI values than HR7A1 and HR7A1.Tr1, which we similarly observed with HR7A1.Tr4 when compared to HR7A1.Tr2 in **Figure S4.4B**. This reduced fluorescence may be attributed to Cy5 fluorescence quenching caused by neighboring nucleotides or the closer proximity of the fluorophore to the aptamer-protein binding interface as the aptamer is truncated.[62] Comparing HR7A1 to Sgc4f, the two aptamers displayed similar apparent binding affinities to H9 cells whereas HR7A1 had slightly higher affinity over Sgc4f towards Jurkat cells.

To assess whether HR7A1 and Sgc4f share a binding site on α4β1, we performed competitive binding studies on Jurkat cells. Increasing concentrations of HR7A1, but not a TfR1-binding tJBA8.1 control aptamer, robustly outcompeted a fixed concentration of Sgc4f for binding to Jurkat cells, demonstrating that the two aptamers share overlapping binding sites on α4β1 (**Figure S4.5A**). Furthermore, the relative affinity of HR7A1 for Jurkat cells appeared to be at least three-fold higher than that of Sgc4f, as only 0.3-fold excess of HR7A1 was required to compete off 50% of Sgc4f binding. We repeated the assay with a fixed concentration of HR7A1 and increasing concentrations of Sgc4f and similarly observed selective competition between the two aptamers, with more than three-fold excess of Sgc4f required to compete off 50% of HR7A1 binding to Jurkat cells (**Figure S4.5B**). Collectively, these results demonstrate that the HR7A1 aptamer family shares an overlapping binding epitope on α4β1 with the Sgc4 aptamer family despite having dissimilar sequences (**Table S4.4**). Moreover, the HR7A1 aptamer family binds more tightly to the α4β1protein and with a smaller minimal binding motif than the Sgc4 aptamer family (37-nt

HR7A1.Tr4 versus 56-nt Sgc4f). Further studies will be needed to conclusively determine if Sgc4f binds α4 alone as reported or the α4β1 heterodimer.

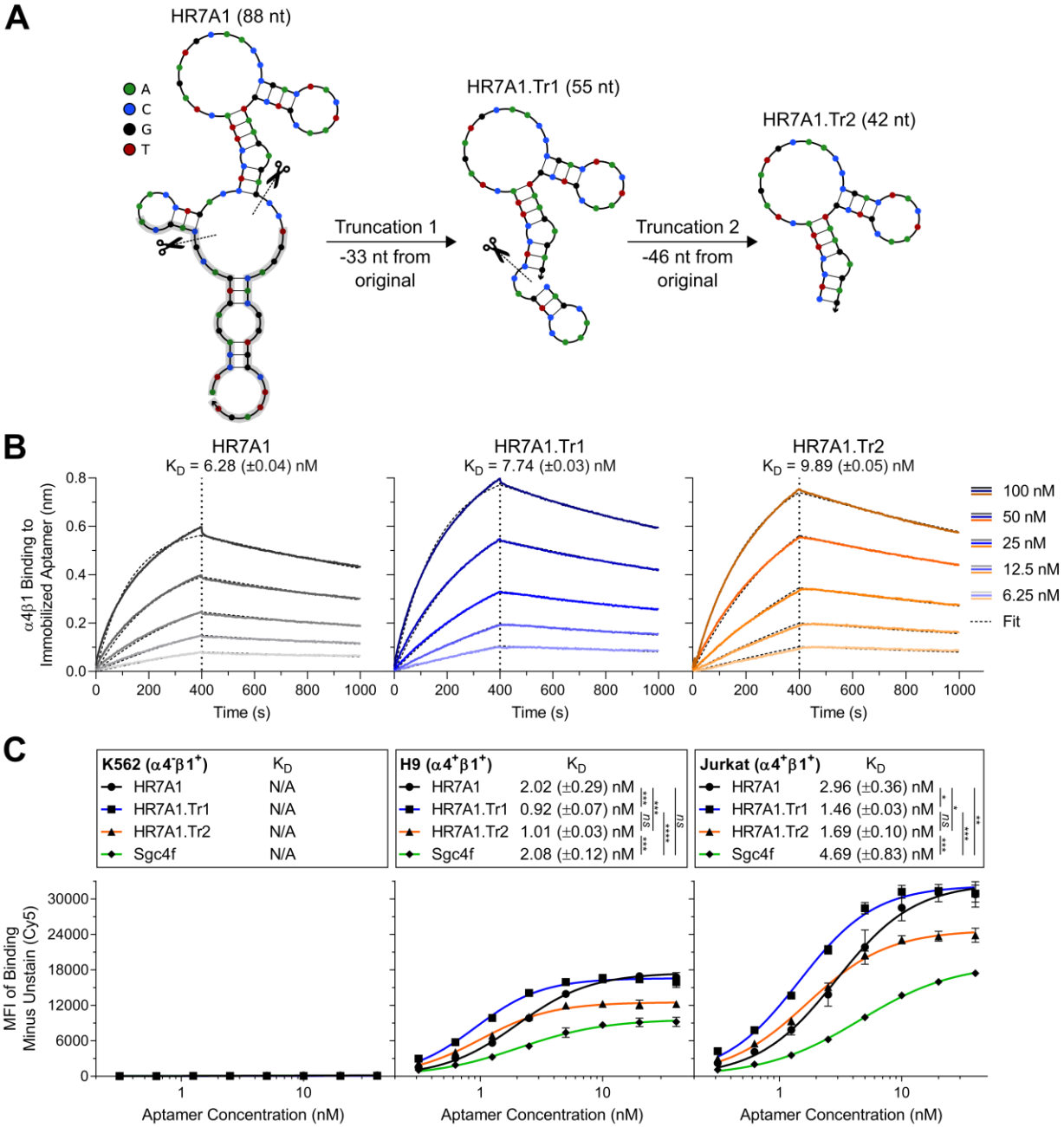

Figure 4.4 | HR7A1 binds α4β1 with single-digit nanomolar affinity and can be significantly truncated without loss of function. (A) Rational truncation of the HR7A1 sequence to remove stem-forming constant regions (grey), resulting in HR7A1.Tr1 and HR7A1.Tr2. MFE secondary structures for each sequence are shown, predicted using NUPACK (temperature = 4 °C; Na^+ = 137 mM; Mg^{2+} = 5.5 mM). The dashed lines indicate the sites of truncation. (B) Association and dissociation kinetics of serially diluted α4β1 binding to

biotinylated HR7A1, HR7A1.Tr1, and HR7A1.Tr2 aptamers immobilized on streptavidin biosensors by BLI. The association phase is illustrated from 0-400 s, and the dissociation phase is illustrated from 400-1000 s (separated by the vertical dotted line). K_D values were calculated by performing a global fit of the multi-concentration kinetic data to a 1:1 binding model. K_D values represent mean ± SD; n = 5 individual concentrations of protein. (C) Flow cytometry binding curves of Cy5-labeled HR7A1, HR7A1.Tr1, HR7A1.Tr2, and Sgc4f to K562, H9, and Jurkat cells, as determined by MFI. The curves represent a nonlinear regression assuming one-site specific binding with Hill slope. K_D values were calculated by averaging the individual regression values of the independent experiments. Data points and error bars, and K_D values, represent mean ± SD; n = 3 independent experiments. *ns* > 0.05, **P* < 0.05, ***P* < 0.01, ****P* < 0.001, *****P* < 0.0001 (ordinary one-way ANOVA with Tukey's test). Cy5, cyanine 5.

4.2.5 Characterization of cancer-selective properties of HR7A1.Tr2

While the integrin α4β1 is overexpressed in leukemia, it is also expressed by hematopoietic stem cells (HSCs) and healthy peripheral immune cells,[48] posing a risk of on-target off-tumor toxicities if the integrin is therapeutically targeted. Accordingly, cancer targeting must be sufficiently selective to mitigate these potential side effects. To characterize the on-target off-tumor labeling with our aptamers *in vitro*, we compared the relative binding of HR7A1.Tr2 at multiple concentrations to healthy donor PBMCs and immortalized Jurkat, H9, and K562 cells. As PBMCs have lower baseline MFI values than immortalized cancer cells on flow cytometry, which can negatively skew raw binding MFIs, we evaluated aptamer binding as a fold change in MFI from each cell's baseline. HR7A1.Tr2 displayed low but specific binding to PBMCs over $\alpha4^{-}\beta1^{+}$ K562 cells (**Figure 4.5A**), binding on average 90% PBMCs at 10 nM (**Figure S4.6A, B**). Despite this, aptamer binding to Jurkat and H9 cells was statistically higher at almost all concentrations, labeling these cancer cells 2.5-4.3 times more than PBMCs depending on the concentration (**Figure 4.5B**). While further comparative screening of aptamer binding to $CD34^{+}$ hematopoietic stem cells (HSCs) and patient-derived leukemia/lymphoma samples is required, these data provide

encouraging evidence that HR7A1.Tr2 can selectively target T-lineage leukemia and lymphoma cells over healthy counterparts via α4β1 binding.

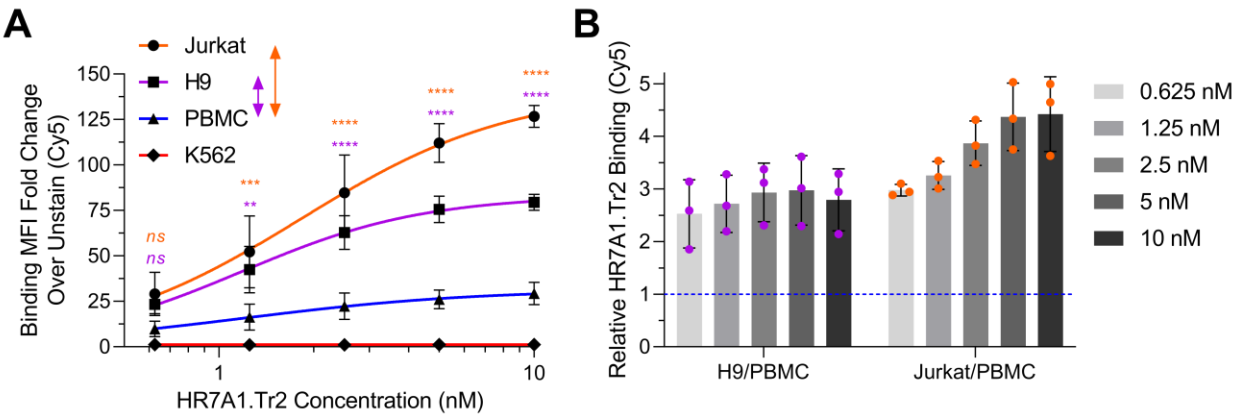

Figure 4.5 | HR7A1.Tr2 selectively binds immortalized T-leukemia and T-lymphoma cancer cells over healthy PBMCs. (A) Flow cytometry binding curves of Cy5-labeled HR7A1.Tr2 to T-leukemia Jurkat cells, T-lymphoma H9 cells, healthy donor PBMCs, and erythroleukemia K562 cells, as determined by MFI fold change over unstained controls. The curves represent a nonlinear regression assuming one-site specific binding with Hill slope. Data points and error bars represent mean ± SD; $n = 3$ independent experiments with different PBMC donors. *ns* > 0.05, $^{**}P < 0.01$, $^{***}P < 0.001$, $^{****}P < 0.0001$ (orange: significance between aptamer binding to Jurkat cells and PBMCs; purple: significance between aptamer binding to H9 cells and PBMCs; ordinary two-way ANOVA with Dunnett's test). (B) Relative binding of Cy5-labeled HR7A1.Tr2 to H9 and Jurkat cells over PBMCs at each of the concentrations tested. Values that fall above the dashed blue line represent cancer-selective binding over PBMCs. Graph bars and error bars represent mean ± SD; $n = 3$ independent experiments with different PBMC donors. Cy5, cyanine 5.

4.2.6 Modification of HR7A1.Tr2.TS for overcoming barriers to *in vivo* translation

Aptamers face many barriers for *in vivo* usage, including poor serum stability, temperature-sensitive binding, and rapid kidney clearance.[63,64] Post-SELEX modification of aptamers can address these barriers, allowing translation of aptamers from binding ligands that function solely under controlled *in vitro* conditions to robust targeting reagents that can actualize a therapeutic effect *in vivo*.[65] To this end, we evaluated the impact of serum, temperature, and renal clearance on the functionality of our aptamers and then modified our aptamers accordingly to address any

major issues that would impede future *in vivo* translation. First investigating serum stability, we found that HR7A1, HR7A1.Tr1, and HR7A1.Tr2 exhibit modest half-lives of 2.075, 1.794, and 2.686 h, respectively, in 50% normal mouse serum (**Figure S4.7A,B**). Given that the timescale of targeting *in vivo* is expected to be shorter than these half-lives, we elected to not introduce non-natural nucleotides into our aptamer sequences for enhancing serum stability.

We next tested the temperature-sensitive binding of HR7A1.Tr2, as it is close to the minimal binding motif of HR7A1 and it slightly outperformed HR7A1 and HR7A1.Tr1 in the previous serum stability assessment. To mimic an *in vivo* setting where the aptamer would circulate at physiological temperature for a period before encountering target cells, we pre-equilibrated HR7A1.Tr2 at 4, 20 and 37 °C before performing cell binding at these respective temperatures. Strikingly, HR7A1.Tr2 retained only 39% and 9% of its 4 °C binding at 20 and 37 °C, respectively, identifying a major issue for *in vivo* translation (**Figure S4.8A**). We speculate that this loss of binding is due to the predicted denaturation of the aptamer structure as temperature increases (**Figure S4.8B**), which effectively lowers the equilibrium probability of correctly folded aptamer and thereby decreases aptamer affinity. In an attempt to overcome this temperature barrier, we substituted two adenine-thymine (AT) base pairs in the HR7A1.Tr2 stem region with more stable GC base pairs and also appended two more GC base pairs at the 5' and 3' end of the aptamer, resulting in the HR7A1.Tr2.S2E2 sequence that maintains it predicted MFE structure between 4 and 37 °C (**Figure S4.9A** and **Table S4.4**). Encouragingly, HR7A1.Tr2.S2E2 preserved the binding affinity of the parental HR7A1.Tr2 aptamer and even exhibited higher maximal binding (**Figure S4.9B**), suggesting that the nucleotide substitutions and additions we made to the HR7A1.Tr2 stem reversed the fluorescence quenching observed in **Figure 4.4C**. Analyzing the sensitivity of HR7A1.Tr2.S2E2 binding to increasing temperature, we observed a small 14.7% and

7.0% improvement in normalized binding at 20 and 37 °C, respectively, over the parental HR7A1.Tr2 aptamer (**Figure S4.9C**). While these results are promising, there is ample room for further improvement in aptamer binding at 37 °C. Cryogenic electron microscopy (cryo-EM) of the HR7A1-α4β1 complex in the future will be imperative to realizing this goal, as it will inform us which nucleotides directly participate in aptamer binding and structure formation.

Lastly, to estimate the circulation half-life of our aptamers, we injected 1 nmol of a 50-nt Cy5-labeled scrambled aptamer into NOD scid mice and monitored the aptamer plasma concentration over 60 min. The scramble aptamer cleared rapidly from the blood, displaying a circulation half-life of only 6.54 min (**Figure S4.10)**. Additionally, this calculated circulation half-life is possibly inflated, as the earliest we sampled the mice was 2 min post-injection. We detected merely 150 nM aptamer in the plasma at this time, which is 3-6 times lower than the theoretical peak concentration of 500-1000 nM assuming a 1-2 mL blood volume in a mouse. Hence, there was likely significant clearance of the aptamer from the plasma within the first two minutes after injection that our analysis does not account for.

As this fast clearance would preclude successful cancer targeting with our aptamers *in vivo*, we sought to increase the size of HR7A1.Tr2.S2E2 via polymeric display to extend its circulation time.[66–69] For the polymer itself, we synthesized 2-hydroxypropyl methacrylamide (HPMA) and 11-azido-3,6,9-trioxaundecan-1-methacrylamide (AzP3MA) monomers and then copolymerized them via reversible addition-fragmentation chain transfer (RAFT) to create the HPMA-AzP3MA polymer (**Figure 4.6A**). ^{1}H NMR confirmed successful copolymerization of the monomers (data not shown), and conversion calculations estimated a polymer molecular weight of 25 kDa with ~30 azide groups/polymer. The azide groups allow conjugation of dibenzocyclooctyne (DBCO) functionalized aptamers to the polymer via strain-promoted azide-alkyne cycloaddition (SPAAC)

(**Figure 4.6A**), a metal-free click reaction that occurs efficiently under mild aqueous conditions to form a stable triazole (Taz).[70] To optimize both the conjugation efficiency and multivalent display of the aptamer on the polymer, we performed small-scale SPAAC reactions with a fixed concentration of DBCO-labeled HR7A1.Tr2.S2E2 aptamer and varying amounts HPMA-AzP3MA polymer and assessed conjugation using a electrophoretic mobility shift assay (**Figure 4.6B**). Aptamer conjugation to the polymer unsurprisingly resulted in a major upward shift in the aptamer band on urea-PAGE (i.e., less mobile aptamer), and a laddering effect was also observed, meaning a given reaction produced a dispersity of aptamer valencies on the polymer. Importantly, varying the aptamer-to-polymer ratio in the SPAAC reactions provided flexible control over the average aptamer valency on the polymer, as indicated by the shift in the conjugate band at different ratios. Using the disappearance of the unconjugated aptamer band to interpret the conjugation efficiency, we found that a 5:1 aptamer-to-polymer ratio, which translates to a 6-fold excess of azide groups over DBCO groups, maximized aptamer conjugation. As adding any more polymer would only reduce aptamer valency, we selected this ratio to produce a large batch of aptamer-polymer conjugate for cell binding studies. For fluorescent detection of binding by secondary staining, we reacted the excess azide groups on the polymer after aptamer conjugation with a biotin-alkyne via copper-catalyzed click chemistry. Molecular weight cut-off membrane filtration was then used to remove unreacted aptamer, biotin-alkyne, and polymer, yielding the final purified conjugate, which we named HPMA-TazP3MA-HR7A1.Tr2.S2E2. To help assess binding of the conjugate and prepare for future *in vivo* targeting studies with a dual flank $\alpha4^{+}\beta1^{+}/\alpha4^{-}\beta1^{+}$ tumor model, we generated K562 ITGA4 cells that stably express the integrin α4 (**Figure S4.11A,B**). HPMA-TazP3MA-HR7A1.Tr2.S2E2 displayed robust and selective binding to K562 ITGA4 cells over parental K562 cells, suggesting that the aptamer-polymer conjugate retained the targeting

capabilities of the unconjugated aptamer (**Figure 4.6C**). Future work will take the aptamer-polymer conjugate *in vivo*, where we will assess its circulation half-life and tumor targeting ability.

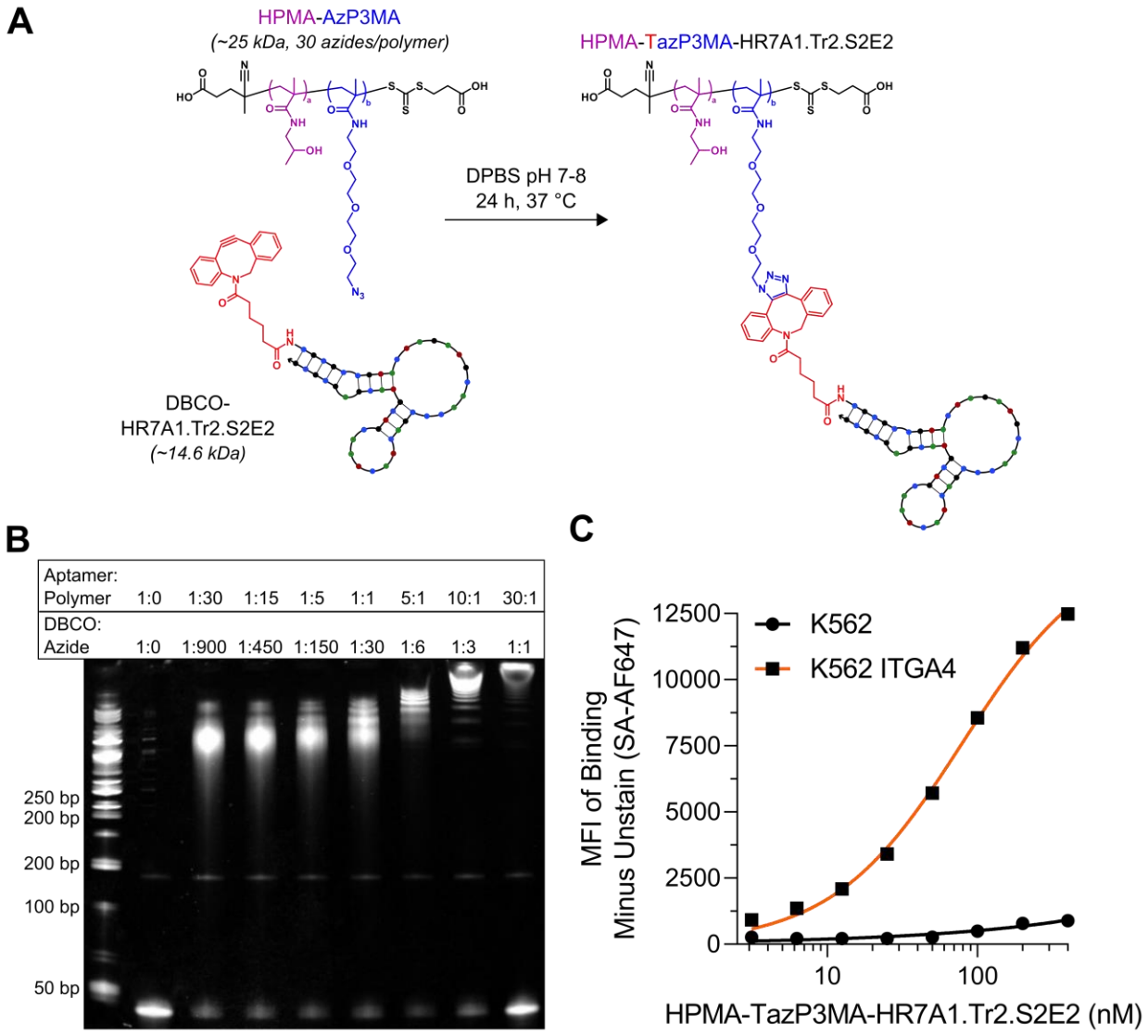

Figure 4.6 | Metal-free click chemistry enables efficient and tunable construction of aptamer-polymer conjugates for multivalent cancer targeting. (A) Schematic representation of DBCO-labeled HR7A1.Tr2.S2E2 aptamer conjugation to HPMA-AzP3MA polymer by strain-promoted azide-alkyne cycloaddition (SPAAC). HPMA and AzP3MA monomers within the polymer structure are shown in purple and blue, respectively, whereas DBCO modification on the 5' end of the aptamer is shown in red. (B) SYBR Gold-stained 15% urea-PAGE gel of aptamer conjugation to polymer at different ratios. The large upward shift in the aptamer band size signifies successful conjugation of aptamer onto the polymer via SPAAC, and further shifts in conjugate band size reflects different aptamer valencies on the polymer. Gel is representative of $n = 2$ independent experiments. (C) Flow cytometry binding curves of biotinylated HPMA-TazP3MA-HR7A1.Tr2.S2E2 conjugate to K562 and K562 ITGA4 cells, as determined by MFI.

The curves represent a nonlinear regression assuming one-site specific binding with Hill slope. Data points are representative of $n = 1$ independent experiment. DBCO, dibenzocyclooctyne; HPMA, 2-hydroxypropyl methacrylamide; AzP3MA; 11-azido-3,6,9-trioxaundecan-1-methacrylamide; SA-AF647, streptavidin Alexa Fluor 647.

4.3 DISCUSSION AND FUTURE WORK

Patients with relapsed or refractory T-cell malignancies have few, if any, viable options for treating their diseases. Treatment of newly diagnosed T-cell malignancies usually involves multiagent, escalating chemotherapy, and curative allogeneic hematopoietic stem cell transplantation is only used during successful remission reinduction following disease recurrence, which is achieved in only 30-40% cases of relapsed disease.[71] While targeted immunotherapy has taken center stage in recent years as a revolutionary cancer treatment for B-cell malignancies, these treatments have remained largely ineffective for T-cell malignancies due to challenges in finding markers selectively expressed on malignant cells over healthy T cells.[17,23] Unlike B-cell aplasia and hypogammaglobulinemia than can be tolerated with periodic prophylactic immunoglobulin replacement after immunotherapy targeting of B-cell malignancies,[72] prolonged T-cell aplasia as a result of non-selective therapeutic targeting of T-cell malignancies is a nontrivial toxicity with fatal consequences. The discovery of biomarkers and associated targeting reagents that can sufficiently distinguish T-leukemia and lymphoma cells from healthy counterparts would thus be of high value for designing effective treatments for these diseases.

Here, we report the unintentional discovery of an α4β1-specific DNA aptamer, named HR7A1, that selectively recognizes T-leukemia and lymphoma cell lines over healthy primary immune cells. The aptamer displays antibody-like affinity for α4β1-expressing malignant cells, outperforming other aptamers in its class, and retains its binding ability even after extensive

truncation. As expression of the α4β1 antigen is both associated with chemotherapy-refractory ALL and an adverse risk factor in childhood ALL at first relapse, the HR7A1 aptamer holds great promise to be used in targeted treatments of r/r leukemia and lymphoma, especially T-lineage malignancies that have high expression of this integrin.

Unexplored in this work is the binding site of HR7A1 on the α4β1 integrin. The α4β1 integrin is known to interact with several ligands, including 1) VCAM-1 expressed by activated vascular endothelium and bone marrow stromal cells,[73,74] 2) the highly abundant extracellular matrix (ECM) glycoprotein fibronectin,[75] and 3) the negatively charged ECM glycoprotein osteopontin expressed on the endosteal bone surface.[76,77] Importantly, α4β1 binding to VCAM-1 on bone marrow stromal cells has been shown to mediate drug resistance in B- and T-lineage leukemia and lymphoma cells via various signaling pathways,[49,50,78–80] and blocking this interaction can sensitize these cancer cells to chemotherapy.[52,54,81] Accordingly, the HR7A1 aptamer may block α4β1 binding to VCAM-1 and display a synergizing effect with drug payloads that would make it especially valuable for targeted anti-cancer treatment. Binding competition assays with HR7A1 and VCAM-1, either by flow cytometry with α4β1-expressing cells or BLI with recombinant α4β1 protein, will be critical to determine this. Alternatively, cryo-EM of the HR7A1-α4β1 complex could indirectly show if HR7A1 clashes with the predicted binding site of VCAM-1 on this integrin.[82]

Also untested in this study is the species cross-reactivity of HR7A1. The human integrins α4 and β1 share 85.3% and 92.5% amino acid identity in their extracellular domains with their mouse counterparts, respectively, which is higher than the median amino acid identity of 78.5% between human-mouse orthologues.[83] A human-mouse cross-reactive anti-α4 antibody has been previously reported,[84] suggesting that HR7A1 could potentially interact with mouse α4β1. Binding studies to

recombinant mouse α4β1 by BLI or to $\alpha4\beta1^+$ mouse B16F10 melanoma cells by flow cytometry will be able to ascertain the species cross-reactivity of HR7A1.[85]

Outside of cancer, α4β1 targeting has potential implications for the treatment and diagnosis of other disorders. Natalizumab is an integrin α4-specific antibody approved by the FDA for the treatment of multiple sclerosis and Crohn's disease.[86–88] Natalizumab binds both α4β1 and α4β7, antagonizing their interaction with their respective adhesion molecules VCAM-1 and MAdCAM-1 to block lymphocyte migration to the central nervous system (CNS) and gastrointestinal tract, respectively.[58,82] While HR7A1 lacks binding to α4β7 and thus holds little promise for treating Crohn's disease, it may inhibit α4β1-dependent transmigration of circulating immune cells across the vascular endothelium into the CNS for the treatment of multiple sclerosis. Like before, binding competition assays with HR7A1 and VCAM-1 or Natalizumab will be important to gauge the potential of HR7A1 for this application. Measuring the impact of HR7A1 on leukocyte transmigratory capacity in an *in vitro* blood-brain barrier assay could also determine the feasibility of this approach.[89] Besides autoimmune disorders, α4β1 has been shown to play an important role in sickle cell disease, mediating the adhesion of reticulocytes to inflamed endothelium that drive painful vaso-occlusive episodes (VOEs).[90] Accordingly, HR7A1 could be used in positron emission tomography (PET) imaging of VOEs or as an anti-adhesive therapy in sickle cell disease if proven to antagonize VCAM-1 binding to α4β1.[91,92]

For prospective *ex vivo* usage of HR7A1, our lab has previously developed traceless aptamer-based isolation strategies for cell therapy manufacturing.[37,93] In these approaches, aptamers attached to solid supports (e.g., magnetic beads, chromatography resin) are used to positively enrich specific cells, and complementary reversal agents are used to recover label-free cells for downstream processing. While HR7A1 does not target a specific immune cell type, it broadly

binds to bulk PBMCs, which could have utility for cell sorting. Commonly, the isolation of PBMCs from whole blood or other processed blood products involves density-gradient centrifugation, which is laborious and time-consuming. An approach that quickly isolates label-free PBMCs with few processing steps would thus greatly benefit research and clinical teams that use these cells for various applications. Accordingly, HR7A1 could prove useful in magnetic activated cell sorting (MACS) or affinity chromatography strategies with a complementary reversal agent to isolate label-free PBMCs from whole blood at low cost with high throughput. However, the effect of plasma and anticoagulants (e.g., EDTA) on aptamer binding would need to be evaluated, and a centrifugation wash step prior to aptamer-mediated cell sorting to remove plasma, platelets, and the anticoagulant may be required.

We recognize that HR7A1 and its truncated variants face many barriers for *in vivo* usage. Notably, HR7A1.Tr2 loses most of its binding ability at physiological temperature, and similar sized aptamers are eliminated rapidly from circulation. To address the issue of temperature, we attempted to stabilize HR7A1.Tr2 by increasing the GC content of a predicted stem structure within the aptamer sequence. However, we only observed a small improvement in 37 °C binding with these changes, necessitating further stabilization of the aptamer. Rather than relying on error-prone software prediction of aptamer folding to guide additional changes to the HR7A1.Tr2 sequence and risk ablating aptamer binding, we plan to definitively determine the structure of HR7A1.Tr2 bound to α4β1 by cryo-EM. Our collaborators previously used this technique to create a *de novo* model of our tJBA8.1 aptamer bound to TfR1, allowing us to identify nucleotides that contribute directly to aptamer binding and structure.[39] We will use similar findings to accurately distinguish which nucleotides in HR7A1.Tr2 are amenable to stabilizing substitutions. As for addressing the issue of short circulation time, we conjugated our aptamer to a polymer to increase

its size above the threshold for renal filtration. Unlike PEGylation, which can cause life-threatening allergic reactions in patients with pre-existing anti-PEG antibodies,[94] polymer conjugation is generally considered non-immunogenic and enables multivalent display of aptamer.[66,95,96] We demonstrate efficient and high-valency display of our aptamer on polymer that retain binding to α4β1-expressing cells *in vitro*. Future work will explore the circulation half-life of our aptamer-polymer conjugate and assess its stability in serum, since other groups have reported improved nuclease resistance of aptamers conjugated on polymers due to a shielding effect.[68] Assuming we see extended circulation time with the aptamer-polymer conjugate, we will evaluate its tumor targeting capabilities in a dual flank K562/K562 ITGA4 mouse model. Ultimately, we hope to demonstrate the feasibility of using an aptamer-based biomaterial for robust and selective targeting of T-cell malignancies *in vivo*.

4.4 MATERIALS AND METHODS

4.4.1 Oligonucleotides, buffers, and aptamer folding

All oligonucleotides used were synthesized by Integrated DNA Technologies. Both the ssDNA library used in cell-SELEX and the primers used for library amplification between SELEX rounds are as previously described.[37] The individual synthesized ssDNA aptamers are listed in **Table S4.4**. Wash buffer was prepared from DPBS with calcium and magnesium (Corning) supplemented with 4.5 g/L glucose and 5 mM $MgCl_2$, as previously described.[97] Binding buffer for flow cytometry studies was prepared from wash buffer that was further supplemented with 1% BSA (w/v) and 0.1 mg/mL yeast tRNA (Invitrogen). Before binding, aptamers were folded by preparing a 1 μM stock in wash buffer and heating at 95 °C for 5 min followed by snap-cooling on ice.

4.4.2 Antibodies and flow cytometry

The following dyes and antibodies were used for cell staining: Zombie Violet (1:500 in 100 μL per 10^6 cells, BioLegend), APC anti-human CD276 (1:200, 351006, BioLegend), FITC anti-human CD49d (1:50, 304315, BioLegend), PE anti-human CD29 (1:50, 303004, BioLegend), and Alexa Fluor 647 streptavidin (1:500, BioLegend). Stained cells were assessed on an Attune NxT Flow Cytometer (Life Technologies), and data was analyzed and plotted in FlowJo V10 software (Becton Dickinson). The median fluorescence intensity of singlet live cell events was used as a measurement of aptamer binding. Binding curves, K_D values, and graphs were generated using GraphPad Prism 9 software (San Diego, CA).

4.4.3 Cloning of 4IgB7H3 constructs and lentivirus production

The DNA sequence for 4IgB7H3 (UniProtKB: Q5ZPR3-1) was synthesized and cloned into epHIV7.2 lentiviral vectors by GeneArt using NheI and NotI restriction enzymes. 5-alpha chemically competent *E. coli* (NEB) were transformed with the resulting plasmid and selected by kanamycin. Correct cloning was verified by sangar sequencing (GENEWIZ) of miniprep DNA (QIAGEN) before transfection-grade plasmid DNA was prepared by maxiprep (MACHEREY-NAGEL).

HEK293T cells were purchased from ATCC and used before passage 20. HEK 293T cells were seeded 24 h prior to transfection in eight 10 cm plates at 3×10^6 cells per plate in 8 mL virus prep medium comprised of DMEM with high-glucose, L-glutamine, and sodium pyruvate (Gibco) supplemented with 10% heat-inactivated FBS (VWR). The next day, each plate was transfected with 40 μL Lipofectamine 2000 reagent (Life Technologies) mixed with 1000 μL Opti-MEM containing transgene lentiviral vector (15 μg), pCMV-Rev2 (1 μg), pCHGP-2 (10 μg), and pCMV-G (2 μg). After 24 h, the top media was aspirated and replaced with virus prep medium further

supplemented with sodium butyrate (Gibco). At 48 h after the media change, virus-containing supernatant was harvested (80 mL total for eight 10 cm plates) and cell debris was removed by centrifugation and 0.45 μm filtration. Virus was pelleted by ultracentrifugation at 24,500 rpm for 94 min at 4 °C in a Beckman Coulter Optima L90K Ultracentrifuge using a SW 28 rotor and 38.5 mL open-top tubes (Beckman Coulter). Virus pellets were then resuspended in a combined volume of 300 μL serum-free DMEM and stored at -80 °C until further use.

4.4.4 Cell line culture and T-cell activation

H9, Jurkat (clone E6-1), Raji, and K562 cell lines used for SELEX and binding studies were purchased from ATCC. The H9 4IgB7H3 cell line was generated by transducing 10^5 H9 cells with 3 μL lentivirus encoding 4IgB7H3 with 40 μg/mL protamine sulfate (AAP Pharmaceuticals). Transduced cells were later purified by magnetic activated cell sorting (MACS) using PE anti-human B7H3 antibody (1 μL per 10^6 cells, 351004, BioLegend) and Anti-PE Microbeads (Miltenyi) according to the manufacturer's instructions. All the above cell lines were cultured in complete RPMI comprised of RPMI 1640 medium with L-glutamine (Corning) supplemented with 10% FBS. Human peripheral blood mononuclear cells (PBMCs) were isolated from TRIMA LRS chambers (Bloodworks Northwest) using Ficoll-Paque density gradient centrifugation (GE).

4.4.5 Cell-SELEX

The SELEX procedure was adapted from reported methods.[41,97] Conditions used in the individual rounds of SELEX are summarized in **Table S4.1**. Briefly, in round 1, 10 nmol of the initial ssDNA library (10^{15}-10^{16} individual sequences) was incubated with 10^6 H9 4IgB7H3 cells for 1 h at 4 °C in 700 μL wash buffer containing 0.1% BSA and 0.1 mg/mL tRNA. After washing, bound aptamers were extracted by heating cells at 95 °C for 10 min in 500 μL molecular-grade H_2O

(Corning) and cell debris was removed by centrifugation. Extracted aptamers were amplified with FAM-labeled forward and biotin-labeled reverse primers by PCR using Phusion High-Fidelity DNA Polymerase (NEB) with the following conditions: a 30 s hot start at 98 °C, 10-18 cycles of 10 s at 98 °C, 30 s at 56 °C, and 30 s at 72 °C, and lastly a 60 s final extension at 72 °C. The resulting double-stranded DNA (dsDNA) product was separated from the PCR solution using High Capacity Streptavidin Agarose Resin (Thermo Fisher), and FAM-labeled ssDNA was eluted from the resin with 0.2 M NaOH. The ssDNA was de-salted using a NAP-5 column (GE Healthcare) and dried on a Savant ISS110 SpeedVac Concentrator (Thermo Fisher) for the next round of SELEX.

For subsequent rounds of SELEX, the ssDNA concentration, H9 4IgB7H3 cell numbers, and incubation time were slowly decreased during positive selection whereas the concentration of BSA was increased or swapped with FBS. At the same time, additional anionic competitors were introduced for positive selection in later rounds such as salmon sperm DNA (Invitrogen) and poly(I:C) (InvivoGen), and the number of washes after binding was gradually extended. After positive selection in rounds 2-6, bound aptamers were extracted by heating positive selection cells at 95 °C for 10 min in 400 μL wash buffer with 0.1% BSA and 0.1 mg/mL tRNA, and cell debris was removed by centrifugation. The extracted aptamers were placed on ice for re-folding before undergoing negative selection with H9 parental cells, whereafter unbound ssDNA was PCR amplified to generate ssDNA pools for use in the next round of SELEX. Starting in round 4, successive negative selections were performed and gradually increased to maximize removal of non-selective binders. In round 7, instead of negative selection, antibody competition was conducted after positive selection by incubating aptamer bound H9 4IgB7H3 cells with 100 nM

APC anti-human CD276 (~1:13 dilution, BioLegend). The eluted ssDNA from this round was used for NGS.

4.4.6 NGS and analysis

The ssDNA pool from round 7 of cell-SELEX was PCR amplified with the barcoded primers listed in **Table S4.2**, purified to remove PCR reagents (Qiagen), and then sequenced using the MiSeq Reagent Kit v2 (300 cycles) and MiSeq System (Illumina) according to the manufacturer's instructions. Exported FASTA files were analyzed with FASTAptamer v1.0.3;[43] specifically, FASTAptamer-Count was used to determine the rank and reads per million for each sequence identified (**Table S4.3**). For the top 50 sequences in round 7, phylogenetic trees were generated with FigTree v1.4.4 (http://tree.bio.ed.ac.uk/software/figtree/) and motifs were discovered with MEME Suite v5.3.0.[45] Minimum free energy structures of select aptamer sequences were predicted with the NUPACK web application.[46]

4.4.7 Aptamer binding studies

Cells (2×10^5) were pre-stained with Zombie Violet in DPBS for 15 min at room temperature, washed once with wash buffer supplemented with 1% BSA, and incubated with 100 µL folded FAM-labeled ssDNA pools or FAM/Cy5-labeled individual aptamers for 30 min at 4 °C in binding buffer at the indicated concentrations. For antibody co-staining, antibodies were added to the incubation with aptamers. For competitive binding studies, unique aptamers with different fluorescent labels were co-incubated on cells at different concentrations. Cells were then washed twice with 200 µL wash buffer 1% BSA to remove excess staining reagent. If biotinylated aptamers were used for primary staining, cells received a secondary stain with 100 µL fluorescently labeled streptavidin for 20 min at 4 °C and then washed twice as before. Lastly, stained cells were lightly

fixed in 200 μL wash buffer 1% BSA with 0.1-0.2% PFA before immediate analysis via flow cytometry as described above. If required, unstained and single-stained cell controls were used for compensation.

4.4.8 Aptamer pull-down assay for receptor identification

The aptamer pull-down assay from cell membrane extracts was adapted from a previously published method.[36] For each group (control, HR7A1, and tJBA8.1), 7.5-9×10^7 cells (Jurkat or H9 cells) were washed three times with DPBS and lysed for 30 min at 4 °C with end-over-end mixing in ~3.3 mL hypotonic buffer comprised of 10 mM Tris-HCl pH 7.5 supplemented with EDTA-free cOmplete Protease Inhibitor Cocktail (Roche) and 1mM PMSF. The resulting cell membranes were pelleted at 16,000 xg for 15 min at 4 °C and washed three times with 3.3 mL of the same hypotonic buffer to remove released intracellular proteins. The membrane pellet was then resuspended in 1mL wash buffer containing 1% Triton X-100, protease inhibitors, and 1mM PMSF to extract and solubilize membrane proteins. The extraction was conducted for 30 min at 4 °C with end-over-end mixing followed by a brief 5-min sonication in an ice water bath. Afterwards, the samples were centrifuged as before and the supernatant containing the extracted proteins was collected and stored at -80 °C until further use.

For pre-clearing, the extracts (1 mL) were thawed and spiked with 100nM of biotinylated random aptamer from the naïve library (RN) and 0.1 mg/mL yeast tRNA. After incubating for 30 min at 4 °C with end-over-end mixing, 200 μL (2 mg) MyOne Streptavidin C1 Dynabeads (Thermo Fisher) were added to the extracts and incubated for another 15 min at 4 °C to remove protein-RN complexes via magnet. For HR7A1 and tJBA8.1 groups, pre-cleared extracts were then spiked with 100 nM of appropriate biotinylated aptamer and 0.1 mg/mL salmon sperm DNA. After

incubating for 30 min at 4 °C with end-over-end mixing, 150 µL (1.5 mg) Streptavidin Dynabeads were added to the binding reaction and incubated for another 15 min at 4 °C to capture aptamer-bound proteins. For the control group, 150 µL (1.5 mg) Streptavidin Dynabeads were instead saturated with 50 nmol biotin and added to the pre-cleared extract for a 30-min incubation at 4 °C. Afterwards, the beads for all groups were washed 5 times for 5 min each with 1 mL cold wash buffer containing 0.01% Triton X-100 to remove unbound proteins. The captured proteins were eluted by heating the beads for 15 min a 47 °C in 50 µL Laemmli Sample Buffer (Bio-Rad) containing 2.5% 2-mercaptoethanol (Bio-Rad), 4.6M urea (Fisher), and 0.01% Triton X-100 (Sigma). Eluted proteins were stored at -80 °C unless used immediately.

Eluted proteins (25 µL) were loaded onto a Novex WedgeWell 8% Tris-Glycine gel (Invitrogen) and separated by SDS-PAGE. The gel was stained with a Colloidal Blue Staining Kit (Invitrogen) according to the manufacturer's instructions and imaged on a Gel Doc EZ system (Bio-Rad). Enriched protein bands were excised and submitted to the Proteomics division at the Fred Hutchinson Cancer Research Center for processing by tandem mass spectrometry on an OrbiTrap Fusion (Thermo Fisher). The data were searched using Proteome Discoverer 2.2 against a Uniprot Human database that included common contaminants. Results were filtered for high confidence 1% false discovery rate at the peptide level.

4.4.9 siRNA knockdown

Some 2×10^6 Jurkat cells in logarithmic growth phase were nucleofected with 100 pmol NS or CD29 siRNA listed in **Table S4.5** using the Human T cell Nucleofector Kit (Lonza) with Program X-001 following the manufacturer's instructions. The cells were analyzed 42 h later for HR7A1 binding and anti-CD29 and anti-CD49d antibody staining by flow cytometry. A CD8.A3 negative

aptamer control was also included to subtract off any non-specific aptamer binding to the nucleofected cells before data normalization.

4.4.11 Bio-layer interferometry

BLI studies were performed on an Octet RED96 instrument (Sartorius) using streptavidin biosensors (Sartorius) as previously described.[39] Briefly, wash buffer supplemented with 1% BSA, 0.1 mg/mL yeast tRNA, 0.1 mg/mL salmon sperm DNA, and 0.01% Tween-20 (Sigma) was used as the sample buffer for all steps. All steps were performed at 25 °C with sample agitation at 1000 r.p.m. Biosensors were allowed to equilibrate in buffer for at least 10 min before loading. For sensor loading, 50 nM biotinylated aptamers were loaded until a 0.5 nm threshold before performing rinse and baseline steps in buffer alone for 100 s each. Afterwards, aptamer-loaded sensors were associated with His-tagged human α4β1 (IT1-H52W1, ACROBiosystems) or His-tagged human α4β7 (IT7-H52W4, ACROBiosystems) at concentrations and times indicated in the figures and captions. Lastly, sensors were transferred to wells containing buffer alone for dissociation. Data analysis was performed with the Octet Data Analysis 9.0 software (Sartorius). Association and dissociation curves were normalized to sensors that received capture ligand alone. Kinetic constants were calculated for datasets with several analyte concentrations by conducting a global fit of the association and dissociation curves to a 1:1 ligand binding model. The quality of each fit was evaluated using R^2 and χ^2 values, which are listed in **Table S4.6** for the appropriate datasets along with the calculated kinetic constants.

4.4.12 Aptamer serum stability

Normal mouse serum for serum stability studies was prepared in-house. Briefly, whole blood was terminally drawn from mice and allowed to clot for 30 min in BD Microtainer serum-separating

tubes (Becton Dickinson). After centrifuging the tubes per the manufacturer's instructions, serum was aliquoted into single-use tubes and stored at -20 °C until needed.

For qualitative assessment of aptamer serum stability, we adapted a previously published protocol.[98] Briefly, 6 µM of folded FAM-labeled aptamer in wash buffer was mixed 1:1 with normal mouse serum (3 µM aptamer in 50% serum final) and incubated for up to 8 h at 37 °C. At 0, 1, 2, 4, 6, and 8 h during the incubation, 10 µl aptamer-serum mixture was removed and frozen at -80 °C to halt nuclease activity until all timepoints were harvested. After the incubation, timepoint samples were then thawed and denatured in 1X loading dye (NEB) containing ~4 M urea for 3 min at 70 °C. Approximately 12.5 pmol denatured sample was then loaded onto a Novex 15% TBE-urea gel (Invitrogen) and separate by urea-PAGE. FAM-labeled aptamer bands were imaged on a Xenogen IVIS Spectrum (PerkinElmer) with 465 nm excitation and 520 nm emission.

For quantitative assessment of functional aptamer serum stability, 2 µM of folded Cy5-labeled aptamer in wash buffer was mixed 1:1 with normal mouse serum (1 µM aptamer in 50% serum final) and incubated for 4, 3, 2, 1.5, 1, 0.5, 0.25 and 0 h at 37 °C (staggered timepoints). After the incubation, timepoint samples were placed on ice and diluted to 10 nM in binding buffer for staining cells by flow cytometry as described above. Aptamer binding for each timepoint sample was normalized to the 0-h control to assess serum-mediated loss of aptamer functionality.

4.4.13 Aptamer temperature-sensitive binding

Aptamer binding was performed as described above, except aliquots of 2X (10 nM) folded FAM-labeled aptamer in binding buffer were pre-equilibrated for 30 min at 4, 20, and 37 °C before mixing 1:1 with Jurkat and K562 cells that were similarly pre-equilibrated at the respective temperatures in binding buffer (5 nM aptamer final). The aptamer-cell binding reactions were

carried out at the appropriate temperatures for a reduced 20 min incubation to limit non-specific uptake of aptamers in the 37 °C group. Non-specific aptamer binding to the K562 cells was subtracted from the specific binding to the Jurkat cells at each temperature before normalizing data to the 4 °C binding controls to assess temperature-mediated loss of aptamer functionality.

4.4.14 Aptamer plasma circulation half-life

All animal experiments were performed in compliance with the University of Washington IACUC guidelines. Cy5-labeled scrambled aptamer (1 nmol) in wash buffer was retro-orbitally injected into three female NOD scid mice (8-12 weeks old). Blood (>10 μL) was drawn at 2, 20, and 60 min post-injection and collected into pre-weighed tubes with 50 μL DPBS 5 mM EDTA. After blood collection, the tubes were re-weighed to determine the volume of blood collected. The diluted blood was then centrifuged at 1000 xg for 10 min at 4 °C, and 50 μL of the supernatant was measured for Cy5 fluorescence (Ex: 633/9 nm; Em: 670/20 nm) using an Infinite 200 PRO plate reader (Tecan). The measured fluorescence values at each timepoint were compared to a standard curve of Cy5-labeled scrambled aptamer and normalized by their respective dilution factors to estimate the aptamer concentration in undiluted plasma.

4.4.15 N-(2-Hydroxypropyl) methacrylamide (HPMA) synthesis

Amino-2-propanol (Sigma, 76 mL, 0.96 mol) was dissolved in 1 L of dichloromethane (DCM, Sigma) and chilled over an ice bath. Methacryloyl chloride (Sigma, 46mL, 0.47mol) was then added dropwise, and the reaction was kept over ice for 30 min after the last drop of methacryloyl chloride was added. The reaction was covered with a glass bung and allowed to warm to room temperature overnight. The next day, an oil/salt solution was removed and discarded from the DCM by filtering the solution through cotton. The DCM was then washed by brine, dried over

sodium sulfate, and concentrated at 25 °C by rotary evaporation. Care was taken to not over-concentrate the DCM, which would lead to the HPMA precipitating out. The mixture was then purified by repeated precipitation and recrystallization in acetone (Sigma), with acetone being evaporated off in between. A fine, clear, white crystal (20 g) was obtained and characterized by ^{1}H NMR (data not shown).

4.4.16 11-azido-3,6,9-trioxaundecan-1-methacrylamide (AzP3MA) synthesis

To a 25 mL round-bottom flask with a stir bar, 800 mg of 11-azido-3,6,9-trioxaundecan-1-amine (Tokyo Chemical Industries, 1 eq), 409 mg of triethylamine (Sigma, 1.1 eq) and 15 mL of anhydrous DCM was added. An addition funnel was installed and sealed with a septum, and the flask was immersed into an ice bath. The setup was purged with dry argon for 15 min. Afterwards, 422 mg of methacryloyl chloride (1.1 eq) was added into the addition funnel alongside 1 mL of anhydrous DCM via syringe. The contents of the addition funnel were slowly dripped into the reaction flask under vigorous stirring, and the reaction mixture was left overnight. The reaction was quenched by adding 2 mL of methanol and allowing to bubble until subsided. The mixture was diluted to 50 mL with DCM, extracted twice with saturated sodium carbonate and once with brine, and concentrated with a rotary evaporator to obtain a crude yellow oil. The crude mixture was purified with column chromatography (5% v/v methanol:ethyl acetate) and characterized by ^{1}H NMR (vinyl 5.5-6.0 ppm, trioxaundecan 3.5-3.7 ppm) (data not shown).

4.4.17 HPMA-AzP3MA synthesis and characterization

For polymer synthesis, briefly, 120 mg of AzP3MA (33 eq) was combined with 229.2 mg of HPMA (127 eq) and 1 mL of 0.1 M pH 5.0 sodium acetate buffer in a 5 mL pear-shaped flask. Thereafter, 773 uL and 163 uL of 5 mg/mL solutions of 4-((((2-

carboxyethyl)thio)carbonothioyl)thio)-4-cyanopentanoic acid (CCC, Boron Molecular, 1 eq) and 2,2'-Azobis[2-(2-imidazolin-2-yl)propane]dihydrochloride (VA-044, Wako Chemicals, 0.1 eq), respectively, in 0.1M pH 5.0 sodium acetate buffer were added. The solution was purged with argon for 20 min and allowed to react at 50 °C for 20 h. The polymer was purified via dialysis (10k MWCO RC membrane) in nanopure water for 3 d, with a water change every day, and finally lyophilized.

The polymer molar mass was estimated with conversion ^{1}H NMR. Briefly, aliquots of the polymerization reaction at times 0 and 20 h were resuspended into D2O and analyzed. Overall conversion was determined by quantifying the depletion of the monomeric vinyl peaks (5.5-6.0 ppm) against the solvent peak. The estimation is further refined by NMR of the finished polymer in D2O, taking the ratio of the HPMA peak (4 ppm) and the AzP3MA peak (3.5-3.7 ppm) to obtain the HPMA:AzP3MA ratio. The HPMA and AzP3MA conversions are then individually determined based on overall conversion and the HPMA:AzP3MA ratio.

4.4.18 HPMA-TazP3MA-HR7A1.Tr2.S2E2 synthesis, purification and characterization

For small-scale optimization of aptamer conjugation to polymer, 50 μM DBCO-labeled HR7A1.Tr2.S2E2 was reacted with varying amounts of HPMA-AzP3MA ranging from 1.667 μM (30:1 aptamer-to-polymer ratio) to 1.5 mM (1:30 aptamer-to-polymer ratio) in 5 μL DPBS with calcium and magnesium for 24 h at 37 °C on a thermal cycler (Bio-Rad). Afterwards, 500 ng 50 bp DNA ladder (Thermo Scientific), 100 ng unconjugated aptamer, and 100 ng aptamer-polymer conjugates were denatured in 1X loading dye containing ~4 M urea for 3 min at 70 °C and separated on a Novex 15% TBE-urea gel by urea-PAGE. The gel was stained with SYBR Gold

(1:10000, Invitrogen) in TBE buffer (Thermo Scientific) for 30 min at room temperature and imaged on a Xenogen IVIS Spectrum (PerkinElmer) with 500 nm excitation and 540 nm emission.

For large-scale conjugation of aptamer to polymer, 100 μM DBCO-labeled HR7A1.Tr2.S2E2 was reacted with 20 μM HPMA-AzP3MA (5:1 aptamer-to-polymer ratio) in 30 μL DPBS with calcium and magnesium for 24 h at 37 °C on a thermal cycler. The next day, 200 μM biotin-alkyne (10:1 biotin-to-polymer ratio), 250 μM copper(II) sulfate, 500 μM PMDETA, and 5 mM sodium ascorbate were added to the reaction mixture for biotinylation of the polymer. The reaction was then purged with nitrogen and allowed to incubate for another 24 h at 37 °C. The biotinylated HPMA-TazP3MA-HR7A1.Tr2.S2E2 conjugate was purified and exchanged into wash buffer using a Amicon Ultra-0.5 mL centrifugal filter unit (EMD Millipore) with a nominal molecular weight limit (NMWL) of 30 kDa. The concentration of aptamer and biotin in the purified conjugate solution was determined using a NanoDrop UV-Vis spectrophotometer (Thermo Fisher) and a QuantTag Biotin Quantification Kit (Vector Labs), respectively. Cell binding studies with the aptamer-polymer conjugate were carried out as described above based on the measured aptamer concentration.

4.4.19 K562 ITGA4 cell line generation

pcDNA3.1-alpha4 wt was a gift from Chinten James Lim (Addgene plasmid # 80016; http://n2t.net/addgene:80016; RRID:Addgene_80016).[99] The pcDNA3.1-alpha4 wt plasmid and epHIV7.2 lentiviral vector were digested with NheI and NotI restriction enzymes (NEB) to create an insert DNA sequence encoding the human integrin α4 (ITGA4) and an empty lentiviral vector expression cassette, respectively, that were subsequently gel purified (QIAGEN) and ligated with T4 DNA ligase (NEB). DH10B chemically competent *E. coli* (Invitrogen) were transformed with

the ligated product and kanamycin-selected colonies were screened by PCR for the correct insert length. Correct cloning was verified by sangar sequencing of miniprep DNA before transfection-grade plasmid DNA was prepared by maxiprep.

HEK 293T cells were seeded 24 h prior to transfection in ten 10-cm plates at 3×10^6 cells per plate in 10 mL DMEM with high-glucose, L-glutamine, and sodium pyruvate supplemented with 10% gamma-irradiated FBS (Life Tech) and 1X penicillin-streptomycin (Life Tech). The next day, half of the plating media (5 mL) was removed from the cells and each plate was transfected with 15 µL BioT transfection reagent (Bioland Scientific) mixed with 150 µL serum-free DMEM containing pMDL-RRE (2.9 µg), pRSV-Rev (1.1 µg), pVSV-G (1.6 µg), and ITGA4 lentiviral vectors (4.5 µg). After 24 h, 5 mL complete DMEM media was added to the plates to make the supernatant 10 mL total and virus-containing supernatant was collected and replaced with 5 mL fresh media at 48 and 72 h post-transfection. At 96 h post-transfection, the last of the virus-containing supernatant was collected (200 mL total for ten 10-cm plates) and cell debris was removed by 0.22 µm filtration. Virus was pelleted by ultracentrifugation at 18,500 rpm (58,486 xg) for 2 h at 4 °C in a Beckman Coulter Optima L-100XP Ultracentrifuge using a SW 32 Ti rotor and six 38.5 mL open-top tubes (Beckman Coulter). Pellets were resuspended and combined in 12 mL HBSS before being pelleted again by ultracentrifugation at 19,500 rpm (65,2020 xg) for 2 h at 4 °C using a SW 41 Ti rotor and a single 13.2 mL open-top tube (Beckman Coulter). The resulting viral pellet was resuspended in 50 µL HBSS and used immediately for transduction.

K562 cells (5×10^5) were transduced with 50 µL ITGA4 lentivirus in 0.5 mL complete RPMI with 5 µg/mL polybrene in a 24-well plate. After 24 h, 1.5 mL complete RPMI was added to the cells to dilute the polybrene. The cells were then allowed to expand for an additional 8 d with regular passaging to reach sufficient cell numbers needed for purification of transduced cells by aptamer-

based MACS. Briefly, transduced cells (60×10^6) were stained with 2.5 nM biotinylated HR7A1.Tr2 aptamer in binding buffer at 2×10^6 cells per mL for 30 min at 4 °C. Aptamer-stained cells were washed once with wash buffer containing 1% BSA to remove excess aptamer and then labeled with Anti-Biotin Microbeads (Miltenyi, 20 μL per 10^7 cells) in wash buffer 1% BSA at 10^8 cells per mL for 15 min at 4 °C. After bead labeling, cells were washed once with wash buffer 1% BSA to remove unbound beads, resuspended in 1 mL wash buffer 1% BSA, and applied over two pre-rinsed LS Columns (Miltenyi) in parallel mounted on a QuadroMACS separator (Miltenyi). Each column was then washed three times with 3 mL wash buffer 1% BSA to remove unlabeled cells. Captured cells were recovered by removing the columns from the magnet and flushing them with 5 mL wash buffer 1% BSA. The purified cells were lastly cultured overnight in complete media to allow for receptor recycling before staining the next day with aptamer and antibody to confirm homogenous integrin α4 expression.

4.5 AUTHOR CONTRIBUTIONS

S.H.P. and M.C.J. conceived the idea and provide funding support. S.H.P., M.C.J., and N.K. provided experimental advice. I.I.C., N.K., M.C.J., and S.H.P. designed the project. I.I.C. conceived, performed, and interpreted the experiments. I.I.C. designed and performed the SELEX procedure. I.I.C., J.R., and S.J.S. analyzed the NGS data. I.I.C. performed the aptamer pull-down assay for receptor identification. I.I.C. and J.R. validated receptor binding. I.I.C. designed and tested aptamer truncations. J.R. performed aptamer competition studies with Sgc4f. J.R. conducted PBMC binding studies. J.R. evaluated aptamer serum stability and temperature-sensitive binding. I.I.C. designed stabilized aptamer variants. I.I.C., D.L.S., and J.R. evaluated aptamer circulation half-life. D.C.N. synthesized AzP3MA monomer and HPMA-AzP3MA polymer. I.I.C. and J.R. performed aptamer-polymer conjugation and assessed binding. D.L.S. prepared ITGA4 lentivirus

and I.I.C. generated K562 ITGA4 cells. I.I.C. prepared the figures and wrote the chapter with input from M.C.J. and S.H.P.

4.6. ACKNOWLEDGEMENTS

We are grateful to Dr. Emmeline Cheng for optimizing the aptamer pull-down procedure for receptor identification and to Trey Pichon for synthesizing the HPMA monomer. We thank Dr. Philip Gafken and Lisa Jones (Fred Hutch) for handling mass spectrometry samples. We are also grateful to all Pun and Jensen Lab members, especially Dr. Adam Johnson (Seattle Children's Research Institute), for experimental support and helpful advice. I.I.C. was supported by a National Science Foundation Graduate Research Fellowship under Grant No. DGE-1762114 and by the National Cancer Institute of the National Institutes of Health under Award No. 5T32CA080416-19 during different stages of the research reported here.

4.7 REFERENCES

(1) Siegel, R. L.; Miller, K. D.; Fuchs, H. E.; Jemal, A. Cancer Statistics, 2022. *CA: A Cancer Journal for Clinicians* **2022**, *72* (1), 7–33.

(2) Miller, K. D.; Fidler-Benaoudia, M.; Keegan, T. H.; Hipp, H. S.; Jemal, A.; Siegel, R. L. Cancer Statistics for Adolescents and Young Adults, 2020. *CA: A Cancer Journal for Clinicians* **2020**, *70*, 443–459.

(3) Hunger, S. P.; Lu, X.; Devidas, M.; Camitta, B. M.; Gaynon, P. S.; Winick, N. J.; Reaman, G. H.; Carroll, W. L. Improved Survival for Children and Adolescents With Acute Lymphoblastic Leukemia Between 1990 and 2005: A Report From the Children's Oncology Group. *Journal of Clinical Oncology* **2012**, *30* (14), 1663–1669.

(4) Burkhardt, B.; Reiter, A.; Landmann, E.; Lang, P.; Lassay, L.; Dickerhoff, R.; Lakomek, M.; Henze, G.; von Stackelberg, A. Poor Outcome for Children and Adolescents With Progressive Disease or Relapse of Lymphoblastic Lymphoma: A Report From the Berlin-Frankfurt-Muenster Group. *Journal of Clinical Oncology* **2009**, *27* (20), 3363–3369.

(5) Schrappe, M.; Hunger, S. P.; Pui, C.-H.; Saha, V.; Gaynon, P. S.; Baruchel, A.; Conter, V.; Otten, J.; Ohara, A.; Versluys, A. B.; Escherich, G.; Heyman, M.; Silverman, L. B.; Horibe, K.; Mann, G.; Camitta, B. M.; Harbott, J.; Riehm, H.; Richards, S.; Devidas, M.; Zimmermann, M. Outcomes after Induction Failure in Childhood Acute Lymphoblastic Leukemia. *New England Journal of Medicine* **2012**, *366* (15), 1371–1381.

(6) Bhojwani, D.; Pui, C.-H. Relapsed Childhood Acute Lymphoblastic Leukaemia. *The Lancet Oncology* **2013**, *14* (6), e205–e217.

(7) Sellar, R. S.; Rowntree, C.; Vora, A. J.; Furness, C. L.; Goulden, N.; Mitchell, C.; Moorman, A. v; Hough, R. Relapse in Teenage and Young Adult Patients Treated on a Paediatric Minimal Residual Disease Stratified ALL Treatment Protocol Is Associated with a Poor Outcome: Results from UKALL2003. *British Journal of Haematology* **2018**, *181* (4), 515–522.

(8) Quist-Paulsen, P.; Toft, N.; Heyman, M.; Abrahamsson, J.; Griškevičius, L.; Hallböök, H.; Jónsson, Ó. G.; Palk, K.; Vaitkeviciene, G.; Vettenranta, K.; Åsberg, A.; Frandsen, T. L.; Opdahl, S.; Marquart, H. v; Siitonen, S.; Osnes, L. T.; Hultdin, M.; Overgaard, U. M.; Wartiovaara-Kautto, U.; Schmiegelow, K. T-Cell Acute Lymphoblastic Leukemia in Patients 1–45 Years Treated with the Pediatric NOPHO ALL2008 Protocol. *Leukemia* **2020**, *34* (2), 347–357.

(9) Nguyen, K.; Devidas, M.; Cheng, S.-C.; La, M.; Raetz, E. A.; Carroll, W. L.; Winick, N. J.; Hunger, S. P.; Gaynon, P. S.; Loh, M. L.; Group, for the C. O. Factors Influencing Survival after Relapse from Acute Lymphoblastic Leukemia: A Children's Oncology Group Study. *Leukemia* **2008**, *22* (12), 2142–2150.

(10) Ko, R. H.; Ji, L.; Barnette, P.; Bostrom, B.; Hutchinson, R.; Raetz, E.; Seibel, N. L.; Twist, C. J.; Eckroth, E.; Sposto, R.; Gaynon, P. S.; Loh, M. L. Outcome of Patients Treated for Relapsed or Refractory Acute Lymphoblastic Leukemia: A Therapeutic Advances in Childhood Leukemia Consortium Study. *Journal of clinical oncology : official journal of the American Society of Clinical Oncology* **2010**, *28* (4), 648–654.

(11) Trausti Oskarsson; Stefan Söderhäll; Johan Arvidson; Erik Forestier; Scott Montgomery; Matteo Bottai; Birgitte Lausen; Niels Carlsen; Marit Hellebostad; Päivi Lähteenmäki; Ulla M. Saarinen-Pihkala; Ólafur G.Jónsson; Mats Heyman. Relapsed Childhood Acute Lymphoblastic Leukemia in the Nordic Countries: Prognostic Factors, Treatment and Outcome. *Haematologica* **2016**, *101* (1 SE-Articles), 68–76.

(12) Sun, W.; Malvar, J.; Sposto, R.; Verma, A.; Wilkes, J. J.; Dennis, R.; Heym, K.; Laetsch, T. W.; Widener, M.; Rheingold, S. R.; Oesterheld, J.; Hijiya, N.; Sulis, M. L.; Huynh, V.; Place, A. E.; Bittencourt, H.; Hutchinson, R.; Messinger, Y.; Chang, B.; Matloub, Y.; Ziegler, D. S.; Gardner, R.; Cooper, T.; Ceppi, F.; Hermiston, M.; Dalla-Pozza, L.; Schultz, K. R.; Gaynon, P.; Wayne, A. S.; Whitlock, J. A. Outcome of Children with Multiply Relapsed B-Cell Acute Lymphoblastic Leukemia: A Therapeutic Advances in Childhood Leukemia & Lymphoma Study. *Leukemia* **2018**, *32* (11), 2316–2325.

(13) Karrman, K.; Johansson, B. Pediatric T-Cell Acute Lymphoblastic Leukemia. *Genes, Chromosomes and Cancer* **2017**, *56* (2), 89–116.

(14) Chiaretti, S.; Zini, G.; Bassan, R. Diagnosis and Subclassification of Acute Lymphoblastic Leukemia. *Mediterranean Journal of Hematology and Infectious Diseases* **2014**, *6* (1).

(15) Patel, J. L.; Smith, L. M.; Anderson, J.; Abromowitch, M.; Campana, D.; Jacobsen, J.; Lones, M. A.; Gross, T. G.; Cairo, M. S.; Perkins, S. L. The Immunophenotype of T-Lymphoblastic Lymphoma in Children and Adolescents: A Children's Oncology Group Report. *British Journal of Haematology* **2012**, *159* (4), 454–461.

(16) Leonard, W. J. Cytokines and Immunodeficiency Diseases. *Nature Reviews Immunology* **2001**, *1* (3), 200–208.

(17) Scherer, L. D.; Brenner, M. K.; Mamonkin, M. Chimeric Antigen Receptors for T-Cell Malignancies . *Frontiers in Oncology* **2019**, *9*, 126.

(18) Ali, M.; Giannakopoulou, E.; Li, Y.; Lehander, M.; Virding Culleton, S.; Yang, W.; Knetter, C.; Odabasi, M. C.; Bollineni, R. C.; Yang, X.; Foldvari, Z.; Böschen, M.-L.; Taraldsrud,

E.; Strønen, E.; Toebes, M.; Hillen, A.; Mazzi, S.; de Ru, A. H.; Janssen, G. M. C.; Kolstad, A.; Tjønnfjord, G. E.; Lie, B. A.; Griffioen, M.; Lehmann, S.; Osnes, L. T.; Buechner, J.; Garcia, K. C.; Schumacher, T. N.; van Veelen, P. A.; Leisegang, M.; Jacobsen, S. E. W.; Woll, P.; Olweus, J. T Cells Targeted to TdT Kill Leukemic Lymphoblasts While Sparing Normal Lymphocytes. *Nature Biotechnology* **2022**, *40* (4), 488–498.

(19) Hernandez, I.; Bott, S. W.; Patel, A. S.; Wolf, C. G.; Hospodar, A. R.; Sampathkumar, S.; Shrank, W. H. Pricing of Monoclonal Antibody Therapies: Higher If Used for Cancer. *Am J Manag Care* **2018**, *24* (2), 109–112.

(20) Thurber, G. M.; Schmidt, M. M.; Wittrup, K. D. Antibody Tumor Penetration: Transport Opposed by Systemic and Antigen-Mediated Clearance. *Advanced Drug Delivery Reviews* **2008**, *60* (12), 1421–1434.

(21) Mankarious, S.; Lee, M.; Fischer, S.; Pyun, K. H.; Ochs, H. D.; Oxelius, V. A.; Wedgwood, R. J. The Half-Lives of IgG Subclasses and Specific Antibodies in Patients with Primary Immunodeficiency Who Are Receiving Intravenously Administered Immunoglobulin. *The Journal of Laboratory and Clinical Medicine* **1988**, *112* (5), 634–640.

(22) Mackness, B. C.; Jaworski, J. A.; Boudanova, E.; Park, A.; Valente, D.; Mauriac, C.; Pasquier, O.; Schmidt, T.; Kabiri, M.; Kandira, A.; Radošević, K.; Qiu, H. Antibody Fc Engineering for Enhanced Neonatal Fc Receptor Binding and Prolonged Circulation Half-Life. *mAbs* **2019**, *11* (7), 1276–1288.

(23) Alcantara, M.; Tesio, M.; June, C. H.; Houot, R. CAR T-Cells for T-Cell Malignancies: Challenges in Distinguishing between Therapeutic, Normal, and Neoplastic T-Cells. *Leukemia* **2018**, *32* (11), 2307–2315.

(24) Xiang, D.; Zheng, C.; Zhou, S. F.; Qiao, S.; Tran, P. H. L.; Pu, C.; Li, Y.; Kong, L.; Kouzani, A. Z.; Lin, J.; Liu, K.; Li, L.; Shigdar, S.; Duan, W. Superior Performance of Aptamer in Tumor Penetration over Antibody: Implication of Aptamer-Based Theranostics in Solid Tumors. *Theranostics* **2015**, *5* (10), 1083–1097.

(25) Healy, J. M.; Lewis, S. D.; Kurz, M.; Boomer, R. M.; Thompson, K. M.; Wilson, C.; McCauley, T. G. Pharmacokinetics and Biodistribution of Novel Aptamer Compositions. *Pharmaceutical Research* **2004**, *21* (12), 2234–2246.

(26) Zhou, J.; Rossi, J. Aptamers as Targeted Therapeutics: Current Potential and Challenges. *Nature Reviews Drug Discovery* **2017**, *16* (6), 440.

(27) Shigdar, S.; Schrand, B.; Giangrande, P. H.; de Franciscis, V. Aptamers: Cutting Edge of Cancer Therapies. *Molecular Therapy* **2021**, *29* (8), 2396–2411.

(28) Bohrmann, L.; Burghardt, T.; Haynes, C.; Saatchi, K.; Häfeli, U. O. Aptamers Used for Molecular Imaging and Theranostics - Recent Developments. *Theranostics* **2022**, *12* (9), 4010–4050.

(29) Ruscito, A.; DeRosa, M. C. Small-Molecule Binding Aptamers: Selection Strategies, Characterization, and Applications. *Frontiers in Chemistry* **2016**, *4*.

(30) Bayat, P.; Nosrati, R.; Alibolandi, M.; Rafatpanah, H.; Abnous, K.; Khedri, M.; Ramezani, M. SELEX Methods on the Road to Protein Targeting with Nucleic Acid Aptamers. *Biochimie* **2018**, *154*, 132–155.

(31) Gopinath, S. C. B.; Misono, T. S.; Kawasaki, K.; Mizuno, T.; Imai, M.; Odagiri, T.; Kumar, P. K. R. An RNA Aptamer That Distinguishes between Closely Related Human Influenza Viruses and Inhibits Haemagglutinin-Mediated Membrane Fusion. *Journal of General Virology* **2006**, *87* (3), 479–487.

(32) Yu, X.; Chen, F.; Wang, R.; Li, Y. Whole-Bacterium SELEX of DNA Aptamers for Rapid Detection of E.Coli O157:H7 Using a QCM Sensor. *Journal of Biotechnology* **2018**, *266*, 39–49.
(33) Shangguan, D.; Li, Y.; Tang, Z.; Cao, Z. C.; Chen, H. W.; Mallikaratchy, P.; Sefah, K.; Yang, C. J.; Tan, W. Aptamers Evolved from Live Cells as Effective Molecular Probes for Cancer Study. *Proceedings of the National Academy of Sciences* **2006**, *103* (32), 11838–11843.
(34) Li, L.; Wan, J.; Wen, X.; Guo, Q.; Jiang, H.; Wang, J.; Ren, Y.; Wang, K. Identification of a New DNA Aptamer by Tissue-SELEX for Cancer Recognition and Imaging. *Analytical Chemistry* **2021**, *93* (19), 7369–7377.
(35) Cheng, C.; Chen, Y. H.; Lennox, K. A.; Behlke, M. A.; Davidson, B. L. In Vivo SELEX for Identification of Brain-Penetrating Aptamers. *Molecular Therapy - Nucleic Acids* **2013**, *2*, e67.
(36) Shangguan, D.; Cao, Z.; Meng, L.; Mallikaratchy, P.; Sefah, K.; Wang, H.; Li, Y.; Tan, W. Cell-Specific Aptamer Probes for Membrane Protein Elucidation in Cancer Cells. *Journal of Proteome Research* **2008**, *7* (5), 2133–2139.
(37) Kacherovsky, N.; Cardle, I. I.; Cheng, E. L.; Yu, J. L.; Baldwin, M. L.; Salipante, S. J.; Jensen, M. C.; Pun, S. H. Traceless Aptamer-Mediated Isolation of CD8+ T Cells for Chimeric Antigen Receptor T-Cell Therapy. *Nature Biomedical Engineering* **2019**, *3* (10), 783–795.
(38) Sylvestre, M.; Saxby, C. P.; Kacherovsky, N.; Gustafson, H.; Salipante, S. J.; Pun, S. H. Identification of a DNA Aptamer That Binds to Human Monocytes and Macrophages. *Bioconjugate Chemistry* **2020**, *31* (8), 1899–1907.
(39) Cheng, E. L.; Cardle, I. I.; Kacherovsky, N.; Bansia, H.; Wang, T.; Zhou, Y.; Raman, J.; Yen, A.; Gutierrez, D.; Salipante, S. J.; des Georges, A.; Jensen, M. C.; Pun, S. H. Discovery of a Transferrin Receptor 1-Binding Aptamer and Its Application in Cancer Cell Depletion for Adoptive T-Cell Therapy Manufacturing. *Journal of the American Chemical Society* **2022**, *144* (30), 13851–13864.
(40) Kacherovsky, N.; Yang, L. F.; Dang, H. v; Cheng, E. L.; Cardle, I. I.; Walls, A. C.; McCallum, M.; Sellers, D. L.; DiMaio, F.; Salipante, S. J.; Corti, D.; Veesler, D.; Pun, S. H. Discovery and Characterization of Spike N-Terminal Domain-Binding Aptamers for Rapid SARS-CoV-2 Detection. *Angewandte Chemie International Edition* **2021**, *60* (39), 21211–21215.
(41) Zumrut, H. E.; Ara, M. N.; Fraile, M.; Maio, G.; Mallikaratchy, P. Ligand-Guided Selection of Target-Specific Aptamers: A Screening Technology for Identifying Specific Aptamers against Cell-Surface Proteins. *Nucleic acid therapeutics* **2016**, *26* (3), 190–198.
(42) Yang, L. F.; Kacherovsky, N.; Panpradist, N.; Wan, R.; Liang, J.; Zhang, B.; Salipante, S. J.; Lutz, B. R.; Pun, S. H. Aptamer Sandwich Lateral Flow Assay (AptaFlow) for Antibody-Free SARS-CoV-2 Detection. *Analytical Chemistry* **2022**, *94* (20), 7278–7285.
(43) Alam, K. K.; Chang, J. L.; Burke, D. H. FASTAptamer: A Bioinformatic Toolkit for High-Throughput Sequence Analysis of Combinatorial Selections. *Molecular Therapy - Nucleic Acids* **2015**, *4* (3), e230.
(44) Caroli, J.; Taccioli, C.; De La Fuente, A.; Serafini, P.; Bicciato, S. APTANI: A Computational Tool to Select Aptamers through Sequence-Structure Motif Analysis of HT-SELEX Data. *Bioinformatics* **2015**, *32* (2), 161–164.

(45) Bailey, T. L.; Boden, M.; Buske, F. A.; Frith, M.; Grant, C. E.; Clementi, L.; Ren, J.; Li, W. W.; Noble, W. S. MEME Suite: Tools for Motif Discovery and Searching. *Nucleic Acids Research* **2009**, *37* (SUPPL. 2), W202–W208.

(46) Zadeh, J. N.; Steenberg, C. D.; Bois, J. S.; Wolfe, B. R.; Pierce, M. B.; Khan, A. R.; Dirks, R. M.; Pierce, N. A. NUPACK: Analysis and Design of Nucleic Acid Systems. *Journal of Computational Chemistry* **2011**, *32* (1), 170–173.

(47) Teixidó, J.; Parker, C. M.; Kassner, P. D.; Hemler, M. E. Functional and Structural Analysis of VLA-4 Integrin Alpha 4 Subunit Cleavage. *Journal of Biological Chemistry* **1992**, *267* (3), 1786–1791.

(48) Imai, Y.; Shimaoka, M.; Kurokawa, M. Essential Roles of VLA-4 in the Hematopoietic System. *International Journal of Hematology* **2010**, *91* (4), 569–575.

(49) Matsunaga, T.; Takemoto, N.; Sato, T.; Takimoto, R.; Tanaka, I.; Fujimi, A.; Akiyama, T.; Kuroda, H.; Kawano, Y.; Kobune, M.; Kato, J.; Hirayama, Y.; Sakamaki, S.; Kohda, K.; Miyake, K.; Niitsu, Y. Interaction between Leukemic-Cell VLA-4 and Stromal Fibronectin Is a Decisive Factor for Minimal Residual Disease of Acute Myelogenous Leukemia. *Nature Medicine* **2003**, *9* (9), 1158–1165.

(50) Kurtova, A. v; Tamayo, A. T.; Ford, R. J.; Burger, J. A. Mantle Cell Lymphoma Cells Express High Levels of CXCR4, CXCR5, and VLA-4 (CD49d): Importance for Interactions with the Stromal Microenvironment and Specific Targeting. *Blood* **2009**, *113* (19), 4604–4613.

(51) Shishido, S.; Bönig, H.; Kim, Y.-M. Role of Integrin Alpha4 in Drug Resistance of Leukemia. *Frontiers in Oncology* **2014**, *4*.

(52) Shalapour, S.; Hof, J.; Kirschner-Schwabe, R.; Bastian, L.; Eckert, C.; Prada, J.; Henze, G.; von Stackelberg, A.; Seeger, K. High VLA-4 Expression Is Associated with Adverse Outcome and Distinct Gene Expression Changes in Childhood B-Cell Precursor Acute Lymphoblastic Leukemia at First Relapse. *Haematologica* **2011**, *96* (11), 1627–1635.

(53) Choi, J.; Beaino, W.; Fecek, R. J.; Fabian, K. P. L.; Laymon, C. M.; Kurland, B. F.; Storkus, W. J.; Anderson, C. J. Combined VLA-4-Targeted Radionuclide Therapy and Immunotherapy in a Mouse Model of Melanoma. *Journal of Nuclear Medicine* **2018**, *59* (12), 1843–1849.

(54) Hsieh, Y.-T.; Gang, E. J.; Geng, H.; Park, E.; Huantes, S.; Chudziak, D.; Dauber, K.; Schaefer, P.; Scharman, C.; Shimada, H.; Shojaee, S.; Klemm, L.; Parameswaran, R.; Loh, M.; Kang, E.-S.; Koo, H. H.; Hofmann, W.-K.; Andrade, J.; Crooks, G. M.; Willman, C. L.; Müschen, M.; Papayannopoulou, T.; Heisterkamp, N.; Bönig, H.; Kim, Y.-M. Integrin Alpha4 Blockade Sensitizes Drug Resistant Pre-B Acute Lymphoblastic Leukemia to Chemotherapy. *Blood* **2013**, *121* (10), 1814–1818.

(55) Bing, T.; Shangguan, D.; Wang, Y. Facile Discovery of Cell-Surface Protein Targets of Cancer Cell Aptamers. *Molecular & Cellular Proteomics* **2015**, *14* (10), 2692–2700.

(56) Hemler, M. E.; Huang, C.; Schwarz, L. The VLA Protein Family. Characterization of Five Distinct Cell Surface Heterodimers Each with a Common 130,000 Molecular Weight Beta Subunit. *Journal of Biological Chemistry* **1987**, *262* (7), 3300–3309.

(57) Petrovic, A.; Alpdogan, O.; Willis, L. M.; Eng, J. M.; Greenberg, A. S.; Kappel, B. J.; Liu, C.; Murphy, G. J.; Heller, G.; van den Brink, M. R. M. LPAM (A4β7 Integrin) Is an Important Homing Integrin on Alloreactive T Cells in the Development of Intestinal Graft-versus-Host Disease. *Blood* **2004**, *103* (4), 1542–1547.

(58) Kurmaeva, E.; Lord, J. D.; Zhang, S.; Bao, J. R.; Kevil, C. G.; Grisham, M. B.; Ostanin, D. v. T Cell-Associated A4β7 but Not A4β1 Integrin Is Required for the Induction and Perpetuation of Chronic Colitis. *Mucosal Immunology* **2014**, *7* (6), 1354–1365.
(59) Wang, G.; Liu, J.; Chen, K.; Xu, Y.; Liu, B.; Liao, J.; Zhu, L.; Hu, X.; Li, J.; Pu, Y. Selection and Characterization of DNA Aptamer against Glucagon Receptor by Cell-SELEX. *Scientific reports* **2017**, *7* (1), 1–10.
(60) Shangguan, D.; Tang, Z.; Mallikaratchy, P.; Xiao, Z.; Tan, W. Optimization and Modifications of Aptamers Selected from Live Cancer Cell Lines. *ChemBioChem* **2007**, *8* (6), 603–606.
(61) Shangguan, D.; Cao, Z. C.; Li, Y.; Tan, W. Aptamers Evolved from Cultured Cancer Cells Reveal Molecular Differences of Cancer Cells in Patient Samples. *Clinical Chemistry* **2007**, *53* (6), 1153–1155.
(62) Kretschy, N.; Sack, M.; Somoza, M. M. Sequence-Dependent Fluorescence of Cy3- and Cy5-Labeled Double-Stranded DNA. *Bioconjugate Chemistry* **2016**, *27* (3), 840–848.
(63) White, R. R.; Sullenger, B. A.; Rusconi, C. P. Developing Aptamers into Therapeutics. *The Journal of Clinical Investigation* **2000**, *106* (8), 929–934.
(64) Wang, C.; Liu, L.; Zhao, Q. Low Temperature Greatly Enhancing Responses of Aptamer Electrochemical Sensor for Aflatoxin B1 Using Aptamer with Short Stem. *ACS Sensors* **2020**, *5* (10), 3246–3253.
(65) Ni, S.; Yao, H.; Wang, L.; Lu, J.; Jiang, F.; Lu, A.; Zhang, G. Chemical Modifications of Nucleic Acid Aptamers for Therapeutic Purposes. *International Journal of Molecular Sciences* **2017**, *18* (8), 1683.
(66) Yang, L.; Meng, L.; Zhang, X.; Chen, Y.; Zhu, G.; Liu, H.; Xiong, X.; Sefah, K.; Tan, W. Engineering Polymeric Aptamers for Selective Cytotoxicity. *Journal of the American Chemical Society* **2011**, *133* (34), 13380–13386.
(67) Fletcher, N. L.; Houston, Z. H.; Simpson, J. D.; Veedu, R. N.; Thurecht, K. J. Designed Multifunctional Polymeric Nanomedicines: Long-Term Biodistribution and Tumour Accumulation of Aptamer-Targeted Nanomaterials. *Chemical Communications* **2018**, *54* (82), 11538–11541.
(68) Deng, Z.; Yang, Q.; Peng, Y.; He, J.; Xu, S.; Wang, D.; Peng, T.; Wang, R.; Wang, X.-Q.; Tan, W. Polymeric Engineering of Aptamer–Drug Conjugates for Targeted Cancer Therapy. *Bioconjugate Chemistry* **2020**, *31* (1), 37–42.
(69) Nerantzaki, M.; Loth, C.; Lutz, J.-F. Chemical Conjugation of Nucleic Acid Aptamers and Synthetic Polymers. *Polymer Chemistry* **2021**, *12* (24), 3498–3509.
(70) Lutz, J.-F. Copper-Free Azide–Alkyne Cycloadditions: New Insights and Perspectives. *Angewandte Chemie International Edition* **2008**, *47* (12), 2182–2184.
(71) Raetz, E. A.; Teachey, D. T. T-Cell Acute Lymphoblastic Leukemia. *Hematology* **2016**, *2016* (1), 580–588.
(72) Hill, J. A.; Giralt, S.; Torgerson, T. R.; Lazarus, H. M. CAR-T – and a Side Order of IgG, to Go? – Immunoglobulin Replacement in Patients Receiving CAR-T Cell Therapy. *Blood Reviews* **2019**, *38*, 100596.
(73) Elices, M. J.; Osborn, L.; Takada, Y.; Crouse, C.; Luhowskyj, S.; Hemler, M. E.; Lobb, R. R. VCAM-1 on Activated Endothelium Interacts with the Leukocyte Integrin VLA-4 at a Site Distinct from the VLA-4/Fibronectin Binding Site. *Cell* **1990**, *60* (4), 577–584.
(74) Oostendorp, R. A. J.; Reisbach, G.; Spitzer, E.; Thalmeier, K.; Dienemann, H.; Mergenthaler, H.-G.; Dörmer, P. VLA-4 and VCAM-1 Are the Principal Adhesion

Molecules Involved in the Interaction between Blast Colony-Forming Cells and Bone Marrow Stromal Cells. *British Journal of Haematology* **1995**, *91* (2), 275–284.
(75) Garcia-Pardo, A.; Wayner, E. A.; Carter, W. G.; Ferreira, O. C. Human B Lymphocytes Define an Alternative Mechanism of Adhesion to Fibronectin. The Interaction of the Alpha 4 Beta 1 Integrin with the LHGPEILDVPST Sequence of the Type III Connecting Segment Is Sufficient to Promote Cell Attachment. *The Journal of Immunology* **1990**, *144* (9), 3361.
(76) Bayless, K. J.; Meininger, G. A.; Scholtz, J. M.; Davis, G. E. Osteopontin Is a Ligand for the Alpha4beta1 Integrin. *Journal of Cell Science* **1998**, *111* (9), 1165–1174.
(77) Nilsson, S. K.; Johnston, H. M.; Whitty, G. A.; Williams, B.; Webb, R. J.; Denhardt, D. T.; Bertoncello, I.; Bendall, L. J.; Simmons, P. J.; Haylock, D. N. Osteopontin, a Key Component of the Hematopoietic Stem Cell Niche and Regulator of Primitive Hematopoietic Progenitor Cells. *Blood* **2005**, *106* (4), 1232–1239.
(78) Mudry, R. E.; Fortney, J. E.; York, T.; Hall, B. M.; Gibson, L. F. Stromal Cells Regulate Survival of B-Lineage Leukemic Cells during Chemotherapy. *Blood* **2000**, *96* (5), 1926–1932.
(79) Jacamo, R.; Chen, Y.; Wang, Z.; Ma, W.; Zhang, M.; Spaeth, E. L.; Wang, Y.; Battula, V. L.; Mak, P. Y.; Schallmoser, K.; Ruvolo, P.; Schober, W. D.; Shpall, E. J.; Nguyen, M. H.; Strunk, D.; Bueso-Ramos, C. E.; Konoplev, S.; Davis, R. E.; Konopleva, M.; Andreeff, M. Reciprocal Leukemia-Stroma VCAM-1/VLA-4-Dependent Activation of NF-KB Mediates Chemoresistance. *Blood* **2014**, *123* (17), 2691–2702.
(80) Berrazouane, S.; Doucet, A.; Boisvert, M.; Barabé, F.; Aoudjit, F. VLA-4 Induces Chemoresistance of T Cell Acute Lymphoblastic Leukemia Cells via PYK2-Mediated Drug Efflux. *Cancers* **2021**, *13* (14), 3512.
(81) Berrazouane, S.; Boisvert, M.; Salti, S.; Mourad, W.; Al-Daccak, R.; Barabé, F.; Aoudjit, F. Beta1 Integrin Blockade Overcomes Doxorubicin Resistance in Human T-Cell Acute Lymphoblastic Leukemia. *Cell Death & Disease* **2019**, *10* (5), 357.
(82) Yu, Y.; Schürpf, T.; Springer, T. A. How Natalizumab Binds and Antagonizes A4 Integrins. *Journal of Biological Chemistry* **2013**, *288* (45), 32314–32325.
(83) Mouse Genome Sequencing Consortium. Initial Sequencing and Comparative Analysis of the Mouse Genome. *Nature* **2002**, *420* (6915), 520–562.
(84) Miyake, K.; Hasunuma, Y.; Yagita, H.; Kimoto, M. Requirement for VLA-4 and VLA-5 Integrins in Lymphoma Cells Binding to and Migration beneath Stromal Cells in Culture. *Journal of Cell Biology* **1992**, *119* (3), 653–662.
(85) García-Martín, A. B.; Zwicky, P.; Gruber, T.; Matti, C.; Moalli, F.; Stein, J. v; Francisco, D.; Enzmann, G.; Levesque, M. P.; Hewer, E.; Lyck, R. VLA-4 Mediated Adhesion of Melanoma Cells on the Blood–Brain Barrier Is the Critical Cue for Melanoma Cell Intercalation and Barrier Disruption. *Journal of Cerebral Blood Flow & Metabolism* **2018**, *39* (10), 1995–2010.
(86) Polman, C. H.; O'Connor, P. W.; Havrdova, E.; Hutchinson, M.; Kappos, L.; Miller, D. H.; Phillips, J. T.; Lublin, F. D.; Giovannoni, G.; Wajgt, A.; Toal, M.; Lynn, F.; Panzara, M. A.; Sandrock, A. W. A Randomized, Placebo-Controlled Trial of Natalizumab for Relapsing Multiple Sclerosis. *New England Journal of Medicine* **2006**, *354* (9), 899–910.
(87) Targan, S. R.; Feagan, B. G.; Fedorak, R. N.; Lashner, B. A.; Panaccione, R.; Present, D. H.; Spehlmann, M. E.; Rutgeerts, P. J.; Tulassay, Z.; Volfova, M.; Wolf, D. C.; Hernandez, C.; Bornstein, J.; Sandborn, W. J. Natalizumab for the Treatment of Active Crohn's Disease: Results of the ENCORE Trial. *Gastroenterology* **2007**, *132* (5), 1672–1683.

(88) Butzkueven, H.; Kappos, L.; Wiendl, H.; Trojano, M.; Spelman, T.; Chang, I.; Kasliwal, R.; Jaitly, S.; Campbell, N.; Ho, P.-R. Long-Term Safety and Effectiveness of Natalizumab Treatment in Clinical Practice: 10 Years of Real-World Data from the Tysabri Observational Program (TOP). *Journal of Neurology, Neurosurgery & Psychiatry* **2020**, *91* (6), 660–668.

(89) Khatri, B. O.; Man, S.; Giovannoni, G.; Koo, A. P.; Lee, J. C.; Tucky, B.; Lynn, F.; Jurgensen, S.; Woodworth, J.; Goelz, S. Effect of Plasma Exchange in Accelerating Natalizumab Clearance and Restoring Leukocyte Function. *Neurology* **2009**, *72* (5), 402–409.

(90) Swerlick, R. A.; Eckman, J. R.; Kumar, A.; Jeitler, M.; Wick, T. M. A4β1-Integrin Expression on Sickle Reticulocytes: Vascular Cell Adhesion Molecule-1-Dependent Binding to Endothelium. *Blood* **1993**, *82* (6), 1891–1899.

(91) Perkins, L. A.; Nyiranshuti, L.; Little-Ihrig, L.; Latoche, J. D.; Day, K. E.; Zhu, Q.; Tavakoli, S.; Sundd, P.; Novelli, E. M.; Anderson, C. J. Integrin VLA-4 as a PET Imaging Biomarker of Hyper-Adhesion in Transgenic Sickle Mice. *Blood Advances* **2020**, *4* (17), 4102–4112.

(92) White, J.; Krishnamoorthy, S.; Gupta, D.; Lancelot, M.; Moore, N.; Sarnaik, S.; Hobbs II, W. E.; Light, D. R.; Hines, P. VLA-4 Blockade by Natalizumab Inhibits Sickle Reticulocyte and Leucocyte Adhesion during Simulated Blood Flow. *British Journal of Haematology* **2016**, *174* (6), 970–982.

(93) Cheng, E. L.; Kacherovsky, N.; Pun, S. H. Aptamer-Based Traceless Multiplexed Cell Isolation Systems. *ACS Applied Materials & Interfaces* **2022**, *14* (39), 44136–44146.

(94) Ganson, N. J.; Povsic, T. J.; Sullenger, B. A.; Alexander, J. H.; Zelenkofske, S. L.; Sailstad, J. M.; Rusconi, C. P.; Hershfield, M. S. Pre-Existing Anti–Polyethylene Glycol Antibody Linked to First-Exposure Allergic Reactions to Pegnivacogin, a PEGylated RNA Aptamer. *Journal of Allergy and Clinical Immunology* **2016**, *137* (5), 1610-1613.e7.

(95) Hoang Thi, T. T.; Pilkington, E. H.; Nguyen, D. H.; Lee, J. S.; Park, K. D.; Truong, N. P. The Importance of Poly (Ethylene Glycol) Alternatives for Overcoming PEG Immunogenicity in Drug Delivery and Bioconjugation. *Polymers* **2020**, *12* (2), 298.

(96) Ozer, I.; Pitoc, G. A.; Layzer, J. M.; Moreno, A.; Olson, L. B.; Layzer, K. D.; Hucknall, A. M.; Sullenger, B. A.; Chilkoti, A. PEG-Like Brush Polymer Conjugate of RNA Aptamer That Shows Reversible Anticoagulant Activity and Minimal Immune Response. *Advanced Materials* **2022**, *34* (10), 2107852.

(97) Sefah, K.; Shangguan, D.; Xiong, X.; O'Donoghue, M. B.; Tan, W. Development of DNA Aptamers Using Cell-Selex. *Nature Protocols* **2010**, *5* (6), 1169–1185.

(98) Wu, X.; Zhao, Z.; Bai, H.; Fu, T.; Yang, C.; Hu, X.; Liu, Q.; Champanhac, C.; Teng, I.-T.; Ye, M.; Tan, W. DNA Aptamer Selected against Pancreatic Ductal Adenocarcinoma for In Vivo Imaging and Clinical Tissue Recognition. *Theranostics* **2015**, *5* (9), 985–994.

(99) Chi-Chao, L.; Pascal, L.; Quin, Y. S.; James, L. C. The Membrane-Proximal KXGFFKR Motif of α-Integrin Mediates Chemoresistance. *Molecular and Cellular Biology* **2013**, *33* (21), 4334–4345.

4.8 SUPPORTING INFORMATION

Table S4.1 | Experimental conditions used in rounds (R) 1-7 of cell-SELEX.

R	DNA (μM)	(+) Selection	BSA (%)	FBS (%)	Yeast tRNA (0.1 mg/mL)	Salmon Sperm DNA (0.1mg/mL)	Poly(I:C) (0.1mg/mL)	(+) Time (min)	Washes	(-) Selection	(-) Time (min)
1	14	10^7 H9 4IgB7H3	0.1	0	Yes	No	No	60	3x, 30 s	None	None
2	0.5	10^7 H9 4IgB7H3	0.1	0	Yes	No	No	60	3x, 3 min	10^7 H9 Parental	60
3	0.5	5×10^6 H9 4IgB7H3	0.5	0	Yes	Yes	No	45	3x, 5 min	2×10^7 H9 Parental	60
4	0.5	4×10^6 H9 4IgB7H3	1	0	Yes	Yes	No	30	4x, 5min	2x, 2×10^7 H9 Parental	30 each
5	0.25	2×10^6 H9 4IgB7H3	1	0	Yes	Yes	No	30	5x, 5min	4x, 2×10^7 H9 Parental	30 each
6	0.25	2×10^6 H9 4IgB7H3	0	2.5	Yes	Yes	Yes	30	6x, 5min	6x, 2×10^7 H9 Parental	20 each
7	0.1	2×10^6 H9 4IgB7H3	0	5	Yes	Yes	Yes	30	6x, 5min	100nM B7H3 Antibody	30

Table S4.2 | Primers used for next generation sequencing (NGS) of round 7 pools in the cell-SELEX.

Primer Name	Sequence	Barcode (in red)
Aptamer_F	AATGATACGGCGACCACCGAGATCTACACCGAGGAGATAC CACTAAGCCACCGTGTCCA	
Aptamer_R_80	CAAGCAGAAGACGGCATACGAGATGAATGGACACAGACC GTCGATCCAGAGTGACGCAGCA	GTCCATTC

Table S4.3 | Top 50 round 7 (R7) aptamer sequences. Sequences do not include constant regions.

R7 Rank	% Representation	Motif	Sequence
1	41.61	1	AACCTGACCTCCTTACTAGATGCAACCCGACTACTAACGTCGTAAGAGAGCC
2	23.77	2	TAGTCAAGGCGATAGACGAAAAACATTGTTTTCCTGGAAGGCCCAGAATCTG
3	6.02	4	CGCAGCAGCGTAAAGGGGGTGTTTGTGCGGTGTGGAGTGCGCGTGCTGCTGC
4	0.83	2	TAGTCAAGGCGATAGACGAAAAACATTGTTTTCCTGGAAGGCCCGGAATCTG
5	0.78		GGTTGCTGTACCTACAATTGACAATAAAAAATCTAGCGGGCTTAGAGACAGT
6	0.57	3	AGGCGCTAGACGCAAACACTTAAGCACCATGAGTGCCAAGTTTTCCTAATGG
7	0.39	2	ATAAGTACGCAGTCAAGGCGATAGACGAAAAGAACACTTTCCCGGAAGGGCC
8	0.29	2	ATAGTCAAGGCGATAGACGAAAAACATTGTTTTCCTGGAAGGCCCAGAATCG
9	0.21		GCGGAACCGAAGATTTGGCCAAAAAAATCAATCGGGCTTTGGCTCACCCCGT
10	0.13	3	GATGCAAATGCTCGAGAGAGGCACGGCGCAAATCTGGTAGATGAGCAACGTA
11	0.13	1	AGCCTGACCTCCTTACTAGATGCAACCCGACTACTAACGTCGTAAGAGAGCC
12	0.12	1	AACCTGACCTCCTTACTAGATGCAACCCGACTACTAACGTCGTAAGAGAGTC
13	0.11	1	AACCTGACCTCCTTACTAGATGCAGCCCGACTACTAACGTCGTAAGAGAGCC
14	0.11	5	GCGCAAGTATGGACTATCCCAACAAGGCGTTAGACGTAAATGAATTATTTCC
15	0.10	3	TCACATCTCGGCAGATGCAAATGCCTGGCCAGGAACCCGAAACCTGTGATAG
16	0.09	3	CGCAGCAACCCAAACCACCAGCCGGGGATGCAAACACCGCACAGGGAACGGC
17	0.09		AGCTGTAGGTGTGCGGTTAACTCCGTGCTAGATAGGAGGTATCTCCACAGGG
18	0.09	5	CGCAGCAATCACAGGGCTACAAGGTGCTAAACGTAAACTAGCAAGAGAACTA
19	0.07	5	GAGTAGGAAGAGTAACCAACAAGGCGGTAGACGTAAAAAGATCAATTTTCCG
20	0.07	3	GACGTTGATTAGGCGGATGCAAACGCACGGTCGTGGTACCAAAACGCACTGC
21	0.07	3	GAAGAGAGTCCGGATGCAAACGCCTGACTAGGATAGACGATGGTTCTGTGTA
22	0.06		AGGTGCTAAACGCAAACCTACCTCTGCTGAGGGCAAGGTGTTTCCTACGGTG
23	0.06		ACGCAGCAAGCGGTTTTCGGGTTCGGGTCTGGGGGTTGGGTTGTCGGCACTA
24	0.05	3	GTGACACGTTCCAAATCCACCAACATCGGATGCAAACGCCAGACATGGGTAA
25	0.05	1	AACCTGACCTCCTTACTAGATGCAACCCGACTACTAACGTCGTAAGAGATCC
26	0.05	4	CGCAGCAGCTTAAAGGGGGTGTTTGTGCGGTGTGGAGTGCGCGTGCTGCTGC
27	0.04	1	AACCTGACCTCCTTGCTAGATGCAACCCGACTACTAACGTCGTAAGAGAGCC
28	0.04	3	AAGCTTTATTGGGGATGCAAACACCGAACAGGGAACAATAGATTCCAGAGCA
29	0.04	1	AACCTGACCTCCTTACTAGATGCAACCCGACTGCTAACGTCGTAAGAGAGCC
30	0.04	2	CGGCCCCAAGCATCAAGGCGTTAGACGAAACCCAGGGTTCACGTAGTGTAAT
31	0.04	3	CGACGTGGTTGACGGATGCAAACGCCTGACAAGGGAATCAATAGTGGTGTAA

32	0.04	3	TTCCAGACAGGGGGGATGCAAACACATGATAATGGGACCATGGTTGGAAATC
33	0.04	1	AACCCGACCTCCTTACTAGATGCAACCCGACTACTAACGTCGTAAGAGAGCC
34	0.04	1	AACCTGACCTCCTTACTAGATGCATCCCGACTACTAACGTCGTAAGAGAGCC
35	0.04	3	GATGCAAATGCCTGACGAGGGTGACAGCGAAACTTTGGTATATAAGCACCTC
36	0.03	3	GCAAGATGCAACTGATGACTATCTAGGTGGAAGCTAAGTTTCACCGTAATGC
37	0.03	3	TTATCGGGGATGCAACCAACGAATGTGGTACGGGAATGTCTGATGCTACAAA
38	0.03	3	AGAAATGAGCAACGGATGCAAACGCCCAAACGGGGAACTGCGTATATTTTCT
39	0.03	3	TTGCGTGAAGGGAGATGCAACTAACGATAGTGGTACCTGCACCCGCACTGCA
40	0.03	4	CGCAGCAGCGTAAAGGGGGTGTTTGTGCGGTGTGGAGTGCGCTTGCTGCTGC
41	0.03	3	CCATCTTGACTTCGGATGCAAACGCTTGACCAAGGGAAAGACATGATGCGCT
42	0.03	3	AGAAGCTGGACTGAGGGGATGCAACCAGAGAATACGGTACTCATGTCATTGG
43	0.03	3	GAGAATCGGGGATGCAACCAGCTACGCGGTACGGTTCACAACTTGTACACAC
44	0.03	2	TAGTCAAGGCGATAGGCGAAAAACATTGTTTTCCTGGAAGGCCCAGAATCTG
45	0.03	1	AACCTGACCTCCTTACTAGATGCACCCCGACTACTAACGTCGTAAGAGAGCC
46	0.03	2	TAGTCAAGGCGATAGACGAAAAACATTGTTTTCCTGGAAGGCCCATAATCTG
47	0.03	5	AAAAACGGCCAAGTCATCAAGGCGATAGACGAAAACGAATCCCTGATTTCCG
48	0.03	5	AGAACAAGGTGTTAAACGTTATGCCCCAGCATACCATCGAAGAGGTCGGCAA
49	0.03	5	ACAGGTCAAGGCGCTAGACGAAGGAAATCTCCTCCATACGGCAATGTTGATT
50	0.03	3	CAAAAGAGATGGATGCAAACACCTGAAAAGGGCATGTCTGAGAAGTGATATA

Table S4.4 | Sequences of aptamers used in experiments. Aptamers were modified on their 5'-end with either 6-FAM, Cy5, biotin-hexa-ethyleneglycol, or DBCO depending on the assay. The exact modifications are specified in the figures and captions. Underlined nucleotides represent constant regions. Red text represents nucleotides that were gradually deleted to make the truncated aptamer variants. Green and blue text represents nucleotides that were added to and substituted into aptamer sequences, respectively.

Name	Sequence
RN	5'-ATCCAGAGTGACGCAGCAAATTCCAAACTCGAGTAAGCGTAGAGCCTCTCATCGCCTCAATAA TGGACACGGTGGCTTAGT-3'
HR7A1	5'-ATCCAGAGTGACGCAGCAAACCTGACCTCCTTACTAGATGCAACCCGACTACTAACGTCGTAA GAGAGCCTGGACACGGTGGCTTAGT-3'
tJBA8.1	5'-GCAGCAGCGTAAAGGGGGTGTTTGTGCGGTGTGGAGTGCGCGTGCTGCTGC-3'
CD8.A3	5'-ATCCAGAGTGACGCAGCAACAGAGGTGTAGAAGTACACGTGAACAAGCTTGAAATTGTCTCT GACAGAGGTGGACACGGTGGCTTAGT-3'
HR7A1.Tr1	5'-CAGCAAACCTGACCTCCTTACTAGATGCAACCCGACTACTAACGTCGTAAGAGAG-3'
HR7A1.Tr2	5'-CTCCTTACTAGATGCAACCCGACTACTAACGTCGTAAGAGAG-3'
HR7A1.Tr3	5'-CTAGATGCAACCCGACTACTAACGTCG-3'
HR7A1.Tr4	5'-GCGTACTAGATGCAACCCGACTACTAACGTCGTACGC-3'
Sgc4f	5'-ATCACTTATAACGAGTGCGGATGCAAACGCCAGACAGGGGGACAGGAGATAAGTGA-3'
HR7A1.Tr2.S2E2	5'-CGCGCCGTACTAGATGCAACCCGACTACTAACGTCGTACGAGCGCG-3'

Table S4.5 | siRNA duplexes used for CD29 (integrin β1) knockdown.

Name	Sequence
hs.Ri.ITGB1.13.1-SEQ1	5'-rArCrUrCrUrUrGrUrCrArGrCrUrArArGrGrUrCrArCrArUTG-3'
hs.Ri.ITGB1.13.1-SEQ2	5'-rCrArArUrGrUrGrArCrCrUrUrArGrCrUrGrArCrArArGrArGrUrArA-3'

Table S4.6 | Bio-layer interferometry (BLI) measured affinity kinetics of immobilized HR7A1, HR7A1.Tr1, and HR7A1.Tr2 aptamer binding to recombinant α4β1 protein. Data are mean ± SD, n = 5 individual protein concentrations. Values were calculated by performing a global fit of the binding curve data in **Figure 4.4B** to a 1:1 binding model. The ratio between the dissociation rate constant (K_{dis}) and the association rate constant (K_{on}) give the equilibrium dissociation constant (K_D). The goodness of fit was evaluated by a reduced chi-square (χ^2) and a R^2 value approaching 1.

Aptamer	K_D (nM)	K_{on} ($nM^{-1}s^{-1}$) × 10^{-5}	K_{dis} (s^{-1}) × 10^{-4}	Full χ^2	Full R^2
HR7A1	6.28 (±0.04)	7.43 (±0.03)	4.67 (±0.02)	0.2548	0.9980
HR7A1.Tr1	7.74 (±0.03)	5.82 (±0.02)	4.50 (±0.01)	0.1694	0.9993
HR7A1.Tr2	9.89 (±0.05)	4.16 (±0.01)	4.12 (±0.01)	0.1619	0.9993

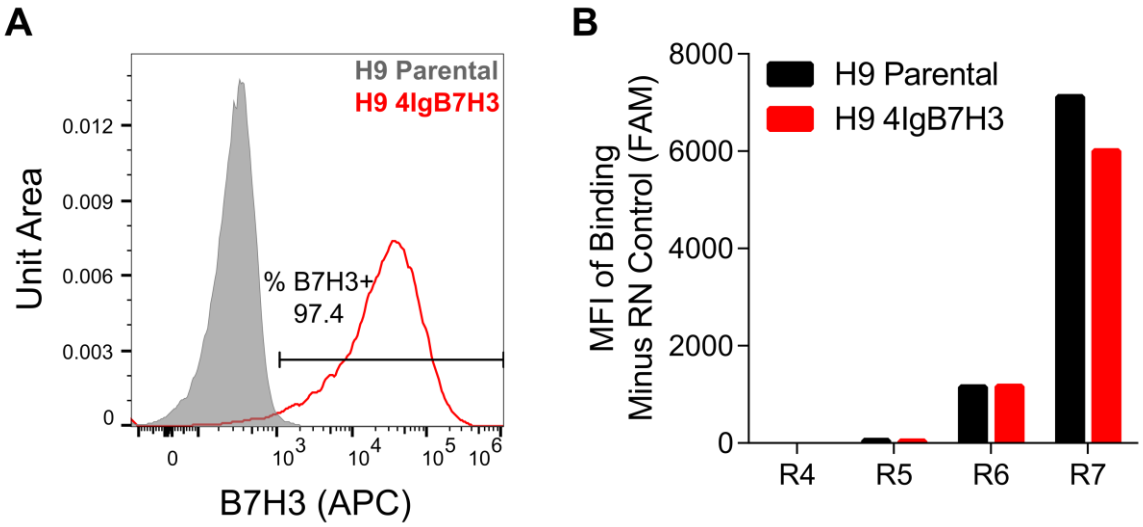

Figure S4.1 | Aptamer pools from rounds 4-7 (R4-7) of cell-SELEX non-selectively bind both H9 parental and H9 4IgB7H3 cells. (A) Flow cytometry histograms of extracellular B7H3 expression on H9 parental and H9 4IgB7H3 cells, as measured by antibody staining. Histograms are representative of three independent experiments. (B) Flow cytometry binding of 250 nM aptamer pools to H9 parental and H9 4IgB7H3 cells after consecutive rounds of SELEX, as measured by MFI. Binding of a random aptamer from the naïve library (RN) at the same concentration was subtracted from values to report specific binding. The bars graphs are representative of one independent experiment. APC, allophycocyanin; FAM, 6-carboxyfluorescein.

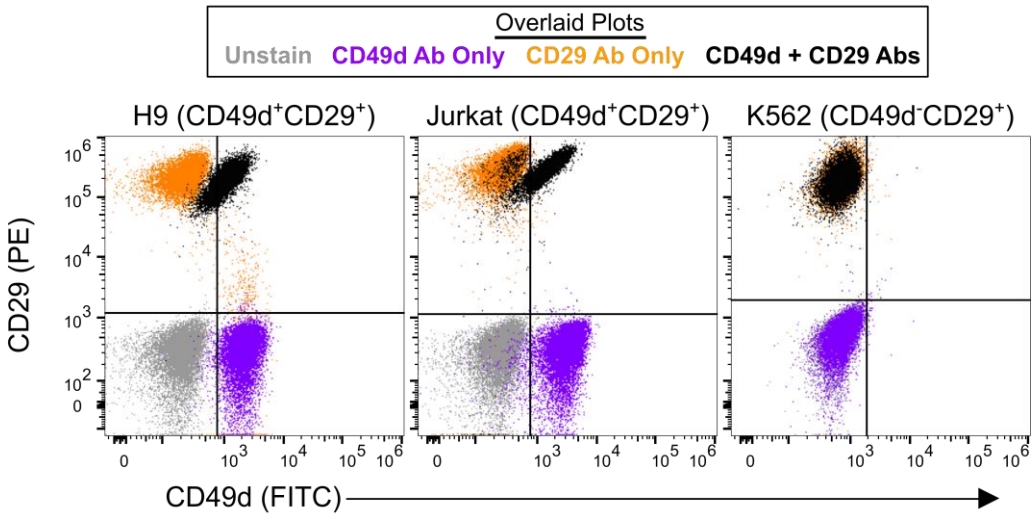

Figure S4.2 | CD49d and CD29 expression on $\alpha4^{+}\beta1^{+}$ cell lines correlate with each other. Overlaid flow cytometry plots of FITC-labeled anti-CD49d antibody (CD49d Ab) and PE-labeled anti-CD29 antibody (CD29 Ab) co-staining on H9, Jurkat, and K562 cells. Plots are representative of one independent experiment. FITC, fluorescein isothiocyanate; PE, phycoerythrin.

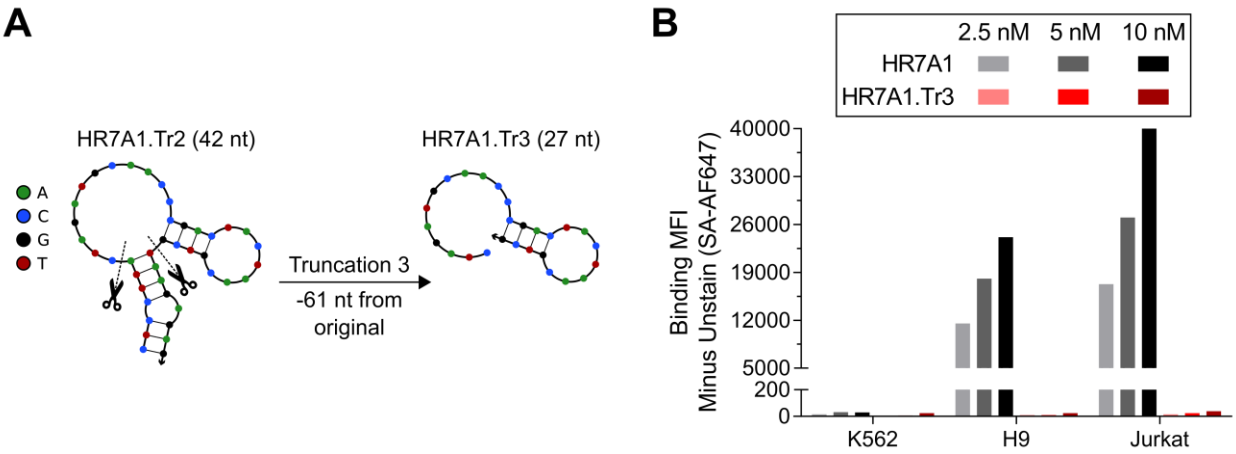

Figure S4.3 | HR7A1.Tr3 does not retain binding capabilities of full-length aptamer. (A) Truncation of the HR7A1.Tr2 sequence to create HR7A1.Tr3. MFE secondary structures for each sequence are shown, predicted using NUPACK (temperature = 4 °C; Na^+ = 137 mM; Mg^{2+} = 5.5 mM). The dashed lines indicate the sites of truncation. (B) Flow cytometry binding of biotinylated HR7A1 and HR7A1.Tr3 to K562, H9, and Jurkat cells, as measured by MFI. The bars graphs represent one independent experiment. SA-AF647, streptavidin Alexa Fluor 647.

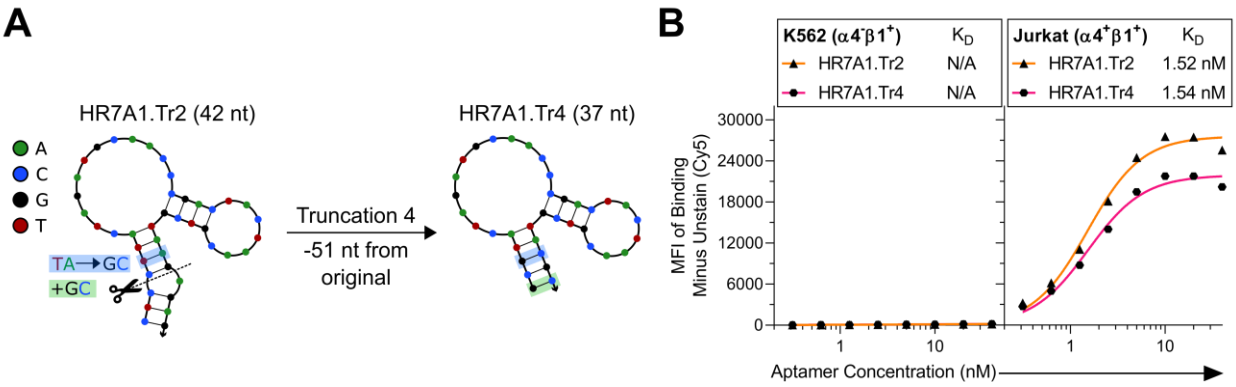

Figure S4.4 | HR7A1.Tr4 is the minimal binding motif of HR7A1. (A) Truncation of the HR7A1.Tr2 sequence to create HR7A1.Tr4. MFE secondary structures for each sequence are shown, predicted using NUPACK (temperature = 4 °C; Na^+ = 137 mM; Mg^{2+} = 5.5 mM). The dashed lines indicate the sites of truncation. Highlighting denotes GC base pairs that were substituted into (blue) or appended to (green) the truncated stem for added stability. (B) Flow cytometry binding curves of Cy5-labeled HR7A1.Tr2 and HR7A1.Tr4 to K562 and Jurkat cells, as determined by MFI. The curves represent a nonlinear regression assuming one-site specific binding with Hill slope. Data points are representative of n = 1 independent experiment. Cy5, cyanine 5.

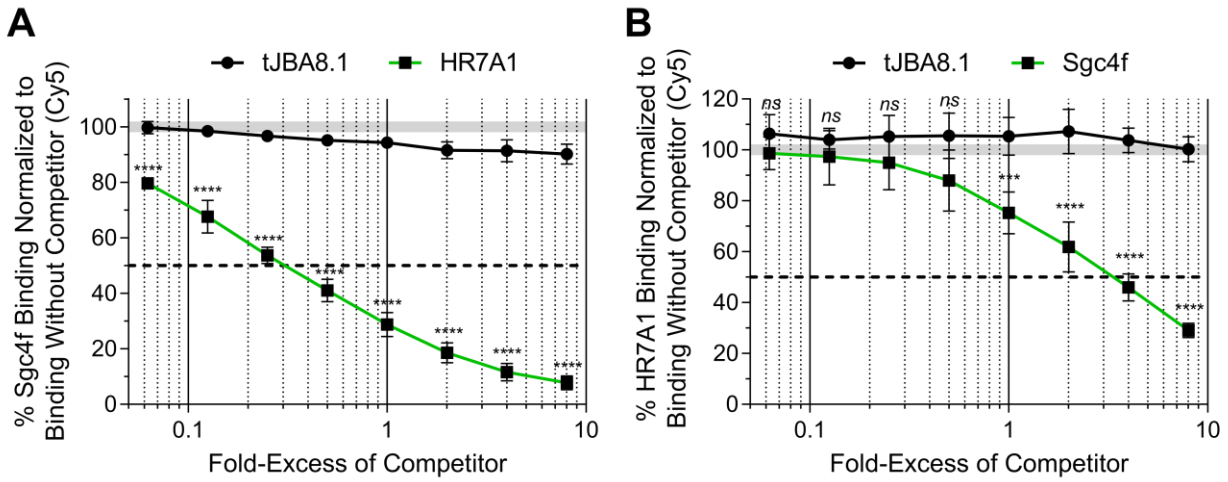

Figure S4.5 | HR7A1 outcompetes Sgc4f for binding to α4β1-expressing cells. Competitive binding of (A) 20 nM Cy5-labeled Sgc4f with varying fold excess of HR7A1 and (B) 20 nM Cy5-labeled HR7A1 with varying fold excess of Sgc4f to Jurkat cells by flow cytometry. Varying fold excess of TfR1-binding tJBA8.1 was also included in each assay as a negative competitor control. Binding was normalized to aptamer-stained cells without competitor aptamer. Data points and error bars represent mean ± SD; $n = 3$ independent experiments. *ns* > 0.05, ***$P < 0.001$, ****$P < 0.0001$ (ordinary two-way ANOVA with Sidak correction). Cy5, cyanine 5.

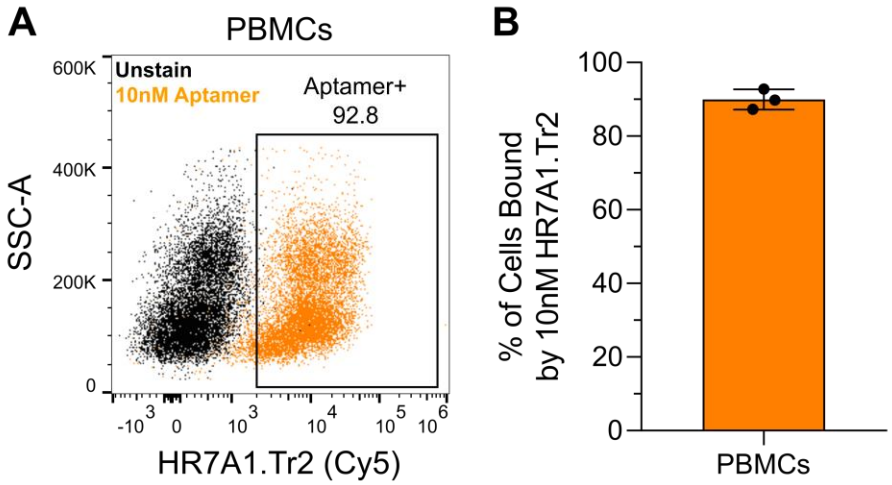

Figure S4.6 | HR7A1.Tr2 binds the majority of PBMCs. (A) Overlaid flow cytometry plot of 0 nM (unstain) and 10 nM Cy5-labeled HR7A1.Tr2 aptamer binding to PBMCs. The plot is representative of $n = 3$ independent experiments with different PBMC donors. (B) Corresponding percentage of PBMCs labeled by 10 nM Cy5-labeled HR7A1.Tr2 staining. Bar graph and error bars represent mean ± SD; $n = 3$ independent experiments with different PBMC donors. Cy5, cyanine 5.

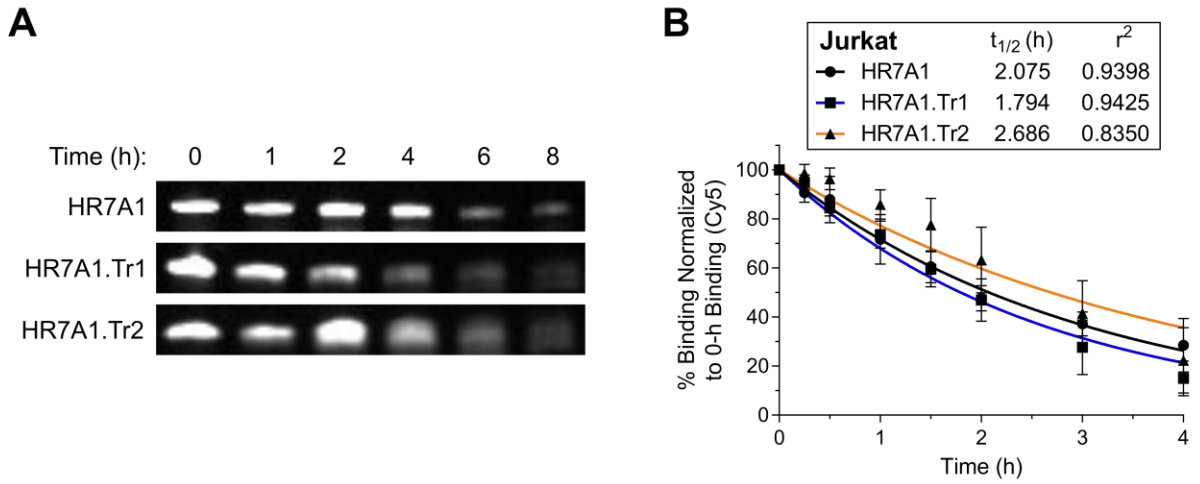

Figure S4.7 | HR7A1 and truncated variants are modestly stable in serum. (A) 15% TBE-urea gel of FAM-labeled HR7A1, HR7A1.Tr1, and HR7A1.Tr2 after 8-h incubation in 50% normal mouse serum at 37 °C. Gel image is representative of n = 1 independent experiment. (B) Flow cytometry binding of 10 nM Cy5-labeled HR7A1, HR7A1.Tr1, and HR7A1.Tr2 to Jurkat cells after 4-h incubation in 50% normal mouse serum at 37 °C, normalized to a 0-h no incubation control. The curves represent a nonlinear regression assuming one-phase exponential decay. Serum half-life values were calculated from a single regression of the averaged experimental data. Data points and error bars represent mean ± SD; n = 3-5 independent experiments. FAM, 6-carboxyfluorescein; Cy5, cyanine 5.

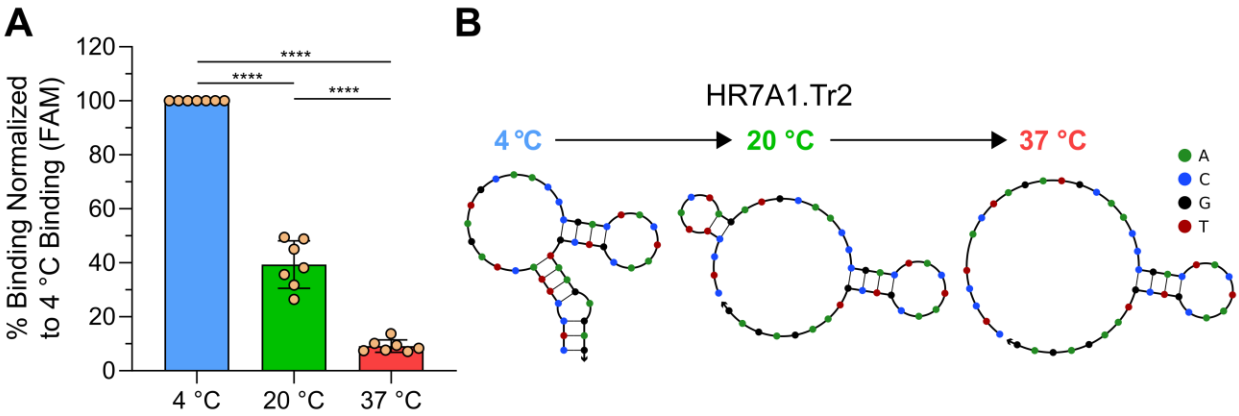

Figure S4.8 | HR7A1.Tr2 loses most of its binding at physiological temperature. (A) Flow cytometry binding of 5 nM FAM-labeled HR7A1.Tr2 to Jurkat cells at 4, 20, and 37 °C, normalized to binding at 4 °C. Non-specific aptamer binding to K562 cells at each temperature was subtracted before normalizing data. Data points and error bars represent mean ± SD; n = 7 independent experiments. ****P < 0.0001 (ordinary two-way ANOVA with Tukey's test). (B) MFE secondary structure of HR7A1.Tr2 at 4, 20, and 37 °C, predicted using NUPACK (Na^+ = 137 mM; Mg^{2+} = 5.5 mM). FAM, 6-carboxyfluorescein.

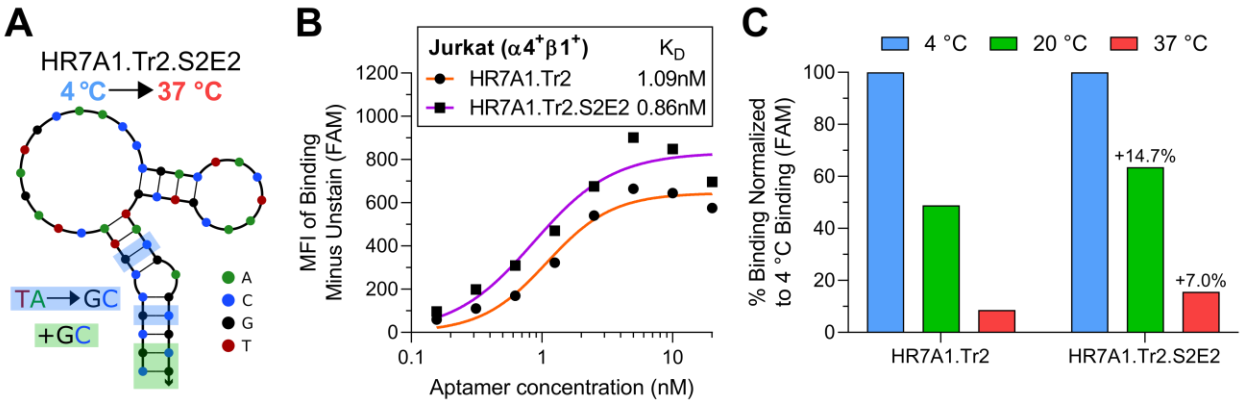

Figure S4.9 | HR7A1.Tr2.S2E2 preserves binding affinity of HR7A1.Tr2 while minorly improving binding at physiological temperature. (A) MFE secondary structure of HR7A1.Tr2.S2E2 at 4 and 37 °C, predicted using NUPACK (Na^+ = 137 mM; Mg^{2+} = 5.5 mM). Highlighting denotes base pairs that were substituted into (blue) or appended to (green) the parental HR7A1.Tr2 sequence to create HR7A1.Tr2.S2E2. (B) Flow cytometry binding curves of FAM-labeled HR7A1.Tr2 and HR7A1.Tr2.S2E2 to Jurkat cells, as determined by MFI. The curves represent a nonlinear regression assuming one-site specific binding with Hill slope. Data points are representative of n = 1 independent experiment. (C) Flow cytometry binding of 5 nM FAM-labeled HR7A1.Tr2 and HR7A1.Tr2.S2E2 to Jurkat cells at 4, 20, and 37 °C, normalized to binding at 4 °C. Non-specific aptamer binding to K562 cells at each temperature was subtracted before normalizing data. Bar graphs are representative of n = 1 independent experiment. FAM, 6-carboxyfluorescein.

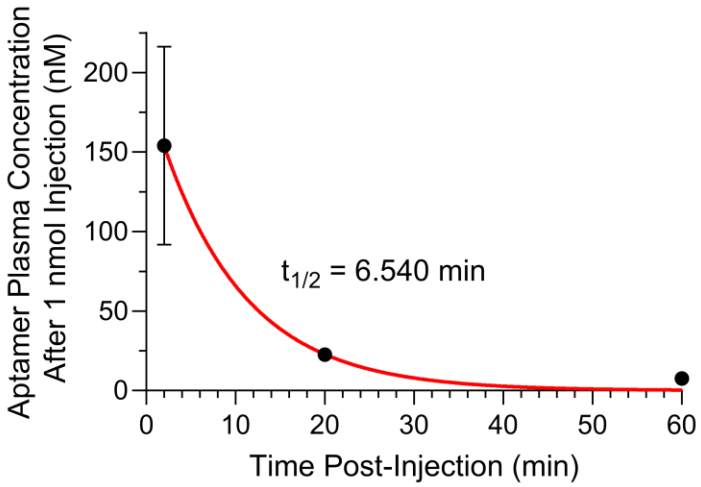

Figure S4.10 | Unmodified aptamers are rapidly eliminated from circulation *in vivo*. Plasma half-life of a 50-nt Cy5-labeled scrambled aptamer in NOD scid mice following a 1 nmol retro-orbital injection. The curve represents a nonlinear regression assuming one-phase exponential decay. Data points and error bars represent the mean ± SD; n = 3 mice. Cy5, cyanine 5.

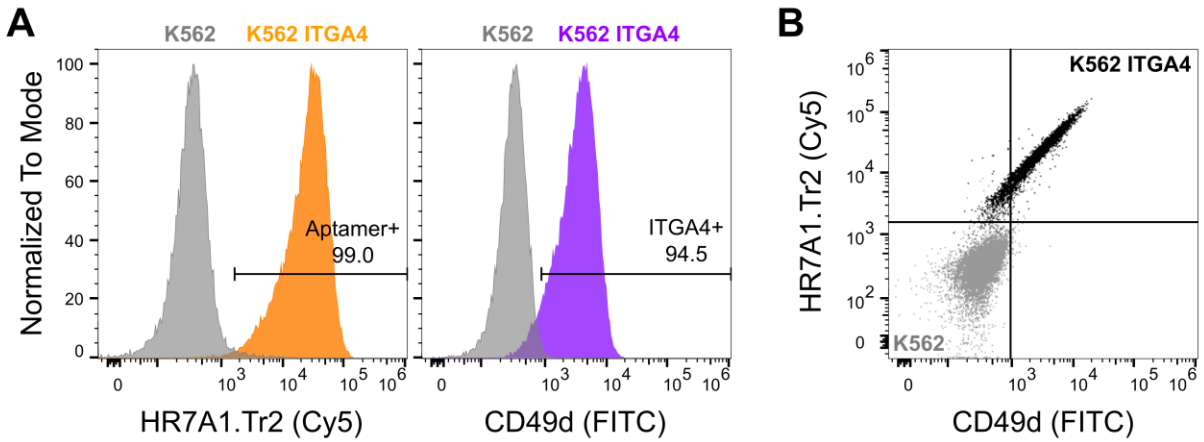

Figure S4.11 | K562 ITGA4 cells have enforced expression of integrin α4 that allows HR7A1.Tr2 binding. (A) Flow cytometry histograms of 10 nM Cy5-labeled HR7A1.Tr2 aptamer and FITC-labeled anti-CD49d antibody staining of K562 and K562 ITGA4 cells. Plots are representative of $n = 1$ independent experiment. (B) Overlaid flow cytometry plot of 10 nM Cy5-labeled HR7A1.Tr2 aptamer co-staining with FITC-labeled anti-CD49d antibody on K562 and K562 ITGA4 cells. Plots are representative of $n = 1$ independent experiment. Cy5, cyanine 5; FITC, fluorescein isothiocyanate.

Chapter 5: Optimized serum stability and specificity of an αvβ6 integrin-binding peptide for tumor targeting

Ian I. Cardle, Michael C. Jensen, Suzie H. Pun, Drew L. Sellers

ABSTRACT

The integrin αvβ6 is an antigen expressed at low levels in healthy tissue but upregulated during tumorigenesis, which makes it a promising target for cancer imaging and therapy. A20FMDV2 is a 20-mer peptide derived from the foot-and-mouth disease virus that exhibits nanomolar and selective affinity for αvβ6 over other integrins. Despite this selectivity, A20FMDV2 has had limited success in imaging and treating $\alpha v\beta 6^{+}$ tumors *in vivo* because of its poor serum stability. Here, we explore the cyclization and modification of the A20FMDV2 peptide to improve its serum stability without sacrificing its affinity and specificity for αvβ6. Using cysteine amino acid substitutions and cyclization by perfluoroarylation with decafluorobiphenyl, we synthesized six cyclized A20FMDV2 variants and discovered that two retained binding to αvβ6 with modestly improved serum stability. Further D-amino acid substitutions and C-terminal sequence optimization outside of the cyclized region greatly prolonged peptide serum stability without reducing binding affinity. While the cyclized A20FMDV2 variants exhibited increased nonspecific integrin binding compared to the original peptide, additional modifications with the non-natural amino acids citrulline, hydroxyproline, and D-alanine were found to restore binding specificity, with some modifications leading to greater αvβ6 integrin selectivity than the original A20FMDV2 peptide. The peptide modifications detailed herein greatly improve the potential for utilization of A20FMDV2 to target αvβ6 *in vivo*, expanding opportunities for cancer theranostics.[4]

[4]Chapter reproduced from: Cardle, I.I. *et al*. Optimized serum stability and specificity of an αvβ6 integrin-binding peptide for tumor targeting. *J. Biol. Chem.* **296**, 100657 (2021). Copyright 2021 ASBMB.

5.1 INTRODUCTION

From 2009 through 2015, pancreatic, liver, lung, and esophageal cancers had the lowest survival rates of any cancer and are projected to contribute to 38% of cancer-related deaths in 2020.[1] Patients are often asymptomatic at early stages with these cancers, preventing timely diagnosis and thereby limiting effective treatment options at later stages of disease. Consequentially, there is a significant need for targeted diagnostics and therapeutics that could identify and treat these cancers at early stages to improve patient outcomes.

Integrins are a family of heterodimeric transmembrane receptors that interact with proteins in the extracellular matrix (ECM) and on other cells to mediate cell adhesion and migration. While integrins are involved in a variety of healthy biological functions, including embryogenesis, tissue regeneration, and immune cell trafficking,[2] their aberrant expression and activity can drive cancer initiation and metastasis.[3–5] Integrins have thus garnered considerable interest as diagnostic and therapeutic targets for cancer.[6,7] One such integrin, αvβ6, is an epithelial-restricted integrin involved in wound healing that has low basal expression in healthy tissue.[8] αvβ6 is broadly upregulated in many solid tumor types, including pancreatic,[9] liver,[10,11] lung,[12,13] esophageal,[14] cervical,[15] breast,[16] head and neck,[17] colon,[18] ovarian,[19] stomach,[20] and oral cancers[21] and its overexpression often correlates with a poor prognosis.[22,23] The role of αvβ6 in tumorigenesis is correspondingly extensive; αvβ6 binds to fibronectin and tenascin for cell adhesion and migration,[14,24,25] it activates pro-transforming growth factor beta to promote the epithelial-to-mesenchymal transition,[22,26–28] and it mediates secretion of matrix metalloproteinases that remodel the ECM for cancer growth and invasion.[18,29–31] Given these qualities, the integrin αvβ6 has become the focus of considerable research efforts in the last two decades as a potential target for cancer imaging and therapy.[32,33]

Peptides are attractive targeting ligands for cancer due to their chemical synthesis and small size, enabling inexpensive production, ease of modification, and enhanced solid tumor penetration compared to antibodies.[34–37] A20FMDV2 is a 20-amino acid, arginine-glycine-aspartate (RGD)-containing peptide derived from the G-H loop of the capsid protein VP1 from foot-and-mouth disease virus (FMDV) serotype O_1 that binds integrin αvβ6 with low nanomolar affinity and high specificity.[38–40] With its favorable binding properties and demonstrated preclinical safety,[41,42] A20FMDV2 has been used in many cancer research applications, including imaging of αvβ6$^+$ tumors in mice and humans,[40,43] αvβ6-specific drug delivery *in vitro* and *in vivo*,[44] and engineering chimeric antigen receptors for αvβ6-directed adoptive T-cell immunotherapy.[45] Recent studies also show the utility of the peptide for imaging idiopathic pulmonary fibrosis and those associated with connective tissue disease, radiation therapy, and severe acute respiratory syndrome coronavirus 2 (SARS-CoV-2) infection.[46–48]

However, the clinical translation of A20FMDV2 has been limited, in part, by poor metabolic stability of the peptide that impairs its pharmacokinetics.[40,49] Modification of A20FMDV2 with two short PEG chains (~1 kDa each) reduces peptide degradation and thereby increases tumor retention, but also slows peptide clearance from healthy tissue and increases renal retention.[50,51] For these reasons, we sought to engineer an A20FMDV2 peptide with chemistries and amino acid modifications that increase the peptide's inherent metabolic stability. Here, we report the design of cyclized A20FMDV2 variants with selective amino acid modifications and their characterization *in vitro*. We demonstrate that these peptide variants have prolonged stability in serum and retain their binding affinity for αvβ6$^+$ cells. Importantly, some of these optimized peptides demonstrate improved αvβ6 specificity over the original A20FMDV2 peptide, further increasing the benefit for future *in vivo* application.

5.2 RESULTS

5.2.1 Synthesis of DFBP-cyclized A20FMDV2 variants and binding evaluation

A20FMDV2 has a hairpin loop structure with the RGD motif at the tip of hairpin turn followed by a 3_{10} helix (**Figure 5.1A**),[38,39] and previous reports have demonstrated that the extended RGDLXXL motif is most critical for αvβ6 binding whereas amino acids at the N-terminus and C-terminus of the peptide are not as critical for binding.[52] Accordingly, we postulated that chemistries involving the N- and C-terminal amino-acid positions of the peptide could increase serum stability without negatively affecting peptide binding to αvβ6.

Cyclization is a well-established technique for stabilizing peptides and improving their pharmacokinetic profiles,[35] and cysteine perfluoroarylation is a facile cyclization approach that uses perfluoroaromatic molecular linkers to staple together cysteine thiol moieties on unprotected peptides.[53] Our lab has previously used this technique for peptide cyclization with a decafluorobiphenyl (DFBP) linker (**Figure 5.1B**) and demonstrated increased serum stability and affinity of DFBP-cyclized peptides compared to counterparts with disulfide, amide, or triazole cyclization.[54,55] We therefore synthesized six unique A20FMDV2 peptide sequences with cysteine substitutions primarily at N- and C-terminal amino-acid positions for cyclization by DFBP to stabilize and close the hairpin peptide structure (**Figure 5.1C**). Biotin was conjugated on the N-terminus of all peptides for labeling with streptavidin-AF647 to assess cell binding by flow cytometry. Peptides were also synthesized with a C-terminal lysine to mimic a prospective methyltrityl-lysine that could be added for selective modification or synthesis of branched peptides at the lysine side-chain.

The binding of cyclized A20FMDV2 sequences to αvβ6 were evaluated with the matched erythroleukemia K562 and K562 αvβ6:mCherry cell lines. Both cell lines endogenously express the α5β1 integrin,[56] but only the K562 αvβ6:mCherry cells express the αvβ6 integrin. Of the DFBP-cyclized sequences, we observed binding of the C1C18 DFBP (N1C; A18C), C1C20 DFBP (N1C; T20C), and C2C18 DFBP (A2C; A18C) peptides to K562 αvβ6:mCherry cells with high affinity and specificity comparable to the original A20FMDV2 peptide (**Figure 5.1D**). Interestingly, peptide sequences C1C19 DFBP (N1C; R19C) and C2C19 DFBP (A2C; R19C) exhibited high binding to K562 αvβ6:mCherry cells but also poor specificity. Both peptides significantly bound to parental K562 cells at high concentrations, suggesting that the R19 amino acid in A20FMDV2 is important for αvβ6 specificity. Similarly, the peptide cyclized via cysteine substitutions proximal to the RGDLXXL motif, C6C17 DFBP (L6C; V17C), displayed minimal binding to K562 αvβ6:mCherry cells. It is known that the V12 and V17 amino acids are important for the structure of the post-RGD helix in A20FMDV2,[57] so the cysteine substitutions in the C6C17 DFBP peptide and their cyclization likely impaired the 3_{10} helix structure. Given that the DFBP-cyclized C1C18, C1C20, and C2C18 peptides retained the favorable binding properties of the original A20FMDV2 peptide, we moved forward with these variants for characterization of serum stability.

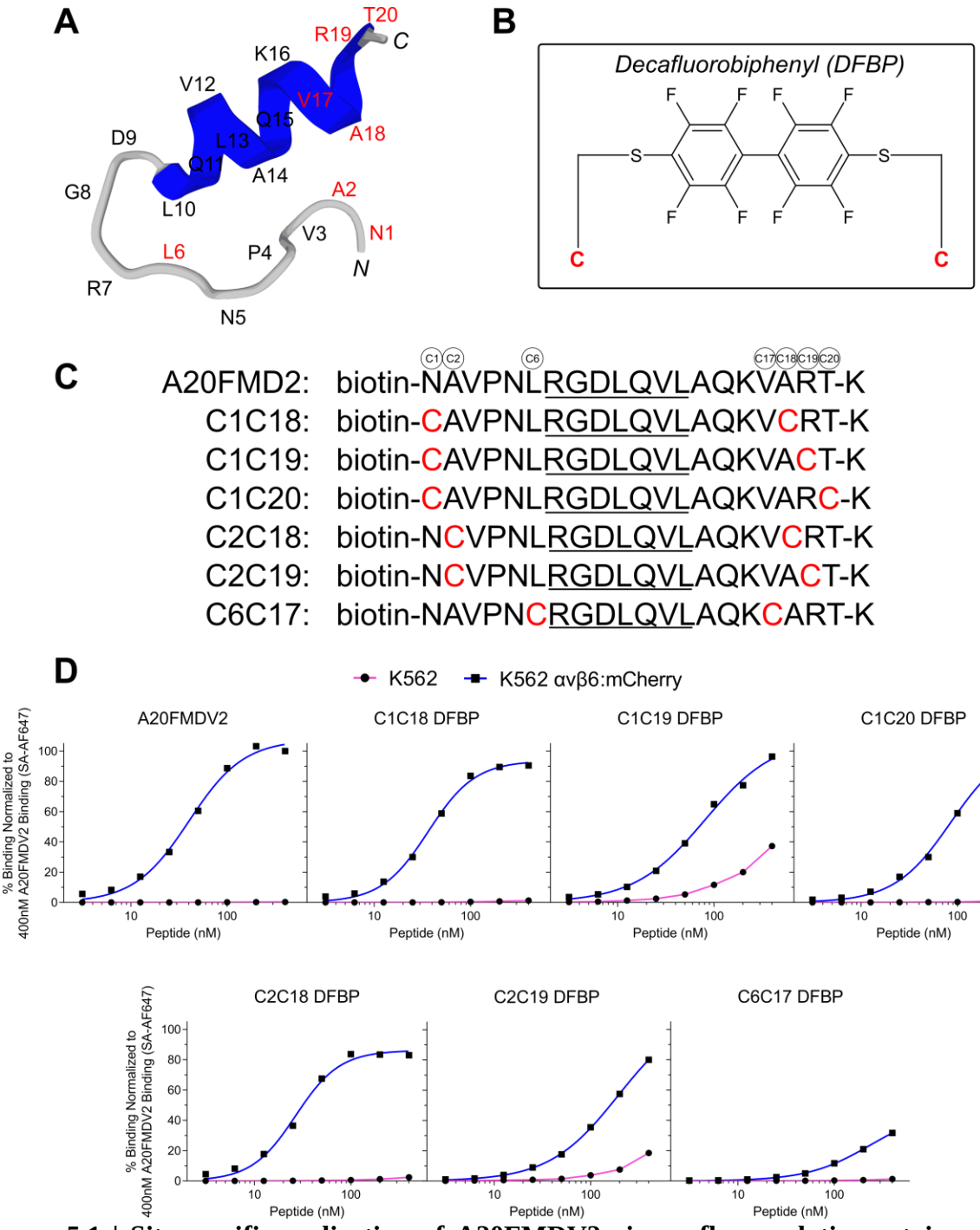

Figure 5.1 | Site-specific cyclization of A20FMDV2 via perfluorarylation retains peptide binding to αvβ6^{+} cancer cells. (A) 3D model of A20FMDV2 peptide predicted by PEP-FOLD3 computational framework.[58] Amino acids are listed, and positions substituted with cysteines for cyclization are shown in red. (B) Chemical structure of DFBP molecular linker used for cyclization. (C) Amino-acid sequences of A20FMDV2 peptide and DFBP-cyclized variants. Cysteine substitutions for cyclization by perfluoroarylation are shown in red. The RGDLXXL motif that is important for αvβ6 recognition is underlined in all sequences. (D) Flow cytometry binding curves of A20FMDV2 peptide and DFBP-cyclized variants to K562 and K562 αvβ6:mCherry cells, normalized to 400nM A20FMDV2 binding to K562 αvβ6:mCherry cells. The

curves represent a nonlinear regression of one independent experiment in which binding data are fitted to a Hill equation. K_D values are not shown here and will be reported for promising peptides in a later figure with triplicate datasets. SA-AF647, streptavidin Alexa Fluor 647.

5.2.2 MALDI-ToF MS serum stability of DFBP-cyclized A20FMDV2 variants

As the original A20FMDV2 peptide is degraded by over 50% in normal mouse serum within a 4 h incubation at 37 °C,[59] we hypothesized that our DFBP-cyclized variants would have prolonged serum stability due to added structural stability from their cyclization. To investigate this, we incubated the DFBP-cyclized C1C18, C1C20, and C2C18 peptides in normal mouse serum a 37 °C for up to 6 h and measured the presence of intact peptide and any degradation products at different time points by MALDI-ToF MS (**Figure 5.2A-C**). As shown, the partially cyclized C1C18 DFBP and C2C18 DFBP peptides formed degradation products that are 385 Da smaller after incubation in serum for 2 h, corresponding C-terminal cleavage of the arginine-threonine-lysine (RTK) group outside of the DFBP-cyclized region (**Figure 5.2A,C**). C1C18 DFBP had prolonged intact peptide presence compared to C2C18 DFBP (6 h versus 2 h), suggesting that the C1C18 cyclization scheme better protects the exocyclic C-terminal RTK group. Importantly, the 385 Da smaller degradation products for both peptides persisted up to the last timepoint sampled and no further degradation peaks were observed, demonstrating good protection of amino acids within their cyclized regions. We also assayed a disulfide-cyclized C1C18 peptide (C1C18 S-S) and observed faster degradation to the 385 Da smaller product compared to C1C18 DFBP (**Figure S5.1**), emphasizing the importance of the DFBP molecular linker.

To our surprise, the fully cyclized C1C20 DFBP peptide degraded within 2 h in serum; we could not detect any peptide or degradation products at the 4 and 6 h timepoints (**Figure 5.2B**). We detected a low-intensity 135 smaller Da degradation product at the 2 h timepoint but it was near

background and we could not predict the amino acid sequence. The molecular weight difference is near what would be expected from an internal arginine deletion (138 Da smaller), so Arg7 or Arg19 may have been metabolically cleaved from the sequence. This data suggests that the complete cyclization of a peptide from N- to C-terminus is not always beneficial for stability, and that peptide structure should rationally guide cyclization positioning. Since peptides C1C18 DFBP and C2C18 DFBP were stable outside of the exocyclic C-terminal RTK groups, we proceeded to further optimize these two peptides with amino acid modifications.

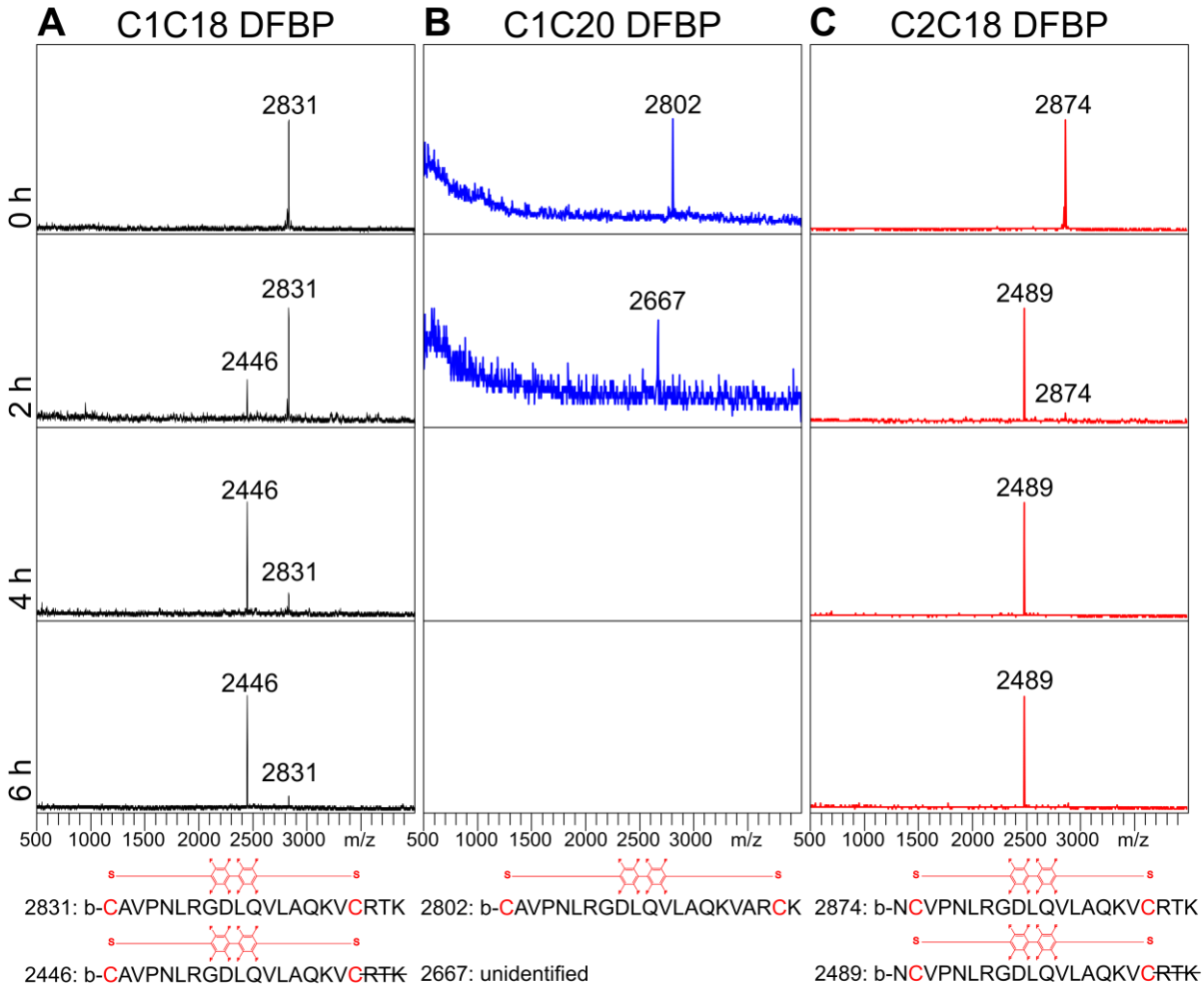

Figure 5.2 | Partial DFBP-cyclized A20FMDV2 candidates display moderate serum stability with exocyclic C-terminal degradation. (A-C) MALDI-ToF spectra of DFBP-cyclized C1C18, C1C20, and C2C18 peptide variants incubated in normal mouse serum for 0, 2, 4, and 6 h at 37 °C. Molecular weights of prominent peaks are shown. No peptide-fragment peaks were observed for C1C20 DFBP at the 4 and 6 h timepoints. Bottom: predicted amino acid sequences of degradation products based on measured molecular weights.

5.2.3 Modification of DFBP-cyclized C1C18 and C2C18 variants and binding characterization

To further stabilize the DFBP-cyclized C1C18 and C2C18 peptides against proteolytic degradation, we turned to non-proteinogenic D-amino acids and naturally occurring analogs for additional amino acid modification (**Figure 5.3A**). As other groups have shown increased serum stability of peptides flanked with D-amino acids,[60] we capped the C-terminus of our peptides with D-alanine (A_D) in an effort to reduce degradation of the exocyclic C-terminal RTK group. Moreover, as the exocyclic C-terminal arginine is readily cleaved by many endopeptidases,[61] we substituted it with D-arginine (R_D) or the nonprotein precursor L-citrulline (Cit) as a way to further limit degradation. These peptide modifications resulted in the synthesis of DFBP-cyclized C2C18 R_DTKA_D (R19R_D; +22A_D) and C2C18 CitTKA_D (R19Cit; +22A_D) for testing. We also attempted to enhance the binding kinetics of our cyclized peptides by substituting the N-terminal proline within the cyclized region with hydroxyproline (P_h), since this modification has previously demonstrated affinity improvements for other peptides.[62] This led to the synthesis of DFBP-cyclized C2C18 P_h R_DTKA_D (P4P_h; R19R_D; +22A_D) for comparison against C2C18 R_DTKA_D DFBP which lacks the hydroxyproline group. Lastly, as the alanines within the cyclized region and the exocyclic C-terminal lysine likely do not contribute to peptide binding, we substituted these amino acids with D-alanine and D-lysine (K_D), respectively, for additional proteolytic stability. Accordingly, DFBP-cyclized C1C18 A_D $R_DTK_DA_D$ (A2A_D; A14A_D; R19R_D; K21K_D; +22A_D) was created to reflect these changes. In total, four modified versions of either DFBP-cyclized C1C18 or C2C18 were synthesized for subsequent binding characterization.

As detailed previously, we compared the K562 cell-binding of these newly modified variants against the original A20FMDV2 peptide and the parental DFBP-cyclized C1C18 and C2C18 peptides. As shown, all DFBP-cyclized modified peptides retain selective binding to K562

αvβ6:mCherry cells with negligible background binding to K562 parental cells (**Figure 5.3B**). Notably, the apparent binding affinities of these modified peptides (C2C18 R_DTKA_D DFBP: 55.3 ± 6.06 nM; C2C18 CitTKA_D DFBP: 75.8 ± 24.0 nM; C2C18 P_h R_DTKA_D DFBP: 67.4 ± 10.5 nM; C1C18 A_D $R_DTK_DA_D$ DFBP: 77.0 ± 16.8 nM), as well as those of the parental DFBP-cyclized C1C18 and C2C18 peptides (85.3 ± 18.6 nM and 70.8 ± 20.3 nM, respectively), did not statistically differ from the affinity of the original A20FMDV2 peptide (63.1 ± 20.6 nM). We did, however, observe less maximal fluorescence signal for the newly modified peptides compared to A20FMDV2, C1C18 DFBP, and C2C18 DFBP. Given their similar affinities, we attributed these differences to reduced fluorescence quantum yield or biotin accessibility of the streptavidin Alexa Fluor 647 stain. Also of importance, the binding affinities observed here differ from the single digit nanomolar values reported for A20FMDV2 previously.[41] These discrepancies likely stem from differences in the binding model (cells versus purified recombinant proteins) and conditions (buffer, temperature, time) used for peptide characterization.

There were no obvious differences when comparing the larger effects of the cyclization schemes and modifications on binding affinity. DFBP-cyclized C1C18 and C2C18 peptides exhibited equivalent apparent binding affinity for K562 αvβ6:mCherry cells, and further stabilizing the C-terminus with D-arginine, citrulline, D-lysine, and/or D-alanine did not impact affinity. Interestingly, substituting proline for hydroxyproline and alanine for D-alanine within the cyclized region did not impact apparent binding affinity, suggesting that these amino acids are not critical for high-affinity αvβ6 binding. The effects of these cyclization schemes and modifications on peptide specificity for the αvβ6 integrin will be evaluated in a later section. Considering that all the newly modified DFBP-cyclized peptides retained their binding affinity for $\alpha v\beta 6^+$ cells, we

advanced forward with these peptides for qualitative and quantitative assessment of serum stability.

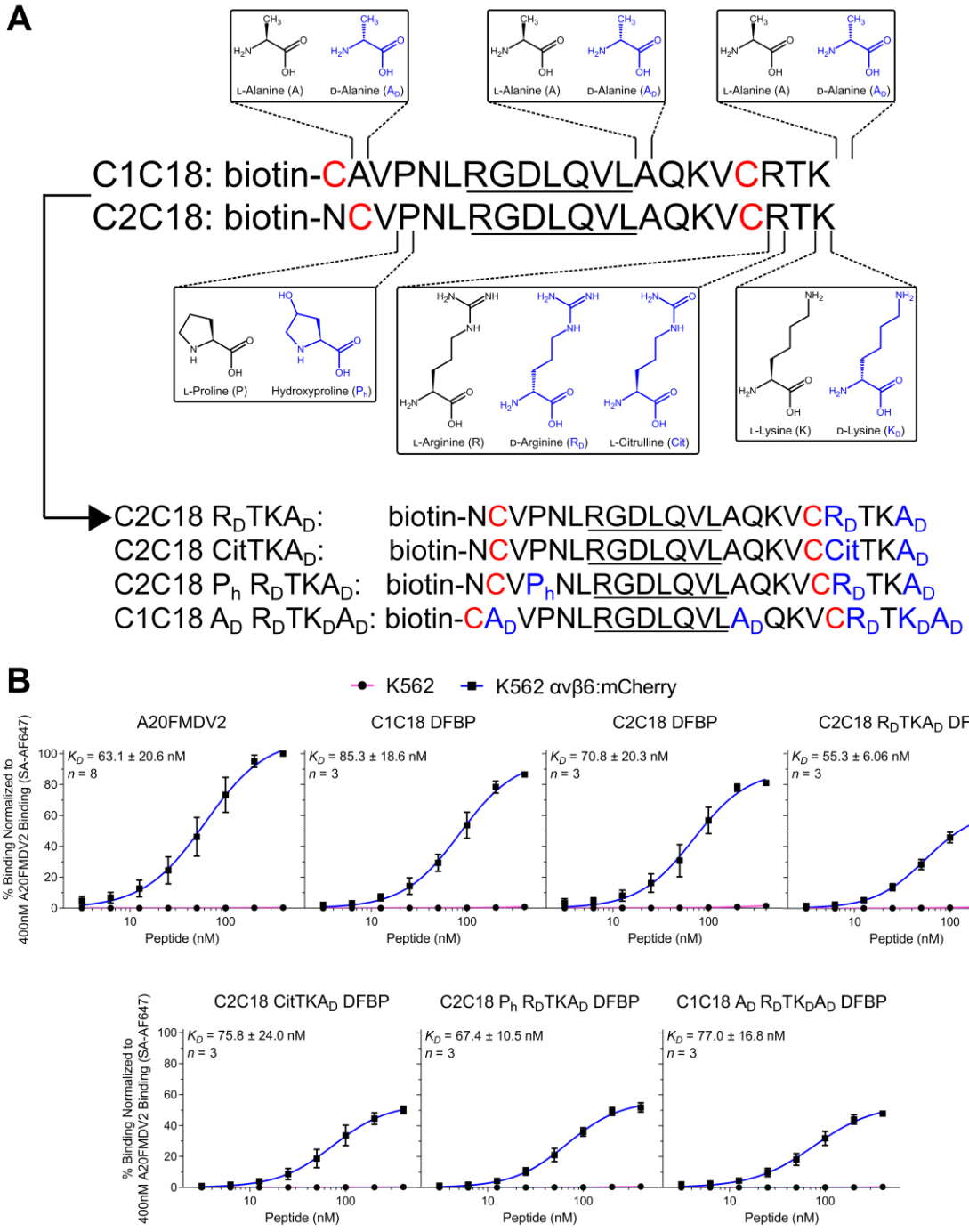

Figure 5.3 | Further modifications to DFBP-cyclized A20FMDV2 peptides do not impact binding αvβ6$^+$ cancer cells. (A) Schematic of modifications made to the sequences of C1C18 DFBP and C2C18 DFBP to further improve their serum stability. Chemical structures of the original (black) and modified (blue) amino acids are shown at positions of incorporation. The

resulting modified peptide sequence are also listed, with cysteine substitutions for DFBP cyclization shown in red and amino acid modifications shown in blue. The RGDLXXL motif that is important for αvβ6 recognition is underlined in all sequences. (B) Flow cytometry binding curves of A20FMDV2, C1C18 DFBP, C2C18 DFBP, and additionally modified peptides to K562 and K562 αvβ6:mCherry cells, normalized to 400nM A20FMDV2 binding to K562 αvβ6:mCherry cells. The curves represent a nonlinear regression of at least three independent experiments in which binding data are fitted to a Hill equation. K_D values were calculated by averaging the individual regression values of the independent experiments. Data points, error bars, and K_D values represent the mean ± s.d.; n = 3-8 independent experiments. K_D values of cyclized and modified peptides were not statistically different than that of the original peptide (P > 0.05, one-way ANOVA with Dunnett's test) and each other (P > 0.05, one-way ANOVA with Tukey's test). SA-AF647, streptavidin Alexa Fluor 647.

5.2.4 MALDI-ToF MS serum stability of additionally modified C1C18 and C2C18 DFBP

We next qualitatively assessed the serum stability of the newly modified peptides by MALDI-ToF MS. Fully intact peptide was still present after 24 h for each of the newly modified peptides (**Figure 5.4A-D**), a large improvement compared to the original DFBP-cyclized C1C18 and C2C18 peptides that were degraded completely within 6 h. Nonetheless, degradation products were still detected at later timepoints and the relative intact peptide signal decreased over time, an indication of slow degradation of each of the peptides. Interestingly, Arg7 of the RGD motif appeared to be a primary target/site for proteolytic cleavage, as a 138 Da smaller degradation product was seen after 8 h for C2C18 R_DTKA_D DFBP, C2C18 P_h R_DTKA_D DFBP, and C1C18 A_D $R_DTK_DA_D$ DFBP (**Figure 5.4A,C-D**). Many degradation products at 24 h show peptides missing even larger fragments between the cysteine-linkages, suggesting that the initial Arg7 cleave accelerated endopeptidase activity. Additionally, the relative signal of the 138 Da smaller degradation product increased over time for C1C18 A_D $R_DTK_DA_D$ DFBP (**Figure 5.4D**), which may signify that the C1C18 cyclization scheme better prevents further internal degradation than the C2C18 configuration after initial Arg7 cleavage. Outside of the cyclized region, we also observed N-terminal cleavage of the biotinylated Asn1 for some of the modified C2C18 peptides

(**Figure 5.4A,C**) as well as C-terminal cleavage at Thr20 for all the modified peptides (**Figure 5.4A-D**). While further peptide design addressing these observed cleavage products warrants future research, the presence of intact cyclized peptides after 24 h in serum demonstrates markedly improved serum stability.

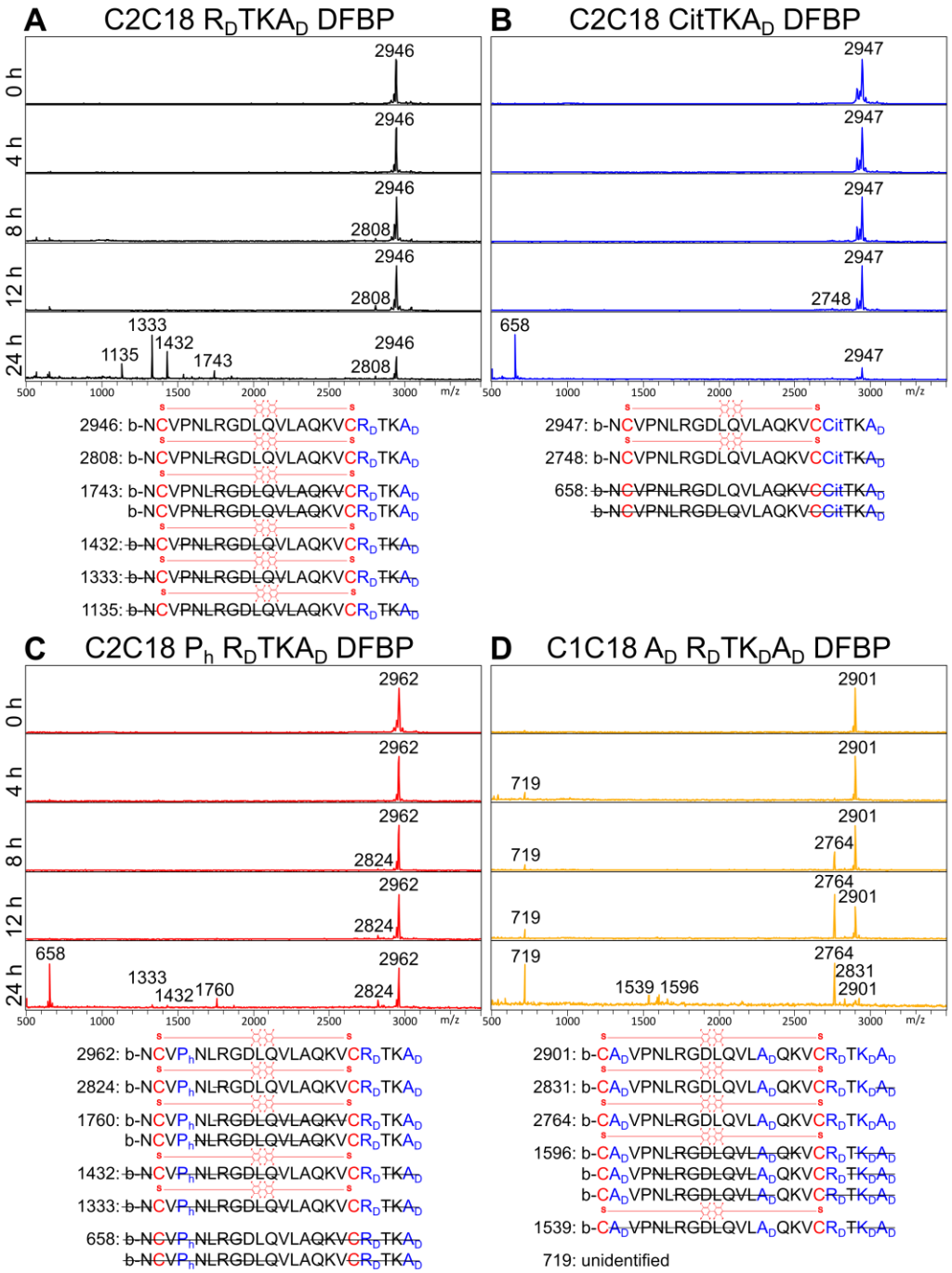

Figure 5.4 | Further modified DFBP-cyclized A20FMDV2 peptides exhibit prolonged serum stability with slow internal arginine cleavage. (A-D) MALDI-ToF spectra of DFBP-cyclized

C2C18 R_DTKA_D, C2C18 $CitTKA_D$, C2C18 P_h R_DTKA_D, and C1C18 A_D $R_DTK_DA_D$ peptides incubated in normal mouse serum for 0, 4, 8, 12, and 24 h at 37 °C. Molecular weights of prominent peaks are shown. Bottom: predicted amino acid sequences of degradation products based on measured molecular weights. For some molecular weights, multiple predictions are listed.

5.2.5 LC-MS serum stability of additionally modified C1C18 and C2C18 DFBP

Since MALDI-ToF MS results are qualitative, we next sought to quantify the rate of degradation in normal mouse serum of the modified DFBP-cyclized C2C18 R_DTKA_D, C2C18 $CitTKA_D$, C2C18 P_h R_DTKA_D, and C1C18 A_D $R_DTK_DA_D$ peptides by LC-MS. Peptides were prepared, treated in serum, and extracted as they were for the MALDI-ToF MS studies before submission for LC-MS analysis. While some of the data points are erratic due to variability in peptide extraction after acetonitrile precipitation of serum proteins, we were able to reasonably fit the LC-MS results to a one phase exponential decay model (**Figure 5.5**). Consistent with the MALDI results, the DFBP-cyclized and additionally modified peptides were found to degrade slowly in serum, with serum half-lives of intact peptides stretching between 4.5-6.6 h. After 24 h, the amount of remaining fully intact peptide in serum for DFBP-cyclized C2C18 R_DTKA_D, C2C18 $CitTKA_D$, C2C18 P_h R_DTKA_D, and C1C18 A_D $R_DTK_DA_D$ ranged tightly at 12.6%, 10.4%, 10.9%, and 8.6%, respectively, demonstrating that they have similar basal stabilities. These results broadly suggest that citrulline and D-arginine substitutions at the peptide C-terminus (R19Cit and $R19R_D$, respectively) confer comparable proteolytic stabilities, whereas substitutions with hydroxyproline and D-alanine in the cyclized region ($P4P_h$, $A2A_D$, and $A14A_D$, respectively) have negligible impact on intact peptide serum stability.

For C1C18 A_D $R_DTK_DA_D$ DFBP specifically, LC-MS also revealed significant accumulation of the 138 Da smaller degradation product that was identified previously by MALDI-ToF (**Figure**

S5.2). After 12 h in serum, the amount of the 138 Da smaller degradation product peaked, representing nearly 60% of the starting (t = 0 h) fully intact peptide; even after 24 h in serum, the presence of the degradation product was still significant, representing over 40% of the starting fully intact peptide. These data indicate that internal cleavage of Arg7 from the RGD motif is a primary degradation pathway for these modified peptides and that the resulting product remains relatively stable for the C1C18 A_D $R_DTK_DA_D$ DFBP formulation despite the cleavage. Thus, even more stable cyclized peptides could be potentially made by further modifying the Arg7 in the RGD motif.

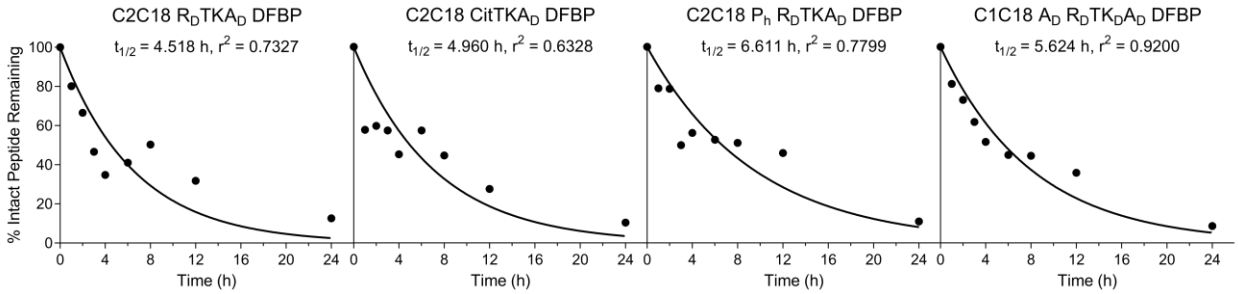

Figure 5.5 | Further modified DFBP-cyclized A20FMDV2 peptides have long and comparable serum half-lives. Stability of DFBP-cyclized C2C18 R_DTKA_D, C2C18 CitTKA_D, C2C18 P_h R_DTKA_D, and C1C18 A_D $R_DTK_DA_D$ peptides over a 24-h incubation in normal mouse serum, as measured by LC-MS. Values are normalized to the 0 h timepoint. Curves represent a non-linear regression of one independent experiment assuming one phase exponential decay.

5.2.6 Assessment of Arginine Mimetics for Modification of the RGD Motif

Given the previous observations, we were interested in substituting arginine within the RGD motif with non-proteinogenic mimetics to prolong the already enhanced stability of our modified DFBP-cyclized A20FMDV2 variants. Phenylalanine analogs have previously demonstrated to be good mimetics for arginine replacement in other peptides.[63] We therefore synthesized three versions of DFBP-cyclized C2C18 containing either 4-amino-L-phenylalanine ($_A$F), citrulline, or 4-guanidino-L-phenylalanine ($_G$F) as substitutions for Arg7 within the RGD motif (**Figure S5.3A**). These peptides were respectively named C2C18 $_A$FGD $RTKA_D$ DFBP, C2C18 CitGD DFBP, and C2C18

$_{G}$FGD R$_{D}$TKA$_{D}$ DFBP. The three peptides have varying degrees of C-terminal modifications, as some of these peptides were synthesized before we discovered the benefit of having D-amino acids at the C-terminus. We assumed these differences would not affect our evaluation of binding potential since we showed earlier that these modifications do not influence peptide affinity for αvβ6.

C2C18 $_{A}$FGD RTKA$_{D}$ DFBP and C2C18 $_{G}$FGD R$_{D}$TKA$_{D}$ DFBP completely lost the ability to bind K562 αvβ6:mCherry cells, whereas C2C18 CitGD DFBP retained some selective binding to these cells at high concentrations, albeit low and non-saturating (**Figure S5.3B**). Owing to the highly conserved nature of the RGD motif in integrin binding, these negative results are not surprising. Other groups have also reported drastic loss of binding for an αvβ3-specific peptide when replacing arginine in the RGD motif with closely resembling homologues.[64] Nonetheless, the small binding we observed with a citrulline substitution is promising, warranting future investigation with a more expansive panel of mimetics and analogs.

5.2.7 Non-specific binding of DFBP-cyclized and modified A20FMDV2 peptides to A375P cells

As there are eight known integrins that recognize the RGD motif (αvβ1, αvβ3, αvβ5, αvβ6, αvβ8, α5β1, α8β1, and αIIbβ3),[65] it is critical that RGD-containing peptides developed for diagnostic and therapeutic applications are highly specific for their targeted integrin with minimal off-target binding. The matched K562 cell model we used previously only expresses the α5β1 integrin, and thus does not rigorously test the non-specific binding of our engineered A20FMDV2 peptides to other RGD-recognizing integrins closely related to αvβ6. Accordingly, we next sought to compare the non-specific integrin binding of our serum-stabilized peptides against the original A20FMDV2 peptide and the parental DFBP-cyclized C1C18 and C2C18 peptides to melanoma A375P cells,

which expresses the αvβ3, αvβ5, αvβ8, and α5β1 integrins but not the β6 integrin.[66] We decided to use A375P cells as a proxy to distinguish how our peptide cyclizations and modifications affect promiscuous integrin binding. To this end, we evaluated binding of A20FMDV2 and DFBP-cyclized C1C18, C2C18, C2C18 R_DTKA_D, C2C18 CitTKA_D, C2C18 P_h R_DTKA_D, and C1C18 A_D $R_DTK_DA_D$ to A375P cells at four high peptide concentrations (125, 250, 500, and 1000 nM) by flow cytometry.

We demonstrate that DFBP-cyclized C1C18 and C2C18 exhibit high non-specific binding for A375P cells, with on average 462 ± 158% and 575 ± 196% binding, respectively, relative to the original A20FMDV2 peptide across all four concentrations (**Figure 5.6**). These results are consistent with findings made by Wagstaff et al.,[67] which showed that disulfide cyclization of the A20FMDV2 peptide at certain positions altered the backbone dynamics of the peptide, driving loss of αvβ6 specificity. The only exception that they found not to affect A20FMDV2 specificity was a complete N-to-C terminal disulfide cyclization, but we demonstrated earlier that this cyclization scheme likely underwent rapid degradation in serum (**Figure 5.2B**, C1C20 DFBP). Interestingly, even higher non-specific binding was shown for C2C18 R_DTKA_D DFBP (1072 ± 612% on average relative to A20FMV2), suggesting that C-terminal substitution with D-arginine (R19R_D) has structural effects that aggravate promiscuous integrin binding.

Most notably, DFBP-cyclized C2C18 CitTKA_D, C2C18 P_h R_DTKA_D, and C1C18 A_D $R_DTK_DA_D$ peptides did not display high non-specific binding, showing on average 22 ± 6%, 60 ± 16%, 145 ± 96% binding relative to the original A20FMDV2 peptide, respectively, across all four concentrations. While some of these effects may be attributed to the reduced binding fluorescence we observed previously with these peptides (~50%, **Figure 5.3B**), it does not completely account for their low non-specific binding, especially for C2C18 CitTKA_D DFBP. Furthermore, the C2C18

R_DTKA_D DFBP peptide has high non-specific binding despite also exhibiting reduced binding fluorescence (~60%, **Figure 5.3B**), so these two observations do not always track with each other. This data thus suggests that the electrostatic effects of the citrulline substitution ($Cit19R_D$), the hydrogen bonding or stereoelectronic effects of the hydroxyproline substitution ($P4P_h$), and the structural effects of the D-alanine substitutions ($A2A_D$ and $A14A_D$) offset the high non-specific integrin binding observed for the DFBP-cyclized C1C18, C2C18, and C2C18 R_DTKA_D peptides, with some ($Cit19R_D$) instilling even improved αvβ6 integrin specificity compared to the original A20FMDV2 peptide. Combined with their greatly enhanced serum stability, the DFBP-cyclized C2C18 $CitTKA_D$, C2C18 P_h R_DTKA_D, and C1C18 A_D $R_DTK_DA_D$ peptides demonstrate the potential to increase αvβ6 targeting for high-fidelity *in vivo* diagnostic and therapeutic applications.

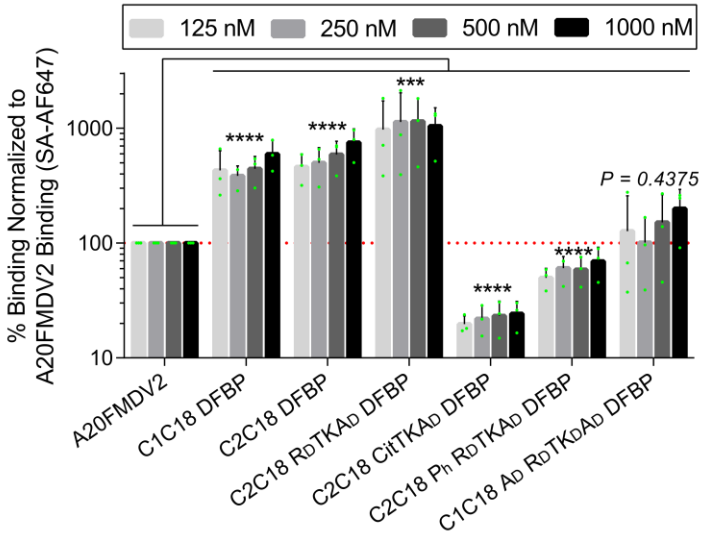

Figure 5.6 | Citrulline, hydroxyproline, and D-alanine substitutions reduced non-specific integrin binding of DFBP-cyclized A20FMDV2 peptides. Non-specific binding of DFBP-cyclized and modified peptides to A375P cells by flow cytometry, normalized to 125, 250, 500, and 1000 nM A20FMDV2 binding. Values that fall above the dotted red line represent increased non-specific binding compared to the original A2FMDV2 peptide, whereas those that fall below represent decreased non-specific binding. The green dots represent the data from individual experiments. Columns and error bars represent the mean ± s.d.; $n = 3$ independent experiments. For statistical testing, values from independent experiments and all four concentrations were pooled together for each peptide before comparison to the original peptide ($n = 12$, $P > 0.05$, ***$P < 0.001$, ****$P < 0.0001$, paired one-way ANOVA with Dunnett's test). SA-AF647, streptavidin Alexa Fluor 647.

5.3 DISCUSSION AND FUTURE WORK

The use of peptides for cancer targeting is limited by their rapid degradation from proteases *in vivo*. High and repeated doses of peptides or PEGylation are thus often required to achieve sufficient delivery to the tumor site, which can negatively impact the sensitivity and safety of medical applications that use these ligands. The virus-derived A20FMDV2 peptide, despite its high affinity and specificity for the tumor-associated integrin αvβ6, is one such peptide that suffers from poor proteolytic stability, hindering its translation into the clinic for cancer imaging and therapy. Modification of A20FMDV2 to bolster its resistance against proteases is difficult due to the highly adapted and conserved structure of the peptide; its 20-amino acid sequence contains a short β sheet, followed by the tripeptide RGD motif, and then lastly a longer 3_{10} helix that together form a loop structure.[38,39] The amino acids in the β sheet and 3_{10} helix that flank the RGD motif strongly influence the affinity and specificity of A20FMDV2 for αvβ6,[57] and thus modifying these amino acids runs the risk of compromising either or both of these attributes that are equally critical for the peptide's successful translation.

In this study, we synthesized a panel of more than 10 re-engineered A20FMDV2 variants that were cyclized by cysteine perfluoroarylation with DFBP and further modified with D-amino acids and non-proteinogenic analogs to improve the A20FMDV2 peptide's serum stability without sacrificing its affinity and specificity for αvβ6. From this panel, we identified three variants (DFBP-cyclized C2C18 CitTKA$_D$, C2C18 P$_h$ R$_D$TKA$_D$, and C1C18 A$_D$ R$_D$TK$_D$A$_D$) that persist in serum for ≥ 24 h and retain binding affinity and specificity to αvβ6$^+$ cells, with the first variant demonstrating even better αvβ6 specificity than the original A20FMDV2 peptide. Given these enhanced properties, future *in vivo* usage of the cyclization and modifications reported herein

could greatly improve the bioavailability of the A20FMDV2 peptide for applications concerning cancer diagnosis and treatment.

Despite our improvements to the A20FMDV2 peptide, there are opportunities for further peptide optimization and design. In our MALDI-ToF MS serum stability studies, we observed N-terminal cleavage of the biotinylated asparagine in modified C2C18 DFBP formulations as well as C-terminal cleavage at or adjacent to threonine for all the cyclized formulations. Hung *et al.* reported that this N-terminal asparagine and C-terminal threonine can be substituted with D-amino acid analogs to improve A20FMDV2 serum stability without diminishing binding affinity.[59] They further showed that Lys16 following the RGDLXXL motif can be replaced with L-ornithine, L-2,4-diaminobutryic acid, or L-2,3-diaminopropionic acid and that Leu13 within the RGDLXXL motif can be replaced with L-2-aminoisobutryic acid or L-norvaline without reducing αvβ6 binding. Accordingly, future work combining these modifications with the cyclization and modifications described here could lead to the generation of "super-stable" A20FMDV2 peptide variants. We also speculate that finding suitable mimetics for arginine substitution in the RGD motif, while difficult, will be equally important for this goal, as cleavage of this amino acid potentially accounted for a large portion of observed degradation products in our experiments.

Another facet of our re-engineered A20FMDV2 variants that we do not explore in this study is their potential for decreased immunogenicity. Our lab has previously shown that repeated doses of PEG-containing micelles loaded with melittin peptides derived from bee venom can cause fatal anaphylactic reactions in immunocompetent mice that are characterized by high titers of serum IgM antibodies that bind PEG.[68] Switching to micelles loaded with melittin peptides modified with D-amino acids was found to eliminate this immune hypersensitivity, suggesting that the unmodified melittin peptides served as adjuvants to induce anti-PEG antibody responses. While

the A20FMDV2 peptide does not appear to be immunogenic in humans after a single microdose,[42] its derivation from FMDV should raise concerns for human application, especially with PEGylation and after repeated doses. Given all this, the incorporation of D-amino acids and non-proteinogenic analogs into the A20FMDV2 sequence described in this work may also lower the potential immunogenicity of this virus-derived peptide, further increasing its safety profile for clinical applications.

5.4 MATERIALS AND METHODS

5.4.1 Materials

Solvents, including N,N-dimethylformamide (DMF), dichloromethane (DCM), trifluoroacetic acid (TFA), etheyl ether anhydrous, and acetonitrile (ACN), were purchased from Fisher Scientific (Waltham, MA). Standard protected L-amino acids, D(+)-Biotin, Fmoc-D-Ala-OH, Fmoc-D-Lys(Boc)-OH, Fmoc-D-Arg(Pbf)-OH, Fmoc-Cit-OH, Fmoc-L-Hyp(tBu)-OH, Fmoc-L-Phe(4-Boc-amino)-OH, Fmoc-L-Phe(4-Boc2-guanidino)-OH, Rink Amide resin, ethyl (hydroxyamino)cyanoacetate (Oxyma), N,N'-diisopropylcarbodiimide (DIC), piperidine, and tris-(carboxyethyl)phosphine hydrochloride (TCEP) were purchased from Novabiochem (Darmstadt, Germany), AnaSpec (Fremont, CA), Chem-Impex International (Wood Dale, IL), and Sigma-Aldrich (St. Louis, MO). 1,3-dimethoxybenzene (DMB), triisopropylsilane (TIPS), 1,2-ethanedithiol (EDT), and decafluorobiphenyl (DFBP) were purchased from Acros Organics (Fair Lawn, NJ). The QuantTag Biotin Quantification Kit was purchased from Vector Laboratories (Burlingame, CA). RPMI and DPBS with magnesium and calcium were purchased from Corning (Corning, NY). DMEM, fetal bovine serum (FBS), and StemPro Accutase were purchased from Life Technologies (Carlsbad, CA). Zombie Violet and Streptavidin Alexa Fluor 647 were

purchased from BioLegend (San Diego, CA). Bovine serum albumin was purchased from Miltenyi Biotec (Bergisch Gladbach, Germany). 4% paraformaldehyde was purchased from Alfa Aesar (Haverhill, MA). Normal mouse serum for stability studies was prepared in-house. Briefly, mouse whole blood was collected by cardiac puncture into BD Microtainer SST tubes (Becton Dickinson, Franklin Lanes, NJ) and allowed to clot for 30 min. Tubes were then centrifuged according to the manufacturer's instructions and serum was collected and stored at -20 °C until needed. All animal handling protocols were approved by the University of Washington Institutional Animal Care and Use Committee.

5.4.2 Peptide synthesis

Sequences of synthesized peptides are listed in **Table S5.1**. Peptide synthesis was performed with a Liberty Blue HT12 automated microwave peptide synthesizer (CEM, Matthews, NC) by Fmoc solid-phase peptide synthesis on a Rink Amide resin support at 0.1 mmol scale. The resin was swelled in 50:50 (v/v) DMF:DCM for 20 min prior to synthesis. Deprotection of Fmoc groups occurred in 20% piperidine in DMF at 90 °C for 65 sec followed by three washes with DMF. Carbodiimide chemistry was used to activate amino acids (AA) at a molar ratio of 1:2:1 AA:DIC:Oxyma in DMF and couplings occurred at 90 °C for 4 min, with the exception for the first amino acid in the synthesis process which was allowed to couple to the resin for 10 min. Double couplings were used for Fmoc-Arg(Pbf)-OH and Fmoc-D-Arg(Pbf)-OH due to the large Pbf group that sterically hinders coupling of these amino acids. After synthesis, side-chain deprotection and cleavage of the peptides from the resin was carried out in 89:5:2.5:2.5:1 (v/v) TFA:DMB:TIPS:EDT:H_2O for 4 h at room temperature with end-over-end mixing. EDT was included in the cleavage cocktail only for cysteine-containing peptides. Cleaved peptides were then double precipitated in cold ethyl ether anhydrous and pelleted at 4500 xg for 5 min at 4°C

after each precipitation before drying overnight under vacuum. A small amount of cleaved product was retained and analyzed by MALDI-ToF MS (Bruker AutoFlexII, Billerica, MA) to confirm proper cleavage and deprotection of each peptide. For some of the D-arginine containing peptides, a second 1 h cleavage of the precipitated crude peptide was required due to challenges with removing the Pbf protecting group on D-arginine. Those cleavage reactions were similarly precipitated in ether before being dried overnight. The next day, crude peptides were dissolved in methanol and re-precipitated in ether to wash away remaining protecting groups. Finally, the crude peptide was dried again overnight under vacuum before HPLC purification.

5.4.3 Reverse-phase HPLC purification

Crude peptides were resuspended at 80 mg/mL in 20% ACN in H_2O containing 0.1% TFA (v/v), syringe filtered, and purified to >95% purity by reverse-phase HPLC on an Agilent 1260 Infinity (Santa Clara, CA) equipped with a Synergi 4u Fusion-RP C18 semipreparative column (Phenomenex). Monitoring 220 nm absorbance, a flow rate of 5 mL/min and a 20-65% 8-min linear solvent gradient of ACN in H_2O with 0.1% TFA were used for purification of these peptides. The molecular weights of purified peptides were confirmed by MALDI-ToF MS and were consistently within 1-2 g/mol of the expected values. After purification, organic solvent was removed by rotary evaporation and peptides were lyophilized and stored at -20 °C until further usage.

5.4.4 Peptide cyclization by perfluoroarylation

In-solution cyclization of peptides with DFBP was conducted as previously described,[54] but with some modifications. Briefly, 20 mg purified linear peptide was dissolved in 3mL DMF with 2 molar equivalents of each TCEP and DFBP. Then, 1.5mL 50mM tris base in DMF was freshly

prepared and added to the reaction before vortexing (4.5mL total). After an overnight incubation at room temperature with end-over-end mixing, the cyclization reaction was diluted in 10mL H_2O containing 0.1% TFA and peptide was desalted with a Sep-Pak C18 cartridge (Waters, Milford, MA). Peptide was eluted from the cartridge in 50:50 (v/v) ACN:H_2O containing 0.1% TFA and proper cyclization was confirmed by MALDI-ToF MS. Organic solvent was subsequently removed by rotary evaporation and cyclized peptides were lyophilized and stored at -20 °C until further usage.

5.4.5 Cell line culture

The K562 and A375P cell lines used in binding studies were purchased from ATCC. The K562 αvβ6:mCherry cell line was a kind gift from Audrey Olshefsky (Pun and King Labs, University of Washington) and was generated by nucleofection of K562 cells with two linear DNA fragments, one encoding the αv integrin and a puromycin resistance gene and the other encoding the β6 integrin and a fluorescent mCherry reporter. After nucleofection, K562 αvβ6:mCherry cells were purified by puromycin selection and FACS sorting. K562 and K562 αvβ6:mCherry suspension cells were cultured in RPMI 1640 medium with L-glutamine and 10% FBS. Adherent A375P cells were cultured in high-glucose DMEM medium with L-glutamine and 10% FBS and were detached with StemPro Accutase prior to flow cytometry binding studies to preserve extracellular integrin expression.

5.4.6 Flow cytometry binding studies

Biotinylated peptide stocks were prepared in H_2O at approximately 5 mM and the exact concentration was measured using a QuantTag Biotin Quantification Kit. Stocks were stored at 4 °C and used for binding studies within two weeks of preparation. Prior to binding, cells were pre-

stained with Zombie Violet in DPBS (0.2 μL per 100 μL per 10^6 cells) for 15 min at room temperature for dead cell discrimination. Meanwhile, peptide stocks were serially diluted in DPBS with calcium and magnesium over ice. Cells were then washed at 4 °C with DPBS 1% BSA to neutralize the Zombie Violet, plated in a U-bottom black 96-well plate (2×10^5 per well) over ice, and stained with 100 μL peptide solutions for 20 min at 4 °C. Cells were then washed twice with 200 μL cold DPBS and incubated with 100 μL streptavidin Alexa Fluor 647 in DPBS (1:500) for 20 min at 4 °C. Cells were subsequently washed twice as before and resuspended in 200 μL DPBS 0.1% PFA for assaying on an Attune NxT Flow Cytometer (Life Technologies, Carlsbad, CA). Data was analyzed by FlowJo v10 software (Becton Dickinson, Ashland, OR) and median fluorescence intensity of singlet live cell events were used as measurements of binding. Data was normalized to A20FMDV2 binding prior to generating binding curves, apparent K_D values, bar graphs, and statistical testing in GraphPad Prism 6 software (San Diego, CA).

5.4.7 MALDI ToF MS serum stability

Peptides were incubated and extracted from serum as previously described,[54,55] but with some adjustments to limit serum protein carryover during extractions. Briefly, peptide stocks were diluted to 10 mg/mL in H_2O and subsequently diluted 1:10 (v/v) in normal mouse serum for incubation at 37 °C in an incubator. At specified timepoints, 40 μL of the peptide/serum mixture was removed and precipitated in an equal volume of cold ACN. Precipitated serum proteins were pelleted by centrifugation at 15000 xg for 5 min and the supernatant with peptides (80 μL) was collected. To extract any remaining peptides, 80 μL cold 1:3 (v/v) H_2O:ACN was added to the pellet, sonicated for 10 min, and centrifuged as before. The resulting supernatant was combined with the old one and dried under vacuum on a Savant ISS110 SpeedVac Concentrator (Thermo Fisher, Waltham, MA). The peptide pellet was then resuspended in 50 μL H_2O and sonicated for

10 min. A small aliquot of resuspended peptide was further diluted 1:10 (v/v) in H_2O and analyzed by MALDI-ToF MS. Resulting mass spectrums at the different timepoints were aligned and plotted in FlexAnalysis software (Bruker, Billerica, MA). Predicted sequences of degradation products based on product molecular weight were determined using a custom Java program called stability.jar (https://github.com/juliomarcopineda/peptide-serum-stability/releases).[55]

5.4.8 LC-MS serum stability

Remaining extracted peptides from MALDI ToF MS serum stability studies were dried as before and stored as dried pellets at room temperature. Within a day of LC-MS runs, pellets were resuspended in 100 µL 95:5 (v/v) H_2O:ACN, sonicated for 10 min, and submitted for LC-MS analysis at the University of Washington School of Pharmacy Mass Spectrometry Center. Samples were injected on a TripleTOF 5600+ instrument (AB Sciex, Framingham, MA) equipped with a 2.1 mm x 50 mm BEH C18 column (Waters, Milford, MA). Peptides were separated over a 5-100% 4-min linear solvent gradient of ACN in H_2O with 0.1% formic acid, and peak area corresponding to the peptide molecular weight was used for quantification of remaining intact peptide. Peak areas across different timepoints were normalized to that of a 0 h control sample that was extracted immediately after mixing the peptide with the serum. Exponential decay curves were generated in GraphPad Prism 6 software.

5.5 AUTHOR CONTRIBUTIONS

D. L. S. conceptualization and project administration; D. L. S. and I. I. C. methodology and investigation; I. I. C. validation, formal analysis, visualization, data curation, and writing-original draft; D. L. S. and S. H. P. resources; D. L. S., S. H. P., and I. I. C. writing - review and editing; D. L. S., S. H. P., and M. C. J. supervision and funding acquisition.

5.6 ACKNOWLEDGEMENTS

This research was supported by the National Institutes of Health under grant nos. R01NS118247 (to D. L. S.), R21NS099654 (to D. L. S.), and R01CA177272 (to S. H. P.), and by a National Science Foundation Graduate Research Fellowship under Grant No. DGE-1762114 (to I. I. C.). The content is solely the responsibility of the authors and does not necessarily represent the official views of the National Institutes of Health. We are grateful to Dr. Scott Edgar (Mass Spectrometry Center, UW School of Pharmacy) for running and analyzing LC-MS samples and Julio Pineda (former Department of Bioengineering, University of Washington) for development of the peptide fragment analyzer software used to predict the sequences of degradation products in our MALDI-ToF MS studies. We also thank Audrey Olshefsky (Department of Bioengineering, University of Washington) for providing the K562 αvβ6:mCherry cell line.

5.7 REFERENCES

(1) Siegel, R. L.; Miller, K. D.; Jemal, A. Cancer Statistics, 2020. *CA: A Cancer Journal for Clinicians* **2020**, *70* (1), 7–30.
(2) Huttenlocher, A.; Horwitz, A. R. Integrins in Cell Migration. *Cold Spring Harbor perspectives in biology* **2011**, *3* (9), a005074.
(3) Hamidi, H.; Ivaska, J. Every Step of the Way: Integrins in Cancer Progression and Metastasis. *Nature Reviews Cancer* **2018**, *18* (9), 533–548.
(4) Munshi, H. G.; Stack, M. S. Reciprocal Interactions between Adhesion Receptor Signaling and MMP Regulation. *Cancer and Metastasis Reviews* **2006**, *25* (1), 45–56.
(5) Khan, Z.; Marshall, J. F. The Role of Integrins in TGFβ Activation in the Tumour Stroma. *Cell and tissue research* **2016**, *365* (3), 657–673.
(6) Sun, C.-C.; Qu, X.-J.; Gao, Z.-H. Arginine-Glycine-Aspartate–Binding Integrins as Therapeutic and Diagnostic Targets. *American Journal of Therapeutics* **2016**, *23* (1), e198–e207.
(7) Raab-Westphal, S.; Marshall, J. F.; Goodman, S. L. Integrins as Therapeutic Targets: Successes and Cancers. *Cancers* **2017**, *9* (9), 110.
(8) Breuss, J. M.; Gallo, J.; DeLisser, H. M.; Klimanskaya, I. V; Folkesson, H. G.; Pittet, J. F.; Nishimura, S. L.; Aldape, K.; Landers, D. V; Carpenter, W. Expression of the Beta 6 Integrin Subunit in Development, Neoplasia and Tissue Repair Suggests a Role in Epithelial Remodeling. *Journal of Cell Science* **1995**, *108* (6), 2241–2251.
(9) Reader, C. S.; Vallath, S.; Steele, C. W.; Haider, S.; Brentnall, A.; Desai, A.; Moore, K. M.; Jamieson, N. B.; Chang, D.; Bailey, P.; Scarpa, A.; Lawlor, R.; Chelala, C.; Keyse, S. M.;

Biankin, A.; Morton, J. P.; Evans, T. R. J.; Barry, S. T.; Sansom, O. J.; Kocher, H. M.; Marshall, J. F. The Integrin Avβ6 Drives Pancreatic Cancer through Diverse Mechanisms and Represents an Effective Target for Therapy. *The Journal of Pathology* **2019**, *249* (3), 332–342.

(10) Patsenker, E.; Wilkens, L.; Banz, V.; Österreicher, C. H.; Weimann, R.; Eisele, S.; Keogh, A.; Stroka, D.; Zimmermann, A.; Stickel, F. The Avβ6 Integrin Is a Highly Specific Immunohistochemical Marker for Cholangiocarcinoma. *Journal of Hepatology* **2010**, *52* (3), 362–369.

(11) Peng, Z.-W.; Ikenaga, N.; Liu, S. B.; Sverdlov, D. Y.; Vaid, K. A.; Dixit, R.; Weinreb, P. H.; Violette, S.; Sheppard, D.; Schuppan, D.; Popov, Y. Integrin Avβ6 Critically Regulates Hepatic Progenitor Cell Function and Promotes Ductular Reaction, Fibrosis, and Tumorigenesis. *Hepatology* **2016**, *63* (1), 217–232.

(12) Elayadi, A. N.; Samli, K. N.; Prudkin, L.; Liu, Y.-H.; Bian, A.; Xie, X.-J.; Wistuba, I. I.; Roth, J. A.; McGuire, M. J.; Brown, K. C. A Peptide Selected by Biopanning Identifies the Integrin Avβ6 as a Prognostic Biomarker for Nonsmall Cell Lung Cancer. *Cancer Research* **2007**, *67* (12), 5889–5895.

(13) Yan, P.; Zhu, H.; Yin, L.; Wang, L.; Xie, P.; Ye, J.; Jiang, X.; He, X. Integrin Avβ6 Promotes Lung Cancer Proliferation and Metastasis through Upregulation of IL-8-Mediated MAPK/ERK Signaling. *Translational oncology* **2018**, *11* (3), 619–627.

(14) Koopman Van Aarsen, L. A.; Leone, D. R.; Ho, S.; Dolinski, B. M.; McCoon, P. E.; LePage, D. J.; Kelly, R.; Heaney, G.; Rayhorn, P.; Reid, C.; Simon, K. J.; Horan, G. S.; Tao, N.; Gardner, H. A.; Skelly, M. M.; Gown, A. M.; Thomas, G. J.; Weinreb, P. H.; Fawell, S. E.; Violette, S. M. Antibody-Mediated Blockade of Integrin Avβ6 by a Transforming Growth Factor-β–Regulated Mechanism. *Cancer Research* **2008**, *68* (2), 561–570.

(15) Hazelbag, S.; Kenter, G. G.; Gorter, A.; Dreef, E. J.; Koopman, L. A.; Violette, S. M.; Weinreb, P. H.; Fleuren, G. J. Overexpression of the Avβ6 Integrin in Cervical Squamous Cell Carcinoma Is a Prognostic Factor for Decreased Survival. *The Journal of Pathology* **2007**, *212* (3), 316–324.

(16) Moore, K. M.; Thomas, G. J.; Duffy, S. W.; Warwick, J.; Gabe, R.; Chou, P.; Ellis, I. O.; Green, A. R.; Haider, S.; Brouilette, K.; Saha, A.; Vallath, S.; Bowen, R.; Chelala, C.; Eccles, D.; Tapper, W. J.; Thompson, A. M.; Quinlan, P.; Jordan, L.; Gillett, C.; Brentnall, A.; Violette, S.; Weinreb, P. H.; Kendrew, J.; Barry, S. T.; Hart, I. R.; Jones, J. L.; Marshall, J. F. Therapeutic Targeting of Integrin Avβ6 in Breast Cancer. *JNCI: Journal of the National Cancer Institute* **2014**, *106* (8).

(17) Hsiao, J.-R.; Chang, Y.; Chen, Y.-L.; Hsieh, S.-H.; Hsu, K.-F.; Wang, C.-F.; Tsai, S.-T.; Jin, Y.-T. Cyclic Avβ6-Targeting Peptide Selected from Biopanning with Clinical Potential for Head and Neck Squamous Cell Carcinoma. *Head & Neck* **2010**, *32* (2), 160–172.

(18) Yang, G.-Y.; Guo, S.; Dong, C.-Y.; Wang, X.-Q.; Hu, B.-Y.; Liu, Y.-F.; Chen, Y.-W.; Niu, J.; Dong, J.-H. Integrin Avβ6 Sustains and Promotes Tumor Invasive Growth in Colon Cancer Progression. *World journal of gastroenterology* **2015**, *21* (24), 7457–7467.

(19) Ahmed, N.; Riley, C.; Rice, G. E.; Quinn, M. A.; Baker, M. S. Avβ6 Integrin-A Marker for the Malignant Potential of Epithelial Ovarian Cancer. *Journal of Histochemistry & Cytochemistry* **2002**, *50* (10), 1371–1379.

(20) Zhuang, Z.; Zhou, R.; Xu, X.; Tian, T.; Liu, Y.; Liu, Y.; Lian, P.; Wang, J.; Xu, K. Clinical Significance of Integrin Avβ6 Expression Effects on Gastric Carcinoma Invasiveness and Progression via Cancer-Associated Fibroblasts. *Medical Oncology* **2013**, *30* (3), 580.

(21) Regezi, J. A.; Ramos, D. M.; Pytela, R.; Dekker, N. P.; Jordan, R. C. K. Tenascin and B6 Integrin Are Overexpressed in Floor of Mouth in Situ Carcinomas and Invasive Squamous Cell Carcinomas. *Oral Oncology* **2002**, *38* (4), 332–336.
(22) Bates, R. C.; Bellovin, D. I.; Brown, C.; Maynard, E.; Wu, B.; Kawakatsu, H.; Sheppard, D.; Oettgen, P.; Mercurio, A. M. Transcriptional Activation of Integrin B6 during the Epithelial-Mesenchymal Transition Defines a Novel Prognostic Indicator of Aggressive Colon Carcinoma. *The Journal of Clinical Investigation* **2005**, *115* (2), 339–347.
(23) Desnoyers, A.; González, C.; Pérez-Segura, P.; Pandiella, A.; Amir, E.; Ocaña, A. Integrin Avβ6 Protein Expression and Prognosis in Solid Tumors: A Meta-Analysis. *Molecular Diagnosis & Therapy* **2020**, *24* (2), 143–151.
(24) Busk, M.; Pytela, R.; Sheppard, D. Characterization of the Integrin Alpha v Beta 6 as a Fibronectin-Binding Protein. *Journal of Biological Chemistry* **1992**, *267* (9), 5790–5796.
(25) Thomas, G. J.; Poomsawat, S.; Lewis, M. P.; Hart, I. R.; Speight, P. M.; Marshall, J. F. Avβ6 Integrin Upregulates Matrix Metalloproteinase 9 and Promotes Migration of Normal Oral Keratinocytes. *Journal of Investigative Dermatology* **2001**, *116* (6), 898–904.
(26) Thomas, G. J.; Hart, I. R.; Speight, P. M.; Marshall, J. F. Binding of TGF-B1 Latency-Associated Peptide (LAP) to Avβ6 Integrin Modulates Behaviour of Squamous Carcinoma Cells. *British journal of cancer* **2002**, *87* (8), 859–867.
(27) Annes, J. P.; Chen, Y.; Munger, J. S.; Rifkin, D. B. Integrin Avβ6-Mediated Activation of Latent TGF-Beta Requires the Latent TGF-Beta Binding Protein-1. *The Journal of cell biology* **2004**, *165* (5), 723–734.
(28) Shi, M.; Zhu, J.; Wang, R.; Chen, X.; Mi, L.; Walz, T.; Springer, T. A. Latent TGF-β Structure and Activation. *Nature* **2011**, *474* (7351), 343–349.
(29) Thomas, G. J.; Lewis, M. P.; Hart, I. R.; Marshall, J. F.; Speight, P. M. Avβ6 Integrin Promotes Invasion of Squamous Carcinoma Cells through Up-Regulation of Matrix Metalloproteinase-9. *International Journal of Cancer* **2001**, *92* (5), 641–650.
(30) Gu, X.; Niu, J.; Dorahy, D. J.; Scott, R.; Agrez, M. V. Integrin Avβ6-Associated ERK2 Mediates MMP-9 Secretion in Colon Cancer Cells. *British Journal of Cancer* **2002**, *87* (3), 348–351.
(31) Morgan, M. R.; Thomas, G. J.; Russell, A.; Hart, I. R.; Marshall, J. F. The Integrin Cytoplasmic-Tail Motif EKQKVDLSTDC Is Sufficient to Promote Tumor Cell Invasion Mediated by Matrix Metalloproteinase (MMP)-2 or MMP-9. *Journal of Biological Chemistry* **2004**, *279* (25), 26533–26539.
(32) Liu, H.; Wu, Y.; Wang, F.; Liu, Z. Molecular Imaging of Integrin Avβ6 Expression in Living Subjects. *American Journal of Nuclear Medicine and Molecular Imaging* **2014**, *4* (4), 333–345.
(33) Bandyopadhyay, A.; Raghavan, S. Defining the Role of Integrin Avβ6 in Cancer. *Current Drug Targets* **2009**, *10* (7), 645–652.
(34) Ladner, R. C.; Sato, A. K.; Gorzelany, J.; de Souza, M. Phage Display-Derived Peptides as Therapeutic Alternatives to Antibodies. *Drug Discovery Today* **2004**, *9* (12), 525–529.
(35) Vlieghe, P.; Lisowski, V.; Martinez, J.; Khrestchatisky, M. Synthetic Therapeutic Peptides: Science and Market. *Drug Discovery Today* **2010**, *15* (1), 40–56.
(36) Firer, M. A.; Gellerman, G. Targeted Drug Delivery for Cancer Therapy: The Other Side of Antibodies. *Journal of Hematology & Oncology* **2012**, *5* (1), 70.

(37) Liu, H.; Zhao, Z.; Zhang, L.; Li, Y.; Jain, A.; Barve, A.; Jin, W.; Liu, Y.; Fetse, J.; Cheng, K. Discovery of Low-Molecular Weight Anti-PD-L1 Peptides for Cancer Immunotherapy. *Journal for ImmunoTherapy of Cancer* **2019**, *7* (1), 270.

(38) Logan, D.; Abu-Ghazaleh, R.; Blakemore, W.; Curry, S.; Jackson, T.; King, A.; Lea, S.; Lewis, R.; Newman, J.; Parry, N.; Rowlands, D.; Stuart, D.; Fry, E. Structure of a Major Immunogenic Site on Foot-and-Mouth Disease Virus. *Nature* **1993**, *362* (6420), 566–568.

(39) DiCara, D.; Rapisarda, C.; Sutcliffe, J. L.; Violette, S. M.; Weinreb, P. H.; Hart, I. R.; Howard, M. J.; Marshall, J. F. Structure-Function Analysis of Arg-Gly-Asp Helix Motifs in Avβ6 Integrin Ligands. *Journal of Biological Chemistry* **2007**, *282* (13), 9657–9665.

(40) Hausner, S. H.; DiCara, D.; Marik, J.; Marshall, J. F.; Sutcliffe, J. L. Use of a Peptide Derived from Foot-and-Mouth Disease Virus for the Noninvasive Imaging of Human Cancer: Generation and Evaluation of 4-[18F]Fluorobenzoyl A20FMDV2 for In Vivo Imaging of Integrin Avβ6 Expression with Positron Emission Tomography. *Cancer Research* **2007**, *67* (16), 7833–7840.

(41) Slack, R. J.; Hafeji, M.; Rogers, R.; Ludbrook, S. B.; Marshall, J. F.; Flint, D. J.; Pyne, S.; Denyer, J. C. Pharmacological Characterization of the Avβ6 Integrin Binding and Internalization Kinetics of the Foot-and-Mouth Disease Virus Derived Peptide A20FMDV2. *Pharmacology* **2016**, *97* (3–4), 114–125.

(42) Keat, N.; Kenny, J.; Chen, K.; Onega, M.; Garman, N.; Slack, R. J.; Parker, C. A.; Lumbers, R. T.; Hallett, W.; Saleem, A.; Passchier, J.; Lukey, P. T. A Microdose PET Study of the Safety, Immunogenicity, Biodistribution, and Radiation Dosimetry of ^{18}F-FB-A20FMDV2 for Imaging the Integrin $\alpha_v\beta_6$. *Journal of Nuclear Medicine Technology* **2018**, *46* (2), 136–143.

(43) Hausner, S. H.; Bold, R. J.; Cheuy, L. Y.; Chew, H. K.; Daly, M. E.; Davis, R. A.; Foster, C. C.; Kim, E. J.; Sutcliffe, J. L. Preclinical Development and First-in-Human Imaging of the Integrin Avβ6 with [18F]Avβ6-Binding Peptide in Metastatic Carcinoma. *Clinical Cancer Research* **2019**, *25* (4), 1206–1215.

(44) Moore, K. M.; Desai, A.; Delgado, B. de L.; Trabulo, S. M. D.; Reader, C.; Brown, N. F.; Murray, E. R.; Brentnall, A.; Howard, P.; Masterson, L.; Zammarchi, F.; Hartley, J. A.; van Berkel, P. H.; Marshall, J. F. Integrin Avβ6-Specific Therapy for Pancreatic Cancer Developed from Foot-and-Mouth-Disease Virus. *Theranostics* **2020**, *10* (7), 2930–2942.

(45) Whilding, L. M.; Parente-Pereira, A. C.; Zabinski, T.; Davies, D. M.; Petrovic, R. M. G.; Kao, Y. V.; Saxena, S. A.; Romain, A.; Costa-Guerra, J. A.; Violette, S.; Itamochi, H.; Ghaem-Maghami, S.; Vallath, S.; Marshall, J. F.; Maher, J. Targeting of Aberrant Avβ6 Integrin Expression in Solid Tumors Using Chimeric Antigen Receptor-Engineered T Cells. *Molecular Therapy* **2017**, *25* (1), 259–273.

(46) Lukey, P. T.; Coello, C.; Gunn, R.; Parker, C.; Wilson, F. J.; Saleem, A.; Garman, N.; Costa, M.; Kendrick, S.; Onega, M.; Kang'ombe, A. R.; Listanco, A.; Davies, J.; Ramada-Magalhaes, J.; Moz, S.; Fahy, W. A.; Maher, T. M.; Jenkins, G.; Passchier, J.; Marshall, R. P. Clinical Quantification of the Integrin Avβ6 by [18F]FB-A20FMDV2 Positron Emission Tomography in Healthy and Fibrotic Human Lung (PETAL Study). *European Journal of Nuclear Medicine and Molecular Imaging* **2020**, *47* (4), 967–979.

(47) Saleem, A.; Helo, Y.; Win, Z.; Dale, R.; Cook, J.; Searle, G. E.; Wells, P. Integrin Avβ6 Positron Emission Tomography Imaging in Lung Cancer Patients Treated With Pulmonary Radiation Therapy. *International Journal of Radiation Oncology*Biology*Physics* **2020**, *107* (2), 370–376.

(48) Foster, C. C.; Davis, R. A.; Hausner, S. H.; Sutcliffe, J. L. Avβ6-Targeted Molecular PET/CT Imaging of the Lungs After SARS-CoV-2 Infection. *Journal of Nuclear Medicine* **2020**, *61* (12), 1717–1719.

(49) Kimura, R. H.; Teed, R.; Hackel, B. J.; Pysz, M. A.; Chuang, C. Z.; Sathirachinda, A.; Willmann, J. K.; Gambhir, S. S. Pharmacokinetically Stabilized Cystine Knot Peptides That Bind Alpha-v-Beta-6 Integrin with Single-Digit Nanomolar Affinities for Detection of Pancreatic Cancer. *Clinical Cancer Research* **2012**, *18* (3), 839–849.

(50) Hausner, S. H.; Abbey, C. K.; Bold, R. J.; Gagnon, M. K.; Marik, J.; Marshall, J. F.; Stanecki, C. E.; Sutcliffe, J. L. Targeted In Vivo Imaging of Integrin Avβ6 with an Improved Radiotracer and Its Relevance in a Pancreatic Tumor Model. *Cancer Research* **2009**, *69* (14), 5843–5850.

(51) Hausner, S. H.; Bauer, N.; Hu, L. Y.; Knight, L. M.; Sutcliffe, J. L. The Effect of Bi-Terminal PEGylation of an Integrin Avβ$_6$-Targeted ^{18}F Peptide on Pharmacokinetics and Tumor Uptake. *Journal of nuclear medicine : official publication, Society of Nuclear Medicine* **2015**, *56* (5), 784–790.

(52) Burman, A.; Clark, S.; Abrescia, N. G. A.; Fry, E. E.; Stuart, D. I.; Jackson, T. Specificity of the VP1 GH Loop of Foot-and-Mouth Disease Virus for Av Integrins. *Journal of Virology* **2006**, *80* (19), 9798–9810.

(53) Spokoyny, A. M.; Zou, Y.; Ling, J. J.; Yu, H.; Lin, Y.-S.; Pentelute, B. L. A Perfluoroaryl-Cysteine SNAr Chemistry Approach to Unprotected Peptide Stapling. *Journal of the American Chemical Society* **2013**, *135* (16), 5946–5949.

(54) Ngambenjawong, C.; Pineda, J. M. B.; Pun, S. H. Engineering an Affinity-Enhanced Peptide through Optimization of Cyclization Chemistry. *Bioconjugate Chemistry* **2016**, *27* (12), 2854–2862.

(55) Sellers, D. L.; Tan, J.-K. Y.; Pineda, J. M. B.; Peeler, D. J.; Porubsky, V. L.; Olden, B. R.; Salipante, S. J.; Pun, S. H. Targeting Ligands Deliver Model Drug Cargo into the Central Nervous System along Autonomic Neurons. *ACS Nano* **2019**, *13* (10), 10961–10971.

(56) Hewish, M. J.; Takada, Y.; Coulson, B. S. Integrins A2β1 and A4β1 Can Mediate SA11 Rotavirus Attachment and Entry into Cells. *Journal of Virology* **2000**, *74* (1), 228236.

(57) DiCara, D.; Burman, A.; Clark, S.; Berryman, S.; Howard, M. J.; Hart, I. R.; Marshall, J. F.; Jackson, T. Foot-and-Mouth Disease Virus Forms a Highly Stable, EDTA-Resistant Complex with Its Principal Receptor, Integrin Avβ6: Implications for Infectiousness. *Journal of Virology* **2008**, *82* (3), 1537–1546.

(58) Lamiable, A.; Thévenet, P.; Rey, J.; Vavrusa, M.; Derreumaux, P.; Tufféry, P. PEP-FOLD3: Faster de Novo Structure Prediction for Linear Peptides in Solution and in Complex. *Nucleic Acids Research* **2016**, *44* (W1), W449–W454.

(59) Hung, K.; Harris, P. W. R.; Desai, A.; Marshall, J. F.; Brimble, M. A. Structure-Activity Relationship Study of the Tumour-Targeting Peptide A20FMDV2 via Modification of Lys16, Leu13, and N- and/or C-Terminal Functionality. *European Journal of Medicinal Chemistry* **2017**, *136*, 154–164.

(60) Tugyi, R.; Uray, K.; Iván, D.; Fellinger, E.; Perkins, A.; Hudecz, F. Partial D-Amino Acid Substitution: Improved Enzymatic Stability and Preserved Ab Recognition of a MUC2 Epitope Peptide. *Proceedings of the National Academy of Sciences of the United States of America* **2005**, *102* (2), 413–418.

(61) Gasteiger, E.; Hoogland, C.; Gattiker, A.; Duvaud, S.; Wilkins, M. R.; Appel, R. D.; Bairoch, A. Protein Identification and Analysis Tools on the ExPASy Server BT - The

Proteomics Protocols Handbook; Walker, J. M., Ed.; Humana Press: Totowa, NJ, 2005; pp 571–607.
(62) Kolodziej, A. F.; Zhang, Z.; Overoye-Chan, K.; Jacques, V.; Caravan, P. Peptide Optimization and Conjugation Strategies in the Development of Molecularly Targeted Magnetic Resonance Imaging Contrast Agents BT - Therapeutic Peptides: Methods and Protocols; Nixon, A. E., Ed.; Humana Press: Totowa, NJ, 2014; pp 185–211.
(63) Weigel, L. F.; Nitsche, C.; Graf, D.; Bartenschlager, R.; Klein, C. D. Phenylalanine and Phenylglycine Analogues as Arginine Mimetics in Dengue Protease Inhibitors. *Journal of Medicinal Chemistry* **2015**, *58* (19), 7719–7733.
(64) Wang, Y.; Xiao, W.; Zhang, Y.; Meza, L.; Tseng, H.; Takada, Y.; Ames, J. B.; Lam, K. S. Optimization of RGD-Containing Cyclic Peptides against Avβ3 Integrin. *Molecular Cancer Therapeutics* **2016**, *15* (2), 232–240.
(65) Nieberler, M.; Reuning, U.; Reichart, F.; Notni, J.; Wester, H.-J.; Schwaiger, M.; Weinmüller, M.; Räder, A.; Steiger, K.; Kessler, H. Exploring the Role of RGD-Recognizing Integrins in Cancer. *Cancers* **2017**, *9* (9), 116.
(66) Kogelberg, H.; Tolner, B.; Thomas, G. J.; Di Cara, D.; Minogue, S.; Ramesh, B.; Sodha, S.; Marsh, D.; Lowdell, M. W.; Meyer, T.; Begent, R. H. J.; Hart, I.; Marshall, J. F.; Chester, K. Engineering a Single-Chain Fv Antibody to Avβ6 Integrin Using the Specificity-Determining Loop of a Foot-and-Mouth Disease Virus. *Journal of Molecular Biology* **2008**, *382* (2), 385–401.
(67) Wagstaff, J. L.; Rowe, M. L.; Hsieh, S.-J.; DiCara, D.; Marshall, J. F.; Williamson, R. A.; Howard, M. J. NMR Relaxation and Structural Elucidation of Peptides in the Presence and Absence of Trifluoroethanol Illuminates the Critical Molecular Nature of Integrin Avβ6 Ligand Specificity. *RSC Advances* **2012**, *2* (29), 11019–11028.
(68) Sylvestre, M.; Lv, S.; Yang, L. F.; Luera, N.; Peeler, D. J.; Chen, B.-M.; Roffler, S. R.; Pun, S. H. Replacement of L-Amino Acid Peptides with D-Amino Acid Peptides Mitigates Anti-PEG Antibody Generation against Polymer-Peptide Conjugates in Mice. *Journal of Controlled Release* **2021**, *331*, 142–153.

5.8 SUPPORTING INFORMATION

Table S5.1 | Original, cyclized, and modified A20FMDV2 peptide sequences used for binding and serum stability studies.

Peptide	Sequence	Weight (g/mol)
A20FMDV2	biotin-NAVPNLRGDLQVLAQKVARTK-amide	2517.0
C1C18 DFBP	biotin-CAVPNLRGDLQVLAQKVCRTK-amide	2832.2
C1C19 DFBP	biotin-CAVPNLRGDLQVLAQKVACTK-amide	2747.1
C1C20 DFBP	biotin-CAVPNLRGDLQVLAQKVARCK-amide	2802.1
C2C18 DFBP	biotin-NCVPNLRGDLQVLAQKVCRTK-amide	2875.2
C2C19 DFBP	biotin-NCVPNLRGDLQVLAQKVACTK-amide	2790.1
C6C17 DFBP	biotin-NAVPNCRGDLQVLAQKCARTK-amide	2805.1
C1C18 S-S	biotin-**C**AVPNLRGDLQVLAQKV**C**RTK-amide	2536.1
C2C18 R_DTKA_D DFBP	biotin-NCVPNLRGDLQVLAQKVCR_DTKA_D-amide	2946.3
C2C18 CitTKA_D DFBP	biotin-NCVPNLRGDLQVLAQKVCCitTKA_D-amide	2947.3
C2C18 P_h R_DTKA_D DFBP	biotin-NCVP_hNLRGDLQVLAQKVCR_DTKA_D-amide	2962.3
C1C18 A_D R_DTK$_D$A$_D$ DFBP	biotin-CA_DVPNLRGDLQVLA_DQKVCR_DTK$_D$A$_D$-amide	2903.2
C2C18 $_A$FGD RTKA_D DFBP	biotin-NCVPNL$_A$FGDLQVLAQKVCRTKA_D-amide	2952.3
C2C18 CitGD DFBP	biotin-NCVPNLCitGDLQVLAQKVCRTK-amide	2876.2
C2C18 $_G$FGD R_DTKA_D DFBP	biotin-NCVPNL$_G$FGDLQVLAQKVCR_DTKA_D-amide	2994.3

C, DFBP-cyclized; **C**, disulfide-cyclized; R_D, D-arginine; A_D, D-alanine; Cit, Citrulline; P_h, hydroxyproline; K_D, D-lysine; $_A$F, 4-aminophenylalanine; $_G$F, 4-guanidinophenylalanine.

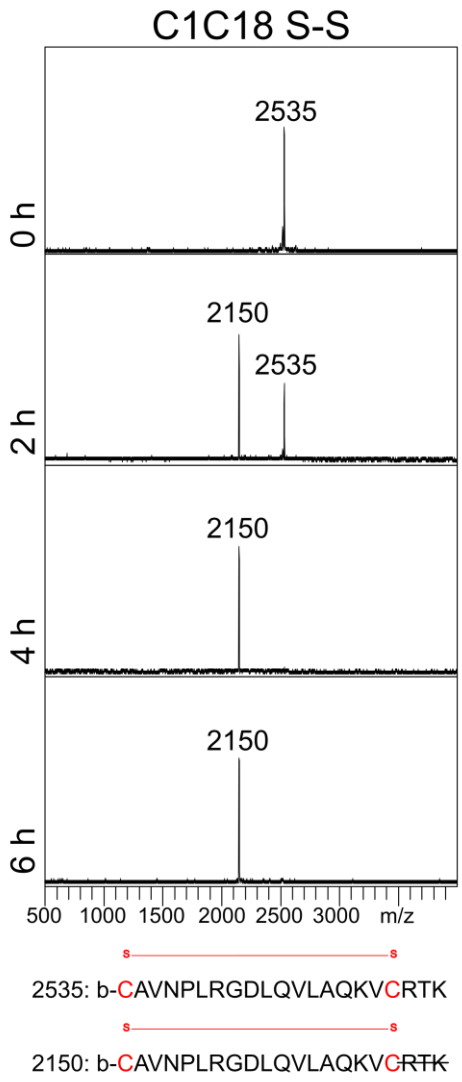

Figure S5.1 | Disulfide cyclization provides less enzymatic stability than DFBP cyclization for the C1C18 peptide. MALDI-ToF spectra of disulfide-cyclized C1C18 S-S incubated in normal mouse serum for 0, 2, 4, and 6 h at 37 °C. Molecular weights of prominent peaks are shown. *Bottom*: predicted amino acid sequences of degradation products based on measured molecular weights.

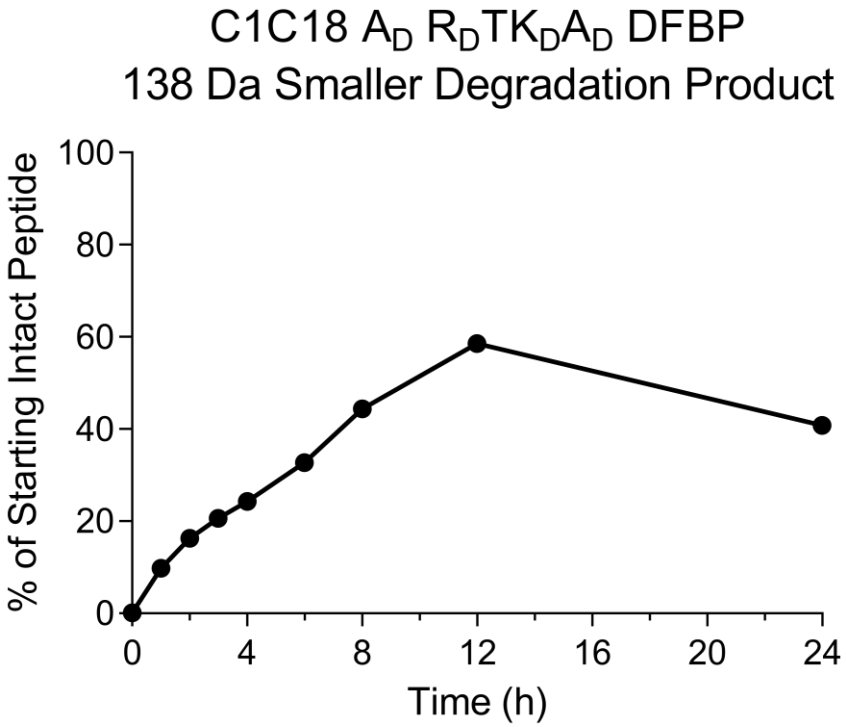

Figure S5.2 | DFBP-cyclized C1C18 A_D R_DTK$_D$$A_D$ is degraded into a stable 138 Da smaller product over serum incubation. Accumulation of a 138 Da smaller degradation product from the DFBP-cyclized C1C18 A_D R_DTK$_D$$A_D$ peptide over a 24-h incubation in normal mouse serum, as measured by LC-MS. Values are normalized to the 0 h timepoint for the intact peptide.

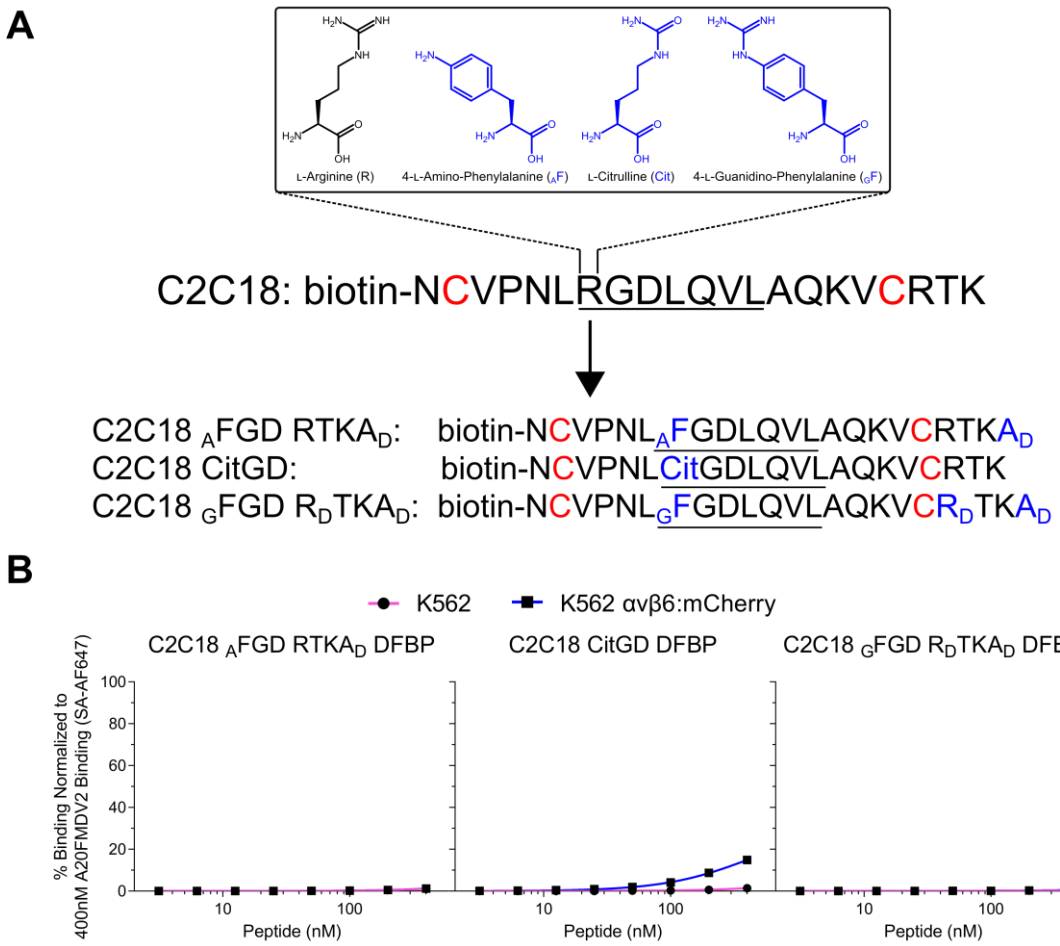

Figure S5.3 | DFBP-cyclized C2C18 peptides with arginine mimetic-modified RGD motifs fail to bind αvβ6$^+$ cancer cells. (A) Schematic of mimetic substitutions made to the sequence of C2C18 DFBP to replace arginine in the RGD motif. Chemical structures of arginine (*black*) and mimetics (*blue*) are shown for comparison. The resulting mimetic-substituted peptide sequences are also listed, with cysteine substitutions for DFBP cyclization shown in *red* and substitutions and C-terminal modifications shown in *blue*. The RGDLXXL motif that is important for αvβ6 recognition is *underlined* in all sequences. (B) Flow cytometry binding curves of mimetic-substituted peptides to K562 and K562 αvβ6:mCherry cells, normalized to 400 nM A20FMDV2 binding to K562 αvβ6:mCherry cells. The curves represent a nonlinear regression of one independent experiment in which binding data are fitted to a Hill equation. SA-AF647, streptavidin Alexa Fluor 647.

Chapter 6: Coupling Bifunctional Synthetic Materials onto Universal Chimeric Antigen Receptor T Cells for Targeted Therapies—Cyborg CAR T-cells

Ian I. Cardle, Dylan R. Scherer, Michael C. Jensen, Suzie H. Pun, Drew. L. Sellers

ABSTRACT

The recent development of modular universal chimeric antigen receptor (CAR) T-cell platforms that use bifunctional adaptor intermediates to redirect engineered T-cell effector function has greatly expanded the capabilities of adoptive T-cell therapy, enabling safer and more comprehensive cancer treatment. However, universal CAR receptor systems rely mostly on unstable transient recognition of tag-coupled intermediates for T-cell function, and the array of targeting ligands used for this application has been limited to antibodies and small molecules. Addressing these shortcomings, we report the development of universal CAR T-cell receptors that can be covalently modified with bifunctional synthetic materials/intermediates by accelerated SpyCatcher003-SpyTag003 chemistry. SpyCatcher003-modified CARs, nicknamed DB5 CARs, displayed fast, low-nanomolar reaction kinetics with synthetic peptides and aptamers that incorporate a SpyTag003 peptide via branched peptide synthesis or conjugation chemistry to comprise a heterobifunctional chimeric material. Pre-arming DB5 CAR T cells or pre-labeling target cells with synthetic targeting materials resulted in robust and selective $CD4^+$ and $CD8^+$ CAR T-cell responses against cancer cells *in vitro*. Furthermore, these synthetic targeting intermediates are capable of arming DB5 CAR T cells *in vivo*, opening opportunities for future animal work. We demonstrate the versatility and therapeutic potential of a universal CAR system that covalently interfaces with synthetic heterobifunctional materials for directed cancer targeting, laying the foundation for next-generation, “cyborg” CAR T-cell therapies.

6.1 INTRODUCTION

The advent of chimeric antigen receptor (CAR) T-cell therapy has significantly changed the cancer treatment landscape, prompting a transition from one-size-fits-all chemotherapy to personalized therapies tailored to a patient's cells. To-date, there has been six CAR T-cell therapies approved by the FDA for treating $CD19^+$ or $BCMA^+$ hematological malignancies—KYMRIAH (tisagenlecleucel) for the treatment of $CD19^+$ relapsed or refractory (r/r) B-lineage acute lymphoblastic leukemia (B-ALL) in young patients and r/r diffuse large B-cell lymphoma (DLBCL) in adults,[1,2] YESCARTA (axicabtagene ciloleucel) for the treatment of specific types of $CD19^+$ r/r B-cell lymphoma in adults,[3,4] TECARTUS (brexucabtagene autoleucel) for the treatment of $CD19^+$ r/r mantle cell lymphoma in adults,[5] BREYANZI (lisocabtagene maraleucel) for the treatment of specific types of $CD19^+$ r/r large B-cell lymphoma in adults,[6] ABECMA (idecabtagene vicleucel) for the treatment of $BCMA^+$ r/r multiple myeloma in adults,[7] and CARVYKTI (ciltacabtagene autoleucel) for the treatment of $BCMA^+$ r/r multiple myeloma in adults.[8] Leading up to their FDA approval, these therapies resulted in 33-67% complete response rates in patients and follow-up real-world outcomes have tracked similarly.[9] This success has led to the pursuit of other indications for these treatments as well as clinical investigation of CAR T cells for targeting solid tumors.[10,11]

Despite the favorable outcomes of current CAR T-cell therapies, they have significant faults. As many as 45% of patients that have complete responses to CD19-directed CAR T-cell therapy will eventually relapse, many with CD19-negative disease.[12,13] Permanent loss of CD19 from the cell surface is thought to occur by many means, including alternative splicing,[14] frameshift mutations,[15] and lineage switching,[16] and therapeutic pressure from CAR treatment drives enrichment of tumor clones with these traits. Importantly, these CD19-negative clones can exist at the onset of disease,[17]

suggesting that hematological malignancies are more antigenically complex than initially surmised. The majority of patients receiving these therapies will also experience some degree of cytokine release syndrome (CRS) and neurotoxicity, and approximately a quarter of patients will present with severe, grade 3 or higher symptoms.[18,19] These side effects are a consequence of on-target CAR T-cell activation, as evidenced by their association with higher pre-infusion tumor burden and higher peak CAR T-cell expansion.[20,21]

The above drawbacks highlight the inflexible design of CAR T-cell therapies used in the clinic. Conventional CARs are composed of an extracellular single-chain variable fragment (scFv) fused to intracellular signaling and costimulatory domains, and T-cell activation occurs when the scFv domain binds to a target antigen on an opposing cell. While highly specific, the single-target nature of these CAR architectures assumes an unrealistic tumor target that has homogenous and static antigen expression; they do not capture the heterogeneity and plasticity of actual tumors. Furthermore, due to their rigid design, conventional CAR T cells cannot be easily controlled post-infusion, and thus toxicities arising from therapy must be curbed symptomatically with anti-IL-6 targeting tocilizumab and corticosteroids.[22] Accordingly, multi-targeting and modular CAR systems are required for comprehensive and adaptable cancer treatment.

Towards this goal, the field has turned to universal CAR receptors that rely on adaptor targeting intermediates for tumor targeting.[23,24] Instead of binding a cancer antigen directly, the universal CAR receptor recognizes a tag on a bifunctional targeting ligand, which in turn targets the cancer antigen to mediate T-cell function. By designing the cancer targeting properties extrinsic to the CAR receptor, this system addresses the weaknesses of conventional CAR architectures mentioned above. For example, multiple targeting intermediates that share the same CAR-specific tag can be employed simultaneously or in sequence depending on the dynamic characteristics of a patient's

cancer, preventing antigen escape via responsive treatment. Additionally, since the targeting intermediates control antigen presentation to the CAR T cells, the amount and frequency at which intermediates are dosed can be used to mitigate toxic side effects normally associated with therapy. For these reasons, a great number of universal CAR systems have been pioneered in recent years. These include systems that use natural binding partner pairs such as avidin and biotin and leucine zipper domains,[25–27] as well as those that use more conventional scFvs that target small molecule or peptide tags such as FITC,[28–30] peptide neo-epitope (PNE) derived from yeast,[31] and E5B9 peptide derived from human nuclear autoantigen La/SS-B.[32]

While these universal CAR systems are powerful, they may be limited by noncovalent recognition of the tag-labeled targeting intermediates. Conventional CARs rely on a single affinity-based interaction for activation, whereas universal CAR systems required two such interactions to occur in sequence. Thus, CAR binding of the tag-labeled ligand and ligand binding to the cancer antigen must synchronize, and the transient properties (i.e. off-rate) of any one event can cause the system to fail. Recognizing the slippery nature of antibody binding to peptide-based tags, Zakeri et al. developed SpyCatcher and SpyTag, a protein and peptide pair split from the collagen adhesion domain from *Streptococcus pyogenes* and rationally optimized to form a covalent isopeptide with each other.[33] The spontaneous reaction between SpyCatcher and SpyTag occurs under diverse conditions (pH 5-10, 4-37 °C), and their ability to be genetically encoded and fused to other proteins at either their N-terminus or C-terminus without loss of function has proven them to be valuable tools for various biological applications.[34–36] Given these favorable attributes, this covalent technology has recently been adopted into universal CAR platforms with SpyCatcher-modified CARs and SpyTag-labeled targeting intermediates such as scFvs, designed ankyrin repeat proteins (DARPins), and antibodies.[37,38]

SpyCatcher and SpyTag, however, have slow reaction kinetics that require micromolar concentrations of both partners for efficient covalent bond formation.[33] Consequentially, universal CAR systems using this pair lose sensitivity if target antigen expression or intermediate ligand concentration is low.[38] Moreover, few of the aforementioned universal CAR systems have explored using synthetic materials to direct universal CAR T-cell function, which naturally lend themselves to SpyCatcher-SpyTag chemistry. To this end, we developed a universal CAR receptor and bifunctional synthetic targeting intermediates that employ enhanced SpyCatcher003-SpyTag003 reaction kinetics to direct T-cell responses against cancer cells. By linking SpyCatcher003 to standard CAR spacer, transmembrane, and signaling domains, we created SpyCatcher003 CARs (nicknamed DB5 CARs) that react efficiently with synthetic SpyTag003 peptides at low-nanomolar concentrations on the order of minutes. For cancer targeting, we attached SpyTag003 to a modified αvβ6-specific peptide via branched peptide design, and the resulting bifunctional peptide intermediate displayed robust bispecific properties, labeling both DB5 CAR-expressing immortalized T cells and $\alpha v\beta 6^+$ cancer cells with high specificity. *In vitro* functional assays with the bifunctional peptide intermediate and primary $CD4^+$ and $CD8^+$ DB5 CAR T cells of different spacer lengths demonstrate sensitive, spacer-dependent immune responses directed against $\alpha v\beta 6^+$ cancer cells. For future preclinical work in tumor-bearing mice, we characterize parameters of bifunctional peptide administration that are important for DB5 CAR T-cell arming *in vivo*. Lastly, we attached an azide-modified SpyTag003 to an octyne-modified cancer-targeting DNA aptamer via copper-free click chemistry, and preliminary results show that the resulting heterobifunctional aptamer-peptide chimera labeled both DB5 CAR-expressing T cells and cancer cells with high specificity. These results demonstrate the ability of diverse

synthetic materials to be covalently attached to DB5 CAR T cells and reconstitute a targeted immunotherapy for cancer treatment, paving the way for universal cyborg CAR T-cell therapies.

6.2 RESULTS

6.2.1 Accelerated CAR reaction kinetics with SpyCatcher003 and SpyTag003

We first attempted to create a universal CAR system based on the original SpyCatcher-SpyTag pair. As the non-signaling extracellular spacer domain is critical for CAR function and the optimal length varies depending on the scFv and targeted epitope,[39] we cloned SpyCatcher (113 amino acids) into three lentiviral CAR constructs with different spacers lengths consisting of either a short IgG4 hinge domain, a medium IgG4 hinge-CH3 domain, or a long IgG4 hinge-CH2-CH3 domain (**Figure S6.1A**). Each spacer was linked to a CD28 transmembrane domain and 41BB-CD3ζ intracellular signaling domains to produce second-generation SpyCatcher-41BB-CD3ζ CARs. Constructs also encoded a double mutant of dihydrofolate reductase (DHFRdm) and truncated EGFR (EGFRt) downstream of the CAR separated by 2A ribosomal skip sequences, allowing for methotrexate drug selection and detection of transduced cells, respectively. To evaluate the covalent reaction kinetics of the SpyCatcher CARs with SpyTag peptide, we transduced immortalized T-lymphoma H9 cells to express the three different SpyCatcher CARs and synthesized biotinylated SpyTag for loading onto the cells. We added a C-terminal glycine to the SpyTag peptide to mimic a prospective linker that could be added when synthesizing bifunctional peptides. After incubating biotinylated SpyTag with the cells at various concentrates for 1 h at room temperature and subsequently staining with streptavidin Alexa Fluor 647, we observed low loading of SpyTag peptides onto the SpyCatcher CARs at nanomolar concentrations (**Figure S6.1B**). Ultimately, 5 μM SpyTag peptide was required for moderate covalent loading

onto SpyCatcher CARs, which was far from ideal compared to the nanomolar and sub-nanomolar affinities of conventional CARs used in the clinic.[40] We posited that improved covalent reaction kinetics compared to the original SpyCatcher-SpyTag pair (1.4×10^3 M^{-1} s^{-1}) would be required to sensitively and effectively direct T-cell function.[33]

The kinetics of the SpyCatcher and SpyTag interaction has been optimized in recent years, with phage display selection and further rational modification of the pair yielding SpyCatcher003 and SpyTag003 that have ~400-fold faster reaction kinetics (5.5×10^5 M^{-1} s^{-1}).[41,42] As this reaction rate approaches diffusion-limited kinetics, we hypothesized that a universal CAR system using SpyCatcher003 and SpyTag003 would be significantly improved compared to a system using old SpyCatcher-SpyTag chemistry. Accordingly, we first evaluated loading of the new SpyTag003 peptide onto the previous H9 cells expressing the original SpyCatcher CAR, since the new 003 variants are back-compatible with previous SpyCatcher/SpyTag generations but with enhanced kinetics.[42] In an effort to increase peptide serum stability, we synthesized biotinylated SpyTag003 with two D-arginine substitutions, which we named SpyTag003 (D2). The arginine residues were originally introduced into SpyTag003 for adding positive charge,[42] so we rationalized that substituting in the D-configuration of these residues would not affect reaction kinetics.

As expected, SpyTag003(D2) displayed remarkedly enhanced loading onto H9 SpyCatcher CAR cells, with comparable loading to the original SpyTag peptide occurring at 10-fold lower concentrations (**Figure S6.1C**). SpyTag003(D2) loading onto SpyCatcher CARs saturated at 1 μM, and the loading signal was approximately 5- to 10-fold higher than that of the original SpyTag peptide at the highest concentration tested. We also qualitatively evaluated the proteolytic stability of SpyTag003(D2) by MALDI-ToF MS. SpyTag003(D2) was stable past 24 hours in cell-spiked complete media (10% FBS) and up to 8 hours in normal mouse serum, indicating good stability

for a linear peptide (**Figure S6.2A,B**). Proteolytic cleavage was frequently observed at or adjacent to the aspartic acid residue in SpyTag003(D2), which is consistent with predicted endoproteinase AspN activity at this position.[43] Mindful that this residue forms the covalent isopeptide bond with all generations of SpyCatcher, we did not pursue further modification of the SpyTag003(D2) peptide.

We next cloned SpyCatcher003 (113 amino acids) into the three lentiviral CAR constructs with different spacers lengths as described before to make second-generation SpyCatcher003-41BB-CD3ζ CARs that would react even more efficiently with SpyTag003(D2) (**Figure 6.1A**). We nicknamed these receptors DB5 CARs and will refer to them as such for the remainder of this chapter. The resulting DB5 CAR lentiviruses were titered in H9 cells, and EGFRt and DB5 CAR expression were assayed in parallel by staining with biotinylated Erbitux antibody and SpyTag003(D2) peptide, respectively. We found that SpyTag003(D2) staining of the DB5 CARs on H9 cells tracked similarly with Erbitux staining of EGFRt across all concentrations of lentivirus tested, even showing greater sensitivity than Erbitux for detecting transduced cells at lower lentivirus concentrations (**Figure S6.3A-C**). The lentiviruses also induced efficient construct expression, providing titers $>10^8$ TU/mL regardless of the CAR spacer length.

To further characterize the reaction kinetics of SpyTag003(D2) with DB5 CARs, we incubated H9 DB5 CAR cells with various concentrations of SpyTag003(D2) and evaluated loading by flow cytometry. SpyTag003(D2) peptides loaded efficiently and selectively onto H9 cells expressing DB5 CARs, with robust loading occurring even below 10 nM (**Figure 6.1B**) Fitting the loading data to a Michaelis-Menten model, K_m values ranged tightly from 20-30 nM regardless of the DB5 CAR spacer length. We also tested the time kinetics of loading at a sub-saturating concentration of peptide (50 nM), and the association half-time of SpyTag003(D2) to H9 DB5 CAR cells was

fast at 5-6 min (**Figure 6.1C**). These results demonstrate a significant improvement in loading kinetics compared to published universal CAR systems that rely on old SpyCatcher-SpyTag chemistry.[38]

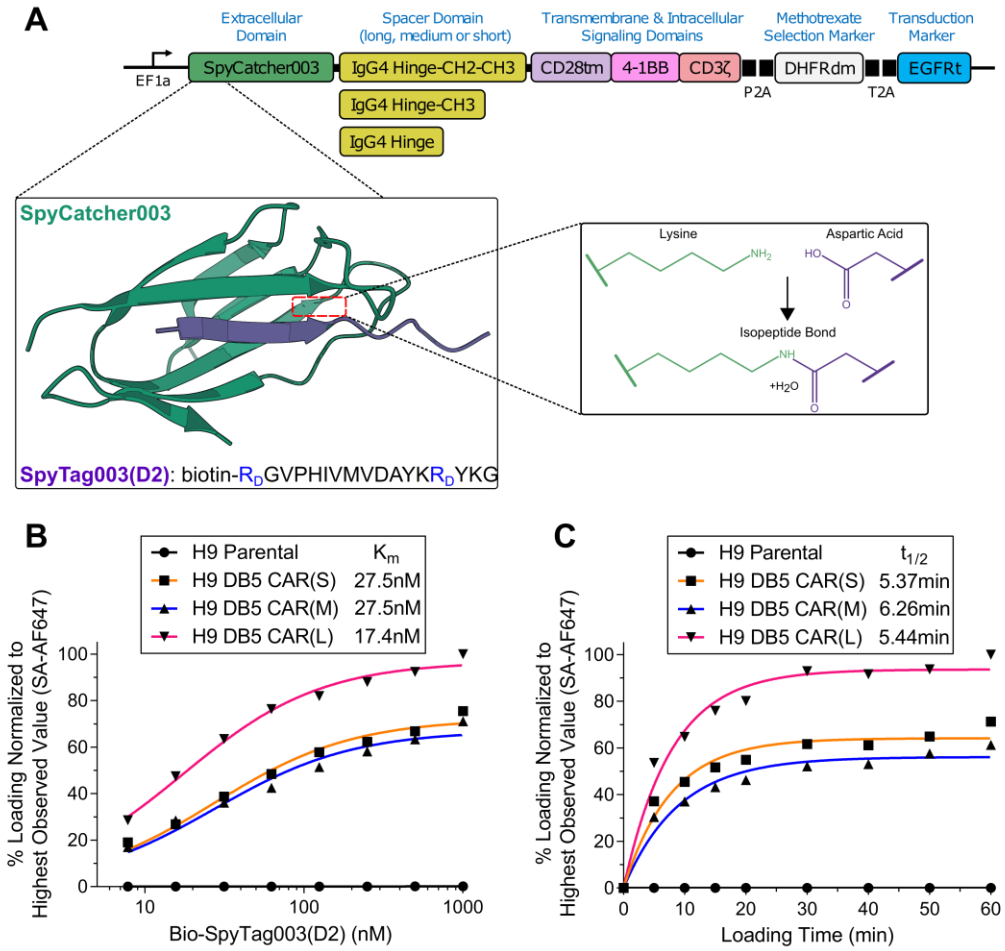

Figure 6.1 | Cell-expressed SpyCatcher003 CARs react sensitively and quickly with modified SpyTag003 peptide. (A) Top: Design of tricistronic lentiviral SpyCatcher003 (DB5) CAR constructs with different extracellular spacer lengths. Bottom: Schematic of isopeptide bond formation between lysine and aspartic acid side chains of SpyCatcher003 CAR (green) and D-arginine substituted SpyTag003(D2) (purple), respectively, based on PDB 4MLI.[44] The D-arginine residues in the SpyTag003(D2) sequence are shown in blue. (B) Flow cytometry loading curves of SpyTag003(D2) peptide onto H9 DB5 CAR cells with different spacers lengths, normalized to the highest observed loading. The curves represent a nonlinear regression of three independent experiments in which loading data are fitted to a Michaelis-Menten equation. (C) Flow cytometry time kinetics of 50 nM SpyTag003(D2) loading onto H9 DB5 CAR cells with different spacer lengths, normalized to the highest observed loading. The curves represent a nonlinear regression assuming one phase association of one independent experiment. SA-AF647, streptavidin Alexa Fluor 647.

6.2.2 Synthesis and characterization of an αvβ6-targeting bifunctional peptide

Peptides offer several advantages over antibodies as therapeutic targeting ligands for cancer. Their small size supports tumor penetration with low accumulation in off-target tissues and organs, their synthetic synthesis enables inexpensive production with high chemical diversity, they have low toxicity, and they can be readily modified with drugs or other peptides for multiplexed properties.[45] We thus sought to create a bifunctional peptide intermediate for directing DB5 CAR function against a relevant cancer target. The integrin αvβ6 is upregulated in many solid cancers and its expression is associated with poor prognosis.[46] As αvβ6 is not expressed in healthy adult epithelia, the integrin has become the focus of research in recent years aiming to develop targeting ligands for cancer imaging and therapeutic applications.[47,48] A20FMDV2, a 20-mer peptide derived from foot-and-mouth disease virus that binds αvβ6 with high affinity and specificity, is the successful culmination of much of this research.[49] A20FMDV2 has been used to image and deliver drugs to $\alpha v\beta 6^{+}$ tumors *in vivo*,[50,51] and researchers have fused it to a CAR receptor for potent αvβ6-directed adoptive T-cell therapy.[52] For these reasons, we chose to construct an αvβ6-targeting bifunctional peptide that incorporates A20FMDV2 to validate our DB5 CAR system.

Previously, our lab designed cysteine substituted A20FMDV2 variants cyclized by perfluoroarylation with decafluorobiphenyl (DFBP) and modified with non-natural amino acids to increase the peptide's poor stability in serum.[53] Therefore, to ensure the proteolytic stability of the peptide intermediate for *in vitro* and *in vivo* usage with DB5 CAR T cells, we selected the DFBP-cyclized C2C18 A20FMDV2 variant that we previously reported to synthesize the αvβ6-targeting arm of the bifunctional peptide. We incorporated hydroxyproline and D-alanine substitutions in between the cysteine linkages since these were found to increase the αvβ6 integrin specificity of the peptide, and D-arginine and D-lysine modifications were made to the C-terminus for added

stability and to decrease potential immunogenicity. The resulting peptide, called C2C18(ChARK) for short, contained an acid-labile 4-methyltrityl (Mtt) group protecting the D-lysine side chain, which was selectively deprotected for branched synthesis of the biotinylated SpyTag003(D2) arm to generated the final C2C18(ChARK)-X-SpyTag003(D2) bifunctional peptide (**Figure 6.2A**).[54] Hexanoic acid and glycine were included as a flexible linker (X) between the two peptide arms to promote proper peptide folding and prevent steric hindrance between αvβ6 and DB5 CAR interactions with the peptide.[55]

To determine if the C2C18(ChARK)-X-SpyTag003(D2) peptide had bispecific properties, we evaluated the peptide's ability to label both αvβ6$^+$ cancer cells and DB5 CAR$^+$ cells. Using the matched erythroleukemia K562 and K562 αvβ6:mCherry cell lines, we found that C2C18(ChARK)-X-SpyTag003(D2) exhibited high-affinity and selective binding for the K562 αvβ6:mCherry cells comparable to that of previously tested monofunctional C2C18 peptides,[53] indicating functionality of the C2C18(ChARK) arm of the bifunctional peptide (**Figure 6.2B**). Similarly, the bifunctional peptide loaded robustly onto H9 DB5 CAR cells with K_m values similar to those observed earlier with the monofunctional SpyTag003(D2) peptide (**Figure 6.2C**). Having confirmed that C2C18(ChARK)-X-SpyTag003(D2) displays potent ambidextrous qualities, we proceeded with testing the peptide in functional assays with CD4$^+$ and CD8$^+$ DB5 CAR T cells.

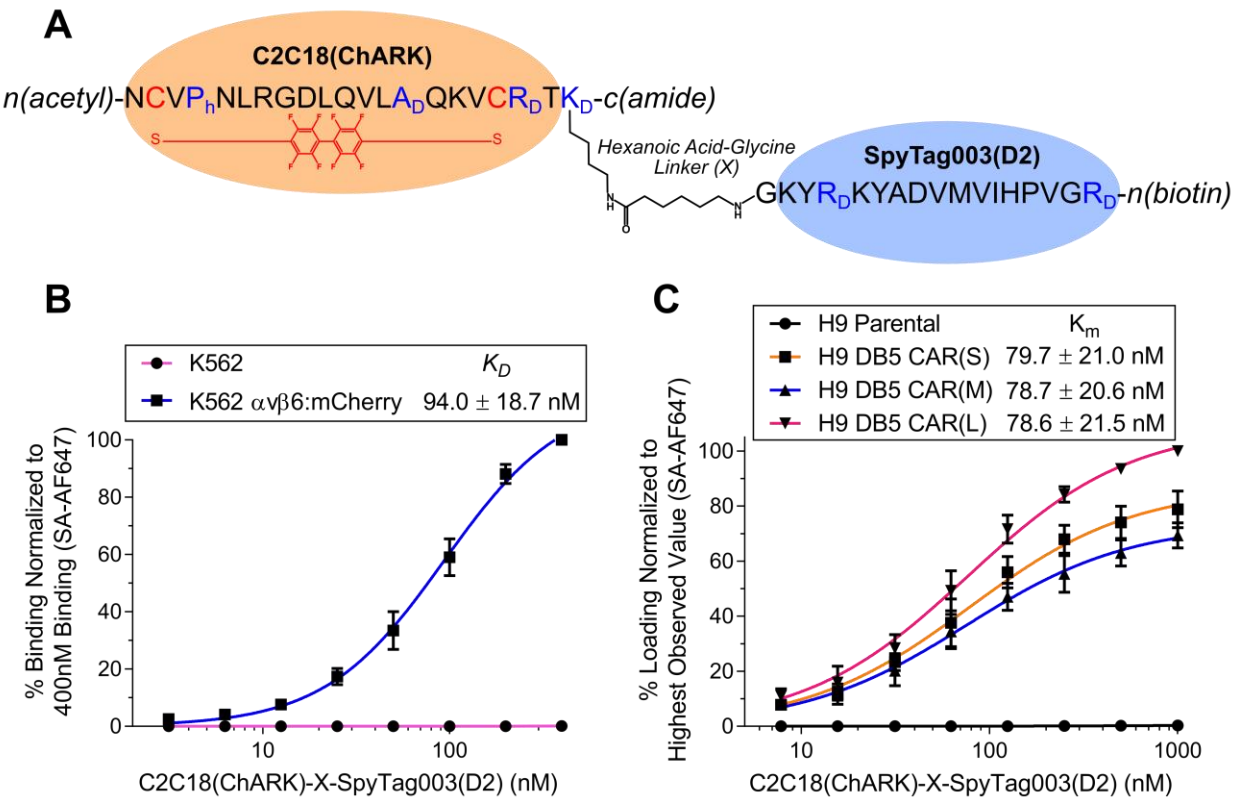

Figure 6.2 | Branched peptide is capable of bispecific properties. (A) Schematic representation of bifunctional C2C18(ChARK)-X-SpyTag003(D2) peptide. Cysteine substitutions and DFBP cyclization are shown in red. Hydroxyproline and D-amino acid modifications are shown in blue. (B) Flow cytometry binding curves of bifunctional peptide to K562 and K562 αvβ6:mCherry cells, normalized to 400 nM binding to K562 αvβ6:mCherry cells. The curves represent a nonlinear regression of three independent experiments in which binding data are fitted to a Hill equation. K_D values were calculated by averaging the individual regression values of the independent experiments. Data points, error bars, and K_D values represent the mean ± SD; n = 3 independent experiments. (C) Flow cytometry loading curves of bifunctional peptide onto H9 DB5 CAR cells with different spacers lengths, normalized to the highest observed loading. The curves represent a nonlinear regression of three independent experiments in which loading data are fitted to a Michaelis-Menten equation. K_m values were calculated by averaging the individual regression values of the independent experiments. Data points, error bars, and K_m values represent the mean ± SD; n = 3 independent experiments. SA-AF647, streptavidin Alexa Fluor 647.

6.2.3 *In vitro* efficacy of $CD4^+$ DB5 CAR T cells directed with bifunctional peptide

To demonstrate whether synthetic peptide intermediates can effectively guide DB5 CAR function, we first generated $CD4^+$ DB5 CAR T cells of all three spacer lengths. $CD4^+$ CAR T cells were

manufactured using a three-week stimulation bead outgrowth protocol, as summarized in **Figure S6.4**, where S_1 denotes the bead stimulation and $D_{\#}$ signifies the number of days since the onset of stimulation. Transduced cells were enriched by methotrexate selection as previously described.[56] After a week of methotrexate selection (S_1D_{11}), high transduction was confirmed by both Erbitux staining for EGFRt (>95%) and SpyTag003(D2) loading on DB5 CARs (>91%) (**Figure 6.3A**). Interestingly, while EGFRt expression was near-identical across all three spacer lengths of the CARs, as indicated by median fluorescence intensity (MFI) values of Erbitux staining, SpyTag003(D2) loading on the $CD4^+$ DB5 CAR T cells varied depending on the CAR spacer length. We observed the highest SpyTag003(D2) loading on T cells expressing the short spacer CAR, followed by the long spacer CAR, and then lastly the medium spacer CAR. As the DB5 CARs should be stoichiometrically translated and expressed with EGFRt, this data suggests that the spacer itself influences the ability of the SpyCatcher003 domain to react with SpyTag003(D2) in solution. Further investigation will be required to determine if the accessibility or folding of the SpyCatcher003 domain is affected when fused to the different spacers. To bring transduction closer to 100%, cells were selected with methotrexate for another three days (10 days total) before being further expanded without selection for functional testing on S_1D_{18}.

We next compared the capacity of these $CD4^+$ DB5 CAR T cells to produce cytokines against $\alpha v\beta 6^+$ target cells when directed by the C2C18(ChARK)-X-SpyTag003(D2) bifunctional peptide. For target cells, we used the matched K562 and K562 αvβ6:mCherry cell lines described earlier as well as pancreatic ductal adenocarcinoma BxPC3 cells which naturally express αvβ6 at more physiologically relevant levels.[52] We also created K562 SpyTag003(L) cells that express SpyTag003 on their surface to be used as a positive control target for the DB5 CAR T cells (**Figure S6.5A,B**). Two orientations of guiding T-cell effector function with the peptide were explored. In

one, we pre-labeled target cells with 500 nM bifunctional peptide for DB5 CAR-driven recognition of SpyTag003(D2) peptide presented on the target cell surface, and successful αvβ6-specific pre-labeling was confirmed by flow cytometry (**Figure 6.3B**). As expected, BxPC3 cells were found to have >10-fold less expression of αvβ6 compared to K562 αvβ6:mCherry cells, making this a more stringent target model for the DB5 CAR system. In the other orientation, we pre-armed T cells with 500 nM bifunctional peptide for peptide-driven recognition of αvβ6 on the target cell surface, and robust pre-arming (>94%) was confirmed by flow cytometry (**Figure 6.3C**). Notably, the MFI of bifunctional peptide pre-arming on the DB5 CAR T cells was spacer-dependent (short > long > medium), reaffirming the previous SpyTag003(D2) loading results on S_1D_{11}.

After pre-labeling and pre-arming with the bifunctional peptide, target cells and $CD4^+$ T cells were co-cultured together for 5 h and intracellular cytokine staining (ICCS) of IL2, TNFα, and IFNγ production was subsequently carried out to assess peptide-induced DB5 CAR T-cell activation (**Figure 6.3D**). $CD4^+$ DB5 CAR T cells actively produced cytokines when co-cultured with K562 SpyTag003(L) cells but not when co-cultured with other bare target cells, with the exception of the short spacer $CD4^+$ DB5 CAR T cells that displayed a small amount of cytokine activity against bare K562 αvβ6:mCherry cells, validating that the DB5 CAR system mostly works as intended. Importantly, K562 αvβ6:mCherry cells pre-labeled with the C2C18(ChARK)-X-SpyTag003(D2) bifunctional peptide induced strong cytokine production in the DB5 CAR T cells, whereas pre-labeled K562 cells did not promote such cytokine responses. Comparable results were found with pre-armed DB5 CAR T cells co-cultured with K562 and K562 αvβ6:mCherry cells, demonstrating that the bifunctional peptide can effectively steer DB5 CAR T cell responses against K562 αvβ6:mCherry regardless of its orientation.

We did, however, observe differences in the efficacy of bifunctional peptide pre-labeling and pre-arming with the BxPC3 cells (**Figure 6.3D**). Whereas pre-labeled BxPC3 cells did not induce cytokine production in DB5 CAR T cells, modest cytokine responses against BxPC3 cells were observed when DB5 CAR T cells were pre-armed with the bifunctional peptide. This may suggest that pre-labeled BxPC3 cells internalize the peptide too quickly for unarmed DB5 CAR T-cell recognition. Indeed, we found that pre-labeled BxPC3 cells internalized the bifunctional peptide with a half-life of approximately 12 min, meaning <5% of starting bifunctional peptide remains on the BxPC3 cell surface after just a 60-min co-incubation with T cells at 37 °C (**Figure S6.6**). Nevertheless, we would expect the bifunctional peptide to both label tumors and arm T cells *in vivo* after intravenous injection, and T-cell arming should outlast tumor labeling given the relatively slower turnover rate of CAR receptors ($t_{1/2}$ = 8-12 h),[57,58] so the observed cytokine production of pre-armed DB5 CAR T cells against BxPC3 cells would suggest *in vivo* translation is possible.

Of the different spacer lengths tested, the long spacer DB5 CAR elicited the greatest cytokine response against BxPC3 cells when armed with the bifunctional peptide intermediate (**Figure 6.3D**). Interestingly, the medium spacer DB5 CAR failed to initiate cytokine responses against BxPC3 cells when armed with bifunctional peptide and also induced the least cytokine responses against K562 αvβ6:mCherry regardless of pre-arming or pre-labeling. The stunted cytokine activity of the medium spacer DB5 CAR is consistent with the low SpyTag003(D2) loading/arming previously observed with this spacer length compared to the short and long spacer DB5 CARs (**Figure 6.3A,C**), suggesting that the medium spacer length does not display fully functional SpyCatcher003 on the T-cell surface.

To see if $CD4^+$ DB5 CAR T-cell activity could be directed with lower bifunctional peptide concentrations, we repeated the ICCS assay with T cells pre-armed with 100 nM bifunctional peptide. While the $CD4^+$ DB5 CAR T cells were less armed with peptide than the T cells in the previous ICCS study (**Figure S6.7A**), they exhibited equivalent if not better cytokine activity against $\alpha v\beta 6^+$ target cells (**Figure S6.7B**), suggesting that the DB5 CAR system operates unhindered even when sub-optimally armed with bifunctional peptide. In contrast, first-generation SpyCatcher CARs developed by Minutolo et al. lose or have reduced activity when armed with 100 nM SpyTag-labeled Herceptin, illustrating the importance of using accelerated SpyCatcher003-SpyTag003 chemistry for enhanced CAR sensitivity.[38] Further titration studies will be required to determine the lowest concentration of bifunctional peptide that can be used to adequately direct $CD4^+$ DB5 CAR T-cell responses via arming, although we suspect the EC_{50} of bifunctional peptide to be <50 nM.

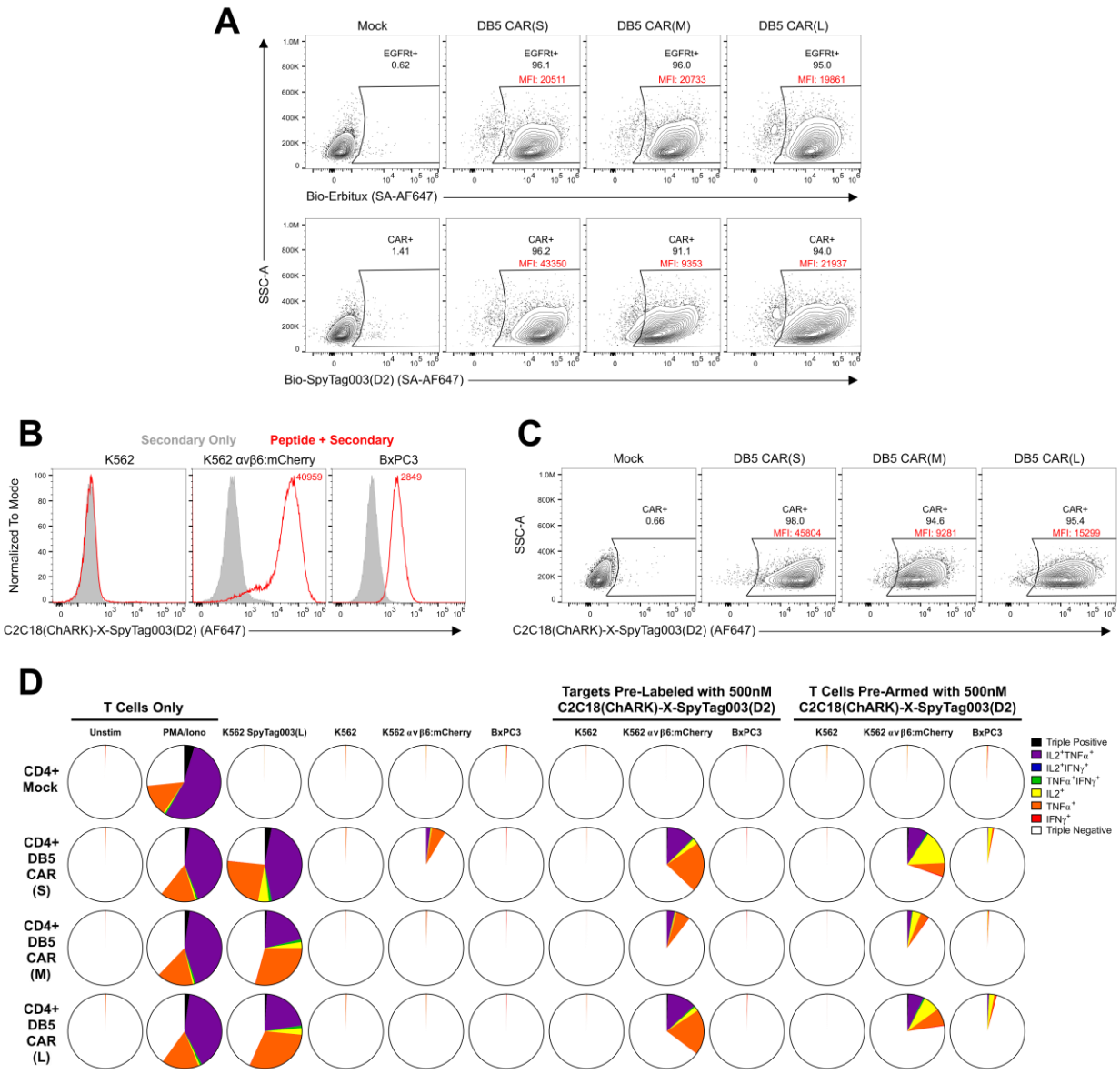

Figure 6.3 | Bifunctional adaptor peptide directs CD4$^+$ DB5 CAR T-cell cytokine responses against αvβ6$^+$ target cells. (A) Flow cytometry plots of biotinylated Erbitux staining and 500 nM SpyTag003(D2) loading on S_1D_{11} CD4$^+$ T cells transduced with lentivirus encoding short, medium, and long spacer DB5 CARs. Plots are representative of 1 biological replicate. MFI values of antibody staining and peptide loading are shown in red. (B) Flow cytometry histograms of target cell pre-labeling with 500 nM bifunctional peptide on the day of the ICCS assay. Histograms are representative of 1 biological replicate. MFI values of peptide labeling are shown in red. (C) Flow cytometry plots of CD4$^+$ DB5 CAR T-cell pre-arming with 500 nM bifunctional peptide on the day of the ICCS assay. Plots are representative of 1 biological replicate. MFI values of peptide arming are shown in red. (D) ICCS pie charts of IL2, TNFα, and IFNγ cytokine production in CD4$^+$ DB5 CAR T cells after 5-h co-culture with target cells. Bifunctional peptide was both pre-labeled on target cells and pre-armed on T cells for directing DB5 CAR T-cell responses against αvβ6$^+$ target cells. Pie charts are representative of 1 biological replicate.

6.2.4 *In vitro* efficacy of $CD8^+$ DB5 CAR T cells directed with bifunctional peptide

We next generated $CD8^+$ DB5 CAR T cells of all three spacer lengths for peptide-directed cytotoxicity studies. $CD8^+$ CAR T cells were sourced from the same donor as the $CD4^+$ T cells used previously, and cell manufacturing comprised a similar three-week stimulation bead outgrowth protocol to that used before, except methotrexate concentrations for selection were reduced given the greater sensitivity of $CD8^+$ T cells to the drug (**Figure S6.8)**. After a week of methotrexate selection (S_1D_{11}), high transduction was confirmed by both Erbitux staining for EGFRt (>94%) and SpyTag003(D2) loading on DB5 CARs (>93%) (**Figure 6.4A**). Consistent with the $CD4^+$ DB5 CAR T cells, while the MFI value of EGFRt expression was near-identical across all three spacer lengths of the CARs, SpyTag003(D2) loading on the $CD8^+$ DB5 CAR T cells was the highest on T cells expressing the short spacer CAR, followed by the long spacer CAR, and then lastly the medium spacer CAR. These data further support that the medium spacer length struggles to properly present SpyCatcher003 on the cell surface.

We next compared the capacity of these $CD8^+$ DB5 CAR T cells to kill $\alpha v\beta 6^+$ target cells when directed by the C2C18(ChARK)-X-SpyTag003(D2) bifunctional peptide. Based on the prior results of pre-arming $CD4^+$ T cells versus pre-labeling target cells in **Figure 6.3C**, we chose to only pre-arm $CD8^+$ T cells with 500 nM bifunctional peptide for the cytotoxicity assay since that was found to be most effective in generating responses against BxPC3 cells. Moderate pre-arming of $CD8^+$ DB5 CAR T cells (>77%) for all space lengths was confirmed by flow cytometry (**Figure 6.4B**). The MFI of bifunctional peptide pre-arming on the DB5 CAR T cells was spacer-dependent (short > long > medium), tracking with both the SpyTag003(D2) loading results on S_1D_{11} and the pre-arming results in the $CD4^+$ DB5 CAR T-cell ICCS study. For target cells, we pre-labeled K562, K562 αvβ6:mCherry, K562 SpyTag003(L), and BxPC3 cells with a CellTrace dye to distinguish

them from effector $CD8^+$ T cells by flow cytometry. Effector $CD8^+$ T-cells and target cells were co-cultured together at different effector-to-target (E:T) ratios for 18 h before staining cells with a viability dye to assess killing of the $CellTrace^+$ target cells by flow cytometry. We chose an 18-h co-culture instead of a 4-h co-culture that is commonly used for chromium release assays since other groups have reported the need for longer co-culture times to adequately measure T cell-mediated cytotoxicity of tumor cells with this more direct, non-radioactive assay.[59]

As shown in **Figure 6.4C**, $CD8^+$ DB5 CAR T cells potently lysed K562 SpyTag003(L) cells over a mock T-cell control, demonstrating that cell surface-displayed SpyTag003 mediates robust DB5 CAR activity. The magnitude of K562 SpyTag003(L) lysis also discernibly increased as the spacer length of $CD8^+$ DB5 CAR T cells decreased, which is expected given that SpyTag003 is spaced distally from the cell surface in this target cell line and thus shorter DB5 CARs should form a narrower synapse with these cells for increased CD45 phosphatase exclusion and T-cell activation.[60] Neither $CD8^+$ mock nor DB5 CAR T cells actively lysed K562 cells, regardless of bifunctional peptide arming, and unarmed $CD8^+$ DB5 CAR T cells did not lyse K562 αvβ6:mCherry and BxPC3 targets over the mock T-cell controls, with the exception of the unarmed short spacer $CD8^+$ DB5 CAR T cells that induced some lysis of K562 αvβ6:mCherry cells. This unusual activity of the unarmed shorter spacer DB5 CAR T cells against K562 αvβ6:mCherry cells was also observed previously in the $CD4^+$ T-cell ICCS study, indicating that this is a real response. However, as this activity is specific only to the K562 αvβ6:mCherry cells, which is a model cell line selected for *in vitro* studies and not representative of real-word $αvβ6^+$ targets like BxPC3 cells, we did not further explore the cause.

Analyzing pre-armed $CD8^+$ DB5 CAR T-cell activity, we observed peptide-directed lysis of K562 αvβ6:mCherry and BxPC3 cells for all DB5 CAR spacer lengths that titrated with the E:T ratio.

The short spacer DB5 CAR elicited the greatest lysis of K562 αvβ6:mCherry and BxPC3 cells by $CD8^+$ T cells when pre-armed with bifunctional peptide, although the background lysis of K562 αvβ6:mCherry cells with unarmed short spacer DB5 CAR makes the K562 αvβ6:mCherry cytotoxicity results difficult to interpret. The pre-armed long spacer DB5 CAR was only slightly inferior at lysing BxPC3 cells than the short spacer DB5 CAR despite having significantly less pre-arming as indicated in **Figure 6.4B**, suggesting that the long spacer DB5 CAR may be more potent with the bifunctional peptide. The pre-armed medium spacer DB5 CAR induced the least lysis of BxPC3 cells, consistent with the previous $CD4^+$ T-cell ICCS results and SpyTag003(D2) loading observations. Altogether, the functional assays with $CD4^+$ and $CD8^+$ T cells demonstrate that the C2C18(ChARK)-X-SpyTag003(D2) peptide can effectively direct DB5 CAR T-cell activity against $\alpha v\beta 6^+$ cancer cell targets, especially when covalently armed onto T cells, and that the DB5 CAR spacer length heavily influences T-cell responses with the bifunctional peptide intermediate.

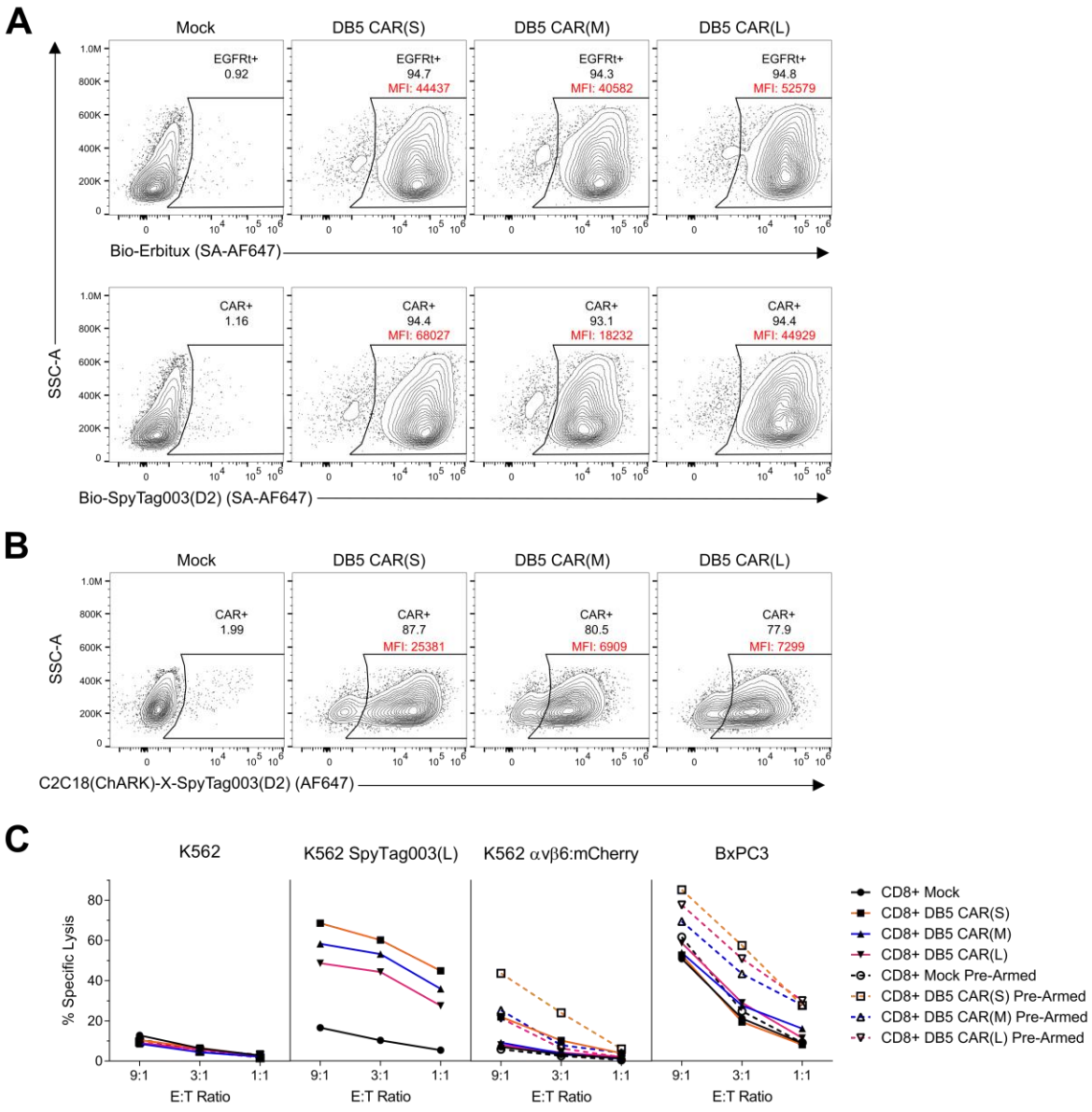

Figure 6.4 | Bifunctional adaptor peptide directs CD8$^+$ DB5 CAR T-cell cytotoxic responses against αvβ6$^+$ target cells. (A) Flow cytometry plots of biotinylated Erbitux staining and 500 nM SpyTag003(D2) loading on S_1D_{11} CD8$^+$ T cells transduced with lentivirus encoding short, medium, and long spacer DB5 CARs. Plots are representative of 1 biological replicate. MFI values of antibody staining and peptide loading are shown in red. (B) Flow cytometry plots of CD8$^+$ DB5 CAR T-cell pre-arming with 500 nM bifunctional peptide on the day of the cytotoxicity assay. Plots are representative of 1 biological replicate. MFI values of peptide arming are shown in red. (C) Specific lysis curves of target cells after 18-h co-culture with effector CD8$^+$ DB5 CAR T cells at 9:1, 3:1, and 1:1 E:T ratios, normalized to lysis in the absence of T cells. Bifunctional peptide was only pre-armed on T cells for directing DB5 CAR T-cell responses against αvβ6$^+$ target cells. Curves are representative of 1 biological replicate.

6.2.5 Optimization of bifunctional peptide administration for arming DB5 CAR T cells *in vivo*

Fluorescein-folate (FITC-folate), a small molecule that targets folate receptor 1 overexpressed on malignant cells, is arguably one of the most successful adaptor intermediates to be used with universal CAR T cells to-date.[29,30,61,62] Unlike larger antibodies that have circulation half-lives of days to weeks,[63] FITC-folate has a circulation half-life of ~87 min in humans and an estimated circulation half-life of ~20-40 min in mice,[64,65] which allows fast and precise control of its concentration *in vivo* for regulating CAR T-cell activity.[62] As peptides are also small targeting agents that can potentially offer the same advantages as small-molecule targeting intermediates, we sought to characterize the plasma circulation half-life of the C2C18(ChARK) peptide. To fluorescently detect peptide in blood and mimic the SpyTag003(D) branching in the bifunctional peptide, we synthesized C2C18(ChARK) and selectively labeled the C-terminal D-lysine side chain with Cy5 via NHS chemistry to create C2C18(ChARK)-Cy5 (**Figure S6.9A**). We then intravenously injected NOD scid mice with 10 nmol C2C18(ChARK)-Cy5 (400-500 nmol/kg) and monitored the peptide plasma concentration for up to 2 h post-injection. C2C18(ChARK)-Cy5 concentration in the plasma peaked at ~10 μM (**Figure S6.9B**), consistent with the mean estimated central blood volume of ~1000 μL for this mouse model.[66] Fitting the exponential decay of peptide plasma concentration over time to a two-compartment pharmacokinetic model, C2C18(ChARK)-Cy5 displayed a short distribution half-life of ~2 min and a longer elimination half-life of ~50 min. As the elimination half-life of our peptide is comparable to that of FITC-folate, we predict that we will have good control of bifunctional peptide concentration *in vivo* for directing DB5 CAR T-cell activity.

We next evaluated how different parameters of bifunctional peptide administration, specifically dosing concentration, frequency, and injection route, affect DB5 CAR T-cell arming *in vivo*. For

this purpose, we intravenously injected immunodeficient NOD scid gamma (NSG) mice with 10 × 10^6 $CD4^+/CD8^+$ mock or short spacer DB5 CAR T cells followed by administration of C2C18(ChARK)-X-SpyTag003(D2) to assess arming of circulating T cells in the blood. Comparing 10, 5, and 2.5 nmol intravenous doses of bifunctional peptide, we observed concentration dependent arming of DB5 CAR T cells in the blood 4 h post-injection over mock controls that received 10 nmol peptide (**Figure 6.5A**). Fitted to a dose-response Hill equation, the *in vivo* arming data suggests that a 4-5 nmol dose of bifunctional peptide (~160-250 nmol/kg) leads to half-maximal arming of DB5 CAR T cells in the blood (**Figure 6.5B**). We also tracked arming of these same DB5 CAR T cells over time in the mice and found that arming decayed over time with a half-life of ~6 h (**Figure 6.5C**), which may be attributed to a combination of CAR turnover, CAR internalization, peptide degradation, and/or T-cell proliferation. After 50 h, there was only a trace amount of peptide arming detected on the T cells, suggesting that dosing bifunctional peptide every 2-3 days would be needed to keep DB5 CAR T cells continually armed *in vivo*. We lastly compared DB5 CAR T-cell arming after retro-orbital (RO), tail vein (TV), subcutaneous (SQ), and intraperitoneal (IP) routes of peptide administration. As shown in **Figure 6.5D**, intravenous administration of bifunctional peptide (RO and TV) provided the highest arming of DB5 CAR T cells in the blood 24 h post-injection, followed by SQ administration, and lastly IP administration. Collectively, these results shed light on dosing regimen parameters that are important for arming DB5 CAR T cells *in vivo* with the bifunctional peptide.

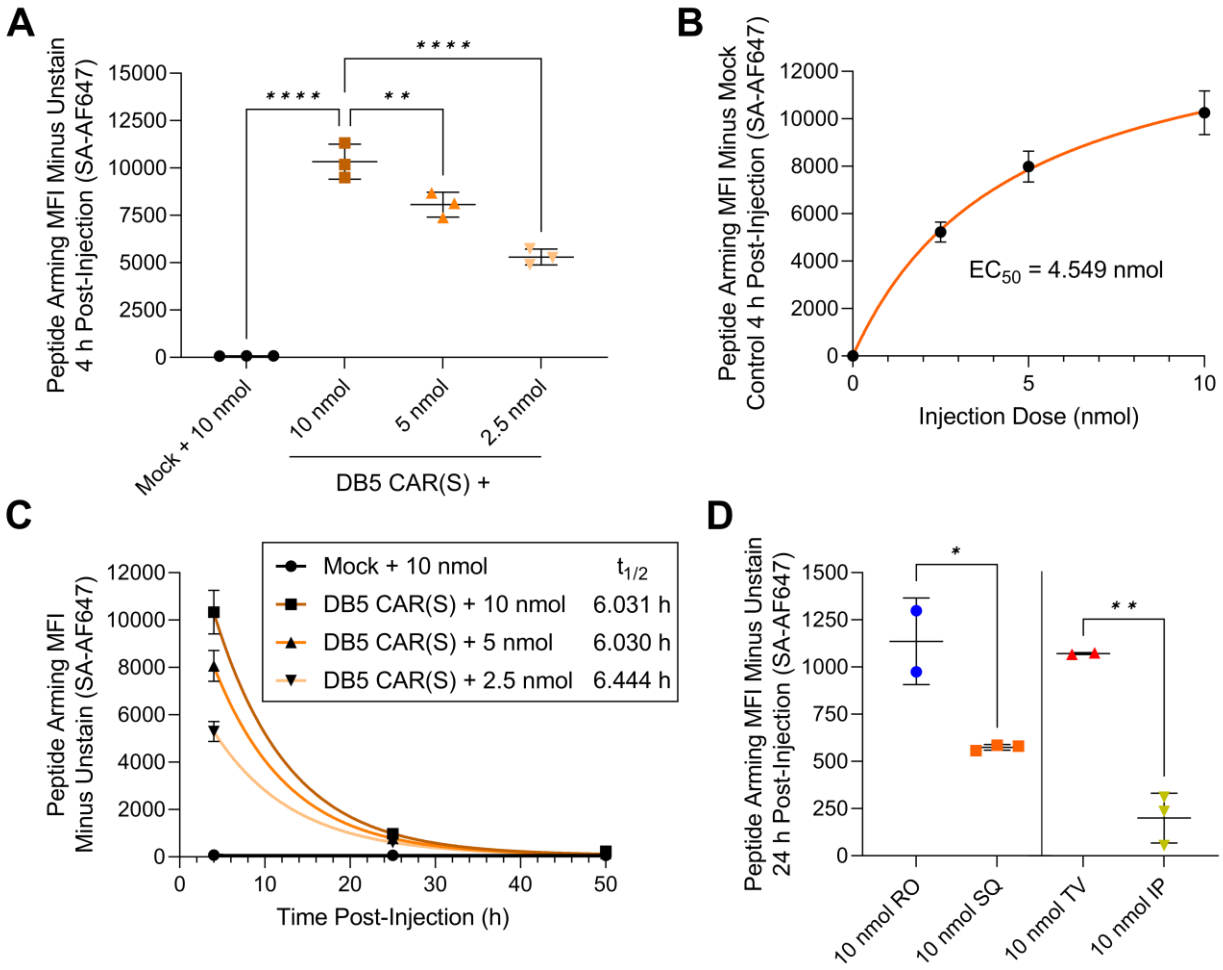

Figure 6.5 | Dose, frequency, and injection route of bifunctional peptide administration impact DB5 CAR T-cell arming *in vivo*. (A) Peptide arming MFI on circulating $CD3^+CD45^+$ DB5 CAR T cells in NSG mice 4 h after injection with 2.5, 5, and 10 nmol bifunctional peptide, measured by flow cytometry. Data points and error bars represent the mean ± SD; *n* = 3 mice per group. $^{**}P < 0.01$, $^{****}P < 0.0001$ (ordinary one-way ANOVA with Dunnett's correction). (B) Corresponding dose-response curve of DB5 CAR T-cell arming MFI as a function of bifunctional peptide dose. The curve represents a nonlinear regression in which arming data are fitted to a Hill equation. Data points and error bars represent the mean ± SD; *n* = 3 mice per dose. (C) Half-life of peptide arming on circulating $CD3^+CD45^+$ DB5 CAR T cells following injection with the above bifunctional peptide doses. The curves represent a nonlinear regression assuming one-phase exponential decay. Data points and error bars represent the mean ± SD; *n* = 2-3 mice per group. (D) Peptide arming MFI on circulating $CD3^+CD45^+$ DB5 CAR T cells in NSG mice 24 h after retro-orbital (RO), subcutaneous (SQ), tail vein (TV), and intraperitoneal (IP) injection with 10 nmol bifunctional peptide, measured by flow cytometry. Data points and error bars represent the mean ± SD; *n* = 2-3 mice per group. $^{*}P < 0.05$, $^{**}P < 0.01$ (two-sided unpaired *t*-test). SA-AF647, streptavidin Alexa Fluor 647.

6.2.6 Synthesis and characterization of a heterobifunctional aptamer-peptide chimera

Besides peptides, we searched for other types of synthetic targeting intermediates that could interface with the DB5 CAR system for cancer targeting. DNA aptamers are single-stranded oligonucleotides that fold into sequence-specific secondary structures capable of recognizing cellular and protein targets with high affinity.[67] Importantly, aptamers are small (10-30 kDa), non-toxic, and amenable to modification with drugs or other peptides for multiplexed properties, highlighting their potential for cancer recognition and treatment.[68,69] Our lab previously discovered a high-affinity DNA aptamer that binds the integrin α4β1 selectively expressed on lymphoid-derived leukemia and lymphoma cells (e.g., Jurkat cells) over myeloid-derived counterparts (e.g., K562 cells) and healthy immune cells (unpublished, Chapter 5). Given the aptamer's favorable cancer targeting traits, we sought to use it in creating a synthetic heterobifunctional aptamer-peptide chimera for directing DB5 CAR T-cell function.

To construct the aptamer-peptide chimera, we used strain-promoted azide-alkyne cycloaddition (SPAAC), a copper-free click reaction that occurs spontaneously with high yield under mild aqueous conditions and is orthogonal to other biochemical reactions.[70] Biotinylated SpyTag003(D2) was first synthesized with a C-terminal D-lysine that contained an acid-labile Mtt group protecting the side chain amino group, which was selectively deprotected and coupled with 5-azidopenatoic acid to produce azide-SpyTag003(D2)-biotin. Our aptamer was then commercially manufactured with a 5' dibenzocyclooctyne (DBCO) modification and reacted with azide-containing peptide to form a triazole bridge, resulting in the chimera called Aptamer-Triazole-SpyTag003(D2)-biotin (**Figure 6.6A**). Denaturing urea polyacrylamide gel electrophoresis (urea-PAGE) confirmed successful conjugation of the aptamer to the peptide with >80% yield, as demonstrated by an upward shift in the DNA band compared to an unconjugated

aptamer control (**Figure S6.10**). The aptamer-peptide chimera was subsequently purified by ethanol precipitation to remove excess unreacted peptide before proceeding to characterization studies.

To determine if the aptamer-peptide chimera had bifunctional properties, we first evaluated binding of the chimera to T-leukemia Jurkat cells (aptamer target positive) and myeloid leukemia K562 cells (aptamer target negative). As expected, Aptamer-Triazole-SpyTag003(D2)-biotin selectively bound Jurkat cells with high affinity, indicating functionality of the aptamer arm of the chimera (**Figure 6.6B**). Furthermore, as streptavidin Alexa Fluor 647 was used as a secondary stain to measure binding, this data also demonstrates successful conjugation of the aptamer to SpyTag003(D2)-biotin, since unconjugated aptamer would not have biotin for streptavidin recognition. We next tested loading of the chimera on primary $CD8^+$ mock and DB5 CAR T cells characterized in **Figure 6.4**. Aptamer-Triazole-SpyTag003(D2)-biotin loaded selectively on $CD8^+$ DB5 CAR T cells of all spacer lengths over the mock control, showing functionality of the peptide arm of the chimera (**Figure 6.6C**). Chimera loading was highest on $CD8^+$ T cells expressing the short spacer CAR, followed by the long spacer CAR, and then lastly the medium spacer CAR, which is consistent with the trend of C2C18(ChARK)-X-SpyTag003(D2) loading on these cells in **Figure 6.4B**. While some chimera loading was observed on mock T cells, this is likely attributed to aptamer binding since our aptamer is known to have low binding to healthy lymphocytes. In comparison, the aptamer exhibits much greater binding to lymphocytic cancer cells, so we do not anticipate off-tumor DB5 activity that would result in unwanted killing of healthy immune cells or fratricide of the CAR T-cell product. However, further testing is needed to determine this. Taken together, the Aptamer-Triazole-SpyTag003(D2)-biotin chimera displays potent heterobifunctional qualities.

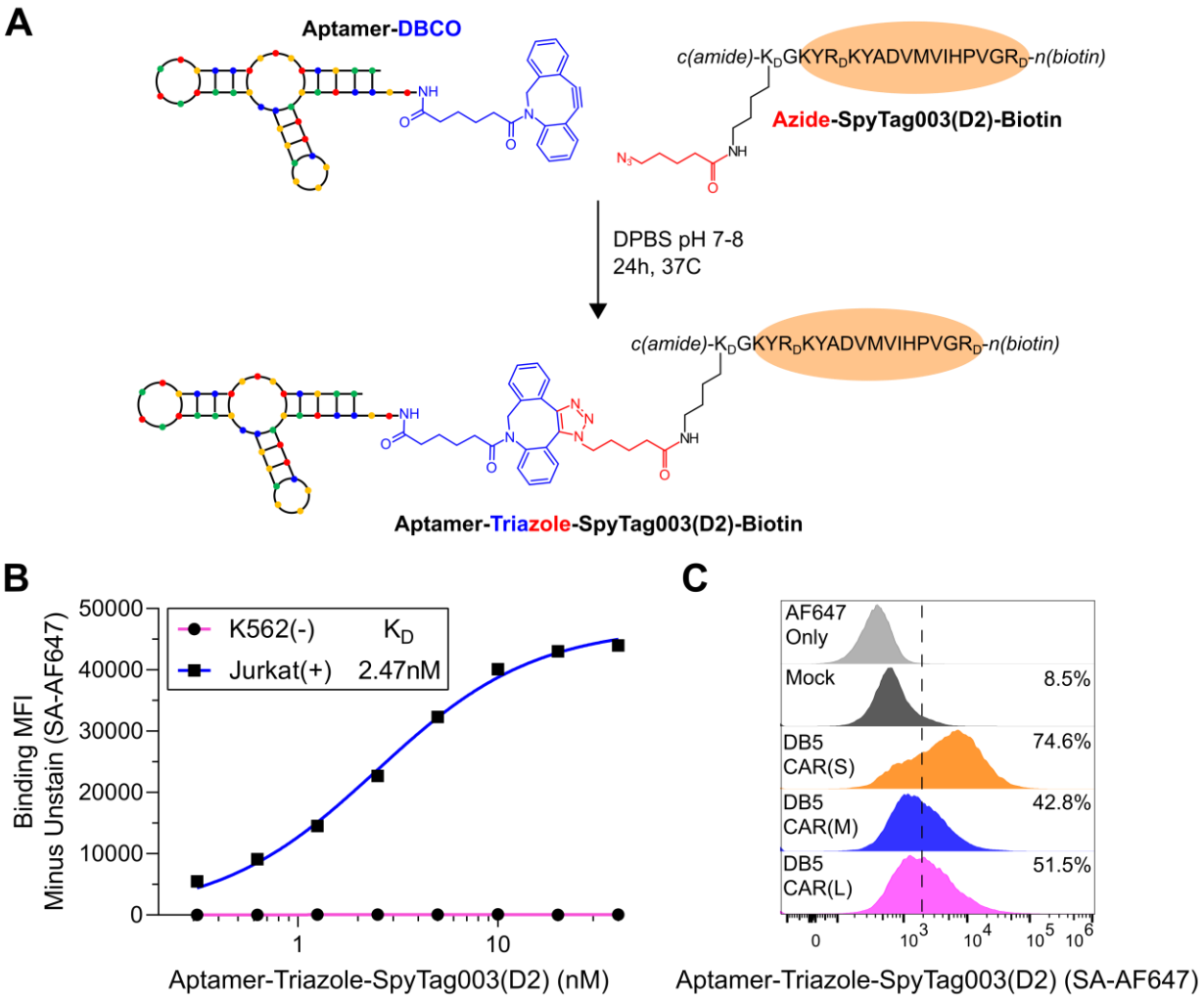

Figure 6.6 | Heterobifunctional aptamer-peptide chimera is capable of bispecific properties. (A) Schematic representation of copper-free click chemistry reaction used to synthesize Aptamer-Triazole-SpyTag003(D2)-biotin chimera. DBCO and azide modifications used for the click reaction are shown in blue and red, respectively. (B) Flow cytometry binding curves of aptamer-peptide chimera to K562 and Jurkat cells. The curves represent a nonlinear regression of one independent experiments in which binding data are fitted to a Hill equation. (C) Flow cytometry histograms of 500nM aptamer-peptide chimera loading on $CD8^+$ DB5 CAR T cells with different spacers lengths. Histograms are representative of two independent experiments. SA-AF647, streptavidin Alexa Fluor 647.

6.3 DISCUSSION AND FUTURE WORK

CAR T-cell therapy has demonstrated great potential to treat cancer but relapse due to antigen escape and toxicities have limited the therapy's broader clinical impact. Universal CAR systems

that decouple antigen targeting from the CAR represent a promising solution to these problems. In these approaches, externally supplemented targeting intermediates are used to bridge CAR T-cell activity with antigen targets, giving researchers and clinicians greater control over the therapy's direction and outcome. A panel of intermediate ligands can be tailored to a patient's heterogenous cancer antigen profile for comprehensive therapy that requires only one CAR T-cell product, and intermediates can be further adapted over treatment to counter a tumor's dynamic plasticity that promotes antigen escape. As the intermediates effectively control antigen presentation and can be cleared from circulation quickly, the concentration and frequency of intermediate dosage can also be precisely regulated to mitigate side effects associated with therapy.

Most universal CAR systems to-date rely on transient noncovalent recognition of tagged targeting intermediates for function, which is unstable and can diminish CAR T-cell activity. For this reason, covalent SpyCatcher-SpyTag chemistry has recently become an attractive method for directing universal CAR T cells function, since T cells can be stably armed with intermediates for prolonged targeting. Indeed, Minutolo et al. showed that covalent recognition of SpyTag-labeled intermediates by SpyCatcher CAR T cells provided better T-cell arming and activation than affinity-based recognition of the same intermediates labeled with a non-reactive SpyTag mutant.[38] Despite this, when compared to conventional CAR T cells, their armed SpyCatcher CAR T cells displayed less overall potency and also lost sensitivity when target antigen expression was low. These results are potentially attributed to the slow kinetics of the SpyCatcher-SpyTag reaction that require micromolar concentrations of each partner, underscoring the need for more efficient covalent universal CAR systems that can be feasibly translated. Additionally, despite the versatility of these approaches, published universal CAR systems have not capitalized on the different classes of ligand intermediates available for cancer targeting, such as synthetic peptides

and aptamers, and instead have relegated their usage to well-established antibody, protein, and small molecule intermediates. Given the unique advantages of synthetic peptides and aptamers, there is an opportunity for expanding the toolkit of intermediates used with universal CAR systems.

In this study, we developed a cyborg universal CAR system that uses accelerated SpyCatcher003-SpyTag003 chemistry to covalently modify T-cell effector function with synthetic targeting materials. These SpyCatcher003 CARs, called DB5 CARs for short, and their cognate peptide SpyTag003 exhibit enhanced arming and reaction kinetics compared to CARs that use original SpyCatcher-SpyTag chemistry. To redirect DB5 CAR T-cell effector function against target cancer antigens, we synthesized a branched peptide intermediate containing both SpyTag003 and a serum-stabilized A20FMDV2 peptide that we previously reported for high-affinity targeting of $\alpha v\beta 6^{+}$ tumor cells. The branched peptide displayed robust bispecific adaptor properties, capable of selectively recognizing both $\alpha v\beta 6^{+}$ cancer cells and DB5 CAR-expressing cells. We demonstrate the bifunctional peptide's ability to induce $CD4^{+}$ DB5 CAR T-cell cytokine production and $CD8^{+}$ DB5 CAR T-cell killing *in vitro* when pre-labeled on $\alpha v\beta 6^{+}$ target cells and pre-armed on DB5 CAR T cells, and we show that these responses are dependent on the extracellular spacing of the DB5 CAR. Arming of DB5 CAR T cells with the bifunctional peptide was also achieved in mice, and parameters of peptide administration that influence DB5 CAR T-cell arming were examined to prepare for future *in vivo* preclinical studies. We lastly synthesized a heterobifunctional aptamer-peptide chimera capable of selectively recognizing both cancer cells and DB5 CAR T cells, diversifying the toolkit of synthetic materials that can interface with the DB5 CAR system,

There are many exciting opportunities afforded by these cyborg CAR T cells. Besides using different concentrations of synthetic targeting materials to titrate DB5 CAR T-cell activation, different generations of SpyTag may be used to a similar effect. SpyTag, SpyTag002, and SpyTag003 react with SpyCatcher003 with rate constants spanning a 20-fold range of values, suggesting that they can be interchanged in the bifunctional peptide to fine-tune the strength of cyborg CAR T-cell activation. Moreover, synthetic materials can be modified to incorporate targeting ligands that permit T-cell accumulation in solid tumors, and synthetic materials can incorporate multiple SpyTag peptides that can group CARs on the surface of a T-cell to potentially augment cytokine release and cell killing. Additionally, DB5 CARs can be partnered with other covalent systems that are orthogonal to SpyCatcher-SpyTag chemistry for logic-gated functions. Split from the same adhesin in *Streptococcus pneumoniae*, SnoopCatcher-SnoopTag and DogCatcher-DogTag are protein-peptide pairs that spontaneously form isopeptide bonds with each other and show no cross-reaction to SpyCatcher and SpyTag.[71,72] Orthogonal SpyCatcher-SpyTag and SnoopCatcher-SnoopTag or DogCatcher-DogTag chemistries can thus be fashioned together in trans-signaling CAR strategies or in synNotch receptor circuits for AND-gated T-cell activation that requires intermediate-guided dual antigen recognition.[57,73]

A limitation of the DB5 CAR system is the non-human origin of the covalent chemistry. The first-generation SpyCatcher-SpyTag pair were sourced from a collagen adhesin domain found in *Streptococcus pyogenes*, so SpyCatcher003 and SpyTag003 may be immunogenic if used in humans. Additionally, the αvβ6-specific A20FMDV2 peptide used for cancer targeting is virus-derived. Alleviating some of these concerns, the D-amino acid substitutions we made to C2C18(ChARK) and SpyTag003(D2) should reduce any potential immunogenicity of the bifunctional peptide, and administration of the bifunctional peptide into immunocompetent mice

can validate this claim. As for SpyCatcher003, it was previously shown that N-terminal truncation of the SpyCatcher protein can lower the antibody responses it induces in immunocompetent mice without affecting its reaction with SpyTag.[74] Given that the mutations made from SpyCatcher002 to SpyCatcher003 are all localized at the protein's C-terminus (**Figure S6.11**),[42] and that the N-terminus of SpyCatcher is known to not have any direct interaction with SpyTag,[44] we anticipate that an N-terminal truncated version of SpyCatcher003 can likely be swapped into the DB5 CARs to reduce immunogenicity without sacrificing the augmented reaction kinetics of the system.

Unexplored in this work is the effect of different T-cell signaling domains on DB5 CAR T-cell function. We only tested DB5 CARs containing 41BB-CD3ζ intracellular signaling domains, which are known to signal less strongly and with slower kinetics than CD28-CD3ζ signaling domains.[75] In settings of chronic antigen stimulation, CARs with 41BB-CD3ζ signaling domains can be more advantageous, promoting increased memory differentiation that enhance T-cell persistence and long-term potency.[76] However, recent work has shown that CARs with low-affinity tumor-recognition domains serve better with CD28-CD3ζ signaling domains since CD28 costimulation lowers the affinity threshold for efficient effector function.[77,78] Similarly, targeting tumor antigens with low surface density may demand the stronger signaling of CD28-CD3ζ CARs to achieve sufficient T-cell activation.[38,79] The C2C18(ChARK)-X-SpyTag003(D2) peptide described in this work binds αvβ6$^+$ target cells with a K_D ~100 nM, which is 100-fold lower than the reported binding affinity of FITC-folate for FOLR1$^+$ target cells (K_D ~1 nM).[30] Furthermore, recycling of αvβ6 to the cell surface after A20FDMV2-induced internalization is known to be slow,[49] suggesting that injection of the bifunctional peptide *in vivo* will reduce αvβ6 density on the surface of tumor cells concurrently with arming DB5 CAR T cells. Given these barriers that raise

the threshold for DB5 CAR T-cell activation with the bifunctional peptide, a more sensitive CD28-CD3ζ signaling domain may be critical for successful translation of this system *in vivo*.

In summary, we demonstrate the potential to utilize synthetic materials to arm a universal CAR system via efficient SpyCatcher003-SpyTag003 chemistry for directing T-cell responses against cancer cells *in vitro*. Future work will take the platform *in vivo* and test alternative CAR signaling domains with the current synthetic intermediates. We will also explore other synthetic targeting materials like peptide- and aptamer-co-polymer conjugates to further expand the toolkit of adaptor ligands available to this system.

6.4 MATERIALS AND METHODS

6.4.1 Cloning of lentiviral constructs and lentivirus production

DNA fragments with a Kozak sequence and an open reading frame encoding a GM-CSF signal peptide followed by SpyCatcher, SpyCatcher003, or SpyTag003 were synthesized by GeneArt and amplified by PCR prior to cloning. The three epHIV7.2 lentiviral vectors encoding scFv-spacer-CD28tm-41BB-CD3ζ-P2A-DHFRdm-T2A-EGFRt with short (IgG4 hinge), medium (IgG4 hinge-CH3), and long (IgG4 hinge-CH2-CH3) extracellular spacers were a gift from the Jensen Lab (Seattle Children's Research Institute). DNA fragments and lentiviral vectors were digested with NheI and RsrII restriction enzymes (NEB) to create inserts and scFv-excised backbones, respectively, that were subsequently gel purified (QIAGEN) and ligated with T4 DNA ligase (NEB). DH10B and Stbl2 chemically competent *E. coli* (Thermo Fisher) were transformed with ligated products and kanamycin-selected colonies were screened by PCR for correct insert length. Correct cloning was verified by sangar sequencing (GENEWIZ) of miniprep DNA (QIAGEN) before transfection-grade plasmid DNA was prepared by maxiprep (MACHEREY-NAGEL).

HEK 293T cells were purchased from ATCC and used before passage 20. For each lentivirus production run, HEK 293T cells were seeded 24 h prior to transfection in twenty 10 cm plates at 3×10^6 cells per plate in 10 mL DMEM with high-glucose, L-glutamine, and sodium pyruvate (Life Tech) supplemented with 10% gamma-irradiated FBS (Life Tech) and 1X penicillin-streptomycin (Life Tech). The next day, half of the plating media (5 mL) was removed from the cells and each plate was transfected with 15 μL BioT transfection reagent (Bioland Scientific) mixed with 150 μL serum-free DMEM containing pMDL-RRE (2.9 μg), pRSV-Rev (1.1 μg), pVSV-G (1.6 μg), and transgene lentiviral vectors (4.5 μg). After 24 h, 5 mL complete DMEM media was added to the plates to make the supernatant 10 mL total and virus-containing supernatant was collected and replaced with 5 mL fresh media at 48 and 72 h post-transfection. At 96 h post-transfection, the last of the virus-containing supernatant was collected (400 mL total for twenty 10 cm plates) and cell debris was removed by 0.22 μm filtration. Virus was pelleted in two batches by ultracentrifugation at 18,500 rpm (58,486 xg) for 2 h at 4 °C in a Beckman Coulter Optima L-100XP Ultracentrifuge using a SW 32 Ti rotor and 38.5 mL open-top tubes (Beckman Coulter). Pellets from both batches were resuspended and combined in 12 mL HBSS before being pelleted again by ultracentrifugation at 19,500 rpm (65,2020 xg) for 2 h at 4 °C using a SW 41 Ti rotor and 13.2 mL open-top tubes (Beckman Coulter). The resulting viral pellet was resuspended in 200 μL HBSS and stored at -80 °C until further use.

6.4.2 Peptide synthesis, purification, and cyclization

Sequences of synthesized peptides are listed in **Table S6.1**. Materials for peptide synthesis are as previously described,[53] with the addition of Fmoc-D-Lys(Mtt)-OH, Fmoc-Lys(Mtt)-OH, Fmoc-ε-Ahx-OH, acetic anhydride, pyridine, NHS-rhodamine, NHS-Cy5, and 5-azidopentanoic acid purchased from Alfa Aesar (Haverhill, MA), Novabiochem (Darmstadt, Germany), AAPPTec

(Louisville, Kentucky), EMD Millipore (Burlington, MA), Thermo Fisher (Waltham, MA), and BroadPharm (San Diego, CA). Peptide synthesis was done as previously described,[53] with the addition of peptide end-capping and Lys(Mtt) deprotection steps for the synthesis of branched peptides or addition of C-terminal rhodamine, Cy5, or 5-azidopentanoic acid. After synthesis of the first peptide arm, on-resin acetylation of the peptide N-terminus was carried out twice in 10 mL 3:2:1 (v/v) DCM:pyridine:acetic anhydride for 1 h at room temperature with end-over-end mixing. Resin with peptide was then washed 3 times with DCM and a Kaiser Test was used to qualitatively check N-acetylation as previously described.[80] The Mtt-protecting group on Lys(Mtt) was removed by repeatedly incubating the resin with N-acetylated or N-biotinylated peptide in 10 mL 2% TFA in DCM (v/v) for 15 min at room temperature with end-over-end mixing until the deprotection solution turned from yellow-orange to clear (5-10 times). Resin was then washed 3 times with each DCM, DMF, and methanol before successful Mtt-deprotection was qualitatively confirmed by Kaiser Test. For further synthesis of branched peptides or on-resin coupling of 5-azidopentanoic acid, the resin with N-acetylated or N-biotinylated and Mtt-deprotected peptide was swelled in 50:50 (v/v) DMF:DCM for 20 min prior to further synthesis on a Liberty Blue HT12 automated microwave peptide synthesizer (CEM, Matthews, NC). For on-resin coupling of NHS-rhodamine or NHS-Cy5, resin with N-acetylated and Mtt-deprotected peptide was swelled in DCM and then exchanged to 5mL DCM with 2 molar equivalents NHS-dye, 3 molar equivalents EDC, and 8 molar equivalents of triethylamine. After an overnight incubation at room temperature with end-over-end mixing, the resin with dye-coupled peptide was washed 3 times in DCM before cleavage. All peptides were cleaved and ether precipitated as previously described,[53] with the exception of azide-SpyTag003(D2)-biotin that was cleaved in 92.5:2.5:2.5:2.5 TFA:triisopropylsilane:H_2O:thioanisol to limit azide to amine reduction.[81]

Peptides were purified by reverse-phase HPLC (Agilent 1260 Infinity, Santa Clara, CA) using a ZORBAX 300SB-C18 semi-preparative column (Agilent). For SpyTag peptides, a flow rate of 5 mL/min and a 30-60% or 25-65% 8-min linear solvent gradient of ACN in H_2O with 0.1% TFA were used for purification by monitoring 280 nm absorbance. For bifunctional peptides, purification conditions were similar but required a shallower and longer 30-55% 12-min linear solvent gradient. Bifunctional peptides were cyclized with DFBP as previously described.[53] Molecular weights of peptides were screened by MALDI-ToF MS (Bruker AutoFlexII, Billerica, MA) multiple times throughout the production process and were consistently within 1-2 g/mol of expected values.

6.4.3 Cell line culture and T-cell isolation

The H9, K562, and BxPC3 cell lines were purchased from ATCC. The K562 αvβ6:mCherry cell line was a gift from A. Olshefsky (Pun and King Labs, University of Washington) and were generated as previously described.[53] The K562 SpyTag003(L) cell line was generated by transduction of 10^6 K562 cells with lentivirus (3.26e8 TU/mL) encoding a SpyTag003 long-spacer CAR at a multiplicity of infection (MOI) of 3 with 5 μg/mL polybrene (EMD Millipore). The H9 cell lines expressing SpyCatcher and DB5 CARs of different spacer lengths were generated in lentivirus titering studies described below. All the above cell lines were cultured in complete RPMI comprised of RPMI 1640 medium with L-glutamine (Corning) supplemented with 10% FBS. Human peripheral blood mononuclear cells (PBMCs) were isolated from TRIMA LRS chambers (Bloodworks Northwest) using Ficoll-Paque density gradient centrifugation (GE). $CD4^+$ and $CD8^+$ T cells were positivity selected in sequence from PBMCs by magnetic-activated cell sorting (MACS) using CD4 and CD8 Microbeads (Miltenyi) according to the manufacturer's instructions and were banked for later CAR T-cell production.

6.4.4 Extracellular flow cytometry binding studies

Peptide stocks were prepared in H_2O at 5 mM and the exact concentration of biotinylated stocks was measured using a QuantTag Biotin Quantification Kit (Vector Labs). SC50Ai SpyCatcher nanocages were a kind gift from the Baker Lab (University of Washington) and were used at a 1:75 dilution (~16.67 nM). Biotinylated Erbitux antibody was a kind from the Jensen Lab (Seattle Children's Therapeutics) and was used at a 1:1000 dilution. Prior to binding, cells were pre-stained with 1:500 Zombie Violet (BioLegend) in 100 μL DPBS (Gibco) per 10^6 cells for 15 min at room temperature for dead cell discrimination. Cells were then washed with DPBS 1% BSA (Miltenyi) to neutralize remaining Zombie Violet and plated in a U-bottom black 96-well plate at 2×10^5 cells per well. Primary staining (100 μL) was carried out under different conditions depending on the assay. For EGFRt staining, cells were stained with antibody diluted in DPBS 1% BSA for 20-30 min at room temperature. For αvβ6-binding experiments, cells were stained with peptides diluted in DPBS with calcium and magnesium (Corning) for 20 min at 4 °C. For loading via covalent SpyCatcher-SpyTag chemistry, cells were stained with peptides or nanocages diluted in DPBS for 30-60 min at room temperature. After primary staining, cells were washed twice with 200 μL appropriate buffer and then stained with the appropriate secondary (100 μL). For cells labeled with biotinylated ligands, cells were stained with streptavidin Alexa Fluor 647 diluted 1:500 in DPBS with calcium and magnesium (αvβ6) or DPBS 1% BSA (antibody, peptide loading) for 20 min at 4 ℃ or room temperature, respectively. For cells labeled with nanocages, cells were stained with SpyTag-Rhodamine diluted in DPBS for 1 h at room temperature. After secondary staining, cells were washed twice as before and resuspended in 200 μL DPBS 0.1% PFA before running on an Attune NxT Flow Cytometer (Life Technologies). Data was analyzed and plotted in FlowJo v10 software and MFI of singlet live cell events were used as measurements of binding or

loading. The background of a secondary only control was subtracted from MFI values before they were normalized to either a positive control (A20FMDV2) or the highest observed value to account for machine-variability across experiments. GraphPad Prism 6 software was used to generate binding and loading curves and their associated apparent K_D and K_m values.

6.4.5 Lentivirus titering

H9 cells (10^5) were transduced with 0, 0.05, 0.1, 0.25, 0.5, 1, 3, and 6 μL lentivirus in 0.5 mL complete RPMI with 5 μg/mL polybrene in a 24-well plate. After 24 h, 1 mL complete RPMI was added to cells to dilute the polybrene. The cells were stained with biotinylated Erbitux and SpyTag003(D2) 96 h post-transduction to measure the percentage of EGFRt and CAR positive cells, respectively. Titers were calculated from virus dilutions that gave percent positive cells in the linear titering range (10-45%) using the following equation: $\frac{TU}{mL} = \frac{(\%\ EGFRt^{+} or\ CAR^{+})(10^5\ cells)}{mL\ of\ lentivirus}$. Leftover H9 cells with near-100% transduction were used to generate H9 SpyCatcher CAR and DB5 CAR cell lines used in early studies.

6.4.6 MALDI-ToF MS proteolytic stability

Normal mouse serum was prepared in-house as previously described.[53] SpyTag003(D2) peptides were incubated and extracted from serum as previously described,[53] except peptides (10 mg/mL in H_2O) were also incubated 1:10 (v/v) in complete RPMI media from BxPC3 cultures spiked further with 10^6 BxPC3 cells at 37 °C to evaluate any protease activity stemming from the cancer cells. For these peptide-cell mixtures, cells were pelleted prior to sampling peptide at specific timepoints for subsequent acetonitrile extraction and stability analysis. Peptide degradation was qualitatively assessed by MALDI-ToF MS, and mass spectrums at the different timepoints were plotted and aligned in FlexAnalysis software (Bruker). A Java program called stability.jar

(https://github.com/juliomarcopineda/peptide-serum-stability/releases) was used to predict sequences of degradation products based on their observed molecular weights.

6.4.7 DB5 CAR T-cell manufacturing

$CD4^+$ and $CD8^+$ T cells (5×10^6 each) were thawed and separately stimulated 1:1 with Dynabeads Human T-Activator CD3/CD28 (Invitrogen) in 4 ml complete RPMI media with 50 U/mL rhIL-2 (Miltenyi, $CD8^+$ T cells), 5 ng/mL rhIL-7 (Miltenyi, $CD4^+$ T cells), and/or 0.5 ng/mL rhIL-15 (Miltenyi, $CD4^+$ and $CD8^+$ T cells) in a 12-well plate. After 2 d (S_1D_2), the activated T cells were individually split into four 10^6 cell groups and each transduced with lentivirus encoding DB5 CARs of different spacer lengths at an MOI of 3 in 0.5 mL complete RPMI media with 5 μg/mL polybrene, with the exception of a mock group that did not receive lentivirus. After a 4-h incubation with the lentivirus at 37 °C, T cells were diluted 1:4 in complete RPMI media containing the appropriate cytokines to dilute the polybrene. Thereafter, media exchanges were conducted every 2-3 d to replenish cytokines and cells were moved to larger culture vessels when they appeared visually dense with yellowing media. Lentivirus-transduced cells were selected with 50-100 nM methotrexate (Teva) starting 2 d after transduction (S_1D_4) for 10 d total. The activator beads were removed 9 d poststimulation (S_1D_9), and T cells were stained for EGFRt and CAR expression 11 d poststimulation (S_1D_{11}) to assess transduction efficiency. T cells were functionally evaluated in ICCS and cytotoxicity assays 18-21 d poststimulation (S_1D_{18}-S_1D_{21}) after sufficiently expanding, and remaining cells were banked for future *in vivo* studies.

6.4.8 T-cell ICCS assay

K562, K562 αvβ6:mCherry, and BxPC3 cells were pre-labeled with 500 nM bifunctional peptide at 2×10^6 cells/mL in DPBS with calcium and magnesium for 30 min at 4 °C. $CD4^+$ T cells were

similarly pre-armed with the bifunctional peptide except the incubation was conducted at room temperature. After washing, T cells (unarmed and pre-armed) and target cells (unlabeled and pre-labeled) were resuspended in complete RPMI and co-cultured at a 1:1 effector-to-target ratio with 5×10^5 cells each in 100 µL in a 96-well U-bottom plate. A cell stimulation cocktail (Invitrogen) containing phorbol 12-myristate 13-acetate (PMA) and ionomycin was added to certain wells as a positive control according to the manufacturer's instructions. Cells were incubated for 5 h at 37 °C and a protease transport inhibitor cocktail (Invitrogen) was added to all wells 1 h into the incubation to prevent cytokine secretion. During the incubation, leftover pre-labeled target cells and pre-armed T cells were stained with streptavidin Alexa Fluor 647 by flow cytometry as described earlier to confirm successful pre-labeling and pre-arming with the bifunctional peptide.

At the end of the 5-h incubation, cells were washed twice with 200 µL DPBS and then stained with 100 µL Zombie Violet (1:500) in DPBS for 15 min at room temperature. After live/dead staining, cells were washed twice with 200 µL DPBS and resuspended in 10 µL FcR Blocking Reagent (Miltenyi) for 10 min at room temperature. After blocking Fc receptors, cells were stained directly with FITC anti-human CD4 antibody (BioLegend, 1:50) in 50 µL DPBS for 20 min at room temperature. After extracellular staining, cells were washed twice with 200 µL DPBS and resuspended in 100 µL cold Cytofix/Cytoperm buffer (BD) for 20 min at 4 °C. After fixation and permeabilization, cells were washed twice with 200 µL cold 1X Perm/Wash buffer (BD) and stained with BV510 anti-human IFNγ antibody (BioLegend, 1:25), PE-Cyanine 7 anti-human TNFα antibody (Invitrogen, 1:100), and APC anti-human IL-2 antibody (Invitrogen, 1:100) in 50 µL 1X Perm/Wash buffer for 30 min at 4 °C. After intracellular staining, cells were washed twice with 200 µL cold 1X Perm/Wash buffer and resuspended in 200 µL DPBS for running on the

cytometer. Single-stain controls were included for compensation and fluorescence minus one (FMO) controls were used for gating.

6.4.9 Peptide internalization study

Trypsin-lifted BxPC3 cells were pre-stained with Zombie Violet as described above. Meanwhile, bifunctional peptide was diluted to 400 nM in DPBS with calcium and magnesium over ice. Cells were then washed at 4 °C with DPBS 1% BSA to neutralize the Zombie Violet, plated in a U-bottom 96-well plate (2×10^5 per well) over ice, and stained with 100 μL 400 nM peptide solution for 20 min at 4 °C. Cells were then washed twice with 200 μL cold DPBS, resuspended in complete media on ice, and transferred to a 37℃ incubator at different times over a 60-min period to induce internalization. Afterwards, the cells were transferred back on ice to stop further internalization, washed twice with 200 μL cold DPBS to remove media, and incubated with 100 μL streptavidin Alexa Fluor 647 in DPBS (1:500) for 20 min at 4 °C. Cells were subsequently washed twice as before and resuspended in 200 μL DPBS 0.1% PFA for running on the cytometer. The MFI of remaining peptide bound to the cell surface was normalized to peptide binding MFI on cells without 37 °C incubation (no internalization control), and normalized data was fit to an exponential decay curve in GraphPad Prism 6 software.

6.4.10 T-cell cytotoxicity assay

$CD8^+$ T cells were pre-armed with bifunctional peptide and washed as was done before for the $CD4^+$ T cells in the ICCS assay. K562, K562 SpyTag003(L), K562 αvβ6:mCherry, and BxPC3 target cells were washed once with DPBS with calcium and magnesium and then pre-labeled with 0.5 μM CellTrace Far Red (Invitrogen) in the same buffer at 10^6 cells/mL for 20 min at room temperature. After target labeling, excess dye was neutralized by adding equal volume of DPBS

with calcium and magnesium supplemented with 1% BSA to the cells and incubating for another 5 min at room temperature. Dye-labeled target cells were then transferred into complete RPMI media at 10^6 cells/mL for a 30-min incubation at 37 °C in a CO_2 incubator to limit leakage of the dye to T cells during co-culture. For plating, T cells and dye-labeled target cells were resuspended in fresh complete RPMI media before co-culturing at 9:1, 3:1, and 1:1 effector-to-target ratios with 5×10^4 total target cells in 200 μL in a 96-well U-bottom plate. Co-cultures were then pelleted and allowed to incubate for 18 h at 37 °C. During the incubation, leftover pre-armed T cells were stained with streptavidin Alexa Fluor 647 by flow cytometry as described earlier to confirm successful pre-arming with the bifunctional peptide.

At the end of the 18-h incubation, cells were washed once with 200 μL DPBS to remove excess serum and then stained with 100 μL Live-Dead Fixable Green (Invitrogen, 1:2000) in DPBS for 30 min at room temperature. After incubation, remaining dye was inactivated by adding 100 μL DPBS supplemented with 1% BSA directly to the live-dead stained cells and incubating them for another 5 min at room temperature. Wells with suspension target cells (K562 and derivative cell lines) were then washed with 200 μL DPBS, whereas wells with adherent target cells (BxPC3) were washed with 50 μL Accutase (Innovative Cell Tech) for 5 min at room temperature to detach live cells and then volumed up to 200 μL with DPBS to complete the wash. Cells were lastly resuspended in 200 μL DPBS 0.2% PFA and run on the cytometer to determine the percentage of Live-Dead Fixable Green$^+$ dead cells within CellTrace Far Red$^+$ target cells. Wells with only target cells were used to determine the amount of spontaneous cell death without T cells. T-cell specific lysis was calculated using the following equation: $\left(\frac{\%\ Killing - \%\ Spontaneus\ Death}{100\% - \%\ Spontaneous\ Death}\right)$.

6.4.11 Peptide circulation half-life

All animal experiments were performed in compliance with the University of Washington IACUC guidelines. C2C18(ChARK)-Cy5 (10 nmol) in DPBS was injected into four 8–12-week-old NOD scid mice via retro-orbital route. Blood was drawn at 10, 15, 30, 60, and 120 min post-injection and collected into pre-weighed tubes with 50 μL DPBS 5 mM EDTA. After blood collection, the tubes were re-weighed to determine the volume of blood collected. The diluted blood was then centrifuged at 1000 xg for 10 min at 4 °C, and 50 μL of the supernatant was measured for Cy5 fluorescence (Ex: 633/9 nm; Em: 670/20 nm) using an Infinite 200 PRO plate reader (Tecan). The measured fluorescence values at each timepoint were compared to a standard curve of C2C18(ChARK)-Cy5 and normalized by their respective dilution factors to estimate the peptide concentration in undiluted plasma. Data from samples with less than 1 μL collected blood (two mice at 10-min post-injection and one mouse at 15-min post-injection) were excluded prior to generating two-phase exponential decay curves in GraphPad Prism 6 software.

6.4.12 *In vivo* DB5 CAR T-cell arming

All animal experiments were performed in compliance with the University of Washington IACUC guidelines. NSG mice were retro-orbitally injected with 10×10^6 mock or DB5 CAR(S) T cells at a 75:25 CD4/CD8 ratio and enrolled into different studies within 21 days post-injection. For evaluating the concentration dependence and kinetics of DB5 CAR T-cell arming with bifunctional peptide, the same mice were retro-orbitally injected with 2.5, 5, and 10 nmol C2C18(ChARK)-X-SpyTag003(D2) 10 days after the initial T-cell injection. The mice with mock T cells received 10 nmol bifunctional peptide as a negative arming control. At 4, 25, and 50 h post-injection of peptide, ~50 μL blood was collected via tail prick into K2 EDTA tubes (Greiner) and stored on ice before

flow cytometry assessment of T-cell arming. For evaluating the influence of different routes of bifunctional peptide administration on DB5 CAR T-cell arming, mice were administered 10 nmol bifunctional peptide 16 days (retro-orbital versus subcutaneous) and 21 days (tail vein versus intraperitoneal) after the initial T-cell injection. Blood was similarly collected 24 h after peptide injections to measure T-cell arming.

To evaluate arming of circulating T cells with bifunctional peptide, 40 µL collected blood was mixed with 450 µL ACK Lysing Buffer (Gibco) for 30 min at room temperature to lyse red blood cells. Pelleted white blood cells were treated a second time with 450 µL ACK Lysing Buffer for 10 min at room temperature to remove residual red blood cells and then washed with 500 µL DPBS 0.5% BSA. The cells were then stained with FITC anti-human CD3 antibody (BioLegend, 1:100), PE anti-human CD45 antibody (BioLegend, 1:200), and streptavidin Alexa Fluor 647 (BioLegend, 1:500) in 100 µL DPBS 0.5% BSA for 20 min at room temperature. After staining, cells were volumed up with 400 µL DPBS 0.5% BSA to dilute out the staining cocktail and washed once with 500 µL DPBS 0.5% BSA. The stained cells were lastly fixed in 300 µL DPBS 0.5% PFA before running on the flow cytometer to determine the MFI of streptavidin Alexa Fluor 647 staining (i.e., peptide arming) on $CD3^{+}CD45^{+}$ T cells. Depending on the dataset, the background of an unstained or mock control was subtracted from the MFI values. GraphPad Prism 6 software was used to generate dose-response and exponential decay curves and perform the appropriate statistical analyses.

6.4.13 Aptamer-chimera synthesis, purification, and characterization

DBCO-modified DNA aptamer was synthesized by Integrated DNA technologies. For preparation of the aptamer-peptide chimera, 20 µM DBCO-modified aptamer was reacted with 200 µM azide-

SpyTag003(D2)-biotin in DPBS with calcium and magnesium for 24 h at 37 °C on a thermal shaker. After aptamer-peptide conjugation, the reaction mixture was lyophilized and resuspended in 0.3 M sodium acetate pH 7.0 for purification of the aptamer-peptide chimera by ethanol precipitation. As unconjugated peptide is soluble in ethanol, ethanol only precipitates unconjugated aptamer and the aptamer-peptide chimera, removing excess peptide. Precipitated aptamer-peptide chimera was resuspended in a wash buffer designed for aptamer folding, which is comprised of DPBS with calcium and magnesium further supplemented with 5 mM MgCl2 (Fisher) and 25 mM D-glucose (Sigma-Aldrich). The concentration of the resuspended aptamer-peptide chimera was determined by both a NanoDrop UV-Vis spectrophotometer (Thermo Fisher) and a QuantTag Biotin Quantification Kit.

To characterize the conjugation efficiency of the peptide to the aptamer, 500 ng 50 bp DNA ladder (Thermo Scientific), 100 ng free aptamer, and 100 ng aptamer-peptide chimera were denatured in 1X loading dye (NEB) containing ~4 M urea (Fisher) for 3 min at 70 °C and separated on a Novex 15% TBE-urea gel (Invitrogen) by urea-PAGE. The gel was stained with SYBR Gold (1:10000, Invitrogen) in TBE buffer (Thermo Scientific) for 30 min at room temperature and imaged on a Xenogen IVIS Spectrum (PerkinElmer) with 500 nm excitation and 540 nm emission. Conjugation yield of the aptamer-peptide chimera was measured semi-quantitatively by measuring the reduction in free aptamer band intensity with Fiji/ImageJ.[82]

Aptamer-peptide chimera folding and binding to Jurkat and K562 cells was performed as previously described.[83] Loading of the aptamer-peptide chimera onto $CD8^+$ DB5 CAR T cells was carried out as mentioned earlier for the bifunctional peptide.

6.5 AUTHOR CONTRIBUTIONS

D.LS. conceived the idea. D.L.S., S.H.P., and M.C.J. provided experimental advice and funding support. I.I.C., D.L.S., M.C.J., and S.H.P. designed the project. I.I.C. and D.L.S. conceived, performed, and interpreted the experiments. I.I.C. and D.L.S. cloned plasmids and prepared lentivirus. D.L.S. and I.I.C. designed and synthesized peptides. I.I.C. and D.R.S manufactured CAR T cells. I.I.C. conducted the rest of the experiments. I.I.C. prepared the figures and wrote the chapter with input from D.L.S., S.H.P., and M.C.J.

6.6. ACKNOWLEDGEMENTS

This research was supported by NIH R01AG063845 and NIH R01NS118247. We are grateful to all Pun and Jensen Lab members for experimental support and helpful advice. I.I.C. was supported by a National Science Foundation Graduate Research Fellowship under Grant No. DGE-1762114 and by the National Cancer Institute of the National Institutes of Health under Award No. 5T32CA080416-19 during different stages of the research reported here.

6.7 REFERENCES

(1) Maude, S. L.; Laetsch, T. W.; Buechner, J.; Rives, S.; Boyer, M.; Bittencourt, H.; Bader, P.; Verneris, M. R.; Stefanski, H. E.; Myers, G. D.; Qayed, M.; De Moerloose, B.; Hiramatsu, H.; Schlis, K.; Davis, K. L.; Martin, P. L.; Nemecek, E. R.; Yanik, G. A.; Peters, C.; Baruchel, A.; Boissel, N.; Mechinaud, F.; Balduzzi, A.; Krueger, J.; June, C. H.; Levine, B. L.; Wood, P.; Taran, T.; Leung, M.; Mueller, K. T.; Zhang, Y.; Sen, K.; Lebwohl, D.; Pulsipher, M. A.; Grupp, S. A. Tisagenlecleucel in Children and Young Adults with B-Cell Lymphoblastic Leukemia. *New England Journal of Medicine* **2018**, *378* (5), 439–448.

(2) Schuster, S. J.; Bishop, M. R.; Tam, C. S.; Waller, E. K.; Borchmann, P.; McGuirk, J. P.; Jäger, U.; Jaglowski, S.; Andreadis, C.; Westin, J. R.; Fleury, I.; Bachanova, V.; Foley, S. R.; Ho, P. J.; Mielke, S.; Magenau, J. M.; Holte, H.; Pantano, S.; Pacaud, L. B.; Awasthi, R.; Chu, J.; Anak, Ö.; Salles, G.; Maziarz, R. T. Tisagenlecleucel in Adult Relapsed or Refractory Diffuse Large B-Cell Lymphoma. *New England Journal of Medicine* **2018**, *380* (1), 45–56.

(3) Neelapu, S. S.; Locke, F. L.; Bartlett, N. L.; Lekakis, L. J.; Miklos, D. B.; Jacobson, C. A.; Braunschweig, I.; Oluwole, O. O.; Siddiqi, T.; Lin, Y.; Timmerman, J. M.; Stiff, P. J.; Friedberg, J. W.; Flinn, I. W.; Goy, A.; Hill, B. T.; Smith, M. R.; Deol, A.; Farooq, U.;

McSweeney, P.; Munoz, J.; Avivi, I.; Castro, J. E.; Westin, J. R.; Chavez, J. C.; Ghobadi, A.; Komanduri, K. V; Levy, R.; Jacobsen, E. D.; Witzig, T. E.; Reagan, P.; Bot, A.; Rossi, J.; Navale, L.; Jiang, Y.; Aycock, J.; Elias, M.; Chang, D.; Wiezorek, J.; Go, W. Y. Axicabtagene Ciloleucel CAR T-Cell Therapy in Refractory Large B-Cell Lymphoma. *New England Journal of Medicine* **2017**, *377* (26), 2531–2544.

(4) Locke, F. L.; Ghobadi, A.; Jacobson, C. A.; Miklos, D. B.; Lekakis, L. J.; Oluwole, O. O.; Lin, Y.; Braunschweig, I.; Hill, B. T.; Timmerman, J. M.; Deol, A.; Reagan, P. M.; Stiff, P.; Flinn, I. W.; Farooq, U.; Goy, A.; McSweeney, P. A.; Munoz, J.; Siddiqi, T.; Chavez, J. C.; Herrera, A. F.; Bartlett, N. L.; Wiezorek, J. S.; Navale, L.; Xue, A.; Jiang, Y.; Bot, A.; Rossi, J. M.; Kim, J. J.; Go, W. Y.; Neelapu, S. S. Long-Term Safety and Activity of Axicabtagene Ciloleucel in Refractory Large B-Cell Lymphoma (ZUMA-1): A Single-Arm, Multicentre, Phase 1-2 Trial. *The Lancet Oncology* **2019**, *20* (1), 31–42.

(5) Wang, M.; Munoz, J.; Goy, A.; Locke, F. L.; Jacobson, C. A.; Hill, B. T.; Timmerman, J. M.; Holmes, H.; Jaglowski, S.; Flinn, I. W.; McSweeney, P. A.; Miklos, D. B.; Pagel, J. M.; Kersten, M.-J.; Milpied, N.; Fung, H.; Topp, M. S.; Houot, R.; Beitinjaneh, A.; Peng, W.; Zheng, L.; Rossi, J. M.; Jain, R. K.; Rao, A. V; Reagan, P. M. KTE-X19 CAR T-Cell Therapy in Relapsed or Refractory Mantle-Cell Lymphoma. *New England Journal of Medicine* **2020**, *382* (14), 1331–1342.

(6) Abramson, J. S.; Palomba, M. L.; Gordon, L. I.; Lunning, M. A.; Wang, M.; Arnason, J.; Mehta, A.; Purev, E.; Maloney, D. G.; Andreadis, C.; Sehgal, A.; Solomon, S. R.; Ghosh, N.; Albertson, T. M.; Garcia, J.; Kostic, A.; Mallaney, M.; Ogasawara, K.; Newhall, K.; Kim, Y.; Li, D.; Siddiqi, T. Lisocabtagene Maraleucel for Patients with Relapsed or Refractory Large B-Cell Lymphomas (TRANSCEND NHL 001): A Multicentre Seamless Design Study. *The Lancet* **2020**, *396* (10254), 839–852.

(7) Munshi, N. C.; Anderson, L. D.; Shah, N.; Madduri, D.; Berdeja, J.; Lonial, S.; Raje, N.; Lin, Y.; Siegel, D.; Oriol, A.; Moreau, P.; Yakoub-Agha, I.; Delforge, M.; Cavo, M.; Einsele, H.; Goldschmidt, H.; Weisel, K.; Rambaldi, A.; Reece, D.; Petrocca, F.; Massaro, M.; Connarn, J. N.; Kaiser, S.; Patel, P.; Huang, L.; Campbell, T. B.; Hege, K.; San-Miguel, J. Idecabtagene Vicleucel in Relapsed and Refractory Multiple Myeloma. *New England Journal of Medicine* **2021**, *384* (8), 705–716.

(8) Berdeja, J. G.; Madduri, D.; Usmani, S. Z.; Jakubowiak, A.; Agha, M.; Cohen, A. D.; Stewart, A. K.; Hari, P.; Htut, M.; Lesokhin, A.; Deol, A.; Munshi, N. C.; O'Donnell, E.; Avigan, D.; Singh, I.; Zudaire, E.; Yeh, T.-M.; Allred, A. J.; Olyslager, Y.; Banerjee, A.; Jackson, C. C.; Goldberg, J. D.; Schecter, J. M.; Deraedt, W.; Zhuang, S. H.; Infante, J.; Geng, D.; Wu, X.; Carrasco-Alfonso, M. J.; Akram, M.; Hossain, F.; Rizvi, S.; Fan, F.; Lin, Y.; Martin, T.; Jagannath, S. Ciltacabtagene Autoleucel, a B-Cell Maturation Antigen-Directed Chimeric Antigen Receptor T-Cell Therapy in Patients with Relapsed or Refractory Multiple Myeloma (CARTITUDE-1): A Phase 1b/2 Open-Label Study. *The Lancet* **2021**, *398* (10297), 314–324.

(9) Vitale, C.; Strati, P. CAR T-Cell Therapy for B-Cell Non-Hodgkin Lymphoma and Chronic Lymphocytic Leukemia: Clinical Trials and Real-World Experiences. *Frontiers in Oncology* **2020**, *10*, 849.

(10) Martinez, M.; Moon, E. K. CAR T Cells for Solid Tumors: New Strategies for Finding, Infiltrating, and Surviving in the Tumor Microenvironment. *Frontiers in Immunology* **2019**, *10*, 128.

(11) Bagley, S. J.; O'Rourke, D. M. Clinical Investigation of CAR T Cells for Solid Tumors: Lessons Learned and Future Directions. *Pharmacology & Therapeutics* **2020**, *205*, 107419.
(12) Xu, X.; Sun, Q.; Liang, X.; Chen, Z.; Zhang, X.; Zhou, X.; Li, M.; Tu, H.; Liu, Y.; Tu, S.; Li, Y. Mechanisms of Relapse After CD19 CAR T-Cell Therapy for Acute Lymphoblastic Leukemia and Its Prevention and Treatment Strategies. *Frontiers in Immunology* **2019**, *10*, 2664.
(13) Gardner, R. A.; Finney, O.; Annesley, C.; Brakke, H.; Summers, C.; Leger, K.; Bleakley, M.; Brown, C.; Mgebroff, S.; Kelly-Spratt, K. S.; Hoglund, V.; Lindgren, C.; Oron, A. P.; Li, D.; Riddell, S. R.; Park, J. R.; Jensen, M. C. Intent-to-Treat Leukemia Remission by CD19 CAR T Cells of Defined Formulation and Dose in Children and Young Adults. *Blood* **2017**, *129* (25), 3322–3331.
(14) Sotillo, E.; Barrett, D. M.; Black, K. L.; Bagashev, A.; Oldridge, D.; Wu, G.; Sussman, R.; Lanauze, C.; Ruella, M.; Gazzara, M. R.; Martinez, N. M.; Harrington, C. T.; Chung, E. Y.; Perazzelli, J.; Hofmann, T. J.; Maude, S. L.; Raman, P.; Barrera, A.; Gill, S.; Lacey, S. F.; Melenhorst, J. J.; Allman, D.; Jacoby, E.; Fry, T.; Mackall, C.; Barash, Y.; Lynch, K. W.; Maris, J. M.; Grupp, S. A.; Thomas-Tikhonenko, A. Convergence of Acquired Mutations and Alternative Splicing of CD19 Enables Resistance to CART-19 Immunotherapy. *Cancer Discovery* **2015**, *5* (12), 1282–1295.
(15) Orlando, E. J.; Han, X.; Tribouley, C.; Wood, P. A.; Leary, R. J.; Riester, M.; Levine, J. E.; Qayed, M.; Grupp, S. A.; Boyer, M.; De Moerloose, B.; Nemecek, E. R.; Bittencourt, H.; Hiramatsu, H.; Buechner, J.; Davies, S. M.; Verneris, M. R.; Nguyen, K.; Brogdon, J. L.; Bitter, H.; Morrissey, M.; Pierog, P.; Pantano, S.; Engelman, J. A.; Winckler, W. Genetic Mechanisms of Target Antigen Loss in CAR19 Therapy of Acute Lymphoblastic Leukemia. *Nature Medicine* **2018**, *24* (10), 1504–1506.
(16) Gardner, R.; Wu, D.; Cherian, S.; Fang, M.; Hanafi, L.-A.; Finney, O.; Smithers, H.; Jensen, M. C.; Riddell, S. R.; Maloney, D. G.; Turtle, C. J. Acquisition of a CD19-Negative Myeloid Phenotype Allows Immune Escape of MLL-Rearranged B-ALL from CD19 CAR-T-Cell Therapy. *Blood* **2016**, *127* (20), 2406–2410.
(17) Fischer, J.; Paret, C.; El Malki, K.; Alt, F.; Wingerter, A.; Neu, M. A.; Kron, B.; Russo, A.; Lehmann, N.; Roth, L.; Fehr, E.-M.; Attig, S.; Hohberger, A.; Kindler, T.; Faber, J. CD19 Isoforms Enabling Resistance to CART-19 Immunotherapy Are Expressed in B-ALL Patients at Initial Diagnosis. *Journal of Immunotherapy* **2017**, *40* (5), 187–195.
(18) Santomasso, B.; Bachier, C.; Westin, J.; Rezvani, K.; Shpall, E. J. The Other Side of CAR T-Cell Therapy: Cytokine Release Syndrome, Neurologic Toxicity, and Financial Burden. *American Society of Clinical Oncology Educational Book* **2019**, No. 39, 433–444.
(19) Gust, J.; Taraseviciute, A.; Turtle, C. J. Neurotoxicity Associated with CD19-Targeted CAR-T Cell Therapies. *CNS Drugs* **2018**, *32* (12), 1091–1101.
(20) Teachey, D. T.; Lacey, S. F.; Shaw, P. A.; Melenhorst, J. J.; Maude, S. L.; Frey, N.; Pequignot, E.; Gonzalez, V. E.; Chen, F.; Finklestein, J.; Barrett, D. M.; Weiss, S. L.; Fitzgerald, J. C.; Berg, R. A.; Aplenc, R.; Callahan, C.; Rheingold, S. R.; Zheng, Z.; Rose-John, S.; White, J. C.; Nazimuddin, F.; Wertheim, G.; Levine, B. L.; June, C. H.; Porter, D. L.; Grupp, S. A. Identification of Predictive Biomarkers for Cytokine Release Syndrome after Chimeric Antigen Receptor T-Cell Therapy for Acute Lymphoblastic Leukemia. *Cancer Discovery* **2016**, *6* (6), 664–679.
(21) Santomasso, B. D.; Park, J. H.; Salloum, D.; Riviere, I.; Flynn, J.; Mead, E.; Halton, E.; Wang, X.; Senechal, B.; Purdon, T.; Cross, J. R.; Liu, H.; Vachha, B.; Chen, X.; DeAngelis,

L. M.; Li, D.; Bernal, Y.; Gonen, M.; Wendel, H.-G.; Sadelain, M.; Brentjens, R. J. Clinical and Biological Correlates of Neurotoxicity Associated with CAR T-Cell Therapy in Patients with B-Cell Acute Lymphoblastic Leukemia. *Cancer Discovery* **2018**, *8* (8), 958–971.

(22) Gardner, R.; Leger, K. J.; Annesley, C. E.; Summers, C.; Rivers, J.; Gust, J.; Tarlock, K.; Cooper, T. M.; Pinto, N. R.; Finney, O.; Smithers, H.; Oron, A.; Li, D.; Park, J. R.; Jensen, M. C. Decreased Rates of Severe CRS Seen with Early Intervention Strategies for CD19 CAR-T Cell Toxicity Management. *Blood* **2016**, *128* (22), 586.

(23) Minutolo, N. G.; Hollander, E. E.; Powell Jr, D. J. The Emergence of Universal Immune Receptor T Cell Therapy for Cancer. *Frontiers in Oncology* **2019**, *9*, 176.

(24) Liu, D.; Zhao, J.; Song, Y. Engineering Switchable and Programmable Universal CARs for CAR T Therapy. *Journal of Hematology & Oncology* **2019**, *12* (1), 69.

(25) Urbanska, K.; Lanitis, E.; Poussin, M.; Lynn, R. C.; Gavin, B. P.; Kelderman, S.; Yu, J.; Scholler, N.; Powell, D. J. A Universal Strategy for Adoptive Immunotherapy of Cancer through Use of a Novel T-Cell Antigen Receptor. *Cancer Research* **2012**, *72* (7), 1844–1852.

(26) Lohmueller, J. J.; Ham, J. D.; Kvorjak, M.; Finn, O. J. MSA2 Affinity-Enhanced Biotin-Binding CAR T Cells for Universal Tumor Targeting. *Oncoimmunology* **2018**, *7* (1), e1368604.

(27) Cho, J. H.; Collins, J. J.; Wong, W. W. Universal Chimeric Antigen Receptors for Multiplexed and Logical Control of T Cell Responses. *Cell* **2018**, *173* (6), 1426–1438.

(28) Ma, J. S. Y.; Kim, J. Y.; Kazane, S. A.; Choi, S.-H.; Yun, H. Y.; Kim, M. S.; Rodgers, D. T.; Pugh, H. M.; Singer, O.; Sun, S. B.; Fonslow, B. R.; Kochenderfer, J. N.; Wright, T. M.; Schultz, P. G.; Young, T. S.; Kim, C. H.; Cao, Y. Versatile Strategy for Controlling the Specificity and Activity of Engineered T Cells. *Proceedings of the National Academy of Sciences* **2016**, *113* (4), E450–E458.

(29) Lee, Y. G.; Marks, I.; Srinivasarao, M.; Kanduluru, A. K.; Mahalingam, S. M.; Liu, X.; Chu, H.; Low, P. S. Use of a Single CAR T Cell and Several Bispecific Adapters Facilitates Eradication of Multiple Antigenically Different Solid Tumors. *Cancer Research* **2019**, *79* (2), 387–396.

(30) Lu, Y. J.; Chu, H.; Wheeler, L. W.; Nelson, M.; Westrick, E.; Matthaei, J. F.; Cardle, I. I.; Johnson, A.; Gustafson, J.; Parker, N.; Vetzel, M.; Xu, L.-C.; Wang, E. Z.; Jensen, M. C.; Klein, P. J.; Low, P. S.; Leamon, C. P. Preclinical Evaluation of Bispecific Adaptor Molecule Controlled Folate Receptor CAR-T Cell Therapy With Special Focus on Pediatric Malignancies. *Frontiers in Oncology* **2019**, *9*, 151.

(31) Rodgers, D. T.; Mazagova, M.; Hampton, E. N.; Cao, Y.; Ramadoss, N. S.; Hardy, I. R.; Schulman, A.; Du, J.; Wang, F.; Singer, O.; Ma, J.; Nunez, V.; Shen, J.; Woods, A. K.; Wright, T. M.; Schultz, P. G.; Kim, C. H.; Young, T. S. Switch-Mediated Activation and Retargeting of CAR-T Cells for B-Cell Malignancies. *Proceedings of the National Academy of Sciences* **2016**, *113* (4), E459–E468.

(32) Cartellieri, M.; Feldmann, A.; Koristka, S.; Arndt, C.; Loff, S.; Ehninger, A.; von Bonin, M.; Bejestani, E. P.; Ehninger, G.; Bachmann, M. P. Switching CAR T Cells on and off: A Novel Modular Platform for Retargeting of T Cells to AML Blasts. *Blood Cancer Journal* **2016**, *6* (8), e458.

(33) Zakeri, B.; Fierer, J. O.; Celik, E.; Chittock, E. C.; Schwarz-Linek, U.; Moy, V. T.; Howarth, M. Peptide Tag Forming a Rapid Covalent Bond to a Protein, through Engineering a

Bacterial Adhesin. *Proceedings of the National Academy of Sciences* **2012**, *109* (12), E690–E697.
(34) Sun, F.; Zhang, W.-B.; Mahdavi, A.; Arnold, F. H.; Tirrell, D. A. Synthesis of Bioactive Protein Hydrogels by Genetically Encoded SpyTag-SpyCatcher Chemistry. *Proceedings of the National Academy of Sciences* **2014**, *111* (31), 11269–11274.
(35) Reddington, S. C.; Howarth, M. Secrets of a Covalent Interaction for Biomaterials and Biotechnology: SpyTag and SpyCatcher. *Current Opinion in Chemical Biology* **2015**, *29*, 94–99.
(36) Brune, K. D.; Leneghan, D. B.; Brian, I. J.; Ishizuka, A. S.; Bachmann, M. F.; Draper, S. J.; Biswas, S.; Howarth, M. Plug-and-Display: Decoration of Virus-Like Particles via Isopeptide Bonds for Modular Immunization. *Scientific Reports* **2016**, *6* (1), 19234.
(37) Liu, X.; Wen, J.; Yi, H.; Hou, X.; Yin, Y.; Ye, G.; Wu, X.; Jiang, X. Split Chimeric Antigen Receptor-Modified T Cells Targeting Glypican-3 Suppress Hepatocellular Carcinoma Growth with Reduced Cytokine Release. *Therapeutic Advances in Medical Oncology* **2020**, *12*, 1–12.
(38) Minutolo, N. G.; Sharma, P.; Poussin, M.; Shaw, L. C.; Brown, D. P.; Hollander, E. E.; Smole, A.; Rodriguez-Garcia, A.; Hui, J. Z.; Zappala, F.; Tsourkas, A.; Powell, D. J. Quantitative Control of Gene-Engineered T-Cell Activity through the Covalent Attachment of Targeting Ligands to a Universal Immune Receptor. *Journal of the American Chemical Society* **2020**, *142* (14), 6554–6568.
(39) Hudecek, M.; Lupo-Stanghellini, M.-T.; Kosasih, P. L.; Sommermeyer, D.; Jensen, M. C.; Rader, C.; Riddell, S. R. Receptor Affinity and Extracellular Domain Modifications Affect Tumor Recognition by ROR1-Specific Chimeric Antigen Receptor T Cells. *Clinical Cancer Research* **2013**, *19* (12), 3153–3164.
(40) Ghorashian, S.; Kramer, A. M.; Onuoha, S.; Wright, G.; Bartram, J.; Richardson, R.; Albon, S. J.; Casanovas-Company, J.; Castro, F.; Popova, B.; Villanueva, K.; Yeung, J.; Vetharoy, W.; Guvenel, A.; Wawrzyniecka, P. A.; Mekkaoui, L.; Cheung, G. W.-K.; Pinner, D.; Chu, J.; Lucchini, G.; Silva, J.; Ciocarlie, O.; Lazareva, A.; Inglott, S.; Gilmour, K. C.; Ahsan, G.; Ferrari, M.; Manzoor, S.; Champion, K.; Brooks, T.; Lopes, A.; Hackshaw, A.; Farzaneh, F.; Chiesa, R.; Rao, K.; Bonney, D.; Samarasinghe, S.; Goulden, N.; Vora, A.; Veys, P.; Hough, R.; Wynn, R.; Pule, M. A.; Amrolia, P. J. Enhanced CAR T Cell Expansion and Prolonged Persistence in Pediatric Patients with ALL Treated with a Low-Affinity CD19 CAR. *Nature Medicine* **2019**, *25* (9), 1408–1414.
(41) Keeble, A. H.; Banerjee, A.; Ferla, M. P.; Reddington, S. C.; Anuar, I. N. A. K.; Howarth, M. Evolving Accelerated Amidation by SpyTag/SpyCatcher to Analyze Membrane Dynamics. *Angewandte Chemie International Edition* **2017**, *56* (52), 16521–16525.
(42) Keeble, A. H.; Turkki, P.; Stokes, S.; Khairil Anuar, I. N. A.; Rahikainen, R.; Hytönen, V. P.; Howarth, M. Approaching Infinite Affinity through Engineering of Peptide–Protein Interaction. *Proceedings of the National Academy of Sciences* **2019**, *116* (52), 26523–26533.
(43) Gasteiger, E.; Hoogland, C.; Gattiker, A.; Duvaud, S.; Wilkins, M. R.; Appel, R. D.; Bairoch, A. Protein Identification and Analysis Tools on the ExPASy Server BT - The Proteomics Protocols Handbook; Walker, J. M., Ed.; Humana Press: Totowa, NJ, 2005; pp 571–607.

(44) Li, L.; Fierer, J. O.; Rapoport, T. A.; Howarth, M. Structural Analysis and Optimization of the Covalent Association between SpyCatcher and a Peptide Tag. *Journal of Molecular Biology* **2014**, *426* (2), 309–317.
(45) Marqus, S.; Pirogova, E.; Piva, T. J. Evaluation of the Use of Therapeutic Peptides for Cancer Treatment. *Journal of Biomedical Science* **2017**, *24* (1), 21.
(46) Bandyopadhyay, A.; Raghavan, S. Defining the Role of Integrin Avβ6 in Cancer. *Current Drug Targets* **2009**, *10* (7), 645–652.
(47) Liu, H.; Wu, Y.; Wang, F.; Liu, Z. Molecular Imaging of Integrin Avβ6 Expression in Living Subjects. *American Journal of Nuclear Medicine and Molecular Imaging* **2014**, *4* (4), 333–345.
(48) Goodman, S. L.; Picard, M. Integrins as Therapeutic Targets. *Trends in Pharmacological Sciences* **2012**, *33* (7), 405–412.
(49) Slack, R. J.; Hafeji, M.; Rogers, R.; Ludbrook, S. B.; Marshall, J. F.; Flint, D. J.; Pyne, S.; Denyer, J. C. Pharmacological Characterization of the Avβ6 Integrin Binding and Internalization Kinetics of the Foot-and-Mouth Disease Virus Derived Peptide A20FMDV2. *Pharmacology* **2016**, *97* (3–4), 114–125.
(50) Saha, A.; Ellison, D.; Thomas, G. J.; Vallath, S.; Mather, S. J.; Hart, I. R.; Marshall, J. F. High-Resolution in Vivo Imaging of Breast Cancer by Targeting the pro-Invasive Integrin Alphavbeta6. *The Journal of Pathology* **2010**, *222* (1), 52–63.
(51) Moore, K. M.; Desai, A.; Delgado, B. de L.; Trabulo, S. M. D.; Reader, C.; Brown, N. F.; Murray, E. R.; Brentnall, A.; Howard, P.; Masterson, L.; Zammarchi, F.; Hartley, J. A.; van Berkel, P. H.; Marshall, J. F. Integrin Avβ6-Specific Therapy for Pancreatic Cancer Developed from Foot-and-Mouth-Disease Virus. *Theranostics* **2020**, *10* (7), 2930–2942.
(52) Whilding, L. M.; Parente-Pereira, A. C.; Zabinski, T.; Davies, D. M.; Petrovic, R. M. G.; Kao, Y. V.; Saxena, S. A.; Romain, A.; Costa-Guerra, J. A.; Violette, S.; Itamochi, H.; Ghaem-Maghami, S.; Vallath, S.; Marshall, J. F.; Maher, J. Targeting of Aberrant Avβ6 Integrin Expression in Solid Tumors Using Chimeric Antigen Receptor-Engineered T Cells. *Molecular Therapy* **2017**, *25* (1), 259–273.
(53) Cardle, I. I.; Jensen, M. C.; Pun, S. H.; Sellers, D. L. Optimized Serum Stability and Specificity of an Avβ6 Integrin-Binding Peptide for Tumor Targeting. *Journal of Biological Chemistry* **2021**, *296*.
(54) Li, D.; Elbert, D. L. The Kinetics of the Removal of the N-Methyltrityl (Mtt) Group during the Synthesis of Branched Peptides. *The Journal of Peptide Research* **2002**, *60* (5), 300–303.
(55) Karle, I. L.; Banerjee, A.; Balaram, P. Design of Two-Helix Motifs in Peptides: Crystal Structure of a System of Linked Helices of Opposite Chirality and a Model Helix-Linker Peptide. *Folding & Design* **1997**, *2* (4), 203–210.
(56) Jonnalagadda, M.; Brown, C. E.; Chang, W. C.; Ostberg, J. R.; Forman, S. J.; Jensen, M. C. Efficient Selection of Genetically Modified Human T Cells Using Methotrexate-Resistant Human Dihydrofolate Reductase. *Gene Therapy* **2013**, *20* (8), 853–860.
(57) Roybal, K. T.; Rupp, L. J.; Morsut, L.; Walker, W. J.; McNally, K. A.; Park, J. S.; Lim, W. A. Precision Tumor Recognition by T Cells With Combinatorial Antigen-Sensing Circuits. *Cell* **2016**, *164* (4), 770–779.
(58) Choe, J. H.; Watchmaker, P. B.; Simic, M. S.; Gilbert, R. D.; Li, A. W.; Krasnow, N. A.; Downey, K. M.; Yu, W.; Carrera, D. A.; Celli, A.; Cho, J.; Briones, J. D.; Duecker, J. M.; Goretsky, Y. E.; Dannenfelser, R.; Cardarelli, L.; Troyanskaya, O.; Sidhu, S. S.; Roybal, K.

T.; Okada, H.; Lim, W. A. SynNotch-CAR T Cells Overcome Challenges of Specificity, Heterogeneity, and Persistence in Treating Glioblastoma. *Science Translational Medicine* **2021**, *13* (591), eabe7378.

(59) Nelson, N.; Lopez-Pelaez, M.; Palazon, A.; Poon, E.; de La Roche, M.; Barry, S.; Valge-Archer, V.; Wilkinson, R. W.; Dovedi, S. J.; Smith, P. D. A Cell-Engineered System to Assess Tumor Cell Sensitivity to CD8+ T Cell-Mediated Cytotoxicity. *OncoImmunology* **2019**, *8* (8), 1–10.

(60) Xiao, Q.; Zhang, X.; Tu, L.; Cao, J.; Hinrichs, C. S.; Su, X. Size-Dependent Activation of CAR-T Cells. *Science Immunology* **2022**, *7* (74), eabl3995.

(61) Kim, M. S.; Ma, J. S. Y.; Yun, H.; Cao, Y.; Kim, J. Y.; Chi, V.; Wang, D.; Woods, A.; Sherwood, L.; Caballero, D.; Gonzalez, J.; Schultz, P. G.; Young, T. S.; Kim, C. H. Redirection of Genetically Engineered CAR-T Cells Using Bifunctional Small Molecules. *Journal of the American Chemical Society* **2015**, *137* (8), 2832–2835.

(62) Lee, Y. G.; Chu, H.; Lu, Y.; Leamon, C. P.; Srinivasarao, M.; Putt, K. S.; Low, P. S. Regulation of CAR T Cell-Mediated Cytokine Release Syndrome-like Toxicity Using Low Molecular Weight Adapters. *Nature Communications* **2019**, *10* (1), 2681.

(63) Unverdorben, F.; Richter, F.; Hutt, M.; Seifert, O.; Malinge, P.; Fischer, N.; Kontermann, R. E. Pharmacokinetic Properties of IgG and Various Fc Fusion Proteins in Mice. *mAbs* **2016**, *8* (1), 120–128.

(64) Tummers, Q. R. J. G.; Hoogstins, C. E. S.; Gaarenstroom, K. N.; de Kroon, C. D.; van Poelgeest, M. I. E.; Vuyk, J.; Bosse, T.; Smit, V. T.; van de Velde, C. J. H.; Cohen, A. F. Intraoperative Imaging of Folate Receptor Alpha Positive Ovarian and Breast Cancer Using the Tumor Specific Agent EC17. *Oncotarget* **2016**, *7* (22), 32144–32155.

(65) Mordenti, J. Man versus Beast: Pharmacokinetic Scaling in Mammals. *Journal of Pharmaceutical Sciences* **1986**, *75* (11), 1028–1040.

(66) Blessinger, S. A.; Tran, J. Q.; Jackman, R. P.; Gilfanova, R.; Rittenhouse, J.; Gutierrez, A. G.; Heitman, J. W.; Hazegh, K.; Kanias, T.; Muench, M. O. Immunodeficient Mice Are Better for Modeling the Transfusion of Human Blood Components than Wild-Type Mice. *PLOS ONE* **2020**, *15* (7), e0237106.

(67) Zhou, J.; Rossi, J. Aptamers as Targeted Therapeutics: Current Potential and Challenges. *Nature Reviews Drug Discovery* **2017**, *16* (6), 440.

(68) Bouchard, P. R.; Hutabarat, R. M.; Thompson, K. M. Discovery and Development of Therapeutic Aptamers. *Annual Review of Pharmacology and Toxicology* **2010**, *50* (1), 237–257.

(69) Tan, Y.; Li, Y.; Qu, Y.-X.; Su, Y.; Peng, Y.; Zhao, Z.; Fu, T.; Wang, X.-Q.; Tan, W. Aptamer-Peptide Conjugates as Targeted Chemosensitizers for Breast Cancer Treatment. *ACS Applied Materials & Interfaces* **2021**, *13* (8), 9436–9444.

(70) Yoon, H. Y.; Lee, D.; Lim, D.-K.; Koo, H.; Kim, K. Copper-Free Click Chemistry: Applications in Drug Delivery, Cell Tracking, and Tissue Engineering. *Advanced Materials* **2022**, *34* (10), 2107192.

(71) Veggiani, G.; Nakamura, T.; Brenner, M. D.; Gayet, R. v; Yan, J.; Robinson, C. v; Howarth, M. Programmable Polyproteams Built Using Twin Peptide Superglues. *Proceedings of the National Academy of Sciences* **2016**, *113* (5), 1202–1207.

(72) Keeble, A. H.; Yadav, V. K.; Ferla, M. P.; Bauer, C. C.; Chuntharpursat-Bon, E.; Huang, J.; Bon, R. S.; Howarth, M. DogCatcher Allows Loop-Friendly Protein-Protein Ligation. *Cell Chemical Biology* **2022**, *29* (2), 339-350.e10.

(73) Lanitis, E.; Poussin, M.; Klattenhoff, A. W.; Song, D.; Sandaltzopoulos, R.; June, C. H.; Powell, D. J. Chimeric Antigen Receptor T Cells with Dissociated Signaling Domains Exhibit Focused Antitumor Activity with Reduced Potential for Toxicity In Vivo. *Cancer Immunology Research* **2013**, *1* (1), 43–53.
(74) Liu, Z.; Zhou, H.; Wang, W.; Tan, W.; Fu, Y.-X.; Zhu, M. A Novel Method for Synthetic Vaccine Construction Based on Protein Assembly. *Scientific Reports* **2014**, *4* (1), 7266.
(75) Salter, A. I.; Ivey, R. G.; Kennedy, J. J.; Voillet, V.; Rajan, A.; Alderman, E. J.; Voytovich, U. J.; Lin, C.; Sommermeyer, D.; Liu, L.; Whiteaker, J. R.; Gottardo, R.; Paulovich, A. G.; Riddell, S. R. Phosphoproteomic Analysis of Chimeric Antigen Receptor Signaling Reveals Kinetic and Quantitative Differences That Affect Cell Function. *Science Signaling* **2018**, *11* (544), eaat6753.
(76) Kawalekar, O. U.; O'Connor, R. S.; Fraietta, J. A.; Guo, L.; McGettigan, S. E.; Posey, A. D.; Patel, P. R.; Guedan, S.; Scholler, J.; Keith, B.; Snyder, N. W.; Blair, I. A.; Milone, M. C.; June, C. H. Distinct Signaling of Coreceptors Regulates Specific Metabolism Pathways and Impacts Memory Development in CAR T Cells. *Immunity* **2016**, *44* (2), 380–390.
(77) Drent, E.; Poels, R.; Ruiter, R.; van de Donk, N. W. C. J.; Zweegman, S.; Yuan, H.; de Bruijn, J.; Sadelain, M.; Lokhorst, H. M.; Groen, R. W. J.; Mutis, T.; Themeli, M. Combined CD28 and 4-1BB Costimulation Potentiates Affinity-Tuned Chimeric Antigen Receptor–Engineered T Cells. *Clinical Cancer Research* **2019**, *25* (13), 4014–4025.
(78) Wang, D.; Starr, R.; Chang, W.-C.; Aguilar, B.; Alizadeh, D.; Wright, S. L.; Yang, X.; Brito, A.; Sarkissian, A.; Ostberg, J. R.; Li, L.; Shi, Y.; Gutova, M.; Aboody, K.; Badie, B.; Forman, S. J.; Barish, M. E.; Brown, C. E. Chlorotoxin-Directed CAR T Cells for Specific and Effective Targeting of Glioblastoma. *Science Translational Medicine* **2020**, *12* (533), eaaw2672.
(79) Walker, A. J.; Majzner, R. G.; Zhang, L.; Wanhainen, K.; Long, A. H.; Nguyen, S. M.; Lopomo, P.; Vigny, M.; Fry, T. J.; Orentas, R. J.; Mackall, C. L. Tumor Antigen and Receptor Densities Regulate Efficacy of a Chimeric Antigen Receptor Targeting Anaplastic Lymphoma Kinase. *Molecular Therapy* **2017**, *25* (9), 2189–2201.
(80) Coin, I.; Beyermann, M.; Bienert, M. Monitoring Solid Phase Peptide Synthesis. *Protocol Exchange* **2007**, *10*.
(81) Schneggenburger, P. E.; Worbs, B.; Diederichsen, U. Azide Reduction during Peptide Cleavage from Solid Support—the Choice of Thioscavenger? *Journal of Peptide Science* **2010**, *16* (1), 10–14.
(82) Schindelin, J.; Arganda-Carreras, I.; Frise, E.; Kaynig, V.; Longair, M.; Pietzsch, T.; Preibisch, S.; Rueden, C.; Saalfeld, S.; Schmid, B.; Tinevez, J.-Y.; White, D. J.; Hartenstein, V.; Eliceiri, K.; Tomancak, P.; Cardona, A. Fiji: An Open-Source Platform for Biological-Image Analysis. *Nature Methods* **2012**, *9* (7), 676–682.
(83) Cheng, E. L.; Cardle, I. I.; Kacherovsky, N.; Bansia, H.; Wang, T.; Zhou, Y.; Raman, J.; Yen, A.; Gutierrez, D.; Salipante, S. J.; des Georges, A.; Jensen, M. C.; Pun, S. H. Discovery of a Transferrin Receptor 1-Binding Aptamer and Its Application in Cancer Cell Depletion for Adoptive T-Cell Therapy Manufacturing. *Journal of the American Chemical Society* **2022**, *144* (30), 13851–13864.

6.8 SUPPORTING INFORMATION

Table S6.1 | Peptide sequences used in studies.

Peptide	Sequence	Weight (g/mol)
Biotin-SpyTag	biotin-AHIVMVDAYKPTKG-amide	1755.1
Biotin-SpyTag003(D2)	biotin-R_DGVPHIVMVDAYKR_DYKG-amide	2214.7
C2C18(ChARK) -X- SpyTag003(D2)	acetyl-NCVP_hNLRGDLQVLA_DQKVCR_DTK_D-amide **X** biotin-R_DGVPHIVMVDAYKR_DYKG	5017.7
SpyTag-Rhodamine	acetyl-AHIVMVDAYKPTKK(rhodamine)-amide	2054.4
C2C18(ChARK)-Cy5	acetyl- NCVP_hNLRGDLQVLA_DQKVCR_DTK_D(Cy5)-amide	3172.6
Azide-SpyTag003(D2)-Biotin	biotin-R_DGVPHIVMVDAYKR_DYKGK_D(azide)-amide	2467.9

C, DFBP-cyclized; R_D, D-arginine; P_h, hydroxyproline; A_D, D-alanine; K_D, D-lysine; **X**, hexanoic acid.

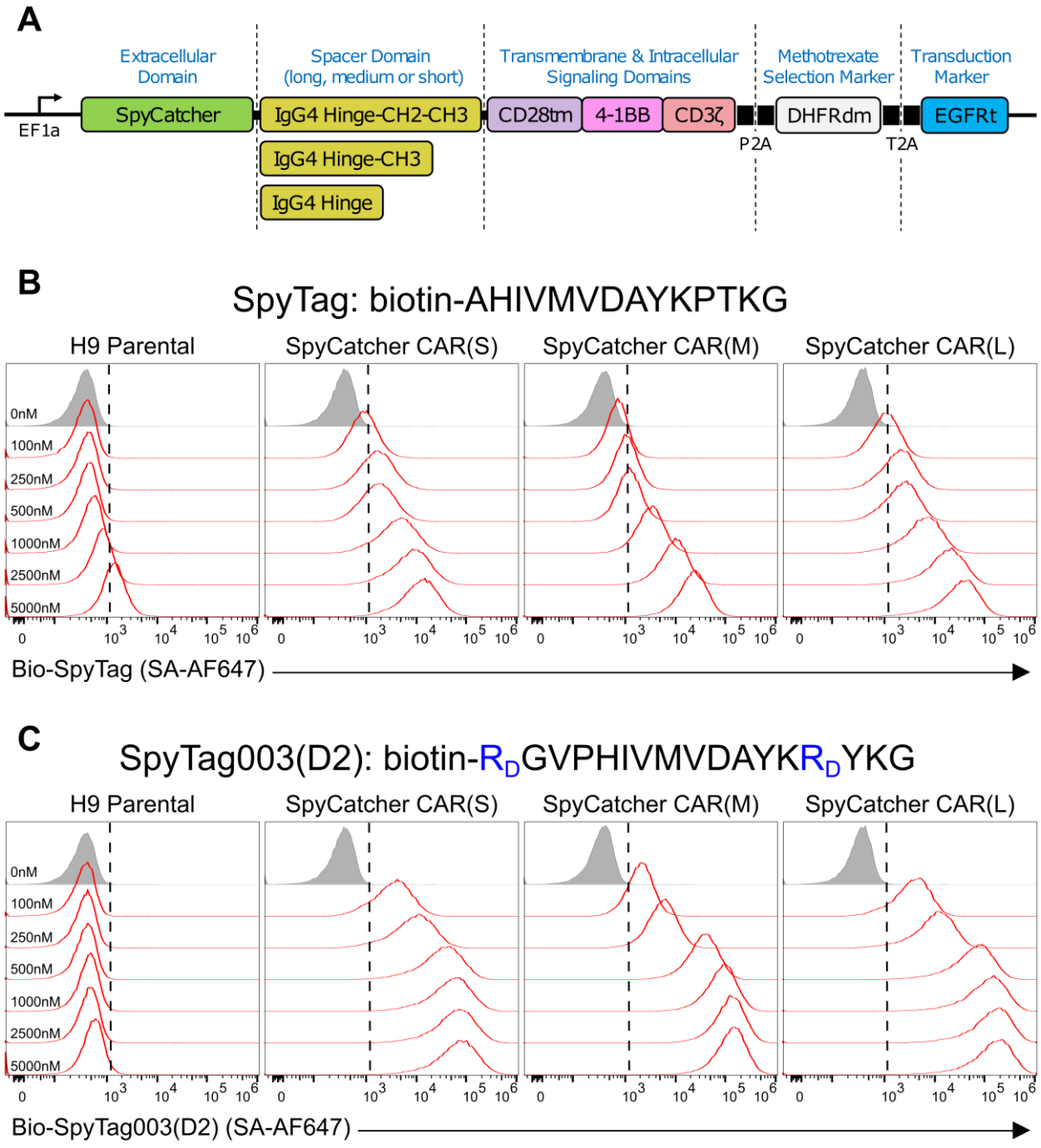

Figure S6.1 | SpyTag003(D2) exhibits enhanced loading onto the original SpyCatcher CAR than SpyTag. (A) Design of tricistronic lentiviral SpyCatcher CAR constructs with different extracellular spacer lengths. (B) Flow cytometry histograms of biotinylated SpyTag loading onto H9 SpyCatcher CAR cells. Histograms are representative of 1 biological replicate. (C) Flow cytometry histograms of biotinylated SpyTag003(D2) loading onto H9 SpyCatcher CAR cells. Histograms are representative of 1 biological replicate. D-arginine substitutions in the SpyTag003(D2) sequence are shown in blue. SA-AF647, streptavidin Alexa Fluor 547.

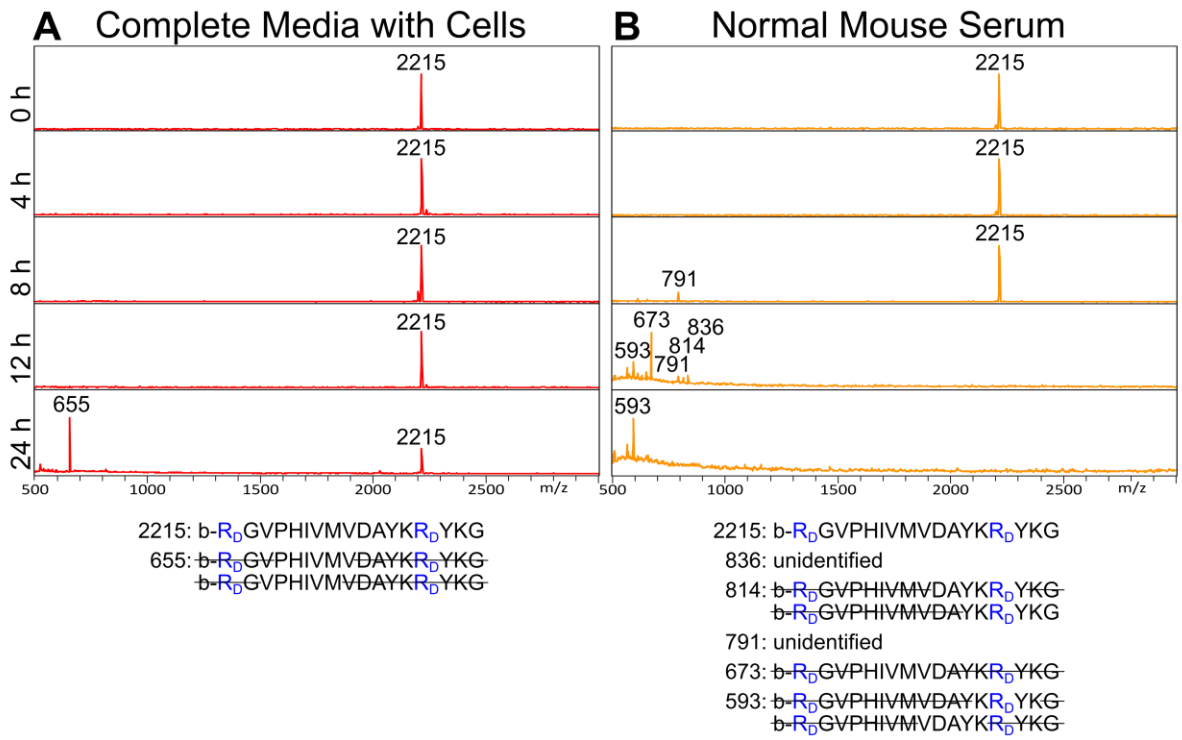

Figure S6.2 | SpyTag003(D2) displays modest proteolytic stability in serum. MALDI-ToF spectra of SpyTag003(D2) peptide incubated in (A) complete media spiked with BxPC3 cells and (B) normal mouse serum for 0, 4, 8, 12, and 24 h at 37 °C. Molecular weights of prominent peaks are shown. Bottom: predicted amino acid sequences of degradation products based on measured molecular weights.

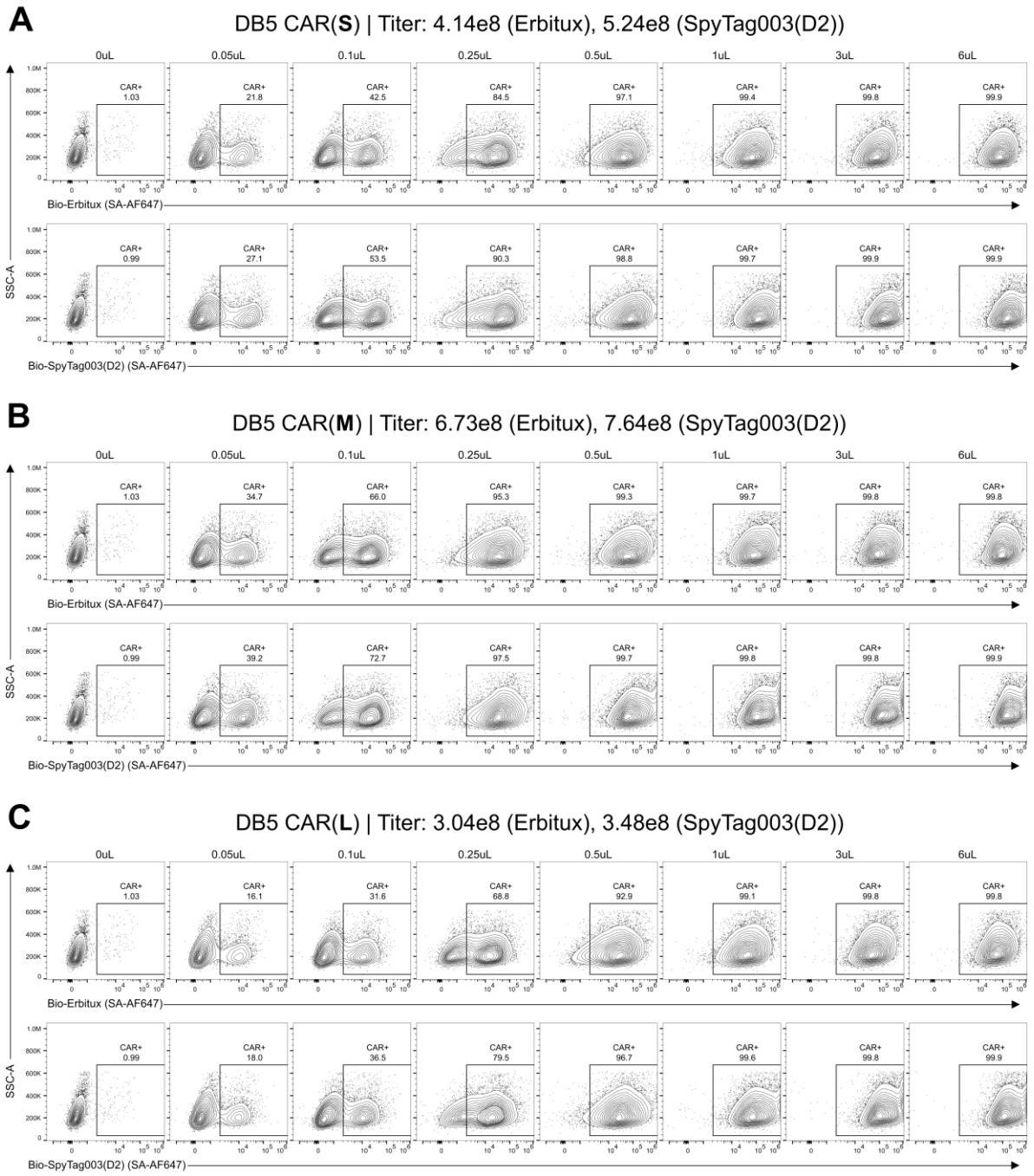

Figure S6.3 | DB5 CAR-encoding lentivirus transduces immortalized T cells with high titers. Flow cytometry plots of biotinylated Erbitux and 500 nM SpyTag003(D2) staining of H9 cells transduced with different concentrations of lentivirus encoding (A) short spacer, (B) medium spacer, and (C) long spacer DB5 CARs. Plots are representative of 1 biological replicate. Titers in TU/mL are listed for each lentivirus and were calculated using data from both the Erbitux and SpyTag003(D2) staining. SA-AF647, streptavidin Alexa Fluor 647.

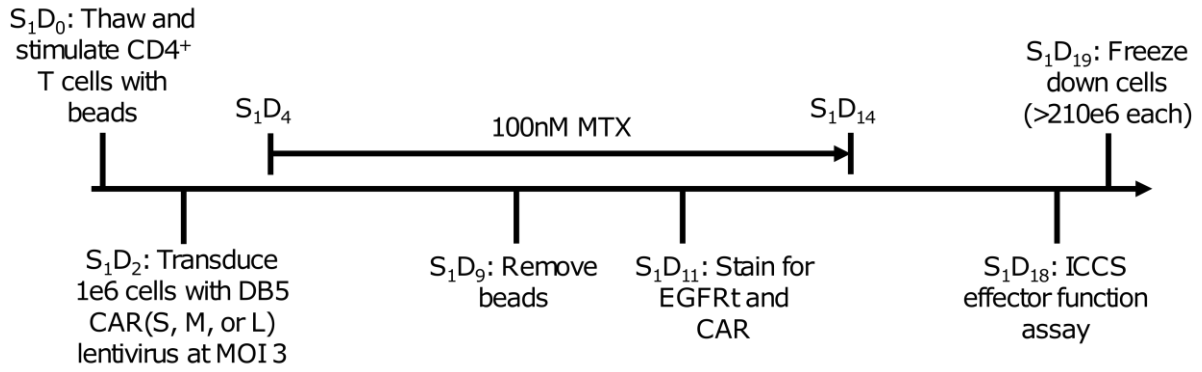

Figure S6.4 | CD4$^+$ DB5 CAR T-cell were successfully produced within a 3-week timeline. Positively-selected CD4$^+$ T cells from a healthy donor were thawed and stimulated with activator beads on Day 0 (S_1D_0). On Day 2 (S_1D_2), 1 $\times 10^6$ cells were transduced with lentivirus encoding either short, medium, or long spacer DB5 CAR. Transduced cells were then put under 100 nM methotrexate selection on Day 4 to enrich CAR$^+$ cells (S_1D_4), activator beads were removed on Day 9 (S_1D_9), and cells were stained for EGFRt transduction reporter and CAR expression on Day 11 (S_1D_{11}). Methotrexate was removed on Day 14 (S_1D_{14}) and cells were functionally characterized by an intracellular cytokine staining (ICCS) on Day 18 (S_1D_{14}). Remaining cells were frozen and banked on Day 19 (S_1D_{19}).

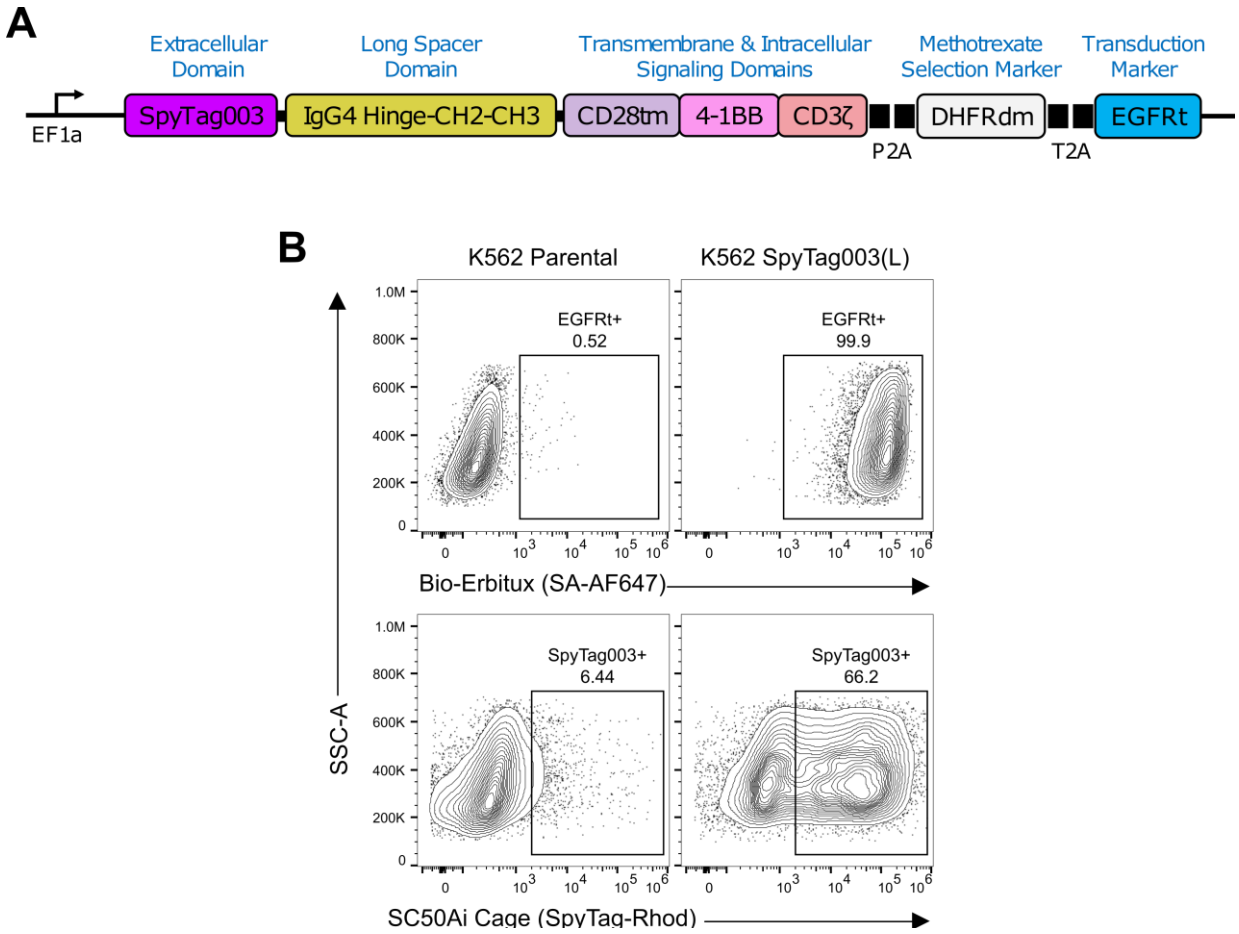

Figure S6.5 | K562 SpyTag003(L) cells express detectable SpyTag003 on their surface. (A) Design of tricistronic lentiviral SpyTag003(L) construct. (B) Flow cytometry plots of biotinylated Erbitux and 16.67 nM SpyCatcher Nanocage (SC50Ai Cage) staining of K562 cells transduced with SpyTag003(L) lentivirus. Unreacted SpyCatcher proteins on cage-labeled cells were stained with 1 μM SpyTag-rhodamine as a secondary stain. Surface expression of SpyTag003 was confirmed by cage staining. Plots are representative of 1 biological replicate. SA-AF647, streptavidin Alexa Fluor 647; SpyTag-Rhod, SpyTag-rhodamine.

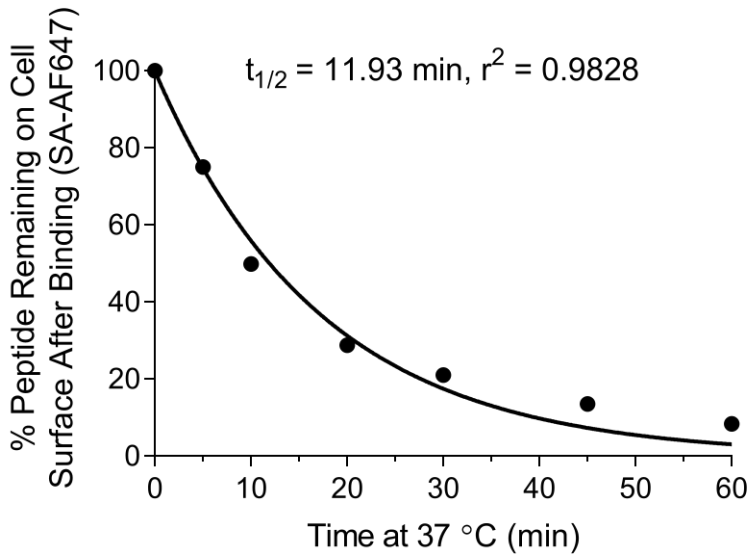

Figure S6.6 | C2C18(ChARK)-X-SpyTag003(D2) peptide is rapidly internalized by αvβ6$^+$ pancreatic BxPC3 cells. Flow cytometry detection of bound C2C18(ChARK)-X-SpyTag003(D2) peptide remaining on the surface of BxPC3 cells over a 60-min incubation at 37℃, normalized to a 0-min no incubation control. The curve represents a nonlinear regression of one independent experiment assuming one-phase exponential decay. SA-AF647, streptavidin Alexa Fluor 647.

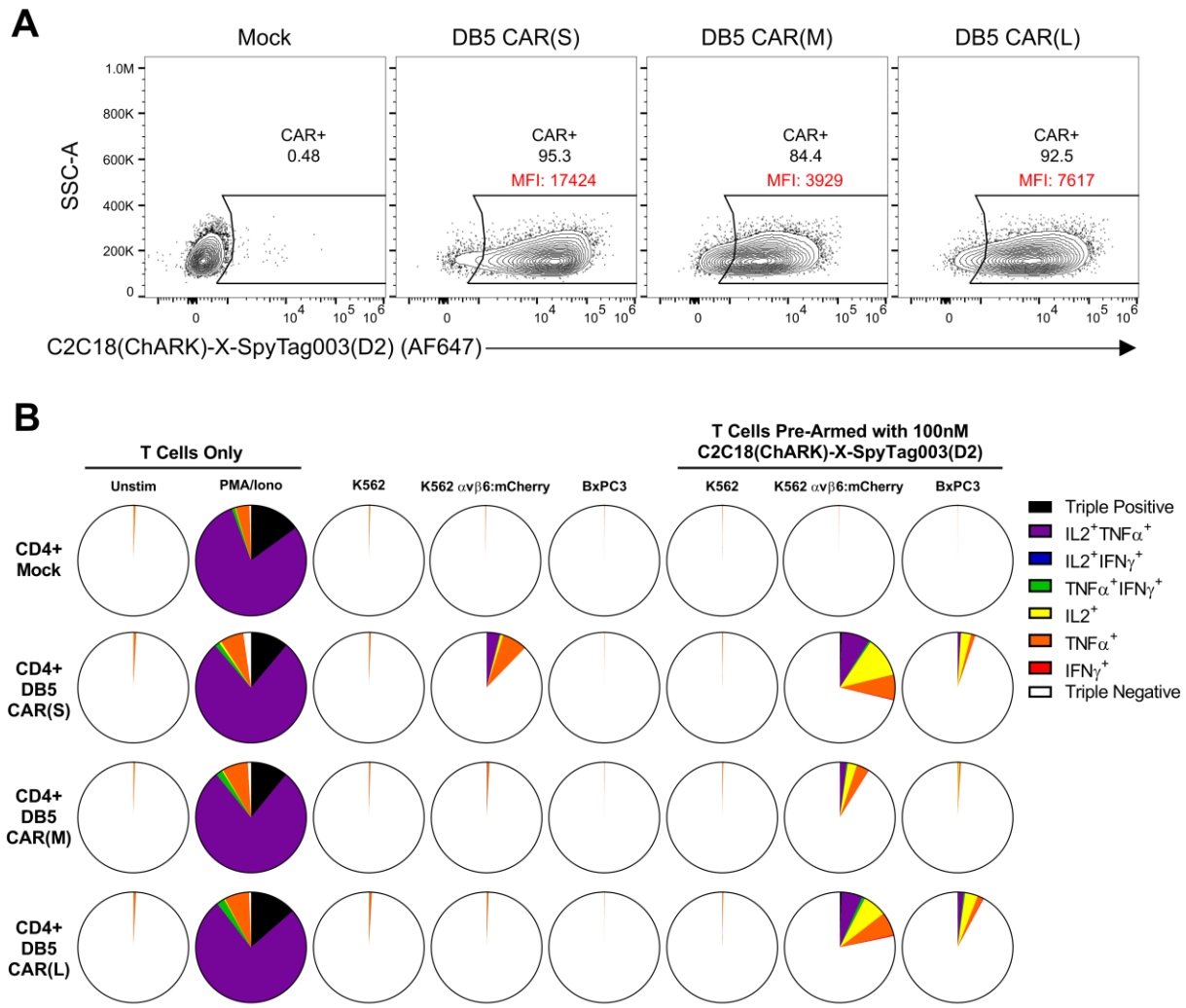

Figure S6.7 | 100nM bifunctional peptide sufficiently directs CD4$^+$ DB5 CAR T-cell cytokine responses against αvβ6$^+$ target cells. (A) Flow cytometry plots of CD4$^+$ DB5 CAR T-cell pre-arming with 100 nM bifunctional peptide on the day of the ICCS assay. Plots are representative of 1 biological replicate. MFI values of peptide arming are shown in red. (B) ICCS pie charts of IL2, TNFα, and IFNγ cytokine production in CD4$^+$ DB5 CAR T cells after 5-h co-culture with target cells. Bifunctional peptide was pre-armed on T cells for directing DB5 CAR T-cell responses against αvβ6$^+$ target cells. Pie charts are representative of 1 biological replicate.

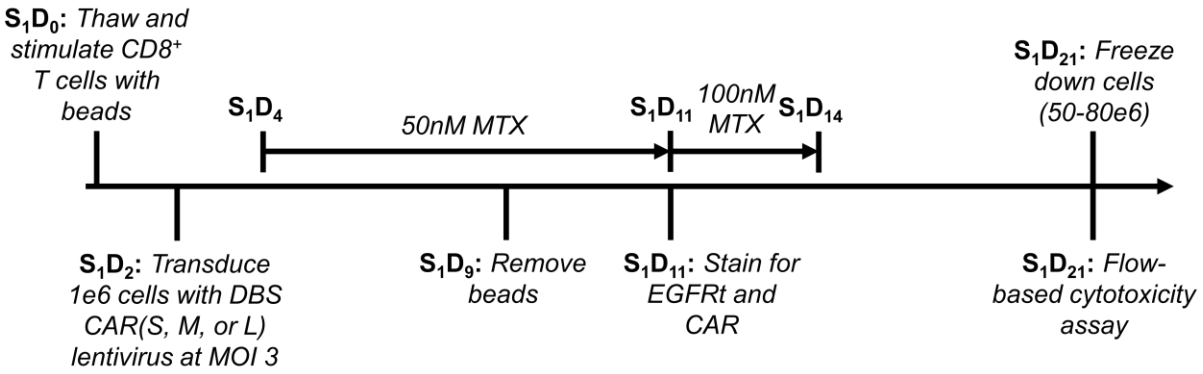

Figure S6.8 | CD8$^+$ DB5 CAR T-cell were successfully produced within a 3-week timeline. Positively-selected CD8$^+$ T cells from a healthy donor were thawed and stimulated with activator beads on Day 0 (S_1D_0). On Day 2 (S_1D_2), 1 ×10^6 cells were transduced with lentivirus encoding either short, medium, or long spacer DB5 CAR. Transduced cells were then put under 50 nM methotrexate selection on Day 4 to enrich CAR$^+$ cells (S_1D_4), activator beads were removed on Day 9 (S_1D_9), and cells were stained for EGFRt transduction reporter and CAR expression on Day 11 (S_1D_{11}). Methotrexate selection was increased to 100 nM on Day 11 (S_1D_{11}) before being removed on Day 14 (S_1D_{14}). Cells were both functionally characterized by a flow-based cytoxicity assay and frozen/baked on Day 21 (S_1D_{21}).

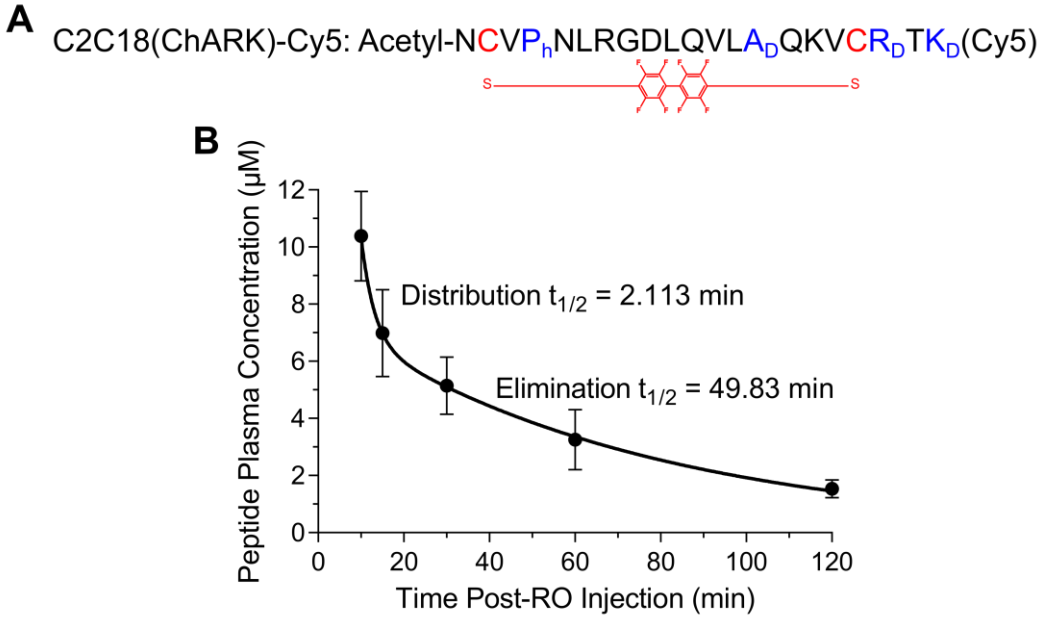

Figure S6.9 | C2C18(ChARK) displays moderately fast plasma circulation half-life in mice. (A) Peptide sequence of C2C18(ChARK)-Cy5. Cysteine substitutions for DFBP cyclization are shown in red and amino acid modifications are shown in blue. The N-terminus of the peptide is acetylated whereas Cy5 was selectively conjugated to the C-terminal D-lysine via its side-chain amino group. (B) Plasma half-life of C2C18(ChARK)-Cy5 in NOD scid mice following a 10 nmol retro-orbital (RO) injection. The curve represents a nonlinear regression assuming two-phase exponential decay. Data points and error bars represent the mean ± SD; *n* = 2-4 mice. Cy5, cyanine 5.

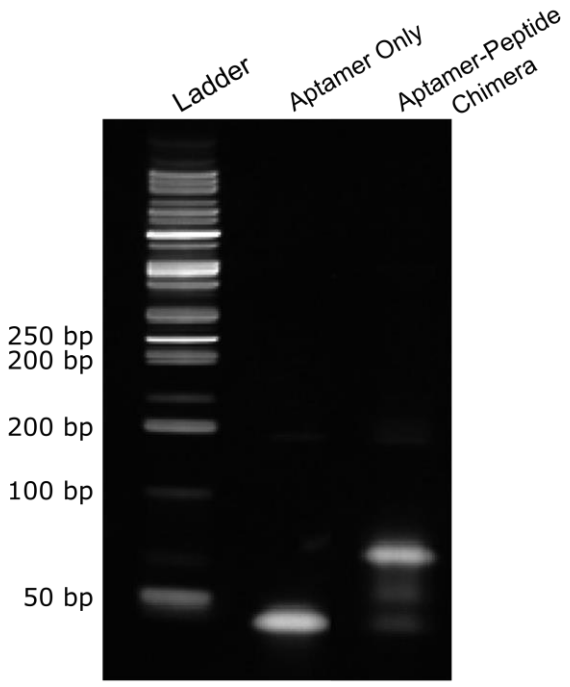

Figure S6.10 | Urea-PAGE confirms successful synthesis of aptamer-peptide chimera. SYBR Gold-stained 15% urea-PAGE gel of aptamer alone and aptamer-peptide chimera. The upward shift in the aptamer band size signifies successful conjugation of peptide onto the aptamer via copper-free click chemistry.

```
SpyCatcherΔN        ----------------------DSATHIKFSKRDEDGKELAGATMELRDSSGKTISTWISD 39
SpyCatcher003       VTTLSGLSGEQGPSGDMTTEEDSATHIKFSKRDEDGRELAGATMELRDSSGKTISTWISD 60
                                          ***************:**********************

SpyCatcherΔN        GQVKDFYLYPGKYTFVETAAPDGYEVATAITFTVNEQGQVTVNGKATKGDAHI         92
SpyCatcher003       GHVKDFYLYPGKYTFVETAAPDGYEVATPIEFTVNEDGQVTVDGEATEGDAHT        113
                    *:************************* * *****:*****:*:**:****
```

Figure S6.11 | An N-terminal truncated SpyCatcher003 would retain all the mutations made to SpyCatcher002 for increased reaction kinetics. Protein sequence alignment of a N-terminal truncated SpyCatcher (SpyCatcherΔN) and SpyCatcher003 using the Clustal Omega program. Red font represents mutations made from SpyCatcher to SpyCatcher002. Green font represents mutations made from SpyCatcher002 to SpyCatcher003.